



HAL
open science

Modélisation des impacts des arbres sur la qualité de l'air de l'échelle de la rue à la ville.

Alice Maison

► **To cite this version:**

Alice Maison. Modélisation des impacts des arbres sur la qualité de l'air de l'échelle de la rue à la ville.. Environnement et Société. École des Ponts ParisTech, 2023. Français. NNT : 2023ENPC0034 . tel-04604417

HAL Id: tel-04604417

<https://pastel.hal.science/tel-04604417v1>

Submitted on 7 Jun 2024

HAL is a multi-disciplinary open access archive for the deposit and dissemination of scientific research documents, whether they are published or not. The documents may come from teaching and research institutions in France or abroad, or from public or private research centers.

L'archive ouverte pluridisciplinaire **HAL**, est destinée au dépôt et à la diffusion de documents scientifiques de niveau recherche, publiés ou non, émanant des établissements d'enseignement et de recherche français ou étrangers, des laboratoires publics ou privés.

Modélisation des impacts des arbres sur la qualité de l'air de l'échelle de la rue à la ville

École doctorale N° 531, Sciences, Ingénierie et Environnement (SIE)

Sciences et Techniques de l'Environnement

Thèse préparée au CEREAA et à l'UMR 1402 ECOSYS

Thèse soutenue le 28/11/2023, par
Alice MAISON

Composition du jury:

Aude, LEMONSU Directrice de recherche, CNRM (CNRS)	<i>Présidente</i>
Jean-Christophe, CALVET Directeur de recherche, CNRM (Météo-France)	<i>Rapporteur</i>
Pierre-Emmanuel, BOURNET Professeur, Institut Agro Rennes-Angers	<i>Rapporteur</i>
Aude, LEMONSU Directrice de recherche, CNRM (CNRS)	<i>Examinatrice</i>
Olivier, SANCHEZ Ingénieur, Airparif	<i>Examineur</i>
Karine, KATA-SARTELET Directrice de recherche, CEREAA (ENPC)	<i>Directrice de thèse</i>
Andrée, TUZET Chargée de recherche, UMR 1402 ECOSYS (INRAE)	<i>Co-encadrante de thèse</i>



École des Ponts
ParisTech



THÈSE DE DOCTORAT DE L'ÉCOLE NATIONALE DES PONTS ET CHAUSSÉES

Soutenue publiquement le 28 novembre 2023 par

Alice MAISON

pour l'obtention du grade de
Docteur de l'École nationale des ponts et chaussées

Spécialité Sciences et Techniques de l'Environnement
École doctorale Sciences, Ingénierie et Environnement - SIE

Modélisation des impacts des arbres sur la qualité de l'air de l'échelle de la rue à la ville

**Modeling the impacts of trees on air quality from the street
to the city level**

Jury composé de

Pierre-Emmanuel BOURNET	Institut Agro Rennes-Angers	Rapporteur
Jean-Christophe CALVET	CNRM	Rapporteur
Aude LEMONSU	CNRM	Examinatrice
Olivier SANCHEZ	Airparif	Examinateur
Karine KATA-SARTELET	ENPC	Directrice de thèse
Andrée TUZET	INRAE	Co-encadrante de thèse

Remerciements

Durant plus de trois ans, cette thèse m'a permis de rencontrer, échanger et collaborer avec de nombreuses personnes que je souhaite remercier.

Je remercie d'abord Pierre-Emmanuel Bournet, Jean-Christophe Calvet, Aude Lemonsu et Olivier Sanchez qui ont accepté d'être membres de mon jury de thèse et dont les remarques et les suggestions ont contribué à l'amélioration de ce manuscrit.

Je souhaite remercier chaleureusement ma directrice de thèse Karine Kata-Sartelet et ma co-encadrante Andrée Tuzet pour leur confiance, leurs précieux conseils, leur investissement et leur disponibilité. Merci à toutes les deux de m'avoir transmis votre passion pour la recherche.

Je remercie aussi Cédric Flageul qui a co-encadré le début de mes travaux de thèse et m'a aidé dans la prise en main de code_saturne.

Je souhaite remercier tous mes collègues du CEREAs et de l'INRAE pour leur accueil. Merci à Lya, Soo-Jin, Youngseob, Alexis, Yelva, Thibaud, Yunyi qui ont contribué à mes travaux, en particulier dans le développement et la mise en place des simulations CHIMERE-MUNICH. Merci aussi à Lydie pour son aide sur les questions administratives.

Cette thèse a été menée en collaboration avec l'équipe VILLE du CNRM, je tiens donc aussi à remercier Aude Lemonsu, Valéry Masson et Cécile De Munck qui m'ont accueillie à Toulouse et pour leur aide précieuse dans la prise en main et le développement de TEB-SPAC.

Mes remerciements vont aussi à mes collègues de l'ANR sTREEt, pour nos échanges enrichissants concernant la partie expérimentale.

Je tiens à remercier affectueusement ma famille et mes amis pour leur soutien inconditionnel tout au long de mes études.

Enfin, je remercie Antoine pour sa patience, son aide et ses conseils.

Résumé

Les arbres apportent de nombreux services écosystémiques en ville, ils permettent de diminuer certaines conséquences de l'urbanisation comme l'îlot de chaleur urbain et le ruissellement de l'eau. Leur effet thermo-radiatif améliore le confort thermique.

Les arbres peuvent également impacter la qualité de l'air en ville via différents processus. Le dépôt de polluants gazeux et particulaires sur les feuilles des arbres peut contribuer à la diminution des concentrations. Cependant, l'effet aérodynamique des arbres modifie l'écoulement dans les rues canyons et limite la dispersion des polluants émis dans la rue. Par ailleurs, les arbres émettent des composés organiques volatils biogéniques (COVb) qui peuvent participer à la formation d'O₃ et d'aérosols organiques secondaires. Les émissions de COVb varient selon l'espèce d'arbre, et sont influencées par des facteurs climatiques (température, rayonnement) mais aussi par le statut hydrique des arbres.

Cette thèse a pour objectif de quantifier les impacts de ces différents processus sur la qualité de l'air en ville. Des simulations numériques sont réalisées sur la ville de Paris pendant l'été 2022 avec la chaîne de modèles CHIMERE/MUNICH afin de quantifier l'impact des arbres sur les concentrations atmosphériques de polluants à l'échelle locale et régionale. Les concentrations simulées sont comparées à des mesures.

Les arbres urbains ne sont généralement pas pris en compte dans les modèles de qualité l'air, aussi bien à l'échelle régionale qu'à l'échelle de la rue. Pour intégrer les émissions de COVb dans le modèle régional CHIMERE, un inventaire est réalisé à partir de la base de données des arbres de la ville de Paris. Une méthode est développée afin d'estimer les caractéristiques des arbres qui sont utilisées en données d'entrée des différents modèles (surface de feuille, biomasse sèche, taille de la couronne, etc.). En moyenne sur les mois de juin et juillet 2022 à Paris, les émissions biogéniques locales des arbres induisent une augmentation de 1,0% d'O₃, 4,6% de PM₁ organiques et 0,6% de PM_{2.5}. Les émissions biogéniques des arbres urbains augmentent très fortement les concentrations d'isoprène et de monoterpènes. Par comparaison aux mesures, les concentrations de terpènes ont tendance à être sous-estimées, compte tenu des incertitudes liées aux facteurs d'émissions et à la part de végétation manquante dans l'inventaire. Les émissions de terpène de la végétation urbaine et suburbaine influencent fortement la formation de particules organiques, il est donc important de bien les caractériser dans les modèles de qualité de l'air.

Les différents effets des arbres urbains sur la qualité de l'air à l'échelle de la rue sont ensuite ajoutés dans le modèle de réseau de rue MUNICH. L'effet aérodynamique des arbres dans les rues est paramétré à partir de simulations de mécanique des fluides. Il induit une augmentation des concentrations des composés émis dans la rue. Cette augmentation peut atteindre +37% pour le NO₂ dans les rues avec une surface de feuilles importante et un trafic élevé. Le dépôt sur les feuilles des arbres est calculé à partir d'une approche résistive adaptée à l'échelle de l'arbre urbain dans la rue. Cependant, son impact sur les concentrations reste limité sur les gaz et particules étudiés (< -3%).

Pour mieux représenter les impacts des hétérogénéités du microclimat urbain et de l'effet thermo-radiatif des arbres sur les concentrations de gaz et de particules, un couplage entre les modèles de surface urbaine (TEB), de continuum sol-plante-atmosphère (SPAC) et de qualité de l'air à l'échelle des rues (MUNICH) a été mis en place. Les résultats montrent qu'à l'été 2022 les arbres plantés dans des fosses avec un volume de sol restreint souffrent rapidement de stress hydrique (vers le 15

juin). Quand les arbres sont bien alimentés en eau, ils induisent une diminution de la température moyenne de l'air dans la rue de $-0,12^{\circ}\text{C}$ et qui peut atteindre $-0,8^{\circ}\text{C}$ localement dans certaines rues. Après le 15 juin, les arbres limitent fortement leurs transpirations ce qui réduit aussi leur effet rafraichissant dans les rues avec une diminution de la température moyenne de l'air dans la rue de $-0,02^{\circ}\text{C}$ et qui atteint $-0,5^{\circ}\text{C}$ localement.

Le couplage entre les modèles MUNICH, TEB et SPAC permet également de calculer plus précisément les émissions de COVb, en les faisant varier avec la température de surface des feuilles et le rayonnement solaire reçu par les feuilles dans la rue (prenant en compte les réflexions entre les différentes surfaces de la rue et les effets d'ombrages). Les émissions ainsi calculées sont plus élevées, entre +23 et +48% selon l'espèce de COVb. Le contenu en eau du sol simulé par TEB-SPAC est aussi utilisé pour estimer l'impact direct du stress hydrique sur les émissions d'isoprène en comparant trois paramétrisations de la littérature. Les trois paramétrisations montrent une diminution des émissions d'isoprène à partir du 15 juin, mais qui est d'intensité variable (entre -28 et -58% de diminution moyenne des émissions d'isoprène sur les deux mois). Ces variations soulignent l'importance de la météorologie locale sur les émissions de COVb.

Abstract

Trees provide numerous ecosystem services in cities, helping to reduce some of the consequences of urbanization, such as the urban heat island and water run-off. Their thermo-radiative effect improves thermal comfort.

Trees can also have an impact on urban air quality through various processes. The deposition of gaseous and particulate pollutants on tree leaves can help to reduce concentrations. However, the aerodynamic effect of trees modifies the airflow in street canyons and limits the dispersion of pollutants emitted in the street. Trees also emit biogenic volatile organic compounds (BVOCs), which can contribute to the formation of O₃ and secondary organic aerosols. BVOC emissions vary depending on the tree species, and are influenced by climatic factors (temperature, radiation) and by the tree water status.

The objective of this thesis is to quantify the impacts of these different processes on urban air quality. Numerical simulations are performed over the city of Paris during summer 2022 using the CHIMERE/MUNICH model chain in order to quantify the impact of trees on atmospheric concentrations of pollutants at the local and regional scales. The simulated concentrations are compared to measurements.

Urban trees are not generally taken into account in air quality models, either at regional or street level. In order to integrate BVOC emissions into the CHIMERE regional model, an inventory is developed using the tree database of the city of Paris. A method is set up to estimate the characteristics of the trees, which are used as input data for the various models (leaf area, dry biomass, crown size, etc.). On average over the months of June and July 2022 in Paris, local biogenic emissions from trees lead to an increase of 1.0% in O₃, 4.6% in organic PM₁ and 0.6% in PM_{2.5}. Biogenic emissions from urban trees strongly increase concentrations of isoprene and monoterpenes. Compared with measurements, terpene concentrations tend to be underestimated, given the uncertainties associated with emission factors and the missing part of the vegetation in the inventory. Terpene emissions from urban and suburban vegetation greatly influence the formation of organic particles, it is therefore important to characterize them properly in air quality models.

The various effects of urban trees on air quality at street level are then added into the MUNICH street network model. The aerodynamic effect of street trees is parameterized using computational fluid dynamics simulations. It leads to an increase in the concentrations of compounds emitted into the street. This increase can reach +37% for NO₂ in streets with a large leaf surface and high traffic. Deposition on tree leaves is computed using a resistive approach adapted to the scale of the tree in the street. However, its impact on concentrations remains limited for the gases and particles studied (< -3%).

To better represent the impacts of urban micro-climate heterogeneities and the thermo-radiative effect of trees on gas and particle concentrations, a coupling between the models of urban surface (TEB), soil-plant-atmosphere continuum (SPAC) and street-scale air quality (MUNICH) was implemented. The results show that during 2022 summer, trees planted in pits with limited soil volume suffer from water stress (around June 15). When trees have a good water supply, they induce a decrease in average street air temperature of -0.12°C, which can reach -0.8°C locally in some streets.

After June 15, trees significantly reduce their transpiration, which also reduces their cooling effect, with a decrease in average street air temperature of -0.02°C , reaching -0.5°C locally.

The computation of the BVOC emissions are also refined by using the variables simulated by TEB-SPAC. BVOC emissions are calculated using the surface temperature of the leaves and the solar radiation received by the leaves in the street (taking into account reflections between different street surfaces and shading effects). These emissions are higher, between +23 and +48% depending on the species of BVOC. The soil water content simulated by TEB-SPAC is also used to estimate the direct impact of water stress on isoprene emissions, by comparing three parameterizations from the literature. The three parameterizations show a decrease in isoprene emissions from June 15, but of variable intensity (between -28 and -58% average decrease in isoprene emissions over the two months). These variations underline the importance of local meteorology on BVOC emissions.

Table of Contents

Abstract	12
1 Introduction	13
1.1 Urban air quality and climate	13
1.1.1 Air pollution, issues and processes	13
1.1.2 Urbanization and air quality	15
1.1.3 Urban climate	17
1.2 Greening the city	19
1.2.1 Ecosystem services provided by the urban vegetation	19
1.2.2 Effects of vegetation on air quality	20
1.2.3 Urban-related stress	21
1.3 Modeling urban vegetation and their effects on air quality and climate	22
1.3.1 Modeling urban vegetation and their effect on air quality	22
1.3.2 Modeling urban vegetation and their effect on climate	23
1.4 Objectives of the PhD thesis and problematic	24
2 Parameterization of air flow in a street with trees	27
2.1 Introduction	27
2.2 Parameterization of air flows in street canyons	28
2.2.1 Introduction	29
2.2.2 Materials and Methods	31
2.2.3 Adaptation of a flow parametrization and comparison with existing MUNICH parametrizations	37
2.2.4 Conclusions	43
2.2.5 Appendices	44
2.3 Parameterization of the tree aerodynamic effect in street canyons	48
2.3.1 Introduction	50
2.3.2 Materials and Methods	51
2.3.3 Quantification of the tree crown effect on horizontal and vertical transfers by Code_Saturne simulations	54
2.3.4 Parameterization of the aerodynamic effect of tree crowns in MUNICH	55
2.3.5 Conclusions	59
2.3.6 Appendices	60
2.4 Conclusion	69
3 Bottom-up inventory of urban-tree biogenic emissions in Paris and impact on regional-scale air quality	71
3.1 Introduction	73
3.2 Materials and Methods	74
3.2.1 Tree-based BVOC emission model	74
3.2.2 Tree inventory and characteristics	75
3.2.3 Description of regional-scale air-quality simulations	75
3.2.4 Description of the air-quality experimental measurements	77
3.3 Bottom-up inventory of tree BVOC emissions and comparison to the land-use approach	79
3.3.1 Calculation of BVOC emissions at the tree level	79
3.3.2 Integration of individual tree BVOC emissions in CHIMERE	86

3.3.3	Complementarity of the emissions computed by the bottom-up and the land-use approaches	87
3.4	Quantification of the impact of BVOC emissions from urban trees on air quality at the regional scale	90
3.4.1	Validation of the reference simulations	90
3.4.2	Impact of biogenic emissions from urban trees on concentrations	97
3.5	Conclusions	106
3.6	Appendices	108
4	Quantifying the effects of trees on air quality at the street and city scales	129
4.1	Introduction	130
4.2	Materials and Methods	131
4.2.1	Description of the reference simulation	131
4.2.2	Integration of the tree effects in MUNICH	133
4.2.3	Simulation set-up	141
4.3	Results and discussion	142
4.3.1	Reference simulation	142
4.3.2	Tree effects on isoprene and monoterpene concentrations	143
4.3.3	Tree effects on NO ₂ and O ₃ concentrations	151
4.3.4	Tree effects on particle concentrations	157
4.4	Conclusion	164
4.A	List of measurement stations	166
4.B	Computation of the dry deposition of gas and aerosols on street and leaf surfaces	167
4.B.1	Dry deposition of gaseous species	167
4.B.2	Dry deposition of aerosols	171
4.B.3	Computation of the surface friction velocity	173
4.C	Impact on tree aerodynamical effect on isoprene and monoterpene emissions in the street . .	174
4.D	Definition of the statistical indicators	175
5	Towards a finer representation of the urban micro-climate and BVOC emissions in air-quality models.	177
5.1	Introduction	178
5.2	Materials & Methods	178
5.2.1	Presentation of TEB-Veg	178
5.2.2	Presentation of SPAC	179
5.2.3	TEB-SPAC coupling	181
5.2.4	TEB-SPAC-MUNICH coupling	183
5.2.5	Simulation set-up and input data	187
5.3	Results	197
5.3.1	Comparison of simulated and observed meteorological fields in HdV	197
5.3.2	Analysis of the tree energetic and hydraulic functioning	199
5.3.3	Impacts of the MUNICH-TEB-SPAC coupling on the modeled urban micro-climate .	205
5.3.4	Impacts of the urban micro-climate on street concentrations	212
5.3.5	Impacts of the urban micro-climate and tree water stress simulated by TEB-SPAC on BVOC emissions	217
5.4	Conclusion	222
6	Conclusions and perspectives	225
6.1	Conclusions	225
6.2	Perspectives	228

List of Figures	230
List of Tables	239
Bibliography	241

Chapter 1

Introduction

Contents

1.1	Urban air quality and climate	13
1.1.1	Air pollution, issues and processes	13
1.1.2	Urbanization and air quality	15
1.1.3	Urban climate	17
1.2	Greening the city	19
1.2.1	Ecosystem services provided by the urban vegetation	19
1.2.2	Effects of vegetation on air quality	20
1.2.3	Urban-related stress	21
1.3	Modeling urban vegetation and their effects on air quality and climate	22
1.3.1	Modeling urban vegetation and their effect on air quality	22
1.3.2	Modeling urban vegetation and their effect on climate	23
1.4	Objectives of the PhD thesis and problematic	24

1.1 Urban air quality and climate

1.1.1 Air pollution, issues and processes

The World Health Organization (WHO) estimates that air pollution is responsible for 6 to 7 million of premature deaths annually. It is the fourth biggest global health risk factor mainly, because of its contribution to ischemic heart disease and stroke, two leading causes of death worldwide. Air pollution is defined as the contamination of the outdoor and indoor air by chemical, physical or biological substances that modify the composition of the atmosphere. Air quality (AQ) is related to concentration level of pollutants in the air. Air pollution is a problematic that affects the entire population, and is border-less. WHO estimates that 99% of the global population breathe air that exceeds WHO guideline limits. The effects on health are multiple and depend on the nature of pollutants, on the size for particles and the duration of exposure (Bernstein et al., 2004; Pénard-Morand and Annesi-Maesano, 2004; Kampa and Castanas, 2008). Air pollution is also complex because a large variety of pollutant types, sources and a large range of scales coexist (Pénard-Morand and Annesi-Maesano, 2004; Sportisse, 2009; Vallero, 2014). Pollutants are present in two forms in the atmosphere: gas (nitrogen oxides (NO_x , where $\text{NO}_x = \text{NO}_2 + \text{NO}$), ozone (O_3), carbon monoxide (CO), sulfur oxides (SO_2 , SO_3), volatile organic compounds (VOCs) etc.) and liquid/solid particles called aerosols or particulate matter (PM) (dust, sea salt, black carbon etc.) with size ranging from 1 nm to 10 μm .

The pollutant concentrations in the air are governed by complex physico-chemical processes, as shown in Fig. 1.1.

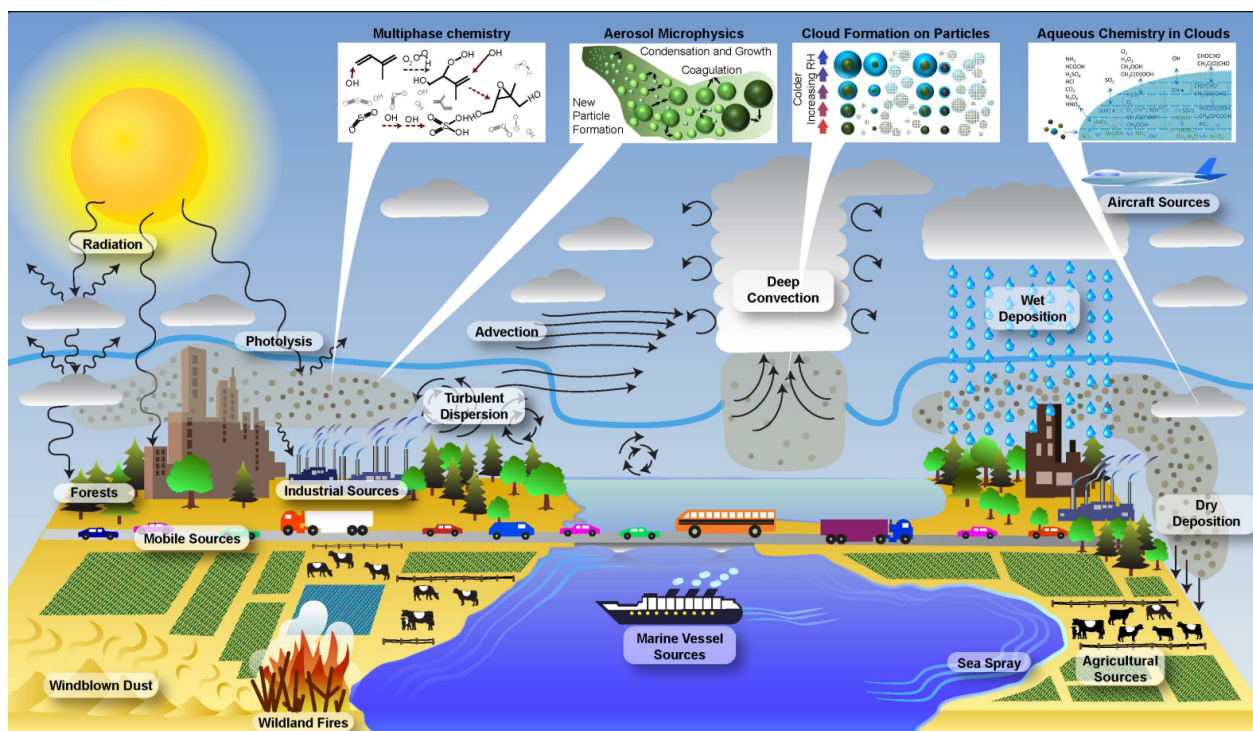


Figure 1.1: Processes affecting air quality and atmospheric chemistry (EPA).

First, they are emitted by anthropic activities (industry, transport, heating, agriculture etc.) or naturally (wind erosion, sea spray, volcanic eruption etc.). Then, depending on their lifetime in the atmosphere, they are transported and dispersed by the wind and turbulence and they can undergo physical and chemical transformations. Pollutants directly emitted are called primary pollutants, and those which are produced in the atmosphere by these reactions are called secondary pollutants. Multiple transformations exist, depending on their properties, gas may be oxidized, photolysed, nucleate, condense or evaporate from aerosols. Aerosols may also coagulate, undergo particle-phase reactions and activation into cloud droplets (Fig. 1.2). Besides, pollutants can be deposited on surfaces by dry or wet deposition (leaching). If they are not re-suspended (Martuzevicius et al., 2011; Askariyeh et al., 2020), they are removed from the atmosphere but can still have negative impacts, such as acid rain (Irwin and Williams, 1988), water contamination (Arimoto, 1989; Huston et al., 2009; Pandey et al., 2009) and vegetation oxidation (Katz and Shore, 1955; Smith, 2012). Finally, air pollution interacts with meteorology (ie. cloud formation), climate (i.e. radiative effect of aerosols) and the biochemical cycle (Ramanathan et al., 2001; Akimoto, 2003; Stier et al., 2007; Li et al., 2011; Vallero, 2014; Fiore et al., 2015; Fuzzi et al., 2015; Feng et al., 2019).

Although air quality is improving in Europe and France for many pollutants, a large part of the population, especially in urban areas, are exposed to concentrations above the health-based guideline level set by the WHO (European Environment Agency, 2023; Elichegaray et al., 2010). Several pollutants are known to have negative effects on human health based on toxicological studies and their concentrations in the ambient air are regulated in Europe by the Ambient Air Quality Directive 2008/50/EC. They include: nitrogen dioxide (NO_2), O_3 , SO_2 , CO , lead (Pb), benzene (C_6H_6) and particulate matter with a diameter of less than $2.5 \mu\text{m}$ ($\text{PM}_{2.5}$) and than $10 \mu\text{m}$ (PM_{10}). The air

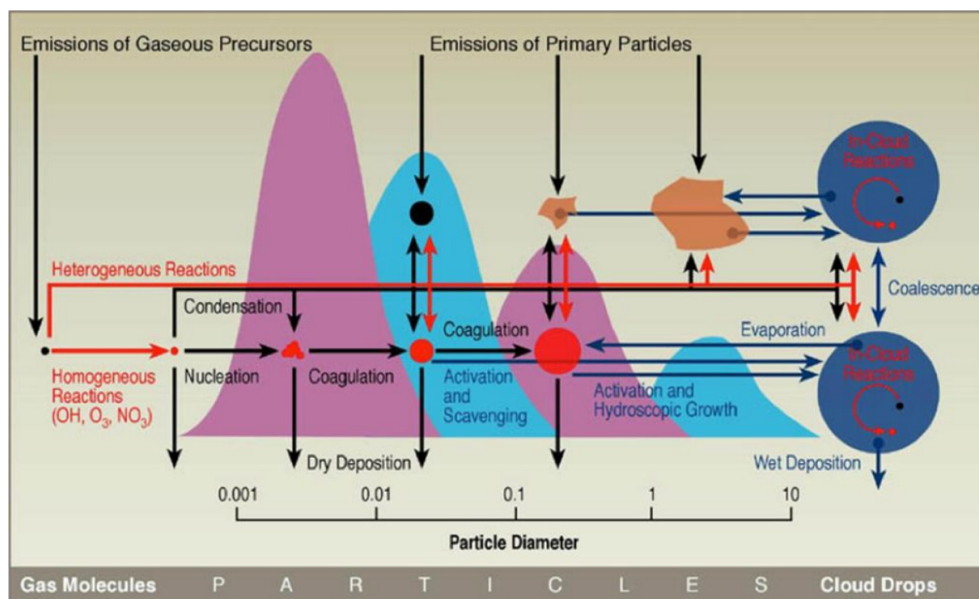


Figure 1.2: Major micro-physical and chemical processes that influence the size distribution and chemical composition of atmospheric aerosols (Brasseur and Jacob, 2017).

quality standards for urban areas under the EU Air Quality Directive, and WHO air quality guidelines are summarized here: <https://www.eea.europa.eu/airs/2016/environment-and-health/outdoor-air-quality-urban-areas>. For particles, threshold values are specified for two size ranges, but the effect on health may also vary according to the chemical composition of the particles (Rohr and Wyzga, 2012; Atkinson et al., 2015). The diversity of pollutant types, sources, processes and consequences makes air pollution still a key topic for scientific research.

1.1.2 Urbanization and air quality

Today, 55% of the world's population lives in cities, and this should reach 68% by 2050 (Angel et al., 2011; Department of Economics and Social Affairs, 2018). The gathering of populations in urban areas leads to the high density of infrastructures and activities (e.g. building and transport), inducing issues. First, air flows are modified due to the presence of high buildings and heterogeneities inducing the reduction of the dispersion of pollutants emitted in the streets (Arnfield, 2003; Li et al., 2019). Combined with high local anthropic emissions (due to traffic, residential heating or cooling, industries etc.), the air quality is deteriorated in urban areas and much higher concentrations are observed in the streets than above it (background) (Lyons et al., 1990; Fenger, 1999; Thunis, 2018; Yang et al., 2020b). One solution to improve urban air quality is to attempt to decrease emissions at the street level by implementing low-emission zones (Ku Donggyun et al., 2020) or at the regional level by banning chimney fires for example. The other is to improve urban planning (Borrego et al., 2006; Huang et al., 2021; Piracha and Chaudhary, 2022). Therefore, to understand the key processes and to guide planning policies in improving air quality, a growing number of studies are focusing on wind speed, turbulence and pollutant dispersion in streets (Chan et al., 2003; Voordeckers et al., 2021). As shown in Fig. 1.3, at the city level, an increase of the boundary layer above the urban area compared to the country side is observed during day, and at night, the boundary layer does not return to stable conditions (Uno et al., 1988; Rotach, 1995; Lemonsu and Masson, 2002). However, at the urban canopy layer (UCL) scale, the wind speed is reduced and the turbulence intensity is increased (Auer, 1981; Collier, 2006; Chan et al., 2013).

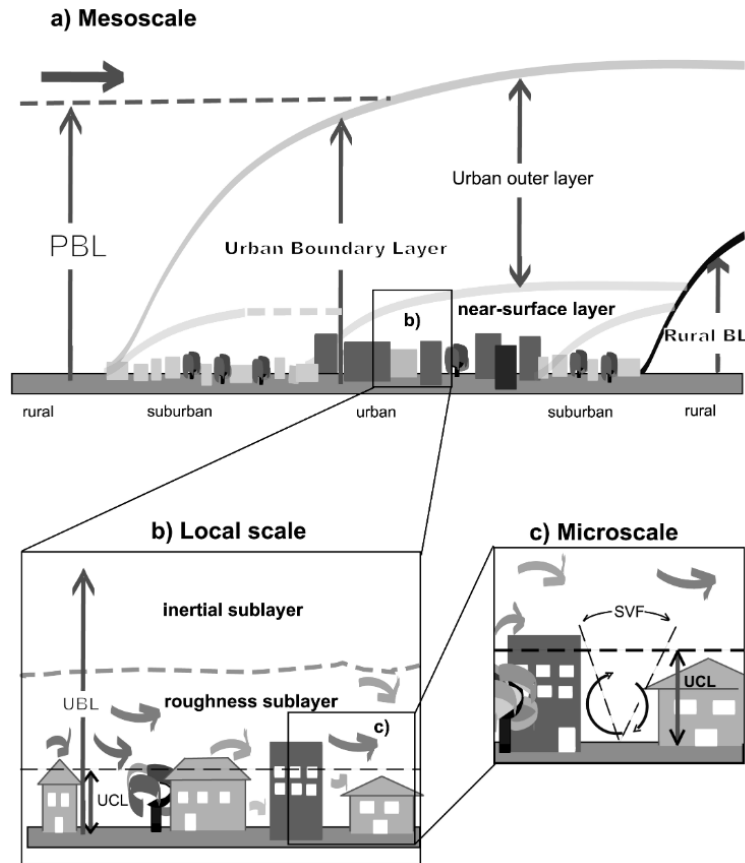


Figure 1.3: Schematic diagram showing flow and scale lengths within an urban boundary layer (UBL) (PBL: Planetary boundary layer) (Fisher et al., 2006).

In the 70s, the concept of street canyon, a road and its two flanking buildings, was used to study the main characteristics of pollutant dispersion within urban streets (Johnson et al., 1973; Nicholson, 1975; Dabberdt et al., 1973; Hotchkiss and Harlow, 1973). The street canyon is a basic geometry unit that can be used to build larger urban structures, and is since used in numerous studies on air flow, air quality and surface energy balance at the street level (Vardoulakis et al., 2003-01; Yazid et al., 2014; Zhang et al., 2020; Zhao et al., 2020; Wankhade et al., 2023). Based on this simplified street geometry, Oke (1998) proposed to classify flow patterns depending on the street aspect ratio (ratio of building height to street width). The street can be divided into two regions: a recirculation zone, and if the street is sufficiently wide a ventilated zone (Harman et al., 2004a). One or more vortex can be formed in the street depending on its aspect ratio and the wind direction (Hunter et al., 1992; Sini et al., 1996; Salizzoni et al., 2009) but also on stability and atmospheric conditions (Nakamura and Oke, 1988). When the wind direction is close to perpendicular to the street, this particular recirculation induces an accumulation of the pollutants emitted in the street at the bottom leeward side of the street (Fig. 1.4) and exposes people in this zone to higher concentrations of pollutants (Ahmad et al., 2005; Salim et al., 2011). Even if flows in heterogeneous street canyons are more complex (Kastner-Klein et al., 2004; Karra et al., 2017), this concept of canyon is very useful to study the general processes affecting the flow and air quality.

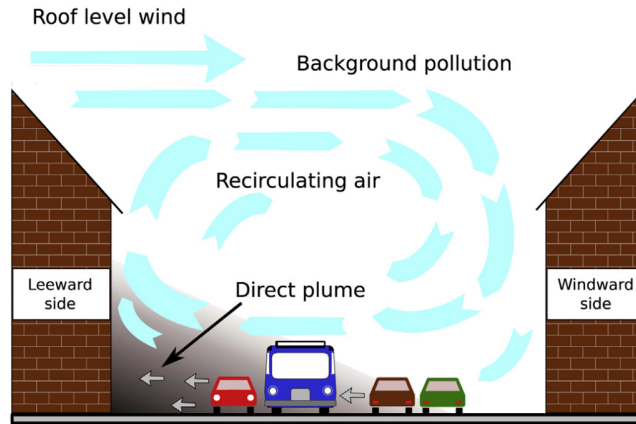


Figure 1.4: Schematic diagram of air flow and pollutant dispersion within a street canyon (Silver et al., 2013).

To better understand these processes, wind speed and turbulence measurements were performed in streets (Eliasson et al., 2006; Zajic et al., 2011). However, this type of experimental studies are limited because conclusion cannot always be generalized to other sites due to local heterogeneities and installation constraints are high in urban areas (people and sensor safety). Wind tunnel experiments in controlled and repeated conditions are also used to study air flows but still required suitable infrastructures (Ahmad et al., 2005). A growing number of studies rely on modeling tools (Vardoulakis et al., 2003-01; El-Harbawi, 2013; Oliveri Conti et al., 2017; Rybarczyk and Zalakeviute, 2018). Indeed, numerical models are very useful because simulations can be easily repeated and parameter configurations modified. Models are often validated on outdoor or wind tunnel experiments, showing that methods are interdependent and complementary. Several types of numerical models are presented in Section 1.3.

1.1.3 Urban climate

Air flow and air quality in the UCL are also closely dependent on meteorological processes, that are themselves modified by the urban environment. In fact, the energy and water budgets in cities are strongly modified because of many processes summarized in Fig. 1.5 (Nunez and Oke, 1977; Taha, 1997; Kuttler, 2008b; Oke et al., 2017; Masson et al., 2020). First, the artificialization of surfaces with darker materials of lower albedo (fraction of solar radiation reflected by a surface), such as asphalt or tile, causes a larger absorption of solar radiation which can be stored and released as sensible heat inducing an increase in surface temperatures (Taha et al., 1988). The release of anthropogenic heat by heating and cooling systems and by traffic also participates to the temperature increase (Pigeon et al., 2007). Multiple reflections of short wave radiation occur between the street surfaces and cause a radiative trapping in the street (Harman et al., 2004b). In addition, vegetation, which has a positive effect on human thermal comfort through evapotranspiration and shading, is often lacking in cities (Oke, 1982; Hass et al., 2016; Walle et al., 2022). Then, water infiltration into the soil is limited by the dominance of impervious surfaces, and heavy runoff can cause flooding (Leopold, 1968; Wissmar et al., 2004; Walsh et al., 2012). At the city scale, an increase of temperature is observed compared to the countryside (Fig. 1.6), this local difference of temperature is called the Urban Heat Island effect (UHI) (Kim, 1992). This effect is particularly visible during the summer nights when the radiative energy is stored during the day and released during the night. Besides, human thermal comfort is also affected by pedestrian level wind turbu-

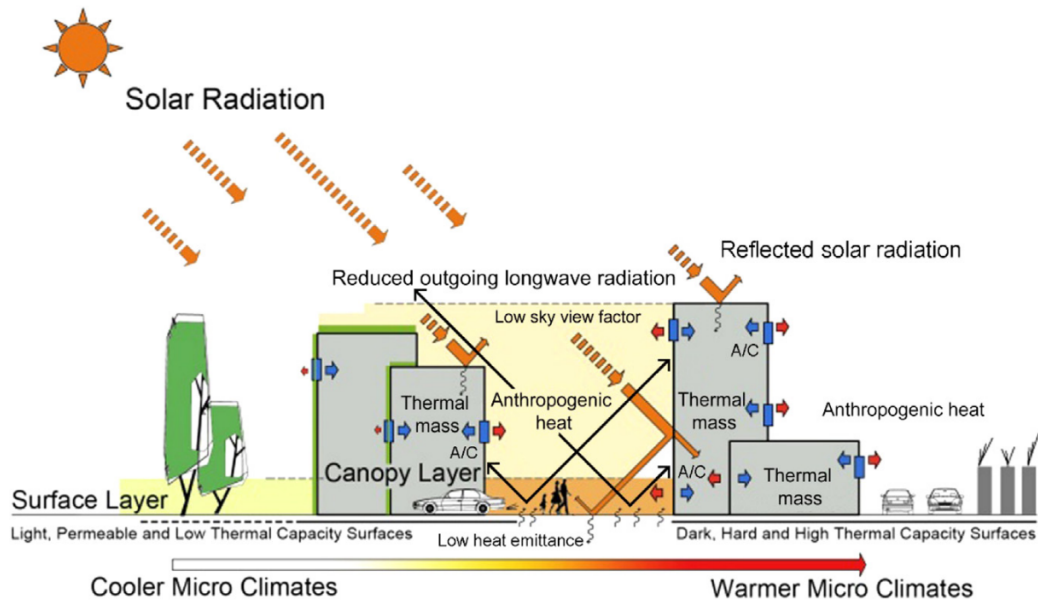


Figure 1.5: Urban structure, cover, fabric and metabolism contribute to the UHI effect in highly developed areas (Soltani and Sharifi, 2017).

lence (Zou et al., 2021). The UHI impacts the turbulent fluxes, and therefore the concentrations of primary and secondary pollutants in urban areas (Sarrat et al., 2006).

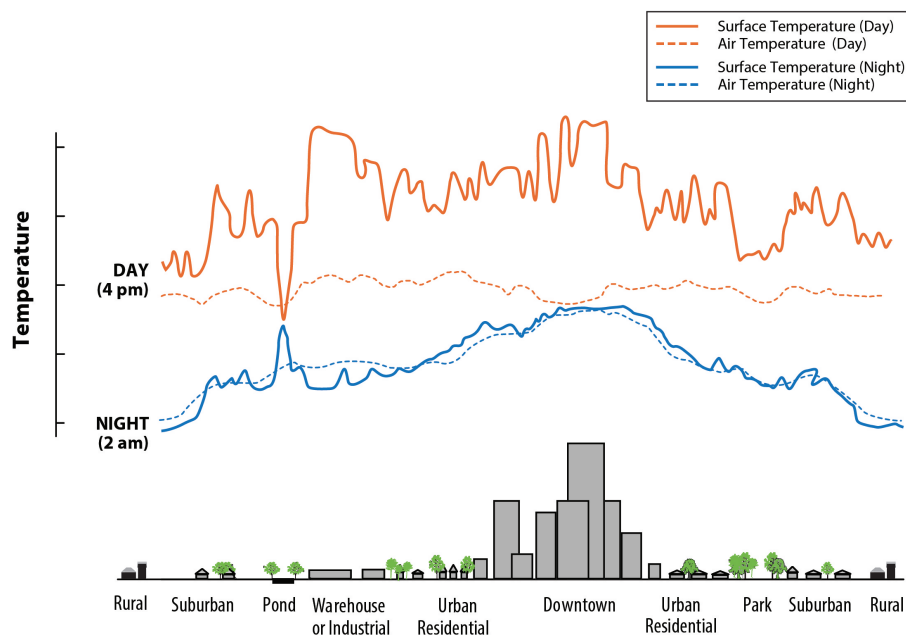


Figure 1.6: UHI diagram - spatial variations of day and nighttime temperatures over a city (US EPA, 2014).

These local climate modifications have a negative impact on human health especially during extreme events (pollution peaks, heatwave, heavy rains) (Robine et al., 2007; Le Tertre et al., 2006; Baccini et al., 2008; Basu, 2009; D'Ippoliti et al., 2010; Laaidi et al., 2012; Mitchell et al., 2016; Heaviside et al., 2017), that, for some of them, may happen more often in the future due to climate change (Patz et al., 2005; Huang et al., 2011; Vardoulakis et al., 2014; Hajat et al., 2014; Lemonsu et al., 2015; IPCC, 2021).

1.2 Greening the city

1.2.1 Ecosystem services provided by the urban vegetation

To mitigate the negative effects of urbanization, nature-based solutions are often promoted (Fig. 1.7) (Livesley et al., 2016; Chang et al., 2017; Roeland et al., 2019). The best-known ecosystem service of vegetation is the improvement of the human thermal comfort. Recent review studies (Jamei et al., 2016; Taleghani, 2018; Lai et al., 2019; Hami et al., 2019; Nasrollahi et al., 2020) have shown that urban greening is an efficient solution to decrease temperatures in urban outdoor spaces. The efficiency of the cooling depends in particular on the type and configuration of vegetation, the street aspect ratio and orientation, and the climate of the city.

In terms of mechanisms involved, high vegetation (trees) intercepts, reflects and absorbs solar radiation preventing it from reaching other surfaces. This creates shade and decreases indirectly temperatures under the trees (Armson et al., 2013a; Konarska et al., 2014; Upreti et al., 2017). Then, the transpiration of water by the vegetation, which is an endothermic reaction, induces a decrease in the surrounding air temperature (Konarska et al., 2016; Gao et al., 2020). Transpiration is the loss of water by evaporation and diffusion, which occurs mainly at leaf level through small pores called stomata. The tension (negative pressure) created by transpiration on sap is transmitted by the cohesion of water molecules from leaves to root apex, where roots absorb water and minerals from the soil. Transpiration is a passive mechanism but is tightly controlled by the opening and closing of stomata which responds to environmental and meteorological conditions such as light, leaf water status, and carbon dioxide concentration.

Urban vegetation also brings additional ecosystem services such as the intercepting of water by leaves that can limit water runoff and the conservation of zones of permeable soil in which water can infiltrate (Armson et al., 2013b; Livesley et al., 2016; Berland, 2017). Photosynthesis removes carbon dioxide, a greenhouse gas, from the atmosphere, stores carbon in the plant tissues, and produces oxygen. The carbon sequestration intensity depends on the area and time of year (Nowak and Crane, 2002; Svirejeva-Hopkins et al., 2004; Velasco et al., 2016; Fares et al., 2017; Kinnunen et al., 2022). Vegetation also enhances biodiversity in cities and improves human well-being and quality of life (Shackell et al., 2012; Bertram and Rehdanz, 2015; Sulaiman, 2016).

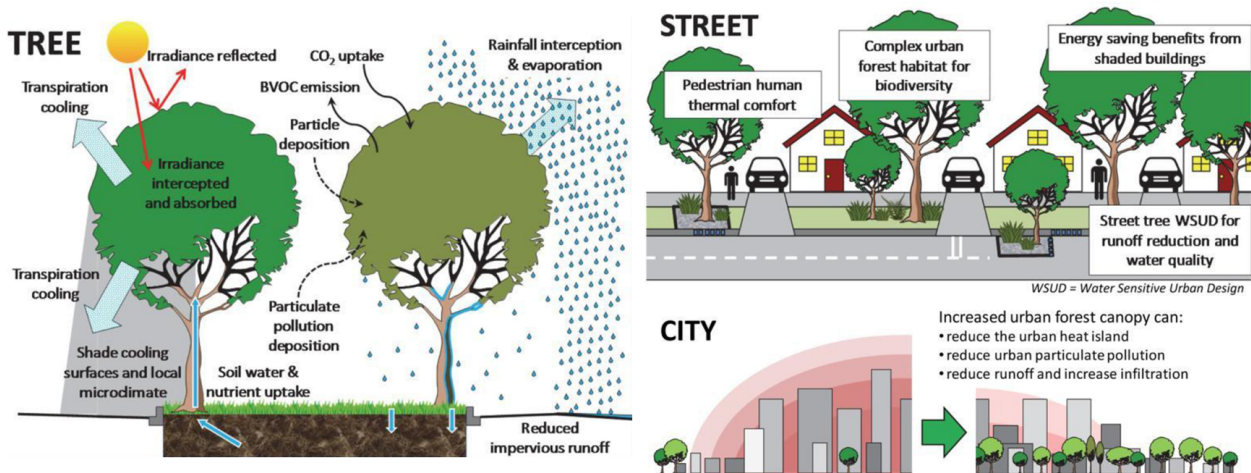


Figure 1.7: Ecosystem services provided by trees in cities (Livesley et al., 2016).

Because of all the ecosystem services vegetation and especially trees can provide in cities, the number of research studies and publications on urban vegetation have been increasing exponentially in recent years (Fig. 1.8).

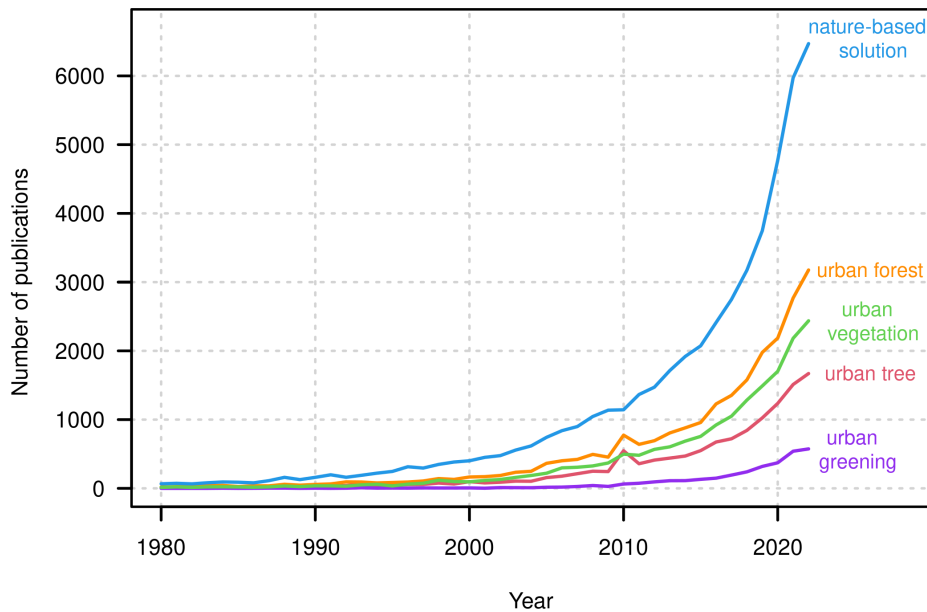


Figure 1.8: Number of publications containing terms related to vegetation in cities in title or abstract (Dimensions, 1980-2022).

1.2.2 Effects of vegetation on air quality

The effects of vegetation on air quality is contrasted (Leung et al., 2011; Janhäll, 2015; Badach et al., 2020; Diener and Mudu, 2021). The dry deposition of gaseous and particulate pollutants on plant surfaces helps to remove pollutants from the atmosphere and reduce concentrations. However, there is a great variability and uncertainties in the magnitude of this process (Nowak et al., 2006; Escobedo and Nowak, 2009; Setälä et al., 2013; Selmi et al., 2016; Xing and Brimblecombe, 2019; Nemitz et al., 2020; Lindén et al., 2023). Certain tree species emit pollen that can trigger allergies (Charalampopoulos et al., 2018; Kasprzyk et al., 2019). The rows of trees planted in streets slow down the air flow, thus limiting the dispersion of pollutants emitted by traffic and increasing concentrations as shown in Fig. 1.9 (Gromke and Ruck, 2007; Vos et al., 2013; Jeanjean et al., 2016). Then, vegetation naturally emits a large range of Biogenic Volatile Organic Compounds (BVOCs), that modulate plant protection to heat, pollutants and water stress. VOCs also operate as messengers in plant-plant and plant-insect interactions. BVOC emissions are strongly dependent on the vegetation type and on environmental conditions (temperature, radiation, soil humidity) (Niinemets et al., 2004). They play an important role in atmospheric chemistry, especially in the formation of ozone and secondary organic aerosols (SOAs). Unlike specific Anthropogenic Volatile Organic Compounds (AVOCs), BVOCs do not pose a direct risk to human health. However, they react with other compounds to form harmful pollutants for health, such as O_3 and SOAs (Owen et al., 2003; Calfapietra et al., 2013; Ren et al., 2017).

The variation of temperature, humidity and solar radiation due to urban micro-climate and the presence of vegetation can also affect air quality through the change of chemical reaction kinetic and photolysis rates (Walcek and Yuan, 1995).

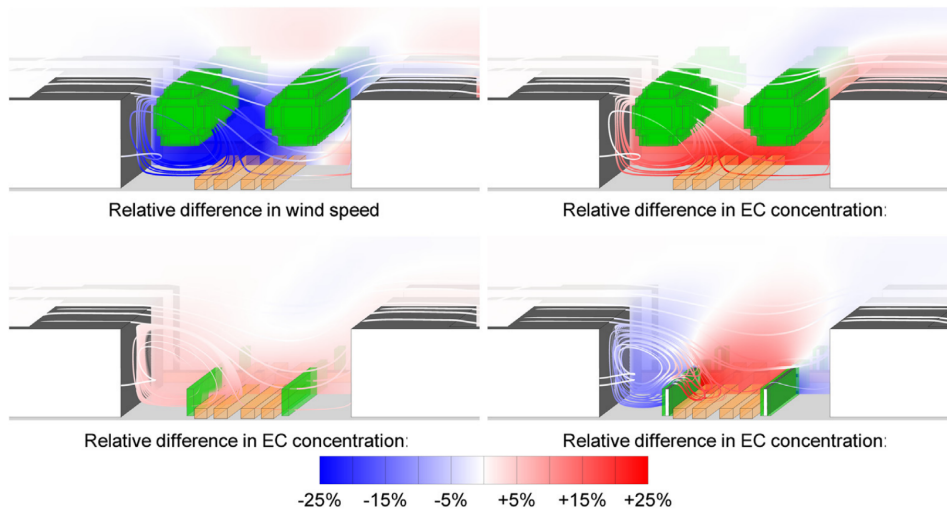


Figure 1.9: Impact of rows of trees and hedges on wind speed and dispersion of pollutants emitted by traffic in a street canyon modeled by Vos et al. (2013).

1.2.3 Urban-related stress

Urban environments are stressful for plants and can cause plant mortality (Lüttge and Buckeridge, 2023; Czaja et al., 2020). These stress of various types are represented in Fig. 1.10.

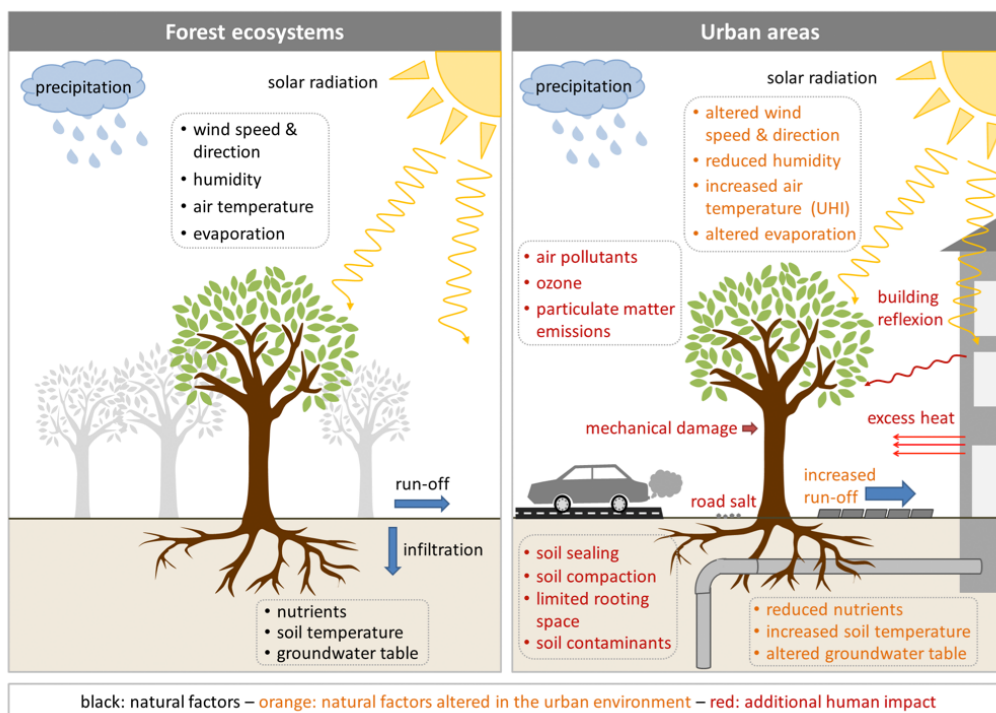


Figure 1.10: Impact of urban environment on tree development compared to forest (www.eskp.de).

First, the plants' growth is contained as they are planted in a limited soil volume and crowns are pruned. Roadside trees also have a very uncertain access to water and often suffer from water stress. Lining pits with low-permeability materials limits the surface of water infiltration. There is also a great uncertainty in the capability of trees to find water deep underground (the soil can be supplied with water by leaks, roots penetrating pipes etc.).

Furthermore, the urban environment induces higher temperatures than rural areas. This means that the vegetation is more likely to suffer from heat stress. Air quality also has an impact on vegetation, which can suffer from pollutant stress. Indeed, air pollutants can oxidize leaves and the water can be contaminated by heavy metals for example. Finally, the urban environment and the associated constraints also impact BVOC emissions which are sensitive to water, heat and ozone stress (Niinemets, 2010).

1.3 Modeling urban vegetation and their effects on air quality and climate

Models are powerful tools to understand processes, interpret observations and make short- and long-term forecasts. Particularly in the field of urban management and planning, where the city heterogeneity limits the representativity of experimental measurements. Numerical simulations have the advantage of being repeatable and parameters can be easily modified. Numerous scenarios can be therefore simulated and compared. With the increase in computing resources, a growing number of studies are based on modeling tools. To ensure the accuracy of the results, simulations need to be evaluated and compared to experimental measurements.

This section presents different types of models designed to simulate air quality and urban climate with or without consideration of urban trees.

1.3.1 Modeling urban vegetation and their effect on air quality

Chemistry-Transport Models (CTMs) (CHIMERE (Menut et al., 2021), Polair3D (Boutahar et al., 2004), WRF-Chem (NOAA/ESRL, 2023), CMAQ (Byun and Schere, 2006; Appel et al., 2021), MOCAGE (Peuch et al., 1999) etc.) can be used to compute air pollutant concentrations on eulerian cell grids over urban areas. However, concentrations are averaged over meshes with horizontal resolutions typically larger than one kilometer, and they can not represent the heterogeneities of pollutant concentrations within a grid, such as the high concentrations found at the street level (Lugon et al., 2020, 2021a). In addition, the land-use at the city scale is of urban type and no vegetation effect is usually modeled. CTMs can be used to provide background concentrations for local models (Fig. 1.4). They can also be coupled to street models to account for more local processes (Lugon et al., 2020).

At the local scale (street and neighborhood), Computational Fluid Dynamics (CFD) codes such as Fluent (<https://www.ansys.com/en-gb/products/fluids/ansys-fluent>), OpenFOAM (<https://www.openfoam.com/>) and code_saturne (<https://www.code-saturne.org/cms/web/>; Archambeau et al. (2004)), are used to simulate pollutant dispersion and air quality with a fine resolution in the meter range (Blocken et al., 2013; Tominaga and Stathopoulos, 2013; Pantusheva et al., 2022). Some are coupled with chemistry and aerosol dynamics models to represent the formation of secondary pollutants and aerosols (Zhong et al., 2016; Lin et al., 2023b). Many models contain a representation of the vegetation effects and most of the studies focus on the aerodynamic effect of trees in a street canyon (Buccolieri et al., 2009; Huang et al., 2019; Yang et al., 2020a; Lin et al., 2023a) or in an existing neighborhood (Buccolieri et al., 2011; Amorim et al., 2013). Some studies also take into account the dry deposition on vegetated surfaces (Vos et al., 2013; Jeanjean et al., 2016; Santiago et al., 2017b; Xue and Li, 2017), the thermal effects (Buccolieri et al., 2018; San Jose and Perez-Camanyo, 2022) and the BVOC emissions (Moradpour and Hosseini, 2020; Wang et al.,

2023). Studies on the impact of vegetation are carried out in the two main types of CFD model: Reynolds-Averaged Navier–Stokes (RANS) models (Gromke and Blocken, 2015; Santiago et al., 2017a) and Large-Eddy Simulation (LES) (Salim et al., 2011; Moonen et al., 2013). CFD models can simulate local variations in wind speed, turbulence and pollutant concentrations. However, due to their accuracy, they require a detailed representation of the urban geometry, and computer resources that are too extensive to simulate an entire city.

To simulate air quality at the street level but covering large areas such as neighborhoods or cities, parameterized models are developed. They assume a simplified street geometry and processes such as transport and pollutant deposition which are parameterized. There are different types of models: street canyon models (SIRANE (Soulhac et al., 2011, 2012, 2017), MUNICH (Kim et al., 2018, 2022)), gaussian (ADMS-Urban (McHugh et al., 1997; Carruthers et al., 2000; Stocker et al., 2012)) or mixed (street canyon with gaussian emissions) (OSPM (Berkowicz, 2000)). Trees are not included in parameterized models because first, they need parameterizations of the different tree effects at the street scale and then, precise information on trees (location, size etc.) is needed at the city scale.

Finally, another method to simulate city-scale pollution is to use a catalog of pre-computed simulations (Berchet et al., 2017). Hourly concentration maps are produced by selecting the hourly situation from the pre-calculated catalog that best matches the meteorological variables.

1.3.2 Modeling urban vegetation and their effect on climate

As for air-quality models, climatic models are of various resolutions and types. As presented by Yang et al. (2019), models used to simulate the effect of vegetation on the micro-climate can be divided into two categories: Energy Balance Models (EBMs) and Computational Fluid Dynamics (CFD) models. EBMs (e.g. RayMan (Matzarakis et al., 2007, 2010), SOLWEIG (Lindberg et al., 2008; Lindberg and Grimmond, 2011), green-CTTC (Shashua-Bar and Hoffman, 2002), TEB-Veg (Lemonsu et al., 2012; Redon et al., 2017, 2020)) are based on the law of conservation of energy for a control volume, and make it possible to study many factors of the thermal environment. CFD models (Fluent, OpenFOAM, ENVI-met (<https://www.envi-met.com/>; Bruse and Fleer (1998)), PALM-4U (<https://palm.muk.uni-hannover.de/trac/wiki/palm4u>) etc.) couples explicitly the velocity, temperature, humidity and pollution fields, and resolves the flow field and the energy budget at finer scales compared to EBMs. However, computational cost is much higher and they need a detailed representation of urban geometry. Within the two types of models, the plant description can be more or less complex (Yang et al., 2019).

1.4 Objectives of the PhD thesis and problematic

Among the types of urban vegetation highlighted in nature-based solutions, roadside trees are of major interest for several reasons. They are a tall vegetation type with large leaf surface which effectively improves thermal comfort through both evapotranspiration and shading. However, due to these same characteristics, they can limit air flows and dispersion of pollutants emitted in streets. Secondly, unlike green walls and roofs, urban trees are already widely planted in cities. This study therefore focuses on urban trees, and more specifically on roadside trees. The objective is to set up a modeling chain to simulate the various effects of trees on meteorology and air quality at the street and city scale, and understand the links between them. The urban micro-meteorology may not only affect the formation of secondary pollutants, it may also influence the tree biogenic emissions of volatile organic compounds. Those may also be very much impacted by water stress. To this end, multi-scale and several types of models are coupled (Fig. 1.11) and applied over the city of Paris.

Chapter 2 is dedicated to the parametrizations of air flows in street canyons with and without trees. The parameterizations are developed for a large range of street and tree characteristics and depend on the meteorology above the street. Then, the Chapter 3 presents the development of a bottom-up inventory of biogenic emissions from urban tree trees (dash-dotted arrows in Fig. 1.11) and the impact on regional air quality. Biogenic emissions are computed by combining different databases and modeling tools, and are then integrated in the mesoscale air-quality model (CHIMERE) to quantify their impact on air quality over the Paris region and during June and July 2022.

In Chapter 4, the impact of trees on local and regional air quality is estimated without taking into account the potential modification of micro-meteorology. To do so, biogenic emissions of road side trees are integrated at the street level in the Paris street network in MUNICH (dashed arrows in Fig. 1.11). The aerodynamical effect of tree parameterized in Chapter 2 is considered as well as the dry deposition of gas and particles on tree leaves. The three effects of trees on air quality at the street level (BVOC emissions, aerodynamic effect and dry deposition on leaves) are quantified by CHIMERE/MUNICH simulations performed on the same 2-month period and over the Paris street network.

Finally, the Chapter 5 evaluates the impact of the street micro-meteorology both with and without trees on street pollutant concentrations. The calculation of biogenic emissions, which is closely dependent on micro-meteorology, tree hydraulic functioning and water stress, is also refined (dotted arrows in Fig. 1.11). This is done by coupling the air-quality model (MUNICH) to the Town Energy Balance model, that computes the energy budget in the street including vegetation-related processes (TEB-Veg), and the soil-plant-atmosphere continuum model (SPAC) to refine the representation of the water transfers within trees.

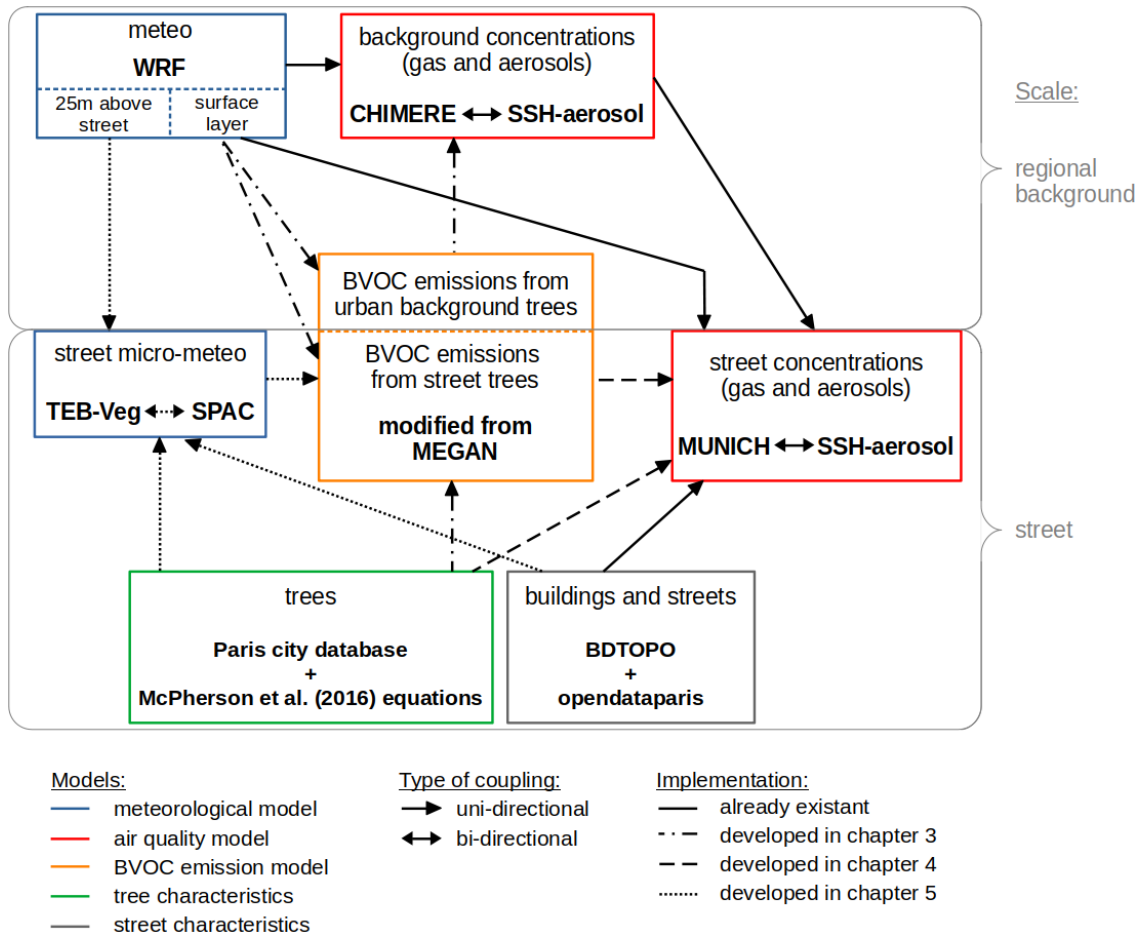


Figure 1.11: Modeling chain developed to simulate the effects of trees on climate and air quality at the street and city scale. Variables are in normal font and models and database in bold.

Chapter 2

Parameterization of air flow in a street with trees

Contents

2.1	Introduction	27
2.2	Parameterization of air flows in street canyons	28
2.2.1	Introduction	29
2.2.2	Materials and Methods	31
2.2.3	Adaptation of a flow parametrization and comparison with existing MU-NICH parametrizations	37
2.2.4	Conclusions	43
2.2.5	Appendices	44
2.3	Parameterization of the tree aerodynamic effect in street canyons	48
2.3.1	Introduction	50
2.3.2	Materials and Methods	51
2.3.3	Quantification of the tree crown effect on horizontal and vertical transfers by Code_Saturne simulations	54
2.3.4	Parameterization of the aerodynamic effect of tree crowns in MUNICH	55
2.3.5	Conclusions	59
2.3.6	Appendices	60
2.4	Conclusion	69





2.1 Introduction

The aim of this chapter is to parameterize the first effect of trees on air quality in MUNICH. First, a new parameterization of air flow in street canyons without tree is developed in MUNICH. This parameterization is based on analytical wind and transfer coefficient vertical profiles designed for sparse canopies, and is adapted to the case of the street canyon based on CFD simulations. The development of this parametrization and a comparison with the existing parametrizations in MUNICH was published in Atmosphere (freely available at <https://doi.org/10.3390/atmos13040527>) and the article is presented in the section 2.2. This parametrization allows us to represent vertical profiles of horizontal wind and vertical exchange coefficient, while being mathematically simple enough to add the effect of trees. The tree aerodynamical effect, i.e. the modification of wind speed and vertical transfer coefficient due to tree leaves in the street, is then parameterized also based on CFD simulations. This work was published in Atmospheric Chemistry and Physics (freely available at <https://doi.org/10.5194/acp-22-9369-2022>) and the article is presented in the section 2.3. The parameterizations use general street and tree characteristics (building height, street width, Leaf Area Index, tree crown height and radius etc.), so they can be applied to any street at any time.

2.2 Parameterization of air flows in street canyons

Article

Parametrization of Horizontal and Vertical Transfers for the Street-Network Model MUNICH Using the CFD Model Code_Saturne

Alice Maison ^{1,2,*} , Cédric Flageul ³ , Bertrand Carissimo ¹ , Andrée Tuzet ² and Karine Sartelet ^{1,*} ¹ CEREA, École des Ponts, EDF R&D, 77455 Marne-la-Vallée, France; bertrand.carissimo@enpc.fr² INRAE, AgroParisTech, UMR EcoSys, Université Paris-Saclay, 78850 Thiverval-Grignon, France; andree.tuzet@inrae.fr³ Curiosity Group, PPRIME Institute, Université de Poitiers, CNRS, ISAE-ENSMA, 86961 Poitiers, France; cedric.flageul@univ-poitiers.fr

* Correspondence: alice.maison@enpc.fr (A.M.); karine.sartelet@enpc.fr (K.S.)

Abstract: Cities are heterogeneous environments, and pollutant concentrations are often higher in streets compared with in the upper roughness sublayer (urban background) and cannot be represented using chemical-transport models that have a spatial resolution on the order of kilometers. Computational Fluid Dynamics (CFD) models coupled to chemistry/aerosol models may be used to compute the pollutant concentrations at high resolution over limited areas of cities; however, they are too expensive to use over a whole city. Hence, simplified street-network models, such as the Model of Urban Network of Intersecting Canyons and Highways (MUNICH), have been developed. These include the main physico-chemical processes that influence pollutant concentrations: emissions, transport, deposition, chemistry and aerosol dynamics. However, the streets are not discretized precisely, and concentrations are assumed to be homogeneous in each street segment. The complex street micro-meteorology is simplified by considering only the vertical transfer between the street and the upper roughness sublayer as well as the horizontal transfer between the streets. This study presents a new parametrization of a horizontal wind profile and vertical/horizontal transfer coefficients. This was developed based on a flow parametrization in a sparse vegetated canopy and adapted to street canyons using local-scale simulations performed with the CFD model Code_Saturne. CFD simulations were performed in a 2D infinite street canyon, and three streets of various aspect ratios ranging from 0.3 to 1.0 were studied with different incoming wind directions. The quantities of interest (wind speed in the street direction and passive tracer concentration) were spatially averaged in the street to compare with MUNICH. The developed parametrization depends on the street characteristics and wind direction. This effectively represents the average wind profile in a street canyon and the vertical transfer between the street and the urban roughness sublayer for a wide range of street aspect ratios while maintaining a simple formulation.

Keywords: meteorological modeling; street-network; urban areas

Citation: Maison, A.; Flageul, C.; Carissimo, B.; Tuzet, A.; Sartelet, K. Parametrization of Horizontal and Vertical Transfers for the Street-Network Model MUNICH Using the CFD Model Code_Saturne. *Atmosphere* **2022**, *13*, 527. <https://doi.org/10.3390/atmos13040527>

Academic Editor: Amir A. Aliabadi

Received: 22 December 2021

Accepted: 22 March 2022

Published: 25 March 2022

Publisher's Note: MDPI stays neutral with regard to jurisdictional claims in published maps and institutional affiliations.



Copyright: © 2022 by the authors. Licensee MDPI, Basel, Switzerland. This article is an open access article distributed under the terms and conditions of the Creative Commons Attribution (CC BY) license (<https://creativecommons.org/licenses/by/4.0/>).

1. Introduction

Cities are areas of highly concentrated human activities that induce large amounts of air pollutants emitted by anthropic activities, such as traffic, industry and residential activities. Cities are also heterogeneous environments, and the presence of high buildings represents obstacles that reduce air flow inside streets and limit the dispersion of pollutants emitted within [1–4]. These two processes lead to poor air quality, thus, imposing a risk for human health. In addition, the growing number of people living in cities increases the vulnerability, and massive urbanization has negative consequences on the environment and human health especially during pollution peaks [5–9]. In the case of a street canyon, air

recirculates inside the canyon, as shown by Harman et al. [10] for the wind perpendicular to the street.

Pollutants emitted in the street—by traffic for example—tend to accumulate on the leeward side of the street, and the concentrations at this location may be much higher than the background concentrations [11–13]. Knowing that people spend most of their time indoors, the vertical distribution of pollutant concentrations is also a key research topic. People are not only exposed to air pollution at street pedestrian level but also to air pollution inside buildings, which may be influenced by outdoor pollution and the height levels of the building [14–16].

Models are powerful tools to study air flow and pollutant concentration because the conditions can be fixed and the simulations are easily replicable, thus, allowing the analysis of different processes influencing the concentrations. Currently, chemistry-transport models (CTMs) are widely used at the meso-scale to understand processes, interpret observations and forecast the evolution of pollutant concentrations [17–20]. Informed by emissions inventories, meteorological, initial and boundary conditions, these models use numerical techniques to simulate pollutant transport, chemical transformation in the atmosphere and compute air concentrations and deposition fluxes.

In CTMs, concentrations are averaged over mesh cells with a horizontal resolution ranging from kilometers to hundreds of kilometers. Due to their coarse spatial resolution, CTMs are not able to capture the high pollutant concentrations observed in streets, and thus city-scale models, such as simplified street-network or street-in-grid models are used to represent the street level concentrations [21–26].

Street models use parametrizations to represent the dispersion of pollutants at the street level over a neighborhood or a city. The streets are not discretized finely; however, concentrations are assumed to be homogeneous in each street segment, as in the Model of Urban Network of Intersecting Canyons and Highways (MUNICH) [24,25], or in part of the street (lee side versus wind side, for example, as in the OSPM (Operational Street Pollution Model) [21].

To study wind fields and pollutant dispersion at a local scale (100 m to 1 km), Computational Fluid Dynamics (CFD) are commonly used [27–29]. The simulation domain is composed of grid cells with a resolution ranging from centimeters to meters. To solve air flow in two or three dimensions, several turbulence schemes are used, such as $k - \epsilon$ and Large Eddy Simulation (LES). This type of model allows capturing the complex street micro-meteorology; however, the computational cost is high to study pollutant dispersion at city scale as this requires billions of grids.

As concentrations are assumed to be homogeneous in each street segment, the computational cost associated with MUNICH is low compared to CFD, allowing simulations over a whole city [25]. To model the dispersion of pollutants, the street-network model MUNICH separates air flow into two components related to transfer velocities. First, the horizontal wind speed is assumed to follow the street direction and to be homogeneous across the street. Second, the vertical transfer velocity between the street and the background domain is calculated at the roof level.

These horizontal and vertical air flows depend on the canyon geometry, wind angle, above-street flow and atmospheric stability [30]. Background concentrations above the roughness sublayer can be provided by 3D CTMs, such as Polair3D from the Polyphemus air-quality modeling platform [25,26,31].

The objective of this study is to evaluate the parametrizations that are currently used in MUNICH for the horizontal and vertical transfers as well as to develop a new parametrization as accurate as the existing ones but with a simpler formulation. It is an adaptation of a parametrization originally designed to model flows in sparse and dense vegetated canopies, depending on the leaf area or spacing between trees. The parametrizations are evaluated by comparisons to Computational Fluid Dynamics (CFD) simulations in street canyons.

They are performed with Code_Saturne [32], an open-source code that can represent air and pollutant flows in a street canyon [33]. “It solves the Navier–Stokes equations for 2D, 2D-axisymmetric and 3D flows, steady or unsteady, laminar or turbulent, incompressible or weakly compressible, isothermal or not, with scalars transport” if required (<https://www.code-saturne.org/>, accessed on 17 December 2021).

This code has been adapted to atmospheric flows and can simulate the humid atmosphere with radiative heat transfer (not used here). Code_Saturne has been evaluated with the results of the Mock Urban Setting Test (MUST). This is a near full-scale experiment conducted in Utah’s West Desert area based on the release of a neutral gas in a field of regularly spaced shipping containers [33,34]. In addition, Code_Saturne was used to simulate thermal effect and pollutant dispersion in a real urban neighborhood of Toulouse, France [35] and micro-scale heterogeneities of turbulent variables for different wind directions over a complex semi-urban area located near Paris [36].

In these different studies, the simulated air flow agreed well with the measurements, demonstrating that Code_Saturne was able to accurately simulate airflow and pollutant dispersion over complex urban sites, as well as 2D simplified street canyons. In the present study, Code_Saturne version 6.0 is used. To compare the parametrizations, several simulations are performed with Code_Saturne to consider different street sizes and wind directions. Therefore, the set-up of the model is simplified, and 2D streets are considered to be consistent with the street-network-model approach.

The structure of the paper is as follows. The models MUNICH and Code_Saturne are detailed in Section 2. Then, a new parametrization for horizontal and vertical transfers based on Code_Saturne simulations and Wang [37,38] is proposed for MUNICH and is compared with existing MUNICH parametrizations in Section 3. Our conclusions are provided in Section 4.

2. Materials and Methods

This section first describes the street-network model MUNICH and then the CFD simulations performed with Code_Saturne.

2.1. Description of MUNICH

2.1.1. Street Geometry and Main Hypothesis

As detailed in Kim et al. [24] and Lugon et al. [25], the streets correspond to the volume of the urban canopy, and each street segment is defined by a length L , uniform street width W and height of the buildings H . Each segment is characterized by its aspect ratio calculated as $a_r = \frac{H}{W}$. Air pollutant concentrations are assumed to be homogeneous within each street segment. The wind in the street follows the street direction and determines the advective air flow, which transports pollutants horizontally. They are also transported in and out of the street network by vertical transfer at the top (roof level) of each street segment. The streets are linked to the background concentrations above roof level by a vertical transfer coefficient. Note that the horizontal wind speed and direction may differ from one street segment to another.

2.1.2. MUNICH Existing Parametrizations for Vertical Transfers

The vertical mass vertical flux of pollutants at the roof level is calculated based on a turbulent transfer coefficient [24,39]:

$$Q_{vert} = q_{vert} WL \frac{(C_{street} - C_{bg})}{H} \quad \text{with} \quad q_{vert} = \sigma_W l_m \quad (1)$$

where Q_{vert} is the vertical flux of pollutants at the roof level for the whole street ($\mu\text{g}\cdot\text{s}^{-1}$), q_{vert} is the vertical transfer coefficient ($\text{m}^2\cdot\text{s}^{-1}$) and WL is the exchange surface (m^2). C_{street} and C_{bg} are, respectively, the average street and background air pollutant concentrations ($\mu\text{g}\cdot\text{m}^{-3}$). l_m is the mixing length within the street (m), and σ_W is a velocity scale corre-

sponding to the standard deviation of the vertical wind velocity at roof level ($\text{m}\cdot\text{s}^{-1}$). σ_W is function of the atmosphere stability and the friction velocity above the street u_* ($\text{m}\cdot\text{s}^{-1}$), and is calculated for a neutral atmosphere as [22,40]:

$$\sigma_W = 1.3 u_* \times \left(1 - 0.8 \frac{H}{PBLH} \right) \quad (2)$$

u_* is not computed by MUNICH but is taken as an input data and is equal to the Code_Saturne friction velocity in the present study (Equation (16)). $PBLH$, also an input, is the planetary boundary layer height (m), which is set to 1000 m in the present simulations [41,42]. The σ_W parametrizations for stable and unstable atmospheric conditions can be found in Souhac et al. [22]. The mixing length is assumed to be constant in the street and can be computed in MUNICH either from the Schulte et al. [39] or Souhac et al. [22] parametrizations:

$$l_m = \frac{DH}{1 + a_r} \quad (3)$$

for Schulte et al. [39]

$$l_m = \frac{H}{\sqrt{2\pi}} \quad (4)$$

for Souhac et al. [22]

D is a constant equal to $\frac{2}{\sqrt{2\pi}}$ fixed by assuming that the estimation of l_m from the formulations Schulte et al. [39] and Souhac et al. [22] are equal for $a_r = 1$ [24]. Hereafter, to be able to compare these mixing length parametrizations, they are noted L_{sch} for Schulte et al. [39] and L_{sir} for Souhac et al. [22].

2.1.3. MUNICH Existing Parametrizations for Horizontal Transfers

The horizontal flux of pollutants between the streets, $Q_{in/outflow}$ ($\mu\text{g}\cdot\text{s}^{-1}$), is computed in MUNICH as the product of the average wind speed in the street direction U_{street} ($\text{m}\cdot\text{s}^{-1}$), which can be interpreted as a horizontal transfer velocity, the exchange section HW (m^2) and the average pollutant concentration in the street C_{street} ($\mu\text{g}\cdot\text{m}^{-3}$). Depending on the wind angle φ (angle between the wind direction and the street orientation), this flux can be an incoming or outgoing flux:

$$Q_{in/outflow} = U_{street} HW C_{street} \quad (5)$$

Two different U_{street} parametrizations already exist in MUNICH.

- Exponential attenuation profile (noted U_{exp})

This profile is an empirical parametrization computed from an exponential attenuation of the wind speed at the roof level and is inspired by wind profiles in vegetated canopies. The wind profile is fully dependent on an attenuation coefficient. The higher the attenuation coefficient, the higher the decrease of the wind speed with altitude. Masson [43], Lemonsu et al. [44] and Cherin et al. [45] proposed an attenuation coefficient of $A \times a_r$, where A is a dimensionless constant equal to 0.5 for wind within street canyons. The value of this attenuation coefficient is tested in Section 3.3.2.

Only advection along the street (i.e., the horizontal component of the wind speed in the street direction) is considered in MUNICH (noted U_Y). Therefore, the wind profile is multiplied by $|\cos(\varphi)|$ to select only this component. The exponential profile is computed as (modified from Kim et al. [24]):

$$U_Y(z) = U_{H,\varphi} \exp \left[A a_r \left(\frac{z}{H} - 1 \right) \right] \quad \forall a_r \quad \text{with } U_{H,\varphi} = U_H |\cos(\varphi)|, \quad (6)$$

where U_H is the norm of the horizontal wind speed at the building height H ($\text{m}\cdot\text{s}^{-1}$), which can be calculated either from Macdonald et al. [46] and Grimmond and Oke [47] or Soulhac et al. [22], z is the vertical elevation (m) (upward orientation and $z = 0$ at the ground level), $A a_r$ corresponds to the dimensionless attenuation coefficient.

In MUNICH, the average wind velocity in the street (U_{street}) is obtained by analytically integrating the wind profile between the soil roughness z_{0s} (m) and the building height H (m) as:

$$U_{street} = \int_{z_{0s}}^H U_Y(z) dz = U_{H,\varphi} \times \frac{1}{A a_r} \left(1 - \exp \left[A a_r \left(\frac{z_{0s}}{H} - 1 \right) \right] \right) \tag{7}$$

- SIRANE profile (noted U_{sir})

Soulhac et al. [22,48] developed an analytical solution of the momentum equation in a street canyon by dividing the canyon into two parts: the region influenced by the walls and the region influenced by the ground. In the region influenced by the walls (in the upper part of the canyon), the horizontal and vertical variations of U are separated and, respectively, represented by the functions f and h . h is a function of z and f is function of x , the horizontal distance with a rightward orientation and $x = 0$ at the left wall level of the street (a different reference is used in Code_Saturne because the wind profile is also defined above the buildings, see Section 2.2.1). In the region influenced by the ground, the walls have no influence on the wind profile; however, the wind speed at $z = \delta$ and at all x is taken to ensure the match between the profiles of the two regions.

In the region influenced by the walls ($\delta \leq z \leq H$ and $z_{0s} \leq x \leq W - z_{0s}$):

$$U(x, z) = U_m f(x/\delta) h(z/\delta) \tag{8}$$

$$f(x/\delta) = \frac{J_1(C)Y_0(Cx/\delta) - J_0(Cx/\delta)Y_1(C)}{J_1(C)Y_0(C) - J_0(C)Y_1(C)} \tag{9}$$

$$h(z/\delta) = \exp \left[\frac{C}{\sqrt{2}} \left(\frac{z - H}{\delta} \right) \right] \tag{10}$$

In the region influenced by the ground ($z_{0s} \leq z < \delta$ and $z_{0s} \leq x \leq W - z_{0s}$):

$$U(x, z) = U(x, \delta) \times \frac{\ln \left(\frac{z}{z_{0s}} \right)}{\ln \left(\frac{\delta}{z_{0s}} \right)} \tag{11}$$

$$\text{with } U(x, \delta) = U_m f(x/\delta) \exp \left[\frac{C}{\sqrt{2}} \left(\frac{\delta - H}{\delta} \right) \right] \tag{12}$$

where J_0, J_1, Y_0 and Y_1 are the first and second kind Bessel functions of order 0 and 1. Unlike U_{exp} , the SIRANE profile is not calculated from the average wind speed at $z = H$, U_H and, instead, from the wind speed at the top of the street in the middle, U_m (at $z = H$ and $x = W/2$). U_m is determined from the shear stress and friction velocity values at $z = H$. Knowing the wall roughness z_{0s} , C has to be determined by an iterative method (see Equation (14) with γ as the Euler constant equal to 0.577).

The wind profile is then integrated in each region of the canyon to compute the average horizontal wind speed in the street [22,24,48]:

$$U_{street} = U_m |\cos(\varphi)| \frac{\delta^2}{HW} \left[\frac{2\sqrt{2}}{C} (1 - B_2) \left(1 - \frac{C^2}{3} + \frac{C^4}{45} \right) + B_2 \frac{2B_1 - 3}{B_1} + \left(\frac{W}{\delta} - 2 \right) \frac{B_1 - 1}{B_1} \right] \tag{13}$$

$$\text{with } \begin{cases} B_1 = \ln\left(\frac{\delta}{z_{0s}}\right) \\ B_2 = \exp\left[\frac{C}{\sqrt{2}}\left(1 - \frac{H}{\delta}\right)\right] \\ U_m = u_* \sqrt{\frac{\pi}{\sqrt{2}k^2 C}} \left[Y_0(C) - \frac{I_0(C) Y_1(C)}{I_1(C)} \right] \\ C \text{ solution of } \frac{\delta}{z_{0s}} = \frac{2}{C} \exp\left[\frac{\pi}{2} \frac{Y_1(C)}{I_1(C)} - \gamma\right] \\ \delta = \min(H, W/2) \end{cases} \quad (14)$$

Note that the vertical wind profiles shown in Section 3.3.2 are determined by averaging the two-dimensional profile $U(x, y)$ through the street width (along the x axis) and by multiplying it by $|\cos(\varphi)|$ to select only the component in the Y axis direction:

$$U_Y(z) = |\cos(\varphi)| U(z) = |\cos(\varphi)| \int_{x=z_{0s}}^{x=W-z_{0s}} U(x, z) dx \quad (15)$$

where z_{0s} (m) is the wall roughness length equal to the ground street roughness.

See Soulhac et al. [48] for the detailed computation of the wind profile. Note that the SIRANE model is not used directly in this study; however, the SIRANE q_{vert} and U_{street} parametrizations are available in MUNICH from the formulations of Soulhac et al. [22].

U_{exp} computation is simple; however, Castro [49] shows that this parametrization is not well adapted to reproduce spatially-averaged mean velocity profiles within the urban canopy. Additionally, the no-slip condition at the ground is not satisfying and leads to an overestimation of the wind speed compared to Code_Saturne simulations (see Section 3). U_{sir} gives more realistic wind profiles, but the computation is complex due to the iterative method necessary to compute the variable C . A new parametrization is added in MUNICH to compute the wind and vertical transfer coefficient profiles: the Wang [37,38] parametrization for the sparse vegetated canopy is adapted to the urban canopy based on Code_Saturne simulations. The advantages of using this parametrization are presented in Section 3.

2.2. Description of the CFD Simulations

2.2.1. Street Canyon Geometry

In the CFD code Code_Saturne, the computational domain is represented by a geometry and a mesh. In the present study, three street canyons are considered: a wide street canyon (WC) with the same characteristics as the one used in the study of Kim et al. [24], an intermediate canyon (IC) and a narrow canyon (NC). Their main characteristics are presented in Table 1 and Figure 1:

Table 1. Characteristics of the three canyons studied.

Canyon	Building Height H (m)	Street Width W (m)	Street Aspect Ratio a_r (-)	Reference Height $z_{ref} = H + 17$ (m)	Maximum Height of the Domain (m)
WC	8.5	27.5	0.3	25.5	25.5
IC	14.0	27.5	0.5	31.0	42.0
NC	27.5	27.5	1.0	44.5	82.5

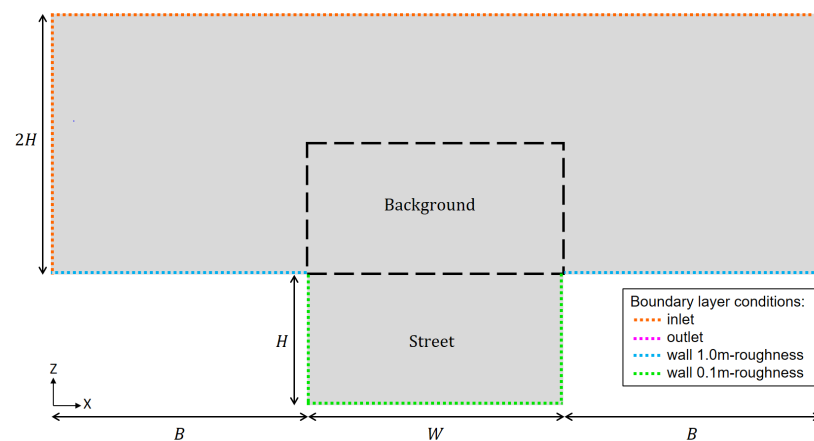


Figure 1. 2D scheme of the canyon geometry with the street and background domain borders, and the boundary conditions.

Code_Saturne simulations are performed in a periodic 2D-canyon of length $L = 1$ m. This configuration is equivalent to an infinite street. The periodicity in the Y direction enables simulations with a wind that is not perpendicular with respect to the canyon axis. The flow and the wind speed vector are 3D. Note that the building height H varies, but the street and building widths (W and B) are constant for the three canyons and equal to 27.5 m.

The mesh used is homogeneous (hexahedral elements) with only one cell for the discretization in the Y direction. The size of each cell in the X and Z directions is 0.5×0.5 m. To compare to MUNICH, the values of the fields averaged over a given cell are located at the center of the cell. The present configuration does not reproduce the complex 3D effects (e.g., variations of width and height of buildings or obstacles in the canyon) encountered in real applications. However, it is suited for comparison with the homogeneous street hypothesis used in MUNICH.

To simplify the reading of the figures, a color code is introduced: red symbols for the wide canyon (WC), purple ones for the intermediate canyon (IC) and blue ones for the narrow canyon (NC). A list of the abbreviations, parameters and variables used can be found in Appendix A.

2.2.2. Set-Up of the Simulations

- Turbulence closure and fluid properties

The $k - \varepsilon$ linear production turbulence model is used in which the Reynolds-averaged Navier–Stokes equations for momentum (U), turbulent kinetic energy (k) and the dissipation rate (ε) are solved. The equations used are presented in Zaïdi et al. [36], Katul et al. [50] and Guimet and Laurence [51]. The atmosphere is assumed to be thermally neutral and dry. The air temperature is set to 293.15 K, and there is no radiative heat transfer. The air properties are summarized in Table 2:

Table 2. Air properties used in the Code_Saturne simulations.

Parameter	Value	Unit
Temperature	293.15	K
Pressure	101,325.0	Pa
Density	1.204	$\text{kg}\cdot\text{m}^{-3}$
Viscosity	1.83×10^{-5}	Pa·s
Specific heat	1017.24	$\text{J}\cdot\text{kg}^{-1}\cdot\text{K}^{-1}$
Thermal conductivity	0.02495	$\text{W}\cdot\text{m}^{-1}\cdot\text{K}^{-1}$

- Initial and boundary conditions

At the inlet (see Figure 1), a logarithmic wind profile is assumed. The norm of the horizontal wind speed ($\|\vec{u}\| = \sqrt{U_X^2 + U_Y^2} = U$) is equal to zero at the roof level ($U(H) = U_H = 0$) [52], and the friction velocity (u_*) is calculated as detailed below. This friction velocity is used in both Code_Saturne and MUNICH:

$$U(z) = \frac{u_*}{\kappa} \times \ln\left(\frac{z - H + z_0}{z_0}\right) \text{ with } z \geq H \text{ and } u_* = \frac{\kappa \times U_{ref}}{\ln\left(\frac{z_{ref} - H + z_0}{z_0}\right)} \quad (16)$$

where κ is the Von Kármán constant ($\kappa = 0.42$) and z_{ref} is the reference altitude equal to $z_{ref} = H + 17$ m (top of the WC domain). The roof roughness length, z_0 , does represent not only the roughness length of the roof surface but also the roughness of the city, and therefore it is taken equal to 1.0 m [53]. The local roughness length of the walls and road surfaces within the canyon, considering typically urban features (balcony, windows, pavement...), is set to 0.10 m (Figure 1).

The wind velocity above the street at $z = z_{ref}$, U_{ref} , is set to $5 \text{ m}\cdot\text{s}^{-1}$ and the friction velocity u_* is then equal to $0.73 \text{ m}\cdot\text{s}^{-1}$. The direction of the above-roof wind can be modified by setting the angle between the wind direction and the street orientation ($U_X(z) = \sin(\varphi)U(z)$ and $U_Y(z) = \cos(\varphi)U(z)$). Note that, as the canyon is symmetrical, simulations are performed with φ ranging between 0 and 90° , where 0° corresponds to a wind parallel to the street and 90° is perpendicular.

The inlet boundary condition associated with the passive tracer is assumed to correspond to a zero concentration (fresh air). Regarding the turbulent variables k and ϵ , the logarithmic velocity profile is associated with a constant turbulent kinetic energy and a variable dissipation rate as follows:

$$k = \frac{u_*^2}{\sqrt{C_\mu}} \quad \text{and} \quad \epsilon(z) = \frac{u_*^3}{\kappa(z - H + z_0)} \quad (17)$$

with $C_\mu = 0.09$ as a dimensionless constant of the $k - \epsilon$ model. The proposed configuration with a fully developed inlet profile provides a simple workbench to study the transport inside the street canyon, in line with our objective. This does not take into account possible interactions between adjacent street canyons that one could investigate using an array of canyons [54].

The simulations run until the flow reaches a stationary state. To reach a stationary state faster, a variable time step in space and time is used with an initial time step of 0.5 s, a maximum Courant number of 1.5 and a maximum Fourier number of 10 (see documentation at <https://www.code-saturne.org/>, accessed on 17 December 2021). This results in larger time step when the velocity is lower and smaller time step when the velocity is higher.

2.2.3. Calculation of Vertical and Horizontal Transfers in Code_Saturne for Comparison to MUNICH

To estimate the vertical transfer between the street and the background domain, a passive tracer is emitted in each cell of the street canyon ($z \leq H$, see Figure 1) with a stationary emission rate $e = 1000 \text{ }\mu\text{g}\cdot\text{s}^{-1}$ for a street canyon with a unit length L . The wind angle is assumed to be normal to the street orientation ($\varphi = 90^\circ$), and thus the horizontal transfers are negligible. The initial street and background tracer concentration is zero.

At the end of the simulation, the tracer concentration is averaged in the street and in the background zone ($B \leq x \leq B + W$ and $H \leq z \leq 2H$, see Figure 1) to reproduce the MUNICH homogeneous street assumption. Knowing C_{street} , C_{bg} and e , a transfer coefficient can be calculated from these simulations that allows us to compare both models. Chemistry and deposition on built surfaces are not considered, as the aim of the study is to parametrize the air flow for dispersion modeling.

To study horizontal transfers, the horizontal wind speed in the street direction (Y axis in Code_Saturne simulations) is averaged across the street in the X -direction. The vertical profile in every mesh cell on the X axis is calculated (once every 0.5 m). The 55 profiles are then averaged over the street width to obtain the averaged vertical wind profile. The averaged wind speed in the street U_{street} is calculated by averaging the Code_Saturne wind speed over the street height and width (for each mesh between $0 \leq z \leq H$ and $B \leq x \leq B + W$). As this work focuses on the wind attenuation inside the street canyon, all the wind profiles and average wind speed are normalized by $U_{H,\varphi}$.

3. Adaptation of a Flow Parametrization and Comparison with Existing MUNICH Parametrizations

Wang [37,38] developed a formulation of the wind profile in sparse vegetated canopies. This is presented in Section 3.1 and then adapted to urban street canyons based on Code_Saturne simulations in Sections 3.2 and 3.3 for the vertical and horizontal transfers, respectively. In those sections, the parametrization developed is also compared to MUNICH's existing one and to Code_Saturne simulations. To illustrate the effect of the parametrization on concentrations, a comparison of Code_Saturne and the MUNICH simulated tracer concentrations is performed in Appendix B.

3.1. Flow in Dense and Sparse Vegetated Canopies

Wang [37] developed an analytical resolution of the momentum equations assuming a first-order closure for a homogeneous canopy under a thermally neutral atmospheric boundary layer. This method is suitable to compute wind and transfer coefficient profiles in dense as well as in sparse canopies, which is particularly convenient to simulate air flows in sparse canopies, such as a street canyon with few trees. The profile is computed from the boundary conditions $U(z_{0s}) = 0$ and $U(H) = U_H$ [37]. Parametrizations of the characteristic length and wind attenuation coefficient presented above were derived from Wang [37,38] and adapted to the street canyon based on CFD simulations.

The vertical profile is computed as an attenuation of the wind speed in the street direction and at the roof level, $U_{H,\varphi}$ as:

$$U_Y(z) = U_{H,\varphi} [C_1 I_0(g(z)) + C_2 K_0(g(z))] \tag{18}$$

where C_1 and C_2 are integration coefficients, and I_0 and K_0 are the first and second type modified Bessel functions of order 0. As with U_{exp} , the wind speed at the roof level U_H has to be multiplied by $|\cos(\varphi)|$ to select only the component of the wind speed in the street direction. The function g is calculated as [37,38]:

$$g(z) = 2\sqrt{\alpha \frac{z}{H}} \tag{19}$$

and [37]:

$$C_1 = \frac{1}{I_0(g(H)) - I_0(g(z_{0s})) K_0(g(H)) / K_0(g(z_{0s}))} \quad \text{and} \quad C_2 = -\frac{C_1 I_0(g(z_{0s}))}{K_0(g(z_{0s}))} \tag{20}$$

α can be interpreted as a dimensionless attenuation coefficient independent of z and as a function of the frontal area of canopy elements per ground area, also called the frontal area index (FAI) [38]:

$$\alpha = \frac{C_D C_u FAI}{\kappa S_H} \tag{21}$$

C_D is the canopy drag coefficient, and C_u is an empirical dimensionless parameter independent of height but dependent on the canopy density. For vegetated canopies, FAI is considered to be half of the Leaf Area Index (leaf surface per ground area). $C_D C_u$ will be parametrized as a function of the building frontal area per ground area based on

Code_Saturne simulations in Section 3.3.1. s_H is a dimensionless factor representing the effect of canopy elements on the mixing length [37,38] (see Equations (22) and (23)).

The mixing length is parametrized as [37]:

$$\frac{1}{l_m} = \frac{1}{\kappa z} + \frac{1}{l_c} \implies l_m = \kappa z \frac{l_c}{l_c + \kappa z} = \kappa z s(z) \tag{22}$$

where κz is the mixing length over a rough bare soil without canopy and l_c is the characteristic length of the canopy elements, corresponding to the mixing length of the canopy alone. To solve the system, the value $s(z)$ is taken at $z = H$ and assumed to be constant in the street:

$$s_H = s(H) = \frac{l_c}{l_c + \kappa H} \tag{23}$$

where l_c is calculated based on Wang [38] considering that l_c is inversely proportional to $C_D \lambda_F / H$:

$$l_c \propto \frac{H}{C_D \lambda_F} \tag{24}$$

This characteristic length is modified in the next section to adapt the mixing length profile to the transfer in a street canyon.

3.2. Vertical Transfers

3.2.1. Vertical Transfer Coefficient Parametrization

Street canyons could also be considered as sparse or dense canopies. As shown by Oke [55], the flow regime in the street depends on the street aspect ratio. Thus, to adapt the Wang [37,38] equations to street canyons, the density of the canyon is estimated with the street aspect ratio a_r , which could be viewed as the local frontal area density and which is equal to the wall area of buildings (HL) divided by the street area (WL). This formulation assumes that the flow reduction in the street is independent of the building width.

To calculate the vertical transfer coefficient adapted from Wang [37,38], the mixing length is first computed at the roof level ($z = H$). Then, to account for atmospheric stability, it is multiplied by σ_W , which includes the friction velocity and the stability function of Soulhac et al. [22]. The vertical transfer coefficient at the roof level is, therefore, equal to:

$$q_{vert} = \sigma_W l_m = \sigma_W \kappa H s_H \tag{25}$$

s_H is calculated from Equation (23) and as the building drag coefficient C_D is complex to determine for street canyons, l_c is computed with a proportionality constant E that includes C_D :

$$l_c = E \frac{H}{a_r} = E W_r \tag{26}$$

Based on Code_Saturne simulations, the value $E = 0.5$ gives a better fit for q_{vert} . The building characteristic length is half the street width and is independent of H . However, s_H is a function of H through the κH term. This modified l_m parametrization based on Wang [37] and Code_Saturne simulations is called, hereafter, L_{mw} .

3.2.2. Comparison of MUNICH Vertical Transfer Coefficient Parametrizations with Code_Saturne Simulations

Figure 2 shows a comparison of the normalized vertical transfer coefficient ($q_{vert} / (u_* H)$) calculated with MUNICH parametrizations (including the method developed based on Wang [37,38]) and simulated with Code_Saturne. The relative deviations for each canyon are presented in Table 3 (see Appendix C for the relative deviation calculation).

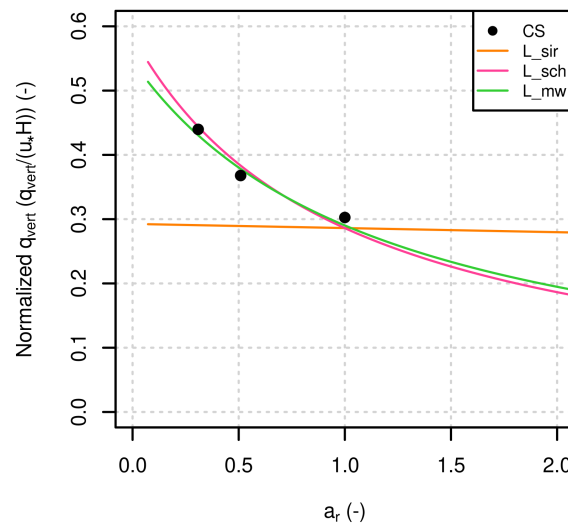


Figure 2. Comparison of the normalized vertical transfer coefficient ($q_{vert}/(u_* H)$) between Code_Saturne (CS), Soulhac et al. [22] (L_sir), Schulte et al. [39] (L_sch) and modified Wang [37] (L_mw) depending on a_r .

Table 3. The q_{vert} relative deviation (%) between Code_Saturne and MUNICH parametrizations for the three canyon heights.

Canyon	L_sir [22]	L_sch [39]	L_mw
WC	−33.9	0.9	−2.1
IC	−21.3	4.2	2.8
NC	−5.4	−5.5	−4.1

L_sir considers a mixing length proportional to the street length (Equation (4)), and thus the normalized q_{vert} is almost constant with a_r (the small variation is due to the term H in σ_W) (Figure 2). L_sir gives a good estimation of q_{vert} for NC but overestimates the concentrations for WC and IC (Table 3). For L_sch and L_mw, the normalized q_{vert} are similar and are close to the Code_Saturne estimation for the three canyons (Figure 2 and Table 3). This parametrized l_m will be used in the next section to compute $U_Y(z)$ and U_{street} .

3.3. Horizontal Transfers

3.3.1. Horizontal Wind Speed Parametrization

To find a relation between α and the street aspect ratio, simulations with varying wind directions φ were performed in Code_Saturne for the three street canyons considered. Figure 3a–c presents the vertical profiles of the wind in the street direction simulated in Code_Saturne for the three canyons and for the varying wind angle φ . Figure 3d presents the average wind speed U_{street} associated with those wind profiles.

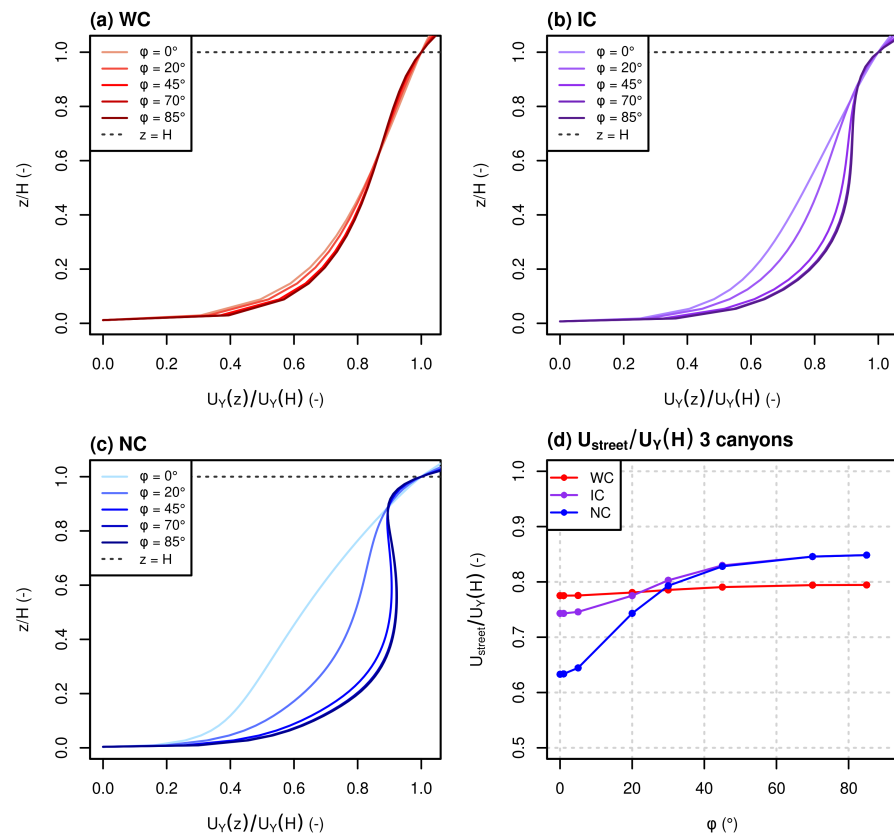


Figure 3. Comparison of the Code_Saturne vertical profile of wind speed in the street direction ($U_V(z)$) normalized by the wind speed at the roof level ($U_{H,\varphi}$) for different wind angle (φ) and for (a) WC, (b) IC and (c) NC. (d) Comparison of the Code_Saturne average wind speed in the street (U_{street}) normalized by $U_{H,\varphi}$ depending on φ and for the three canyons.

Figure 3 shows that the dependence of the wind profiles to φ is limited for WC and increases when the canyon aspect ratio increases. For IC and NC, the wind attenuation in the street, calculated with the ratio $U_{street} / U_{H,\varphi}$, decreases when the wind tends to be parallel to the street. Based on these Code_Saturne simulations, the Wang [38] formulation of the $C_D C_u$ term in Equation (21) is modified to parametrize the attenuation of the wind speed in a street canyon. As for l_c (Equation (26)), C_D and C_u are gathered into a variable called C_B . Note that the s_H coefficient parametrized based on vertical transfers was used in α equation (Equation (21)). To consider the effects of the wind angle on wind attenuation in the street, C_B is a function of φ and a_r deduced from Code_Saturne simulations:

$$\alpha = \frac{C_B a_r}{\kappa s_H} \quad \text{with } C_B = 0.31[1 - \exp(-1.6 a_r)] f_\varphi \tag{27}$$

$$\text{and } f_\varphi = \begin{cases} |\cos(2\varphi)|^3 & \text{if } \varphi = 0^\circ \pm 45^\circ \\ 0 & \text{if } \varphi = 90^\circ \pm 45^\circ \end{cases} \tag{28}$$

f_φ is zero when the wind is perpendicular to the street plus or minus 45° ($45 < \varphi < 135^\circ$ or $225 < \varphi < 315^\circ$) and varies with φ when the wind is parallel to the street plus or minus 45° ($0 \leq \varphi \leq 45^\circ$ or $135 \leq \varphi \leq 225^\circ$ or $315 \leq \varphi \leq 360^\circ$). This modified U_{street} parametrization based on Wang [37,38] and Code_Saturne simulations is called U_{mw} .

Figure 4 presents (a) the variation of α as a function of φ and for the three canyons and (b) as a function of the street aspect ratio for the case $\varphi = 0^\circ$. It shows that the parametrized α is slightly overestimated for WC compared to Code_Saturne. For IC and NC, the parametrized α agrees well with Code_Saturne. Finally, the Wang profile (Equation (18)) is integrated between $z = z_{0_s}$ and $z = H$ to calculate U_{street} .

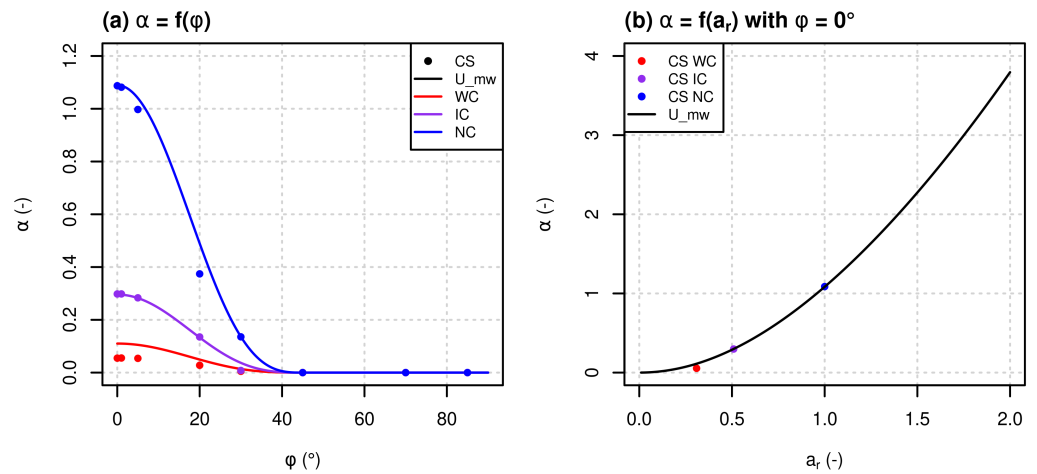


Figure 4. Comparison of the wind speed attenuation coefficient (α) between Code_Saturne and the modified Wang [37,38] parametrization (U_{mw}) (a) depending on ϕ and (b) canyon aspect ratio (a_r) in the $\phi = 0^\circ$ case for the three canyons.

3.3.2. Comparison of MUNICH Horizontal Wind Profiles to Code_Saturne Simulations

Figures 5 and 6 compare, respectively, the U_{street} and wind speed profiles between Code_Saturne and MUNICH parametrizations. The Normalized Mean Absolute Error (NMAE) and Bias (NMB) (Appendix C) are calculated for each canyon and for all angles ϕ in Table 4 to compare MUNICH parametrized with Code_Saturne simulated U_{street} .

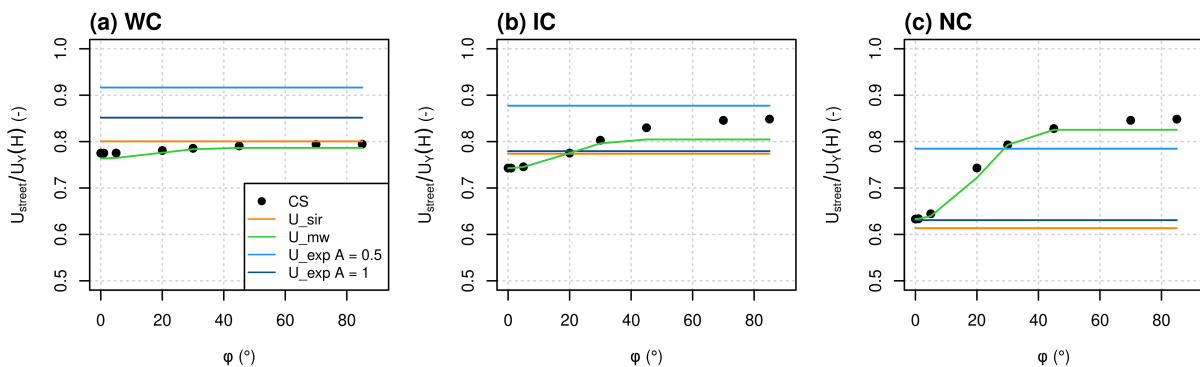


Figure 5. Comparison of U_{street} normalized by $U_{H,\phi}$ between Code_Saturne and the different MUNICH parametrizations for (a) WC, (b) IC and (c) NC and depending on ϕ .

Table 4. Normalized Mean Absolute Error (NMAE) and Bias (NMB) (%) between Code_Saturne and MUNICH parametrized U_{street} for the three canyons studied and for all ϕ ($n = 8$).

Canyon	U_exp A = 0.5		U_exp A = 1		U_sir		U_mw	
	NMAE	NMB	NMAE	NMB	NMAE	NMB	NMAE	NMB
WC	16.9	16.9	8.6	8.6	2.1	2.1	1.0	-1.0
IC	10.8	10.8	5.1	-1.6	5.1	-2.3	1.9	-1.9
NC	11.1	5.2	15.5	-15.5	17.8	-17.8	1.2	-1.2

Figures 5 and 6 and Table 4 show that the U_{exp} profile with an attenuation coefficient of $a_r/2$ as suggested by Masson [43] and Cherin et al. [45] overestimates the wind speed in the street for WC and IC. For NC, it gives a rather good estimation for $\phi \approx 30^\circ$ but overestimates the wind attenuation in the street for smaller ϕ and underestimates it for larger ϕ . U_{sir} and U_{exp} profiles with a coefficient attenuation equal to a_r give better results for WC, IC and NC for $\phi < 5^\circ$. For U_{exp} profiles, the no-slip condition at the ground is not satisfied ($U_Y(z_0) \neq 0$),

and the wind speed near the ground is largely overestimated. The no-slip condition at the ground is satisfied only with a high attenuation coefficient (above 15).

U_{sir} and U_{mw} parametrizations can be both interpreted as a mixed profile that tends to a logarithmic profile when the street aspect ratio is close to zero and to an exponential attenuation profile when the street aspect ratio increases. Unlike the U_{exp} profile, the no-slip condition at the ground is always satisfied. As the U_{mw} profile has been modified to account for the effect of the wind angle on the wind attenuation in the street, it gives values that are close for the wind profiles and U_{street} compared to Code_Saturne for every φ .

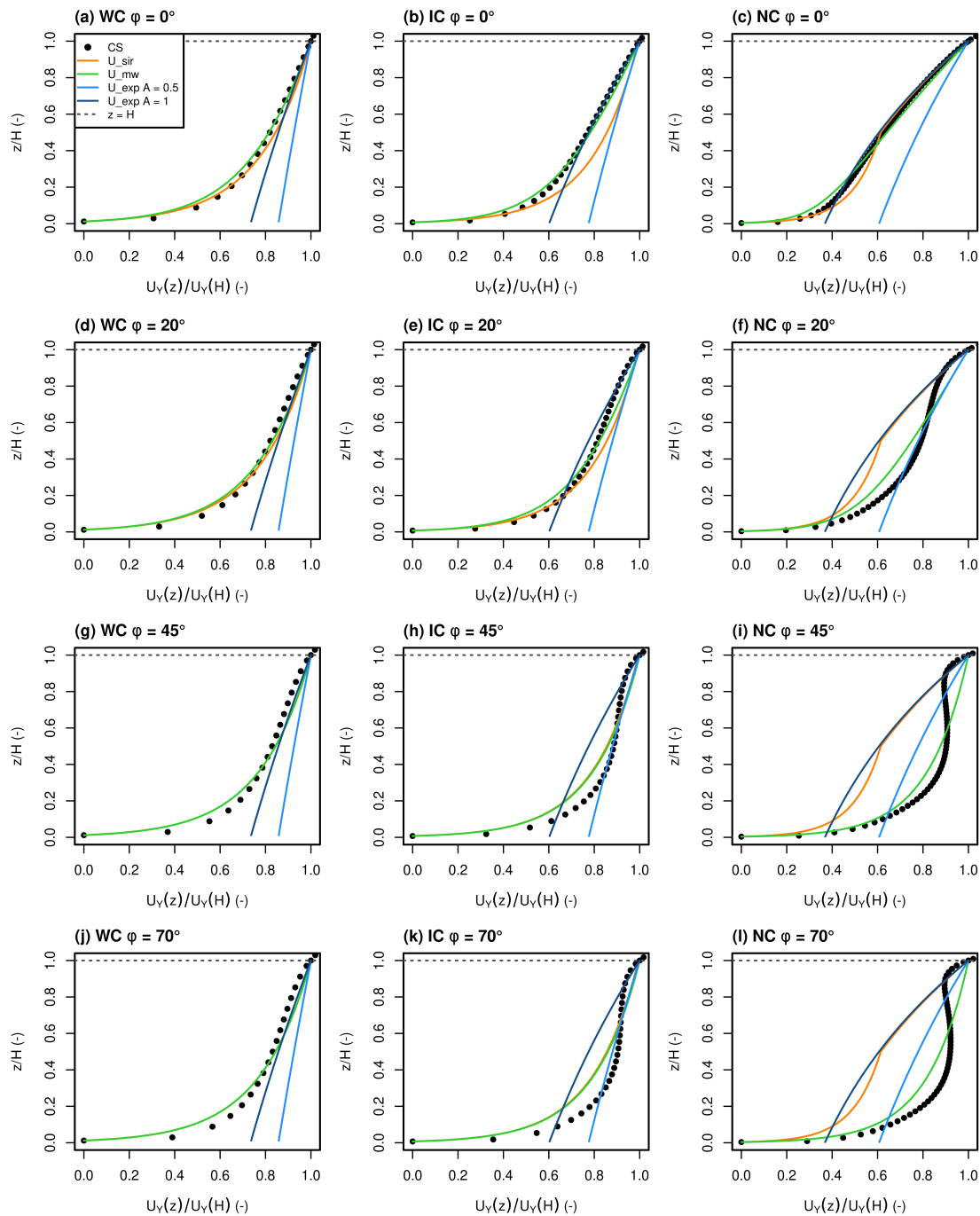


Figure 6. Comparison of $U_Y(z)$ normalized by $U_{H,\varphi}$ between Code_Saturne and the different MU-NICH parametrizations for (a,d,g,j) WC, (b,e,h,k) IC, (c,f,i,l) NC and for (a–c) $\varphi = 0^\circ$, (d–f) $\varphi = 20^\circ$, (g–i) $\varphi = 45^\circ$ and (j,k,l) $\varphi = 70^\circ$.

4. Conclusions

A parametrization that was originally developed for flow in sparse and dense vegetated canopies was adapted to represent the flow in street canyons in the Model of Urban Network of Intersecting Canyons and Highways (MUNICH) based on CFD simulations performed with the Code_Saturne code. The different MUNICH flow parametrizations and Code_Saturne simulations were compared by spatially averaging the wind speed and the passive tracer concentration in the street and the background domains.

The newly adapted parametrization is based on an analytical resolution of the momentum equation within sparse and dense vegetated canopies developed by Wang [37,38]. Assuming a homogeneous canopy, the vertical transfer coefficient profile is proportional to the distance from the ground and depends on the canopy features (the height and frontal area density). The vertical wind speed profile is also a function of the canopy features; this converges to a logarithmic profile in the no-canopy scenario and tends to an exponential profile when the frontal area density of obstacles increases.

The Wang [37,38] equations were adapted to street canyons by modifying the value of two parameters, one involved in the characteristic length calculation and the other one in the wind speed attenuation coefficient. The street canyon aspect ratio was multiplied by a function of the wind angle to consider the variation of the wind speed in the street with this wind angle (only for horizontal transfers). The modified parameters were determined to maximize the agreement with Code_Saturne simulations: for the average wind speed in the street, the normalized mean absolute error ranged from 1.0% to 1.9%, and the normalized mean bias ranged from -1.0% to -1.9% . For the vertical transfer coefficient, the relative deviation ranged from -4.1% to 2.8% .

Compared to other MUNICH parametrizations, this work added a dependence on the wind angle for the horizontal wind speed in the street. The formulation of the wind speed and vertical transfer coefficient is general and valid for a wide range of street-canyon and wind characteristics. Furthermore, it is simple enough to be easily modified to take new features into account. For example, in further work, the tree effect on air flow in street canyons will be parametrized to consider both building and tree effects on the horizontal wind speed and vertical transfer coefficient. In addition, this parametrization developed for pollutant dispersion could also be used in urban climate models to compute heat and water vapor transfers.

Author Contributions: Conceptualization, A.M., K.S., A.T. and C.F.; methodology, A.M., C.F. and B.C.; software, C.F. and B.C.; data curation, A.M.; writing original draft preparation, A.M., K.S. and C.F.; writing review and editing, B.C. and A.T.; visualization, A.M.; supervision, K.S. and C.F.; project administration, K.S. and A.T.; funding acquisition, K.S. and A.T. All authors have read and agreed to the published version of the manuscript.

Funding: This work was partially funded by the sTREEt ANR project (ANR-19-CE22-0012).

Institutional Review Board Statement: Not applicable.

Informed Consent Statement: Not applicable.

Data Availability Statement: The last version of MUNICH source code is available online at <https://doi.org/10.5281/zenodo.4168984> (accessed on 20 December 2021) and <https://github.com/cereal-lab/munich> (accessed on 20 December 2021). For the three 2D canyons considered in the present study, the mesh, the source code and the XML setup file allowing reproduction of the CFD results using Code_Saturne version 6.0 are available online at https://gitlab.enpc.fr/alice.maison/tree_parametrization (accessed on 3 December 2021) and at <http://dx.doi.org/10.17632/fzfrjsz3mv.2> (accessed on 3 December 2021) under the GNU GPL2.0 licence.

Acknowledgments: The authors thank Youngseob KIM and Lya LUGON for their support in the development of the MUNICH model and Martin FERRAND for his support in the understanding of the Code_Saturne model.

Conflicts of Interest: The authors declare no conflict of interest.

Appendix A. Lists of Abbreviations, Variables and Parameters

Table A1. List of abbreviations.

Acronym	Definition
WC	Wide Canyon
IC	Intermediate Canyon
NC	Narrow Canyon
CTM	Chemistry-Transport Model
CFD	Computational Fluid Dynamics

Table A2. List of parameters.

Symbol	Definition	Value	Unit
κ	Von Kármán constant	0.42	-
D	Constant in the vertical transfer coefficient expression [24]	0.45	-
PBLH	Boundary layer height	1000	m
z_0	Code_Saturne city roughness length	1.0	m
z_{0s}	Code_Saturne inside street walls roughness length	0.10	m
u_*	Friction velocity	0.727	$\text{m}\cdot\text{s}^{-1}$
U_{ref}	Wind speed at the reference height	5.0	$\text{m}\cdot\text{s}^{-1}$
e	Passive tracer emission rate	1000	$\mu\text{g}\cdot\text{s}^{-1}$
E	Parameter in modified Wang [38] parametrization	0.5	-

Table A3. List of variables.

Group of Variables	Symbol	Definition	Unit
Street characteristics	H	Building height	m
	W	Street width	m
	B	Building width	m
	L	Street length	m
	V	Street volume	m^3
	a_r	Aspect ratio	-
	z_{ref}	Reference height	m
Horizontal wind speed	U_{street}	Average street horizontal wind speed	$\text{m}\cdot\text{s}^{-1}$
	U	Norm of the horizontal wind speed	$\text{m}\cdot\text{s}^{-1}$
	U_X	Horizontal wind speed in the X direction	$\text{m}\cdot\text{s}^{-1}$
	U_Y	Horizontal wind speed in the Y direction	$\text{m}\cdot\text{s}^{-1}$
	U_H	Average horizontal wind speed at the roof level	$\text{m}\cdot\text{s}^{-1}$
	φ	Wind angle	rad or °
Vertical transfer	A	Constant in the exp. profile attenuation coefficient	-
	Q_{vert}	Vertical flux of pollutant	$\mu\text{g}\cdot\text{s}^{-1}$
	q_{vert}	Vertical transfer coefficient	$\text{m}^2\cdot\text{s}^{-1}$
	σ_W	Standard deviation of the vertical wind speed at $z = H$	$\text{m}\cdot\text{s}^{-1}$
	l_m	Mixing length in the street	m
	C_{street}	Street concentration	$\mu\text{g}\cdot\text{m}^{-3}$
Modified Wang [37] parametrization	C_{bg}	Background concentration	$\mu\text{g}\cdot\text{m}^{-3}$
	α	Wind attenuation coefficient	-
	l_c	Characteristic length in the street	m
	s_H	Characteristic length factor	-
	C_u	Empiric coefficient in α equation	-
	C_B	Function of a_r and φ	-

Appendix B. Comparison of Street-Average Concentrations in Code_Saturne and MUNICH

The average concentration C_{street} of a passive tracer in the street is compared between Code_Saturne and MUNICH on Figure A1. The setup for these simulations is described in the first paragraph of Section 2.2.3.

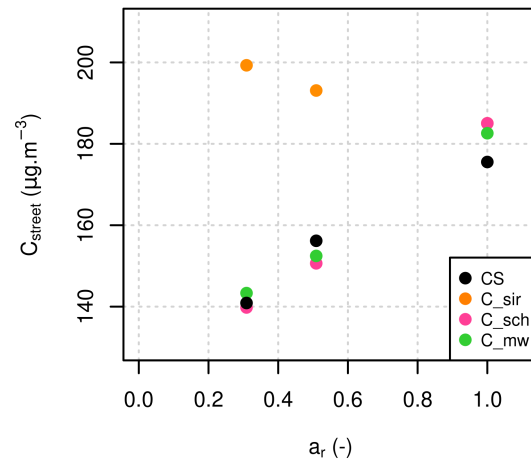


Figure A1. Comparison of average tracer concentration in the street (C_{street}) between Code_Saturne (CS), Soulhac et al. [22] (C_{sir}), Schulte et al. [39] (C_{sch}) and modified Wang [37] (C_{mw}) depending on a_r and for $\varphi = 90^\circ$.

Figure A1 shows a good comparison of the concentrations simulated with the new parametrization and Code_Saturne. Furthermore, C_{street} increases when the street canyon gets deeper, except for the SIRANE parametrization. This increase of C_{street} can be explained by the emission rate, which is the same in the three streets, and the vertical transfer coefficient, which decreases when a_r increases. C_{street} does not increase in SIRANE because the vertical transfer coefficient is constant with a_r (see Figure 2).

Appendix C. Definition of the Statistical Indicators

In this section, cs_i stands for the simulations of the reference model Code_Saturne, m_i stands for the MUNICH simulations and n is the total number of simulations.

- Normalized Mean Absolute Error (%):

$$NMAE = 100 \times \frac{\sum_{i=1}^n |m_i - cs_i|}{\left| \sum_{i=1}^n cs_i \right|} \tag{A1}$$

- Normalized Mean Bias (%):

$$NMB = 100 \times \frac{\sum_{i=1}^n (m_i - cs_i)}{\sum_{i=1}^n cs_i} \tag{A2}$$

- Relative Deviation (%):

$$RD_i = 100 \times \frac{m_i - cs_i}{cs_i} \tag{A3}$$

References

1. Faiz, A. Automotive emissions in developing countries-relative implications for global warming, acidification and urban air quality. *Transp. Res. Part A Policy Pract.* **1993**, *27*, 167–186. [\[CrossRef\]](#)
2. Akimoto, H. Global Air Quality and Pollution. *Science* **2003**, *302*, 1716–1719. [\[CrossRef\]](#) [\[PubMed\]](#)
3. Yuan, C.; Ng, E.; Norford, L.K. Improving air quality in high-density cities by understanding the relationship between air pollutant dispersion and urban morphologies. *Build. Environ.* **2014**, *71*, 245–258. [\[CrossRef\]](#) [\[PubMed\]](#)
4. Zhang, Y.; Gu, Z.; Yu, C.W. Impact Factors on Airflow and Pollutant Dispersion in Urban Street Canyons and Comprehensive Simulations: a Review. *Curr. Pollut. Rep.* **2020**, *6*, 425–439. [\[CrossRef\]](#)
5. Angel, S.; Parent, J.; Civco, D.L.; Blei, A.; Potere, D. The dimensions of global urban expansion: Estimates and projections for all countries, 2000–2050. *Prog. Plan.* **2011**, *75*, 53–107. [\[CrossRef\]](#)
6. Pascal, M.; Corso, M.; Chanel, O.; Declercq, C.; Badaloni, C.; Cesaroni, G.; Henschel, S.; Meister, K.; Haluza, D.; Martin-Olmedo, P.; et al. Assessing the public health impacts of urban air pollution in 25 European cities: Results of the Aphekomp project. *Sci. Total Environ.* **2013**, *449*, 390–400. [\[CrossRef\]](#)
7. West, J.J.; Cohen, A.; Dentener, F.; Brunekreef, B.; Zhu, T.; Armstrong, B.; Bell, M.L.; Brauer, M.; Carmichael, G.; Costa, D.L.; et al. What We Breathe Impacts Our Health: Improving Understanding of the Link between Air Pollution and Health. *Environ. Sci. Technol.* **2016**, *50*, 4895–4904. [\[CrossRef\]](#)
8. Borck, R.; Schrauth, P. Population density and urban air quality. *Reg. Sci. Urban Econ.* **2021**, *86*, 103596. [\[CrossRef\]](#)
9. Demetriou, E.; Hadjistassou, C. Lowering mortality risks in urban areas by containing atmospheric pollution. *Environ. Res.* **2022**, *211*, 113096. [\[CrossRef\]](#)
10. Harman, I.N.; Barlow, J.F.; Belcher, S.E. Scalar fluxes from urban street canyons. Part II Model. *Bound.-Lay. Meteorol.* **2004**, *113*, 387–409. [\[CrossRef\]](#)
11. Cai, X.M.; Barlow, J.F.; Belcher, S.E. Dispersion and transfer of passive scalars in and above street canyons—Large-eddy simulations. *Atmos. Environ.* **2008**, *42*, 5885–5895. [\[CrossRef\]](#)
12. Vardoulakis, S.; Fisher, B.E.; Pericleous, K.; Gonzalez-Flesca, N. Modelling air quality in street canyons: a review. *Atmos. Environ.* **2003**, *37*, 155–182. [\[CrossRef\]](#)
13. Huang, Y.D.; Hou, R.W.; Liu, Z.Y.; Song, Y.; Cui, P.Y.; Kim, C.N. Effects of Wind Direction on the Airflow and Pollutant Dispersion inside a Long Street Canyon. *Aerosol Air Qual. Res.* **2019**, *19*, 1152–1171. [\[CrossRef\]](#)
14. Zhang, K.; Chen, G.; Wang, X.; Liu, S.; Mak, C.M.; Fan, Y.; Hang, J. Numerical evaluations of urban design technique to reduce vehicular personal intake fraction in deep street canyons. *Sci. Total Environ.* **2019**, *653*, 968–994. [\[CrossRef\]](#) [\[PubMed\]](#)
15. Yang, H.; Chen, T.; Lin, Y.; Buccolieri, R.; Mattsson, M.; Zhang, M.; Hang, J.; Wang, Q. Integrated impacts of tree planting and street aspect ratios on CO dispersion and personal exposure in full-scale street canyons. *Build. Environ.* **2020**, *169*, 106529. [\[CrossRef\]](#)
16. Miao, C.; Yu, S.; Zhang, Y.; Hu, Y.; He, X.; Chen, W. Assessing outdoor air quality vertically in an urban street canyon and its response to microclimatic factors. *J. Environ. Sci.* **2022**. [\[CrossRef\]](#)
17. Collett, R.S.; Oduyemi, K. Air quality modelling: a technical review of mathematical approaches. *Meteorol. Appl.* **1997**, *4*, 235–246. [\[CrossRef\]](#)
18. Zhang, Y.; Sartelet, K.; Wu, S.Y.; Seigneur, C. Application of WRF/Chem-MADRID and WRF/Polyphemus in Europe, Part I: Model description, evaluation of meteorological predictions, and aerosol-meteorology interactions. *Atmos. Chem. Phys.* **2013**, *13*, 6845–6875. [\[CrossRef\]](#)
19. Mailler, S.; Menut, L.; Khvorostyanov, D.; Valari, M.; Couvidat, F.; Siour, G.; Turquety, S.; Briant, R.; Tuccella, P.; Bessagnet, B.; et al. CHIMERE-2017: from urban to hemispheric chemistry-transport modeling. *Geosci. Model Dev.* **2017**, *10*, 2397–2423. [\[CrossRef\]](#)
20. Appel, K.W.; Napelenok, S.L.; Foley, K.M.; Pye, H.O.T.; Hogrefe, C.; Luecken, D.J.; Bash, J.O.; Roselle, S.J.; Pleim, J.E.; Foroutan, H.; et al. Description and evaluation of the Community Multiscale Air Quality (CMAQ) modeling system version 5.1. *Geosci. Model Dev.* **2017**, *10*, 1703–1732. [\[CrossRef\]](#)
21. Berkowicz, R. OSPM—A parameterised street pollution model. *Environ. Monit. Assess.* **2000**, *65*, 323–331. [\[CrossRef\]](#)
22. Soulhac, L.; Salizzoni, P.; Cierco, F.X.; Perkins, R. The model SIRANE for atmospheric urban pollutant dispersion; part I, presentation of the model. *Atmos. Environ.* **2011**, *45*, 7379–7395. [\[CrossRef\]](#)
23. Soulhac, L.; Nguyen, C.; Volta, P.; Salizzoni, P. The model SIRANE for atmospheric urban pollutant dispersion. PART III: Validation against NO₂ yearly concentration measurements in a large urban agglomeration. *Atmos. Environ.* **2017**, *167*, 377–388. [\[CrossRef\]](#)
24. Kim, Y.; Wu, Y.; Seigneur, C.; Roustan, Y. Multi-scale modeling of urban air pollution: development and application of a Street-in-Grid model (v1.0) by coupling MUNICH (v1.0) and Polair3D (v1.8.1). *Geosci. Model Dev.* **2018**, *11*, 611–629. [\[CrossRef\]](#)
25. Lugon, L.; Sartelet, K.; Kim, Y.; Vigneron, J.; Chrétien, O. Nonstationary modeling of NO₂, NO and NO_x in Paris using the Street-in-Grid model: coupling local and regional scales with a two-way dynamic approach. *Atmos. Chem. Phys.* **2020**, *20*, 7717–7740. [\[CrossRef\]](#)
26. Lugon, L.; Sartelet, K.; Kim, Y.; Vigneron, J.; Chrétien, O. Simulation of primary and secondary particles in the streets of Paris using MUNICH. *Faraday Discuss.* **2021**. [\[CrossRef\]](#)
27. Li, X.; Liu, C.; Leung, D.; Lam, K. Recent progress in CFD modelling of wind field and pollutant transport in street canyons. *Atmos. Environ.* **2006**, *40*, 5640–5658. [\[CrossRef\]](#)

28. Tominaga, Y.; Stathopoulos, T. CFD simulation of near-field pollutant dispersion in the urban environment: A review of current modeling techniques. *Atmos. Environ.* **2013**, *79*, 716–730. [[CrossRef](#)]
29. Salim, S.M.; Buccolieri, R.; Chan, A.; Di Sabatino, S. Numerical simulation of atmospheric pollutant dispersion in an urban street canyon: Comparison between RANS and LES. *J. Wind Eng. Ind. Aerod.* **2011**, *99*, 103–113. [[CrossRef](#)]
30. Aliabadi, A.A.; Moradi, M.; Byerley, R.A.E. The budgets of turbulence kinetic energy and heat in the urban roughness sublayer. *Environ. Fluid Mech.* **2021**, *21*, 843–884. [[CrossRef](#)]
31. Sartelet, K.; Zhu, S.; Moukhtar, S.; André, M.; André, J.M.; Gros, V.; Favez, O.; Brasseur, A.; Redaelli, M. Emission of intermediate, semi and low volatile organic compounds from traffic and their impact on secondary organic aerosol concentrations over Greater Paris. *Atmos. Environ.* **2018**, *180*, 126–137. [[CrossRef](#)]
32. Archambeau, F.; Méchitoua, N.; Sakiz, M. Code Saturne: A finite volume code for the computation of turbulent incompressible flows-Industrial applications. *Int. J. Finite Vol.* **2004**, *1*, 1–62.
33. Milliez, M.; Carissimo, B. Numerical simulations of pollutant dispersion in an idealized urban area, for different meteorological conditions. *Bound.-Lay. Meteorol.* **2007**, *122*, 321–342. [[CrossRef](#)]
34. Milliez, M.; Carissimo, B. Computational Fluid Dynamical Modelling of Concentration Fluctuations in an Idealized Urban Area. *Bound.-Lay. Meteorol.* **2008**, *127*, 241–259. [[CrossRef](#)]
35. Gao, Z.; Bresson, R.; Qu, Y.; Milliez, M.; de Munck, C.; Carissimo, B. High resolution unsteady RANS simulation of wind, thermal effects and pollution dispersion for studying urban renewal scenarios in a neighborhood of Toulouse. *Urban Clim.* **2018**, *23*, 114–130. [[CrossRef](#)]
36. Zaïdi, H.; Dupont, E.; Milliez, M.; Musson-Genon, L.; Carissimo, B. Numerical Simulations of the Microscale Heterogeneities of Turbulence Observed on a Complex Site. *Bound.-Lay. Meteorol.* **2013**, *147*, 237–259. [[CrossRef](#)]
37. Wang, W. An Analytical Model for Mean Wind Profiles in Sparse Canopies. *Bound.-Lay. Meteorol.* **2012**, *142*, 383–399. [[CrossRef](#)]
38. Wang, W. Analytically Modelling Mean Wind and Stress Profiles in Canopies. *Bound.-Lay. Meteorol.* **2014**, *151*, 239–256. [[CrossRef](#)]
39. Schulte, N.; Tan, S.; Venkatram, A. The ratio of effective building height to street width governs dispersion of local vehicle emissions. *Atmos. Environ.* **2015**, *112*, 54–63. [[CrossRef](#)]
40. Salizzoni, P.; Soulhac, L.; Mejean, P. Street canyon ventilation and atmospheric turbulence. *Atmos. Environ.* **2009**, *43*, 5056–5067. [[CrossRef](#)]
41. Wang, Y.; Sartelet, K.; Bocquet, M.; Chazette, P. Modelling and assimilation of lidar signals over Greater Paris during the MEGAPOLI summer campaign. *Atmos. Chem. Phys.* **2014**, 3511–3532. [[CrossRef](#)]
42. Kim, Y.; Sartelet, K.; Raut, J.C.; Chazette, P. Influence of an urban canopy model and PBL schemes on vertical mixing for air quality modeling over Greater Paris. *Atmos. Environ.* **2015**, *107*, 289–306. [[CrossRef](#)]
43. Masson, V. A Physically-Based Scheme For The Urban Energy Budget In Atmospheric Models. *Bound.-Lay. Meteorol.* **2000**, *94*, 357–397. [[CrossRef](#)]
44. Lemonsu, A.; Grimmond, C.S.B.; Masson, V. Modeling the Surface Energy Balance of the Core of an Old Mediterranean City: Marseille. *J. Appl. Meteorol.* **2004**, *43*, 312–327. [[CrossRef](#)]
45. Cherin, N.; Roustan, Y.; Musson-Genon, L.; Seigneur, C. Modelling atmospheric dry deposition in urban areas using an urban canopy approach. *Geosci. Model Dev.* **2015**, *8*, 893–910. [[CrossRef](#)]
46. Macdonald, R.W.; Griffiths, R.F.; Hall, D.J. An improved method for the estimation of surface roughness of obstacle arrays. *Atmos. Environ.* **1998**, *32*, 1857–1864. [[CrossRef](#)]
47. Grimmond, C.S.B.; Oke, T.R. Aerodynamic Properties of Urban Areas Derived from Analysis of Surface Form. *J. Appl. Meteorol.* **1999**, *38*, 1262–1292. [[CrossRef](#)]
48. Soulhac, L.; Perkins, R.J.; Salizzoni, P. Flow in a Street Canyon for any External Wind Direction. *Bound.-Lay. Meteorol.* **2008**, *126*, 365–388. [[CrossRef](#)]
49. Castro, I.P. Are Urban-Canopy Velocity Profiles Exponential? *Bound.-Lay. Meteorol.* **2017**, *164*, 337–351. s10546-017-0258-x. [[CrossRef](#)]
50. Katul, G.G.; Mahrt, L.; Poggi, D.; Sanz, C. ONE- and TWO-Equation Models for Canopy Turbulence. *Bound.-Lay. Meteorol.* **2004**, *113*, 81–109. [[CrossRef](#)]
51. Guimet, V.; Laurence, D. A linearised turbulent production in the $k-\epsilon$ model for engineering applications. In *Engineering Turbulence Modelling and Experiments 5*; Rodi, W., Fueyo, N., Eds.; Elsevier Science Ltd.: Oxford, UK, 2002; pp. 157–166. [[CrossRef](#)]
52. Richards, P.J.; Hoxey, R.P. Appropriate boundary conditions for computational wind engineering models using the $k - \epsilon$ turbulence model. *J. Wind Eng. Ind. Aerodyn.* **1993**, *46–47*, 145–153. [[CrossRef](#)]
53. Wiernga, J. Representative roughness parameters for homogeneous terrain. *Bound.-Lay. Meteorol.* **1993**, *63*, 323–364. [[CrossRef](#)]
54. An, K.; Fung, J.C.H.; Yim, S.H.L. Sensitivity of inflow boundary conditions on downstream wind and turbulence profiles through building obstacles using a CFD approach. *J. Wind Eng. Ind. Aerod.* **2013**, *115*, 137–149. [[CrossRef](#)]
55. Oke, T.R. *Boundary Layer Climates (Chapter 8, pp. 262–303)*, 2nd ed.; Routledge; Methuen: New York, NY, USA, 1987; p. 435.

2.3 Parameterization of the tree aerodynamic effect in street canyons



Parameterizing the aerodynamic effect of trees in street canyons for the street network model MUNICH using the CFD model Code_Saturne

Alice Maison^{1,2}, Cédric Flageul³, Bertrand Carissimo¹, Yunyi Wang¹, Andrée Tuzet², and Karine Sartelet¹

¹CEREA, École des Ponts, EDF R&D, Marne-la-Vallée, France

²Université Paris-Saclay, INRAE, AgroParisTech, UMR EcoSys, 78850 Thiverval-Grignon, France

³PPRIME Institute, Curiosity Group, Université de Poitiers, CNRS, ISAE-ENSMA, Poitiers, France

Correspondence: Alice Maison (alice.maison@enpc.fr) and Karine Sartelet (karine.sartelet@enpc.fr)

Received: 15 April 2022 – Discussion started: 29 April 2022

Revised: 24 June 2022 – Accepted: 1 July 2022 – Published: 20 July 2022

Abstract. Trees provide many ecosystem services in cities such as urban heat island reduction, water runoff limitation, and carbon storage. However, the presence of trees in street canyons reduces the wind velocity in the street and limits pollutant dispersion. Thus, to obtain accurate simulations of pollutant concentrations, the aerodynamic effect of trees should be taken into account in air quality models at the street level.

The Model of Urban Network of Intersecting Canyons and Highways (MUNICH) simulates the pollutant concentrations in a street network, considering dispersion and physico-chemical processes. It can be coupled to a regional-scale chemical transport model to simulate air quality over districts or cities. The aerodynamic effect of the tree crown is parameterized here through its impact on the average wind velocity in the street direction and the vertical transfer coefficient associated with the dispersion of a tracer. The parameterization is built using local-scale simulations performed with the computational fluid dynamics (CFDs) code Code_Saturne. The two-dimensional CFD simulations in an infinite street canyon are used to quantify the effect of trees, depending on the tree characteristics (leaf area index, crown volume fraction, and tree height to street height ratio) using a drag porosity approach. The tree crown slows down the flow and produces turbulent kinetic energy in the street, thus impacting the tracer dispersion. This effect increases with the leaf area index and the crown volume fraction of the trees, and the average horizontal velocity in the street is reduced by up to 68 %, while the vertical transfer coefficient by up to 23 % in the simulations performed here.

A parameterization of these effects on horizontal and vertical transfers for the street model MUNICH is proposed. Existing parameterizations in MUNICH are modified based on Code_Saturne simulations to account for both building and tree effects on vertical and horizontal transfers. The parameterization is built to obtain similar tree effects (quantified by a relative deviation between the cases without and with trees) between Code_Saturne and MUNICH. The vertical wind profile and mixing length depend on leaf area index, crown radius, and tree height to street height ratio. The interaction between the trees and the street aspect ratio is also considered.

1 Introduction

Cities are, by definition, areas with high densities of people, infrastructure, and activities, and this urbanization causes many issues. First, air quality is poor because of the numerous air pollutants emitted by anthropic activities such as traffic, industries, or residential activities, and the reduction in air flow by high buildings limits the dispersion of these pollutants (Faiz, 1993; Akimoto, 2003; Yuan et al., 2014; Zhang et al., 2020). In addition to air pollution issues, radiative and water budgets are strongly modified in cities compared to the countryside (Bozonnet et al., 2015). Temperatures are, on average, higher than in the countryside because of the urban heat island created by additional anthropogenic energy released, storage of radiative energy in dark materials, radiation multi-reflection, and lack of vegetation and associated evapotranspiration (Oke, 1982; Pigeon et al., 2007; Stewart, 2011; Hebbert and Jankovic, 2013). Impervious soils also decrease water infiltration and intensify runoff (Leopold, 1968). In addition, growing urbanization and increasing extreme events (due to climate change) such as pollution peaks, heat waves, and floods have negative consequences on the environment and human health (Robine et al., 2007; Angel et al., 2011; Pascal et al., 2013; West et al., 2016; IPCC, 2021).

One nature-based solution is to green the city by planting vegetation as lawns, planting trees in streets or in parks, and growing green walls and roofs (Livesley et al., 2016; Revelli and Porporato, 2018). Vegetation and especially trees contribute to improve human thermal comfort by creating a favorable micro-climate with lower air temperature (through solar radiation interception and creation of shade) and higher evaporation (through ground and vegetation evapotranspiration; Taha et al., 1991; Bowler et al., 2010; Gillner et al., 2015; Klemm et al., 2015; Lobaccaro and Acero, 2015; Gunawardena et al., 2017). This positive effect of trees is significant in particular during heat wave episodes, which will be more frequent in the future due to climate change (IPCC, 2021). Trees and vegetated areas also favor infiltration in soils that contributes to offset water runoff induced by soil artificialization (Armson et al., 2013; Berland et al., 2017). Besides, vegetation is known to store carbon (Nowak and Crane, 2002; Svirejeva-Hopkins et al., 2004) and to enhance human well-being (van Dillen et al., 2012; Bertram and Rehdanz, 2015; Krekel et al., 2015). For all these ecosystem services in urban areas, city greening is often promoted and, for example, the city of Paris has about 205 000 trees of which 52 % are roadside trees (Direction des Espaces Verts et de l'Environnement – Mairie de Paris, 2021).

Many studies have tried to figure out the impact of trees on air pollution in a street canyon, and they have shown that trees are an important parameter to take into account if we want to understand and accurately simulate the pollutant concentrations in the streets (Beckett et al., 1998; Nowak et al., 1998; Jayasooriya et al., 2017). Vegetation, and especially trees, represent surfaces available for pollutant dry de-

position and, hence, can contribute to reducing air pollutant concentrations. However, pollutant removal and its impact on air quality vary greatly, depending on tree characteristics, tree species, and pollutant type (Nowak et al., 2006; Hwang et al., 2011; Selmi et al., 2016; Xue and Li, 2017; Ozdemir, 2019). Trees may also affect atmospheric chemistry by emitting biogenic volatile organic compounds (BVOCs), which may lead to the formation of ozone and secondary organic aerosols (Calfapietra et al., 2013; Préndez et al., 2019; Gu et al., 2021). Furthermore, trees may alter air quality by influencing aerodynamic processes and limiting the pollutant dispersion (Buccolieri et al., 2011; Wania et al., 2012; Vos et al., 2013; Gromke and Ruck, 2007, 2009, 2012; Gromke and Blocken, 2015). The aerodynamic effect of trees is defined as the drag force resulting from the friction between the air and the leaves. Since the tree crown can be seen as a porous medium as air passes through it but is slowed down, and the drag force increases with the leaf surface.

For wind perpendicular to a street, the air recirculates inside the street canyon (Harman et al., 2004). Pollutants emitted at the bottom of the street (by traffic) accumulate on the leeward side of the street, inducing higher local concentrations (Vardoulakis et al., 2003; Cai et al., 2008; Huang et al., 2019). Obstacles in the street, such as trees, can strongly impact the air flow and intensify the pollutant accumulation (Vos et al., 2013). This effect has been studied using computational fluid dynamics (CFD) models where the aerodynamic influence of trees on the flow is represented by a porosity model (Buccolieri et al., 2009; Zaïdi et al., 2013; Wei et al., 2016; Jeanjean et al., 2017; Santiago et al., 2017). Vos et al. (2013) showed that pollutant concentrations may increase by 20 % in a street because of the presence of two rows of trees in the street. The effects of vegetation depend on the height, width, and density (leaf area index) of trees (Vos et al., 2013; Janhäll, 2015), as well as the height to width ratio of streets (Wania et al., 2012). Finally, it is necessary to accurately assess the effect of trees on pollutant dispersion in order to find what configurations are more effective in reducing air pollution in street canyon and to guide urban development policy (Janhäll, 2015).

The effect of trees on aerodynamic processes should also be considered at the street level in air quality models. As discussed previously, CFD models including trees are used to study wind fields and pollutant transport in street canyons (Li et al., 2006). However, as the street is discretized with a fine mesh, the computational cost is high, and simulations at the city scale are too expensive today. Fast-running codes, such as simplified street network or street-in-grid models, are developed to simulate street pollutant concentrations over neighborhoods or cities, but they do not take into account the effect of trees in the streets. The objective of this study is to parameterize the effect of trees on air flow in the Model of Urban Network of Intersecting Canyons and Highways (MUNICH; Kim et al., 2018; Lugon et al., 2020, <http://cerea.enpc.fr/munich/>, last access: 17 December 2021). To build this pa-

parameterization, simulations in street canyons are performed with Code_Saturne (Archambeau et al., 2004, <https://www.code-saturne.org/>, last access: 17 December 2021), a CFD code, which can represent the tree aerodynamic effect with a drag porosity approach (Katul et al., 2004) and has previously been compared with field measurements (Zaïdi et al., 2013). MUNICH parameterizations have already been compared with Code_Saturne results in a treeless canyon, and a new parameterization for horizontal and vertical transfers has been developed in MUNICH based on Wang (2012, 2014) and Code_Saturne simulations (Maison et al., 2022). In the present study, the tree aerodynamic effect is added to this parameterization, and Code_Saturne (version 6.0) is used as a reference to parameterize the aerodynamic effect of trees in the street network model MUNICH. CFD simulations are performed in three streets of aspect ratios varying from 0.3 to 1.0, and a large range of tree leaf area index, crown radius, and heights is tested. The tree aerodynamic effect quantified with Code_Saturne is analyzed depending on these street and tree characteristics.

The approach to modeling the dispersion of pollutants in MUNICH and Code_Saturne is fundamentally different due to their physical modeling and discretization in space and time. MUNICH is a street network model that simulates air pollutant concentration in an urban canopy. Street dimensions and pollutant concentrations are assumed to be homogeneous in each street segment. Air flow is divided into a horizontal flux from one street to another and a vertical flux between the street and the background (Maison et al., 2022). Background concentrations above the street can be computed by 3D chemistry transport models (CTMs), such as Polair3D (Sartelet et al., 2018; Lugon et al., 2020, 2021). To build the tree parameterization, the CFD simulation setup is adapted for the comparison with MUNICH, and several simulations are performed with Code_Saturne, considering a range of street and tree characteristics.

The structure of the paper is as follows. The MUNICH and Code_Saturne models are presented in Sect. 2. Then, the tree effect on horizontal wind speed and vertical transfer coefficient is quantified with Code_Saturne simulations in Sect. 3 and parameterized in MUNICH in Sect. 4. Conclusions are presented in Sect. 5.

2 Materials and methods

2.1 Description of MUNICH

In MUNICH, each street segment is assumed to be homogeneous, i.e., with uniform building height H and street width W and of length L (m). The street is characterized by its height-to-width ratio called the aspect ratio, $a_r = H/W$ (–). Only the average pollutant concentrations over the street are considered. Pollutants are transported by the horizontal wind speed (advection) in the street network and by a vertical transfer coefficient between the streets and the background.

Several parameterizations of the horizontal wind speed and of the vertical transfer coefficient exist in MUNICH. The ones recently developed in Maison et al. (2022) and based on Code_Saturne simulations are used and detailed here. The vertical profile of the wind speed in the street direction is calculated as an attenuation of the wind speed in the street direction and at the roof level, $U_{H,\varphi}$ (m s^{-1}), as follows (Maison et al., 2022):

$$U(z) = U_{H,\varphi} [C_1 I_0(g(z)) + C_2 K_0(g(z))] \\ \text{with } U_{H,\varphi} = U_H |\cos(\varphi)|, \quad (1)$$

where C_1 and C_2 are integration coefficients, and I_0 and K_0 are the first and second type modified Bessel functions of order 0. Besides, the wind speed at the roof level U_H has to be multiplied by $|\cos(\varphi)|$ to select the component of the wind speed in the street direction, where φ is the angle between the wind direction and the street orientation ($^\circ$). This vertical wind profile is then integrated between the soil roughness z_{0s} (m) and H to compute the average horizontal wind speed in the street direction. The function g is calculated as follows (Wang, 2012, 2014):

$$g(z) = 2\sqrt{\alpha \frac{z}{H}}, \quad (2)$$

and

$$C_1 = \frac{1}{I_0(g(H)) - I_0(g(z_{0s})) K_0(g(H)) / K_0(g(z_{0s}))} \\ \text{and } C_2 = -\frac{C_1 I_0(g(z_{0s}))}{K_0(g(z_{0s}))}, \quad (3)$$

where α is a dimensionless coefficient expressing the effects of wind angle on wind attenuation in the street. It is computed as follows:

$$\alpha = \frac{C_B a_r}{\kappa s_H} \quad \text{with } C_B = 0.31 [1 - \exp(-1.6 a_r)] f_\varphi \quad (4)$$

$$\text{and } f_\varphi = \begin{cases} |\cos(2\varphi)|^3 & \text{if } \varphi \in [0, 45^\circ] \cup [135, 225^\circ] \\ & \cup [315, 360^\circ] \\ 0 & \text{if } \varphi \in]45, 135^\circ[\cup]225, 315^\circ[, \end{cases} \quad (5)$$

where $s_H = s(z=H)$ is a dimensionless factor describing the effect of canopy on the mixing length l_m (Wang, 2012, 2014). The mixing length is calculated as follows:

$$\frac{1}{l_m} = \frac{1}{\kappa z} + \frac{1}{l_{cb}} \Rightarrow l_m = \kappa z \frac{l_{cb}}{l_{cb} + \kappa z} = \kappa z s(z), \quad (6)$$

where κz corresponds to the mixing length over a rough bare soil (without canopy), and l_{cb} is the characteristic length (m) in the street canyon, corresponding to the mixing length of the urban canopy alone ($l_{cb} = 0.5 W$).

The vertical transfer coefficient that drives pollutant exchange between the street and the background zone is calculated at $z=H$ as follows:

$$q_{\text{vert}} = \sigma_W l_m = \sigma_W \kappa H s_H, \quad (7)$$

where σ_w (in m s^{-1}) is a velocity scale equal to the standard deviation of the vertical wind speed. It depends on both the friction velocity above the urban canopy, u_* , and on atmospheric stability (Soulhac et al., 2011).

In Sect. 4, the tree effect is parameterized by taking into account the characteristic length of the trees in the mixing length l_m (Eq. 19, which leads to modifications in the coefficient α Eq. 23).

2.2 Description of Code_Saturne

2.2.1 Street and tree modeling setup

In the present study, the tree effect is studied in three street canyons of the following different street aspect ratios: a wide street canyon (WC), an intermediate canyon (IC), and a narrow canyon (NC). Their characteristics are presented in Table 1.

A color code is introduced to simplify the reading of the figures, with red symbols for the wide canyon (WC), purple ones for the intermediate canyon (IC), and blue ones for the narrow canyon (NC). Abbreviations, parameters, and variables used are listed in Appendix A.

The $k - \varepsilon$ linear production turbulence model is used in Code_Saturne. Stationary simulations are performed with a thermally neutral atmosphere. A 2D infinite street canyon is modeled with periodic condition on the y axis, but the flow and the wind speed vector are 3D. The mesh is composed of hexahedral cells of 1 m in the y -axis direction and 0.5 m on the x and z axes. The vertical profiles of U , k , and ε are set in the inlet (top left border of the domain). The complete description of Code_Saturne simulation setup in treeless canyons can be found in Maison et al. (2022).

The tree geometry and its representation in Code_Saturne are shown in Fig. 1. Here, two rows of trees ($n = 2$) are considered, with one on each side of the street, and whose positions on the x axis are $x = 34.5$ m and $x = 48.0$ m (the wall positions are $x = 27.5$ and $x = 55.0$ m). The tree crown centers are located in a position on the x axis so that the largest crowns (CVF $\approx 25\%$) do not reach the street walls for the three street canyons studied. r is the tree radius (m), h , h_{\min} , and h_{\max} correspond, respectively, to the middle, minimum, and maximum heights of the tree crown (m). Note that all the simulations verify $h_{\max} \leq H$, i.e., the top of the trees do not exceed the top of the street.

In the cells containing the trees, an additional drag term is added to the Navier–Stokes equations as follows (Katul et al., 2004; Zaïdi et al., 2013):

$$S_{u,i} = -\rho \text{LAD} C_{D_t} |U| U_i, \quad (8)$$

where $|U|$ is the modulus of U , U_i is the velocity in the i -direction, LAD is the leaf area density in square meters of leaf surface per cubic meter of crown volume ($\text{m}_{\text{leaves}}^2 \text{m}_{\text{tree crown}}^{-3}$), ρ is the air density, and C_{D_t} is the tree drag coefficient set to 0.2, which is a representative value for

trees (Katul and Albertson, 1998). The leaf area index (LAI) is the one-sided green leaf area per unit ground surface area, and the leaf area density (LAD) is the one-sided green leaf area per unit volume. They are calculated as follows:

$$\text{LAI} = \frac{\text{surface of leaves}}{\text{soil projected surface area}} \left(\text{m}_{\text{leaf}}^2 \text{m}_{\text{soil}}^{-2} \right)$$

$$\text{and LAD} = \frac{\text{surface of leaves}}{\text{volume of tree crown}} \left(\text{m}_{\text{leaf}}^2 \text{m}_{\text{crown}}^{-3} \right). \quad (9)$$

The source terms for trees are also implemented in the $k - \varepsilon$ equations as follows:

$$S_k = \rho \text{LAD} C_{D_t} \left(\beta_p |U|^3 - \beta_d |U| k \right) \quad (10)$$

$$S_\varepsilon = \rho \text{LAD} C_{D_t} \left(C_{4\varepsilon} \beta_p |U|^3 \frac{\varepsilon}{k} - C_{5\varepsilon} \beta_d |U| \varepsilon \right), \quad (11)$$

where $C_{4\varepsilon} = C_{5\varepsilon} = 0.9$, $\beta_p = 1.0$, and $\beta_d = 5.03$ are constants of the model (Zaïdi et al., 2013). Note that this type of tree aerodynamic effect modeling is commonly used and evaluated by comparison with experimental results (Buccolieri et al., 2018).

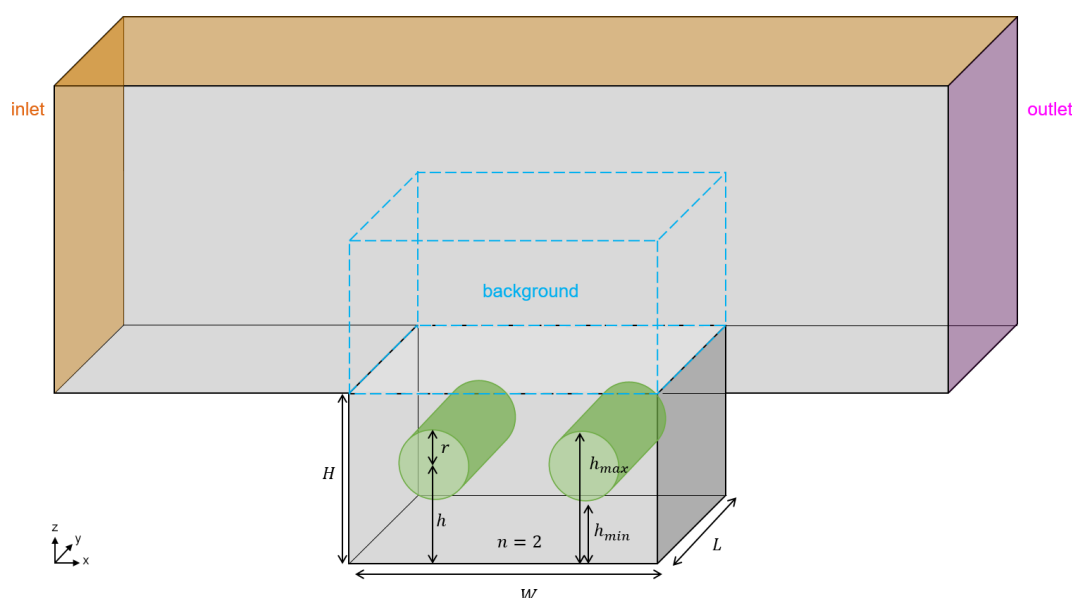
Only the impact of the tree leaves is considered, and the impact of the tree trunk and branches on the flow is not modeled. As the streets are modeled in 2D and an infinite length in the y direction is assumed (see Sect. 2), the LAI considered here is the equivalent cylindrical LAI_{2D}. Usually, studies consider the tree LAI, which is well defined for a 3D tree. The relation between the tree LAI_{3D} and the equivalent cylindrical LAI_{2D} is given in Appendix B. To check that this effect of trees is well modeled using this simplified 2D setup, 3D simulations were performed and compared to some of the 2D simulations presented here, showing very good agreement between the 2D and 3D simulations in terms of the influence of the trees on the flow (Appendix B).

To gain a complete vision of the effect of trees, 45 simulations are performed per canyon, and the impact of three independent tree parameters are studied, including the following:

- The 2D-equivalent LAI, i.e., LAI_{2D} = 0.5, 1, 2, 3, and 4 (see Appendix B, for the conversion between LAI_{3D} and equivalent LAI_{2D}).
- The crown volume fraction (CVF), calculated as the tree (2D cylindrical) crown volume divided by the street volume, i.e., $\text{CVF} = \frac{n\pi r^2}{HW}$. This ratio is already used in studies quantifying the effect of trees on street pollution such as Gromke and Blocken (2015). The relation between 2D and 3D CVF is shown in Appendix B. Note that, apart from Appendix B, all CVF mentioned in the figures and in the text refer to the 2D CVF. In total, the following three CVF ranges are simulated: CVF ≈ 5 , 10, and 25 %.
- The tree-to-street height ratio calculated as the crown middle height divided by the building height (h/H).

Table 1. Characteristics of the three canyons studied.

Canyon	Building height H (m)	Street width W (m)	Street aspect ratio a_r (–)	Maximum height of the domain ($3H$) (m)
WC	8.5	27.5	0.3	25.5
IC	14.0	27.5	0.5	42.0
NC	27.5	27.5	1.0	82.5

**Figure 1.** The 3D scheme of the street canyon with cylindrical tree crown dimensions.

In total, the following three h/H ranges are simulated: $h/H \approx 1/3$, $1/2$, and $2/3$.

Note that these three tree characteristics are normalized by street characteristics, and similar values are chosen in the three canyons to be able to compare them and to quantify if the street aspect ratio influences the tree effect (i.e., if there is an interaction between tree and building effects). However, the normalized tree characteristics are not exactly equal in the three canyons due to the street sizes and the 0.5 m mesh cells that limit the possible range of tree sizes. The detailed list of the tree characteristics and the different values used for the tree parameters are presented in Table A4.

2.2.2 Calculation of vertical and horizontal transfers in Code_Saturne for comparison to MUNICH

To evaluate the vertical transfer between the street and the background zone in Code_Saturne, a passive tracer is emitted in each mesh cell of the street, with an arbitrary stationary emission rate $e = 1000 \mu\text{g s}^{-1}$ for a street canyon of length $L = 1$ m. For the tracer to be dispersed only by vertical transfers and not by horizontal winds within the street, simulations are performed with the wind perpendicular to the street at the inlet ($\varphi = 90^\circ$). The initial street and background tracer

concentrations are zero. At the end of the simulation (stationary state reached), the tracer concentration is averaged in the street and in the background zone (denoted as C_{street} and C_{bg} in $\mu\text{g m}^{-3}$) to reproduce a MUNICH homogeneous street assumption. The background zone corresponds to the area of the same volume as the street but located just above the street (see Maison et al., 2022, for more details). In the absence of other processes (horizontal transport, deposition, and chemical reactions), the tracer mass balance in the street yields the following:

$$Q_{\text{vert}} = e \quad (12)$$

$$\Rightarrow q_{\text{vert}} \text{WL} \frac{C_{\text{street}} - C_{\text{bg}}}{H} = e \quad (13)$$

$$\Rightarrow q_{\text{vert}} = \frac{eH}{\text{WL} (C_{\text{street}} - C_{\text{bg}})}, \quad (14)$$

where Q_{vert} is the vertical flux of pollutant at the roof level for the whole street ($\mu\text{g s}^{-1}$), q_{vert} is the vertical transfer coefficient ($\text{m}^2 \text{s}^{-1}$), and WL is the exchange surface (m^2). Thus, the vertical transfer coefficient can be compared between both models. In Code_Saturne, q_{vert} is calculated from the emission rate e and the concentration gradient $\left(\frac{C_{\text{street}} - C_{\text{bg}}}{H}\right)$,

following Eq. (14), and in MUNICH, it is calculated from Eq. (7).

In MUNICH, the horizontal transfer velocity is equal to the street average horizontal wind speed in the street direction U_{street} , which is calculated by integrating Eq. (1) between $z = z_{0s}$ and $z = H$. In Code_Saturne, U_{street} is estimated from the wind speed in the y direction averaged over the street mesh cells. In addition to U_{street} , the MUNICH vertical profile of the wind speed (Eq. 1) can also be compared to Code_Saturne by averaging the wind speed in the y direction over the street width (x axis).

As the objective of the study is to parameterize the aerodynamic effect of trees, the chemistry and deposition on built and vegetated surfaces are not considered here. Further details on the simulation setup of MUNICH and Code_Saturne and on the comparison of vertical and horizontal transfers in a treeless canyon are presented in Maison et al. (2022).

3 Quantification of the tree crown effect on horizontal and vertical transfers by Code_Saturne simulations

To quantify tree effect on the horizontal wind speed along the street and on the vertical transfer coefficient, Code_Saturne simulations are performed for a large range of tree characteristics (LAI_{2D}, CVF, and height ratio h/H), as summarized in Table A4. The tree effect is expressed as a relative deviation between the simulations without and with trees.

3.1 Tree effect on horizontal transfer

To quantify and compare the effect of tree crowns in Code_Saturne and MUNICH, and thus to overcome eventual differences between the two models observed in a treeless canyon for the horizontal velocity U_{street} , a relative deviation (RD) of U_{street} , between the simulations with and without trees (%), is computed as follows:

$$RD_{U_{\text{street}}} = 100 \times \frac{U_{\text{street}} - U_{\text{street}_0}}{U_{\text{street}_0}}, \quad (15)$$

where U_{street_0} stands for the average wind velocity in a treeless street, and U_{street} is the average wind velocity in a street with trees, as computed with Code_Saturne. This RD between the Code_Saturne simulations with and without trees is shown in Fig. 2a for WC, 2b for IC, and 2c for NC. It shows that $RD_{U_{\text{street}}}$ becomes increasingly negative, meaning that U_{street} decreases as the LAI_{2D} and the CVF increase. On the opposite, the tree height has either no impact or a small impact compared to LAI_{2D} and CVF. When the effect of tree height is noticeable, an increase in the tree height induces a decrease in RD.

In the range of the tree characteristics studied, U_{street} is attenuated from 7.3 % to 62.3 %. The tree effect on U_{street} can be compared between the three canyons. The tree effect

on U_{street} increases as the canyon is deeper, highlighting the complex interaction between the street dimensions and the tree effect on the velocity. This observation is consistent with the study of Wania et al. (2012).

3.2 Tree effect on vertical transfer

The relative deviation of the vertical transfer coefficient ($RD_{q_{\text{vert}}}$) between simulations with and without trees is introduced to quantify the tree effect on the vertical transfer coefficient. Similar to the relative deviation of U_{street} (Eq. 15), the relative deviation $RD_{q_{\text{vert}}}$ (%) is expressed as follows:

$$RD_{q_{\text{vert}}} = 100 \times \frac{q_{\text{vert}} - q_{\text{vert}_0}}{q_{\text{vert}_0}}, \quad (16)$$

where q_{vert_0} stands for the vertical transfer coefficient in a treeless street, and q_{vert} is the vertical transfer coefficient in a street with trees. Code_Saturne $RD_{q_{\text{vert}}}$ is plotted for different tree parameters LAI_{2D}, CVF, and height ratio h/H in Fig. 3a for WC, 3b for IC, and 3c for NC.

For WC, $RD_{q_{\text{vert}}}$ increases with tree LAI_{2D}, CVF, and height ratio (Fig. 3a). For IC, $RD_{q_{\text{vert}}}$ also increases with CVF and height ratio, but $RD_{q_{\text{vert}}}$ tends to slightly decrease as the LAI increase when the LAI is high and the ratio h/H is small (differences between LAI = 3 and 4 for $h/H = 0.36$ and 0.50; Fig. 3b). For NC, a small increase in $RD_{q_{\text{vert}}}$ with LAI_{2D} and CVF is observed for $h/H = 0.65$. However, for the two other smaller height ratios, the tree effect is very low ($-1.1 \leq RD_{q_{\text{vert}}} \leq 0.5$; Fig. 3c).

This reduction in the tree effect on q_{vert} when LAI or CVF increases for small h/H ratios in IC and NC can be explained by micro-scale effects (modified air flow path and turbulent viscosity) and is left out of the scope of the present study due to the corresponding low amplitude. Besides, investigation of such micro-scale effects would probably require more advanced turbulence models, for example, switching from a first-order model, $k - \varepsilon$, to a second-order one (Rij-SSG; Speziale et al., 1991) or a 3D large eddy simulation (LES).

Note that, unlike U_{street} (Sect. 3.1), the tree effect on q_{vert} decreases when the canyon becomes deeper. For example, the tree effect, as quantified by $RD_{q_{\text{vert}}}$, ranges between -1.0 % and -20.3 % for WC, -1.0 % and -18.7 % for IC, and 0.5 % and -2.7 % for NC. The averaged tree effect is relatively less strong when the canyon is deeper. In other words, regarding vertical transfers, the street effect dominates over the tree effect.

For vertical transfer, a wind perpendicular to the street ($\varphi = 90^\circ$) is used to focus on the effects on vertical transfers only. In this case of perpendicular wind, the air flow occurring in street canyons is complex and leads to heterogeneous tracer concentration in the street. In general, for the three canyons, the presence of the two tree crowns tends to increase the tracer concentration on the leeward side of the street and to decrease it on the windward side (Buccolieri et al., 2009; Gromke and Ruck, 2012). Depending on the

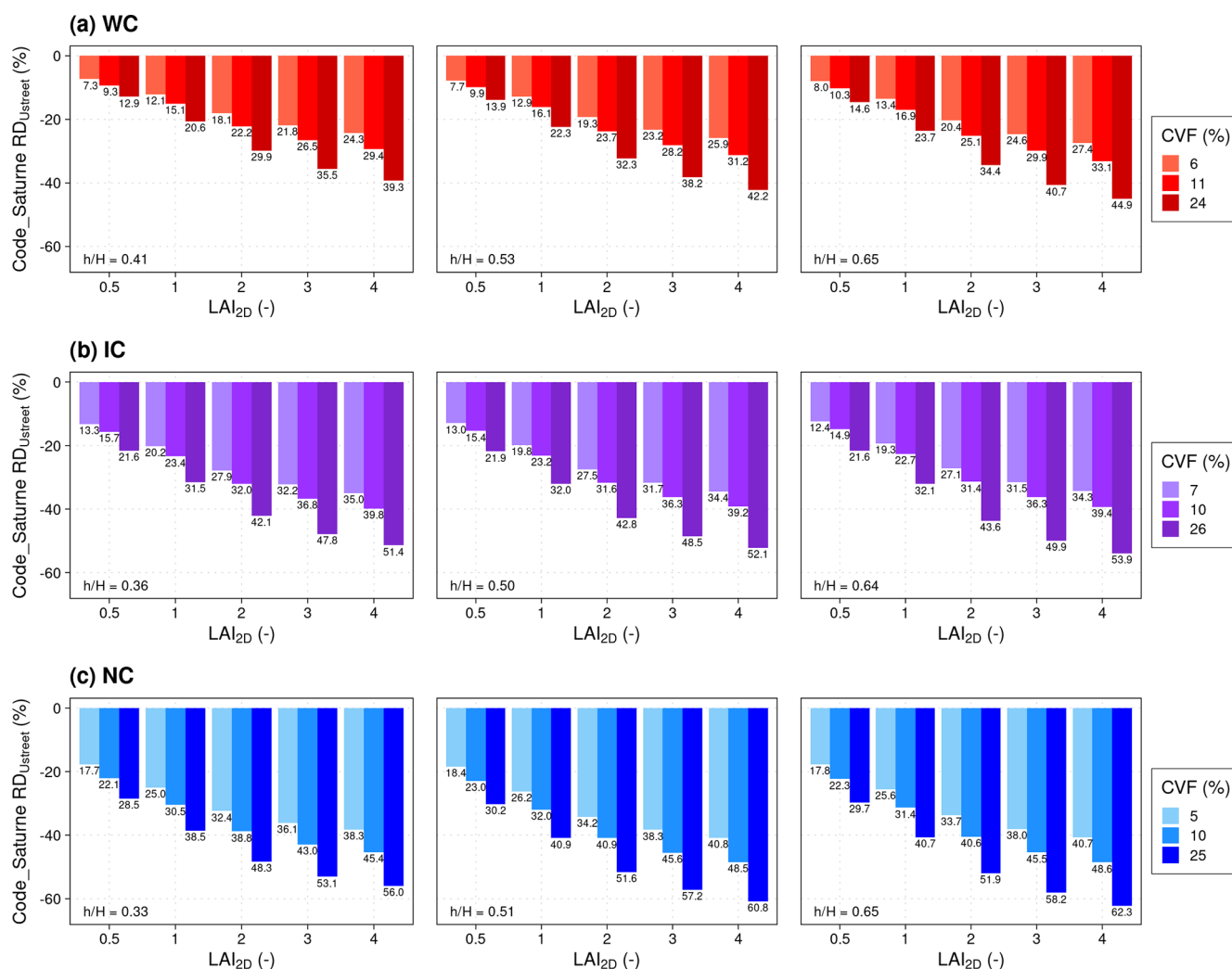


Figure 2. Relative deviation (RD) of U_{street} computed from Code_Saturne simulations for different tree LAI_{2D} , CVF, and height ratio for WC (a), IC (b), and NC (c). The graphic is divided into three columns corresponding to the three height ratios, and higher CVF correspond to darker colors. $|RD_{U_{street}}|$ values are specified with data labels.

street aspect ratio and, therefore, on the air flow regime (Oke, 1988; Harman et al., 2004) and on the tree characteristics, the tree crown effect on local tracer concentration (leeward versus windward side) is more or less important. For example, for NC, the flow regime is skimming, and on average, the variation in C_{street} due to the presence of trees compensates between the two sides of the street, explaining why $RD_{q_{vert}}$ is very low for NC.

This section demonstrated that the tree effect parameterizations should depend on tree characteristics and also on building characteristics to account for the building–tree interactions. The next section aims to parameterize in MUNICH the tree effect on U_{street} and q_{vert} observed in Code_Saturne simulations.

4 Parameterization of the aerodynamic effect of tree crowns in MUNICH

4.1 Model description

The MUNICH parameterizations of horizontal and vertical transfers detailed in Maison et al. (2022) are modified to take into account the tree effects. These parameterizations are based on Wang (2012, 2014) equations, which were originally developed for homogeneous vegetated cover. To remain consistent with this hypothesis, the parameterization will depend on the homogeneous leaf area index in the street, denoted as LAI_{street} . As for the conversion from LAI_{3D} to LAI_{2D} , LAI_{street} is estimated from LAI_{2D} conserving the leaf surface. LAI_{street} is calculated by spreading the tree crown

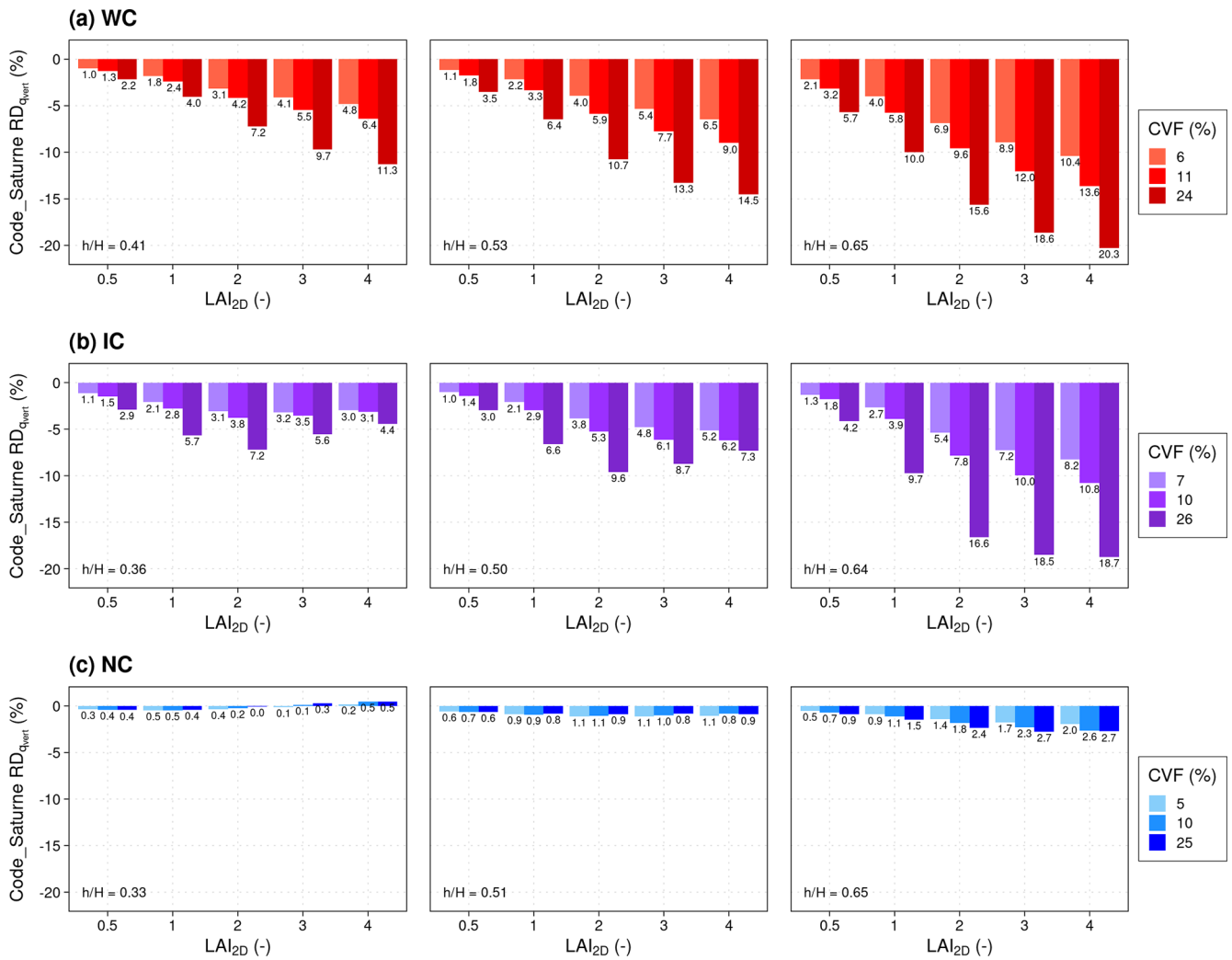


Figure 3. Relative deviation (RD) of q_{vert} computed from Code_Saturne simulations for different tree $\text{LAI}_{2\text{D}}$, CVF, and height ratio for WC (a), IC (b), and NC (c). The graphic is divided into three columns corresponding to the three height ratios, and higher CVF correspond to darker colors. $|\text{RD}_{q_{\text{vert}}}|$ values are specified with data labels.

cylindrical $\text{LAI}_{2\text{D}}$ over the whole street width as follows:

$$\text{LAI}_{\text{street}} \times S_{\text{street}} = \text{LAI}_{2\text{D}} \times S_{2\text{D}} \quad (17)$$

$$\begin{aligned} \Rightarrow \text{LAI}_{\text{street}} &= \text{LAI}_{2\text{D}} \times \frac{S_{2\text{D}}}{S_{\text{street}}} = \frac{2rLn\text{LAI}_{2\text{D}}}{\text{WL}} \\ &= \frac{2rn\text{LAI}_{2\text{D}}}{W}, \end{aligned} \quad (18)$$

where S_{street} is the soil-projected area of the street homogeneous tree crown, and $S_{2\text{D}}$ is the soil-projected area of the Code_Saturne 2D cylindrical tree crown (in m^2). Note that, regardless of the tree crown geometry, $\text{LAI}_{\text{street}}$ is always equal to the street total leaf surface divided by the street ground area (WL).

To account for the tree effect on the mixing length, the characteristic length of the trees (l_{c_t} in m) is added into the

equation describing the mixing length l_m as follows:

$$\frac{1}{l_m} = \frac{1}{\kappa H} + \frac{1}{l_{c_t}} + \frac{1}{l_{c_t} f_{b \times t}}, \quad (19)$$

$$\text{with } l_{c_t} = \frac{E_t H}{C_{D_t} \frac{1}{2} \text{LAI}_{\text{street}}}, \quad (20)$$

where $\frac{1}{2} \text{LAI}_{\text{street}}$ corresponds to the leaf frontal area density, assuming a random leaf orientation distribution, E_t is a proportionality constant taken equal to 0.054 for vegetated cover, as suggested by Wang (2014), and $f_{b \times t}$ is a function parameterized based on Code_Saturne simulations in Sect. 4.2 and representing the interaction between buildings, trees, and the tree crown height.

The dimensionless factor s_H expressing the effects of the tree canopy on the mixing length l_m is calculated using its definition in Eq. (6) and the expression of l_m in Eq. (19) as

follows:

$$l_m = \kappa H s_H \text{ at roof level} \quad (21)$$

$$\text{with } s_H = \begin{cases} \frac{l_{cb}}{l_{cb} + \kappa H} & \text{without tree} \\ \frac{l_{cb} l_{ct} f_{b \times t}}{\kappa H (l_{cb} + l_{ct} f_{b \times t}) + l_{cb} l_{ct} f_{b \times t}} & \text{with trees.} \end{cases} \quad (22)$$

The simulations with and without trees have to be distinguished to avoid any convergence issue since l_{ct} tends to $+\infty$ when $\text{LAI}_{\text{street}}$ tends to 0. This s_H factor now includes rough soil, buildings, and tree effects on the mixing length and is then used in the calculation of the attenuation coefficient α (Eq. 4). In the numerator, the expressions for buildings and trees are added as follows:

$$\alpha = \frac{C_B a_r + C_{D_t} C_u \frac{1}{2} \text{LAI}_{\text{street}}}{\kappa s_H}, \quad (23)$$

where C_{D_t} is the tree drag coefficient (dimensionless) taken equal to the one, as used in Code_Saturne ($C_{D_t} = 0.2$). Wang (2014) presents C_u as a dimensionless coefficient homogeneous on the vertical axis, but that can depend on canopy features. This coefficient has to be determined based on experimental or simulated observation data and will be parameterized in Sect. 4.2 with CFD simulations.

4.2 Parameter determination based on Code_Saturne simulations

There are two parameters introduced in l_m and α equations, i.e., $f_{b \times t}$ and C_u (Eqs. 19 and 23), that have to be determined based on Code_Saturne $\text{RD}_{q_{\text{vert}}}$ and $\text{RD}_{U_{\text{street}}}$. The function $f_{b \times t}$ depends on a_r to account for the interaction between trees and buildings observed in Fig. 3 and also on h_{max} to account for the effect of the tree height. Note that, since tree crowns are assumed to be homogeneous within the canopy in the original Wang formulation, the tree crown height h_{max} is not taken into account (see Eq. 20), and therefore, it needs to be included in the function $f_{b \times t}$. The $f_{b \times t}$ expression is determined by maximizing the fit between Code_Saturne $\text{RD}_{q_{\text{vert}}}$ and MUNICH $\text{RD}_{q_{\text{vert}}}$ as follows:

$$f_{b \times t} = \frac{a_0 + a_1 \exp(a_2 a_r)}{(h_{\text{max}}/H)^2} \quad \text{with } a_0 = 3.26, a_1 = 0.0256 \text{ and } a_2 = 6.70. \quad (24)$$

A comparison of Code_Saturne $\text{RD}_{q_{\text{vert}}}$ and the $\text{RD}_{q_{\text{vert}}}$ parameterized with Eqs. (7), (19), (20), and (24) is presented for the three canyons in Fig. 4a, c, e. The normalized mean absolute error (NMAE) and bias (NMB) are calculated to compare Code_Saturne and MUNICH results (see Appendix C for the definition of the statistical indicators). Figure 4a, c, e show a good agreement between Code_Saturne $\text{RD}_{q_{\text{vert}}}$ and the parameterized $\text{RD}_{q_{\text{vert}}}$ because the $f_{b \times t}$ function was determined to minimize bias. The NMAE can be high for $\text{RD}_{q_{\text{vert}}}$ (up to 63 % in NC) because the parameterization does

Table 2. Statistical indicators (normalized mean absolute error, NMAE, and bias, NMB, in percent) for the comparison of Code_Saturne and MUNICH q_{vert} and U_{street} .

Canyon	q_{vert}		U_{street}	
	NMAE	NMB	NMAE	NMB
WC	2.2	−2.1	3.4	−1.1
IC	3.5	2.8	4.4	−1.7
NC	4.1	−4.1	6.8	−2.8

not reproduce the slight decrease in $\text{RD}_{q_{\text{vert}}}$ when LAI_{2D} increases from $\text{LAI}_{2D} = 3$ to 4 when $h/H \approx 1/3$ and $1/2$ (see Sect. 3.2 and Fig. 3b and c). But this is not an issue for NC since the q_{vert} values are low.

For U_{street} , the parameter C_u also needs to be determined. A constant value of $C_u = 6.7$ is sufficient to obtain a good fit between Code_Saturne $\text{RD}_{U_{\text{street}}}$ and MUNICH $\text{RD}_{U_{\text{street}}}$. No dependency of C_u on building or tree features is needed, as shown in Fig. 4b, d, f, which compares Code_Saturne $\text{RD}_{U_{\text{street}}}$ and the parameterized $\text{RD}_{U_{\text{street}}}$. Note that the parameterizations of l_{ct} and $f_{b \times t}$ impact not only the vertical transfers but also the horizontal wind speed because they are involved in the calculation of the s_H factor and, hence, of the α coefficient. The good comparisons between Code_Saturne $\text{RD}_{U_{\text{street}}}$ and MUNICH $\text{RD}_{U_{\text{street}}}$ also show that the parameterized s_H reproduces the horizontal wind speed well and, therefore, also the interactions between trees and building effects and the influence of h_{max} .

4.3 Comparison of q_{vert} , U_{street} , and wind profiles

Figure 5a and b present, respectively, a comparison of Code_Saturne and parameterized q_{vert} and U_{street} . The statistical indicators are presented in Table 2. As MUNICH was parameterized to reproduce the tree effect observed in Code_Saturne well, and as the two models agree well in a treeless canyon (Maison et al., 2022), the vertical transfer coefficient and wind speed with trees are close between the two models, as expected (Fig. 5 and Table 2). The parameterized vertical transfer coefficients with trees agree well with the Code_Saturne ones, with normalized mean absolute errors ranging from 2.2 % to 4.1 % and bias from −4.1 % to 2.8 %. The parameterized average wind speed with trees agree well with Code_Saturne ones, with normalized mean absolute errors ranging from 3.4 % to 6.8 % and a normalized mean bias from −2.8 % to −1.1 %.

For each street canyon, Fig. 6 compares the Code_Saturne and parameterized vertical wind profiles for fixed CVF and h/H ratio but for five different LAI_{2D} .

Figure 6 shows that an increase in the LAI_{2D} induces a decrease in the wind velocity. Concerning the vertical profile shape, trees induce a lower wind velocity on the entire street and not only in the tree crown. They even slightly

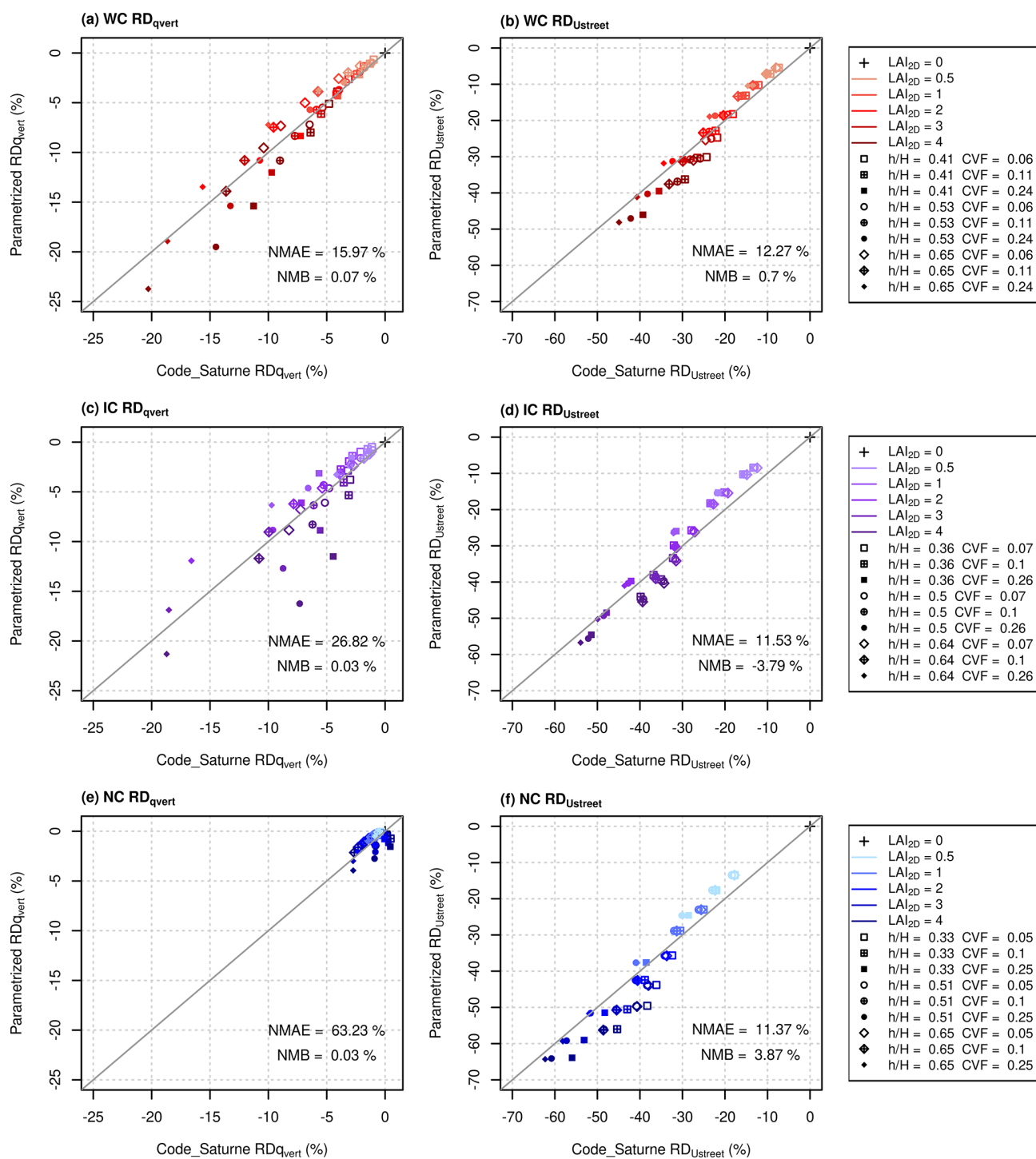


Figure 4. Comparison of (a, c, e) $RD_{q_{vert}}$ and (b, d, f) $RD_{U_{street}}$ computed from Code_Saturne simulations and parameterized in MUNICH for different tree LAI_{2D} , CVF, and height ratio and for (a, b) WC, (c, d) IC, and (e, f) NC.

impact the velocity just above the street. The maximum of attenuation of the wind is located in the middle of the tree crown and the wind velocity is re-accelerated under the tree crown. In the middle of the tree crown, the parameterized wind speed is close to the one of Code_Saturne. In the lower

part and under the tree crown, the parameterized wind speed is underestimated. In fact, the re-acceleration under the tree crown is complex to consider in parameterized models. Besides, in real streets the tree height is not homogeneous, so this re-acceleration under the tree crown might be unrealis-

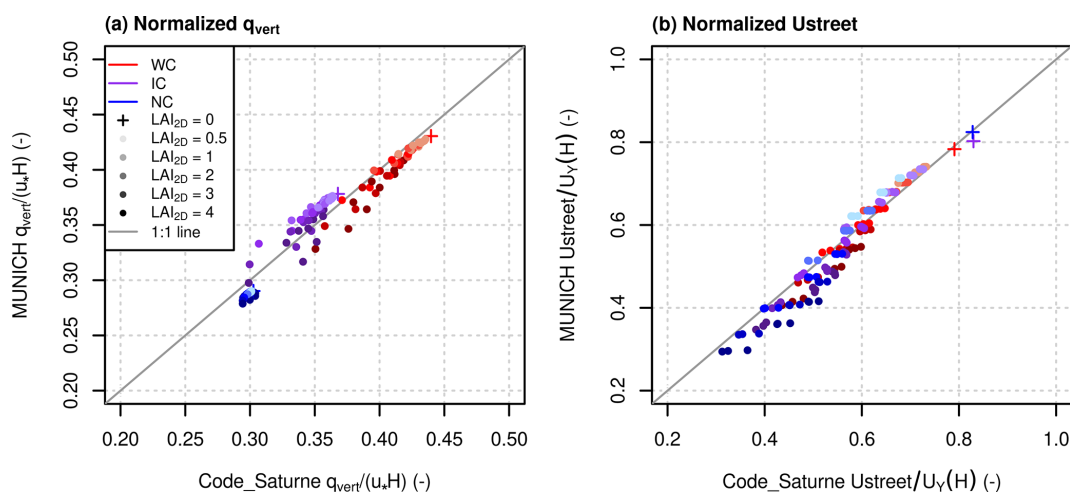


Figure 5. Normalized U_{street} and q_{vert} computed from Code_Saturne simulations for different tree $\text{LAI}_{2\text{D}}$, CVF, and height ratios.

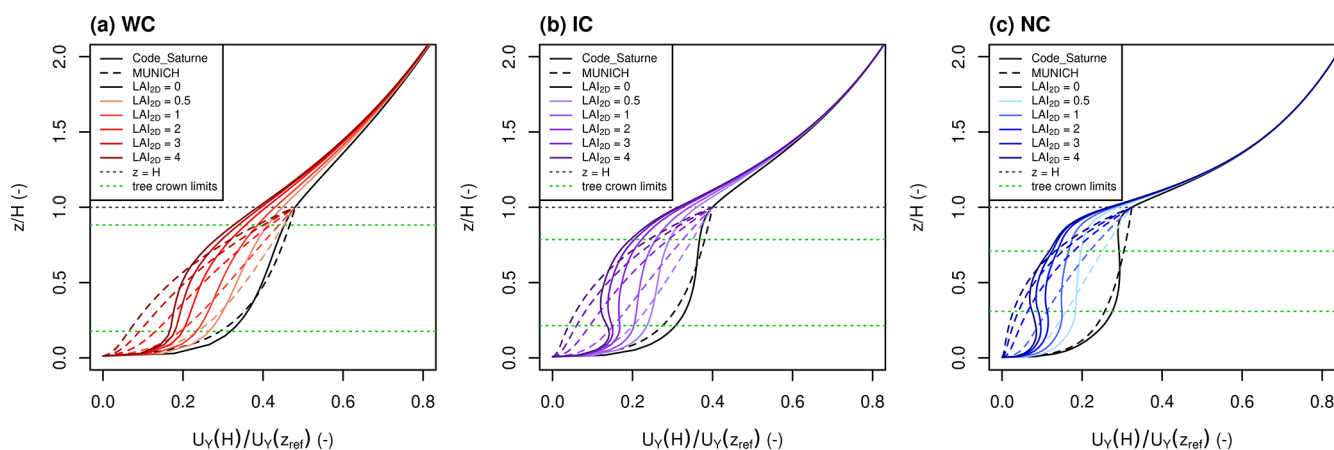


Figure 6. Comparison of Code_Saturne (solid lines) and parameterized (dotted lines) vertical wind profiles. The profiles in a treeless canyon are in black and darker colors correspond to increasing $\text{LAI}_{2\text{D}}$. For the three canyons, $h/H \approx 0.5$ and $\text{CVF} \approx 25\%$.

tic in Code_Saturne simulations. In the parameterized wind profile with trees, the reduction in the wind speed just above the street due to the presence of trees was neglected. So the parameterized wind speed above and in the upper part of the tree crown is overestimated compared to Code_Saturne. Note that Kent et al. (2017) proposed a method to include the vegetation effect in aerodynamic roughness parameters and so to account for vegetation in the above-urban canopy wind profile of Macdonald et al. (1998). This method considers vegetation at the city scale and is not applicable here, since we work at the street scale. For now, as MUNICH assumes a homogeneous street canyon, the profile is averaged to compute U_{street} , and the shape of the profile is not used.

Moreover, to illustrate the impact of the developed parametrization on pollutant concentrations, MUNICH simulations are performed with carbon monoxide emissions in IC without and with trees of various characteristics. The results are presented in Appendix D.

5 Conclusions

Although the discretizations and the physical modeling used in MUNICH and Code_Saturne are fundamentally different, the setup of the CFD simulations was adapted to compare the two models through the average horizontal wind speed along the street and the calculation of the vertical transfer coefficient at the roof level by averaging a passive tracer concentration in the street and the background (above the streets). To build a parametrization suited to the street network model MUNICH, the CFD simulations were simplified with several hypothesis such as an infinite street canyon with 2D CFD simulations and homogeneous emissions over the street. Furthermore, quantities of interest were averaged over the street in the CFD simulations.

The aerodynamic effect of trees in street canyons is quantified with Code_Saturne simulations. Simulations were performed with two rows of trees and a large range of tree

leaf area index, crown radius, and heights. In the range of the simulations performed, the average horizontal velocity in the street is reduced by -7.3% to -62.3% and the vertical transfer coefficient by $+0.5\%$ to -20.3% . This highlights the necessity of adding the tree aerodynamic effects into street models such as MUNICH.

Maison et al. (2022) proposed a parameterization of horizontal and vertical transfers in a treeless canyon, and the present study adds the tree effect to the building effect in this parameterization. The differences in wind speed and vertical transfer coefficient in a treeless canyon are very low between the two models (Maison et al., 2022). However, to overcome any model-specific difference and to build a parameterization for MUNICH of the tree effect on the aerodynamic parameters, relative deviation ratios between cases without and with trees are defined.

First, the Maison et al. (2022) vertical transfer coefficient parameterization is modified by adding a term representing the tree effect and the interaction between the trees and the buildings in the mixing-length expression. This term is a function of two dimensionless parameters to characterize the trees, street leaf area index (LAI_{street}) and tree-to-street height ratio (h_{max}/H), and also of street characteristics, building height (H), and street width (W). A parameterization of the tree mixing length was defined from Code_Saturne simulations to obtain a tree effect as close as possible in the two models. The parameterized vertical transfer coefficients with trees agree well with those of Code_Saturne, with the normalized mean absolute error ranging from 2.2% to 4.1% and bias from -4.1% to 2.8% .

Second, this new mixing length expression is also used to compute the vertical wind profile and average wind speed along the street. Only one constant is fixed in the wind attenuation coefficient to maximize the fit between Code_Saturne and MUNICH tree effect on average wind speed. The comparison of the average wind speed gives a normalized mean absolute error ranging from 3.4% to 6.8% and a normalized mean bias from -2.8% to -1.1% .

MUNICH now includes a relatively simple parameterization of the tree effect on both horizontal and vertical aerodynamic processes, based on commonly used tree parameters that can be easily computed from urban databases and can reproduce the main effects obtained in much more detailed and costly CFD simulations. This parameterization can also be used in urban climate models to compute water and heat transfer in tree-lined streets. The perspectives of this study are to quantify the effect of street trees on air quality from the street level to the scale of the city of Paris. Dry deposition of gaseous pollutants and aerosols on tree leaves and emission of biogenic organic volatile compounds related to tree water stress will be considered in MUNICH. The contribution of biogenic and anthropic precursors to the formation of organic aerosols over an entire city will be compared.

Appendix A: Lists of abbreviations, variable parameters, and tree dimensions

Each line of the Table A4 corresponds to the parameters of a simulation. For each case, simulations with different LAI_{2D} were performed as follows: 0.5, 1, 2, 3, and 4.

Table A1. List of abbreviations.

Acronym	Definition
WC	Wide canyon
IC	Intermediate canyon
NC	Narrow canyon
CTM	Chemistry transport model
CFD	Computational fluid dynamics
RD	Relative deviation
BVOC	Biogenic volatile organic compound

Table A2. List of parameters.

Symbol	Definition	Value	Unit
κ	Von Kàrmàn constant	0.42	–
PBLH	Planetary boundary layer height	1000	m
z_{0s}	Code_Saturne inside street walls roughness length	0.10	m
u_*	Friction velocity	0.727	m s^{-1}
E	Parameter in modified Wang (2014) parameterization	0.5	–
n	Number of tree rows	2	–
C_{Dt}	Tree crown drag coefficient (Katul and Albertson, 1998)	0.2	–

Table A3. List of variables.

Group of variables	Symbol	Definition	Unit
Street characteristics	H	Buildings height	m
	W	Street width	m
	L	Street length	m
	a_r	Street aspect ratio	–
	l_{cb}	Characteristic length in the street	m
Tree characteristics	LAD	Tree leaf area density	$\text{m}_{\text{leaf}}^2 \text{m}_{\text{tree crown}}^{-3}$
	LAI	Tree leaf area index	$\text{m}_{\text{leaf}}^2 \text{m}_{\text{soil}}^{-2}$
	LAI _{3D}	3D leaf area index of the spherical tree crown	$\text{m}_{\text{leaf}}^2 \text{m}_{\text{soil}}^{-2}$
	LAI _{2D}	2D equivalent leaf area index of the cylindrical tree crown	$\text{m}_{\text{leaf}}^2 \text{m}_{\text{soil}}^{-2}$
	LAI _{street}	Leaf area index of the homogeneous street tree crown	$\text{m}_{\text{leaf}}^2 \text{m}_{\text{soil}}^{-2}$
	S_{3D}	Soil projected area of the 3D spherical tree crown	m^2
	S_{2D}	Soil projected area of the 2D cylindrical tree crown	m^2
	S_{street}	Soil projected area of the street homogeneous tree crown	m^2
	r	Tree radius	m
	CVF	Crown volume fraction	– or %
	h	Middle crown height	m
	h_{max}	Maximum tree crown height	m
	h_{min}	Minimum tree crown height	m
δ	Spacing between two trees within a row	m	
l_{ct}	Tree characteristic length	m	
Horizontal wind speed	U_{street}	Average street horizontal wind speed	m s^{-1}
	U	Norm of the horizontal wind speed	m s^{-1}
	U_x	Horizontal wind speed in the x direction	m s^{-1}
	U_y	Horizontal wind speed in the y direction	m s^{-1}
	U_H	Average horizontal wind speed at roof level	m s^{-1}
	φ	Angle of the wind direction	rad or °
	α	Wind attenuation coefficient	–
	s_H	Characteristic length factor	–
Vertical transfer	C_u	Empiric coefficient in α equation	–
	C_B	Function of a_r and φ	–
	Q_{vert}	Vertical flux of pollutant	$\mu\text{g s}^{-1}$
	q_{vert}	Vertical transfer coefficient	$\text{m}^2 \text{s}^{-1}$
	σ_W	Standard deviation of the vertical wind speed at $z = H$ (Soulhac et al., 2011)	m s^{-1}
	l_m	Mixing length in the street	m
	e	Passive tracer emission rate for the street	$\mu\text{g s}^{-1}$
	C_{street}	Street concentration	$\mu\text{g m}^{-3}$
	C_{bg}	Background concentration	$\mu\text{g m}^{-3}$

Table A4. List of tree dimensions simulated with Code_Saturne (r is the radius, h is the middle crown height, h_{\min} is the crown bottom height, and h_{\max} is the crown top height) and calculated tree parameters (CVF is the crown volume fraction, and h/H is the height ratio).

Canyon	r (m)	h (m)	h_{\min} (m)	h_{\max} (m)	CVF (%)	h/H (-)
WC	1.5	3.5	2.0	5.0	6.0	0.41
	1.5	4.5	3.0	6.0	6.0	0.53
	1.5	5.5	4.0	7.0	6.0	0.65
	2.0	3.5	1.5	5.5	10.8	0.41
	2.0	4.5	2.5	6.5	10.8	0.53
	2.0	5.5	3.5	7.5	10.8	0.65
	3.0	3.5	0.5	6.5	24.2	0.41
	3.0	4.5	1.5	7.5	24.2	0.53
	3.0	5.5	2.5	8.5	24.2	0.65
IC	2.0	5.0	3.0	7.0	6.5	0.36
	2.0	7.0	5.0	9.0	6.5	0.50
	2.0	9.0	7.0	11.0	6.5	0.64
	2.5	5.0	2.5	7.5	10.2	0.36
	2.5	7.0	4.5	9.5	10.2	0.50
	2.5	9.0	6.5	11.5	10.2	0.64
	4.0	5.0	1.0	9.0	26.1	0.36
	4.0	7.0	3.0	10.0	26.1	0.50
	4.0	9.0	5.0	13.0	26.1	0.64
NC	2.5	9.0	6.5	11.5	5.2	0.33
	2.5	14.0	11.5	16.5	5.2	0.51
	2.5	18.0	15.5	20.5	5.2	0.65
	3.5	9.0	5.5	12.5	10.2	0.33
	3.5	14.0	10.5	17.5	10.2	0.51
	3.5	18.0	14.5	21.5	10.2	0.65
	5.5	9.0	3.5	14.5	25.1	0.33
	5.5	14.0	8.5	19.5	25.1	0.51
	5.5	18.0	12.5	23.5	25.1	0.65

Appendix B: Comparison of 2D and 3D Code_Saturne simulations with trees

Code_Saturne simulations were performed in a periodic 2D canyon of length $L = 1$ m, and the street was therefore considered infinite due to this periodicity. In this case, the tree crown is represented as an infinite cylinder of radius r . To take into account the fact that, in reality, most of the tree crowns are spherical and are spaced from each other, an equivalent cylindrical LAI_{2D} is calculated in the 2D simulations. For the tree effect to be similar, the surface of the leaves is kept constant between the 2D and 3D simulations, as follows:

$$\text{LAI}_{3D} \times S_{3D} = \text{LAI}_{2D} \times S_{2D} \quad (\text{B1})$$

$$\text{LAI}_{2D} = \text{LAI}_{3D} \times \frac{S_{3D}}{S_{2D}} = \text{LAI}_{3D} \times \frac{\pi r^2}{2r(2r + \delta)}, \quad (\text{B2})$$

where δ is the spacing between two tree crowns within the row, and $2r + \delta$ is the length of the street section for one spherical tree (m). S_{3D} and S_{2D} are, respectively, the soil-projected area of the 3D and 2D tree crowns (m²). In addition to the leaf surface and tree height, the tree radius is also conserved between 2D and 3D simulations; however, the value of the crown volume fraction (CVF) varies, as follows:

$$\text{CVF}_{2D} = \frac{V_{2D}}{V_{\text{street}}} = \frac{n\pi r^2 L}{HWL} \quad \text{and} \quad \text{CVF}_{3D} = \frac{V_{3D}}{V_{\text{street}}} = \frac{n\frac{4}{3}\pi r^3}{HW(2r + \delta)}. \quad (\text{B3})$$

V_{street} is the street volume (m³), and V_{3D} and V_{2D} are, respectively, the 3D and 2D tree crown volumes (m³). The relation between 2D and 3D CVF is therefore as follows:

$$\text{CVF}_{2D} = \frac{3}{4} \times \frac{2r + \delta}{r} \times \text{CVF}_{3D}. \quad (\text{B4})$$

2D and 3D simulations with different LAI are performed to check the validity of the 2D infinite street canyon hypothesis. 3D simulations are realized with a periodic street with a 10 m length and cell meshes of $0.5 \times 0.5 \times 0.5$ m in the x , y , and z directions. In both 2D and 3D simulations, C_{street} and C_{bg} are computed with a normal wind to the street ($\varphi = 90^\circ$) and U_{street} with $\varphi = 45^\circ$. The results are presented in Figs. B1a–d for WC, B1e–h for IC, and B1i–l for NC.

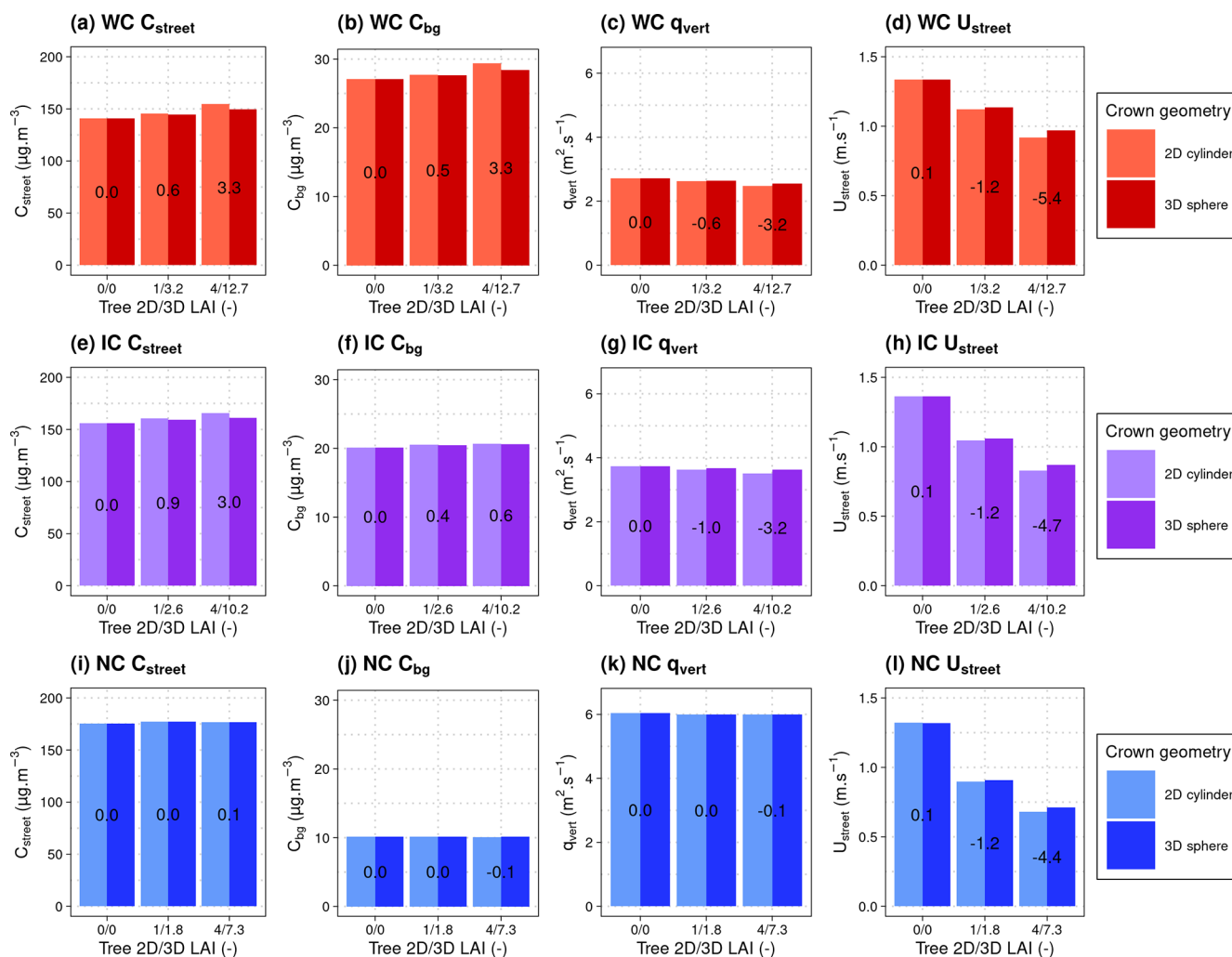


Figure B1. Comparison of C_{street} (a, e, i), C_{bg} (b, f, j), q_{vert} (c, g, k), and U_{street} (d, h, l) for 2D and 3D simulations in the three canyons without and with trees of $\text{LAI}_{2\text{D}} = 1$ and 4. $\text{CVF}_{2\text{D}} \approx 10\%$ and $h/H \approx 0.5$ are fixed. The percentages written in the middle of the histogram bars correspond to the RD between the 2D and 3D cases.

For each canyon, the cases without tree ($LAI = 0$) are equivalent. C_{street} , C_{bg} , q_{vert} , and U_{street} are similar between the 2D and 3D cases, with a maximum relative difference of 0.1 % for U_{street} . For the cases with trees, concerning C_{street} , C_{bg} , and q_{vert} , the differences between the 2D and 3D cases are relatively low over the range of simulations performed with a maximum of 3.3 % for C_{street} and C_{bg} in WC. For U_{street} , slightly larger differences are observed (up to -5.4 % in WC for $LAI = 4(2D)/12.7(3D)$). These differences can be explained by the distribution of the turbulence around the crown. For each variable and canyon, the relative deviation between the 2D and 3D cases increases with the tree LAI. Given the low differences observed between the 2D and 3D simulations, the hypothesis of a 2D canyon with a cylindrical tree crown associated with an equivalent LAI_{2D} to represent a spherical tree crown spaced of δ m in a street of length L is reasonable.

Appendix C: Definition of the statistical indicators

Code_Saturne and MUNICH simulations are denoted cs_i and m_i , respectively. In this section, n is the total number of simulations, which is equal to 45 per street canyon.

- Normalized mean absolute error (%):

$$NMAE = 100 \times \frac{\sum_{i=1}^n |m_i - cs_i|}{\left| \sum_{i=1}^n cs_i \right|}. \quad (C1)$$

- Normalized mean bias (%):

$$NMB = 100 \times \frac{\sum_{i=1}^n (m_i - cs_i)}{\sum_{i=1}^n cs_i}. \quad (C2)$$

Appendix D: Aerodynamic tree effect on concentration

To illustrate the impact of the developed parameterization on pollutant concentrations, MUNICH simulations are performed in the Intermediate Canyon (IC) with carbon monoxide (CO) emissions in the street. The input parameters are detailed in Table D1.

In the simulations, only the tree aerodynamic effect is considered, and there is no chemistry, no deposition of pollutants on urban or tree surfaces, and no biogenic volatile organic compound (BVOC) emission. One street is modeled without any inflow of pollutant from nearby streets. The following three processes are taken into account: pollutant emission in the street, pollutant outflow by horizontal transfer, $Q_{outflow}$ (function of the parameterized U_{street}), and vertical transfer

Table D1. List of parameters fixed in MUNICH simulation.

Fixed parameter	Symbol	Value	Unit
Building height	H	14	m
Street width	W	27.5	m
Street length	L	200	m
Wind angle	φ	45	°
Friction velocity	u_*	0.7	m s^{-1}
CO emission rate	e	1000	$\mu\text{g s}^{-1} \text{m}^{-1}$
CO background concentration	C_{bg}	100	$\mu\text{g m}^{-3}$

between the street and the background, Q_{vert} (function of the parameterized q_{vert}).

The street average CO concentrations (C_{street}) are compared in Fig. D1 for a canyon without trees (Fig. D1a) and for a canyon with trees of various LAI, CVF, and height ratios h/H (Fig. D1b, c).

Figure D1 shows that the increase in tree LAI and CVF induces higher average street CO concentrations. The effect of the tree height ratio h/H is negligible for low LAI and increases when the LAI increases. The variations in the concentrations are due to both the effect of trees on the horizontal transfer velocity, U_{street} , and on the vertical transfer coefficient, q_{vert} .

In this example, the aerodynamical effect of trees leads to a large increase in the CO concentration from 4 % to 45 %. However, to simulate the global effect of trees on air quality at street level, other processes such as dry deposition on leaves and BVOC emissions need to be considered.

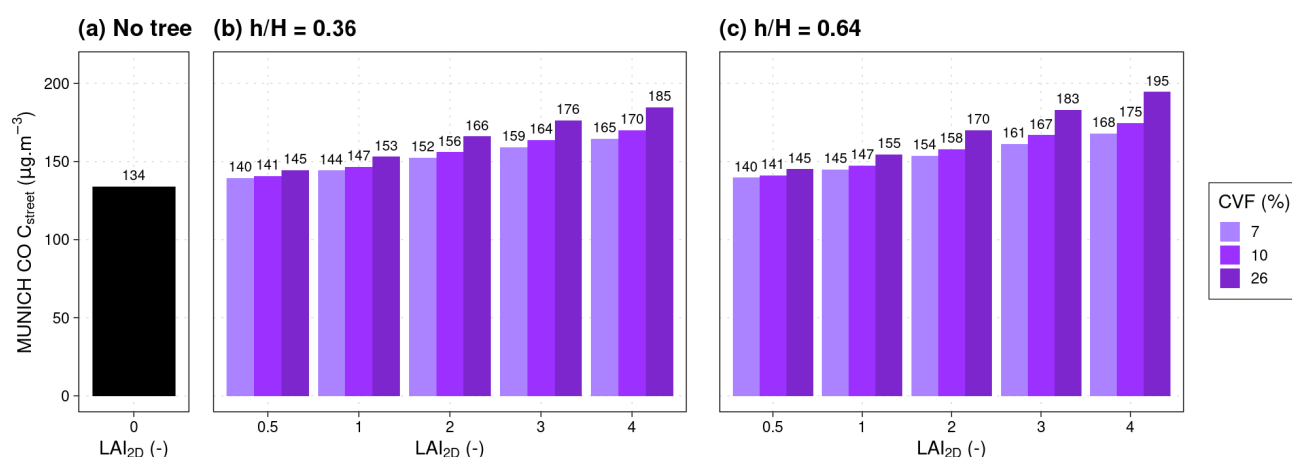


Figure D1. Comparison of CO concentration (C_{street}) simulated with MUNICH in IC for different tree LAI_{2D} , CVF, and tree height ratios h/H . The graphic is divided into three columns corresponding to the treeless canyon (a) and to canyons with trees of height ratios $h/H = 0.36$ (b) and 0.64 (c). The concentrations C_{street} (in $\mu\text{g m}^{-3}$) are specified with data labels.

Code availability. The last version of the MUNICH source code is available online at <https://doi.org/10.5281/zenodo.4168984> (Kim et al., 2022) and <https://github.com/cerea-lab/munich> (last access: 5 January 2022).

Data availability. For the three 2D canyons considered in the present study, the mesh, the source code, and the XML setup file allowing the reproduction of the CFD results using Code_Saturne version 6.0 are available online at https://gitlab.enpc.fr/alice.maison/tree_parametrization (last access: 3 December 2021) and at <https://doi.org/10.17632/fzfrjsz3mv.2> (Maison and Flageul, 2021) under the GNU GPL2.0 license.

Author contributions. KS, CF, BC, and AM were responsible for the conceptualization. AM developed the MUNICH model code and performed the Code_Saturne simulations. AM, KS, CF, and BC performed the formal analysis. AM conducted the visualization. AM, KS, and CF were responsible for writing the original draft, and BC and AT reviewed it. CF, BC, and YW provided support for the Code_Saturne computing resources. KS and AT were responsible for the funding acquisition.

Competing interests. The contact author has declared that none of the authors has any competing interests.

Disclaimer. Publisher's note: Copernicus Publications remains neutral with regard to jurisdictional claims in published maps and institutional affiliations.

Special issue statement. This article is part of the special issue “Air quality research at street level (ACP/GMD inter-journal SI)”. It is not associated with a conference.

Acknowledgements. The authors thank Youngseob Kim and Lya Lugon, for their support in the development of the MUNICH model, and Martin Ferrand, for his support in the understanding of the Code_Saturne model.

Financial support. This work has partially been funded by the sTREEt ANR project (grant no. ANR-19-CE22-0012), the DIM Qi2 (Air Quality Research Network on air quality in the Île-de-France region), and Paris Île-de-France Region.

Review statement. This paper was edited by Yang Zhang and reviewed by two anonymous referees.

References

- Akimoto, H.: Global Air Quality and Pollution, *Science*, 302, 1716–1719, <https://doi.org/10.1126/science.1092666>, 2003.
- Angel, S., Parent, J., Civco, D. L., Blei, A., and Potere, D.: The dimensions of global urban expansion: Estimates and projections for all countries, 2000–2050, *Prog. Plann.*, 75, 53–107, <https://doi.org/10.1016/j.progress.2011.04.001>, 2011.
- Archambeau, F., Méchitoua, N., and Sakiz, M.: Code Saturne: A finite volume code for the computation of turbulent incompressible flows-Industrial applications, *International Journal on Finite*

- Volumes, 1, 1–62, <https://hal.archives-ouvertes.fr/hal-01115371> (last access: 18 July 2022), 2004.
- Armson, D., Stringer, P., and Ennos, A.: The effect of street trees and amenity grass on urban surface water runoff in Manchester, UK, *Urban For. Urban Gree.*, 12, 282–286, <https://doi.org/10.1016/j.ufug.2013.04.001>, 2013.
- Beckett, K., Freer-Smith, P., and Taylor, G.: Urban woodlands: their role in reducing the effects of particulate pollution, *Environ. Pollut.*, 99, 347–360, [https://doi.org/10.1016/S0269-7491\(98\)00016-5](https://doi.org/10.1016/S0269-7491(98)00016-5), 1998.
- Berland, A., Shiflett, S. A., Shuster, W. D., Garmestani, A. S., Goddard, H. C., Herrmann, D. L., and Hopton, M. E.: The role of trees in urban stormwater management, *Landscape Urban Plan.*, 162, 167–177, <https://doi.org/10.1016/j.landurbplan.2017.02.017>, 2017.
- Bertram, C. and Rehdanz, K.: The role of urban green space for human well-being, *Ecol. Econ.*, 120, 139–152, <https://doi.org/10.1016/j.ecolecon.2015.10.013>, 2015.
- Bowler, D. E., Buyung-Ali, L., Knight, T. M., and Pullin, A. S.: Urban greening to cool towns and cities: A systematic review of the empirical evidence, *Landscape Urban Plan.*, 97, 147–155, <https://doi.org/10.1016/j.landurbplan.2010.05.006>, 2010.
- Bozonnet, E., Musy, M., Calmet, I., and Rodriguez, F.: Modeling methods to assess urban fluxes and heat island mitigation measures from street to city scale, *International Journal of Low-Carbon Technologies*, 10, 62–77, <https://doi.org/10.1093/ijlct/ctt049>, 2015.
- Buccolieri, R., Gromke, C., Di Sabatino, S., and Ruck, B.: Aerodynamic effects of trees on pollutant concentration in street canyons, *Sci. Total Environ.*, 407, 5247–5256, <https://doi.org/10.1016/j.scitotenv.2009.06.016>, 2009.
- Buccolieri, R., Salim, M., Leo, L. S., Di Sabatino, S., Chan, A., Ielpo, P., de Gennaro, G., and Gromke, C.: Analysis of local scale tree–atmosphere interaction on pollutant concentration in idealized street canyons and application to a real urban junction, *Atmos. Environ.*, 45, 1702–1713, <https://doi.org/10.1016/j.atmosenv.2010.12.058>, 2011.
- Buccolieri, R., Santiago, J.-L., Rivas, E., and Sanchez, B.: Review on urban tree modelling in CFD simulations: Aerodynamic, deposition and thermal effects, *Urban For. Urban Gree.*, 31, 212–220, <https://doi.org/10.1016/j.ufug.2018.03.003>, 2018.
- Cai, X.-M., Barlow, J., and Belcher, S.: Dispersion and transfer of passive scalars in and above street canyons – Large-eddy simulations, *Atmos. Environ.*, 42, 5885–5895, <https://doi.org/10.1016/j.atmosenv.2008.03.040>, 2008.
- Calfapietra, C., Fares, S., Manes, F., Morani, A., Sgrigna, G., and Loreto, F.: Role of Biogenic Volatile Organic Compounds (BVOC) emitted by urban trees on ozone concentration in cities: A review, *Environ. Pollut.*, 183, 71–80, <https://doi.org/10.1016/j.envpol.2013.03.012>, 2013.
- Faiz, A.: Automotive emissions in developing countries–relative implications for global warming, acidification and urban air quality, *Transportation Res. A-Pol.*, 27, 167–186, [https://doi.org/10.1016/0965-8564\(93\)90057-R](https://doi.org/10.1016/0965-8564(93)90057-R), 1993.
- Gillner, S., Vogt, J., Tharang, A., Dettmann, S., and Roloff, A.: Role of street trees in mitigating effects of heat and drought at highly sealed urban sites, *Landscape Urban Plan.*, 143, 33–42, <https://doi.org/10.1016/j.landurbplan.2015.06.005>, 2015.
- Gromke, C. and Blocken, B.: Influence of avenue-trees on air quality at the urban neighborhood scale. Part II: Traffic pollutant concentrations at pedestrian level, *Environ. Pollut.*, 196, 176–184, <https://doi.org/10.1016/j.envpol.2014.10.015>, 2015.
- Gromke, C. and Ruck, B.: Influence of trees on the dispersion of pollutants in an urban street canyon – Experimental investigation of the flow and concentration field., *Atmos. Environ.*, 41, 3287–3302, <https://doi.org/10.1016/j.atmosenv.2006.12.043>, 2007.
- Gromke, C. and Ruck, B.: On the Impact of Trees on Dispersion Processes of Traffic Emissions in Street Canyons, *Bound.-Lay. Meteorol.*, 131, 19–34, <https://doi.org/10.1007/s10546-008-9301-2>, 2009.
- Gromke, C. and Ruck, B.: Pollutant Concentrations in Street Canyons of Different Aspect Ratio with Avenues of Trees for Various Wind Directions, *Bound.-Lay. Meteorol.*, 144, 41–64, <https://doi.org/10.1007/s10546-012-9703-z>, 2012.
- Gu, S., Guenther, A., and Faiola, C.: Effects of Anthropogenic and Biogenic Volatile Organic Compounds on Los Angeles Air Quality, *Environ. Sci. Technol.*, 55, 12191–12201, <https://doi.org/10.1021/acs.est.1c01481>, 2021.
- Gunawardena, K., Wells, M., and Kershaw, T.: Utilising green and bluespace to mitigate urban heat island intensity, *Sci. Total Environ.*, 584–585, 1040–1055, <https://doi.org/10.1016/j.scitotenv.2017.01.158>, 2017.
- Harman, I. N., Barlow, J. F., and Belcher, S. E.: Scalar fluxes from urban street canyons. Part II Model, *Bound.-Lay. Meteorol.*, 113, 387–409, <https://doi.org/10.1007/s10546-004-6205-7>, 2004.
- Hebbert, M. and Jankovic, V.: Cities and Climate Change: The Precedents and Why They Matter, *Urban Stud.*, 50, 1332–1347, <https://doi.org/10.1177/0042098013480970>, 2013.
- Huang, Y.-D., Hou, R.-W., Liu, Z.-Y., Song, Y., Cui, P.-Y., and Kim, C.-N.: Effects of Wind Direction on the Airflow and Pollutant Dispersion inside a Long Street Canyon, *Aerosol Air Qual. Res.*, 19, 1152–1171, <https://doi.org/10.4209/aaqr.2018.09.0344>, 2019.
- Hwang, H.-J., Yook, S.-J., and Ahn, K.-H.: Experimental investigation of submicron and ultrafine soot particle removal by tree leaves, *Atmos. Environ.*, 45, 6987–6994, <https://doi.org/10.1016/j.atmosenv.2011.09.019>, 2011.
- IPCC: Climate Change 2021: The Physical Science Basis. Contribution of Working Group I to the Sixth Assessment Report of the Intergovernmental Panel on Climate Change, Report, Intergovernmental Panel on Climate Change, United Nations, edited by: Masson-Delmotte, V., Zhai, P., Pirani, A., Connors, S. L., Péan, C., Berger, S., Caud, N., Chen, Y., Goldfarb, L., Gomis, M. I., Huang, M., Leitzell, K., Lonnoy, E., Matthews, J. B. R., Maycock, T. K., Waterfield, T., Yelekçi, O., Yu, R., and Zhou, B., Cambridge University Press, <https://www.ipcc.ch/report/ar6/wg1/> (last access: 18 July 2022), 2021.
- Janhäll, S.: Review on urban vegetation and particle air pollution – Deposition and dispersion, *Atmos. Environ.*, 105, 130–137, <https://doi.org/10.1016/j.atmosenv.2015.01.052>, 2015.
- Jayasooriya, V., Ng, A., Muthukumar, S., and Perera, B.: Green infrastructure practices for improvement of urban air quality, *Urban For. Urban Gree.*, 21, 34–47, <https://doi.org/10.1016/j.ufug.2016.11.007>, 2017.
- Jeanjean, A., Buccolierib, R., Eddy, J., Monks, P., and Leigh, R.: Air quality affected by trees in real street canyons: The case of Marylebone neighbourhood in

- central London., *Urban For. Urban Gree.*, 22, 41–43, <https://doi.org/10.1016/j.ufug.2017.01.009>, 2017.
- Katul, G. and Albertson, J.: An Investigation of Higher-Order Closure Models for a Forested Canopy, *Bound.-Lay. Meteorol.*, 89, 47–74, <https://doi.org/10.1023/A:1001509106381>, 1998.
- Katul, G. G., Mahrt, L., Poggi, D., and Sanz, C.: ONE- and TWO-Equation Models for Canopy Turbulence, *Bound.-Lay. Meteorol.*, 113, 81–109, <https://doi.org/10.1023/B:BOUN.0000037333.48760.e5>, 2004.
- Kent, C. W., Grimmond, S., and Gatey, D.: Aerodynamic roughness parameters in cities: Inclusion of vegetation, *J. Wind Eng. Ind. Aerod.*, 169, 168–176, <https://doi.org/10.1016/j.jweia.2017.07.016>, 2017.
- Kim, Y., Wu, Y., Seigneur, C., and Roustan, Y.: Multi-scale modeling of urban air pollution: development and application of a Street-in-Grid model (v1.0) by coupling MUNICH (v1.0) and Polair3D (v1.8.1), *Geosci. Model Dev.*, 11, 611–629, <https://doi.org/10.5194/gmd-11-611-2018>, 2018.
- Kim, Y., Sartelet, K., Lugon, L., Roustan, Y., Sarica, T., Maison, A., Valari, M., Zhang, Y., and André, M.: The Model of Urban Network of Intersecting Canyons and Highways (MUNICH), Zenodo [code], <https://doi.org/10.5281/zenodo.6167477>, 2022.
- Klemm, W., Heusinkveld, B. G., Lenzholzer, S., and van Hove, B.: Street greenery and its physical and psychological impact on thermal comfort, *Landscape Urban Plan.*, 138, 87–98, <https://doi.org/10.1016/j.landurbplan.2015.02.009>, 2015.
- Krekel, C., Kolbe, J., and Wüstemann, H.: The Greener, The Happier? The Effects of Urban Green and Abandoned Areas on Residential Well-Being, *The German Socio-Economic Panel study at DIW Berlin*, 728, 65, <https://doi.org/10.2139/ssrn.2554477>, 2015.
- Leopold, L. B.: Hydrology for urban land planning – A guidebook on the hydrologic effects of urban land use, *US. Geological Survey*, 554, 18, <https://doi.org/10.3133/cir554>, 1968.
- Li, X., Liu, C., Leung, D., and Lam, K.: Recent progress in CFD modelling of wind field and pollutant transport in street canyons, *Atmos. Environ.*, 40, 5640–5658, <https://doi.org/10.1016/j.atmosenv.2006.04.055>, 2006.
- Livesley, S. J., McPherson, E. G., and Calfapietra, C.: The Urban Forest and Ecosystem Services: Impacts on Urban Water, Heat, and Pollution Cycles at the Tree, Street, and City Scale, *J. Environ. Qual.*, 45, 119–124, <https://doi.org/10.2134/jeq2015.11.0567>, 2016.
- Lobaccaro, G. and Acero, J.: Comparative analysis of green actions to improve outdoor thermal comfort inside typical urban street canyons, *Urban Climate*, 14, 251–267, <https://doi.org/10.1016/j.uclim.2015.10.002>, 2015.
- Lugon, L., Sartelet, K., Kim, Y., Vigneron, J., and Chrétien, O.: Nonstationary modeling of NO₂, NO and NO_x in Paris using the Street-in-Grid model: coupling local and regional scales with a two-way dynamic approach, *Atmos. Chem. Phys.*, 20, 7717–7740, <https://doi.org/10.5194/acp-20-7717-2020>, 2020.
- Lugon, L., Sartelet, K., Kim, Y., Vigneron, J., and Chrétien, O.: Simulation of primary and secondary particles in the streets of Paris using MUNICH, *Faraday Discuss.*, <https://doi.org/10.1039/D0FD00092B>, 2021.
- Macdonald, R., Griffiths, R., and Hall, D.: An improved method for the estimation of surface roughness of obstacle arrays, *Atmos. Environ.*, 32, 1857–1864, [https://doi.org/10.1016/S1352-2310\(97\)00403-2](https://doi.org/10.1016/S1352-2310(97)00403-2), 1998.
- Maison, A. and Flageul, C.: Parameterizing the aerodynamic effect of trees in street canyons for the street-network model MUNICH using the CFD model Code_Saturne – Code_Saturne simulation dataset, V2, Mendeley Data [code], <https://doi.org/10.17632/fzfrjsz3mv.2>, 2021.
- Maison, A., Flageul, C., Carissimo, B., Tuzet, A., and Sartelet, K.: Parametrization of Horizontal and Vertical Transfers for the Street-Network Model MUNICH Using the CFD Model Code_Saturne, *Atmosphere*, 13, 527, <https://doi.org/10.3390/atmos13040527>, 2022.
- Direction des Espaces Verts et de l'Environnement – Mairie de Paris: Les arbres – OpenDataParis, <https://opendata.paris.fr/explore/dataset/les-arbres/>, last access: 17 December 2021.
- Nowak, D. J., McHale, P. J., Ibarra, M., Crane, D., Stevens, J. C., and Luley, C. J.: Modeling the Effects of Urban Vegetation on Air Pollution, in: *Air Pollution Modeling and Its Application XII*, edited by: Gryning, S. E. and Chaumerliac, N., NATO, Challenges of Modern Society, vol 22., Springer, Boston, MA, 1998.
- Nowak, D. J. and Crane, D. E.: Carbon storage and sequestration by urban trees in the USA, *Environ. Pollut.*, 116, 381–389, [https://doi.org/10.1016/S0269-7491\(01\)00214-7](https://doi.org/10.1016/S0269-7491(01)00214-7), 2002.
- Nowak, D. J., Crane, D. E., and Stevens, J. C.: Air pollution removal by urban trees and shrubs in the United States, *Urban For. Urban Gree.*, 4, 115–123, <https://doi.org/10.1016/j.ufug.2006.01.007>, 2006.
- Oke, T.: Street design and urban canopy layer climate, *Energ. Buildings*, 11, 103–113, [https://doi.org/10.1016/0378-7788\(88\)90026-6](https://doi.org/10.1016/0378-7788(88)90026-6), 1988.
- Oke, T. R.: The energetic basis of the urban heat island, *Q. J. Roy. Meteor. Soc.*, 108, 1–24, <https://doi.org/10.1002/qj.49710845502>, 1982.
- Ozdemir, H.: Mitigation impact of roadside trees on fine particle pollution, *Sci. Total Environ.*, 659, 1176–1185, <https://doi.org/10.1016/j.scitotenv.2018.12.262>, 2019.
- Pascal, M., Corso, M., Chanel, O., Declercq, C., Badaloni, C., Cesaroni, G., Henschel, S., Meister, K., Haluza, D., Martin-Olmedo, P., and Medina, S.: Assessing the public health impacts of urban air pollution in 25 European cities: Results of the Aphekom project, *Sci. Total Environ.*, 449, 390–400, <https://doi.org/10.1016/j.scitotenv.2013.01.077>, 2013.
- Pigeon, G., Legain, D., Durand, P., and Masson, V.: Anthropogenic heat release in an old European agglomeration (Toulouse, France), *Int. J. Climatol.*, 27, 1969–1981, <https://doi.org/10.1002/joc.1530>, 2007.
- Prédez, M., Araya, M., Criollo, C., Egas, C., Farías, I., Fuentealba, R., and González, E.: Urban Trees and Their Relationship with Air Pollution by Particulate Matter and Ozone in Santiago, Chile, in: *Urban Climates in Latin America*, edited by: Henríquez, C. and Romero, H., Springer International Publishing, pp. 167–206, https://doi.org/10.1007/978-3-319-97013-4_8, 2019.
- Revelli, R. and Porporato, A.: Ecohydrological model for the quantification of ecosystem services provided by urban street trees, *Urban Ecosyst.*, 21, 489–504, <https://doi.org/10.1007/s11252-018-0741-2>, 2018.
- Robine, J., Cheung, S., and Roy, S. L.: Report on excess mortality in Europe during summer 2003, *Tech. Rep.*, EU Community Action Programme for Public Health, <http://ec.europa.eu/health/>

- ph_projects/2005/action1/docs/action1_2005_a2_15_en.pdf (last access: 18 July 2022), 2007.
- Santiago, J.-L., Rivas, E., Sanchez, B., Buccolieri, R., and Martin, F.: The Impact of Planting Trees on NO_x Concentrations: The Case of the Plaza de la Cruz Neighborhood in Pamplona (Spain), *Atmosphere*, 8, 131, <https://doi.org/10.3390/atmos8070131>, 2017.
- Sartelet, K., Zhu, S., Moukhtar, S., André, M., André, J., Gros, V., Favez, O., Brasseur, A., and Redaelli, M.: Emission of intermediate, semi and low volatile organic compounds from traffic and their impact on secondary organic aerosol concentrations over Greater Paris, *Atmos. Environ.*, 180, 126–137, 2018.
- Selmi, W., Weber, C., Rivière, E., Blond, N., Mehdi, L., and Nowak, D.: Air pollution removal by trees in public green spaces in Strasbourg city, France, *Urban For. Urban Gree.*, 17, 192–201, <https://doi.org/10.1016/j.ufug.2016.04.010>, 2016.
- Soulhac, L., Salizzoni, P., Cierco, F.-X., and Perkins, R.: The model SIRANE for atmospheric urban pollutant dispersion; part I, presentation of the model, *Atmos. Environ.*, 45, 7379–7395, <https://doi.org/10.1016/j.atmosenv.2011.07.008>, 2011.
- Speziale, C., Sarkar, S., and Gatski, T.: Modelling the pressure-strain correlation of turbulence – An invariant dynamical systems approach, *J. Fluid Mech.*, 227, 245–272, <https://doi.org/10.1017/S0022112091000101>, 1991.
- Stewart, I.: A systematic review and scientific critique of methodology in modern urban heat island literature, *Int. J. Climatol.*, 31, 200–217, <https://doi.org/10.1002/joc.2141>, 2011.
- Svirejeva-Hopkins, A., Schellhuber, H., and Pomaz, V.: Urbanised territories as a specific component of the Global Carbon Cycle, *Ecol. Model.*, 173, 295–312, <https://doi.org/10.1016/j.ecolmodel.2003.09.022>, 2004.
- Taha, H., Akbari, H., and Rosenfeld, A.: Heat island and oasis effects of vegetative canopies: Micro-meteorological field-measurements, *Theor. Appl. Climatol.*, 44, 123–138, <https://doi.org/10.1007/BF00867999>, 1991.
- van Dillen, S. M. E., de Vries, S., Groenewegen, P. P., and Spreeuwenberg, P.: Greenspace in urban neighbourhoods and residents' health: adding quality to quantity, *J. Epidemiol. Commun. H.*, 66, e8, <https://doi.org/10.1136/jech.2009.104695>, 2012.
- Vardoulakis, S., Fisher, B. E., Pericleous, K., and Gonzalez-Flesca, N.: Modelling air quality in street canyons: a review, *Atmos. Environ.*, 37, 155–182, [https://doi.org/10.1016/S1352-2310\(02\)00857-9](https://doi.org/10.1016/S1352-2310(02)00857-9), 2003.
- Vos, P. E., Maiheu, B., Vankerkom, J., and Janssen, S.: Improving local air quality in cities: To tree or not to tree?, *Environ. Pollut.*, 183, 113–122, <https://doi.org/10.1016/j.envpol.2012.10.021>, 2013.
- Wang, W.: An Analytical Model for Mean Wind Profiles in Sparse Canopies, *Bound.-Lay. Meteorol.*, 142, 383–399, <https://doi.org/10.1007/s10546-011-9687-0>, 2012.
- Wang, W.: Analytically Modelling Mean Wind and Stress Profiles in Canopies, *Bound.-Lay. Meteorol.*, 151, 239–256, <https://doi.org/10.1007/s10546-013-9899-6>, 2014.
- Wania, A., Bruse, M., Blond, N., and Weber, C.: Analysing the influence of different street vegetation on traffic-induced particle dispersion using microscale simulations., *J. Env. Manag.*, 94, 91–101, <https://doi.org/10.1016/j.jenvman.2011.06.036>, 2012.
- Wei, X., Dupont, E., Gilbert, E., Musson-Genon, L., and Carissimo, B.: Experimental and Numerical Study of Wind and Turbulence in a Near-Field Dispersion Campaign at an Inhomogeneous Site, *Bound.-Lay. Meteorol.*, 160, 475–499, <https://doi.org/10.1007/s10546-016-0148-7>, 2016.
- West, J. J., Cohen, A., Dentener, F., Brunekreef, B., Zhu, T., Armstrong, B., Bell, M. L., Brauer, M., Carmichael, G., Costa, D. L., Dockery, D. W., Kleeman, M., Krzyzanowski, M., Künzli, N., Liou, S.-C. C., Martin, R. V., Pöschl, U., Pope, C. A., Roberts, J. M., Russell, A. G., and Wiedinmyer, C.: What We Breathe Impacts Our Health: Improving Understanding of the Link between Air Pollution and Health, *Environ. Sci. Technol.*, 50, 4895–4904, <https://doi.org/10.1021/acs.est.5b03827>, 2016.
- Xue, F. and Li, X.: The impact of roadside trees on traffic released PM₁₀ in urban street canyon: Aerodynamic and deposition effects, *Sustain. Cities Soc.*, 30, 195–204, <https://doi.org/10.1016/j.scs.2017.02.001>, 2017.
- Yuan, C., Ng, E., and Norford, L. K.: Improving air quality in high-density cities by understanding the relationship between air pollutant dispersion and urban morphologies, *Build. Environ.*, 71, 245–258, <https://doi.org/10.1016/j.buildenv.2013.10.008>, 2014.
- Zaïdi, H., Dupont, E., Milliez, M., Musson-Genon, L., and Carissimo, B.: Numerical Simulations of the Microscale Heterogeneities of Turbulence Observed on a Complex Site, *Bound.-Lay. Meteorol.*, 147, 237–259, <https://doi.org/10.1007/s10546-012-9783-9>, 2013.
- Zhang, Y., Gu, Z., and Yu, C. W.: Impact Factors on Airflow and Pollutant Dispersion in Urban Street Canyons and Comprehensive Simulations: a Review, *Current Pollution Report*, 6, 425–439, <https://doi.org/10.1007/s40726-020-00166-0>, 2020.

2.4 Conclusion

The development of a parameterization to represent air flow in a street canyon with and without tree in MUNICH is the first step to include the effects of urban trees on air quality at the street scale. This parameterization has been developed based on an analytical expression of the wind and turbulent transfer vertical profiles for sparse canopies and was adapted to a street canyon with or without trees with CFD simulations. The parameterization depends on generic street and tree parameters and can be used in various cases. The main limitations are that the tree crowns must not exceed building height and the leaf surface is distributed over the entire street, which is considered homogeneous. The equations have developed for streets with aspect ratios ranging from 0.3 to 1, and its application to wider or narrower streets should be treated with caution.

The impact of parameterizing the aerodynamic effect of trees on concentrations of gaseous and particulate pollutants will be quantified for the city of Paris in Chapter 4.

Chapter 3

Bottom-up inventory of urban-tree biogenic emissions in Paris and impact on regional-scale air quality

Contents

3.1	Introduction	73
3.2	Materials and Methods	74
3.2.1	Tree-based BVOC emission model	74
3.2.2	Tree inventory and characteristics	75
3.2.3	Description of regional-scale air-quality simulations	75
3.2.4	Description of the air-quality experimental measurements	77
3.3	Bottom-up inventory of tree BVOC emissions and comparison to the land-use approach	79
3.3.1	Calculation of BVOC emissions at the tree level	79
3.3.2	Integration of individual tree BVOC emissions in CHIMERE	86
3.3.3	Complementarity of the emissions computed by the bottom-up and the land-use approaches	87
3.4	Quantification of the impact of BVOC emissions from urban trees on air quality at the regional scale	90
3.4.1	Validation of the reference simulations	90
3.4.2	Impact of biogenic emissions from urban trees on concentrations	97
3.5	Conclusions	106
3.6	Appendices	108

This chapter presents the development of a bottom-up inventory of biogenic emissions from urban trees. Emissions are computed by individual trees and integrated in the chemistry-transport model WRF-CHIMERE to quantify the impact on air-quality at the regional scale. This chapter is written as an article and has been submitted to the Atmospheric Chemistry and Physics journal.

Bottom-up inventory of urban-tree biogenic emissions in Paris and impact on regional-scale air quality

Alice Maison^{1,2}, Lya Lugon¹, Soo-Jin Park¹, Alexia Baudic³, Christopher Cantrell⁴, Florian Couvidat⁵, Barbara D'Anna⁶, Claudia Di Biagio⁷, Aline Gratien⁷, Valérie Gros⁸, Carmen Kalalian^{8,a}, Julien Kammer⁶, Vincent Michoud⁷, Jean-Eudes Petit⁸, Marwa Shahin⁶, Leila Simon^{8,b}, Myrto Valari⁹, Jérémy Vigneron³, Andrée Tuzet², and Karine Sartelet¹

¹CEREA, École des Ponts, EDF R&D, IPSL, Marne-la-Vallée, France

²Université Paris-Saclay, INRAE, AgroParisTech, UMR EcoSys, 91120 Palaiseau, France

³Airparif, Association Agréée pour la Surveillance de la Qualité de l'Air en région Île-de-France, 7 rue Crillon, 75004 Paris, France

⁴Univ Paris Est Creteil and Université Paris Cité, CNRS, LISA, F-94010 Créteil, France

⁵Institut National de l'Environnement Industriel et des Risques, Verneuil-en-Halatte, France

⁶Aix Marseille Univ, CNRS, LCE, Marseille, France

⁷Université Paris Cité and Univ Paris Est Creteil, CNRS, LISA, F-75013 Paris, France

⁸Laboratoire des Sciences du Climat et l'Environnement, CEA/Orme des Merisiers, 91191 Gif-sur-Yvette, France

⁹LMD/IPSL, École Polytechnique, Université Paris Saclay, ENS, PSL Research University; Sorbonne Universités, UPMC Univ Paris 06, CNRS, Palaiseau, France

^anow at Université Paris-Saclay, INRAE, AgroParisTech, UMR EcoSys, 91120 Palaiseau, France

^bnow at Atmospheric Composition Research, Finnish Meteorological Institute, 00101 Helsinki, Finland

Correspondence: Alice Maison (alice.maison@enpc.fr), Karine Sartelet (karine.sartelet@enpc.fr)

Abstract. Biogenic Volatile Organic Compounds (BVOCs) play an important role in atmospheric chemistry. They are emitted by vegetation and react with other compounds to form ozone and secondary organic matter (OM). In regional air-quality models, biogenic emissions are often calculated using a Plant Functional Type approach, which depends on the land-use category. However, over cities, the land-use is urban, so trees and their emissions are not represented. In this study we develop a bottom-up inventory of urban-tree biogenic emissions, in which the location of trees and their characteristics are derived from the tree database of the Paris city combined with allometric equations. Biogenic emissions are then computed for each tree based on their leaf dry biomass, tree-species dependent emission factors and activity factors representing the effects of light and temperature. Emissions are integrated in WRF-CHIMERE air-quality simulations performed over June-July 2022. Over Paris city, the urban trees induce an increase of OM of 4.6% on average over the two months and of 5.4% during heatwaves. PM_{2.5} and ozone concentrations increase respectively by 0.6% and 1.0% on average over the two months and by 1.0% and 2.4% during heatwaves. The concentration increase remains spatially localized over Paris, extending to the Paris suburbs in the case of ozone during heatwaves. The inclusion of urban-tree emissions improves the estimation of OM concentrations compared to in situ measurements, but there are still underestimated. OM concentrations are sensitive to monoterpene and sesquiterpene emissions, highlighting the importance of urban and suburban vegetation, which should be better described.

1 Introduction

With an increasing number of people living in cities, urban areas are experiencing continuous expansion (Angel et al., 2011; United Nations, 2018). Artificial surfaces with darker, impermeable materials and high buildings, as well as release of anthropogenic heat strongly modify the energy budget of the urban area (Taha et al., 1988; Taha, 1997; Pigeon et al., 2007a; Kuttler, 2008; Oke et al., 2017; Masson et al., 2020). An increase in temperature in the city compared to the surrounding countryside is often observed and is called Urban Heat Island (UHI) effect (Oke, 1982; Kim, 1992). Due to the high local emission sources (traffic) and the modification of air flows by tall buildings which limits the pollutant dispersion, concentrations of several pollutants, such as NO₂ and particles, are higher in cities than surroundings (Lyons et al., 1990; Fenger, 1999; Thunis, 2018; Li et al., 2019; Yang et al., 2020).

To mitigate the negative effects of urbanization, urban vegetation and trees in particular are now widely promoted (Livesley et al., 2016; Chang et al., 2017; Roeland et al., 2019). Trees can reduce surrounding temperatures by creating shade and by evaporating water through transpiration (Jamei et al., 2016; Taleghani, 2018; Lai et al., 2019; Hami et al., 2019; Nasrollahi et al., 2020). Trees can also remove gaseous and particulate pollutants from the atmosphere by dry deposition, although this effect is quantitatively questionable due to the large variability and uncertainties (Nowak et al., 2006; Escobedo and Nowak, 2009; Setälä et al., 2013; Selmi et al., 2016; Nemitz et al., 2020; Lindén et al., 2023).

Trees are known to naturally emit Biogenic Volatile Organic Compounds (BVOCs). The term BVOC includes gaseous non-methane hydrocarbons and includes many families of molecules: isoprene, terpenes, alkanes, alkenes, carbonyls, alcohols, esters, ethers and acids. BVOC emissions are involved in stress resistance mechanisms (due to heat, water shortage, oxidation, herbivore or pathogen attack) and communication (plant-plant and plant-insect interactions) (Kesselmeier and Staudt, 1999). Emission rates depend on abiotic factors such as temperature and light, and biotic factors such as tree species, leaf age and stress level (Niinemets et al., 2004; Loreto and Schnitzler, 2010; Niinemets, 2010). BVOC emissions are therefore highly variable in space and time. Unlike specific Anthropogenic Volatile Organic Compounds (AVOCs) such as benzene, emitted BVOCs may not be directly harmful to human health. However, BVOCs may form secondary pollutants, such as ozone (Calfapietra, 2013; Atkinson and Arey, 2003a; Churkina et al., 2017) and secondary organic aerosols (Salvador et al., 2020; C. Minguillón et al., 2016; Churkina et al., 2017; Lehtipalo et al., 2018). BVOCs emitted in the gaseous phase are oxidized in the atmosphere, forming more functionalized compounds that are semi-volatile and may be absorbed into aerosols. In the urban VOC-limited environment with high nitrogen oxides (NO_x) (emitted by traffic), ozone formation strongly depends on the VOC concentrations. There are also feedbacks between the urban environment, which is stressful for trees (higher temperatures and concentrations of oxidizing pollutants, difficult access to water) (Lüttge and Buckeridge, 2023; Czaja et al., 2020) and BVOC emissions.

To understand processes and forecast the evolution of pollutant concentrations, numerical models are widely used. Air-quality models of various types and resolutions exist, depending on the scale and processes studied. Chemistry-Transport Models (CTM) are eulerian models that represent the chemistry and transport of pollutants in three-dimensional grid cells, e.g. CHIMERE (Menuet et al., 2021), Polair3D (Boutahar et al., 2004), WRF-Chem (NOAA/ESRL, 2023), CMAQ (Byun and

Schere, 2006; Appel et al., 2021), MOCAGE (CNRM, 2023), etc. Their typical horizontal resolution varies between 1 and 10^2 km and they are used from the global to the regional scales (Mailler et al., 2017). Many input data are necessary: surface characterization, spatio-temporal emissions of each pollutant, boundary and initial conditions. Due to the coarse resolution, the surface type is characterized by land-use categories such as open water, urban, forest, crop, etc. Forest trees are usually divided into 1 to 5 categories based on general characteristics (evergreen or deciduous, broadleaf or needleleaf). Most of the CTMs compute the BVOC emissions from forest and crops based on Plant Functional Type (PFT) and the MEGAN empirical model (Model of Emissions of Gases and Aerosols from Nature) (Guenther et al., 2006, 2012; Matthias et al., 2018). The heterogeneity of the vegetation species is not explicitly modeled, but the model gives a rough estimate of the BVOC emission rates in the grid cells containing vegetation. CTMs can be used to compute air quality over large urban areas, but at this spatial resolution the land-use is urban and no biogenic emission from urban vegetation is taken into account. In parallel, tree inventories are being developed in many cities (Bennett, 2023) and give us a much more accurate description of the urban forest. They can contain the tree precise locations, species and sizes, allowing to study the impact of urban vegetation on air quality (Mircea et al., 2023).

Based on the tree inventory implemented in Paris by the Municipality (Municipality of Paris, 2023) and a series of allometric equations (McPherson et al., 2016), a method is developed to estimate the BVOC emissions by urban trees in Paris. This "bottom-up" inventory of BVOC emissions by urban trees is used to estimate emissions from Paris trees over June and July 2022. This period is chosen because biogenic emissions are expected to be higher in summer, especially during heatwaves, and also because of the numerous in situ measurements that have been performed in Paris region. The effect on isoprene, monoterpene, O_3 and particle concentrations over the Île-de-France (IDF) region is quantified using the CTM CHIMERE.

2 Materials and Methods

2.1 Tree-based BVOC emission model

To compute BVOC emissions in CTMs, an empirical approach is usually used. The emission rate of each BVOC species is computed as the product of several factors: the amount of vegetation (surface of the land-use category, leaf area index or mass), an emission factor at the standard conditions (leaf temperature of 30 °C and Photosynthetic Photon Flux Density (PPFD) of 1000 $\mu\text{mol photons}\cdot\text{m}^{-2}\cdot\text{s}^{-1}$) and activity factors representing physiological or meteorological effects. One emission factor is associated to each PFT. The development of BVOC rate measurements at the leaf or branch scale with chambers and tree inventories allows estimation of BVOC emission rates at the tree level (Owen et al., 2001, 2003; Stewart et al., 2003; Karl et al., 2009; Steinbrecher et al., 2009). The emission rate of a BVOC k for a tree t ($\mu\text{g}\cdot\text{h}^{-1}$ per tree) can be estimated as:

$$ER_{k,t} = DB_t \cdot EF_{k,t} \cdot \gamma_k \quad (1)$$

where:

- $EF_{k,t}$ ($\mu\text{g}\cdot\text{g}_{DW}^{-1}\cdot\text{h}^{-1}$) is the emission factor (or potential) at standard conditions,
- DB_t is the dry leaf biomass (g_{DW} , where DW stands for dry weight),
- γ_k combines the different dimensionless emission activity factors.

2.2 Tree inventory and characteristics

The Paris Tree database (<https://opendata.paris.fr/explore/dataset/les-arbres/map/>) regroups an inventory of the public trees. Many mapped information is available for each tree: precise location (coordinates), address, type (roadside, garden, cemetery etc.), tree species, height, trunk circumference and development stage. It is regularly updated, and the version used in this study was downloaded in March 2023. A map of trees around Avenue des Champs-Élysées taken from the database is shown in Fig. B1. The proportion (P) of the tree genus found in Paris is presented in Fig. B2 and the distributions of their trunk circumferences and crown heights are shown in Fig. B3. The municipality of Paris estimates that around 1/3 of the Parisian trees are missing from their database, mainly trees located in private areas. Without further information on these private trees, they are not taken into account in this study.

To compute the BVOC emissions (eq. (1)) of each individual tree, an estimation of the leaf dry biomass is necessary. Dry biomass such as leaf area, and crown dimensions can be estimated using allometric equations. These allometric relationships are statistical models based on a sample of measurements predicting tree size as a function of parameters such as trunk diameter or age since planting. Many studies propose equations for forest trees (Burton et al., 1991; Bartelink, 1997; Karlik and McKay, 2002), but studies on urban trees are more scarce (Nowak, 1996). The open database of McPherson et al. (2016) is chosen in this study because it was developed specifically for urban trees and includes many genus found in Paris (84% of the trees in the Paris inventory) (365 growth equations for 174 tree species). For missing tree genus, equation from another tree genus in the same family is selected, as described in Section 3. It includes allometric tree measurements for different climates in the United-States, so assumptions are necessary to select the climate for each tree species that is the closest to that of the Paris region (see Section 3).

2.3 Description of regional-scale air-quality simulations

To quantify the impact of the Parisian tree emissions on air quality, regional-scale simulations using the 3D CTM CHIMERE v2020_r3 (Menut et al., 2021) coupled to the chemical module SSH-aerosol v1.3 (Sartelet et al., 2020) are performed. The gas-phase chemical scheme is MELCHIOR2, modified to represent secondary organic aerosol formation, as described in Sartelet et al. (2020). Biogenic emissions are estimated using the MEGANv2.1 algorithm implemented in CHIMERE (Couvidat et al., 2018), which corresponds to a land-use approach. The following section describes the simulation setup.

Simulations are performed during summer 2022, between 6 June and 31 July 2022, with a five-day spin-up period (1-5 June). Summer time is chosen as biogenic emissions are the highest during this period due to meteorological conditions. In France, the summer 2022 was exceptionally hot and sunny, with little precipitation (on average 1 to 3 °C above seasonal values over most of France) (Meteo France, 2023). The domain of study corresponds to the Île-de-France region, with a 1 km × 1 km spatial resolution (IDF1). Initial and boundary conditions are taken from two additional nesting simulations: one over France with a 9 km × 9 km spatial resolution (FRA9), and one over the northwest of France with a 3 km × 3 km spatial resolution

(IDF3), as shown in Fig. 1. For the FRA9 domain, boundary and initial conditions are obtained from the CAMS platform (Inness et al., 2019), with a $10 \text{ km} \times 10 \text{ km}$ spatial resolution.

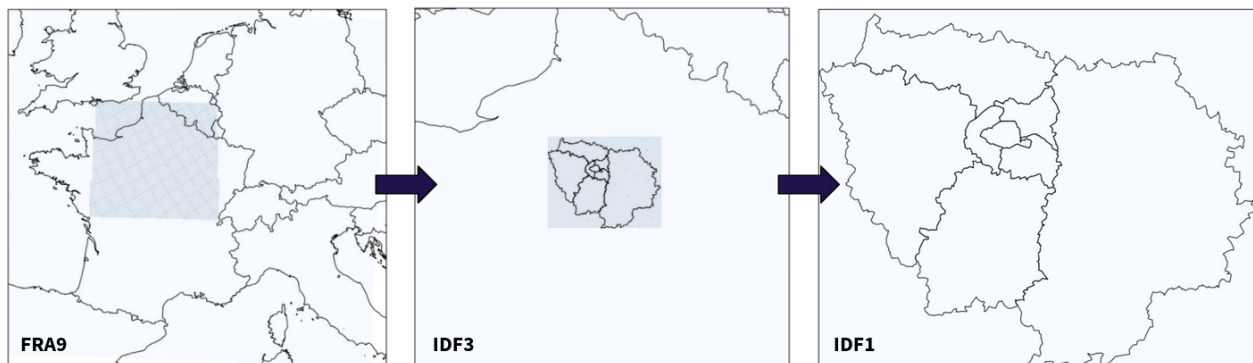


Figure 1. Representation of the simulated domains. The blue rectangles represent the location of the different nested domains.

Meteorological data for all domains are computed using the Weather Research and Forecasting (WRF) model v3.7.1 available in CHIMERE (Powers et al., 2017; Menut et al., 2021). Even if CHIMERE and WRF simulations are performed simultaneously, one-way coupling is used and then concentrations computed in CHIMERE are assumed to have no influence on the meteorological fields computed by WRF. WRF simulations are performed with 33 vertical levels, from 0 to 20 km altitude. A more refined vertical discretization is employed in the first four vertical levels (average heights of 0.12, 25, 50 and 83 meters, respectively), which contains almost all buildings in Paris region. In order to represent more precisely the meteorological fields in urban areas, the single-layer urban canopy model (UCM) (Kusaka et al., 2001) is used in the IDF3 and IDF1 domains. Three urban categories are employed to differentiate street and building dimensions, as well as heat transfer parameters in commercial, high and low intensity residential areas. The spatial distribution of each urban category used in WRF simulations is based on CORINE land-use coverage, with a 250 m resolution (available in <https://doi.org/10.2909/71c95a07-e296-44fc-b22b-415f42acdf0>). In the single-layer UCM model, the sensible heat flux (AH) is assumed to be 45 W.m^{-2} for commercial areas, 10 W.m^{-2} for high intensity residential and 5 W.m^{-2} for low intensity residential areas, based on Pigeon et al. (2007b) and Sailor et al. (2015). Table 1 summarizes the other physical options employed in the WRF simulations.

Anthropogenic emissions in the domains FRA9 and IDF3 are from the latest (2020) EMEP emission inventory (EMEP, 2019) ($0.1^\circ \times 0.1^\circ$ horizontal resolution), and in IDF1, they are from the latest (2019) regional emission inventory of the Air Quality Monitoring Network (AQMN) Airparif for the Greater Paris area. (<https://www.airparif.asso.fr/>) ($1 \text{ km} \times 1 \text{ km}$ spatial resolution). Traffic emissions correspond to those of the summer 2022 calculated using the bottom-up traffic emissions model HEAVEN (<https://www.airparif.asso.fr/heaven-emissions-du-traffic-en-temps-reel>), while non-traffic anthropogenic emissions correspond to the 2019 Airparif inventory.

Table 1. Main physical options employed in WRF simulations.

option in WRF namelist	option complete name	option selected
mp_physics	Microphysics	Thompson graupel scheme
cu_physics	Cumulus	Grell-Devenyi ensemble scheme
ra_lw_physics	Longwave radiation	rrtmg scheme
ra_sw_physics	Shortwave radiation	rrtmg scheme
bl_pbl_physics	Boundary layer	YSU scheme
sf_sfclay_physics	Surface layer	Monin-Obukhov Similarity scheme
sf_surface_physics	Land surface	Noah Land-Surface Model
sf_urban_physics	Urban canopy model	Single-layer (only in IDF3 and IDF1)

2.4 Description of the air-quality experimental measurements

The results of the simulations are compared to experimental measurements performed at different sites in the Paris region. In sections 4.1.2 and 4.2, temporal variations of observed and simulated concentrations are presented in three main sites: the Halles site, a permanent air-quality monitoring station located in the city center and operated by Airparif, the PRG-Paris Rive Gauche site, located at the 7th floor of the Lamark B building of Université Paris Cité (30 m above ground layer), in the south-east side of the city, set up as part of the ACROSS campaign (Cantrell and Michoud, 2022), and the SIRTA site (Site Instrumental de Recherche par Télédétection Atmosphérique), an atmospheric observatory located 20 km south-west of Paris which is integrated in the ACTRIS European Research Infrastructure Consortium (<https://www.actris.eu>) (Haeffelin et al., 2005). The Halles and PRG stations are both urban background sites, while SIRTA is a suburban background site. The three sites and the measurements performed are described in Table 2 and a more complete description of the measurements and their associated uncertainties is provided in Appendix A.

The reference simulations (without urban trees biogenic emissions) are validated in Section 4.1 with the observation sites of the Airparif network. These sites correspond to 21 permanent air-quality monitoring stations included within a large operational stations network operated by Airparif (see Table A1 and <https://www.airparif.asso.fr/carte-des-stations>). The map in Fig. 2 shows the location of all measurement stations which are used to evaluate the simulations (Sections 4.1 and 4.2). It also presents the land-use from GLOBCOVER (Team et al., 2011) used in the CHIMERE simulation over IDF1. It is mainly composed of agricultural lands, forests of varying sizes and a large urban area including Paris and its suburbs.

3. BVOC EMISSIONS FROM URBAN TREES AND IMPACT ON REGIONAL AIR QUALITY

Table 2. Description of the experimental measurements performed at different sites and used in this study. ACSM: Aerosol Chemical Speciation Monitor (Petit et al., 2015), PTR-MS: Proton-Transfer-Reaction Mass Spectrometry (Simon et al., 2023). GC-FID: Gas-Chromatograph with a Flame Ionisation Detector (Gros et al., 2011)

Site	location	typology	species measured	instrument
Halles	1 st district of Paris city (48.862128° N, 2.344622° E)	urban background	NO ₂	AC32M
			O ₃	O3 42e
			PM	FIDAS 200
			OM	ACSM
PRG	13 th district of Paris city (48.827778° N, 2.380562° E)	urban background	C ₅ H ₈	PTR-MS
			monoterpenes	PTR-MS
			OM	ACSM
SIRTA	20 km south-west of Paris (48.709890° N, 2.147938° E)	suburban	C ₅ H ₈	GC-FID
			monoterpenes	PTR-MS
			OM	ACSM

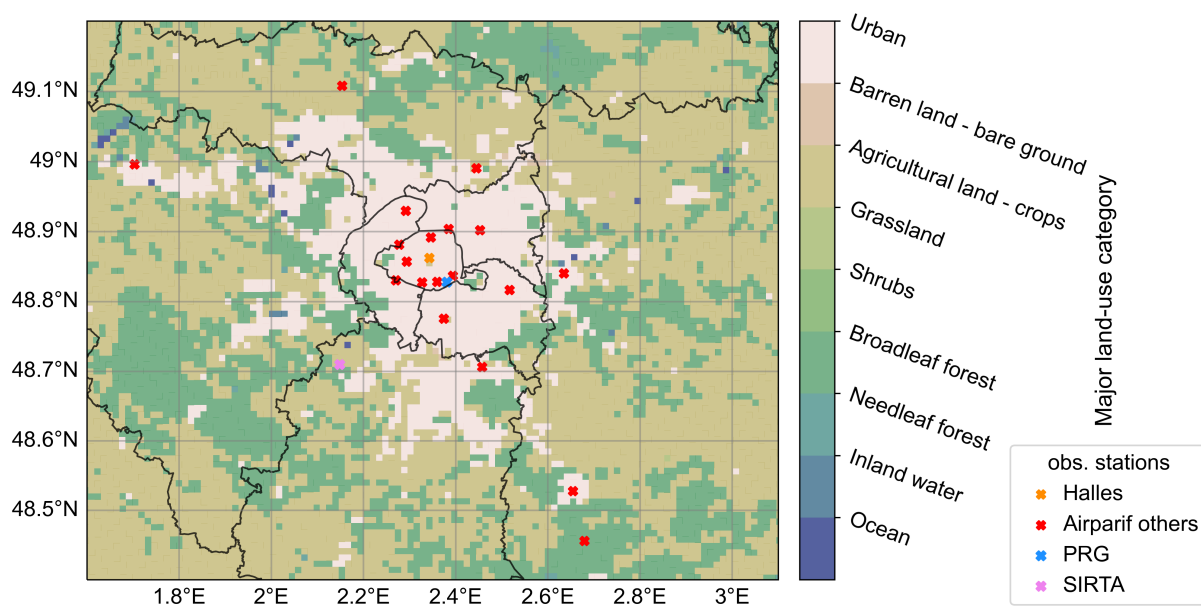


Figure 2. Map of the GLOBCOVER major land-use in each grid cell used in IDF1 CHIMERE simulations. The crosses represent the locations of the different measurement stations.

3 Bottom-up inventory of tree BVOC emissions and comparison to the land-use approach

3.1 Calculation of BVOC emissions at the tree level

3.1.1 Estimation of the tree dry biomass

The total tree leaf dry biomass (in grams of dry weight, g_{DW}) is computed based on the McPherson et al. (2016) allometric equation database. Tree data were collected in 17 reference cities representative of the different US climate zones and analyzed to obtain growth equations. The database contains equations to estimate the tree characteristics from the tree species, climate and the trunk diameter at breast height (at 1.3 m) (DBH). To find the correspondence between Parisian trees and this database, the US climates were first ranked from closest to farthest from the Parisian climate based on a qualitative comparison of annual rainfall and temperatures (see Table 3).

Table 3. US reference cities and climates used in the McPherson et al. (2016) study ranked from the closest to the farthest from the Parisian climate. The last column refers to Köppen climate classification (Paris region: Cfb).

Rank	Region Code	Region Name	City	State	Climate class
1	NoEast	Northeast	Queens	New York	Cfa
2	Piedmt	South	Charlotte	North Carolina	Cfa
3	LoMidW	Lower Midwest	Indianapolis	Indiana	Cfa
4	GulfCo	Coastal Plain	Charleston	South Carolina	Cfa
5	CenFla	Central Florida	Orlando	Florida	Cfa
6	PacfNW	Pacific Northwest	Longview	Oregon	Csb
7	TpIntW	Temperate Interior West	Boise	Idaho	Csa
8	NoCalC	Northern California Coast	Berkeley	California	Csb
9	InlEmp	Inland Empire	Claremont	California	Csb
10	SoCalC	Southern California Coast	Santa Monica	California	Csb
11	SacVal	Sacramento Valley	Sacramento	California	Csa
12	NMtnPr	North	Fort Collins	Colorado	Dfb
13	InterW	Interior West	Albuquerque	New Mexico	Bsk
14	MidWst	Midwest	Minneapolis	Minnesota	Dfa
15	InlVal	Inland Valleys	Modesto	California	Bsk
16	SWDsrt	Southwest Desert	Glendale	Arizona	Bwh
17	Tropic	Tropical	Honolulu	Hawaii	As

For each tree species in the Paris tree inventory, the allometric equations are obtained from the US database, by selecting the closest tree category in terms of tree species and climate following the decision tree shown in Fig. 3. The default species is the plane tree (*Planatus x hispanica*), which is the predominant species in Paris.

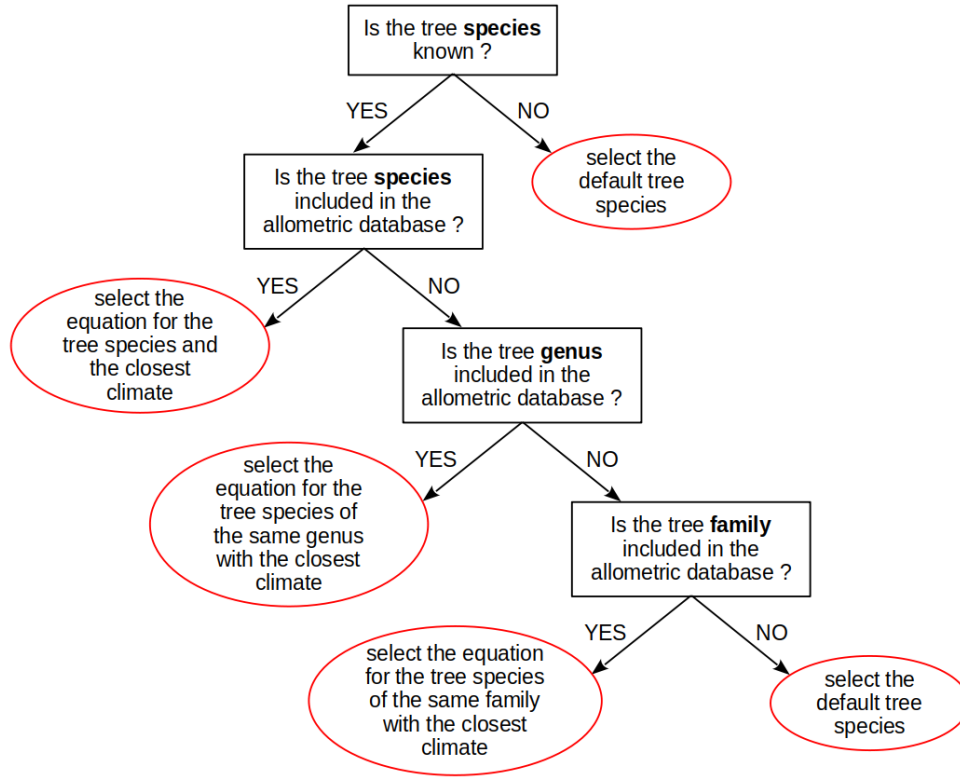


Figure 3. Decision tree to select the tree category to be used for each Paris tree. The tree category and corresponding allometric database refers to McPherson et al. (2016).

Then, the trunk diameter at breast height, DBH (cm), is computed from the trunk circumference, $CIRC$ (cm) available in the Paris tree inventory for each tree, assuming a cylindrical tree trunk, as:

$$DBH = \frac{CIRC}{\pi}. \quad (2)$$

The total tree leaf area (LA in m^2) is then computed from each Parisian tree using the selected equation form and coefficient and the computed DBH . For example, the function $LA = f(DBH)$ is shown for three tree species in equations (3), (4) and (5), where a , b , c , d and MSE (Mean Squared Error) are dimensionless model coefficients.

For *Planatus x hispanica* (London plane):

$$LA = \exp \left[a + b \ln(\ln(DBH + 1)) + \frac{MSE}{2} \right], \quad (3)$$

with $a = -2.06877$, $b = 5.77886$ and $MSE = 0.27978$.

For *Acer platanoides* (Norway maple):

$$LA = \exp \left[a + b \ln(\ln(DBH + 1)) + \left(\sqrt{DBH} \times \frac{MSE}{2} \right) \right],$$

with $a = -0.55184$, $b = 4.27852$ and $MSE = 0.07518$. (4)

For *Prunus serrulata* (Japanese cherry):

$$LA = a + bDBH + cDBH^2 + dDBH^3,$$

with $a = -18.045$, $b = 4.6553$, $c = -0.12798$ and $d = 0.00198$. (5)

Finally, the dry biomass (DB in g_{DW}) is the product of the leaf area and the dry weight density (DWD in $g_{DW}.m^{-2}$):

$$DB_t = LA_t \times DWD_t. \quad (6)$$

The dry weight density depends on tree species and it is also given in the McPherson et al. (2016) database. For instance, $DWD = 500, 520$ and $560 g_{DW}.m^{-2}$ for *Planatus x hispanica*, *Acer platanoides* and *Prunus serrulata* respectively.

The computed LA and DB are shown in Fig. 4 for the predominant tree species ($P > 1\%$) as a function of the DBH . It shows that LA and DB increase with DBH but there is a large variability depending on the tree species. For example, for a tree of $DBH = 100$ cm, the estimation of the leaf surface is equal to $1151.5 m^2$ for *Planatus x hispanica*, $582.5 m^2$ for *Acer platanoides* and $1147.7 m^2$ for *Prunus serrulata*.

As the simulation is performed during the late spring and summer periods, the tree foliage is assumed to be fully developed, so that the leaf area and dry biomass are constant over time. For longer simulations periods, the temporal evolution of leaf area and dry biomass should be introduced.

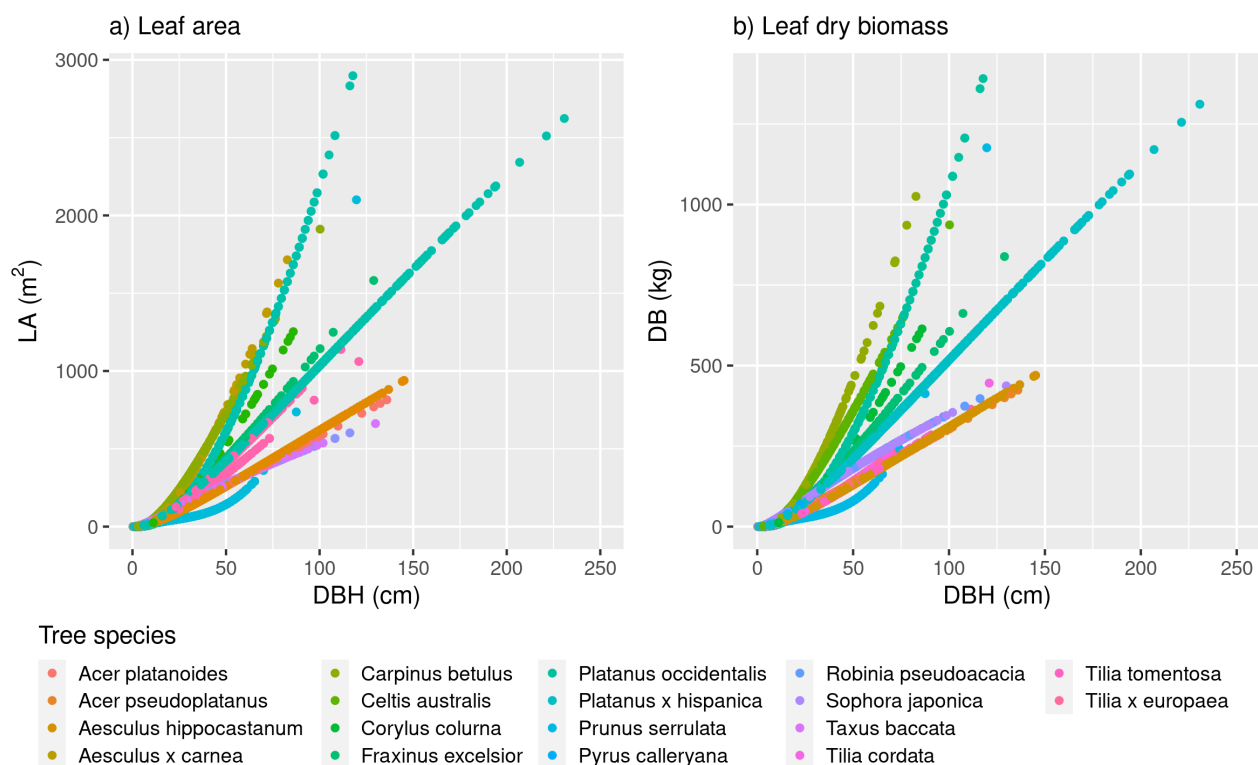


Figure 4. a) Leaf area (LA) and (b) dry biomass (DB) computed for the predominant tree species ($P > 1\%$) in the Paris city inventory as a function of DBH .

3.1.2 Emission factors by tree species

The emission factors by tree species are taken from MEGANv3.2 code, downloaded at <https://bai.ess.uci.edu/megan/data-and-code/megan32>, last accessed on 10/07/2023. The EF presented by tree species are assumed to be identical within the same tree genus. Therefore, EF by tree genus are used for all trees except for the *Quercus* genus (oak), whose species are known to have very different BVOC emission profiles (Loreto, 2002). The EF for the *Quercus* species are taken from Ciccioli et al. (2023) for isoprene and monoterpenes. For the *Quercus* species missing in Ciccioli et al. (2023) but with a known emission type (Loreto, 2002), the EF values are taken from MEGANv3.2. For unknown emission type, the EF value is set by default to oak isoprene emitters in MEGANv3.2. For all tree species the EF values for sesquiterpenes and oxygenated VOC are taken from MEGANv3.2. The emission factors of nitric oxide (NO) and carbon monoxide (CO) are fixed for all tree species and are equal to: $EF_{NO} = 0.05$ and $EF_{CO} = 1.0 \mu\text{g}\cdot\text{g}_{DW}^{-1}\cdot\text{h}^{-1}$, as suggested in MEGANv3.2. The emission factors of isoprene (ISOP), total monoterpenes (MT), total sesquiterpenes (SQT) and total other VOCs (OVOC) are shown in Table 4 for the predominant tree genus and oak species.

3. BVOC EMISSIONS FROM URBAN TREES AND IMPACT ON REGIONAL AIR QUALITY

Table 4. Emission factors (EF in $\mu\text{g}\cdot\text{g}_{DW}^{-1}\cdot\text{h}^{-1}$) of BVOCs for the predominant tree genus found in Paris ($P > 1\%$) and for the predominant Quercus species. ISOP: isoprene, MT: monoterpenes, SQT: sesquiterpenes and OVOC: other VOC

Genus	species	% of trees in Paris	EF_{ISOP}	EF_{MT}	EF_{SQT}	EF_{OVOC}
Platanus	all	22.7	24	0.51	0.10	4.64
Aesculus	all	11.9	0	0.58	0.10	4.64
Tilia	all	10.3	0	0.53	0.10	4.64
Acer	all	7.7	0	0.51	0.10	4.64
Sophora	all	6.3	5.0	0.53	0.10	4.64
Prunus	all	3.9	0	1.18	0.10	4.64
Fraxinus	all	2.6	0	0.26	0.10	4.64
Pyrus	all	2.6	0	0.68	0.10	4.64
Celtis	all	2.3	0	0.33	0.10	4.64
Pinus	all	2.2	0	1.43	0.15	6.94
Carpinus	all	1.5	0	1.07	0.10	4.64
Populus	all	1.5	37	0.44	0.10	4.64
Malus	all	1.5	0	0.44	0.10	4.64
Corylus	all	1.4	1.0	1.81	0.10	4.64
Robinia	all	1.2	20	0.23	0.10	4.64
Ulmus	all	1.1	0	0.62	0.10	4.64
Taxus	all	1.1	0	0.58	0.15	4.64
Betula	all	1.0	0	0.66	0.10	4.64
Gleditsia	all	1.0	0	0.56	0.10	4.64
Quercus	ilex	0.485	0.1	43	0.10	4.64
Quercus	robur	0.365	70	0.3	0.10	4.64
Quercus	rubra	0.272	35	0.1	0.10	4.64
Quercus	cerris	0.257	0.1	0.6	0.10	4.64
Quercus	petraea	0.045	45	0.3	0.10	4.64
Quercus	pubescens	0.044	70	0.3	0.10	4.64
Quercus	frainetto	0.036	85	0.0	0.10	4.64
Quercus	palustris	0.035	34	1.0	0.10	4.64
Quercus	coccinea	0.025	34	1.0	0.10	4.64
Quercus	suber	0.018	0.2	20	0.10	4.64
Quercus	coccifera	0.016	0.1	25	0.10	4.64
Quercus	phellos	0.013	34	1.0	0.10	4.64
Quercus	imbricaria	0.011	34	1.0	0.10	4.64

3.1.3 Choice of activity factors

Emission factors, which are measured at standard conditions, are then multiplied by dimensionless factors representing variations of emissions as a function of biotic and abiotic processes. Photosynthetic Photon Flux Density (PPFD) is the flux of photons in the 400-700 nm spectral range of solar radiation that is used for photosynthesis. It is expressed in $\mu\text{mol.m}^{-2}.\text{s}^{-1}$ and is calculated from the simulated solar radiation in the grid cell where the tree is located (i, j) as:

$$PPFD_{t \in (i, j)} = 4.5 \times 0.5 \times SW g_{t \in (i, j)}, \quad (7)$$

where SWg is the global solar radiation (short wave), 4.5 is a factor to convert the W.m^{-2} into $\mu\text{mol.m}^{-2}.\text{s}^{-1}$ and 0.5 is an approximation of the fraction of the solar radiation energy that is in the 400-700 nm spectral range (Meek et al., 1984).

For each BVOC, the activity factors for light (PPFD), $\gamma_{P_{k, t \in (i, j)}}$, and for temperature, $\gamma_{T_{k, t \in (i, j)}}$, are computed as the weighted average of a light-dependent (LDF_k) and light-independent fraction ($LIF_k = 1 - LDF_k$):

$$\gamma_{P_{k, t \in (i, j)}} = (1 - LDF_k) + LDF_k \gamma_{P_LDF_{k, t \in (i, j)}} \quad (8)$$

$$\gamma_{T_{k, t \in (i, j)}} = (1 - LDF_k) \gamma_{T_LIF_{k, t \in (i, j)}} + LDF_k \gamma_{T_LDF_{k, t \in (i, j)}}. \quad (9)$$

The LDF_k factor depends on the BVOC compound and can be found in Table 4 of Guenther et al. (2012).

- Light effect $\gamma_{P_{k, t \in (i, j)}}$

As no canopy model is used to consider the shadow effects inside the canopy, no distinction between the sunlit and shaded leaves can be done. Therefore, the dependency to the past PPFD that require this distinction is not included and, the light activity factor is computed as (Guenther et al., 1995):

$$\gamma_{P_LDF_{k, t \in (i, j)}} = \frac{C_P \alpha PPFD_{t \in (i, j)}}{\sqrt{1 + \alpha^2 PPFD_{t \in (i, j)}^2}}, \quad (10)$$

with $\alpha = 0.004$ and $C_P = 1.03$.

- Temperature effect $\gamma_{T_{k, t \in (i, j)}}$

$$\gamma_{T_LDF_{k, t \in (i, j)}} = \frac{E_{opt_{k, t \in (i, j)}} C_{T2} \exp(C_{T1_k} x_{t \in (i, j)})}{C_{T2} - (C_{T1_k} [1 - \exp(C_{T2} x_{t \in (i, j)})])} \quad (11)$$

$$\gamma_{T_LIF_{k, t \in (i, j)}} = \exp[\beta_k (T_{t \in (i, j)} - T_s)], \quad (12)$$

$$\text{with } x_{t \in (i, j)} = \frac{1}{R} \left(\frac{1}{T_{opt_{t \in (i, j)}}} - \frac{1}{T_{t \in (i, j)}} \right), \quad (13)$$

and $R = 0.00831$, $T_{t \in (i, j)}$ is the leaf surface temperature (K), approximated here by the air temperature at 2 m above ground layer in the horizontal grid cell (i, j) to which the tree t belongs.

$C_{T2} = 230$, $T_{opt_{t \in (i,j)}}$, $E_{opt_{k,t \in (i,j)}}$ are empirical coefficients:

$$T_{opt_{t \in (i,j)}} = 313 + 0.6(T_{240_{t \in (i,j)}} - T_s) \quad (14)$$

$$E_{opt_{k,t \in (i,j)}} = C_{eo_k} \exp[0.05(T_{24_{t \in (i,j)}} - T_s)] \exp[0.05(T_{240_{t \in (i,j)}} - T_s)] \quad (15)$$

where $T_{24_{t \in (i,j)}}$ and $T_{240_{t \in (i,j)}}$ are the temperature averages over the past 24 and 240 h and $T_s = 297$ K is the standard conditions for leaf temperature. C_{T1_k} , $C_{eo,k}$ and β_k are BVOC dependent empirical coefficients that can be found in the Table 4 of Guenther et al. (2012). To illustrate the variation of the activity factors with light and temperature, Fig. 5 shows averaged γ_T and γ_P for isoprene, α -pinene and β -pinene. Figure 5a shows that BVOC emissions increase with temperature. At high temperatures, isoprene emissions are capped, while monoterpene emissions rise sharply. BVOC emissions also increase with light (Fig. 5b) and the activity factor reaches its maximum value of 1 after $PPFD = 1000 \mu\text{mol photons.m}^{-2}.\text{s}^{-1}$.

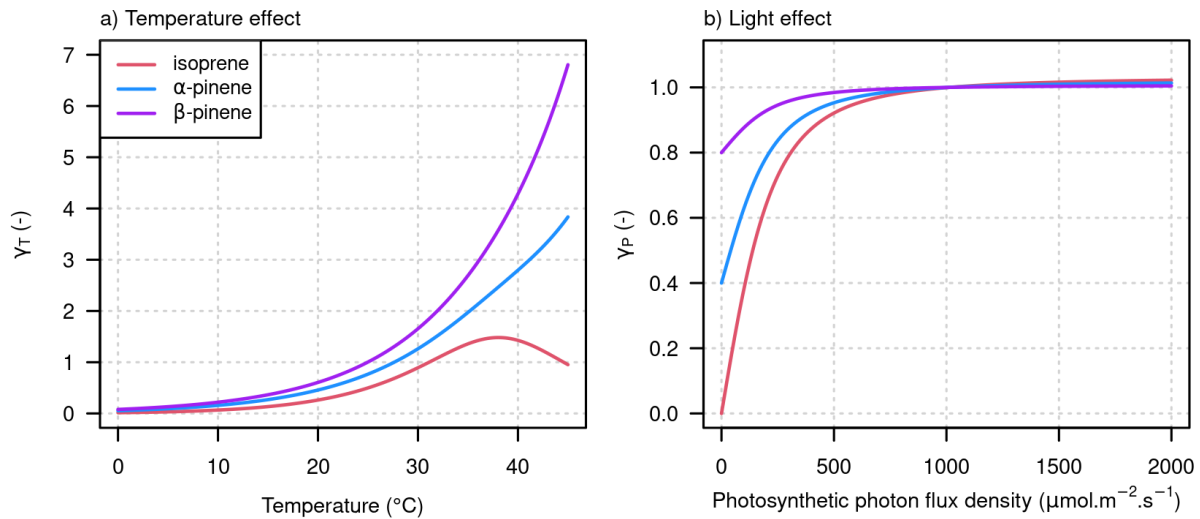


Figure 5. Dependence of activity factors on (a) temperature and (b) light variations for three BVOCs (T_{24} and T_{240} are fixed to 294 K in this figure) (Guenther et al., 2012).

- Other factors

Other activity factors could be added to represent the effect of leaf age and water stress. In this study, emissions are calculated per amount of leaf biomass, considering an average emission for all leaves in the canopy. In addition, we assume that in June and July, tree foliage is fully developed and leaf area and dry biomass are constant. Therefore, no activity factor is added to modulate emissions according to the fraction of growing, mature, growing and old foliage (Guenther et al., 2012).

Several studies also introduce an activity factor to represent the impact of soil moisture and water stress on isoprene emissions (Guenther et al., 2012; Jiang et al., 2018; Bonn et al., 2019; Otu-Larbi et al., 2020; Wang et al., 2022). Although urban trees planted in reduced soil volumes may be subject to water stress (Lüttge and Buckeridge, 2023), the resolution of the CTM does not allow us to accurately simulate the soil water content in an urban environment, so no activity factor modulating isoprene emissions as a function of water content is taken into account here.

3.2 Integration of individual tree BVOC emissions in CHIMERE

After estimating the biogenic emissions of each tree in the city of Paris, these emissions are integrated into the CHIMERE CTM. To do this, they must be spatialized and speciated, as detailed in this section.

3.2.1 Integration of individual tree BVOC emissions on the CTM grid

First, each tree is located within the CTM grid using its precise position given in the Paris Tree inventory and the coordinates of the CTM grid. The product of the dry biomass and the emission factor ($DB_t EF_{t,k}$) is then summed for all trees belonging to the same cell to compute the BVOC emission rates ($ER_{i,j,k}$ in $\mu\text{g}\cdot\text{m}^{-2}\cdot\text{h}^{-1}$) as:

$$ER_{i,j,k} = \frac{1}{\Delta x_{i,j} \Delta y_{i,j}} \sum_{t \in i,j} (DB_t EF_{t,k}) \gamma_{T_{i,j,k}} \cdot \gamma_{P_{i,j,k}}, \quad (16)$$

where $\Delta x_{i,j}$ and $\Delta y_{i,j}$ are the size of the cell (i,j) in the x and y directions (m), here both equal to 1000 m. A map of the dry biomass integrated on the CTM grid cells is shown in Fig. 6. The average cell dry biomass over Paris is $130 \text{ g}\cdot\text{m}^{-2}$ and can reach $390 \text{ g}\cdot\text{m}^{-2}$ in cells containing large parks or cemeteries. The Paris tree inventory does not include all the trees in the Vincennes and Boulogne woods, however, these large woods are considered at the regional scale, so their emissions are calculated using the land-use approach as shown in Fig. 7b.

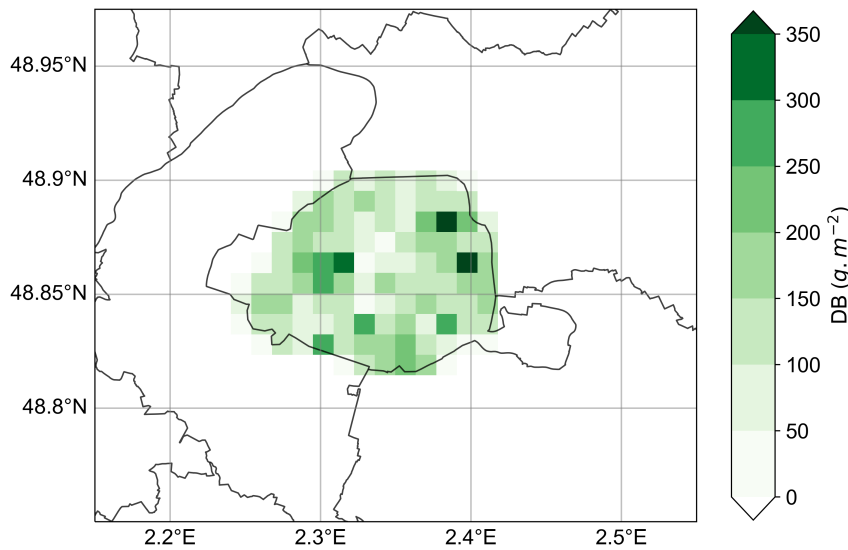


Figure 6. Tree leaf dry biomass computed over Paris from the Paris tree database and McPherson et al. (2016) with a spatial resolution of $1 \text{ km} \times 1 \text{ km}$.

3.2.2 Speciation and aggregation of BVOC species

The emission factors of MEGANv3.2 are estimated for different categories of BVOCs, which are presented in the rows of Table C1. These BVOC categories need to be disaggregated into model species to be used in the CTM. The chemical scheme used in CHIMERE corresponds to MELCHIOR2, and the model species are shown in the columns of Table C1. To disaggregate the BVOC categories into model species, the BVOC categories are first speciated into detailed real species, which are then aggregated into the model species. The speciation in real BVOC species is done with a speciation matrix available in MEGANv3.2 code (downloaded at <https://bai.ess.uci.edu/megan/data-and-code/megan32>). Then, the real BVOC species used in CHIMERE are speciated and aggregated into MELCHIOR2 species. The product of the two matrices gives the speciation/aggregation matrix, described in Table C1. Note that no specific speciation is applied to sesquiterpenes, which are all included in the model species humulene (HUMULE). Monoterpenes are speciated as α -pinene (APINEN), β -pinene (BPINEN), limonene (LIMONE) and ocimene (OCIMEN); and other VOCs (OVOC) represents ethylene (C₂H₄) and oxygenated VOCs (CH₃OH, CH₃CHO, CH₃COE and MEMALD).

Then, the BVOC emissions from urban trees in Paris are added to the regional-scale BVOC emissions to estimate the BVOC emissions over the Île-de-France region. The Section below details the complementarity between the bottom-up inventory for urban trees and the regional-scale PFT-based emissions.

3.3 Complementarity of the emissions computed by the bottom-up and the land-use approaches

At the regional-scale, biogenic emissions are estimated using a land-use approach with emission factors that depend on the land-use and PFT, as described in Guenther et al. (2012). As the land-use is urban over Paris, vegetation is not considered, and there are no biogenic emissions, as shown in Fig. 7, which represents on the left panel (a) the 2-month averaged isoprene emissions computed with the bottom-up inventory and on the right panel (b) isoprene emissions computed with the land-use approach in CHIMERE. The bottom-up inventory allows accounting of local biogenic emissions in the city but Fig. 7 shows that tree inventory and emissions are probably still missing in the Paris suburban area, because there is currently no tree inventory for most of the urban areas outside Paris city. The order of magnitude of isoprene emissions computed by the bottom-up inventory seems coherent compared to regional-scale emissions. Emission rates in Paris ($0.12 \mu\text{g}\cdot\text{m}^{-2}\cdot\text{s}^{-1}$ on average for isoprene) are lower than those simulated over the large Île-de-France forests. This is also the case for other BVOC species as shown in Appendix C. The relative distribution of monoterpenes emitted is different between the urban and the regional scales as shown in Fig. C2. In particular, there is relatively more β -pinene in the regional-scale emissions. This is due to the different vegetation species between the city and the regional scale, and to the speciation of monoterpenes, which may be different.

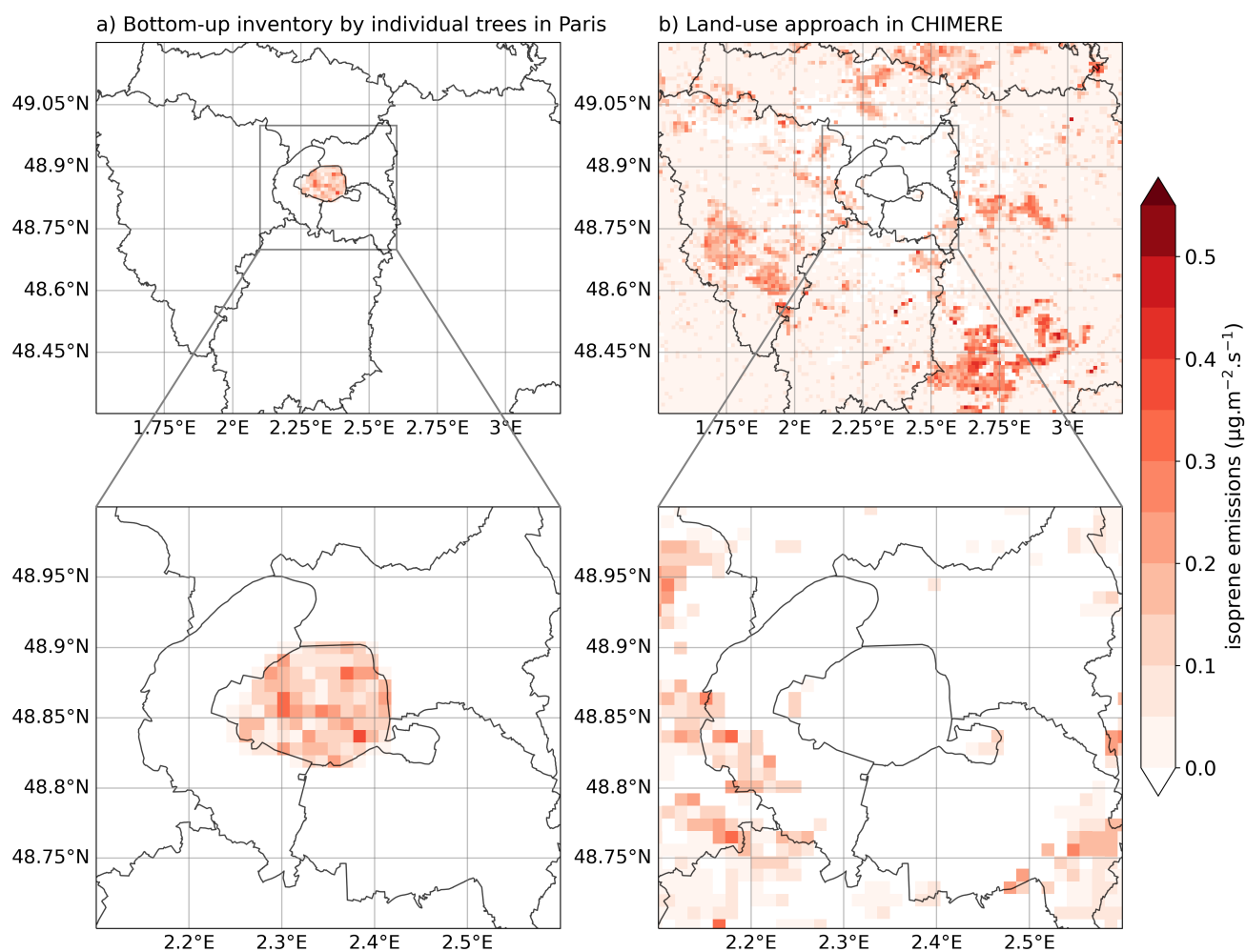


Figure 7. Comparison of the 2-month averaged isoprene emissions with (a) the "bottom-up" inventory and (b) with the land-cover approach in CHIMERE over Île-de-France and Greater Paris.

The temporal variation of the spatially averaged emissions of different biogenic compounds is shown in Fig. 8. For all compounds, emissions are strongly correlated with temperature and sunlight. Over the 2-month periods, there are three emission peaks corresponding to periods of heatwaves with clear-sky conditions and air temperature reaching 35 °C. The impact of BVOC emissions on air quality is expected to be higher during these periods. Therefore, the effect of emissions on pollutant concentrations will be calculated both on the 2-month period and on the heatwave periods, which correspond to the following days: June, 15 to 18, July, 11 to 14 and 17 to 19. In terms of emitted compounds, isoprene is the most emitted biogenic species, followed by OVOC. Monoterpenes and CO are emitted to a lesser extent, followed by sesquiterpenes and NO. This distribution

3. BVOC EMISSIONS FROM URBAN TREES AND IMPACT ON REGIONAL AIR QUALITY

of emissions is fairly typical of emissions calculated using the MEGAN model (Guenther et al., 2012; Ciccioli et al., 2023). In terms of emission intensity, some recent studies computing the BVOC emissions over Europe with plant emission specific models instead of using the PFT approach of MEGAN, have reported that isoprene emissions may be overestimated by a factor 3 in MEGANv2.1, while monoterpene and sesquiterpene emissions may be underestimated by a factor 3 especially in summer (Jiang et al., 2019; Ciccioli et al., 2023). These discrepancies were attributed to the different vegetation classifications and emission factors at standard conditions. Using plant emission specific models, Jiang et al. (2019) found a better comparison to observations for isoprene and organic aerosol concentrations at the European scale, while around the Paris basin in summer, differences in emissions mainly concern monoterpenes and sesquiterpenes. In order to take these emission uncertainties into account in our study, sensitivity simulations are carried out by multiplying monoterpene and sesquiterpene emissions by a factor 2 or 3.

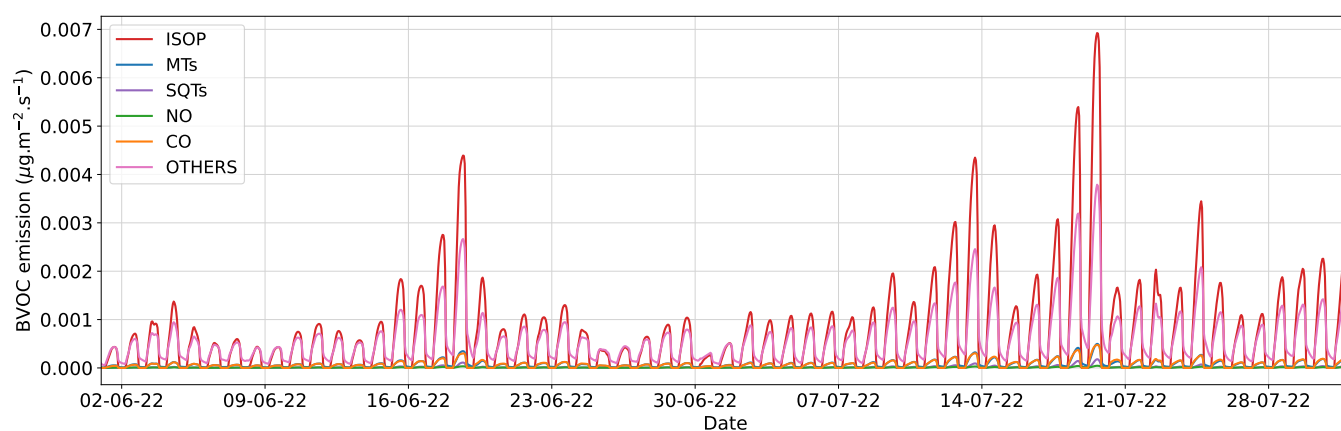


Figure 8. Temporal variation of the spatially averaged biogenic emissions computed over Paris with the bottom-up inventory.

4 Quantification of the impact of BVOC emissions from urban trees on air quality at the regional scale

Before studying the impacts of the bottom-up inventory, comparisons of simulated and observed key variables are performed to evaluate the simulation performance. Meteorological variables are first analyzed in Section 4.1.1, as biogenic emissions are strongly related to them. Then, Section 4.1.2 presents comparisons of modeled and observed pollutant concentrations at different air-quality stations in Île-de-France. Simulations are performed with the emissions factors presented above (REF) and with monoterpene and sesquiterpene emissions multiplied by a factor 2 (REF-TX2) and 3 (REF-TX3).

Then, to quantify the impacts of urban trees on air quality, simulations with the biogenic emissions from urban trees are performed and compared to the simulations without trees in Section 4.2. Three simulations with urban trees are performed: one for each monoterpene and sesquiterpene emissions scenario, which are referred to as bioparis, bioparis-TX2 and bioparis-TX3. All the simulations performed and the corresponding emissions are presented in Table 5.

Table 5. Simulation list with corresponding emission scenarios. ER stands for emission rates, SQT for sesquiterpenes, MT for monoterpenes, LUA for land-use approach and BUI for bottom-up inventory.

Simulation name	Emissions computed with the land-use approach over IDF	Emissions computed with the bottom-up inventory over Paris
REF	yes	no
REF-TX2	yes $ER_{MT\&SQT}^{LUA} \times 2$	no
REF-TX3	yes $ER_{MT\&SQT}^{LUA} \times 3$	no
bioparis	yes	yes
bioparis-TX2	yes $ER_{MT\&SQT}^{LUA} \times 2$	yes $ER_{MT\&SQT}^{BUI} \times 2$
bioparis-TX3	yes $ER_{MT\&SQT}^{LUA} \times 3$	yes $ER_{MT\&SQT}^{BUI} \times 3$

4.1 Validation of the reference simulations

4.1.1 Meteorology

The surface meteorological fields simulated by WRF-CHIMERE are compared to measurements performed at SIRTÀ. The 10-minute averages of meteorological measurements of air temperature (T), relative humidity (RH), pressure (P), precipitation at 2 m, wind speed and direction at 10 m above ground level, as well as longwave (LW), global shortwave (SW) and PPFD incident radiations at the surface are compared. The wind speed and direction observed at 10 m are approximated by the value simulated in the grid cell from 0.15 to 24 m, that is supposed to represent the field at the mid-cell altitude (i.e. ≈ 12 m). The meteorological fields are extracted in the horizontal cell of the IDF1 domain which includes the SIRTÀ. Figure 9 shows the comparison of modeled and observed air temperature at 2 m height and PPFD, which are the two meteorological variables used to calculate BVOC emissions, from June to July 2022. They are also compared with statistical indicators (defined in Appendix D) in the Table 6 along with the other simulated and observed meteorological variables.

3. BVOC EMISSIONS FROM URBAN TREES AND IMPACT ON REGIONAL AIR QUALITY

Figure 9 and Table 6 show that the variations of air temperature at 2 m and PPFD are well modeled with high correlations and low errors. The temperature is slightly overestimated by the model, especially after the 16th of July, resulting in an average positive bias of about 1 °C. For PPFD, the daily maximum is overestimated some days resulting in a positive bias. As PPFD is computed from the global solar radiation (SW) and the bias on this global solar radiation is lower, this overestimation may also come from the conversion coefficient between PPFD and solar radiation. Some tests have been performed to compare the BVOC emission of the bottom-up inventory calculated with the PPFD/SW ratio measured at SIRTAs instead of the ratio used by CHIMERE (2.25) and showed that the impact on BVOC emissions was not significant. Other meteorological variables such as air relative humidity, pressure, wind direction and incident longwave radiation are also well modeled (Table 6). The wind speed is slightly overestimated but this may be due to a difference in representativity between a punctual wind speed measurement and an average value in the 24m-thick vertical cell. The low rainfall intensity limits the significance of statistical indicator calculations but the temporal comparison (not shown) demonstrates that the rainy days are well represented by the model, but the intensity of heavy rains is underestimated.

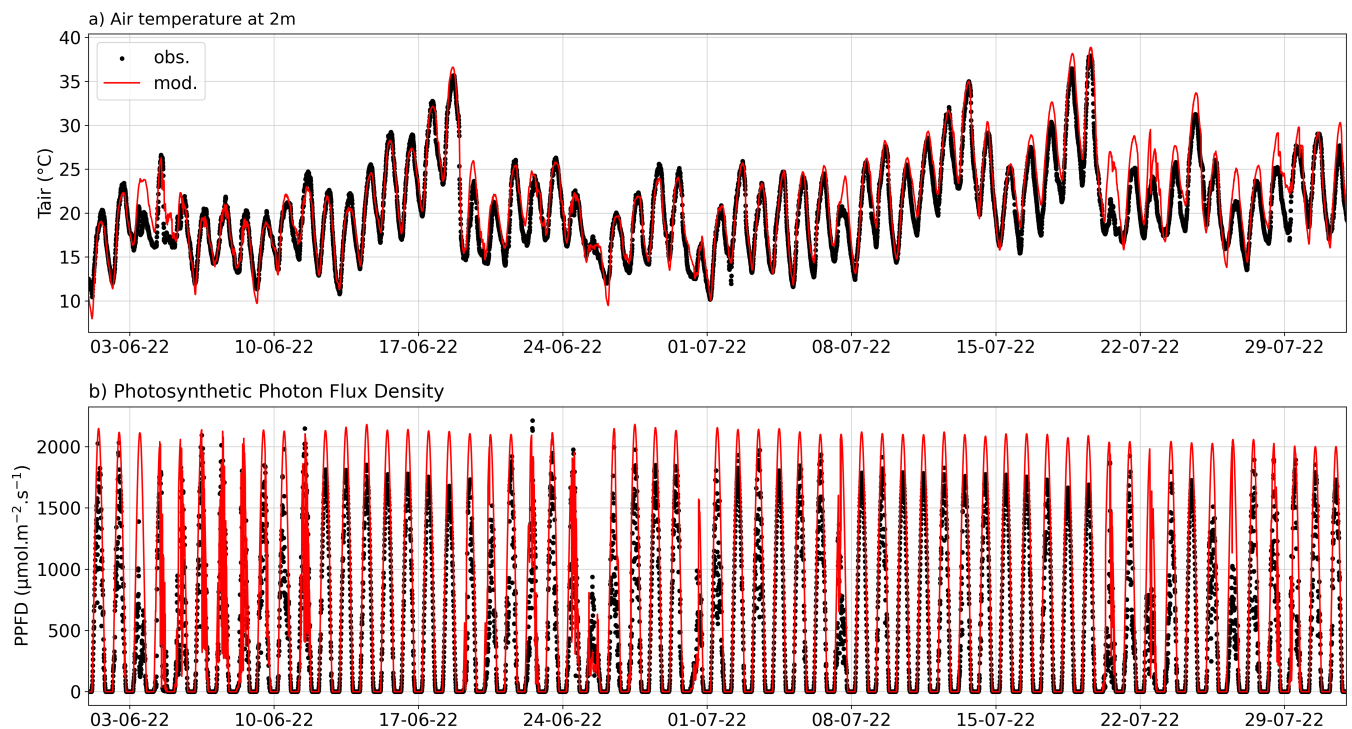


Figure 9. Comparison of the temporal variation of (a) air temperature at 2 m height and (b) photosynthetic photo flux density modeled by WRF (mod) and observed (obs) at the SIRTAs observatory site (48.71734° N, 2.208868° E).

Table 6. Statistical indicators for the comparison of the meteorological variables simulated by WRF and observed at the SIRTA observatory site (48.7° N, 2.2° E). RMSE: Root Mean Square Error, NAD: Normalized Absolute Difference, Bias: Fractional Mean Bias and *R*: Pearson correlation coefficient (Appendix D), AGL: above ground layer, su: same unit as the meteorological variable.

Obs. height	Variable	Unit	mean obs. su	mean mod. su	RMSE su	NAD -	Bias su	<i>R</i> -
2m AGL	T	°C	20.5	21.4	1.80	0.03	0.94	0.96
	RH	%	57.4	51.1	11.23	0.08	-6.27	0.88
	P	hPa	998.1	1000.8	2.82	0.00	2.72	0.99
	rain	mm	0.008	0.010	0.19	0.83	0.00	0.05
10m AGL	wind speed	m.s ⁻¹	2.6	4.5	2.37	0.28	1.85	0.58
	wind direction	°	179.2	179.2	88.26	0.14	1.63	0.68
surface	PPFD	μmol.m ⁻² .s ⁻¹	524.5	733.5	399.66	0.19	205.78	0.91
	SW	W.m ⁻²	278.6	326.0	153.30	0.12	45.26	0.91
	LW	W.m ⁻²	347.5	338.8	23.31	0.02	-8.20	0.72

4.1.2 Model to data comparisons of gas and particle concentrations

In this section the NO₂, O₃, OM, PM_{2.5}, isoprene and monoterpene concentrations simulated by CHIMERE are compared to observations performed at different measurement stations over Île-de-France. The concentrations simulated in the horizontal grid cell containing the station and in the first vertical layer are compared to the observed concentrations in Table 7 for the three emission scenarios REF, REF-TX2 and REF-TX3. Two performance criteria are defined by Hanna and Chang (2012), and they are used here to evaluate the simulations performance. The most strict criteria are accepted when $-0.3 < \text{FB} < 0.3$, $0.7 < \text{MG} < 1.3$, $\text{NMSE} < 3$, $\text{VG} < 1.6$, $\text{FAC2} \geq 0.5$, $\text{NAD} < 0.3$. The less strict criteria are accepted when $-0.67 < \text{FB} < 0.67$, $\text{NMSE} < 6$, $\text{FAC2} \geq 0.3$, $\text{NAD} < 0.5$ (where FB: Fractional Bias, MG: Geometric Mean Bias, NMSE: Normalized Mean Square Error, VG: Geometric Variance, FAC2: Factor of 2, NAD: Normalized Absolute Difference and *R*: correlation coefficient, see Appendix D). Values that respect the most strict performance criteria are represented in green, those that respect the acceptable performance criteria for urban areas are represented in orange, and those that do not respect any criteria are in red. In order to investigate in more detail the model performance in each simulation, the temporal evolution of simulated and observed concentrations in three different stations (the Halles and PRG urban stations, and the SIRTA suburban station) is presented in Figures 10 and 11.

3. BVOC EMISSIONS FROM URBAN TREES AND IMPACT ON REGIONAL AIR QUALITY

Table 7. Statistical comparison of the observed and simulated concentrations on average over 21 stations in IDF1 (listed in Table A1). Values indicated in **green** respect the most strict performance criteria, while those in **orange** respect the acceptable performance criteria, and those in **red** do not respect the performance criteria defined by Hanna and Chang (2012). Correlation coefficients (R) are indicated in black as they are not included in the performance criteria. FB: Fractional Bias, MG: Geometric Mean Bias, NMSE: Normalized Mean Square Error, VG: Geometric Variance, FAC2: Factor of 2, NAD: Normalized Absolute Difference, R : correlation coefficient. The calculation of the statistical indicators and performance criteria are presented in Appendix D. su stands for same unit as the concentration.

species & unit	simulation	Nb stat.	Obs. su	Sim. su	FB -	MG -	NMSE -	VG -	FAC2 -	NAD -	R -
NO ₂ µg.m ⁻³	REF			15.8	0.05	1.16	0.52	1.52	0.67	0.24	0.54
	REF-TX2	20	14.6	15.7	0.04	1.15	0.52	1.52	0.67	0.24	0.54
	REF-TX3			15.6	0.04	1.15	0.53	1.52	0.67	0.24	0.54
O ₃ µg.m ⁻³	REF			82.9	0.19	1.29	0.13	1.31	0.85	0.14	0.69
	REF-TX2	12	68.2	83.8	0.21	1.30	0.14	1.32	0.84	0.14	0.69
	REF-TX3			84.7	0.22	1.32	0.14	1.33	0.84	0.14	0.69
PM _{2.5} µg.m ⁻³	REF			8.4	0.17	1.33	0.51	1.68	0.72	0.23	0.41
	REF-TX2	8	7.2	10.4	0.37	1.60	0.81	2.01	0.65	0.26	0.47
	REF-TX3			12.4	0.53	1.88	1.29	2.60	0.57	0.31	0.49
OM µg.m ⁻³	REF			1.4	-0.99	0.29	2.24	7.59	0.16	0.50	0.58
	REF-TX2	3	4.3	2.6	-0.46	0.54	0.78	2.51	0.37	0.35	0.59
	REF-TX3			3.4	-0.09	0.81	0.58	1.80	0.49	0.26	0.59
C ₅ H ₈ ppb vol	REF			0.09	-0.89	0.25	5.95	12.27	0.15	0.54	0.54
	REF-TX2	2	0.29	0.09	-0.89	0.26	5.88	10.31	0.15	0.54	0.54
	REF-TX3			0.09	-0.89	0.27	5.80	9.23	0.15	0.54	0.55
MTs ppb vol	REF			0.04	-0.91	0.43	12.53	2.8e15	0.26	0.60	0.14
	REF-TX2	2	0.09	0.10	-0.39	0.89	6.11	4.0e12	0.22	0.58	0.13
	REF-TX3			0.16	-0.03	1.36	5.49	1.6e11	0.15	0.59	0.14

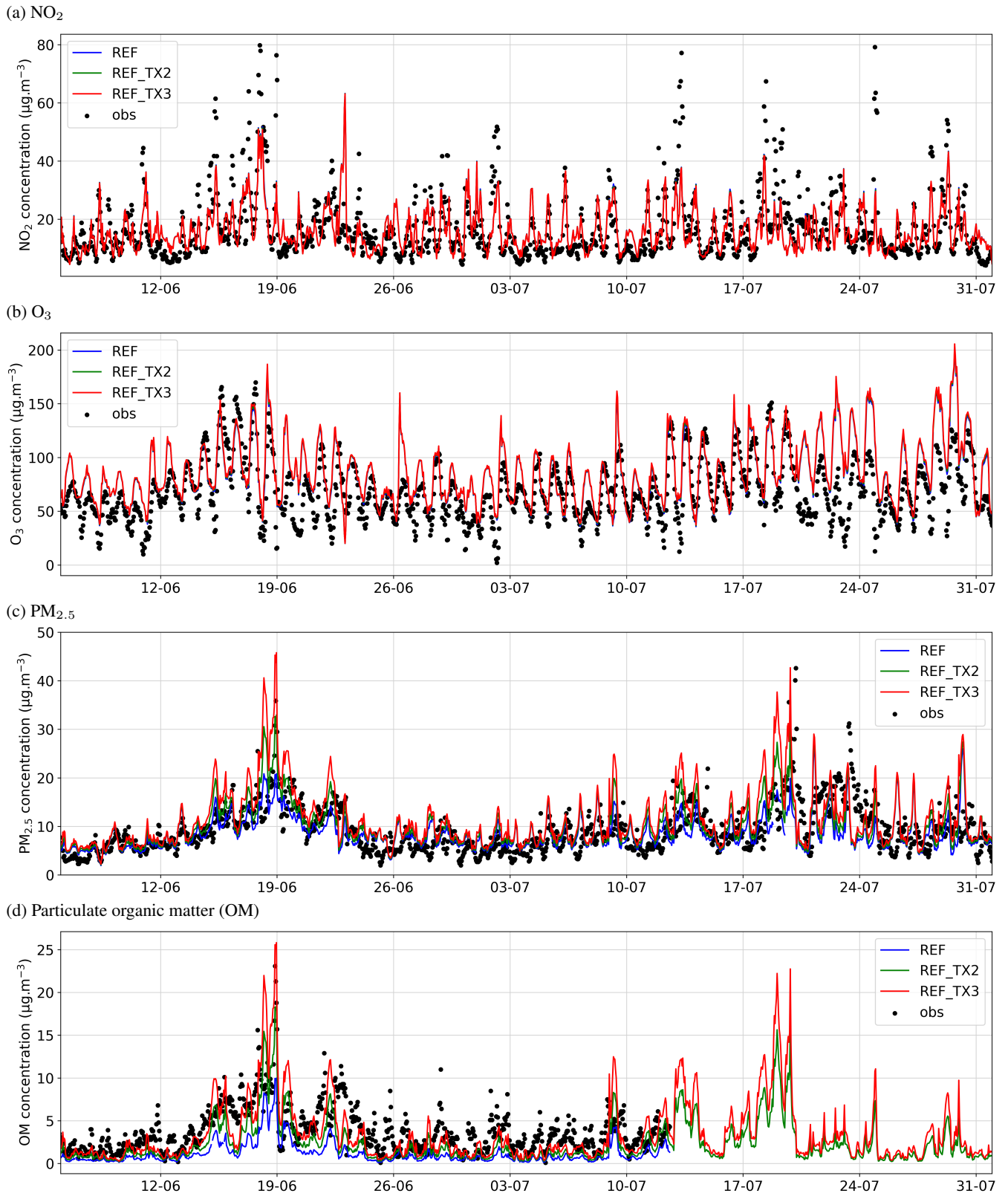


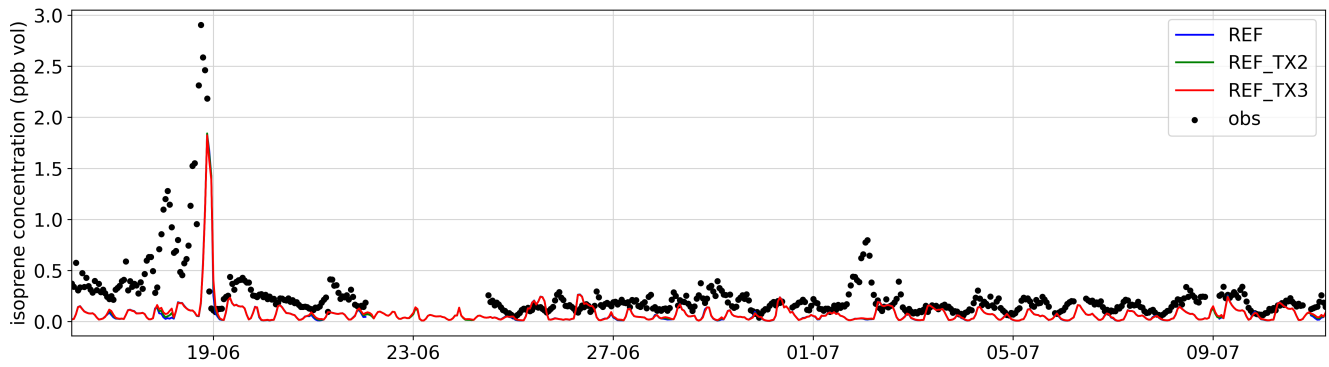
Figure 10. Observed and simulated hourly concentrations of (a) NO_2 , (b) O_3 (c) $\text{PM}_{2.5}$ and (d) OM at the Halles station.

The different hypotheses regarding terpene biogenic emissions have low impact on NO_2 and O_3 concentrations, and all simulations present very similar concentrations and statistical indicators (Table 7). Figure 10a shows good correlation between the NO_2 concentrations measured and observed at the Halles site in all simulations, although a few concentration peaks are underestimated. The most strict performance criteria are respected for all statistical indicators for NO_2 and for O_3 . The O_3 geometric mean bias is at the limit of the acceptance criteria, because of the overestimation of the low O_3 concentrations at night (see Fig. 10b). This overestimation of low O_3 concentrations has previously commonly been observed and might be related to model grid resolution (Jang et al., 1995a, b; Liang and Jacobson, 2000; Arunachalam et al., 2006).

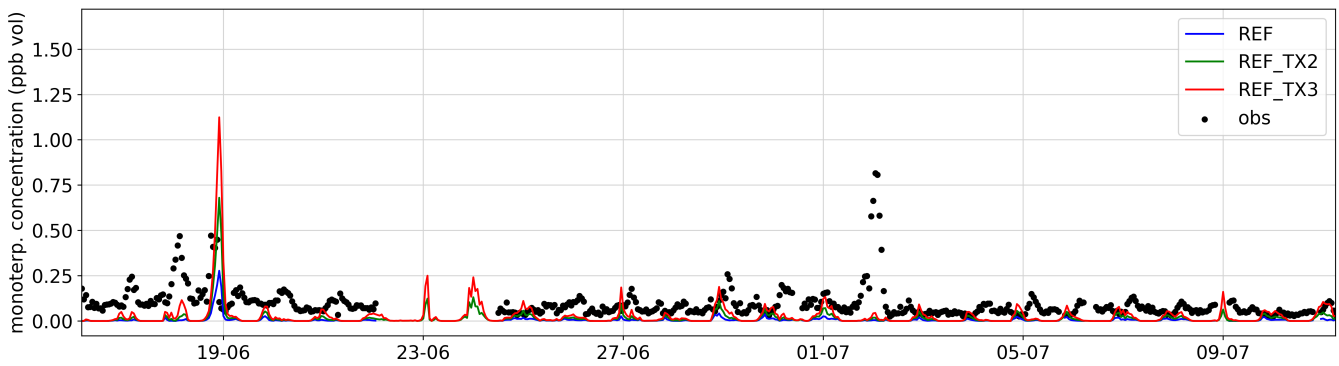
For $\text{PM}_{2.5}$, the less strict criteria are respected for the three simulations, but the fractional bias (FB) increases with the increase of biogenic terpene emissions. This increase is observed mostly in rural stations. In other words, $\text{PM}_{2.5}$ concentrations are overestimated at rural stations when the terpene biogenic emissions are increased, but the increase of terpene biogenic emissions does not degrade the scores at urban and suburban stations, and it even improves the correlation. A $\text{PM}_{2.5}$ concentration peak reaching $80 \mu\text{g}\cdot\text{m}^{-3}$ is observed on July 19 (not shown in Fig. 10c) and is probably due to forest fires in the south-west of France (Menut et al., 2023). Similar to $\text{PM}_{2.5}$, the concentrations of the organic fraction of PM_1 (organic matter, OM) are strongly influenced by the terpene biogenic emissions hypothesis. While OM concentrations are strongly underestimated in the REF simulation (fractional bias of -0.99), they respect all the less strict criteria in the REF-TX2 and REF-TX3 simulations (fractional bias equal to -0.46 and -0.09 respectively). As the stations where OM is measured are suburban and urban stations, this goes hand in hand with the better estimate of $\text{PM}_{2.5}$ at urban stations (not shown). As shown in Fig. 10c, the effect of modifying biogenic terpene emissions is quite significant, even at the Halles station, which is located in a very dense urban area. This increase of $\text{PM}_{2.5}$ concentrations is due to the increase of OM, as shown in Fig. 10d. OM concentrations are especially high between 18 and 19 June, days with very high temperatures and high biogenic emissions. During this period, the differences between the OM concentrations in the REF, REF-TX2 and REF-TX3 simulations are the largest. The highest the terpene emissions, the better the simulated OM concentration compared to observation, suggesting that it is essential to well represent the terpene emission of suburban areas to well represent the OM concentrations.

Regarding BVOC concentrations, no differences in the three simulations are observed for isoprene (C_5H_8) concentrations, as expected, and the mean concentration tends to be underestimated. Monoterpene concentrations are highly influenced by the biogenic terpene emissions. The higher the biogenic terpene emissions are, the smaller are the fractional biases observed in the simulations (-0.91 for REF, -0.39 for REF-TX2 and -0.03 for REF-TX3) (Table 7). Figures 11a and 11c show the hourly isoprene concentrations simulated and observed at the PRG station (dense urban area) and at the SIRTA station (suburban area), respectively. Isoprene is better represented at SIRTA than at the PRG station, because of the absence of biogenic emissions inside Paris in REF, REF-TX2 and REF-TX3 simulations. Figures 11b and 11d illustrate the hourly concentrations of monoterpenes simulated and observed at the PRG and SIRTA stations, respectively. Similarly as observed for isoprene, monoterpene concentrations are also strongly underestimated in urban areas (PRG) and better represented at the SIRTA suburban site. This can be justified by the absence of monoterpene biogenic emissions inside Paris, as analyzed in Section 4.2. The observed values in the urban PRG site point out a “regional background” of the monoterpene concentrations around 0.1 ppb.

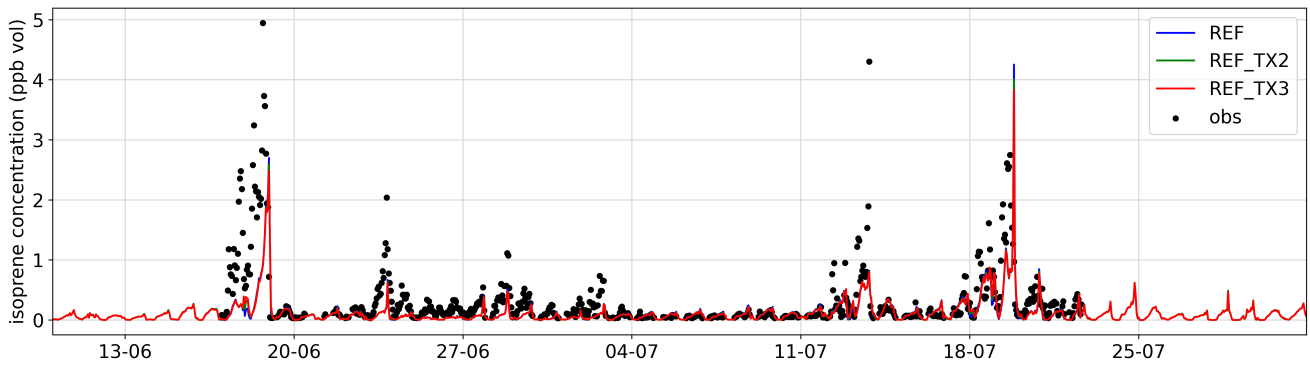
(a) Isoprene concentrations at the PRG station



(b) Monoterpene concentrations at the PRG station



(c) Isoprene concentrations at the SIRTA station



(d) Monoterpene concentrations at the SIRTA station

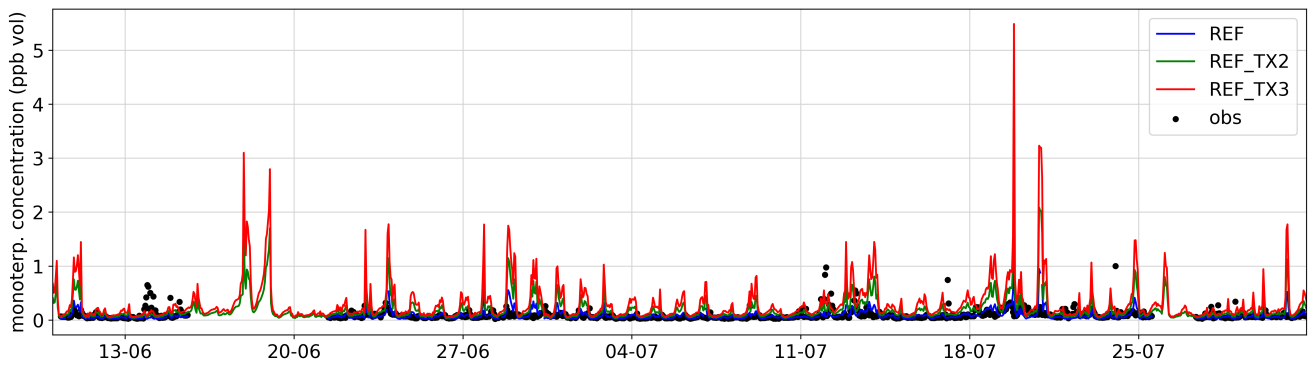


Figure 11. Observed and simulated hourly concentrations of (a) isoprene and (b) monoterpenes at the PRG station and (c) isoprene and (d) monoterpenes at the SIRTA station.

4.2 Impact of biogenic emissions from urban trees on isoprene, monoterpene, ozone, organic matter and PM_{2.5} concentrations

4.2.1 Impact of urban-tree biogenic emissions on isoprene and monoterpene concentrations

Comparisons of the hourly concentrations of isoprene and monoterpenes observed and simulated in the reference case (REF-TX2) and with the urban-tree biogenic emissions (bioparis-TX2) at PRG are presented in Fig. 12.

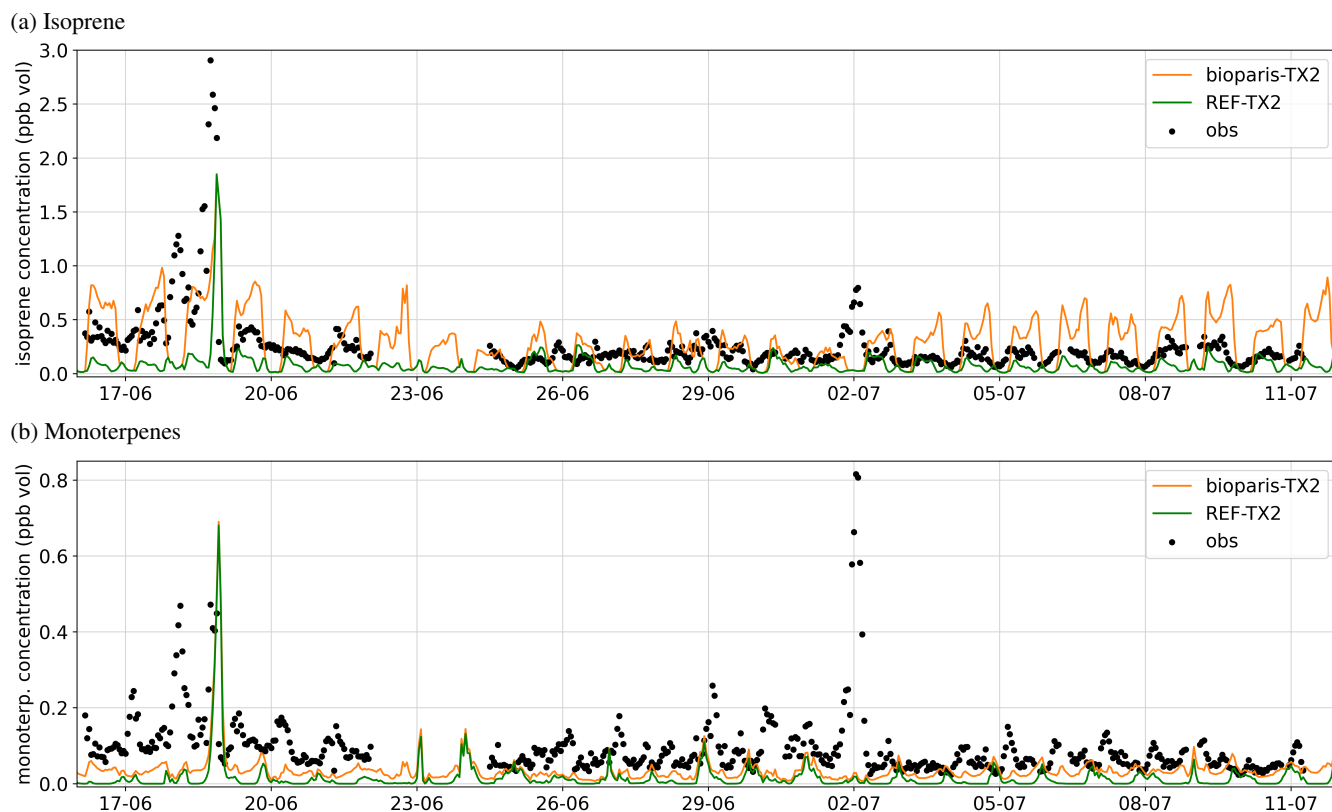


Figure 12. Observed and simulated hourly concentrations of (a) isoprene and (b) monoterpenes at the PRG station with (bioparis-TX2) and without (REF-TX2) the bottom-up biogenic emission inventory.

Figure 12a shows that isoprene concentrations simulated at PRG are underestimated in the reference simulation compared to the measurements. The inclusion of the urban-tree biogenic emissions allows a better representation of the isoprene concentrations (decrease of the NAD from 0.57 (REF-TX2) to 0.38 (bioparis-TX2) and increase of the correlation from 0.38 (REF-TX2) to 0.42 (bioparis-TX2)). However, in the bioparis-TX2 simulation, the daytime concentrations are overestimated on June 16, 17, 19, 20 and between July 2 and 10 by about a factor of 1.5, but the concentration peak around the 18th of June is underestimated. At night, non-zero isoprene concentrations are measured, the simulated concentrations are almost zero

3. BVOC EMISSIONS FROM URBAN TREES AND IMPACT ON REGIONAL AIR QUALITY

because isoprene is emitted only during the day by biogenic emissions and has a short lifetime ($\tau_{OH} \approx 1.5$ h with $[OH] = 10^6$ molecules.cm⁻³ (Atkinson and Arey, 2003b)). Isoprene is also emitted by road-traffic according the VOC speciation used (Theloke and Friedrich, 2007; Baudic et al., 2016), but in the model, traffic emissions are too low at night to represent the measured concentrations. This model to measurement discrepancy could be due to a measurement artefact, or to missing anthropogenic sources of isoprene at night. In view of the uncertainties in the measurements, the model provides a satisfactory representation of the order of magnitude of isoprene concentrations.

Table 8 presents the averaged isoprene and monoterpene concentrations and the relative impact of bioparis during the 2-month period and heatwaves. Note that the relative difference of concentrations is calculated on an hourly time step and then averaged over the 2-month or heatwave periods. As seen previously, biogenic emissions are driven by environmental variables, in particular temperature and solar radiation. To determine whether the effect of local biogenic emissions is greater during heatwaves, isoprene concentrations are also compared during these periods. It is especially relevant to quantify this effect because the frequency of these episodes is expected to increase in the future due to climate change (IPCC, 2021). The heatwave periods refers to the averaged concentrations on the following days: June, 15, 16, 17, 18 and July 11, 12, 13, 14, 17, 18, 19. During these periods, high air temperatures and clear sky conditions were observed as shown in Fig. 9. Table 8 shows that at the scale of the city of Paris, local isoprene emissions significantly increase isoprene concentrations (+1100% on average). The effect of bioparis during the heatwave periods is higher (+2400% on average), because emissions during that period are higher. As the TX2 and TX3 scenarios do not modify isoprene emissions, there is no impact on isoprene concentrations.

The comparison of monoterpene concentrations presented in Fig. 12b shows that monoterpenes are underestimated at PRG in the reference simulation and the addition of the urban-tree emissions strongly increases the monoterpene concentrations. However, the simulated concentrations still underestimate the observations, even with the bioparis-TX2 scenario, probably because of missing anthropogenic sources (Jo et al., 2023). Like isoprene, Table 8 shows that the addition of monoterpene emissions greatly increases the monoterpene concentrations by $6.4 \times 10^{12}\%$ on average over the 2-month period and by $1.4 \times 10^8\%$ during the heatwave periods. Monoterpene concentrations logically increase when their emissions are multiplied by 2 (TX2) or 3 (TX3), but the simulated concentrations underestimate the measurements. This discrepancy raises the question of potentially missing local sources of vegetation that emits monoterpenes in the area of measurement.

3. BVOC EMISSIONS FROM URBAN TREES AND IMPACT ON REGIONAL AIR QUALITY

Table 8. Comparison of minimum, mean and maximum isoprene and monoterpene concentrations averaged in Paris for each simulation and relative difference between the bioparis and the reference simulations during the 2 months and the heatwave periods.

species	simulation	2-month period			Heatwave periods		
Isoprene	concentration (ppb vol)	min	mean	max	min	mean	max
	REF	0.03	0.05	0.13	0.08	0.11	0.23
	REF_TX2	0.03	0.05	0.13	0.08	0.11	0.23
	REF_TX3	0.03	0.05	0.13	0.09	0.12	0.22
	bioparis	0.04	0.28	0.70	0.12	0.61	1.51
	bioparis_TX2	0.04	0.28	0.68	0.12	0.61	1.48
	bioparis_TX3	0.04	0.27	0.67	0.12	0.60	1.45
	Relative difference (%) between bioparis and REF	min	mean	max	min	mean	max
	bioparis_TX2 and REF_TX2	40	1.1e3	7.1e3	58	2.4e3	1.5e4
	bioparis_TX3 and REF_TX3	38	1.1e3	7.1e3	53	2.3e3	1.5e4
Monoterpenes	concentration (ppb vol)	min	mean	max	min	mean	max
	REF	0.005	0.009	0.12	0.009	0.016	0.19
	REF_TX2	0.01	0.02	0.23	0.02	0.03	0.38
	REF_TX3	0.02	0.03	0.35	0.04	0.07	0.57
	bioparis	0.007	0.02	0.12	0.01	0.03	0.21
	bioparis_TX2	0.01	0.04	0.24	0.03	0.08	0.41
	bioparis_TX3	0.03	0.07	0.36	0.05	0.13	0.61
	Relative difference (%) between bioparis and REF	min	mean	max	min	mean	max
	bioparis_TX2 and REF_TX2	3.6	6.4e12	9.0e13	6.3	1.4e8	1.0e9
	bioparis_TX3 and REF_TX3	3.5	1.1e13	1.5e14	6.2	1.5e8	1.2e9
	3.4	1.7e13	2.0e14	6.1	1.6e8	1.6e9	

4.2.2 Impact of urban-tree biogenic emissions on organic matter and particles concentrations

Figure 13, which compares the observed and simulated OM concentrations at PRG, shows that the impact of the urban biogenic emissions is smaller on OM concentrations than on isoprene and monoterpene concentrations. The urban biogenic emissions lead to an increase in OM concentrations on average over Paris during the 2-month period of 4.6% as shown in Table 9. The increase of OM concentrations is slightly larger when terpene emissions are doubled (+5.6%) and tripled (+6.1%). Due to larger biogenic emissions, the increase in OM concentrations is also larger during the heatwave (+5.4%).

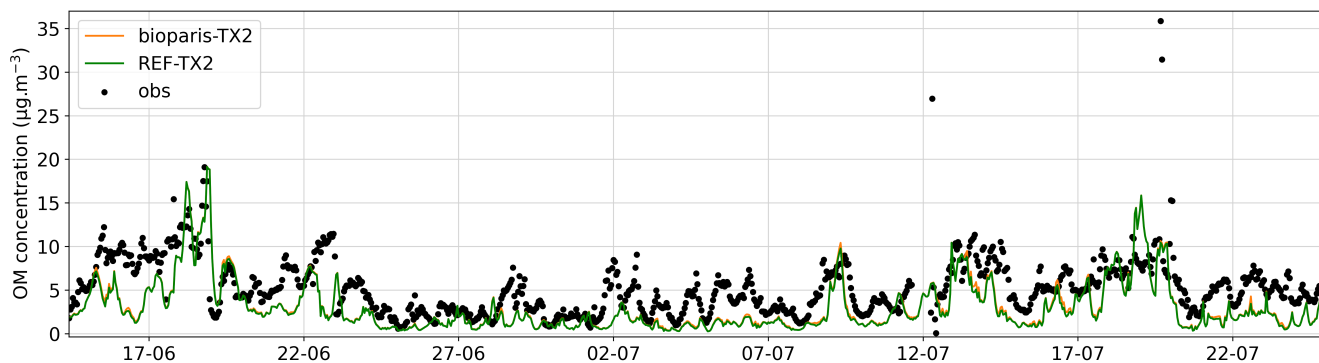


Figure 13. Observed and simulated hourly concentrations of organic matter (OM) at the PRG station with (bioparis-TX2) and without (REF-TX2) the urban biogenic emissions inventory.

The impact of the urban biogenic emissions is also less visible on hourly concentrations of $PM_{2.5}$, so the relative differences in OM and $PM_{2.5}$ concentrations are mapped in Figures 14 and 15. The two top panels present the REF-TX2 concentrations and the relative difference between bioparis-TX2 and REF-TX2 concentrations averaged on the 2-month period. The same maps are presented in the two lower panels but with concentrations averaged on the heatwave periods.

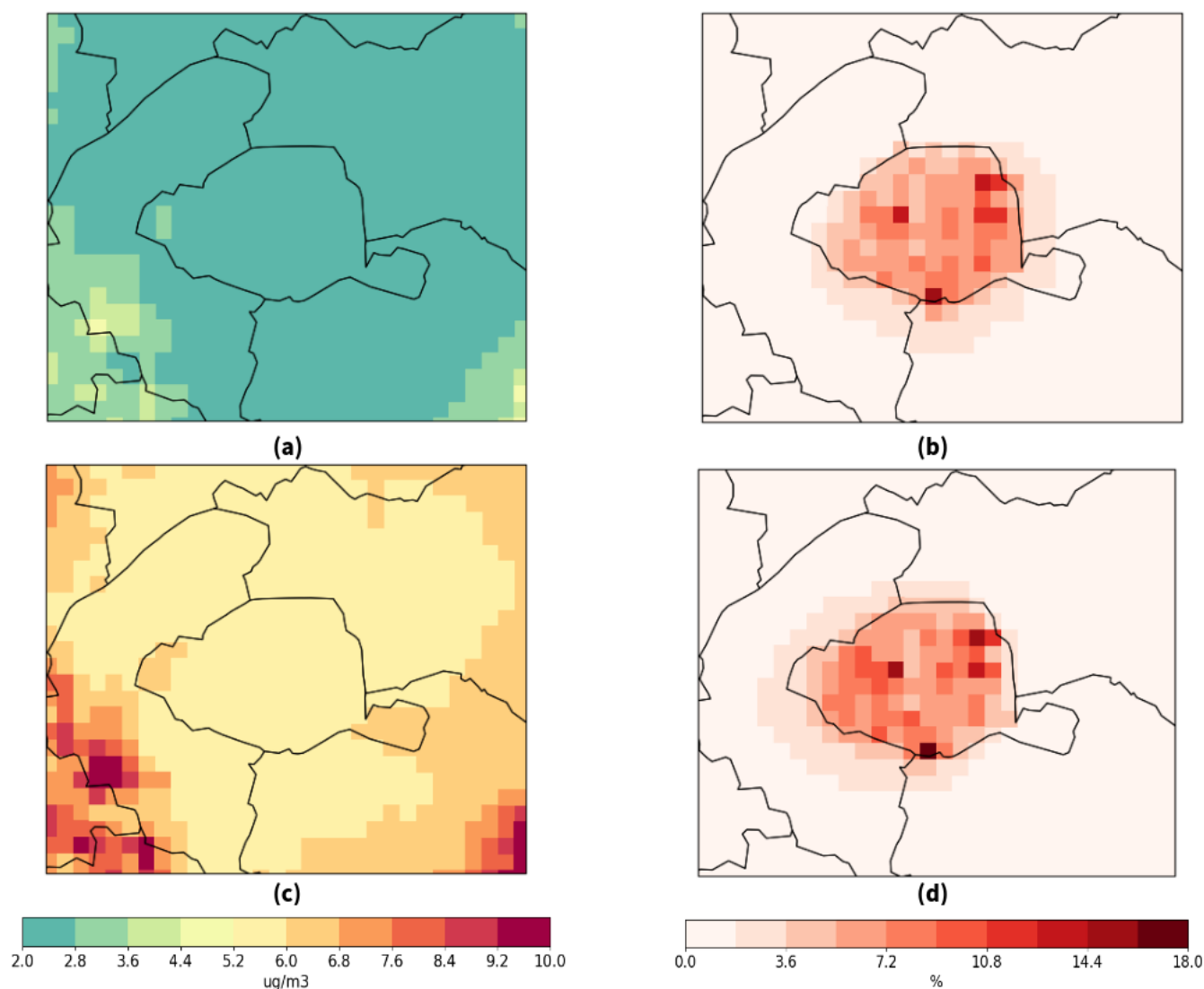


Figure 14. Average OM concentrations ($\mu\text{g}\cdot\text{m}^{-3}$) simulated by CHIMERE (REF-TX2) during (a) the whole period and (c) the heatwave and relative difference of OM concentrations with the urban-tree biogenic emissions (bioparis-TX2) during (b) the whole period and (d) the heatwave.

Figure 14 shows the spatial variability of the local biogenic emission effect and that the increase in OM concentrations due to emissions from urban trees remains localized over Paris. It is greater in cells with a large tree biomass (Fig. 6), where biogenic emissions are also larger, in particular monoterpenes (Fig. C1) and sesquiterpenes (Fig. C3). This correlation shows that biogenic emissions from urban trees contribute strongly to local OM formation. The increase in OM concentrations is slightly larger during the heatwaves periods, as shown in Table 9. The impact of urban emissions extends a little further during these periods.

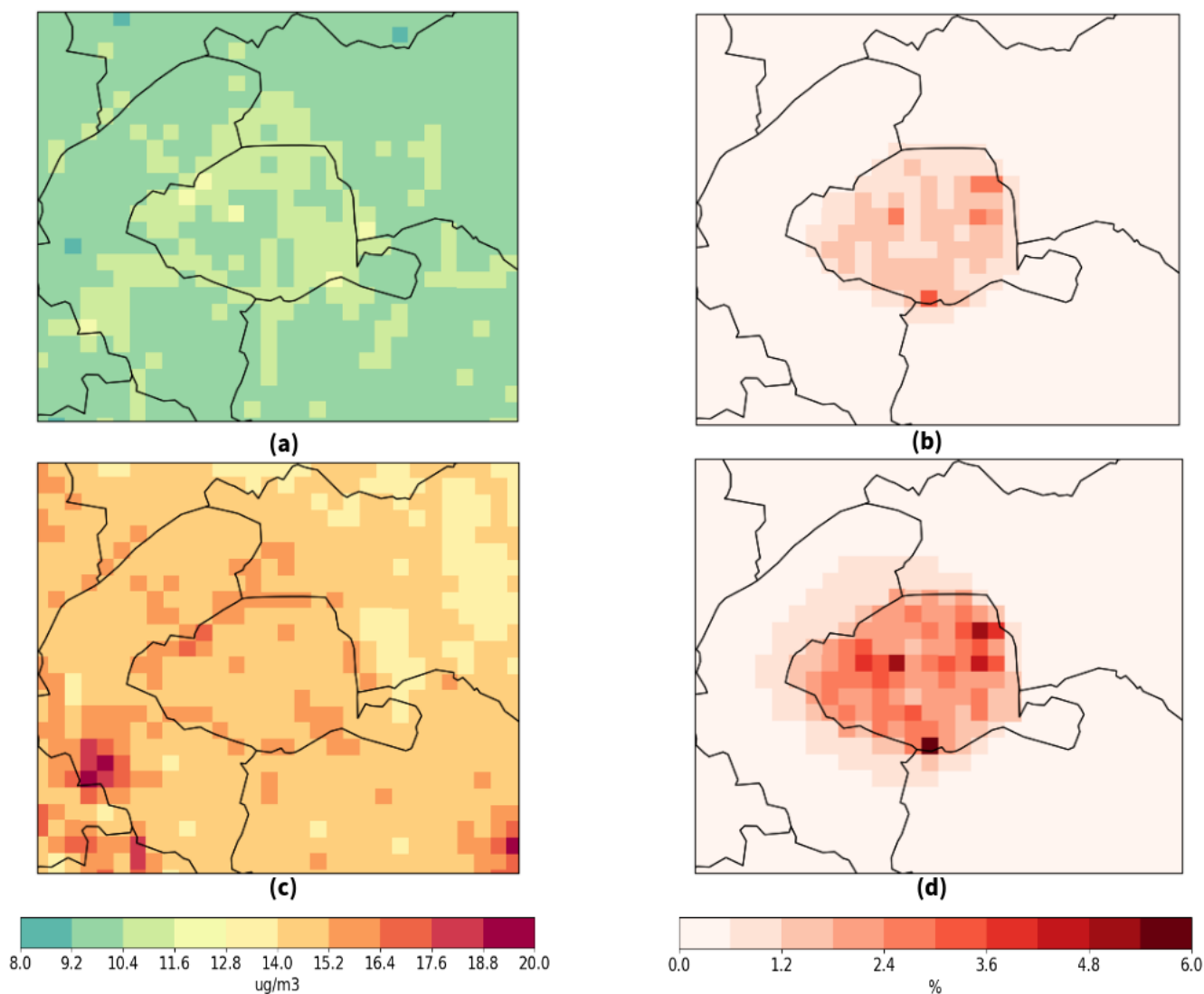


Figure 15. Average PM_{2.5} concentrations (μg.m⁻³) simulated by CHIMERE (REF-TX2) during (a) the whole period and (c) the heatwave and relative difference of PM_{2.5} concentrations with the urban-tree biogenic emissions (bioparis-TX2) during (b) the whole period and (d) the heatwave.

The increase in PM_{2.5} concentrations is lower than for OM, but the spatial distribution is similar. The impact remains localized over Paris (+0.6% on average), and is strongest during heatwaves (+1.3%), as shown by the maps in Fig. 15 and Table 9. The increase in PM_{2.5} is larger when monoterpene and sesquiterpene emissions are doubled (TX2) and tripled (TX3) (Table 9). This underlines the importance of terpenes in the formation of particulate matter.

3. BVOC EMISSIONS FROM URBAN TREES AND IMPACT ON REGIONAL AIR QUALITY

Table 9. Comparison of minimum, mean and maximum organic matter (OM) and PM_{2.5} concentrations averaged in Paris for each simulation and relative difference between the bioparis and the reference simulations during the 2 months and the heatwave periods.

species	simulation	2-month period			Heatwave periods		
OM	concentration ($\mu\text{g}\cdot\text{m}^{-3}$)	min	mean	max	min	mean	max
	REF	1.27	1.35	1.57	2.91	3.01	3.34
	REF_TX2	2.34	2.45	2.79	5.45	5.62	6.31
	REF_TX3	3.45	3.58	4.14	7.94	8.16	9.27
	bioparis	1.32	1.40	1.63	2.95	3.13	3.48
	bioparis_TX2	2.43	2.55	2.87	5.58	5.87	6.59
	bioparis_TX3	3.57	3.74	4.26	8.15	8.55	9.69
	Relative difference (%) between bioparis and REF	min	mean	max	min	mean	max
	bioparis_TX2 and REF_TX2	0.6	4.60	11.51	0.2	5.44	14.37
	bioparis_TX3 and REF_TX3	0.6	5.58	15.86	0.3	6.08	18.00
PM _{2.5}	concentration ($\mu\text{g}\cdot\text{m}^{-3}$)	min	mean	max	min	mean	max
	REF	8.48	9.25	10.85	10.83	11.64	13.36
	REF_TX2	9.85	10.65	12.26	14.13	14.97	16.76
	REF_TX3	11.32	12.15	13.84	17.65	18.52	20.45
	bioparis	8.54	9.31	10.91	10.85	11.78	13.53
	bioparis_TX2	9.98	10.77	12.38	14.18	15.25	17.16
	bioparis_TX3	11.53	12.34	14.06	17.72	18.96	21.07
	Relative difference (%) between REF and bioparis	min	mean	max	min	mean	max
	REF_TX2 and bioparis_TX2	0.12	0.64	1.60	0.09	1.25	3.09
	REF_TX3 and bioparis_TX3	0.20	1.12	3.06	0.14	2.06	5.78
		0.25	1.55	4.52	0.17	2.69	8.29

4.2.3 Impact on ozone concentrations

Ozone concentrations also increase with the urban-tree biogenic emissions (+1% on average), especially during the heatwave periods (+2.4%). The increase in O_3 concentrations is also mostly localized in the Paris city and extends to the Paris suburbs during heatwaves (Fig. 16). Table 10 shows that doubled or tripled monoterpene and sesquiterpene emissions increase ozone concentrations, but the increase is relatively lower than for OM and $PM_{2.5}$. This suggests that ozone formation is less sensitive to monoterpene and sesquiterpene emissions, which mostly impact the formation of organic matter.

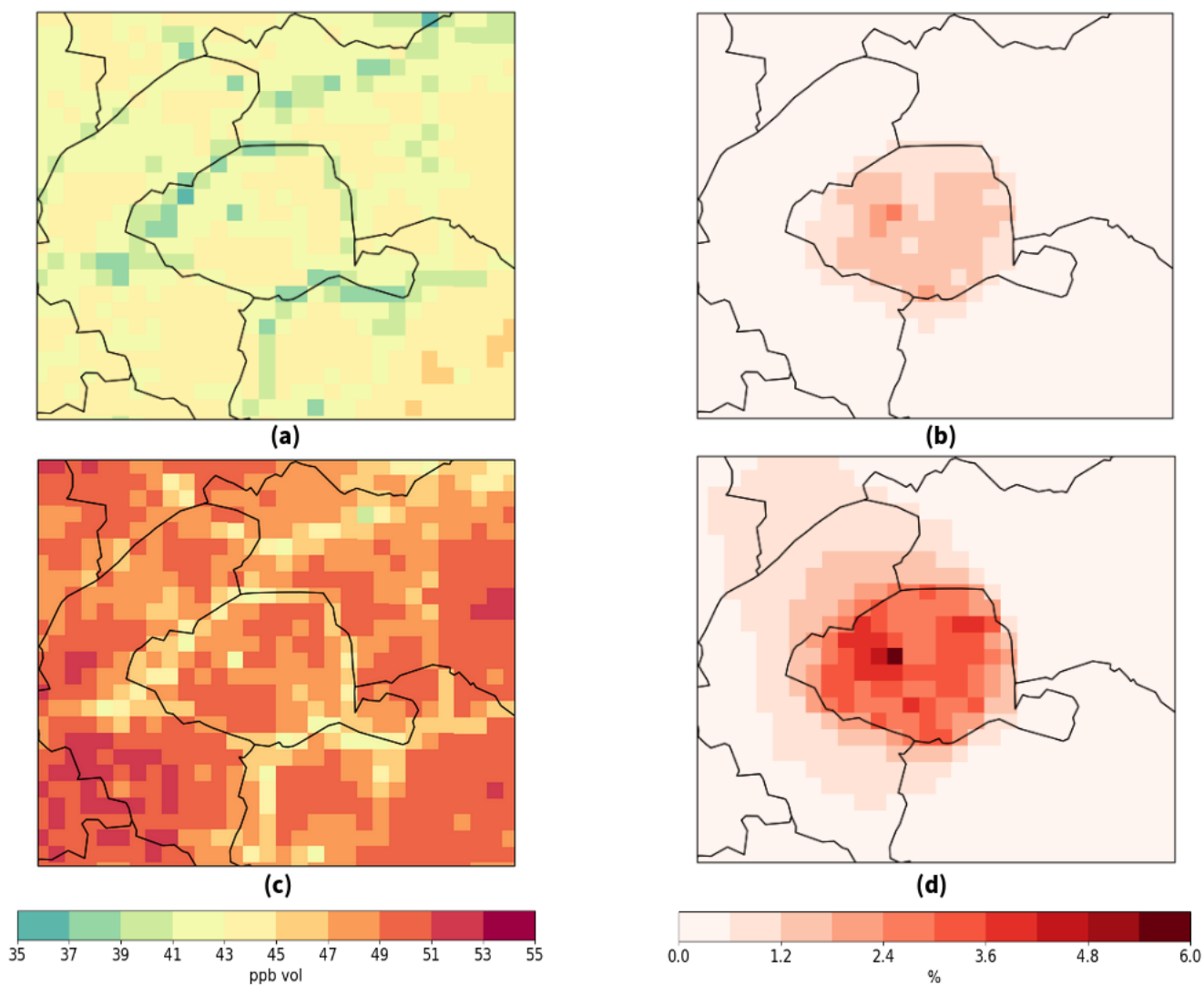


Figure 16. Average O_3 concentrations (ppb vol) simulated by CHIMERE (REF-TX2) during (a) the whole period and (c) the heatwave and relative difference of O_3 concentrations with the urban-tree biogenic emissions (bioparis-TX2) during (b) the whole period and (d) the heatwave.

3. BVOC EMISSIONS FROM URBAN TREES AND IMPACT ON REGIONAL AIR QUALITY

Table 10. Comparison of minimum, mean and maximum ozone concentrations averaged in Paris for each simulation and relative difference between the bioparis and the reference simulations during the 2 months and the heatwave periods.

simulation	2-month period			Heatwave periods		
concentration (ppb vol)	min	mean	max	min	mean	max
REF	34.92	41.54	43.81	40.96	46.94	49.53
REF_TX2	35.42	42.03	44.30	41.65	47.68	50.28
REF_TX3	35.87	42.46	44.73	42.27	48.34	50.95
bioparis	35.48	42.05	44.47	41.63	48.26	51.15
bioparis_TX2	36.06	42.62	45.05	42.36	49.14	52.10
bioparis_TX3	36.59	43.12	45.57	43.01	49.94	52.95
Relative difference (%) between	min	mean	max	min	mean	max
bioparis and REF	0.28	1.03	2.38	0.40	2.42	5.72
bioparis_TX2 and REF_TX2	0.32	1.17	2.67	0.48	2.65	6.21
bioparis_TX3 and REF_TX3	0.35	1.30	2.94	0.45	2.87	6.66

The urban biogenic emissions mainly increase O_3 concentrations during the day, as the concentrations of biogenic species are higher and O_3 is formed during daytime influenced by solar radiation. The impact of the biogenic bottom-up inventory on maximal daily ozone concentrations (8 h moving average) is also evaluated, as this value is used in the French air quality standards (LCSQA, 2016). The bottom-up inventory increases, in average during the 2 months, by around 0.6% the ozone maximal 8 h concentrations and by 1.2% during heatwaves in all scenarios. The maximal impact goes from 4.0% to 4.8% according to the biogenic emission factors scenario on average over the 2-month period and from 7.6 to 8.5% during heatwaves.

5 Conclusions

To conclude, trees naturally emit BVOCs, which can lead to the formation of secondary pollutants such as ozone and secondary organic aerosols. The impact of urban trees on pollutant concentrations is not taken into account in regional air-quality models. To estimate this impact, an inventory of biogenic emissions from urban trees has been developed using a bottom-up approach. Its effect on gas and particle concentrations in the Paris Region has been quantified using the CHIMERE model.

First, the location and characteristics of the urban trees were obtained from the tree database of the Paris city (Municipality of Paris, 2023). This information was combined with allometric equations developed for urban trees in the United-States (US) (McPherson et al., 2016) to compute the leaf dry biomass used in the emissions model. Tree-species emission factors from MEGAN model were used to compute emissions of various BVOC by each tree species per leaf biomass amount and at standard conditions. Then, emissions were modulated by the temperature and radiation with activity factors from Guenther et al. (1995, 2012) and the meteorological variables simulated by WRF. Biogenic emissions were then integrated in the CHIMERE grid and complement the regional biogenic emissions computed with the land-use approach. The order of magnitude of emissions are consistent between the urban and the regional biogenic emissions.

Secondly, the biogenic emissions computed with the bottom-up approach were added to CHIMERE to simulate air quality over the Paris region during the 2 months of June and July 2022. The study presents first a validation of the reference simulations, and then focuses on the impact of the bottom-up inventory on concentrations of isoprene, monoterpenes, organic matter (OM), $PM_{2.5}$ and ozone. To estimate the sensitivity to terpene emissions, for which there are high uncertainties in emission factors, simulations were carried out with monoterpene and sesquiterpene emissions multiplied by 2 (TX2) and 3 (TX3). The results show that simulated NO_2 , O_3 , and $PM_{2.5}$ concentrations are globally consistent with measurements. OM, isoprene and monoterpene concentrations are underestimated but they increase when emissions from urban trees are taken into account. Over Paris city, urban trees induce a significant increase in OM concentrations of 4.6% on average over the two months and of 5.4% during the heatwave periods. This increase can reach 11.5% locally on average over the two months and 14.4% during the heatwave period. The increase in OM concentrations is sensitive to monoterpene and sesquiterpene emissions and remains localized over Paris city where the urban trees are located. Since OM is part of $PM_{2.5}$, $PM_{2.5}$ concentrations also increase, but to a lesser extent (+0.6% on average and +1.3% during the heatwave periods). O_3 concentrations also slightly increase due to the urban-tree emissions by 1.0% on average over the 2 months and by 2.4% during the heatwaves. This increase can locally reach 2.4% on average over the two months and 5.7% during the heatwaves. The increase in O_3 concentrations during the heatwave periods extends to the Paris suburbs, further than for OM. These values correspond to temporal averages but the effect of urban emissions on OM, $PM_{2.5}$ and O_3 could be higher during the day time when biogenic emissions and photolysis occur.

OM concentrations are sensitive to terpene emissions, and they are better modeled when urban trees are taken into account in the model, and when terpene emission factors are increased. So it is essential to better estimate emission factors specifically of urban and suburban trees. The effect of urban-tree emissions on O_3 concentrations is not very high, but can aggravate O_3 peaks during heatwaves. Furthermore, it should be noted that part of the urban vegetation (in private areas) and of the suburban

3. BVOC EMISSIONS FROM URBAN TREES AND IMPACT ON REGIONAL AIR QUALITY

vegetation were not taken into account in this study, as the tree inventory is only available for the public trees of Paris city. The effect of urban and suburban trees on air quality is therefore probably underestimated. Tree inventories should be set up systematically in more cities and their suburbs. This could be completed with methods for characterizing urban vegetation using aerial images, for example. This methodology for building a BVOCs bottom-up inventory could be easily applied to other cities that have a tree inventory. Further work would involve improving the estimation of the tree-scale biogenic emissions by improving the spatial resolution of the meteorological fields. Speciation of monoterpenes and oxygenated VOCs emitted into model chemical species is assumed to be identical for each tree species. A speciation of monoterpenes according to the tree species, as done in Steinbrecher et al. (2009), could be introduced. However as this speciation does not include all the tree species found in Paris, the speciation should be enriched with other data.

Code availability. The version of WRF-CHIMERE code used here is available on request.

Data availability. ACSM data measured at the PRG site are available in the Aeris datacenter: Di Biagio et al. (2023), ACROSS_LISA_PRG_ACSM-nrPM1comp_L2, in preparation. [Dataset]. Aeris.

PTR-MS data measured at the PRG site are available in the Aeris datacenter: <https://www.aeris-data.fr/>.

PTR-MS data measured at the SIRTAs station are available in the ACTRIS database: <https://ebas-data.nilu.no> and in the IPSL data catalog: Simon, L., Gros, V., Truong, F., Sarda-Esteve, R., and Kalalian, C.: PTR-MS measurements in 2020–2021, IPSL Data Catalog [dataset], <https://doi.org/10.14768/f8c46735-e6c3-45e2-8f6f-26c6d67c4723>, 2022a.

Hourly NO₂, O₃ and PM_{2.5} concentrations measured at the Paris Chatelet/Halles station are available on the Airparif's Open Data Portal: <https://data-airparif-asso.opendata.arcgis.com/>. Regional emissions inventory and organic matter data for the Halles site are available on request.

Appendix A: Detailed description of the experimental measurements

A1 Measurements performed at SIRT

Isoprene was measured with a gas-chromatograph equipped with a Flame Ionisation Detector (GC-FID), AIRMOVOC C2-C6 (Chromatotec, Saint Antoine, France). The instrument is described in detailed Gros et al. (2011). Calibration was performed with a NPL (National Physics Laboratory, Teddington, UK) standard. Uncertainty are estimated to be less than 15%. Monoterpenes were measured at SIRT using a Proton-Transfer-Reaction Quadrupole Mass Spectrometer (PTR-Q-MS) from Ionicon (Innsbruck, Austria) with a time resolution of 5 min. This instrument was implemented at SIRT for long-term measurements early 2020 and its operating conditions are described in Simon et al. (2023). The ambient air was sampled at 15m, 1-hour blank measurements were performed every 13 hours, and calibrations every month with a NPL standard containing α -pinene. Monoterpenes were measured at the mass-to-charge ratio (m/z) 137, and the associated uncertainties for the period of June-July 2022 were 32%, while the mean detection limit was of 25 ppt.

A2 Measurements performed at PRG

Gas and aerosol sampling at PRG site are performed at 30 m above ground layer. VOCs were measured at PRG site using a PTR-ToF-MS (PTR 4000x2, Ionicon Analytik, Austria) equipped with a CHARON inlet, already extensively described elsewhere (Jordan et al., 2009; Eichler et al., 2015; Müller et al., 2017; Leglise et al., 2019). The instrument has been programmed to automatically switch between gas and particle phases, and was working at 2.6 mbar and at $E/N=120$ Td. Gas was sampled at the top of a 7th floor building through a 12 m long Teflon tubing, with a 17.5 mm inner diameter. The flow in this main line was fixed at 40 L min⁻¹ until a glass manifold where all gas phase instruments sampled ambient air. Sensitivity and background have been regularly controlled during the course of the experiment using pure nitrogen cylinder (99.99999% purity, Linde) and a certified gas standard (containing 10 VOCs at 100 ppb, NPL) providing quantitative measurement with an uncertainty typically in the order of 10 ppt.

A3 Measurements performed at the Halles

In the Halles station, NO₂ concentrations are measured by chemiluminescence detection with a AC32M, analyzer from ENVEA (formerly Environnement SA), with a measurement uncertainty of 10%. O₃ concentrations are measured by Ultraviolet (UV) photometry with a O3 42e analyzer from ENVEA, with a measurement uncertainty of 11%. PM_{2.5} are measured with a FIDAS 200 analyzer from PALAS, certified technically compliant by the Laboratoire Central de la Surveillance de la Qualité de l'Air (LCSQA) for continuous, real-time regulatory monitoring of PM₁₀ and PM_{2.5} fractions based on the optical detection of light scattered by aerosols (Lorenz-Mie solution). The uncertainties associated with measurement are estimated to 9%. More information on the certified devices for regulatory air quality measurement are available here (in French): https://www.lcsqa.org/system/files/media/documents/Liste%20appareils%20conforme%20mesure%20_qualit%C3%A9%20air%20M%C3%A0J_13-05-20_v2_0.pdf

3. BVOC EMISSIONS FROM URBAN TREES AND IMPACT ON REGIONAL AIR QUALITY

Table A1. List of Airparif stations with the species measured and used in this study.

station	location	type	species measured
PARIS 1er Les Halles	48.862128° N, 2.3446227° E	urban background	NO ₂ , O ₃ , PM _{2.5} , OM
PARIS 7eme	48.8571944° N, 2.2932778° E	urban background	NO ₂
PARIS 12eme	48.8371944° N, 2.3938056° E	urban background	NO ₂
PARIS 13eme	48.8284722° N, 2.3595583° E	urban background	NO ₂ , O ₃
PARIS 15eme	48.8303889° N, 2.2698861° E	urban background	NO ₂
PARIS 18eme	48.8917278° N, 2.345575° E	urban background	NO ₂ , O ₃ , PM _{2.5}
AUBERVILLIERS	48.9039444° N, 2.3847222° E	urban background	NO ₂
ARGENTEUIL	48.8278324° N, 2.3805391° E	urban background	NO ₂
BOBIGNY	48.9024111° N, 2.4526167° E	urban background	NO ₂ , PM _{2.5}
CHAMPIGNY-SUR-MARNE	48.816692° N, 2.516669° E	urban background	NO ₂ , O ₃
EVRY	48.8276389° N, 2.3267111° E	urban background	NO ₂
LOGNES	48.8403167° N, 2.6346611° E	urban background	NO ₂ , O ₃
MONTGERON	48.7065833° N, 2.4570833° E	urban background	NO ₂ , O ₃
NEUILLY-SUR-SEINE	48.8813333° N, 2.2773167° E	urban background	NO ₂ , O ₃
GENNEVILLIERS	48.9298219° N, 2.291413° E	urban background	NO ₂ , PM _{2.5}
VITRY-SUR-SEINE	48.7756628° N, 2.374005° E	urban background	NO ₂ , O ₃ , PM _{2.5}
GONESSE	48.9908583° N, 2.4447722° E	suburban background	NO ₂ , PM _{2.5}
MANTES-LA-JOLIE	48.996225° N, 1.7032972° E	suburban background	NO ₂ , O ₃
MELUN	48.5281028° N, 2.6539472° E	suburban background	NO ₂ , O ₃
FONTAINEBLEAU FOREST	48.4562391° N, 2.6793973° E	rural	NO ₂ , O ₃ , PM _{2.5}
SAINT-MARTIN-DU-TERTRE	49.1082856° N, 2.1531876° E	rural	O ₃ , PM _{2.5}

Appendix B: Characteristics of trees in the Paris Tree database

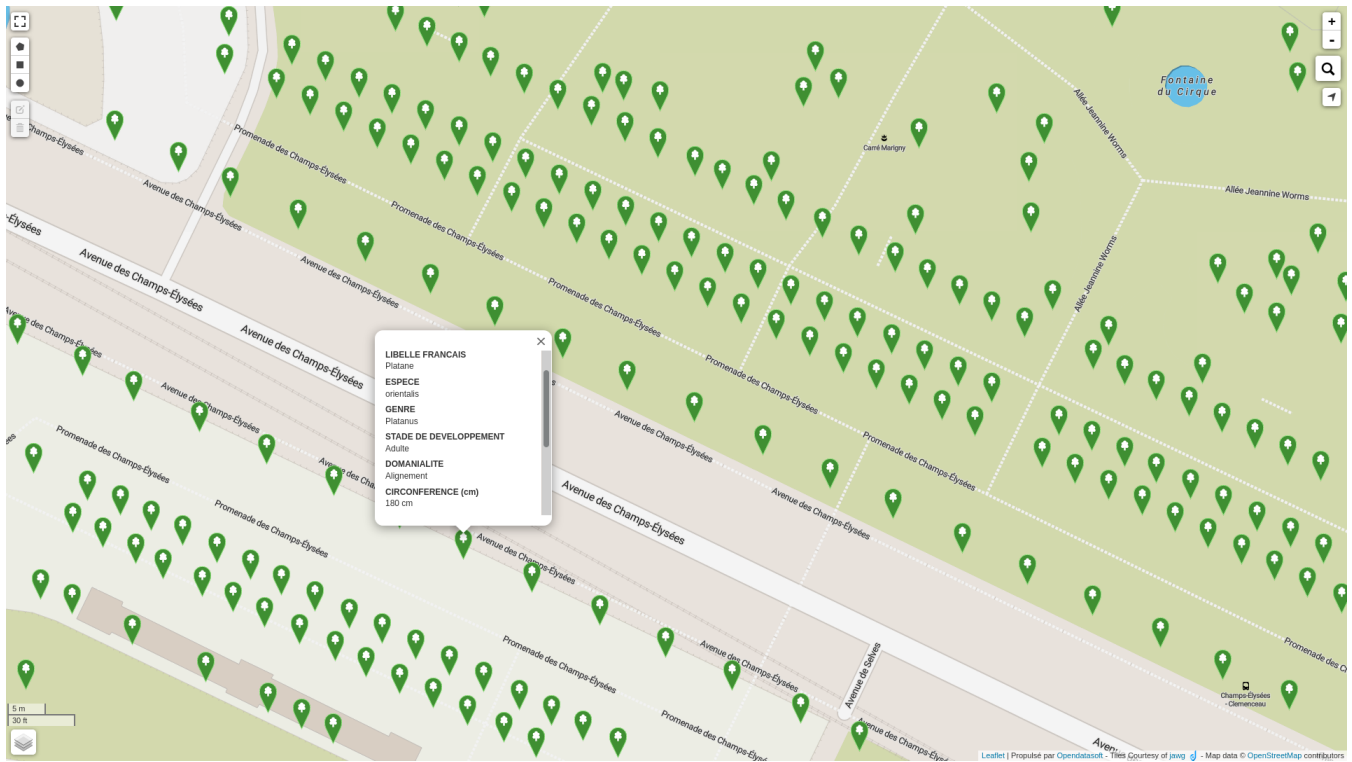


Figure B1. Screenshot of the Paris tree database near Avenue des Champs-Élysées (Municipality of Paris, 2023).

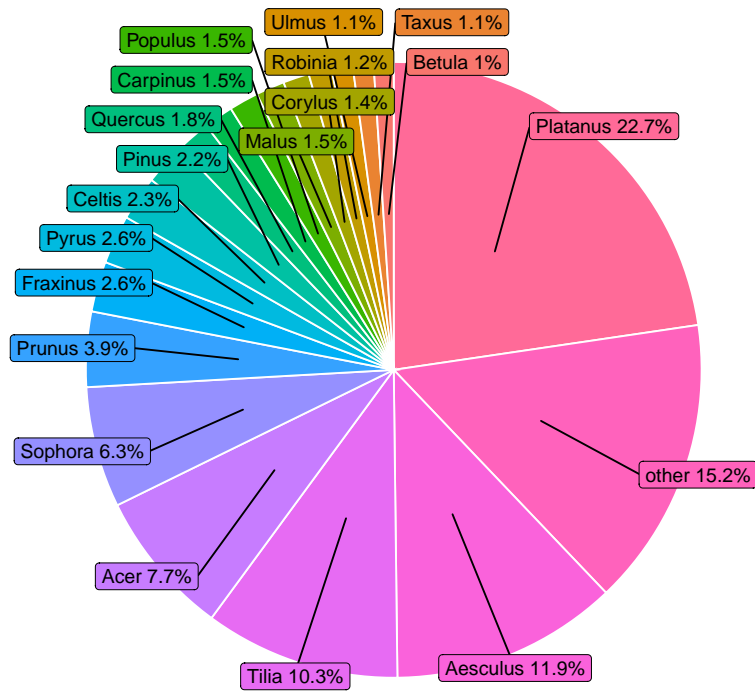


Figure B2. Proportion (%) of each tree genus in Paris (only genus with $P > 1\%$ are shown, the rest of the trees are in the "other" category).

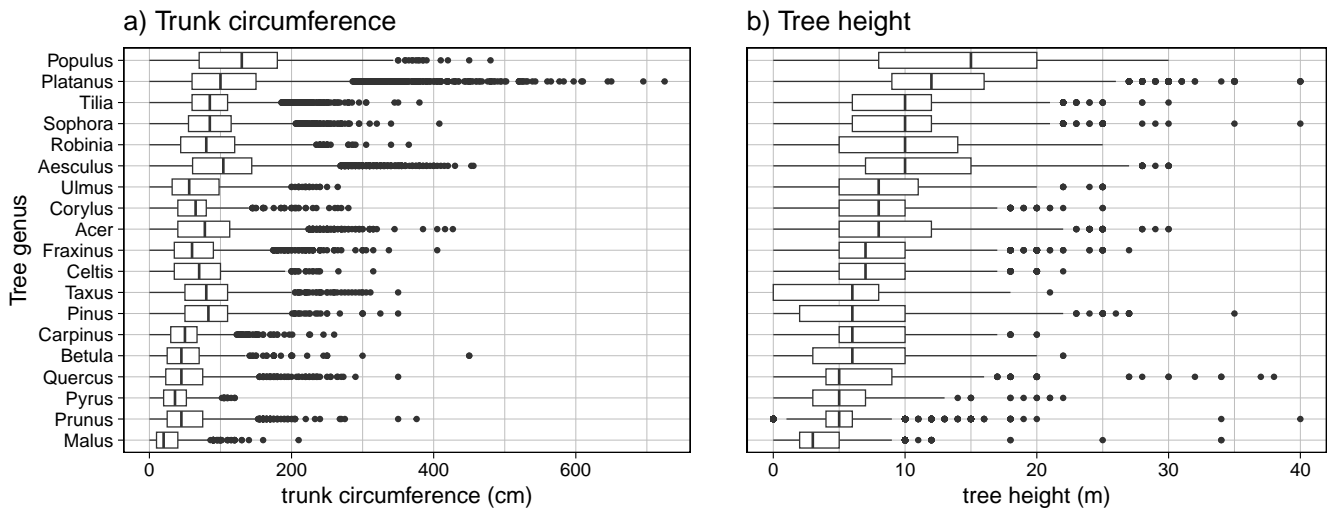


Figure B3. Boxplot of the (a) trunk circumference and (b) tree height of the most dominant tree genus.

Appendix C: BVOC emissions

Table C1. Aggregation matrix of emitted MEGAN v3.2 species to MELCHIOR2 species.

MEGANv3.2/ MELCHIOR2 species	C5H8	APINEN	BPINEN	LIMONE	TERPEN	OCIMEN	HUMULE	NO	CO	CH3OH	C2H4	CH3CHO	CH3COE	MEMALD
ISOP	1.0	0.0	0.0	0.0	0.0	0.0	0.0	0.0	0.0	0.0	0.0	0.0	0.0	0.0
MBO	0.0	0.0	0.0	0.0	0.0	0.0	0.0	0.0	0.0	0.0	0.0	0.0	0.0	1.0
MT_PINE	0.0	1.0	0.0	0.0	0.0	0.0	0.0	0.0	0.0	0.0	0.0	0.0	0.0	0.0
MT_ACYC	0.0	0.0	0.0	0.0	0.0	1.0	0.0	0.0	0.0	0.0	0.0	0.0	0.0	0.0
MT_CAMP	0.0	0.47	0.53	0.0	0.0	0.0	0.0	0.0	0.0	0.0	0.0	0.0	0.0	0.0
MT_SABI	0.0	0.4	0.0	0.6	0.0	0.0	0.0	0.0	0.0	0.0	0.0	0.0	0.0	0.0
MT_AROM	0.0	1.0	0.0	0.0	0.0	0.0	0.0	0.0	0.0	0.0	0.0	0.0	0.0	0.0
NO	0.0	0.0	0.0	0.0	0.0	0.0	0.0	1.0	0.0	0.0	0.0	0.0	0.0	0.0
SQT_HR	0.0	0.0	0.0	0.0	0.0	0.0	1.0	0.0	0.0	0.0	0.0	0.0	0.0	0.0
SQT_LR	0.0	0.0	0.0	0.0	0.0	0.0	1.0	0.0	0.0	0.0	0.0	0.0	0.0	0.0
MEOH	0.0	0.0	0.0	0.0	0.0	0.0	0.0	0.0	0.0	1.0	0.0	0.0	0.0	0.0
ACTO	0.0	0.0	0.0	0.0	0.0	0.0	0.0	0.0	0.0	0.0	0.0	0.0	1.0	0.0
ETOH	0.0	0.0	0.0	0.0	0.0	0.0	0.0	0.0	0.0	0.0	0.0	1.0	0.0	0.0
ACID	0.0	0.0	0.0	0.0	0.0	0.0	0.0	0.0	0.0	0.0	0.0	1.0	0.0	0.0
LVOC	0.0	0.0	0.0	0.0	0.0	0.0	0.0	0.0	0.0	0.0	0.36	0.0	0.64	0.0
OXPROD	0.0	0.0	0.0	0.0	0.0	0.0	0.0	0.0	0.0	0.0	0.0	0.9	0.1	0.0
STRESS	0.0	0.0	0.0	0.0	0.0	0.0	0.0	0.0	0.0	0.0	1.0	0.0	0.0	0.0
OTHER	0.0	0.0	0.0	0.0	0.0	0.0	0.0	0.0	0.0	0.0	0.0	0.0	1.0	0.0
CO	0.0	0.0	0.0	0.0	0.0	0.0	0.0	0.0	1.0	0.0	0.0	0.0	0.0	0.0

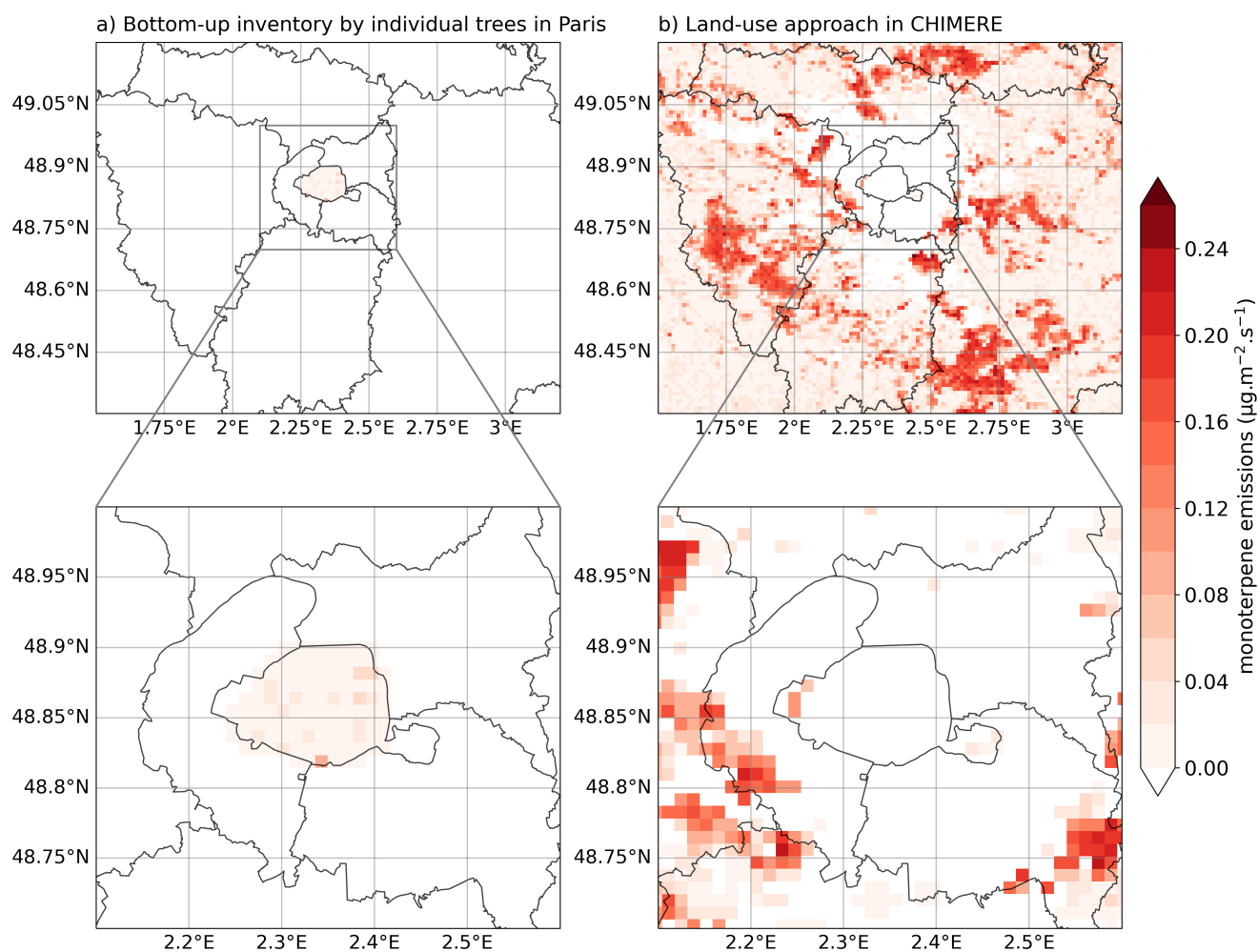


Figure C1. Comparison of the 2 months averaged monoterpene emissions computed with (a) the "bottom-up" inventory and (b) with the land-cover approach in CHIMERE over Île-de-France and Greater Paris.

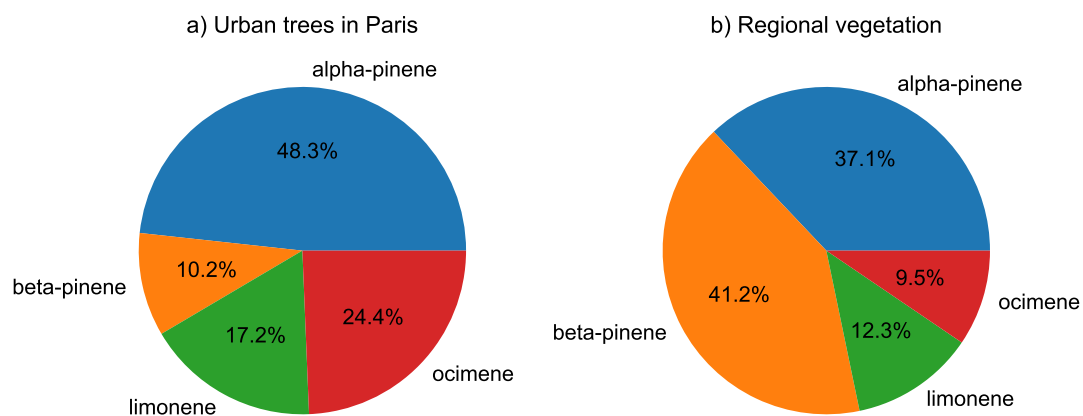


Figure C2. Distribution of monoterpane species emitted, summed over the two months (a) for the urban trees in Paris computed with the bottom-up inventory and (b) for the vegetation over Île-de-France region computed with the land-use approach.

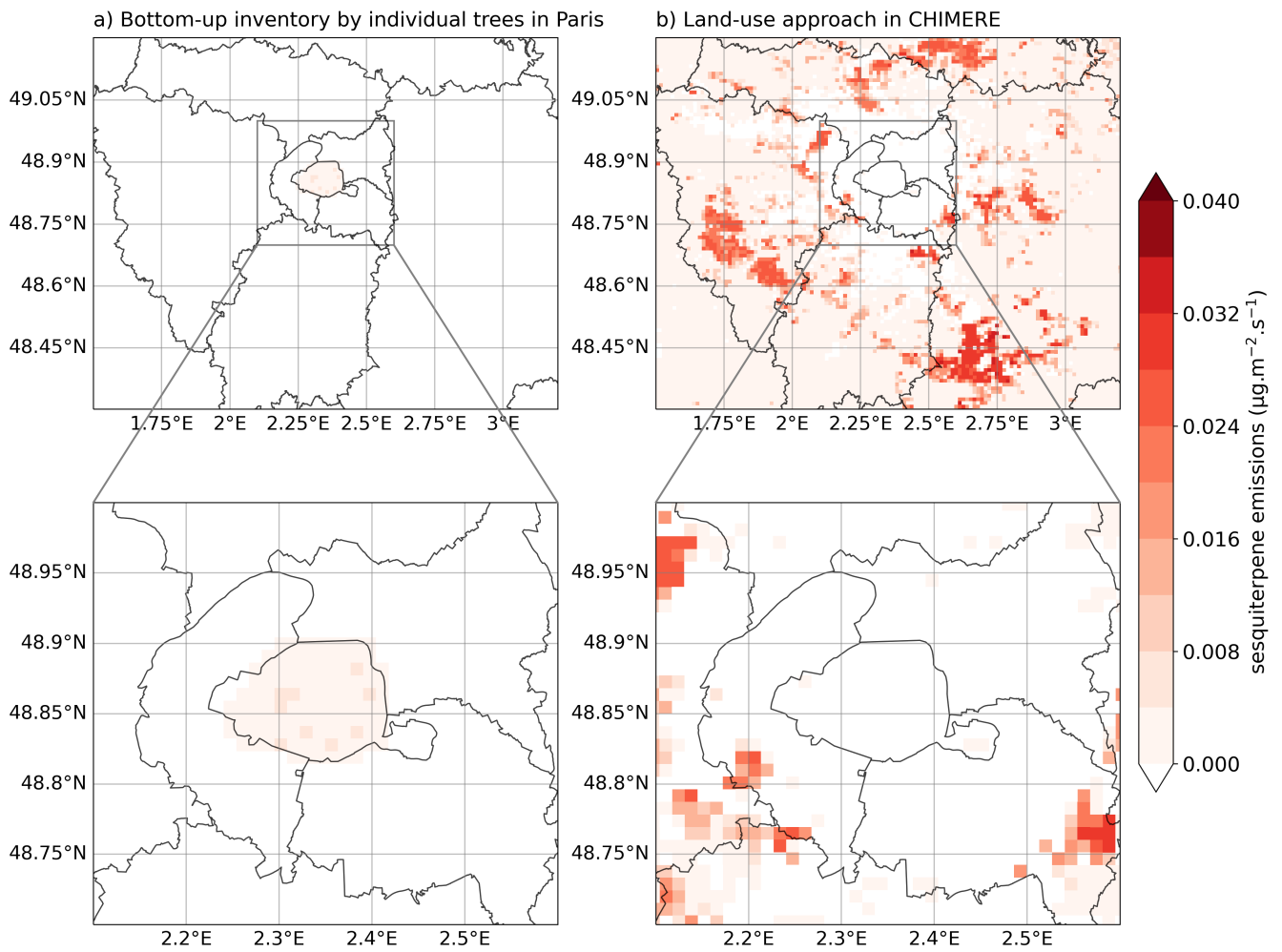


Figure C3. Comparison of the 2 months sesquiterpene emissions computed with (a) the "bottom-up" inventory and (b) with the land-cover approach in CHIMERE over Île-de-France and Greater Paris.

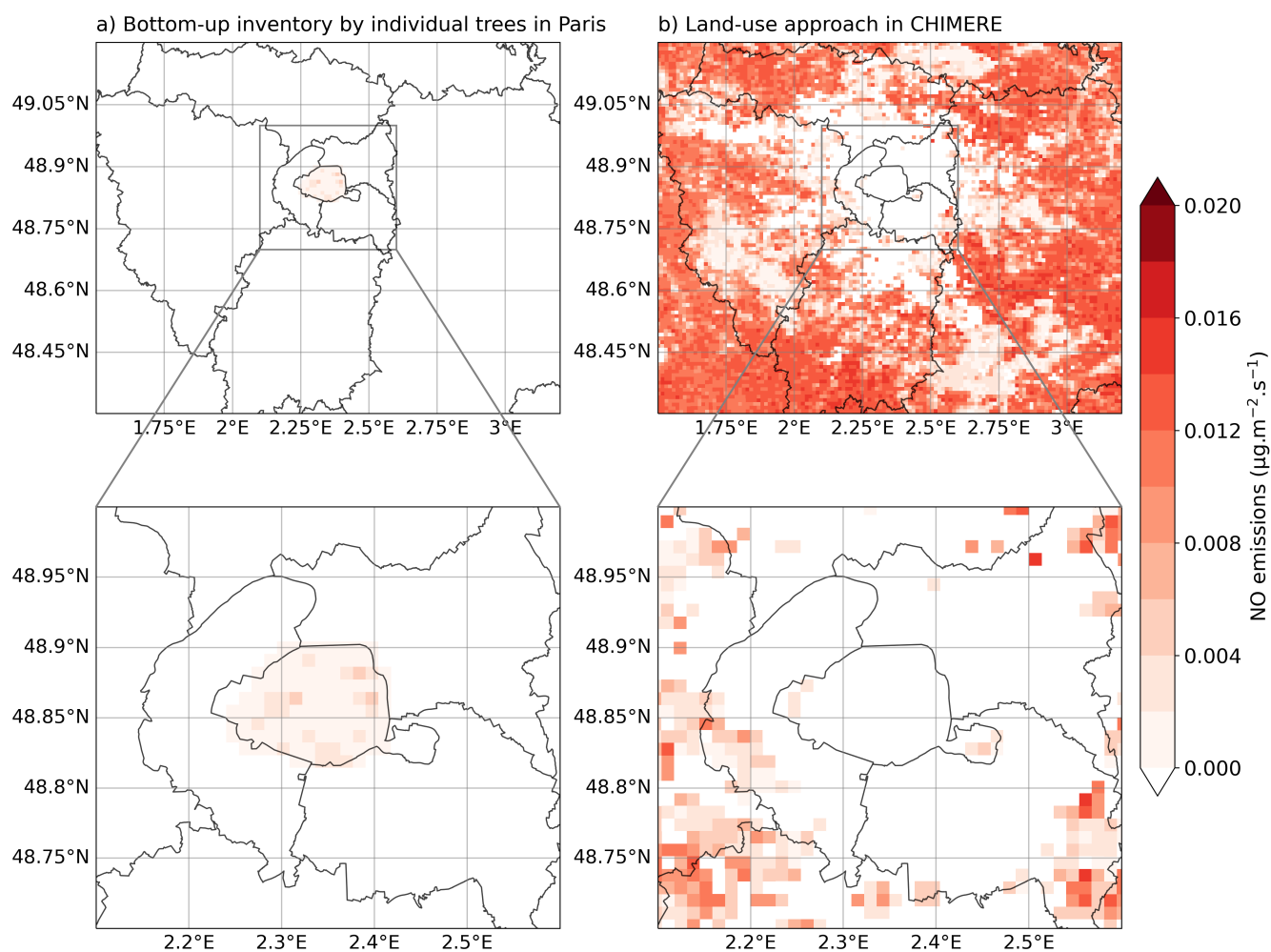


Figure C4. Comparison of the 2 months nitrite oxide (NO) emissions computed with (a) the "bottom-up" inventory and (b) with the land-cover approach in CHIMERE over Île-de-France and Greater Paris.

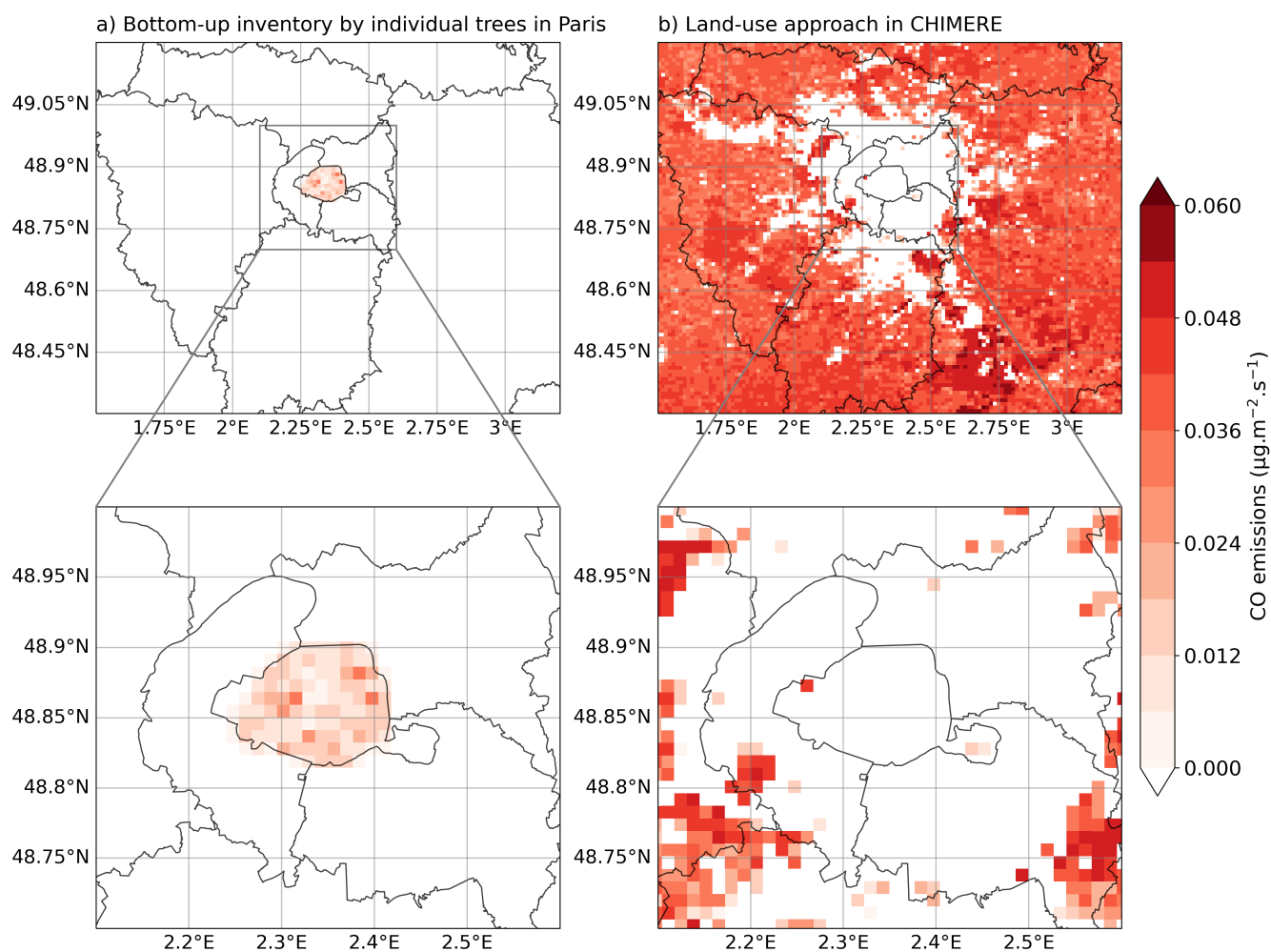


Figure C5. Comparison of the 2 months carbon monoxide (CO) emissions computed with (a) the "bottom-up" inventory and (b) with the land-cover approach in CHIMERE over Île-de-France and Greater Paris.

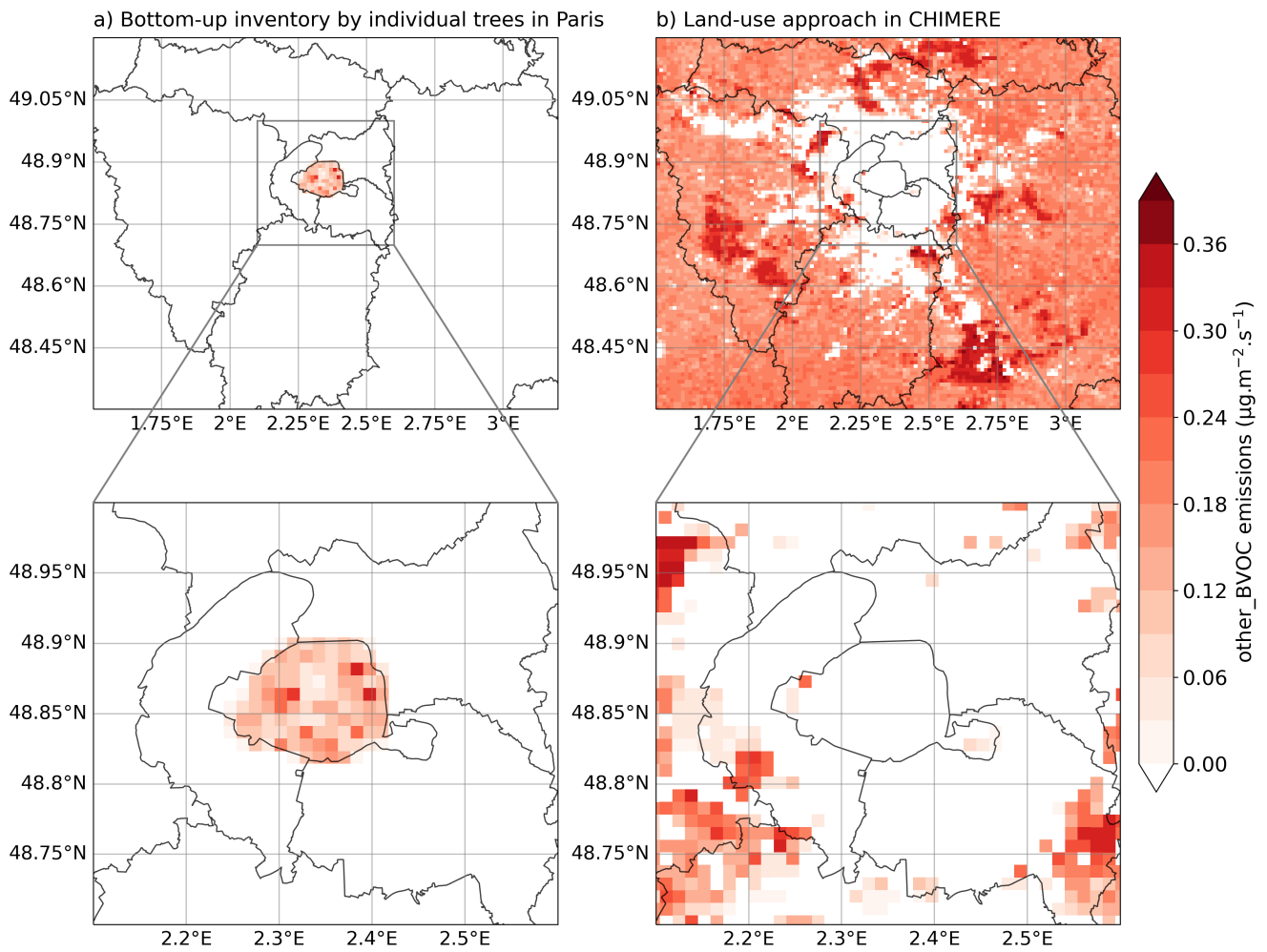


Figure C6. Comparison of the 2 months other VOC (OVOC) emissions computed with (a) the "bottom-up" inventory and (b) with the land-cover approach in CHIMERE over Île-de-France and Greater Paris.

Appendix D: Definition of the statistical indicators

To compare the simulation results to measured data, classical statistical indicators are computed where obs_i and sim_i are respectively the observed and simulated hourly concentrations. n is the total number of concentrations and \overline{obs} and \overline{sim} are the average observed and simulated concentrations.

- Root Mean Square Error (same unit as the concentration):

$$RMSE = \sqrt{\frac{1}{n} \sum_{i=1}^n (obs_i - sim_i)^2}. \quad (D1)$$

- Normalized Mean Square Error (dimensionless):

$$NMSE = \frac{\sum_{i=1}^n (obs_i - sim_i)^2}{\sum_{i=1}^n obs_i \times \sum_{i=1}^n sim_i}. \quad (D2)$$

- Normalized Absolute Difference (dimensionless):

$$NAD = \frac{\sum_{i=1}^n |obs_i - sim_i|}{\sum_{i=1}^n obs_i + \sum_{i=1}^n sim_i}. \quad (D3)$$

- Mean Fractional Error (dimensionless):

$$MFE = \frac{1}{n} \sum_{i=1}^n \frac{|sim_i - obs_i|}{obs_i}. \quad (D4)$$

- Mean Fractional Bias (same unit as the concentration):

$$MFB = \frac{1}{n} \sum_{i=1}^n |sim_i - obs_i|. \quad (D5)$$

- Bias (same unit as the concentration):

$$Bias = \frac{1}{n} \sum_{i=1}^n (sim_i - obs_i). \quad (D6)$$

- Fractional Bias (dimensionless):

$$FB = 2 \times \frac{\sum_{i=1}^n sim_i - \sum_{i=1}^n obs_i}{\sum_{i=1}^n obs_i + \sum_{i=1}^n sim_i}. \quad (D7)$$

- Geometric Mean Bias (dimensionless):

$$MG = \exp \left[\frac{1}{n} \sum_{i=1}^n \ln(sim_i) - \frac{1}{n} \sum_{i=1}^n \ln(obs_i) \right] \quad (D8)$$

- Correlation coefficient (dimensionless):

$$R = \frac{\sum_{i=1}^n [(sim_i - \overline{sim})(obs_i - \overline{obs})]}{\sqrt{\sum_{i=1}^n (sim_i - \overline{sim})^2 \sum_{i=1}^n (obs_i - \overline{obs})^2}}. \quad (D9)$$

- Geometric Variance (dimensionless):

$$VG = \exp \left[\frac{1}{n} \sum_{i=1}^n (\ln(obs_i) - \ln(sim_i))^2 \right] \quad (D10)$$

- Factor of 2 (dimensionless):

$$FAC2 = \text{total fraction where } 0.5 < \frac{sim_i}{obs_i} < 2.0 \quad (D11)$$

Author contributions. KS and AM were responsible for the conceptualization. AM, AT and KS developed the tree biogenic emission inventory. LL, SP, KS, FC and MV prepared the input data for the WRF-CHIMERE model and LL performed the simulations. AM, KS, LL and SP performed the formal analysis. KS was responsible for the supervision. JV provided the regional and traffic emission inventory. AM and LL conducted the visualization. The experimental data were provided by AB and JV for the Airparif sites, by AG, CDB, BD, JK, MS, VM and CC for the PRG site and by VG, JEP, CK and LS for the SIRTa site. AM, LL and KS wrote the original draft, and all authors reviewed it. KS and AT were responsible for the funding acquisition related to the modelling study.

Competing interests. At least one of the (co-)authors is a member of the editorial board of Atmospheric Chemistry and Physics, and the authors have no other competing interests to declare.

Acknowledgements. This work benefited from the French state aid managed by the sTREEt ANR project (ANR-19-CE22-0012), and by the ANR under the "Investissements d'avenir" program (ANR-11-IDEX-0004-17-EURE-0006) with support from IPSL/Composair. The measurements at the PRG site have been supported by the ACROSS project. The ACROSS project has received funding from the French National Research Agency (ANR) under the investment program integrated into France 2030, with the reference ANR-17-MPGA-0002, and it was supported by the French National program LEFE (Les Enveloppes Fluides et l'Environnement) of the CNRS/INSU (Centre National de la Recherche Scientifique/Institut National des Sciences de L'Univers). Contributions to measurements at PRG by A. Bauville, M. Cazaunau, L. Hawkins, D. Pronovost, A. Bergé, L. Di Antonio, F. Maisonneuve, C. Gaimoz, and S. Chevallier are gratefully acknowledged.

References

- Angel, S., Parent, J., Civco, D. L., Blei, A., and Potere, D.: The dimensions of global urban expansion: Estimates and projections for all countries, 2000–2050, *Progress in Planning*, 75, 53–107, <https://doi.org/https://doi.org/10.1016/j.progress.2011.04.001>, 2011.
- Appel, K. W., Bash, J. O., Fahey, K. M., Foley, K. M., Gilliam, R. C., Hogrefe, C., Hutzell, W. T., Kang, D., Mathur, R., Murphy, B. N., Napelenok, S. L., Nolte, C. G., Pleim, J. E., Pouliot, G. A., Pye, H. O. T., Ran, L., Roselle, S. J., Sarwar, G., Schwede, D. B., Sidi, F. I., Spero, T. L., and Wong, D. C.: The Community Multiscale Air Quality (CMAQ) model versions 5.3 and 5.3.1: system upyears and evaluation, *Geoscientific Model Development*, 14, 2867–2897, <https://doi.org/10.5194/gmd-14-2867-2021>, 2021.
- Arunachalam, S., Holland, A., Do, B., and Abraczinskas, M.: A quantitative assessment of the influence of grid resolution on predictions of future-year air quality in North Carolina, USA, *Atmospheric Environment*, 40, 5010–5026, <https://doi.org/https://doi.org/10.1016/j.atmosenv.2006.01.024>, 2006.
- Atkinson, R. and Arey, J.: Gas-phase tropospheric chemistry of biogenic volatile organic compounds: a review, *Atmospheric Environment*, 37, 197–219, [https://doi.org/10.1016/S1352-2310\(03\)00391-1](https://doi.org/10.1016/S1352-2310(03)00391-1), 2003a.
- Atkinson, R. and Arey, J.: Atmospheric degradation of volatile organic compounds, *Chemical Reviews*, 103, 4605–4638, <https://doi.org/10.1021/cr0206420>, 2003b.
- Bartelink, H.: Allometric relationships for biomass and leaf area of beech (*Fagus sylvatica* L), *Annales des Sciences Forestières*, 54, 39–50, <https://doi.org/10.1051/forest:19970104>, 1997.
- Baudic, A., Gros, V., Sauvage, S., Locoge, N., Sanchez, O., Sarda-Estève, R., Kalogridis, C., Petit, J.-E., Bonnaire, N., Baisnée, D., Favez, O., Albinet, A., Sciare, J., and Bonsang, B.: Seasonal variability and source apportionment of volatile organic compounds (VOCs) in the Paris megacity (France), *Atmospheric Chemistry and Physics*, 16, 11 961–11 989, <https://doi.org/10.5194/acp-16-11961-2016>, 2016.
- Bennett, S.: OpenTree.org, <https://opentrees.org/>, 2023.
- Bonn, B., Magh, R.-K., Rombach, J., and Kreuzwieser, J.: Biogenic isoprenoid emissions under drought stress: different responses for isoprene and terpenes, *Biogeosciences*, 16, 4627–4645, <https://doi.org/10.5194/bg-16-4627-2019>, 2019.
- Boutahar, J., Lacour, S., Mallet, V., Quelo, D., Roustan, Y., and Sportisse, B.: Development and validation of a fully modular platform for numerical modelling of air pollution: POLAIR, *International Journal of Environment and Pollution*, 22, 17–28, <https://doi.org/10.1504/IJEP.2004.005474>, 2004.
- Burton, A. J., Pregitzer, K. S., and Reed, D. D.: Leaf Area and Foliar Biomass Relationships in Northern Hardwood Forests Located Along an 800 km Acid Deposition Gradient, *Forest Science*, 37, 1041–1059, <https://doi.org/10.1093/forestscience/37.4.1041>, 1991.
- Byun, D. and Schere, K. L.: Review of the Governing Equations, Computational Algorithms, and Other Components of the Models-3 Community Multiscale Air Quality (CMAQ) Modeling System, *Applied Mechanics Reviews*, 59, 51–77, <https://doi.org/10.1115/1.2128636>, 2006.
- C. Minguillón, M., Pérez, N., Marchand, N., Bertrand, A., Temime-Roussel, B., Agrios, K., Szidat, S., Drooge, B. v., Sylvestre, A., Alastuey, A., Reche, C., Ripoll, A., Marco, E., O. Grimalt, J., and Querol, X.: Secondary organic aerosol origin in an urban environment: influence of biogenic and fuel combustion precursors, *Faraday Discussions*, 189, 337–359, <https://doi.org/10.1039/C5FD00182J>, 2016.
- Calfapietra, C.: Role of Biogenic Volatile Organic Compounds (BVOC) emitted by urban trees on ozone concentration in cities: A review, *Environmental Pollution*, p. 10, 2013.

3. BVOC EMISSIONS FROM URBAN TREES AND IMPACT ON REGIONAL AIR QUALITY

- Cantrell, C. and Michoud, V.: An Experiment to Study Atmospheric Oxidation Chemistry and Physics of Mixed Anthropogenic–Biogenic Air Masses in the Greater Paris Area, *Bulletin of the American Meteorological Society*, 103, 599–603, <https://doi.org/https://doi.org/10.1175/BAMS-D-21-0115.1>, 2022.
- Chang, J., Qu, Z., Xu, R., Pan, K., Xu, B., Min, Y., Ren, Y., Yang, G., and Ge, Y.: Assessing the ecosystem services provided by urban green spaces along urban center-edge gradients, *Scientific Reports*, 7, 11 226, <https://doi.org/10.1038/s41598-017-11559-5>, 2017.
- Churkina, G., Kuik, F., Bonn, B., Lauer, A., Grote, R., Tomiak, K., and Butler, T. M.: Effect of VOC Emissions from Vegetation on Air Quality in Berlin during a Heatwave, *Environmental Science & Technology*, 51, 6120–6130, <https://doi.org/10.1021/acs.est.6b06514>, 2017.
- Ciccioli, P., Silibello, C., Finardi, S., Pepe, N., Ciccioli, P., Rapparini, F., Neri, L., Fares, S., Brilli, F., Mircea, M., Magliulo, E., and Baraldi, R.: The potential impact of biogenic volatile organic compounds (BVOCs) from terrestrial vegetation on a Mediterranean area using two different emission models, *Agricultural and Forest Meteorology*, 328, 109 255, <https://doi.org/10.1016/j.agrformet.2022.109255>, 2023.
- CNRM: MOCAGE - Modèle de Chimie Atmosphérique de Grande Echelle, <https://www.umr-cnrm.fr/spip.php?article128>, last access: 2023-06-06, 2023.
- Couvidat, F., Bessagnet, B., Garcia-Vivanco, M., Real, E., Menut, L., , and Colette, A.: Development of an inorganic and organic aerosol model (CHIMERE 2017 β v1.0): seasonal and spatial evaluation over Europe, *Geoscientific Model Development*, pp. 165–194, <https://doi.org/https://doi.org/10.5194/gmd-11-165-2018>, 2018.
- Czaja, M., Kolton, A., and Muras, P.: The Complex Issue of Urban Trees—Stress Factor Accumulation and Ecological Service Possibilities, *Forests*, 11, 932, <https://doi.org/10.3390/f11090932>, 2020.
- Eichler, P., Müller, M., D’Anna, B., and Wisthaler, A.: A novel inlet system for online chemical analysis of semi-volatile submicron particulate matter, *Atmospheric Measurement Techniques*, pp. 1353–1360, <https://doi.org/https://doi.org/10.5194/amt-8-1353-2015>, 2015.
- EMEP: Transboundary particulate matter, photo-oxidants, acidifying and eutrophying components, 2019.
- Escobedo, F. J. and Nowak, D. J.: Spatial heterogeneity and air pollution removal by an urban forest, *Landscape and Urban Planning*, 90, 102–110, <https://doi.org/10.1016/j.landurbplan.2008.10.021>, 2009.
- Fenger, J.: Urban air quality, *Atmospheric Environment*, 33, 4877–4900, [https://doi.org/10.1016/S1352-2310\(99\)00290-3](https://doi.org/10.1016/S1352-2310(99)00290-3), 1999.
- Gros, V., Gaimoz, C., Herrmann, F., Custer, T., Williams, J., Bonsang, B., Sauvage, S., Locoge, N., d’Argouges, O., Sarda-Estève, R., and Sciare, J.: Volatile organic compounds sources in Paris in spring 2007. Part I: qualitative analysis, *Environmental Chemistry*, 8, 74–90, <https://doi.org/10.1071/EN10068>, 2011.
- Guenther, A., Hewitt, C. N., Erickson, D., Fall, R., Geron, C., Graedel, T., Harley, P., Klinger, L., Lerdau, M., McKay, W., Pierce, T., Scholes, B., Steinbrecher, R., Tallamraju, R., Taylor, J., and Zimmerman, P.: A global model of natural volatile organic compound emissions, *Journal of geophysical research*, 100, 8873–8892, <https://doi.org/10.1029/94JD02950>, 1995.
- Guenther, A., Karl, T., Harley, P., Wiedinmyer, C., Palmer, P. I., and Geron, C.: Estimates of global terrestrial isoprene emissions using MEGAN (Model of Emissions of Gases and Aerosols from Nature), *Atmospheric Chemistry and Physics*, p. 30, 2006.
- Guenther, A., Jiang, X., Heald, C. L., Sakulyanontvittaya, T., Duhl, T., Emmons, L. K., and Wang, X.: The Model of Emissions of Gases and Aerosols from Nature version 2.1 (MEGAN2.1): an extended and upyear framework for modeling biogenic emissions, *Geoscientific Model Development*, 5, 1471–1492, <https://doi.org/10.5194/gmd-5-1471-2012>, 2012.
- Haeffelin, M., Barthès, L., Bock, O., Boitel, C., Bony, S., Bouniol, D., Chepfer, H., Chiriaco, M., Cuesta, J., Delanoë, J., Drobinski, P., Dufresne, J.-L., Flamant, C., Grall, M., Hodzic, A., Hourdin, F., Lapouge, F., Lemaître, Y., Mathieu, A., Morille, Y., Naud, C., Noël, V.,

- O'Hirok, W., Pelon, J., Pietras, C., Protat, A., Romand, B., Scialom, G., and Vautard, R.: SIRTa, a ground-based atmospheric observatory for cloud and aerosol research, *Annales Geophysicae*, 23, 253–275, <https://doi.org/10.5194/angeo-23-253-2005>, 2005.
- Hami, A., Abdi, B., Zarehaghi, D., and Maulan, S. B.: Assessing the thermal comfort effects of green spaces: A systematic review of methods, parameters, and plants' attributes, *Sustainable Cities and Society*, 49, 101 634, <https://doi.org/10.1016/j.scs.2019.101634>, 2019.
- Hanna, S. and Chang, J.: Acceptance criteria for urban dispersion model evaluation, *Meteorology and Atmospheric Physics*, 116, 133–146, <https://doi.org/https://doi.org/10.1007/s00703-011-0177-1>, 2012.
- Inness, A., Ades, M., Agustí-Panareda, A., Barré, J., Benedictow, A., Blechschmidt, A.-M., Dominguez, J. J., Engelen, R., Eskes, H., Flemming, J., et al.: The CAMS reanalysis of atmospheric composition, *Atmospheric Chemistry and Physics*, 19, 3515–3556, 2019.
- IPCC: Climate Change 2021: The Physical Science Basis. Contribution of Working Group I to the Sixth Assessment Report of the Intergovernmental Panel on Climate Change, Report, Intergovernmental Panel on Climate Change, United Nations, [Masson-Delmotte V., Zhai P., Pirani A., Connors S.L., Péan C., Berger S., Caud N., Chen Y., Goldfarb L., Gomis M.I., Huang M., Leitzell K., Lonnoy E., Matthews J.B.R., Maycock T.K., Waterfield T., Yelekçi O., Yu R., and Zhou B. (eds.)]. Cambridge University Press. In Press., 2021.
- Jamei, E., Rajagopalan, P., Seyedmahmoudian, M., and Jamei, Y.: Review on the impact of urban geometry and pedestrian level greening on outdoor thermal comfort, *Renewable and Sustainable Energy Reviews*, 54, 1002–1017, <https://doi.org/10.1016/j.rser.2015.10.104>, 2016.
- Jang, J.-C. C., Jeffries, H. E., Byun, D., and Pleim, J. E.: Sensitivity of ozone to model grid resolution—I. Application of high-resolution regional acid deposition model, *Atmospheric Environment*, 29, 3085–3100, [https://doi.org/https://doi.org/10.1016/1352-2310\(95\)00118-I](https://doi.org/https://doi.org/10.1016/1352-2310(95)00118-I), 1995a.
- Jang, J.-C. C., Jeffries, H. E., and Tonnesen, S.: Sensitivity of ozone to model grid resolution — II. Detailed process analysis for ozone chemistry, *Atmospheric Environment*, 29, 3101–3114, [https://doi.org/https://doi.org/10.1016/1352-2310\(95\)00119-J](https://doi.org/https://doi.org/10.1016/1352-2310(95)00119-J), 1995b.
- Jiang, J., Aksoyoglu, S., Ciarelli, G., Oikonomakis, E., El-Haddad, I., Canonaco, F., O'Dowd, C., Ovadnevaite, J., Minguillón, M. C., Baltensperger, U., and Prévôt, A. S. H.: Effects of two different biogenic emission models on modelled ozone and aerosol concentrations in Europe, *Atmospheric Chemistry and Physics*, 19, 3747–3768, <https://doi.org/10.5194/acp-19-3747-2019>, 2019.
- Jiang, X., Guenther, A., Potosnak, M., Geron, C., Seco, R., Karl, T., Kim, S., Gu, L., and Pallardy, S.: Isoprene emission response to drought and the impact on global atmospheric chemistry, *Atmospheric Environment*, 183, 69–83, <https://doi.org/10.1016/j.atmosenv.2018.01.026>, 2018.
- Jo, O., Han, J. Q., Askari, A., Abbatt, J. P. D., and Chan, A. W. H.: Investigation of Anthropogenic Monoterpenes in Canadian Cities, *ACS Earth and Space Chemistry*, <https://doi.org/10.1021/acsearthspacechem.3c00181>, publisher: American Chemical Society, 2023.
- Jordan, A., Haidacher, S., Hanel, G., Hartungen, E., Märk, L., Seehauser, H., Schotchkowsky, R., Sulzer, P., and Märk, T.: A high resolution and high sensitivity proton-transfer-reaction time-of-flight mass spectrometer (PTR-TOF-MS), *International Journal of Mass Spectrometry*, pp. 122–128, <https://doi.org/https://doi.org/10.1016/j.ijms.2009.07.005>, 2009.
- Karl, M., Guenther, A., Koble, R., Leip, A., and Seufert, G.: A new European plant-specific emission inventory of biogenic volatile organic compounds for use in atmospheric transport models, *Biogeosciences*, 6, 1059–1087, <https://doi.org/https://doi.org/10.5194/bg-6-1059-2009>, 2009.
- Karlik, J. F. and McKay, A. H.: Leaf area index, leaf mass density, and allometric relationships derived from harvest of blue oaks in a California oak savanna, In: Standiford, Richard B., et al, tech. editor. *Proceedings of the Fifth Symposium on Oak Woodlands: Oaks in California's Challenging Landscape*. Gen. Tech. Rep. PSW-GTR-184, Albany, CA: Pacific Southwest Research Station, Forest Service, U.S. Department of Agriculture: 719-729, 184, 719–729, <https://www.fs.usda.gov/research/treesearch/26168>, 2002.

- Kesselmeier, J. and Staudt, M.: Biogenic Volatile Organic Compounds (VOC): An Overview on Emission, Physiology and Ecology, *Journal of Atmospheric Chemistry*, 33, 23–88, <https://doi.org/10.1023/A:1006127516791>, 1999.
- Kim, H. H.: Urban heat island, *International Journal of Remote Sensing*, 13, 2319–2336, <https://doi.org/10.1080/01431169208904271>, 1992.
- Kusaka, H., Kondo, H., Kikegawa, Y., and Kimura, F.: A simple single-layer urban canopy model for atmospheric models: Comparison with multi-layer and slab models, *Boundary-layer meteorology*, 101, 329–358, 2001.
- Kuttler, W.: The Urban Climate – Basic and Applied Aspects, in: *Urban Ecology: An International Perspective on the Interaction Between Humans and Nature*, edited by Marzluff, J. M., Shulenberg, E., Endlicher, W., Alberti, M., Bradley, G., Ryan, C., Simon, U., and ZumBrunnen, C., pp. 233–248, Springer US, https://doi.org/10.1007/978-0-387-73412-5_13, 2008.
- Lai, D., Liu, W., Gan, T., Liu, K., and Chen, Q.: A review of mitigating strategies to improve the thermal environment and thermal comfort in urban outdoor spaces, *Science of The Total Environment*, 661, 337–353, <https://doi.org/10.1016/j.scitotenv.2019.01.062>, 2019.
- LCSQA: Guide méthodologique pour le calcul des statistiques relatives à la qualité de l'air, Tech. rep., Laboratoire Central de Surveillance de la Qualité de l'Air, https://www.lcsqa.org/system/files/media/documents/lcsqa2016-guide_calcul_statistiques_qa-drc-16-159667-08455a.pdf, 2016.
- Leglise, J., Müller, M., Piel, F., Otto, T., and Wisthaler, A.: Bulk Organic Aerosol Analysis by Proton-Transfer-Reaction Mass Spectrometry: An Improved Methodology for the Determination of Total Organic Mass, O:C and H:C Elemental Ratios, and the Average Molecular Formula, *Anal. Chem.*, pp. 12 619–12 624, <https://doi.org/https://doi.org/10.1021/acs.analchem.9b02949>, 2019.
- Lehtipalo, K., Yan, C., Dada, L., Bianchi, F., Xiao, M., Wagner, R., Stolzenburg, D., Ahonen, L. R., Amorim, A., Baccharini, A., Bauer, P. S., Baumgartner, B., Bergen, A., Bernhammer, A.-K., Breitenlechner, M., Brilke, S., Buchholz, A., Mazon, S. B., Chen, D., Chen, X., Dias, A., Dommen, J., Draper, D. C., Duplissy, J., Ehn, M., Finkenzeller, H., Fischer, L., Frege, C., Fuchs, C., Garmash, O., Gordon, H., Hakala, J., He, X., Heikkinen, L., Heinritzi, M., Helm, J. C., Hofbauer, V., Hoyle, C. R., Jokinen, T., Kangasluoma, J., Kerminen, V.-M., Kim, C., Kirkby, J., Kontkanen, J., Kürten, A., Lawler, M. J., Mai, H., Mathot, S., Mauldin, R. L., Molteni, U., Nichman, L., Nie, W., Nieminen, T., Ojdanic, A., Onnela, A., Passananti, M., Petäjä, T., Piel, F., Pospisilova, V., Quéléver, L. L. J., Rissanen, M. P., Rose, C., Sarnela, N., Schallhart, S., Schuchmann, S., Sengupta, K., Simon, M., Sipilä, M., Tauber, C., Tomé, A., Tröstl, J., Väisänen, O., Vogel, A. L., Volkamer, R., Wagner, A. C., Wang, M., Weitz, L., Wimmer, D., Ye, P., Ylisirniö, A., Zha, Q., Carslaw, K. S., Curtius, J., Donahue, N. M., Flagan, R. C., Hansel, A., Riipinen, I., Virtanen, A., Winkler, P. M., Baltensperger, U., Kulmala, M., and Worsnop, D. R.: Multicomponent new particle formation from sulfuric acid, ammonia, and biogenic vapors, *Science Advances*, 4, eaau5363, <https://doi.org/10.1126/sciadv.aau5363>, 2018.
- Li, C., Wang, Z., Li, B., Peng, Z.-R., and Fu, Q.: Investigating the relationship between air pollution variation and urban form, *Building and Environment*, 147, 559–568, <https://doi.org/10.1016/j.buildenv.2018.06.038>, 2019.
- Liang, J. and Jacobson, M. Z.: Effects of subgrid segregation on ozone production efficiency in a chemical model, *Atmospheric Environment*, 34, 2975–2982, [https://doi.org/https://doi.org/10.1016/S1352-2310\(99\)00520-8](https://doi.org/https://doi.org/10.1016/S1352-2310(99)00520-8), 2000.
- Lindén, J., Gustafsson, M., Uddling, J., Watne, A., and Pleijel, H.: Air pollution removal through deposition on urban vegetation: The importance of vegetation characteristics, *Urban Forestry & Urban Greening*, 81, 127 843, <https://doi.org/10.1016/j.ufug.2023.127843>, 2023.
- Livesley, S. J., McPherson, E. G., and Calfapietra, C.: The Urban Forest and Ecosystem Services: Impacts on Urban Water, Heat, and Pollution Cycles at the Tree, Street, and City Scale, *Journal of Environmental Quality*, 45, 119–124, <https://doi.org/10.2134/jeq2015.11.0567>, 2016.

3. BVOC EMISSIONS FROM URBAN TREES AND IMPACT ON REGIONAL AIR QUALITY

- Loreto, F.: Distribution of isoprenoid emitters in the *Quercus* genus around the world: chemo-taxonomical implications and evolutionary considerations based on the ecological function of the trait, *Perspectives in Plant Ecology, Evolution and Systematics*, 5, 185–192, <https://doi.org/10.1078/1433-8319-00033>, 2002.
- Loreto, F. and Schnitzler, J.-P.: Abiotic stresses and induced BVOCs, *Trends in Plant Science*, 15, 154–166, <https://doi.org/10.1016/j.tplants.2009.12.006>, 2010.
- Lyons, T., Kenworthy, J., and Newman, P.: Urban structure and air pollution, *Atmospheric Environment. Part B. Urban Atmosphere*, 24, 43–48, [https://doi.org/10.1016/0957-1272\(90\)90008-I](https://doi.org/10.1016/0957-1272(90)90008-I), 1990.
- Lüttge, U. and Buckeridge, M.: Trees: structure and function and the challenges of urbanization, *Trees*, 37, 9–16, <https://doi.org/10.1007/s00468-020-01964-1>, 2023.
- Mailler, S., Menut, L., Khvorostyanov, D., Valari, M., Couvidat, F., Siour, G., Turquety, S., Briant, R., Tuccella, P., Bessagnet, B., Colette, A., Létinois, L., Markakis, K., and Meleux, F.: CHIMERE-2017: from urban to hemispheric chemistry-transport modeling, *Geoscientific Model Development*, 10, 2397–2423, <https://doi.org/10.5194/gmd-10-2397-2017>, 2017.
- Masson, V., Lemonsu, A., Hidalgo, J., and Voogt, J.: Urban Climates and Climate Change, *Annual Review of Environment and Resources*, 45, 411–444, <https://doi.org/10.1146/annurev-environ-012320-083623>, 2020.
- Matthias, V., Arndt, J. A., Aulinger, A., Bieser, J., Denier van der Gon, H., Kranenburg, R., Kuenen, J., Neumann, D., Pouliot, G., and Quante, M.: Modeling emissions for three-dimensional atmospheric chemistry transport models, *Journal of the Air & Waste Management Association*, 68, 763–800, <https://doi.org/10.1080/10962247.2018.1424057>, 2018.
- McPherson, E. G., van Doorn, N. S., and Peper, P. J.: Urban tree database and allometric equations, Tech. Rep. PSW-GTR-253, U.S. Department of Agriculture, Forest Service, Pacific Southwest Research Station, <https://doi.org/10.2737/PSW-GTR-253>, 2016.
- Meek, D. W., Hatfield, J. L., Howell, T. A., Idso, S. B., and Reginato, R. J.: A Generalized Relationship between Photosynthetically Active Radiation and Solar Radiation¹, *Agronomy Journal*, 76, 939–945, <https://doi.org/10.2134/agronj1984.00021962007600060018x>, 1984.
- Menut, L., Bessagnet, B., Briant, R., Cholakian, A., Couvidat, F., Mailler, S., Pennel, R., Siour, G., Tuccella, P., Turquety, S., and Valari, M.: The CHIMERE v2020r1 online chemistry-transport model, *Geoscientific Model Development*, 14, 6781–6811, <https://doi.org/10.5194/gmd-14-6781-2021>, 2021.
- Menut, L., Cholakian, A., Siour, G., Lapere, R., Pennel, R., Mailler, S., and Bessagnet, B.: Impact of Landes forest fires on air quality in France during the 2022 summer, *Atmospheric Chemistry and Physics*, 23, 7281–7296, <https://doi.org/10.5194/acp-23-7281-2023>, 2023.
- Meteo France: Bilan climatique de l'année 2022, *in french*, https://meteofrance.fr/sites/meteofrance.fr/files/files/editorial/Bilan_climatique_definitif_2022_130123.pdf, 2023.
- Mircea, M., Borge, R., Finardi, S., Briganti, G., Russo, F., de la Paz, D., D'Isidoro, M., Cremona, G., Villani, M. G., Cappelletti, A., Adani, M., D'Elia, I., Piersanti, A., Sorrentino, B., Petralia, E., de Andrés, J. M., Narros, A., Silibello, C., Pepe, N., Prandi, R., and Carlino, G.: The Role of Vegetation on Urban Atmosphere of Three European Cities. Part 2: Evaluation of Vegetation Impact on Air Pollutant Concentrations and Depositions, *Forests*, 14, 1255, <https://doi.org/10.3390/f14061255>, 2023.
- Municipality of Paris: Paris Data : Les arbres, <https://opendata.paris.fr/explore/dataset/les-arbres/>, accessed: 2023-03-03, 2023.
- Müller, M., Eichler, P., D'Anna, B., Tan, W., and Wisthaler, A.: Direct Sampling and Analysis of Atmospheric Particulate Organic Matter by Proton-Transfer-Reaction Mass Spectrometry, *Anal. Chem.*, pp. 10 889–10 897, <https://doi.org/https://doi.org/10.1021/acs.analchem.7b02582>, 2017.
- Nasrollahi, N., Ghosouri, A., Khodakarami, J., and Taleghani, M.: Heat-Mitigation Strategies to Improve Pedestrian Thermal Comfort in Urban Environments: A Review, *Sustainability*, 12, 10 000, <https://doi.org/10.3390/su122310000>, 2020.

3. BVOC EMISSIONS FROM URBAN TREES AND IMPACT ON REGIONAL AIR QUALITY

- Nemitz, E., Vieno, M., Carnell, E., Fitch, A., Steadman, C., Cryle, P., Holland, M., Morton, R. D., Hall, J., Mills, G., Hayes, F., Dickie, I., Carruthers, D., Fowler, D., Reis, S., and Jones, L.: Potential and limitation of air pollution mitigation by vegetation and uncertainties of deposition-based evaluations, *Philosophical Transactions of the Royal Society A: Mathematical, Physical and Engineering Sciences*, 378, 20190 320, <https://doi.org/10.1098/rsta.2019.0320>, 2020.
- Niinemets, U.: Mild versus severe stress and BVOCs: thresholds, priming and consequences, *Trends in Plant Science*, 15, 145–153, <https://doi.org/10.1016/j.tplants.2009.11.008>, 2010.
- Niinemets, U., Loreto, F., and Reichstein, M.: Physiological and physicochemical controls on foliar volatile organic compound emissions, *Trends in Plant Science*, 9, 180–186, <https://doi.org/10.1016/j.tplants.2004.02.006>, 2004.
- NOAA/ESRL: WRF-Chem - Weather Research and Forecasting model coupled to Chemistry, <https://ruc.noaa.gov/wrf/wrf-chem/>, last access: 2023-06-06, 2023.
- Nowak, D. J.: Estimating Leaf Area and Leaf Biomass of Open-Grown Deciduous Urban Trees, *Forest Science*, 42, 504–507, <https://doi.org/10.1093/forestscience/42.4.504>, 1996.
- Nowak, D. J., Crane, D. E., and Stevens, J. C.: Air pollution removal by urban trees and shrubs in the United States, *Urban Forestry & Urban Greening*, 4, 115–123, <https://doi.org/10.1016/j.ufug.2006.01.007>, 2006.
- Oke, T. R.: The energetic basis of the urban heat island, *Quarterly Journal of the Royal Meteorological Society*, 108, 1–24, <https://doi.org/10.1002/qj.49710845502>, 1982.
- Oke, T. R., Mills, G., Christen, A., and Voogt, J. A.: *Urban Climates*, Cambridge University Press, 2017.
- Otu-Larbi, F., Bolas, C. G., Ferracci, V., Staniaszek, Z., Jones, R. L., Malhi, Y., Harris, N. R. P., Wild, O., and Ashworth, K.: Modelling the effect of the 2018 summer heatwave and drought on isoprene emissions in a UK woodland, *Global Change Biology*, 26, 2320–2335, <https://doi.org/10.1111/gcb.14963>, 2020.
- Owen, S. M., Boissard, C., and Hewitt, C. N.: Volatile organic compounds (VOCs) emitted from 40 Mediterranean plant species: VOC speciation and extrapolation to habitat scale, *Atmospheric Environment*, 35, 5393–5409, [https://doi.org/10.1016/S1352-2310\(01\)00302-8](https://doi.org/10.1016/S1352-2310(01)00302-8), 2001.
- Owen, S. M., MacKenzie, A. R., Stewart, H., Donovan, R., and Hewitt, C. N.: BIOGENIC VOLATILE ORGANIC COMPOUND (VOC) EMISSION ESTIMATES FROM AN URBAN TREE CANOPY, *Ecological Applications*, 13, 927–938, <https://doi.org/10.1890/01-5177>, 2003.
- Petit, J.-E., Favez, O., Sciare, J., Crenn, V., Sarda-Estève, R., Bonnaire, N., Močnik, G., Dupont, J.-C., Haeffelin, M., and Leoz-Garziandia, E.: Two years of near real-time chemical composition of submicron aerosols in the region of Paris using an Aerosol Chemical Speciation Monitor (ACSM) and a multi-wavelength Aethalometer, *Atmospheric Chemistry and Physics*, 15, 2985–3005, <https://doi.org/10.5194/acp-15-2985-2015>, 2015.
- Pigeon, G., Legain, D., Durand, P., and Masson, V.: Anthropogenic heat release in an old European agglomeration (Toulouse, France), *International Journal of Climatology*, 27, 1969–1981, <https://doi.org/10.1002/joc.1530>, 2007a.
- Pigeon, G., Legain, D., Durand, P., and Masson, V.: Anthropogenic heat release in an old European agglomeration (Toulouse, France), *International Journal of Climatology: A Journal of the Royal Meteorological Society*, 27, 1969–1981, 2007b.
- Powers, J. G., Klemp, J. B., Skamarock, W. C., Davis, C. A., Dudhia, J., Gill, D. O., Coen, J. L., Gochis, D. J., Ahmadov, R., Peckham, S. E., et al.: The weather research and forecasting model: Overview, system efforts, and future directions, *Bull. Am. Meteorol. Soc.*, 98, 1717–1737, 2017.

3. BVOC EMISSIONS FROM URBAN TREES AND IMPACT ON REGIONAL AIR QUALITY

- Roeland, S., Moretti, M., Amorim, J. H., Branquinho, C., Fares, S., Morelli, F., Niinemets, U., Paoletti, E., Pinho, P., Sgrigna, G., Stojanovski, V., Tiwary, A., Sicard, P., and Calfapietra, C.: Towards an integrative approach to evaluate the environmental ecosystem services provided by urban forest, *Journal of Forestry Research*, 30, 1981–1996, <https://doi.org/10.1007/s11676-019-00916-x>, 2019.
- Sailor, D. J., Georgescu, M., Milne, J. M., and Hart, M. A.: Development of a national anthropogenic heating database with an extrapolation for international cities, *Atmospheric Environment*, 118, 7–18, 2015.
- Salvador, C. M., Chou, C. C.-K., Ho, T.-T., Tsai, C.-Y., Tsao, T.-M., Tsai, M.-J., and Su, T.-C.: Contribution of Terpenes to Ozone Formation and Secondary Organic Aerosols in a Subtropical Forest Impacted by Urban Pollution, *Atmosphere*, 11, 1232, <https://doi.org/10.3390/atmos11111232>, 2020.
- Sartelet, K., Couvidat, F., Wang, Z., Flageul, C., and Kim, Y.: SSH-Aerosol v1.1: A Modular Box Model to Simulate the Evolution of Primary and Secondary Aerosols, *Atmosphere*, 11, 525, <https://doi.org/10.3390/atmos11050525>, 2020.
- Selmi, W., Weber, C., Rivière, E., Blond, N., Mehdi, L., and Nowak, D.: Air pollution removal by trees in public green spaces in Strasbourg city, France, *Urban Forestry & Urban Greening*, 17, 192–201, <https://doi.org/10.1016/j.ufug.2016.04.010>, 2016.
- Setälä, H., Viippola, V., Rantalainen, A.-L., Pennanen, A., and Yli-Pelkonen, V.: Does urban vegetation mitigate air pollution in northern conditions?, *Environmental Pollution*, 183, 104–112, <https://doi.org/10.1016/j.envpol.2012.11.010>, 2013.
- Simon, L., Gros, V., Petit, J.-E., Truong, F., Sarda-Estève, R., Kalalian, C., Baudic, A., Marchand, C., and Favez, O.: Two years of volatile organic compound online in situ measurements at the Site Instrumental de Recherche par Télédétection Atmosphérique (Paris region, France) using proton-transfer-reaction mass spectrometry, *Earth System Science Data*, 15, 1947–1968, <https://doi.org/10.5194/essd-15-1947-2023>, 2023.
- Steinbrecher, R., Smiatek, G., Köble, R., Seufert, G., Theloke, J., Hauff, K., Ciccioli, P., Vautard, R., and Curci, G.: Intra- and inter-annual variability of VOC emissions from natural and semi-natural vegetation in Europe and neighbouring countries, *Atmospheric Environment*, 43, 1380–1391, <https://doi.org/10.1016/j.atmosenv.2008.09.072>, 2009.
- Stewart, H. E., Hewitt, C. N., Bunce, R. G. H., Steinbrecher, R., Smiatek, G., and Schoenemeyer, T.: A highly spatially and temporally resolved inventory for biogenic isoprene and monoterpene emissions: Model description and application to Great Britain, *Journal of Geophysical Research: Atmospheres*, 108, <https://doi.org/10.1029/2002JD002694>, 2003.
- Taha, H.: Urban climates and heat islands: albedo, evapotranspiration, and anthropogenic heat, *Energy and Buildings*, 25, 99–103, [https://doi.org/10.1016/S0378-7788\(96\)00999-1](https://doi.org/10.1016/S0378-7788(96)00999-1), 1997.
- Taha, H., Akbari, H., Rosenfeld, A., and Huang, J.: Residential cooling loads and the urban heat island—the effects of albedo, *Building and Environment*, 23, 271–283, [https://doi.org/10.1016/0360-1323\(88\)90033-9](https://doi.org/10.1016/0360-1323(88)90033-9), 1988.
- Taleghani, M.: Outdoor thermal comfort by different heat mitigation strategies- A review, *Renewable and Sustainable Energy Reviews*, 81, 2011–2018, <https://doi.org/10.1016/j.rser.2017.06.010>, 2018.
- Team, U., Bontemps, S., Defourny, P., Van Bogaert, E., Team, E., Arino, O., Kalogirou, V., and Perez, J. R.: GLOBCOVER 2009 Products Description and Validation Report, 2011.
- Theloke, J. and Friedrich, R.: Compilation of a database on the composition of anthropogenic VOC emissions for atmospheric modeling in Europe, *Atmospheric Environment*, 41, 4148–4160, <https://doi.org/https://doi.org/10.1016/j.atmosenv.2006.12.026>, 2007.
- Thunis, P.: On the validity of the incremental approach to estimate the impact of cities on air quality, *Atmospheric Environment*, 173, 210–222, <https://doi.org/10.1016/j.atmosenv.2017.11.012>, 2018.
- United Nations: World Urbanization Prospects The 2018 Revision, Tech. rep., Department of Economics and Social Affairs, <https://population.un.org/wup/Publications/Files/WUP2018-Report.pdf>, 2018.

3. BVOC EMISSIONS FROM URBAN TREES AND IMPACT ON REGIONAL AIR QUALITY

Wang, H., Lu, X., Seco, R., Stavrakou, T., Karl, T., Jiang, X., Gu, L., and Guenther, A. B.: Modeling Isoprene Emission Response to Drought and Heatwaves Within MEGAN Using Evapotranspiration Data and by Coupling With the Community Land Model, *Journal of Advances in Modeling Earth Systems*, 14, <https://doi.org/10.1029/2022MS003174>, 2022.

Yang, J., Shi, B., Shi, Y., Marvin, S., Zheng, Y., and Xia, G.: Air pollution dispersal in high density urban areas: Research on the triadic relation of wind, air pollution, and urban form, *Sustainable Cities and Society*, 54, 101941, <https://doi.org/10.1016/j.scs.2019.101941>, 2020.

Chapter 4

Quantifying the effects of trees on air quality at the street and city scales

Contents

4.1	Introduction	130
4.2	Materials and Methods	131
4.2.1	Description of the reference simulation	131
4.2.2	Integration of the tree effects in MUNICH	133
4.2.3	Simulation set-up	141
4.3	Results and discussion	142
4.3.1	Reference simulation	142
4.3.2	Tree effects on isoprene and monoterpene concentrations	143
4.3.3	Tree effects on NO ₂ and O ₃ concentrations	151
4.3.4	Tree effects on particle concentrations	157
4.4	Conclusion	164
4.A	List of measurement stations	166
4.B	Computation of the dry deposition of gas and aerosols on street and leaf surfaces	167
4.B.1	Dry deposition of gaseous species	167
4.B.2	Dry deposition of aerosols	171
4.B.3	Computation of the surface friction velocity	173
4.C	Impact on tree aerodynamical effect on isoprene and monoterpene emissions in the street	174
4.D	Definition of the statistical indicators	175

Trees impact air quality at the street level through three main processes: the limitation of the dispersion of pollutants emitted in the street due to the tree aerodynamic effect, the removal of pollutants by dry deposition on tree surfaces, and the emissions of BVOCs, which impact atmospheric chemistry. The effect of BVOC emissions at the regional scale was discussed in the previous chapter. This chapter aims to quantify the impact of each tree effect, as well as the global impact of the combined effects. The modeling chain CHIMERE/MUNICH is used to quantify these effects by performing simulations over Paris and June and July 2022.

4.1 Introduction

Trees in urban environments provide numerous benefits to overcome the side effects of urbanization (Livesley et al., 2016; Roeland et al., 2019). The city energy and water budgets are strongly modified by the presence of artificial materials and high buildings and the release of anthropogenic heat. These processes induce an increase in temperatures compared to the country side, called the urban heat island effect (UHI) (Nunez and Oke, 1977; Taha, 1997; Arnfield, 2003; Kuttler, 2008a; Oke et al., 2017; Masson et al., 2020). Urban air quality is also often deteriorated due to reduced air flows and high local emissions (Lyons et al., 1990; Fenger, 1999; Yang et al., 2020b). By creating shade and transpiring, trees improve human thermal comfort and limit the UHI effect (Taleghani, 2018; Hami et al., 2019). They also preserve permeable soils in which runoff water can infiltrate (Livesley et al., 2016; Berland, 2017). While the effects of trees on climate are widely studied in scientific research and known to the general public, the effects on the urban air quality are much less well known. Trees are often promoted for their capacity to remove pollutant from the atmosphere by dry deposition (Nowak et al., 2006; Escobedo and Nowak, 2009; Setälä et al., 2013; Selmi et al., 2016; Xing and Brimblecombe, 2019; Nemitz et al., 2020; Lindén et al., 2023). However, other direct effects are rather negative for air quality. In the street, the tree crowns strongly modify air flows and limit the dispersion of pollutants emitted by traffic (Gromke and Ruck, 2007; Vos et al., 2013; Jeanjean et al., 2016). Trees naturally emit Biogenic Organic Volatile Compounds (BVOCs) that react with the other compounds of the urban atmosphere to form secondary pollutants such as ozone and secondary organic aerosols (SOAs) (Owen et al., 2003; Calfapietra et al., 2013; Ren et al., 2017). In temperate cities, these effects are mainly present during the vegetative period when trees have leaves. The effect of BVOC emissions, which increases with temperature and light, is expected to be higher in summer and especially during heatwave periods (Niinemets et al., 2004). To estimate the magnitude of these processes, models are useful tools, in particular because they can represent the city heterogeneity, and sensitivity scenarios can be performed to estimate the relative strength of the different tree effects. Computational Fluid Dynamics (CFD) codes are frequently used to study the tree effects on air flows and pollutant concentrations but their fine resolution (~ 1 m) requires high computational resources, limiting the study area to a street or neighborhood and the consideration of complex chemistry (Buccolieri et al., 2011; Santiago et al., 2017a; Gromke and Blocken, 2015). To model air quality at the street scale but over large areas such as cities, parameterized street-network models are developed such as SIRANE (Soulhac et al., 2011, 2012, 2017), the Model of Urban Network of Intersecting Canyons and Highways (MUNICH) (Kim et al., 2018, 2022), OSPM (Berkowicz, 2000) or ADMS-Urban (McHugh et al., 1997; Carruthers et al., 2000; Stocker et al., 2012). They are fast-running codes because air flows are parameterized and streets are considered as an homogeneous volume or are divided into no more than 3-4 zones. The aerodynamic effect of trees in street canyons has been developed in the street-network model MUNICH based on CFD simulations in the Chapter 2 (Maison et al., 2022a,b). It is coupled to the regional-scale chemistry transport model CHIMERE, with an eulerian approach, allowing to fully represent the formation of secondary pollutants from the regional down to the street scale. To estimate the urban tree effects on air quality in Paris, a city tree inventory, which includes tree locations and characteristics, is used.

The objective of the present study is to estimate the impacts of each tree process (aerodynamic effect, dry deposition on leaves, biogenic emissions) on gas and aerosol concentrations separately and combined in the city of Paris. The city of Paris is a relevant place to study because it is dense,

sprawling and regularly subject to air-quality issues. Paris is also rather well vegetated, with more than 200,000 trees in the streets and green spaces and more than 300,000 trees in the Boulogne and Vincennes woods (<https://www.paris.fr/pages/1-arbre-a-paris-199>).

First, Section 4.2 presents the materials and methods. The modeling chain set-up including the input data, and the reference simulation performed without tree are presented in Section 4.2.1. Section 4.2.2 describes the integration of the tree effects in the modeling chain. The tree inventory of the Municipality of Paris ([Municipality of Paris, 2023](#)) is used to integrate trees in the Paris street network and is combined with allometric equations to estimate tree characteristics (leaf area, dry biomass, tree dimension). The parameterization of the tree aerodynamic effect, previously developed, is applied to the whole city of Paris. Dry deposition of gas and aerosols on both street and tree leaf surfaces is computed based on parameterizations of the literature. Biogenic emissions are estimated from the calculated leaf dry biomass of each individual tree, the tree-species dependent emission factors available in the Model of Emissions of Gases and Aerosols from Nature, MEGANv3.2, and the activity factors of [Guenther et al. \(1995, 2012\)](#) which depends on meteorological conditions. CHIMERE/MUNICH simulations are performed over Paris region and the Paris street network for June and July 2022 with the different tree effects added individually and combined. The impacts on isoprene (C_5H_8), monoterpene, nitrogen dioxide (NO_2), ozone (O_3), organic matter (OM) and particulate matter ($PM_{2.5}$) concentrations are presented in Section 4.3.

4.2 Materials and Methods

4.2.1 Description of the reference simulation

4.2.1.1 Presentation of the modeling chain CHIMERE/MUNICH

The Chemistry-Transport Model (CTM) CHIMERE is used to estimate the urban background concentrations ([Menut et al., 2021](#)). It is coupled to the gas-phase mechanism MELCHIOR2, to the aerosol model SSH-aerosol ([Sartelet et al., 2020](#)), and to the meteorological model WRF, where a one-layer urban canopy model is used, with a prescribed anthropogenic heat flux (see previous chapter).

As presented in the Chapter 2, MUNICH is a street-network model that simulates with an eulerian approach, gas and particle concentrations at the street level ([Kim et al., 2022](#)). To be able to simulate concentrations at the street level and over large areas such as cities, each street is considered as an homogeneous volume. So within a street segment, buildings have the same height (H), and the street width (W) is taken as constant. Streets can have various lengths (L) and are linked by punctual intersections. MUNICH includes the main processes affecting street concentrations: emission of gas and particles by traffic, horizontal transport by advection between the streets, vertical transport between the street and the background, dry and wet deposition of gas and aerosols, gas chemistry and aerosols dynamics. MUNICH is one-way coupled to the CTM CHIMERE. Both MUNICH and WRF-CHIMERE are eulerian models, and WRF-CHIMERE is used to estimate the boundary conditions of MUNICH, i.e. meteorological fields and background concentrations above the street. As both CHIMERE and MUNICH are eulerian models using the same gas-phase chemistry MELCHIOR2 and aerosol model SSH-aerosol, primary and secondary pollutant concentrations are represented consistently from street to regional scale. The input data used in this study are presented in the following sections with a focus on tree characteristics in Section 4.2.2.

4.2.1.2 Paris street network

The Paris street network used in the study is composed of 4655 streets and 3040 intersections. It includes the main streets of the Paris city and the close suburbs, as shown in Fig. 4.1. It has been constructed from the BDTOPO database, available at <https://geoservices.ign.fr/bdtopo> and the opendataparis database available at <https://www.data.gouv.fr/fr/datasets/trottoirs-des-rues-de-paris-prs/> (Lugon et al., 2020). The average building height, street width and lengths are respectively equal to 12.4, 18.2 and 221.4 m. The average street aspect ratio is $H/W = 0.79$. Figure 4.1 shows that this street aspect ratio is rather homogeneous in Paris (between 0.66 and 2), with more opened areas along the Seine river, the ring road and the Vincennes and Boulogne woods. Streets with higher aspect ratio (up to 7.9) can be found in the Défense district.

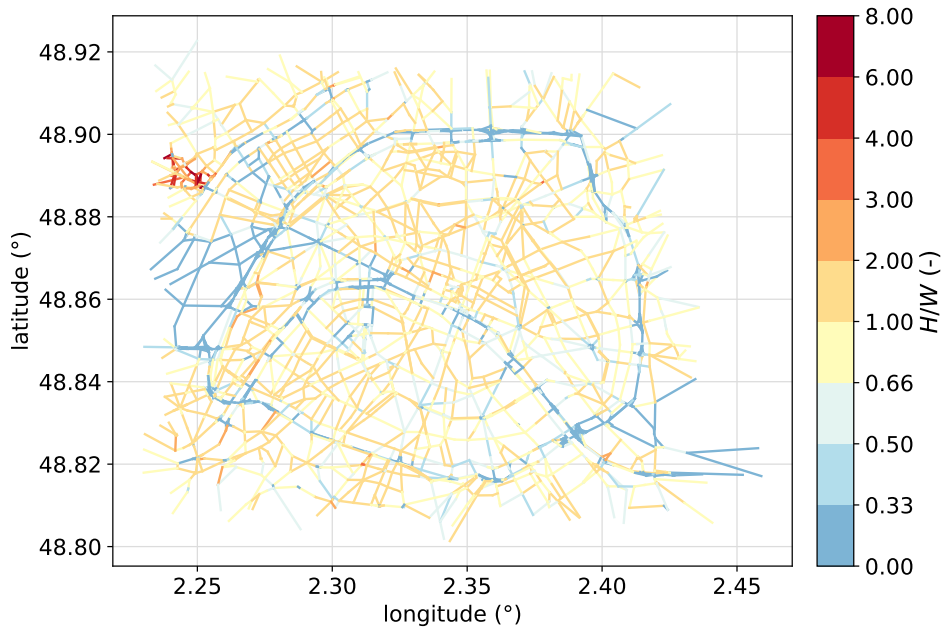


Figure 4.1: Map of the street aspect ratio (H/W) in Paris street network.

4.2.1.3 Anthropogenic and biogenic emissions

Anthropogenic emissions for all activity sectors were provided by the air-quality monitoring association Airparif for the Île de France region. For sectors other than traffic, the inventory represents the year 2019 with a spatial resolution of $1 \text{ km} \times 1 \text{ km}$. For traffic, emissions are those of June and July 2022, they are given by street segment and corrected from traffic counting loops. Biogenic emissions at the regional scale are estimated using MEGANv2.1 in CHIMERE using the land-use approach. At the urban scale in Paris, biogenic emissions are calculated from the tree inventory of the city of Paris, as described in the previous chapter. Special treatments, as detailed below, are necessary to include the trees in the street network used in MUNICH.

4.2.2 Integration of the tree effects in MUNICH

4.2.2.1 Integration of trees in the Paris street network

As presented in Chapter 3, the tree inventory of the municipality of Paris, including tree location, species and dimensions is used. To locate the trees in the street network, streets are considered as rectangles of known four extremity coordinates, and trees are located into the street segments by comparing their coordinates with those of streets. Because of uncertainty about street widths, trees within a perimeter of half of the street width on each side of the street are integrated into the street segment. On the 112,154 roadside trees listed in the Paris tree inventory, 60% are integrated in the MUNICH street network of which 39.5% in the exact street width and 20.5% by widening the street width between 1.2 and $2 \times W$ (Fig. 4.2).

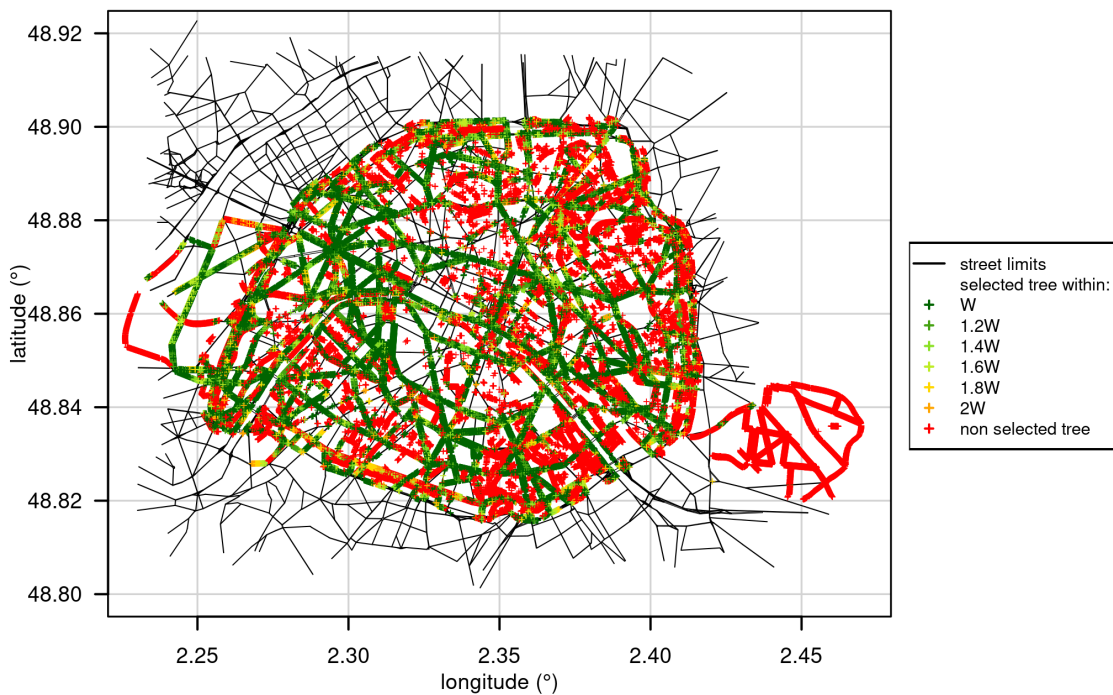


Figure 4.2: Trees integrated in the Paris street network depending on the search street width.

Zooms by districts, as in Fig. 4.3 around the Champs Elysées (a) and the Hôtel de Ville (b), show that the non-integration of some trees into the street network is mainly due to the fact that they are located in secondary streets that are not included in the network, and also because of inaccuracies in the layout and width of streets. Finally, 36.4% of the streets in the network contain at least one tree, a significant effect of trees on concentrations can therefore be expected.

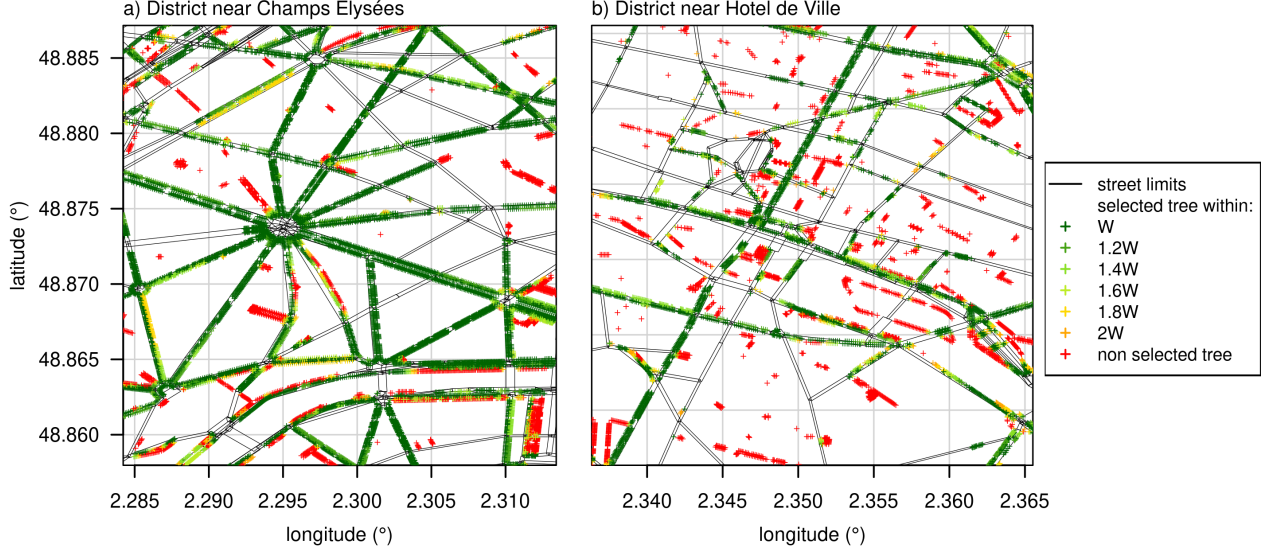


Figure 4.3: Trees integrated in the Paris street network depending on the search street width. Zoom over the a) Champs Elysées and b) Hôtel de Ville neighborhoods.

Although the municipality of Paris estimates that 30% of the trees in the city of Paris are not listed in the database, these missing trees are most likely located in parks and private yards. Roadside trees are rather well documented. The street effects of roadside trees that are not integrated in the street network are not considered. However their biogenic emissions are taken into account in the regional-scale simulation to estimate background concentrations (see Section 4.2.2.5 and Chapter 3).

4.2.2.2 Estimation of the characteristics of the tree canopies in streets

The tree characteristics needed to compute the different tree effects at the street level (leaf area, dry biomass and tree crown height) are estimated, as in the Chapter 3, based on the Paris Tree inventory and a set of allometric equations from McPherson et al. (2016). The canopy characteristics of each street segment take into account all the trees included in the segment. Depending on the nature of the characteristics, they are averaged or summed over the trees of the street segment. The total leaf area normalized by the street area, LAI_{street_s} in $m^2_{leaf} \cdot m^{-2}_{street}$, is computed by summing the leaf area (LA_t in m^2_{leaf}) of all trees included in the street s and by dividing by the street surface ($W_s L_s$ in m^{-2}_{street}):

$$LAI_{street_s} = \frac{\sum_{t \in s} LA_t}{W_s L_s}. \quad (4.1)$$

The total dry biomass per street (DB_s in g of dry weight) is computed by summing the leaf dry biomass (DB_t in g) of all trees included in the street s :

$$DB_s = \sum_{t \in s} DB_t. \quad (4.2)$$

The top tree height is directly taken from the Paris tree inventory. For trees whose height is missing in the Paris inventory, the height is estimated from McPherson et al. (2016) equations. It is then

averaged to obtain the street average top tree height:

$$h_{max_s} = \frac{1}{n_{t \in s}} \sum_{t \in s} h_{max_t}, \quad (4.3)$$

where $n_{t \in s}$ is the number of trees in the street s . To respect the assumption made in Chapter 2, the crown heights that exceed the building heights are reduced to the building heights. This correction was made in 11% of the streets.

The tree fraction in the street, TF_s (-), needed in the Chapter 5 was also used here to check that the crown to street surface ratio is consistent. It is calculated as:

$$TF_s = \frac{\sum_{t \in s} CPA_t}{W_s L_s}, \quad (4.4)$$

$$CPA_t = \pi r_t^2, \quad (4.5)$$

where CPA_t is the crown projected area in m^2 (considered to be circular) and r_t is the tree crown radius (m) estimated from McPherson et al. (2016) equations.

Because in reality trees can be pruned, we assume that the tree canopy cannot cover the street surface by more than 90%, and therefore cannot exceed it. A maximum tree fraction is fixed to $TF_{s_{max}} = 0.9$ and when $TF_s > TF_{s_{max}}$, $TF_s = TF_{s_{max}}$. Trees are "pruned" in 6.1% of the streets and the tree characteristics are modified based on the tree fraction ratio as:

$$CPA'_t = CPA_t \times \frac{TF_{s_{max}}}{TF_s}, \quad (4.6)$$

$$LA'_t = LA_t \times \frac{TF_{s_{max}}}{TF_s}, \quad (4.7)$$

$$DB'_t = DB_t \times \frac{TF_{s_{max}}}{TF_s}, \quad (4.8)$$

where the ' mark stands for the corrected variable. Then, the street canopy characteristics are recomputed with equations (4.1) and (4.2). The street leaf area index, normalized dry biomass and crown height to building height ratios obtained are plotted for the street network in Figures 4.4 and 4.5.

4.2.2.3 The tree aerodynamic effect

The tree aerodynamic effect, i.e. the modification of air flows at the street level by tree crowns, has been parameterized in MUNICH using empirical equations based on Computational Fluid Dynamics (CFD) simulations in Chapter 2. As a reminder, the vertical profile of horizontal wind speed in the street direction and the vertical transfer coefficient between the street and the background are parameterized depending on LAI_{street} and on the average top tree crown height to building height ratio h_{max}/H (-). Among the streets including trees, the average LAI_{street} is equal to 1.3 with heterogeneities due to different number of trees, tree dimensions and species in each street. Few streets (1.12%) have a relatively high LAI_{street} (> 3), these are often wide streets with more than 2 rows of trees. The average top tree crown height to building height ratio seems more homogeneous within Paris and in 82.3% of the streets, trees are taller than half the building height ($h_{max}/H > 0.5$). The tree aerodynamic effect is expected to be higher in the street of high LAI_{street} and high h_{max}/H .

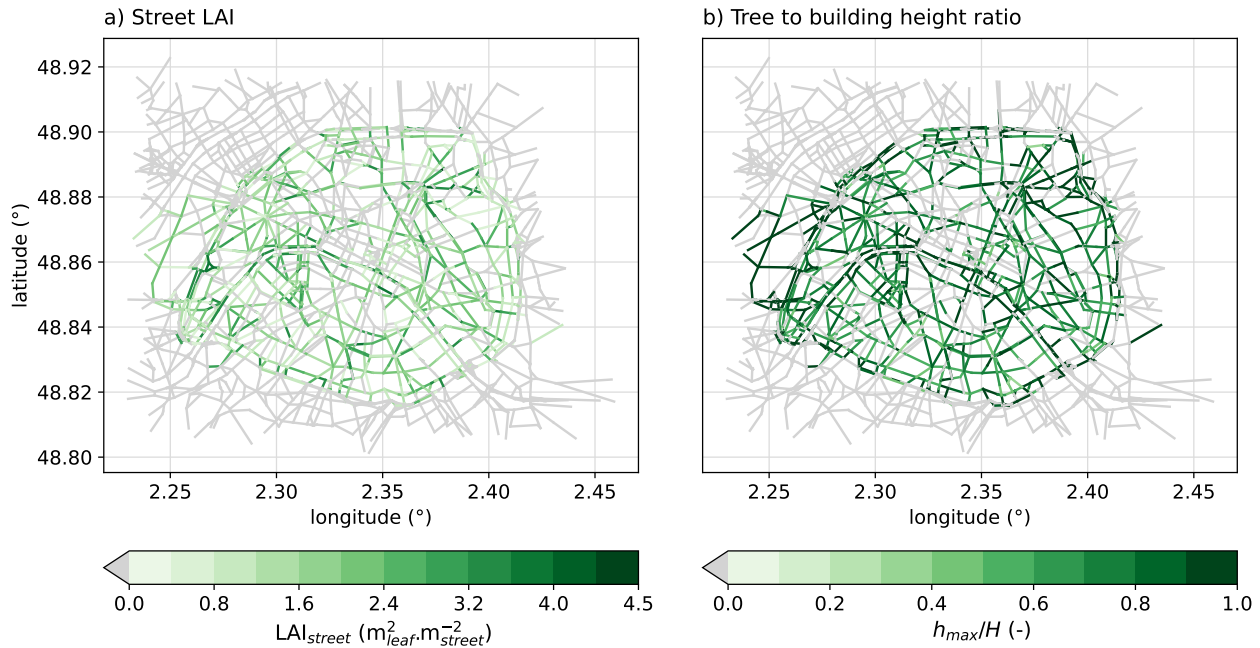


Figure 4.4: Maps of a) the street Leaf Area Index (LAI_{street}) and b) the tree to building height ratio (h_{max}/H) computed in Paris street network.

4.2.2.4 Computation of dry deposition on street surfaces and tree leaves

The ability of trees to reduce air pollutant concentrations via dry deposition is often promoted. However in the literature, the amplitude of this process varies (Nowak et al., 2006; Escobedo and Nowak, 2009; Setälä et al., 2013; Selmi et al., 2016; Xing and Brimblecombe, 2019; Nemitz et al., 2020; Lindén et al., 2023), with sometimes highly simplified representations of pollutant deposition rates. To try to estimate if this process modifies significantly the street concentrations, the dry deposition flux of gas and particles is taken into account in the street mass budget. The deposition fluxes are computed as the product of surface area, deposition velocity and street concentration. Deposition velocities are calculated for each surface (wall, street surface, tree leaf), which is considered homogeneous and in contact with the average concentration in the street. A resistive scheme is used to compute the deposition velocities and the different resistances are estimated using equations from the literature (Hicks et al. (1987); Walmsley and Wesely (1996); Wesely (1989); Venkatram and Pleim (1999); Zhang et al. (2002, 2003) for gas and Zhang et al. (2001) for aerosols). Due to their different physico-chemical properties, the parameterization varies according to the type of compound and the methodology used is detailed first for gaseous species and then for particles. Concerning the deposition of BVOCs, several studies suggest that isoprene and monoterpenes are not directly deposited but are rapidly oxidized in the atmosphere and are therefore indirectly deposited as oxygenated VOCs (Karl et al., 2010; Nguyen et al., 2015; Canaval et al., 2020). Due to the large number of species formed, and the lack of measurements to estimate the deposition model parameters, BVOC deposition on street and tree leaf surfaces is not considered. The resistance and coefficient formulations taken from the literature are presented in Appendices 4.B.1 for gas and 4.B.2 for particles at the end of this chapter.

4.2.2.5 Biogenic emissions

The biogenic emissions are computed with the same empirical approach as in Chapter 3. At the regional scale, the biogenic emissions are estimated from the dry biomass of each tree and then aggregated over the grid cells of the simulation domain. At the street scale, the total dry biomass for each street estimated with eq. (4.2). In streets including trees, the average dry biomass is equal to 647.2 g.m^{-2} . As shown in Fig. 4.5, the streets with the highest leaf areas are logically the streets with the highest leaf dry biomass.

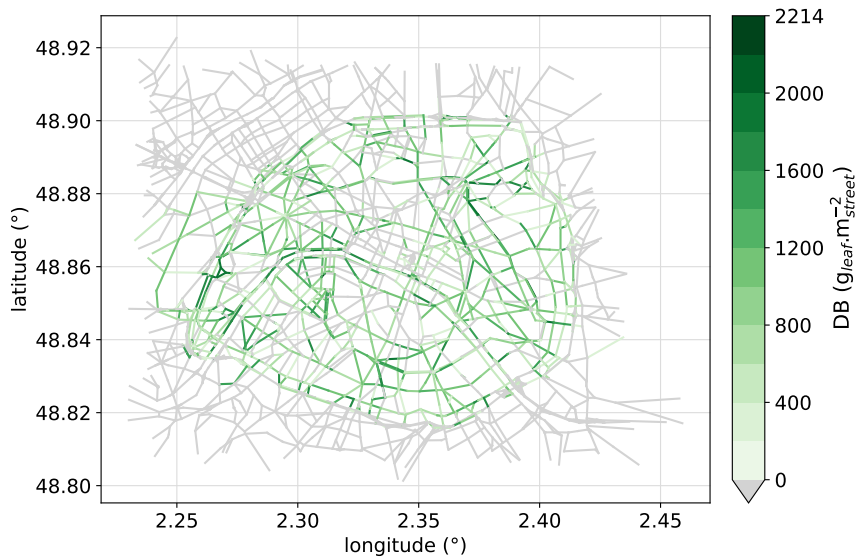


Figure 4.5: Map of the tree leaf dry biomass (DB) per area of street computed in Paris street network.

As in Chapter 3, the tree species emission factors are taken from MEGANv3.2 (<https://bai.ess.uci.edu/megan/data-and-code/megan32>, last accessed on 10/07/2023). At the street scale, the activity factors are computed from equations from (Guenther et al., 2012) for the temperature effect and from (Guenther et al., 1995) for the light effect. The leaf surface temperature is approximated by the air temperature at 2 m simulated by WRF and the Photosynthetic Photon Flux Density (PPFD) is computed from the global solar radiation as: $PPFD = 4.5 \times 0.5 \times SW_g$. These two factors include the selection of the 400-700 nm spectral range of the solar radiation and the conversion of W.m^{-2} into $\mu\text{mol.m}^{-2} \cdot \text{s}^{-1}$. For each street, the temperature and global solar radiation are taken from the CHIMERE-WRF horizontal cell which is located above the middle of the street. The air temperature (T_{air}) and the global solar radiation (SW_g) that are used in the computation of the BVOC emissions at the street level are compared to measurements performed in the Hôtel de Ville station (HdV) and in the Qualair platform in Fig. 4.6. Statistical indicators are also computed to compare observed and modeled meteorological data on the overlapping period at a 10-min time step (Table 4.1).

Table 4.1: Comparison of observed and modeled air temperature (T_{air}) in HdV and global solar radiation (SW_g) in Qualair with statistical indicators (defined in Appendix 4.D). su: same unit as the variable.

Variable		Min	Mean	Max	RMSE	NAD	Bias	R
		su	su	su	su	-	su	-
T_{air} ($^{\circ}\text{C}$)	obs	13.4	21.3	37.6	1.49	0.03	-0.53	0.95
	mod	12.2	20.8	37.3				
SW_g ($\text{W}\cdot\text{m}^{-2}$)	obs	-0.7	267.9	1112.5	154.46	0.13	52.74	0.91
	mod	0.0	320.6	966.4				

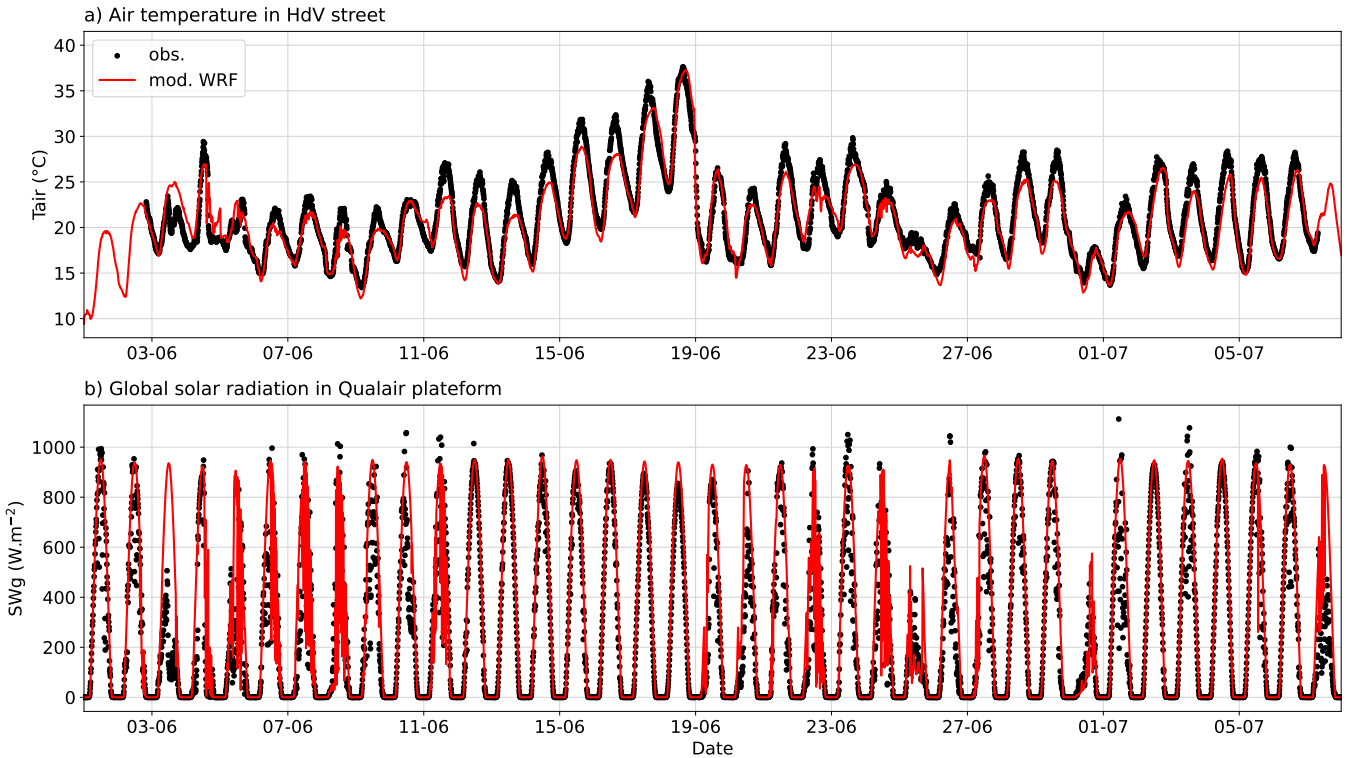


Figure 4.6: Comparison of the temporal variation of a) air temperature at 2 m height and b) global solar radiation modeled by WRF (mod) and observed (obs) at the HdV (48.85574°N , 2.35191°E) and Qualair (48.84638°N , 2.35598°E) sites at a 10 min temporal resolution. T_{air} observations are 10-min average of 10 s data measured by a meteorological station was located at 2 m height on the edge of the Paris city hall garden (HdV). SW_g observations are 10-min average of 1 s data measured by a radiometer located in the Qualair platform, on the roof of Sorbonne university at 35 m above the ground (<https://qualair.fr>).

The comparison shows that the air temperature is rather well modeled, although the mean temperature and the daily maximum are underestimated by the model compared to observations with a mean negative bias of -0.53°C (Table 4.1). Concerning the solar radiation, it is rather well estimated by WRF but with some over-estimations especially on cloudy days. The high air temperatures around the 18th of June and the clear-sky conditions suggest high emission during these period. July also experienced heatwaves, with temperatures exceeding 35°C on July 13, 18 and 19 (Fig. 4.6).

It should be noted that biogenic emissions from other tree organs (trunk, branches, flowers, etc.) or from the soil, although significant at certain times of the year (Baghi et al., 2012), are minor compared to leaf emissions and are not considered.

As in the Chapter 3, the emitted biogenic species are speciated and aggregated into MELCHIOR2 model species. Biogenic species include isoprene, monoterpenes, sesquiterpenes and many other BVOCs (OVOCs), mainly oxygenated compounds, such as methanol, acetone, acetaldehyde, formaldehyde. Note that nitrogen monoxide (NO) and carbon monoxide (CO), which are not BVOCs, are also emitted by trees and considered in the model. The temporal variation and emission maps of the different biogenic species are shown respectively in Fig. 4.7 and 4.8 respectively.

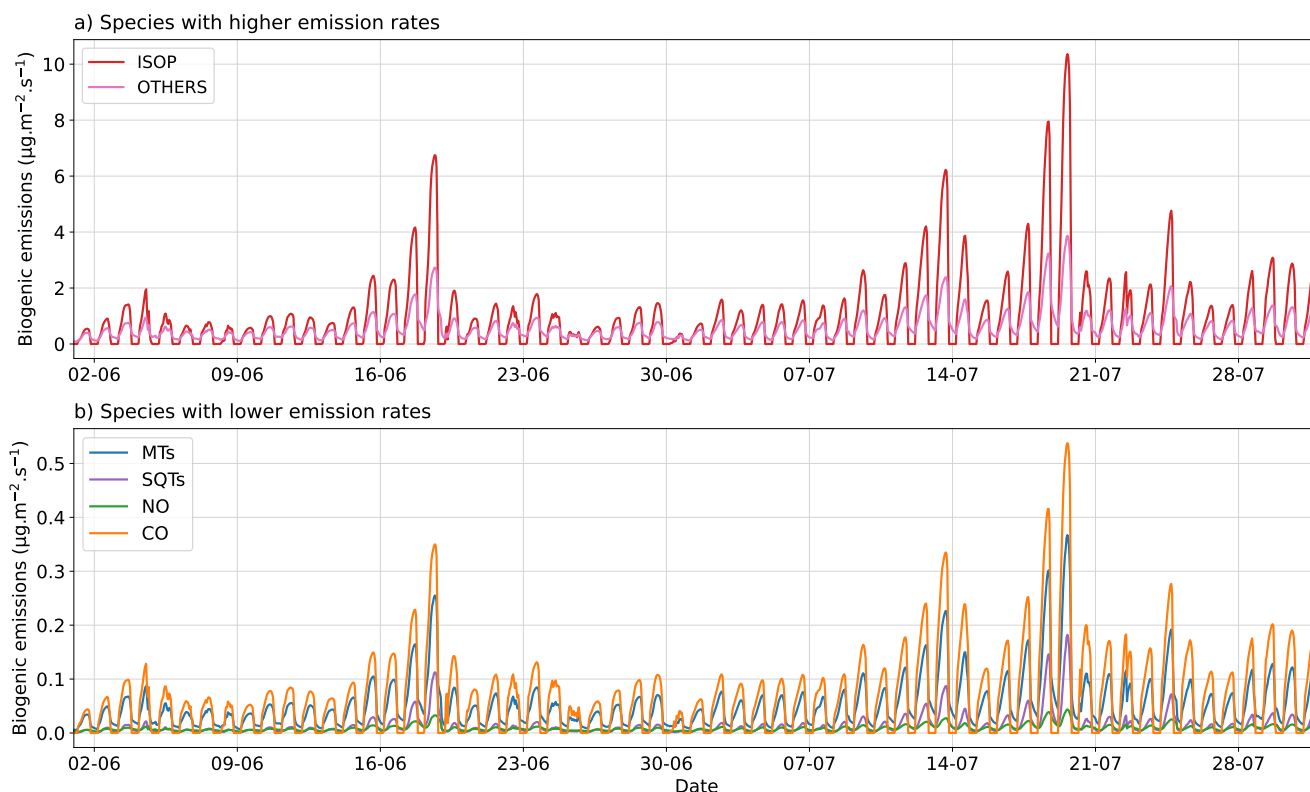


Figure 4.7: Temporal variation of spatially averaged BVOC emissions. Due to their different emission rates, the BVOC species are separated into two panels a) for isoprene and other BVOCs and b) for monoterpenes, sesquiterpenes, NO and CO. Emissions are averaged over the streets with trees.

As shown in the Chapter 3, isoprene is the most emitted biogenic species with 54.7% of the total emissions following by other oxygenated BVOCs (36.7%), CO (4.0%), monoterpenes (3.2%), sesquiterpenes (0.8%) and NO (0.5%) (Fig. 4.7).

Figure 4.8 shows that emissions are located in the streets containing trees and the density of the emissions depends on the quantity of leaf dry biomass and also on tree species via the emission factors.

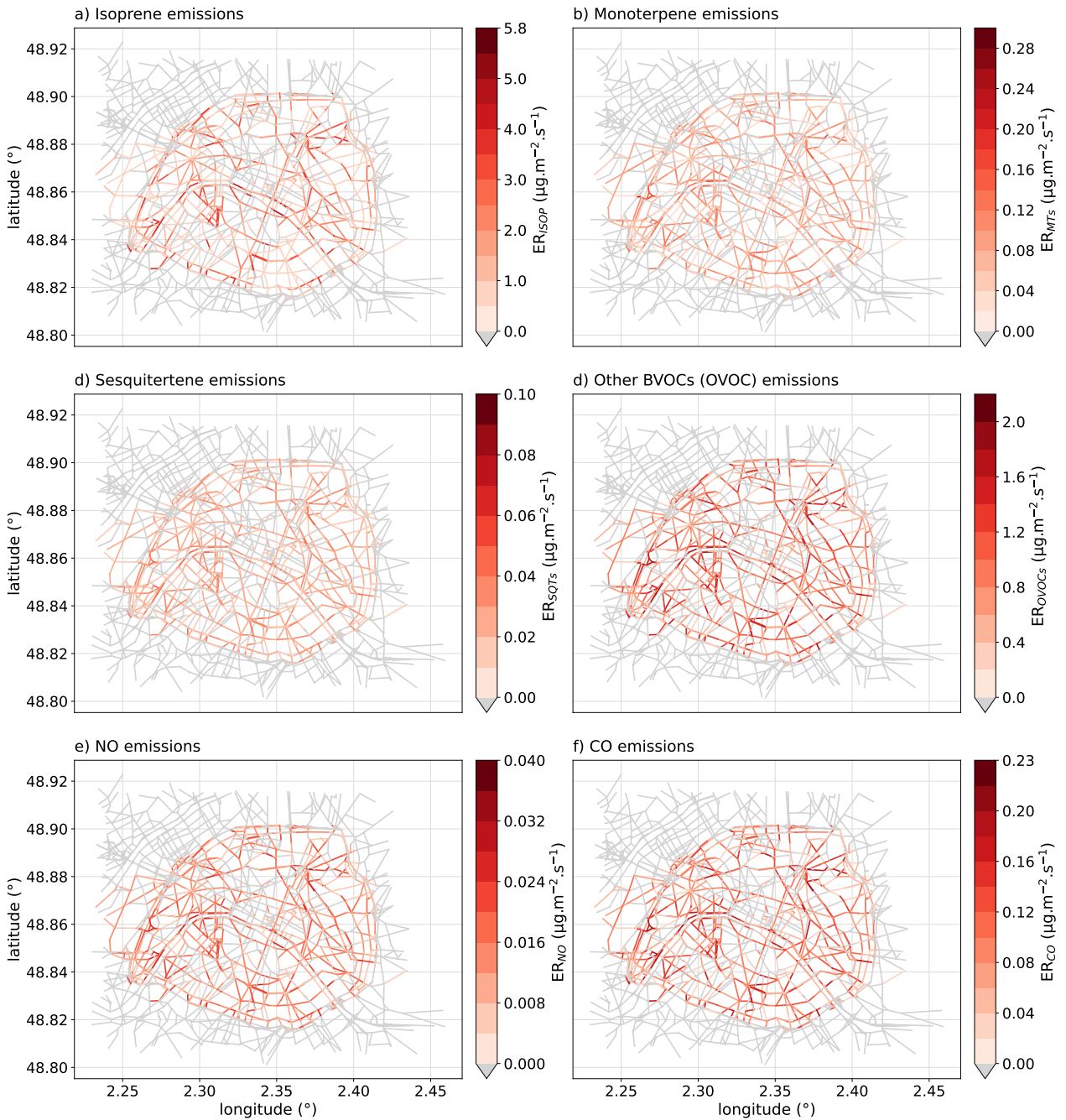


Figure 4.8: Maps of temporal average BVOC emissions over the 2-month period without multiplication of monoterpene emissions. a) Isoprene, e) NO and f) CO are directly emitted whereas b) monoterpenes, d) sesquiterpenes and d) other VOCs (OVOCs, mainly oxygenated BVOCs) represent the sum of several emitted species.

4.2.3 Simulation set-up

CHIMERE/MUNICH simulations are performed over the Paris street network from June 1 to July 31. A spin-up period of 5 days is considered, and the results are analyzed starting from June 6. As a reference and for comparison, a simulation without tree is performed (see Section 4.3.1). Simulations with all tree effects are performed to quantify the overall effect. Specific effects of trees on concentrations are also assessed using shorter simulations (2 weeks). The performed simulations are described in Table 4.2. As explained in Chapter 3, to quantify the impacts of uncertainties in the emission factors of terpenes, simulations are also performed with a TX2 scenario (Table 4.2), where monoterpene and sesquiterpene emissions are doubled.

Table 4.2: Description of the MUNICH simulations performed with the simulated period, the tree effect(s) considered and the corresponding background concentrations.

Simulation name	start and end dates	aero. effect	dry dep. on leaves	urban tree biogenic emissions	CHIMERE background simulation
REF	06/06 - 31/07	-	-	-	REF
AERO	13/06 - 26/06	yes	-	-	REF
DEP	13/06 - 26/06	-	yes	-	REF
BVOC	13/06 - 26/06	-	-	yes	bioparis
3EFF	06/06 - 31/07	yes	yes	yes	bioparis
REF TX2	06/06 - 31/07	-	-	-	REF-TX2
3EFF TX2	06/06 - 31/07	yes	yes	yes $ER_{MT \& SQT} \times 2$	bioparis-TX2

The next section presents, first a validation of the reference simulation, and then the tree impacts on gas and aerosol concentrations are analyzed and discussed.

4.3 Results and discussion

4.3.1 Reference simulation

To quantify the tree effects on concentrations, a reference simulation is performed without urban tree, neither at the regional or local scale. A comparison of observed and simulated concentrations through the average and standard deviation of concentrations along with statistical indicators is summarized in Table 4.3. Observed concentrations have been measured in the Paris HdV station and in Airparif traffic stations located inside the Paris city or in very near suburbs. These sites correspond to 10 permanent air-quality monitoring stations included within a large operational stations network operated by Airparif. The list of stations with measured compounds is presented in Table 4.7 and located in the map in Fig. 4.32.

Table 4.3 shows that the NO₂ concentrations are rather well estimated with a good correlation, a low bias and a NAD lower than 0.3 as recommended by [Hanna and Chang \(2012\)](#). PM_{2.5} concentrations are also rather well simulated by the model, but PM₁₀ are largely underestimated. This may be due the high uncertainties on non-exhaust emissions that affect coarse particle concentrations ([Lugon et al., 2021b](#)). Isoprene and monoterpene concentrations are also largely underestimated by the model. It may be due to the missing biogenic emissions of urban trees that will be added in this study. The fraction of fine organic particles (organic matter, OM) is also underestimated. As they are formed by condensation of BVOCs, their concentrations are expected to increase with the addition of the local urban biogenic emissions.

Table 4.3: Comparison of pollutants and BVOC concentrations observed at HdV and Airparif traffic stations and simulated with MUNICH without tree (REF). The definition of the statistical indicators is given in Appendix 4.D.

species	Nb stations	mean conc.		σ conc.		RMSE	NAD	Bias	R
		obs	mod	obs	mod				
	-	$\mu\text{g}\cdot\text{m}^{-3}$		$\mu\text{g}\cdot\text{m}^{-3}$		$\mu\text{g}\cdot\text{m}^{-3}$	-	$\mu\text{g}\cdot\text{m}^{-3}$	-
NO ₂	10	40.8	40.3	25.4	18.1	21.7	0.19	0.9	0.57
PM _{2.5}	3	11.2	12.3	5.4	4.4	5.4	0.17	1.0	0.42
PM ₁₀	6	25.3	15.7	11.0	5.8	13.6	0.25	-8.9	0.39
C ₅ H ₈	1	3.6	0.1	2.5	0.3	4.5	0.92	-3.6	0.39
MTs	1	1.0	0.03	0.6	0.08	1.1	0.94	-1.0	0.35
OM	2	6.2	2.4	4.2	1.8	5.8	0.49	-4.2	0.56

In the next sections, the impact of the different individual and combined tree effects is quantified by comparing the concentrations of isoprene, monoterpenes, NO₂, O₃, PM_{2.5}, and organic matter. The mean relative difference (MRD, see Appendix 4.D) between the simulation that includes only one tree effect (AERO, DEP, BVOC, 3EFF) and the reference simulation is computed during the period from June 13 to 26 in all the streets of the network. The concentration maps of the reference simulation averaged over this period are presented in panel a). The average concentrations with all tree effects are also compared to the reference simulations without tree (8 weeks between 06/06 and 31/07/22). This comparison is done with default biogenic emission factors, and with terpene emission factors multiplied by 2 (TX2 scenario). For that comparison, the simulation 3EFF TX2 is compared to the reference simulation REF TX2, i.e. terpene emissions are multiplied by 2 not only for urban trees, but also for the vegetation outside Paris.

4.3.2 Tree effects on isoprene and monoterpene concentrations

Figure 4.9 presents a) the average isoprene concentrations and the different tree impacts on average isoprene concentrations: b) the tree aerodynamical effect (AERO), c) the dry deposition on leaves (DEP) and d) the biogenic emissions from urban trees (BVOC).

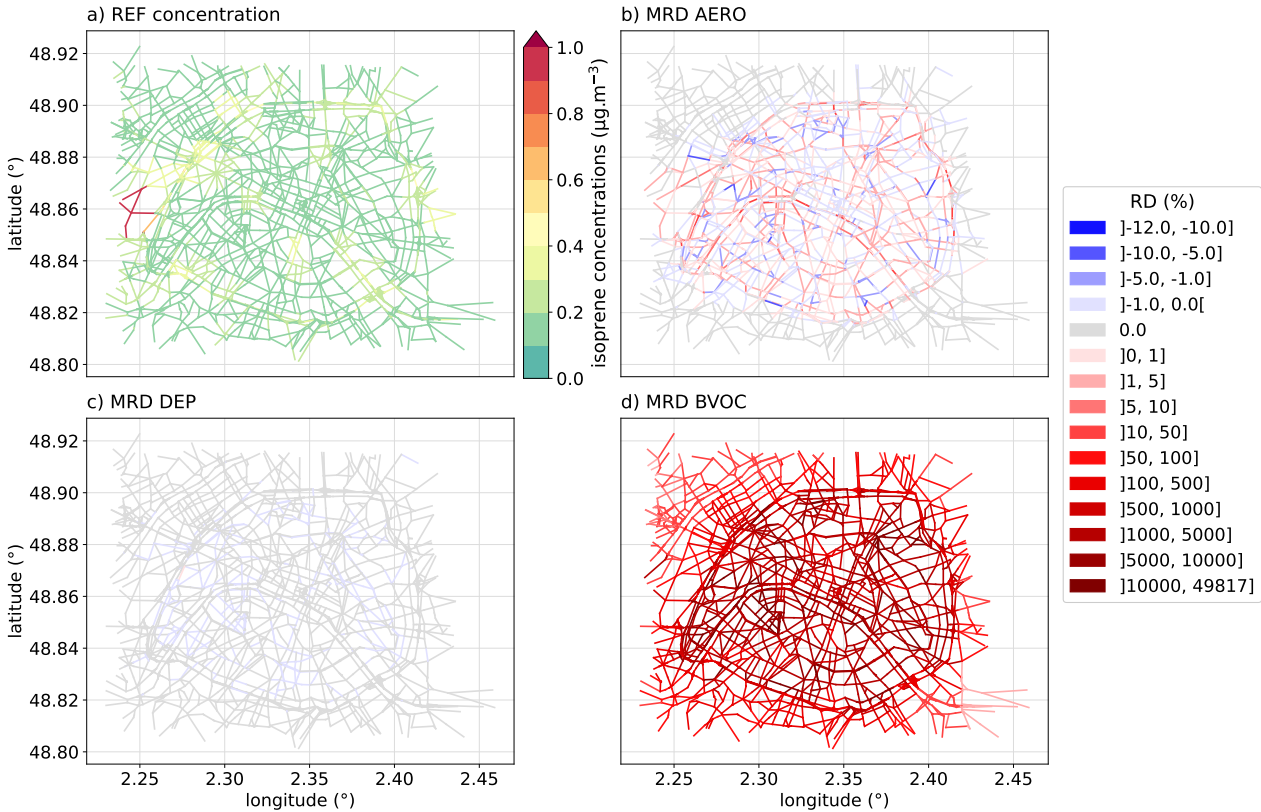


Figure 4.9: a) Average isoprene concentrations in the reference simulation (REF) and mean relative difference (MRD) of isoprene concentrations between the simulation b) with tree aerodynamic effect (AERO), c) with dry deposition on leaves (DEP), d) with urban tree biogenic emissions (BVOC) and the REF simulation without trees averaged from June 13 to 26.

Figure 4.9 shows that isoprene concentrations increase very significantly, when urban biogenic emissions are added to the BVOC simulation. This increase is rather spatially homogeneous, because isoprene life time is sufficiently long for isoprene to be transported over the city and then in the different streets, independently of the presence of trees in the street. As no dry deposition of isoprene on leaves is considered, there is no difference between the REF and the DEP simulations. The aerodynamic effect can lead to an increase of concentrations up to +23% and a decrease up to -11% in certain streets.

As the urban tree impact could be higher during heatwaves, it is analyzed in more details during the heatwave period of June 15 to 18, and compared to the 14-day period. Figure 4.10 shows series of box-plots of MRD of isoprene concentrations averaged either on a) all streets or b) streets with trees, during the all 14-day period (left part), and the heatwave (June 15 to 18) (right part) for each simulation. Note that to maintain the visibility of the figures, outliers, that can be numerous, are not displayed on the box-plots for all chemical species. They are, nevertheless, taken into account in the calculation of the statistics and in the other figures.

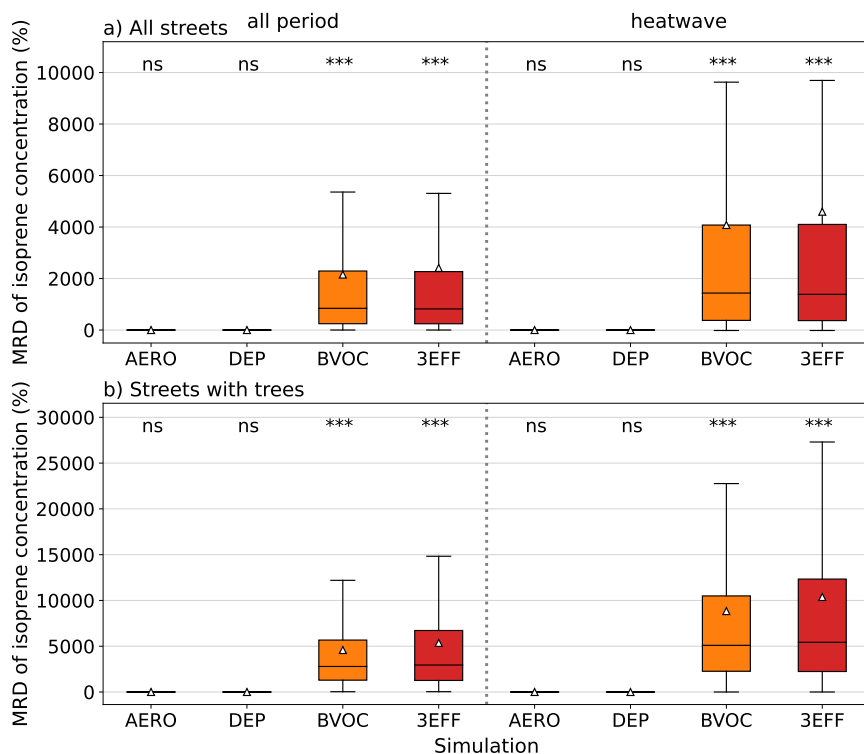


Figure 4.10: Box-plots of the Mean Relative Difference (MRD) of isoprene concentrations in a) all streets and b) streets with trees for each simulation. Concentrations are averaged from June 13 to 26 (left panel) and during the heatwave period (June 15 to 18) (right panel). The mean is represented by a white triangle and the result of a T-test between each simulation with trees and the reference simulation is indicated at the top of each box-plot '***': p-value < 0.001, '**': p-value < 0.01, '*': p-value < 0.05 and 'ns' (non-significant): p-value \geq 0.1.

Figure 4.10 confirms that the increase in isoprene concentration is mainly due to the biogenic emissions. This increase is larger in streets containing trees (Fig. 4.10b), and during the 4-day heatwave, because isoprene emissions increase with temperature and solar radiation (Fig. 4.7). Despite the low impact of the aerodynamical effect and deposition on isoprene concentrations, they are slightly higher in the simulation with the 3 tree effects (3EFF) than in the simulation with only BVOC emissions. Indeed, in the AERO simulation, the tree aerodynamic effect can only affect the isoprene emitted by traffic and in the 3EFF simulation, the aerodynamic effect also influences biogenic isoprene emitted by the trees, as quantified in Appendix 4.C.

On average over the 8-week period, taking into account the effects of trees, isoprene concentrations increase very significantly at both the street and the regional scales (Fig. 4.11). Note that there is no difference between the 3EFF and 3EFF TX2 simulations because unlike monoterpenes and sesquiterpenes, isoprene emissions are the same in the two simulations.

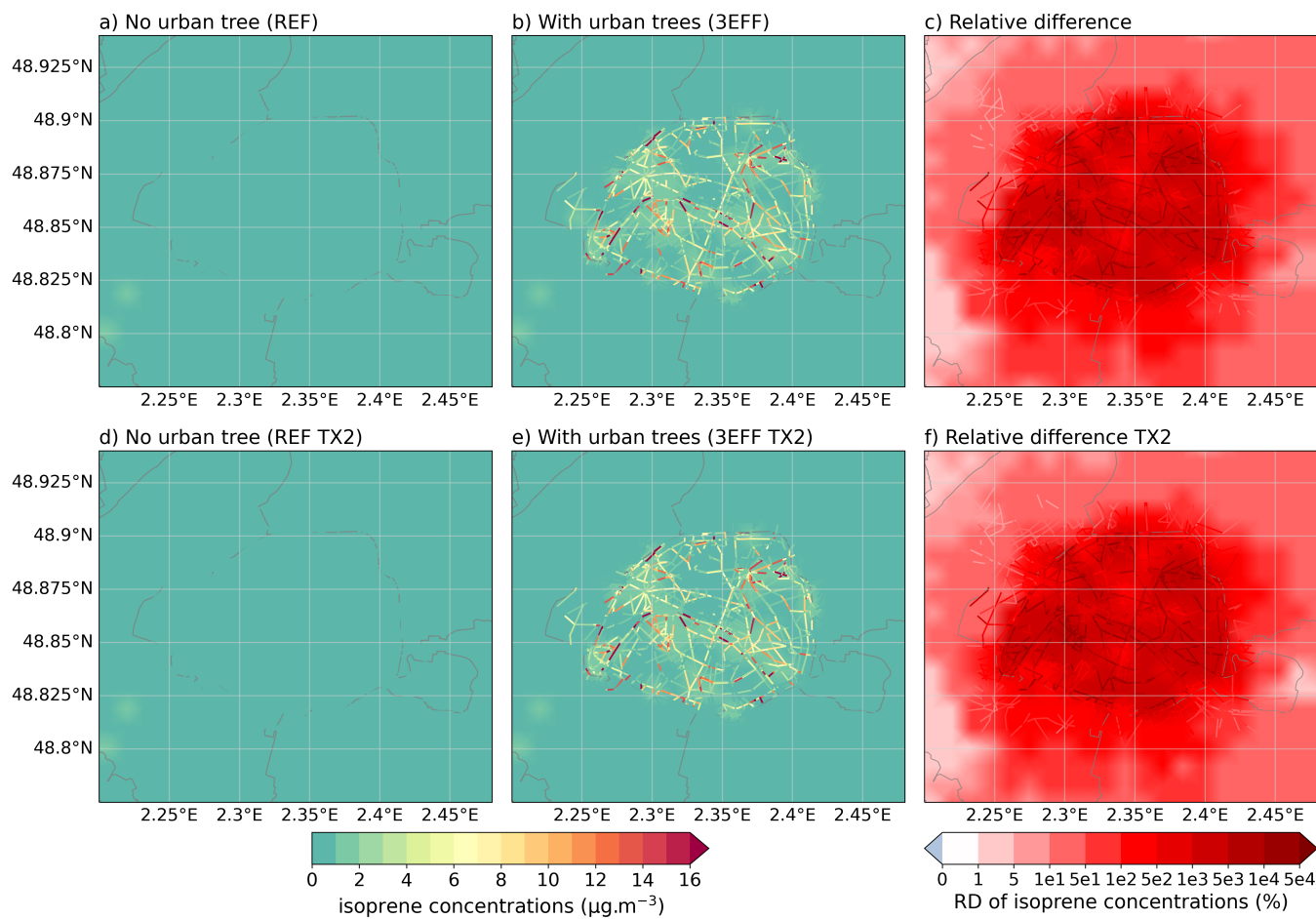


Figure 4.11: Average background and street isoprene concentrations (06/06 to 31/07/22) simulated with CHIMERE/MUNICH a) without trees (REF) and b) with all tree effects (3EFF) and c) mean relative difference between the two. Panels d), e) and f) show the same results with TX2 scenario.

Fig. 4.12 presents the temporal variation of isoprene concentrations measured and simulated at Paris City Hall (Hôtel de Ville, HdV). Isoprene and monoterpene (Fig. 4.16) concentrations are measured in the ambient air by Proton-transfer-reaction mass spectrometry (PTR-MS) in the HdV station. Hourly averages of measurements are calculated to compare to simulated concentrations. In the reference simulations (dotted line), concentrations are very low because anthropogenic isoprene emissions and isoprene background concentrations are low. The isoprene concentrations increase to an order of magnitude close to observations by including of urban tree biogenic emissions. During the heatwave (from June 15 to 18), concentrations are overestimated by up to a factor 3 probably because isoprene emissions are also overestimated. This was also the case in the Chapter 3, where compared to measurements at PRG, isoprene concentrations are overestimated on June, 16, 17, 19 and 20 but largely underestimated on June 18. As the temperature and global radiation are not overestimated by the model (Fig. 4.6 and concentrations on other days are rather well simulated, this overestimation might come from the emission parameterizations. In fact, the effect of water stress could significantly reduce isoprene emissions during this period and is not currently taken into account. Besides, the simulated concentrations are much larger during the day than during the night, strongly under-estimating the night-time concentrations compared to measurements. The low night-time concentrations in the simulations can be explained by the fact that isoprene is mainly emitted by vegetation during the day and is highly reactive. During night

time, isoprene emissions from traffic are low because traffic is much lower than during day time. Further work is needed to identify the cause of the discrepancy between measured and simulated isoprene concentrations at night.

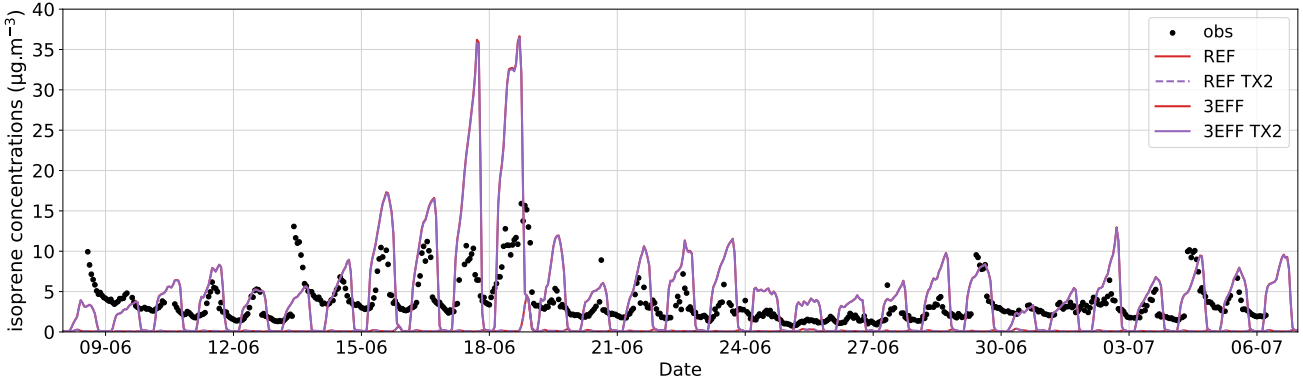


Figure 4.12: Temporal evolution of measured (black dots) and simulated with MUNICH (lines) isoprene concentrations in Paris Hôtel de Ville.

The inclusion of urban trees largely improves the estimation of isoprene concentrations, as shown by the statistical comparison of the simulations with the observations presented in Table 4.4. The normalized absolute difference (NAD) and the correlation (R) are improved, but the overestimation of isoprene concentrations some days induced a positive bias and a slightly higher root mean square error (RMSE).

Table 4.4: Comparison of isoprene concentrations observed and simulated at HdV with and without urban trees and TX2 scenario. The definition of the statistical indicators is given in Appendix 4.D and $n = 619$.

simulation	mean conc.		σ conc.		RMSE $\mu\text{g.m}^{-3}$	NAD -	Bias $\mu\text{g.m}^{-3}$	R -
	obs $\mu\text{g.m}^{-3}$	mod $\mu\text{g.m}^{-3}$	obs $\mu\text{g.m}^{-3}$	mod $\mu\text{g.m}^{-3}$				
REF		0.14		0.28	4.46	0.92	-3.62	0.39
REF TX2	3.56	0.15	2.5	0.28	4.46	0.92	-3.61	0.38
3EFF		6.22		8.22	5.71	0.41	1.5	0.65
3EFF TX2		6.19		8.16	5.65	0.41	1.47	0.65

Concerning monoterpenes, urban biogenic emissions have a large impact on concentrations, up to +10⁶% in the BVOC simulation compared to the reference (Fig. 4.13). The impact of dry deposition is low, and the aerodynamic effect of trees leads to an increase of concentrations by up to +11% or a decrease by up to -15% in some streets, but is not significant at the city scale.

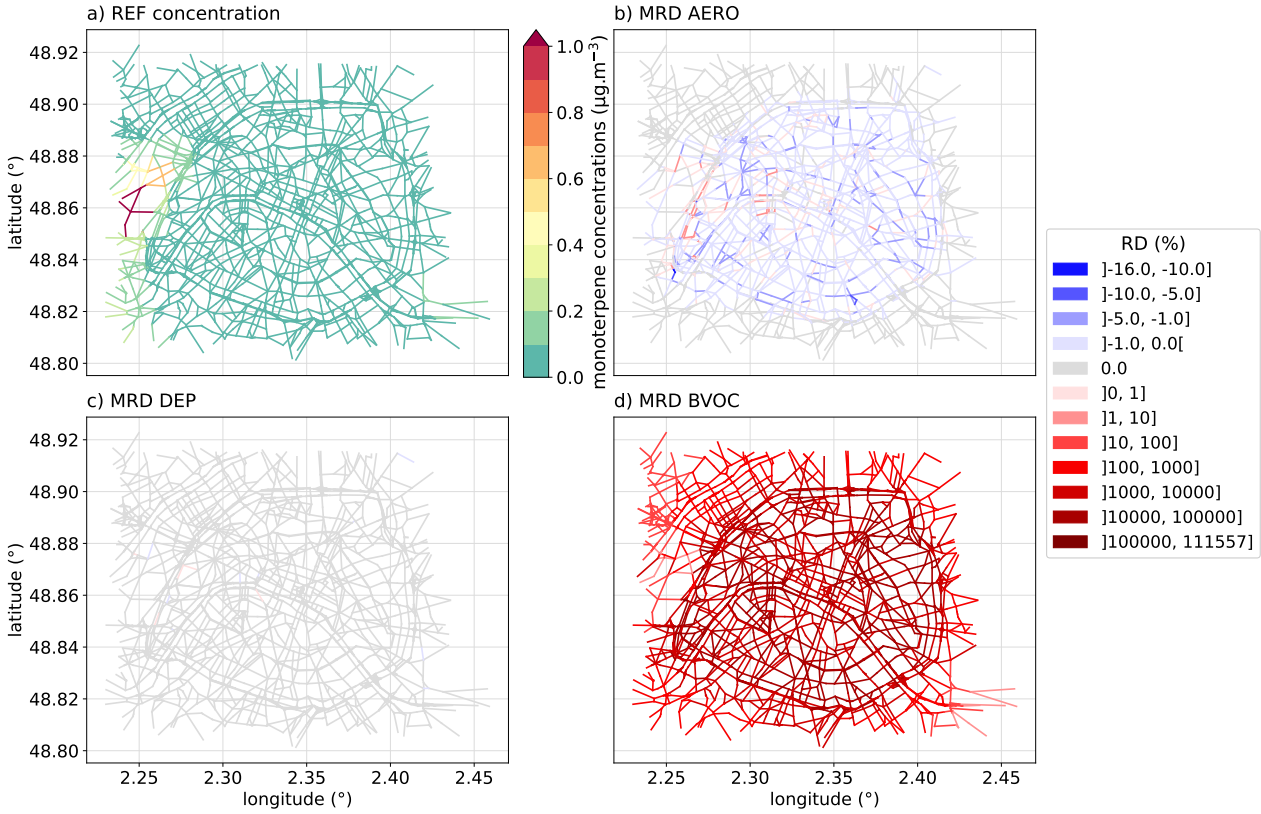


Figure 4.13: a) Average monoterpene concentrations in the reference simulation (REF) and mean relative difference (MRD) of monoterpene concentrations between the simulation b) with tree aerodynamic effect (AERO), c) with dry deposition on leaves (DEP), d) with urban tree biogenic emissions (BVOC) and the REF simulation without trees averaged from June 13 to 26.

As for isoprene, this increase of monoterpene concentrations due to biogenic emissions is larger in street containing trees and during the heatwave (Fig. 4.14). The tree aerodynamic effect also influences the monoterpene emissions from trees in streets (Appendix 4.C).

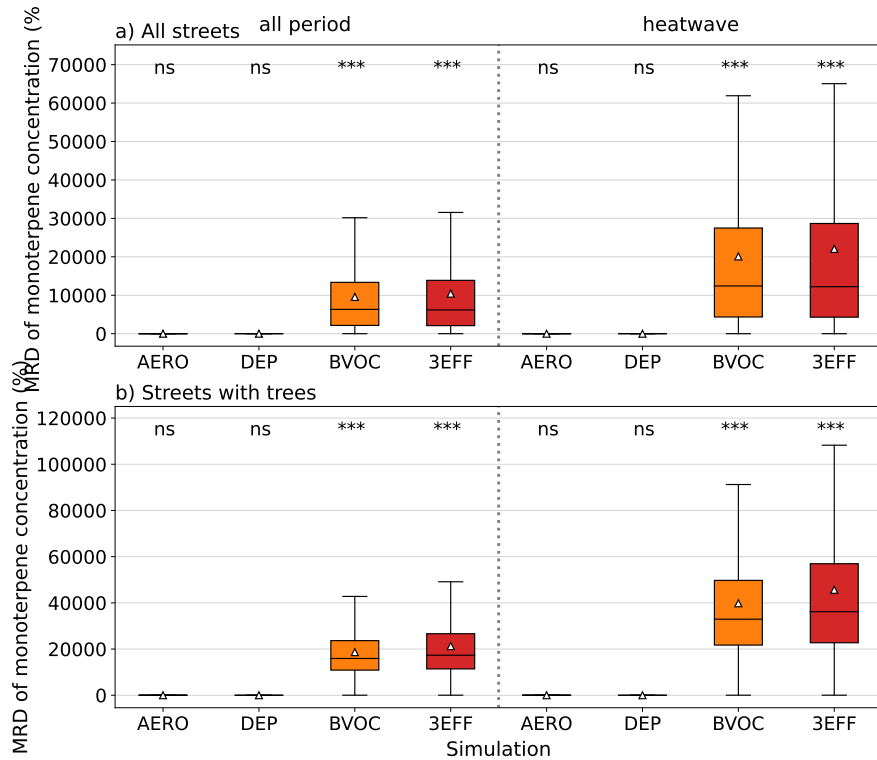


Figure 4.14: Box-plot of the Mean Relative Difference (MRD) of monoterpene concentrations in a) all streets, b) streets with trees and c) streets without tree for each simulation. Concentrations are averaged from June 13 to 26, on the all period (left part), during daytime (middle part) and nighttime (right part). The mean is represented by a white triangle and the result of a T-test between each simulation with trees and the reference simulation is indicated at the top of each box-plot '***': p-value < 0.001, '**': p-value < 0.01, '*': p-value < 0.05 and 'ns' (non-significant): p-value ≥ 0.1.

A map of the 8-week average monoterpene background and street concentrations simulated with CHIMERE/MUNICH with and without trees is presented in Fig. 4.15. The monoterpene concentrations of the REF simulation are very low without urban trees except in western Paris, around the Boulogne wood and the forests of southwestern Paris (Fig. 4.15a). The addition of urban trees, and mainly monoterpene emissions, increase very largely the concentrations both in the streets and the background, as shown in Fig. 4.15b and c. As for isoprene, this increase is mainly due to the addition of biogenic emissions since there is no dry deposition on leaves and the aerodynamic effect of trees leads to a variation of monoterpene concentrations between -15% and $+11\%$ (Fig. 4.9 and 4.10). The increase is larger during heatwaves due to higher emissions (Fig. 4.10). In the TX2 scenario, as monoterpene emissions are doubled, monoterpene concentrations are much higher (Fig. 4.15e). The relative impact of urban trees is also a little higher especially inside Paris city (Fig. 4.15f).

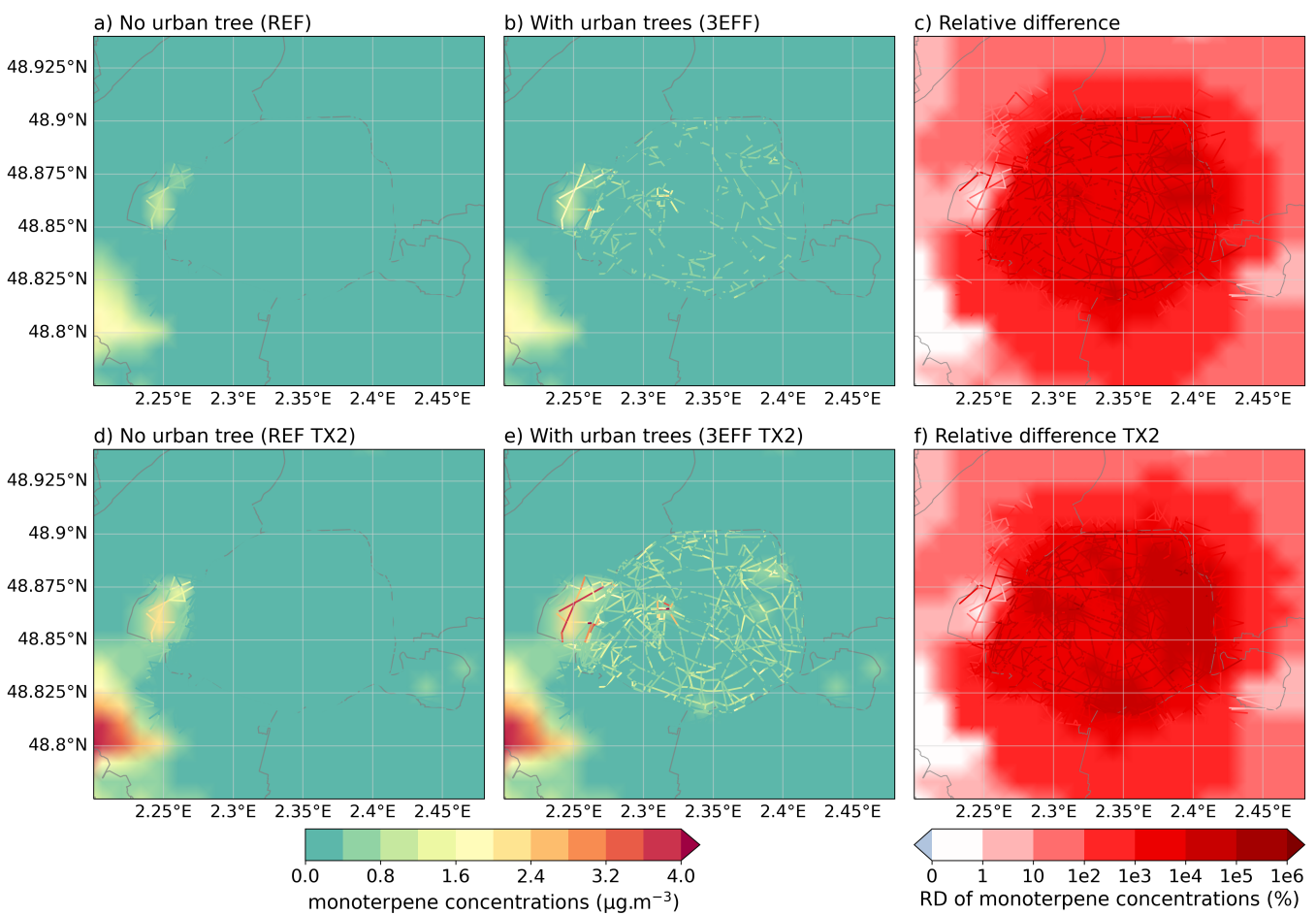


Figure 4.15: Average background and street monoterpene concentrations (06/06 to 31/07/22) simulated with CHIMERE/MUNICH a) without trees (REF) and b) with all tree effects (3EFF) and c) mean relative difference between the two. Panels d), e) and f) show the same results with TX2 scenario.

Figure 4.16 shows a comparison of observed and simulated hourly monoterpene concentrations at Paris HdV station. The statistical comparison of the different simulations to observations is presented in Table 4.5. As for isoprene, the concentrations of monoterpenes in the reference simulation are low and underestimated compared to the measurements. The addition of local monoterpene emissions from urban trees allows to better simulate the observed concentrations, especially when monoterpene concentrations are doubled in TX2 scenario (Table 4.5). The concentration peak during the heatwave around the 18th of June is rather well simulated by MUNICH. However concentration increases on the 8th, 13th, 29th of June and 2nd, 4th of July are not simulated by the model. Overall, as there are also uncertainties in monoterpene measurements, the monoterpene concentrations are reasonably well simulated with the TX2 scenario. This comparison suggests that monoterpenes concentrations are very sensitive to local emissions. It would therefore be important to quantify and characterize the missing trees in Paris ($\sim 30\%$) and its suburbs.

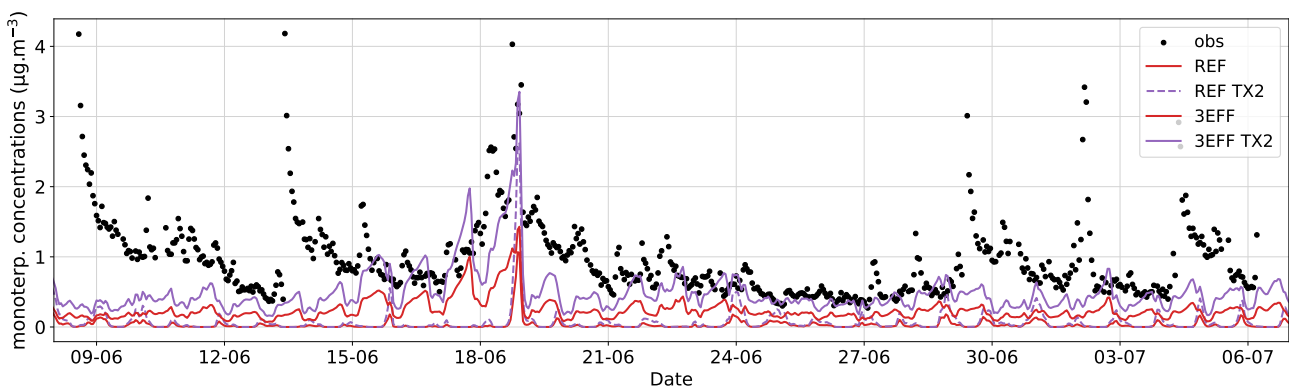


Figure 4.16: Hourly evolution of measured (black dots) and simulated (lines) monoterpene concentrations at Paris HdV station.

Table 4.5: Comparison of monoterpene concentrations observed and simulated at HdV with and without urban trees and TX2 scenario. The definition of the statistical indicators is given in Appendix 4.D.

simulation	mean conc.		σ conc.		RMSE $\mu\text{g.m}^{-3}$	NAD -	Bias $\mu\text{g.m}^{-3}$	R -
	obs $\mu\text{g.m}^{-3}$	mod $\mu\text{g.m}^{-3}$	obs $\mu\text{g.m}^{-3}$	mod $\mu\text{g.m}^{-3}$				
REF		0.03		0.08	1.12	0.94	-0.97	0.35
REF TX2	0.96	0.08	0.57	0.20	1.08	0.86	-0.92	0.34
3EFF		0.29		0.20	0.92	0.59	-0.74	0.39
3EFF TX2		0.59		0.42	0.73	0.34	-0.47	0.4

Due to the addition of biogenic emissions from urban trees, the effect on biogenic concentration is, as expected, very significant. The next section focuses on the impact of trees on NO_2 and O_3 concentrations.

4.3.3 Tree effects on NO₂ and O₃ concentrations

To estimate the impacts of urban trees on NO₂ and O₃ concentrations, the relative impact of each individual tree effect is quantified over the Paris street network on average over 14 days in Figures 4.17 and 4.21, and during the 4-day heatwave in the Figures 4.18 and 4.23. The overall tree effects are evaluated for the 2-month average concentrations in Figures 4.19, 4.24.

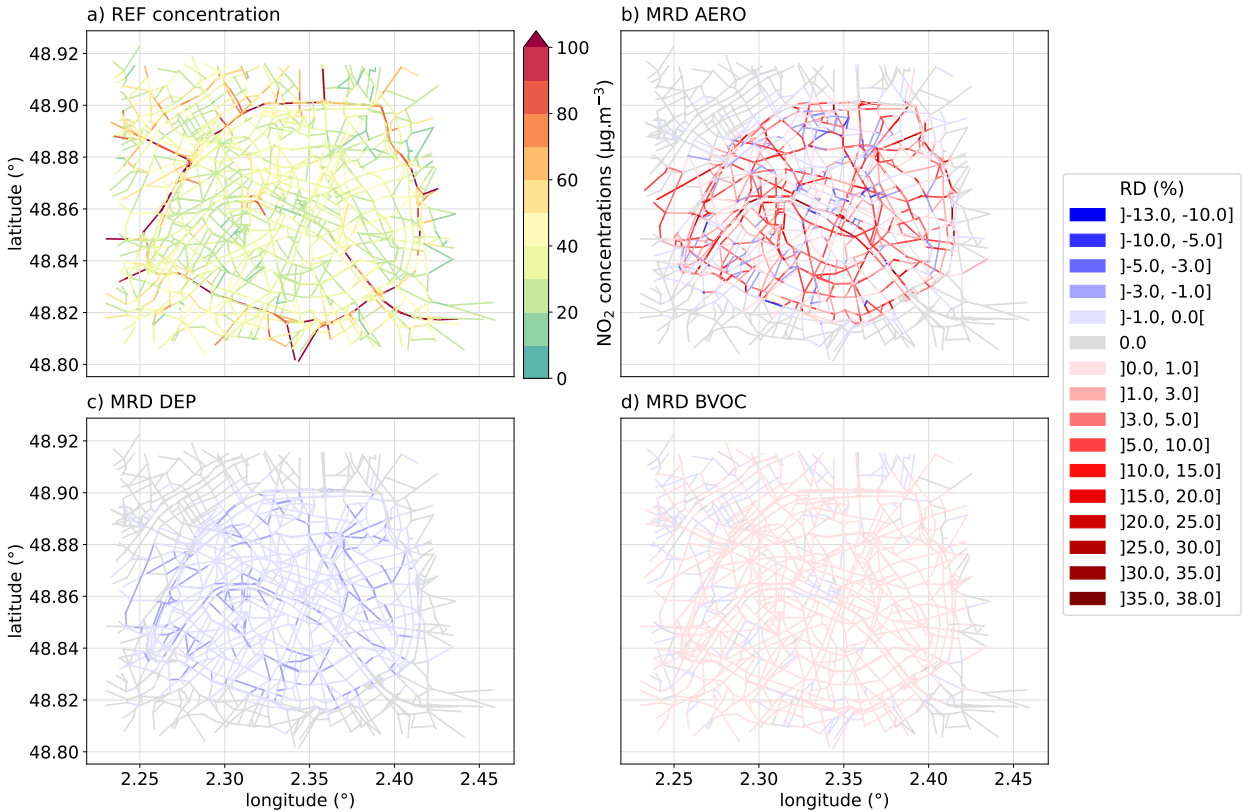


Figure 4.17: a) Average NO₂ concentrations in the reference simulation (REF) and mean relative difference (MRD) of NO₂ concentrations between the simulation b) with tree aerodynamic effect (AERO), c) with dry deposition on leaves (DEP), d) with urban tree biogenic emissions (BVOC) and the REF simulation without trees averaged from June 13 to 26.

Figures 4.17 and 4.18 show that the predominant tree impact that affects NO₂ concentrations is the aerodynamic effect. Depending on the street, it leads to an increase up to +37%, but also to a decrease, which can reach -12% (Fig. 4.17). This effect is especially significant in the streets including trees (Fig. 4.18). The effect of dry deposition of NO₂ on tree leaves leads to a decrease of concentrations up to -2.5%, and it is not significant at the city scale (Fig. 4.18). Although biogenic emissions, particularly isoprene, can have an impact on NO₂ concentrations through the ozone cycle, this effect is low, as shown by the mean relative difference of the BVOC and the REF simulation, which does not exceed ±1%. The impact of trees on NO₂ concentrations is therefore related to the aerodynamic effect and it is not much impacted by the heatwave (Fig. 4.18).

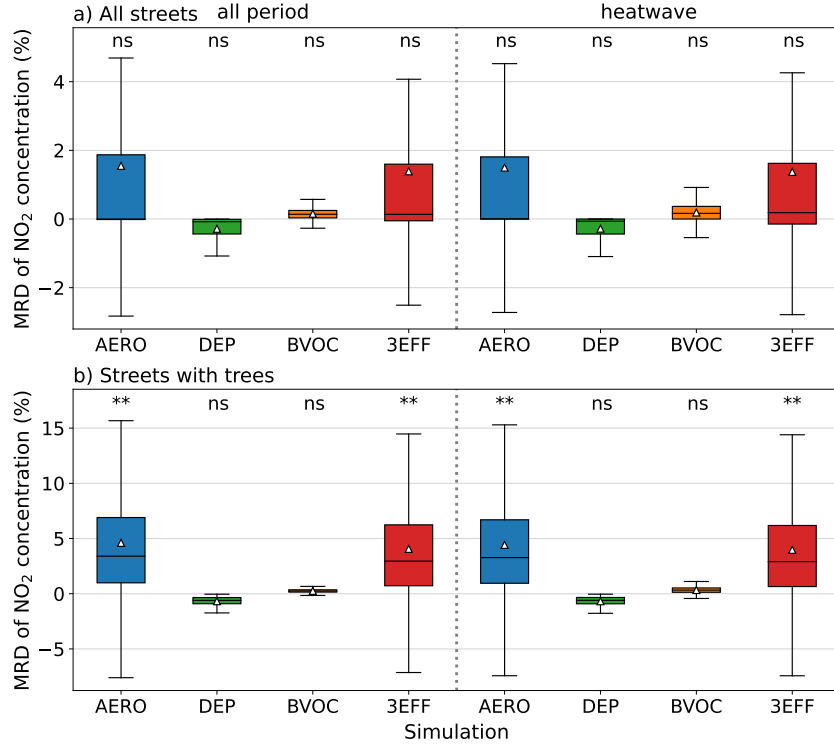


Figure 4.18: Box-plot of the Mean Relative Difference (MRD) of NO₂ concentrations in a) all streets, b) streets with trees and c) streets without tree for each simulation. Concentrations are averaged from June 13 to 26, over the whole period (left part), during daytime (middle part) and nighttime (right part). The mean is represented by a white triangle and the result of a T-test between each simulation with trees and the reference simulation is indicated at the top of each box-plot '* * *': p-value < 0.001, '* *': p-value < 0.01, '*': p-value < 0.05 and 'ns' (non-significant): p-value ≥ 0.1.

The effect is similar over the whole period, as shown in Fig. 4.19. It presents the 8-week average NO₂ concentrations with and without trees along with the relative difference between the two simulations. The increase in NO₂ concentrations is rather well correlated with the street LAI, which is the main tree characteristic involved in the aerodynamic effect (Fig. 4.4). Because NO₂ is emitted in the street by traffic, its dispersion is limited by the presence of trees. In order to quantify the influence of the NO₂ emission intensity on the amplitude of the tree aerodynamic effect, the temporal average of the mean relative difference between the NO₂ concentrations between the simulations AERO and REF (MRD AERO) is plotted as a function of the street LAI and of the NO₂ emissions in Fig. 4.20. It shows that in treeless streets ($LAI_{street} = 0$), the MRD AERO is globally between ±10% and it seems quite independent of the intensity of emissions. This variability observed in treeless streets could be a consequence of transport of concentrations between adjacent streets. In streets where NO₂ emissions are low, the tree aerodynamic effect is relatively low (between about +5 and -10%) for all LAIs. When NO₂ emissions are higher, a strong aerodynamic effect proportional to LAI is observed. Other factors influence the aerodynamic effect, such as the street aspect ratio and the direction of the wind compared to the street. However, on average over the period, the aerodynamic effect is always significant in high-traffic streets when the LAI exceeds 0.5, and in medium-traffic streets when the LAI exceeds $1.0 \text{ m}_{leaf}^2 \cdot \text{m}_{street}^{-2}$.

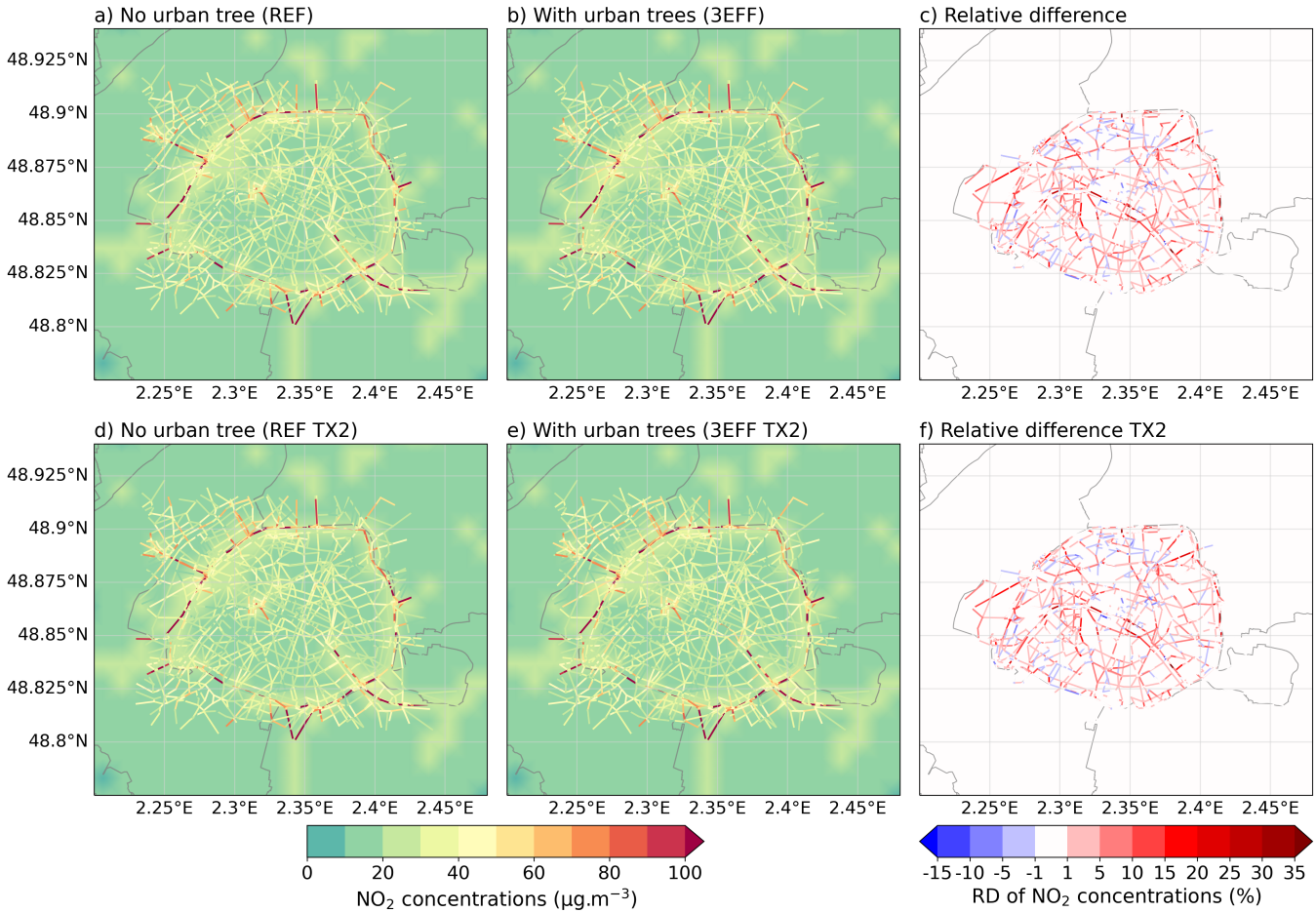


Figure 4.19: Average background and street NO₂ concentrations (06/06 to 31/07/22) simulated with CHIMERE/MUNICH a) without trees (REF) and b) with all tree effects (3EFF) and c) mean relative difference between the two. Panels d), e) and f) show the same results with TX2 scenario.

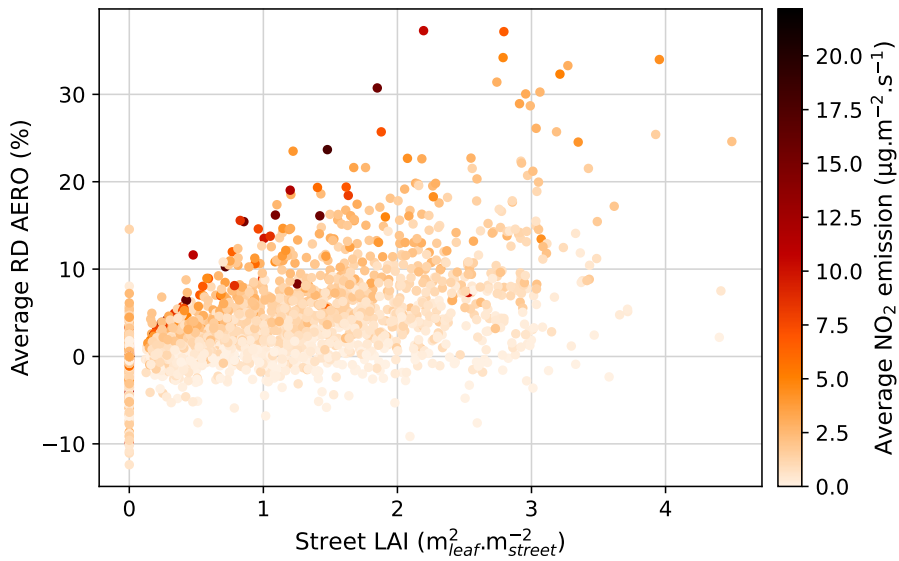


Figure 4.20: Mean relative difference of NO₂ concentrations between the simulations AERO and REF as a function of the street LAI and the average NO₂ emission (for each street averaged from 13 to 26/06).

As shown in the Chapter 3, the urban tree biogenic emissions induce an average increase of background ozone concentrations of about 1% over Paris. The individual impacts of urban trees on ozone concentrations at the street scale are shown in Figures 4.21 and 4.23. The aerodynamical effect leads to a decrease in O₃ concentrations in many streets (up to -23%) and to an increase in others (up to +17%). This effect is more significant in streets containing trees and is anti-correlated with the increase in NO₂ concentrations, as shown in Fig. 4.22 that plots the MRD AERO of O₃ depending on the MRD AERO of NO₂.

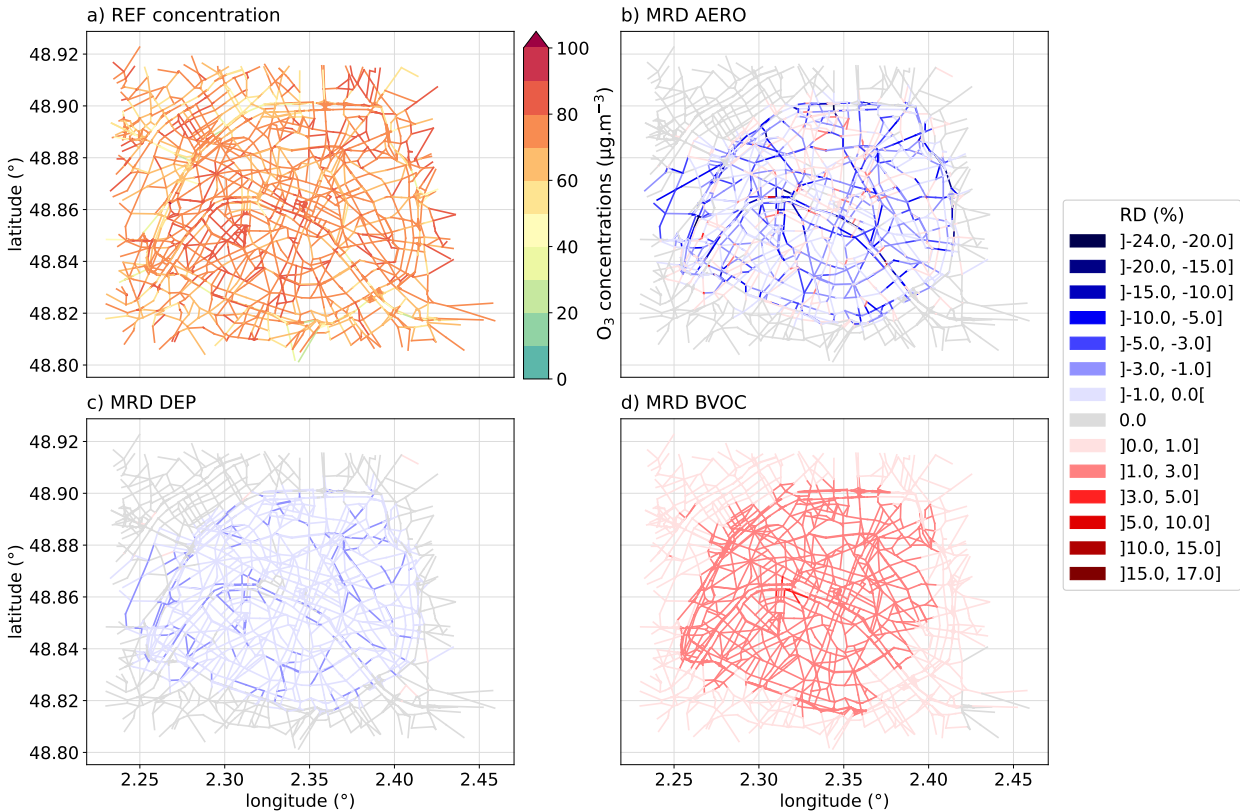
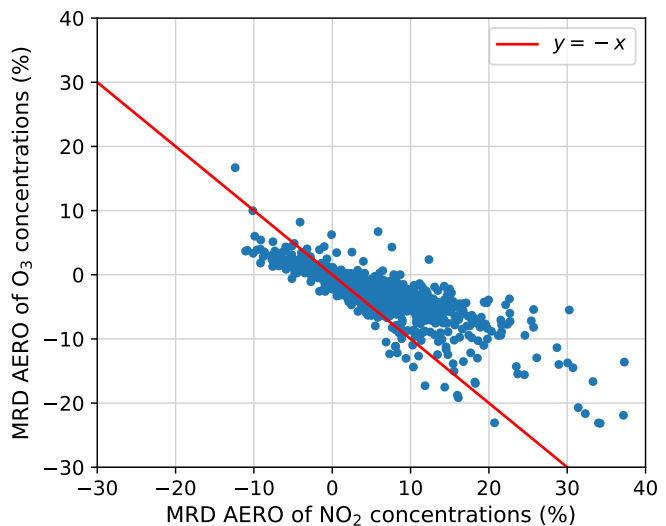


Figure 4.21: a) Average O₃ concentrations in the reference simulation (REF) and mean relative difference (MRD) of O₃ concentrations between the simulation b) with tree aerodynamic effect (AERO), c) with dry deposition on leaves (DEP), d) with urban tree biogenic emissions (BVOC) and the REF simulation without trees averaged from June 13 to 26.

Figure 4.22: Mean relative difference due to aerodynamical effect (MRD AERO) of O₃ concentrations as a function of MRD AERO of NO₂ concentrations (for each street averaged from 13 to 26/06).



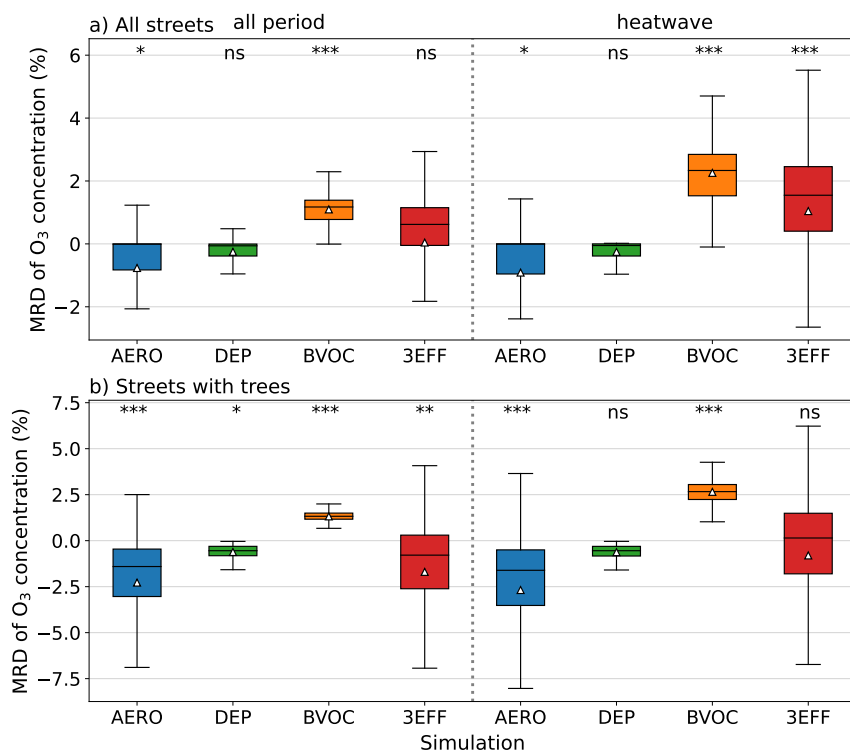


Figure 4.23: Box-plot of the Mean Relative Difference (MRD) of O₃ concentrations in a) all streets, b) streets with trees and c) streets without tree for each simulation. Concentrations are averaged from June 13 to 26, over the whole period (left part), during daytime (middle part) and nighttime (right part). The mean is represented by a white triangle and the result of a T-test between each simulation with trees and the reference simulation is indicated at the top of each box-plot '* * *': p-value < 0.001, '* *': p-value < 0.01, '*': p-value < 0.05 and 'ns' (non-significant): p-value \geq 0.1.

The effect of the dry deposition on ozone concentrations is very low and does not exceed -2.5% . However, the Fig. 4.23b shows that the dry deposition is more significant in the streets with trees (-0.62% on average and up to -2.5%). The biogenic emissions induce an average O₃ increase of $+1\%$ which is very homogeneous over the Paris city highlighting the impact of the background concentrations. This increase is larger during the heatwave period ($+2.1\%$) as shown in Fig. 4.23. As this is a relative difference compared with a simulation without trees, which already includes the effect of weather on O₃ formation, this increase of concentration during the heatwave is due to the increase of biogenic emissions. The comparison of the individual tree effects with the combined effects (3EFF simulation) shows that the three tree effects compensate each other to give an average tree impact that can be negative, nil or positive depending on the street and time period.

Figure 4.24 shows a comparison of average concentrations with and without trees over the 8-week simulations. Urban trees lead to a few percent increase in background O₃ concentrations overlaid by lower concentrations in streets where NO₂ concentrations increase due to the aerodynamic effect of trees. The difference with the TX2 scenario is not clearly visible on the map 4.24, and the doubled monoterpene and sesquiterpenes emissions induce only a slightly higher impact of trees on O₃ concentrations. This suggests that terpenes have a low impact on ozone compared to other VOCs such as isoprene, which are emitted in larger quantities.

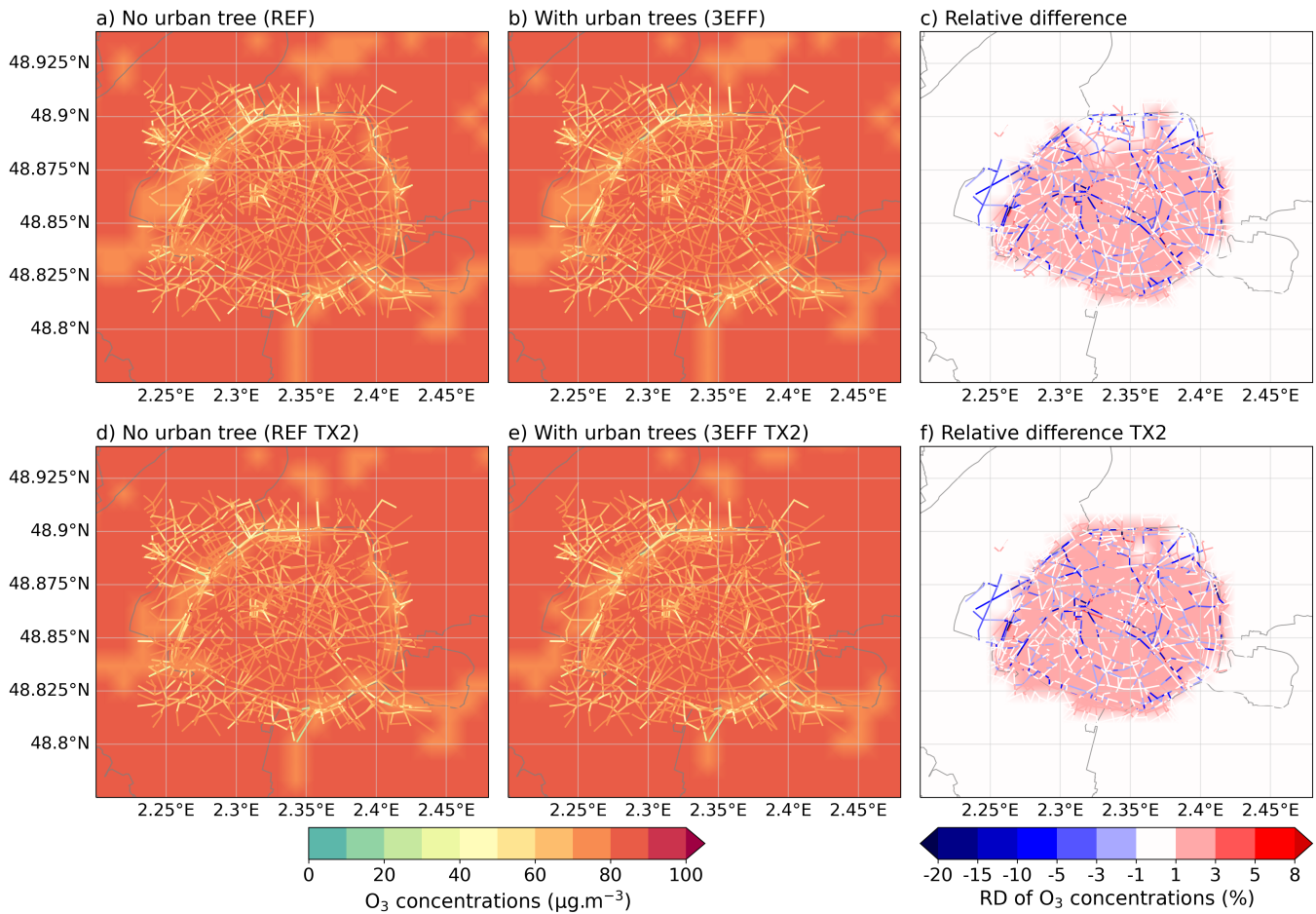


Figure 4.24: Average background and street O₃ concentrations (06/06 to 31/07/22) simulated with CHIMERE/MUNICH a) without trees (REF) and b) with all tree effects (3EFF) and c) mean relative difference between the two. Panels d), e) and f) show the same results with TX2 scenario.

Following the study of gaseous species, the impact of trees on particles, and more specifically on the organic fraction, is quantified in the next section.

4.3.4 Tree effects on particle concentrations

As the BVOCs emitted by trees may be oxidized leading to the formation of organic particles, called organic matter (OM), which may increase because of the urban biogenic emissions. The OM concentration is computed by summing the concentrations of the organic compounds of particles of diameters lower than $1\ \mu\text{m}$. Similarly to the previous chemical species studied, the tree effect on OM concentrations is quantified by calculating and mapping the mean relative difference of the sensitivity simulations with the reference simulation (Fig. 4.25) and by comparing the different MRD over the whole period and the 4-day heatwave (Fig. 4.26).

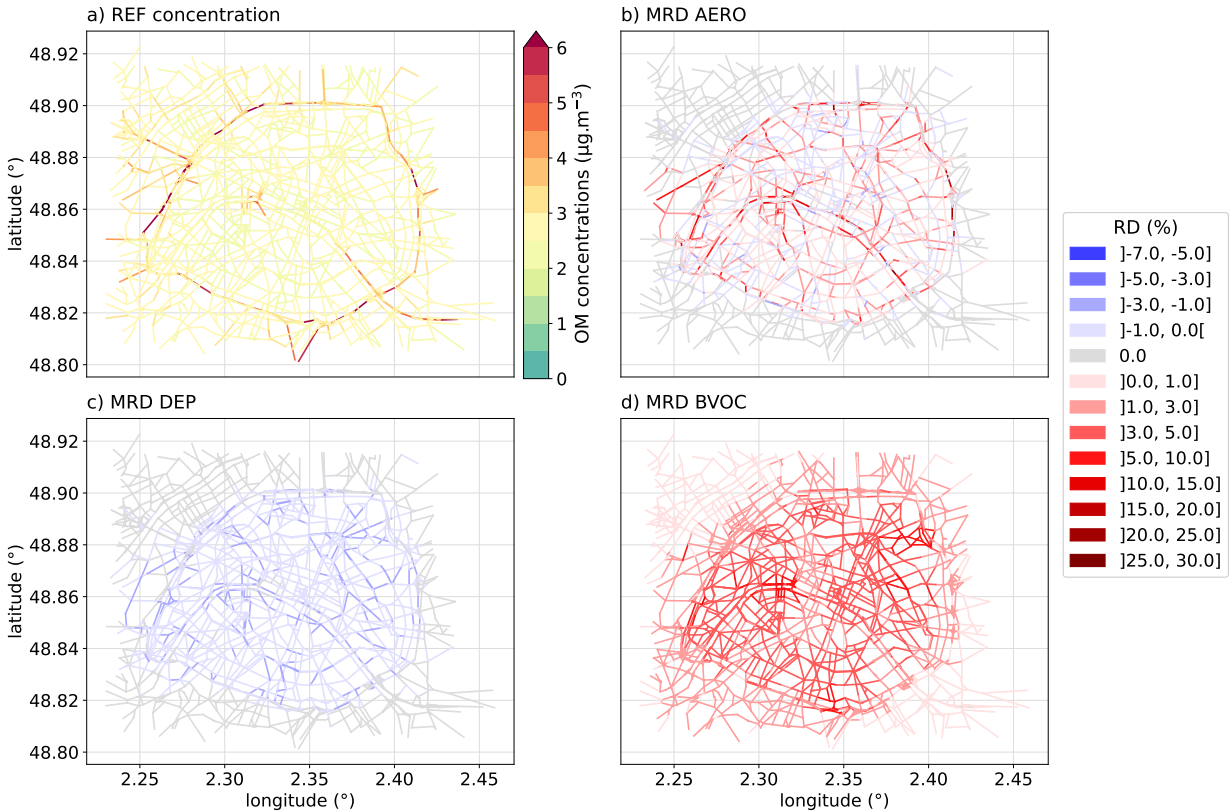


Figure 4.25: a) Average organic matter (OM) concentrations in the reference simulation (REF) and mean relative difference (MRD) of OM concentrations between the simulation b) with tree aerodynamic effect (AERO), c) with dry deposition on leaves (DEP), d) with urban tree biogenic emissions (BVOC) and the REF simulation without trees averaged from June 13 to 26.

Figure 4.25 shows that the tree aerodynamic effect leads to an increase in OM concentrations mainly in street with trees (up to +29%) and to a decrease in others (up to -6.3%). The characteristic time for OM formation in streets from the biogenic species emitted is too long (Wang et al., 2023) to consider that OM is affected by the tree aerodynamic effect. It is in fact the primary organic aerosols (POAs), emitted by traffic, whose concentrations are increased by the aerodynamic effect of the trees. However, statistically at the city scale, this effect is not significant with an average increase of $+0.6\%$ (fig 4.26). The dry deposition of OM on leaves remains limited (up to -2.5%) and non-significant compared to the other effects, in particular biogenic emissions. The comparison of the BVOC simulation with the reference shows that OM concentrations are increased quite uniformly across Paris city by on average $+2.2\%$ and up to $+13\%$. The increase reaches $+3.8\%$ during the heatwave period.

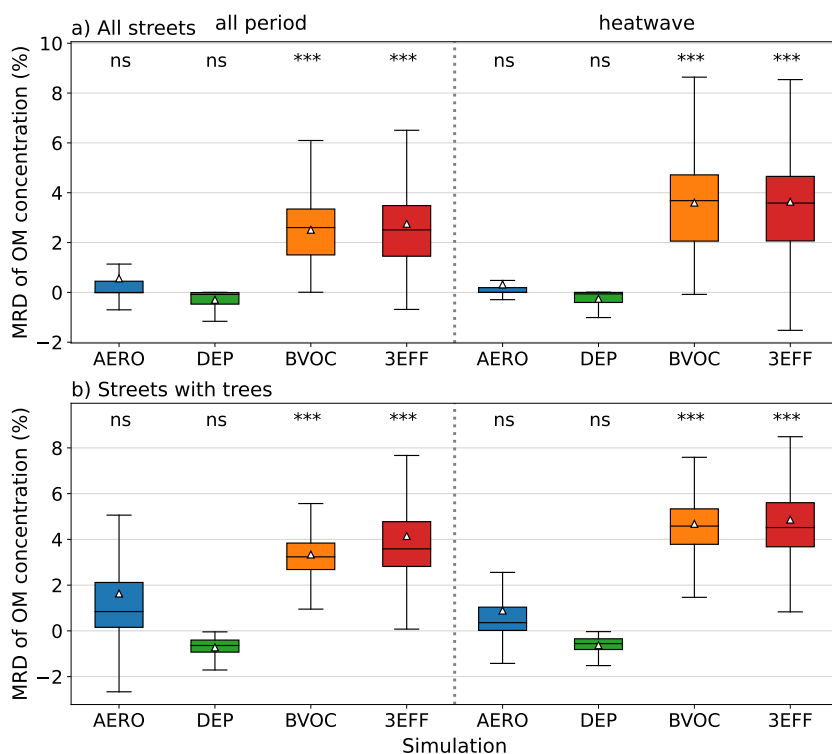


Figure 4.26: Box-plot of the Mean Relative Difference (MRD) of organic matter concentrations in a) all streets, b) streets with trees and c) streets without tree for each simulation. Concentrations are averaged from June 13 to 26, over the whole period (left part), during daytime (middle part) and nighttime (right part). The mean is represented by a white triangle and the result of a T-test between each simulation with trees and the reference simulation is indicated at the top of each box-plot '***': p-value < 0.001, '**': p-value < 0.01, '*': p-value < 0.05 and 'ns' (non-significant): p-value \geq 0.1.

Figure 4.27 compares the observed and simulated OM concentrations at the HdV station (48.85574°N, 2.35191°E). The chemical composition of fine particles (PM_{10}) is measured by an Aerosol Chemical Speciation Monitor (ACSM) in the ambient air. The hourly-average measured concentrations of OM are compared with simulated concentrations in Fig. 4.27, which shows that, both for the unmodified and TX2 emission scenarios, the concentrations of the simulations with all tree effects (solid lines) are slightly higher than the concentrations of the reference simulations (dotted lines). Urban trees contribute significantly to the increase in OM concentrations (on average in the street of the HdV station by 10.6% and 9.5% for TX2). When monoterpene and sesquiterpene emissions are doubled, the simulated concentrations (red lines) compare much better to observations, especially during the concentration peak around the 18th of June. Note that the highly variable concentrations, which are measured at the end of June and beginning of July, are not represented by the model.

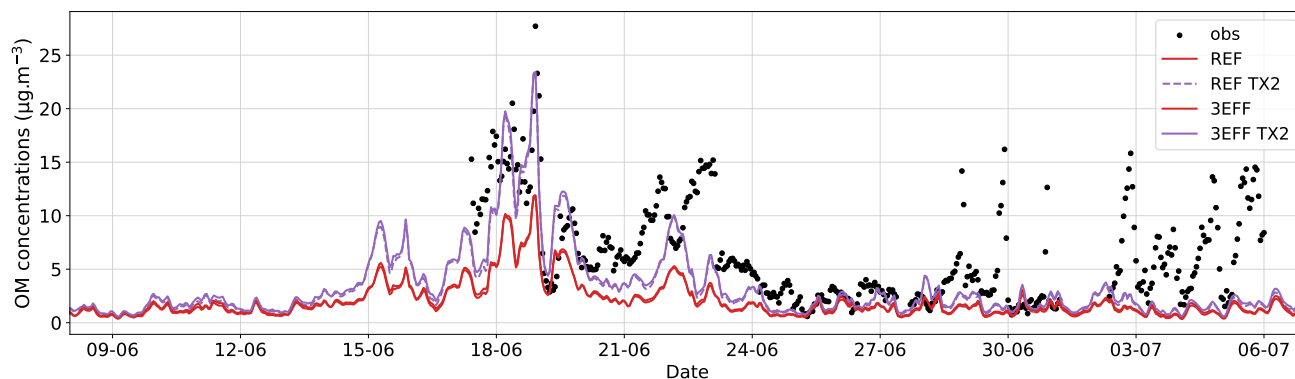


Figure 4.27: Temporal evolution of measured (black dots) and simulated (lines) OM concentrations at Paris HdV station.

The statistical comparison of simulations and observations presented in Table 4.6 shows that the inclusion of urban trees improves the comparison to observations. The best agreement between observed and simulated concentrations is in the TX2 scenario, in particular between June 24 and 27 when monoterpene concentrations compare well to measurements. This suggests that the modeling of terpene concentrations need to be improved to improve the modeling of OM concentrations. As simulated terpene concentrations are very sensitive to urban trees, those need to be better characterized to improve the modeling of OM in summer.

Table 4.6: Comparison of OM concentrations observed and simulated at Paris HdV station with and without urban trees and TX2 scenario. The definition of the statistical indicators is given in Appendix 4.D.

simulation	mean conc.		σ conc.		RMSE $\mu\text{g.m}^{-3}$	NAD -	Bias $\mu\text{g.m}^{-3}$	R -
	obs $\mu\text{g.m}^{-3}$	mod $\mu\text{g.m}^{-3}$	obs $\mu\text{g.m}^{-3}$	mod $\mu\text{g.m}^{-3}$				
REF		1.94		1.62	8.94	0.48	-8.70	0.67
REF TX2	6.45	3.29	4.66	3.12	5.71	0.24	-4.51	0.66
3EFF		2.08		1.64	8.71	0.46	-8.46	0.67
3EFF TX2		3.50		3.17	5.31	0.22	-4.11	0.66

Over the 8-week summer period, the effect of urban trees, and in particular their biogenic emissions, leads to a significant increase of OM concentration. With the TX2 scenario, which gives the best comparison to measurements, the OM concentrations are increased on average by 4.4% in Paris streets, as shown in Fig. 4.28.

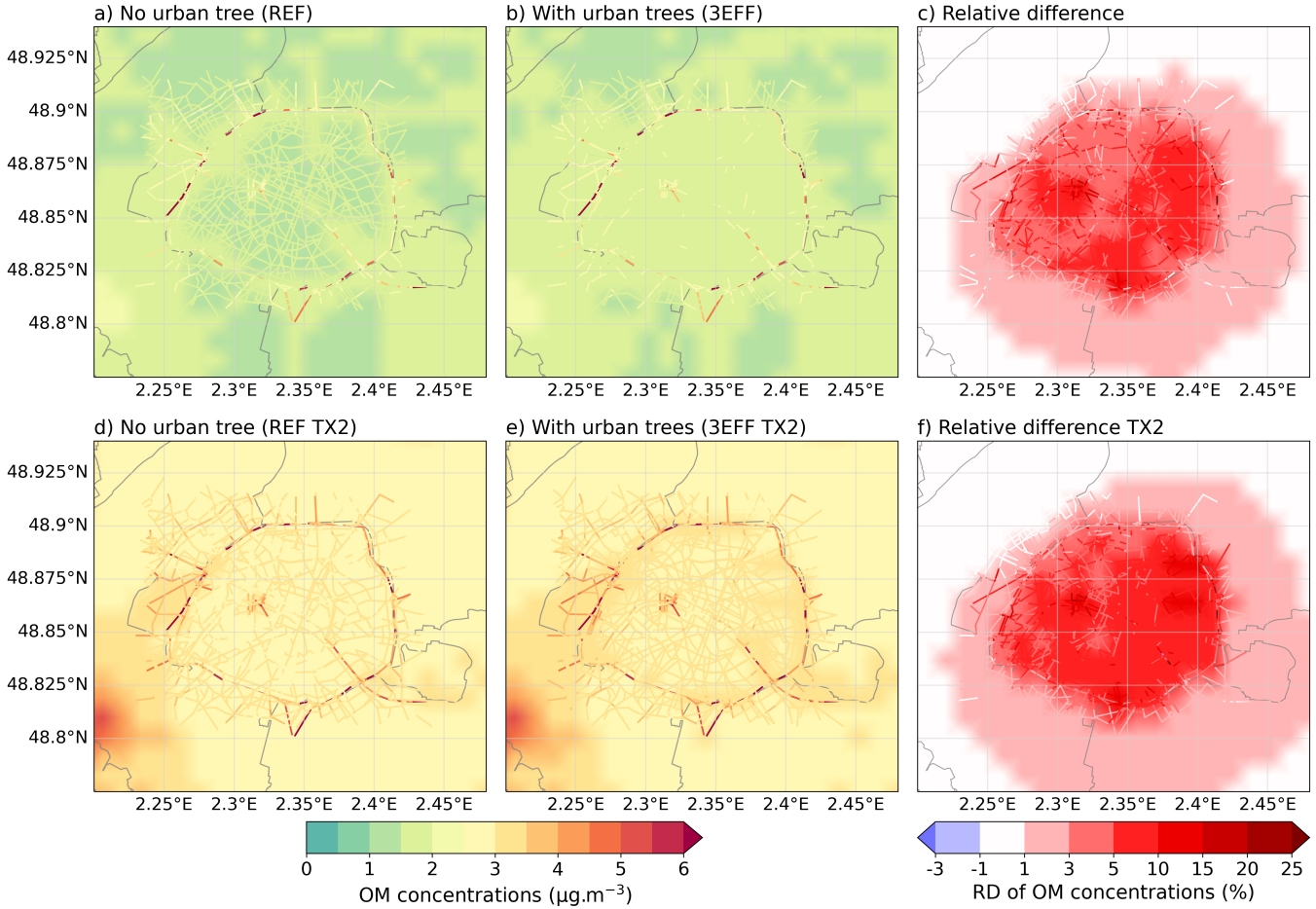


Figure 4.28: Average background and street organic matter (OM) concentrations (06/06 to 31/07/22) simulated with CHIMERE/MUNICH a) without trees (REF) and b) with all tree effects (3EFF) and c) mean relative difference between the two. Panels d), e) and f) show the same results with TX2 scenario.

Although biogenic urban tree emissions strongly influence OM concentrations, they have a limited impact on $PM_{2.5}$ concentrations except in the densely vegetated areas (up to +3%), as shown in Fig. 4.29. The effect of dry deposition on leaves is weak and induces a decrease of $PM_{2.5}$ concentrations by up to -1.6% . The aerodynamic effect of trees induces a large increase in $PM_{2.5}$ concentrations in some streets (up to +22%) and a small decrease in others (up to -5%) (Fig. 4.30). A part of $PM_{2.5}$ are emitted by traffic, so like NO_2 , they are sensitive to the presence of trees in streets and to the emission intensity, which explains the heterogeneity obtained.

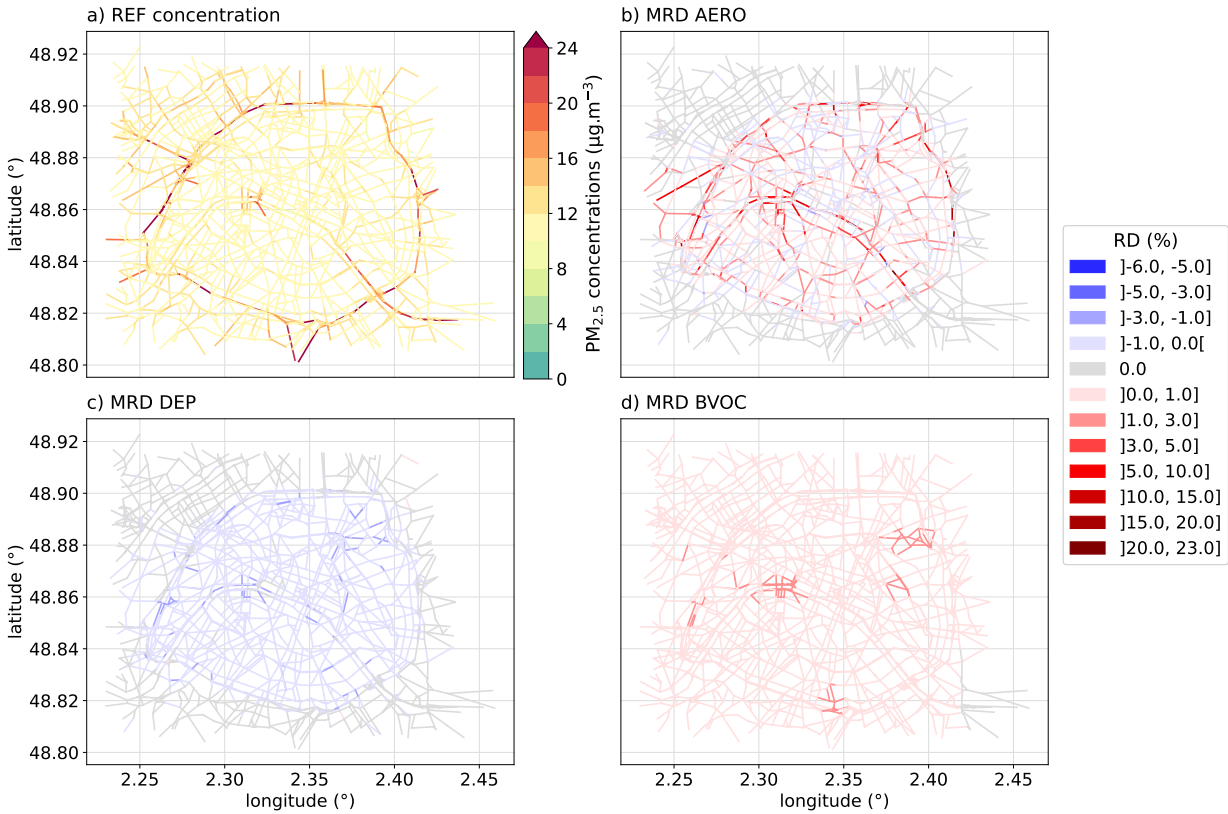


Figure 4.29: a) Average $PM_{2.5}$ concentrations in the reference simulation (REF) and mean relative difference (MRD) of $PM_{2.5}$ concentrations between the simulation b) with tree aerodynamic effect (AERO), c) with dry deposition on leaves (DEP), d) with urban tree biogenic emissions (BVOC) and the REF simulation without trees averaged from June 13 to 26.

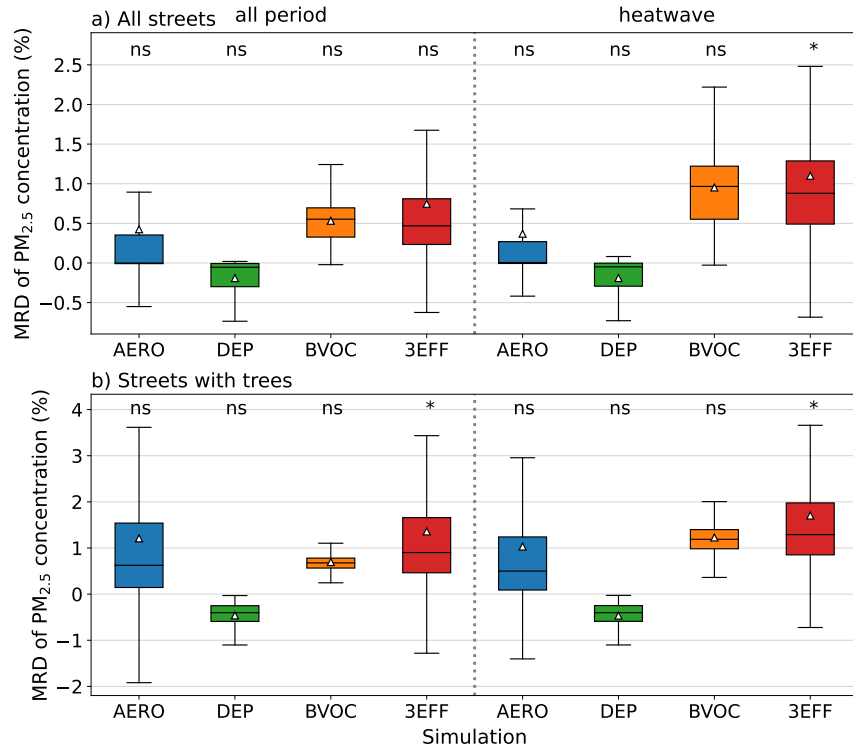


Figure 4.30: Box-plot of the Mean Relative Difference (MRD) of PM_{2.5} concentrations in a) all streets, b) streets with trees and c) streets without tree for each simulation. Concentrations are averaged from June 13 to 26, over the whole period (left part), during daytime (middle part) and nighttime (right part). The mean is represented by a white triangle and the result of a T-test between each simulation with trees and the reference simulation is indicated at the top of each box-plot '***': p-value < 0.001, '**': p-value < 0.01, '*': p-value < 0.05 and 'ns' (non-significant): p-value ≥ 0.1.

Figure 4.31 shows the average global tree effect over the 8 weeks of simulation. The increase in $PM_{2.5}$ due to biogenic emissions is visible locally in the background concentrations over densely vegetated areas (up to +1.6%) and in streets with an increase of +0.8% on average and up to +21.7%. Doubling monoterpene and sesquiterpene emissions (TX2) leads to an increase of $PM_{2.5}$ concentrations of +1.2% on average in all streets.

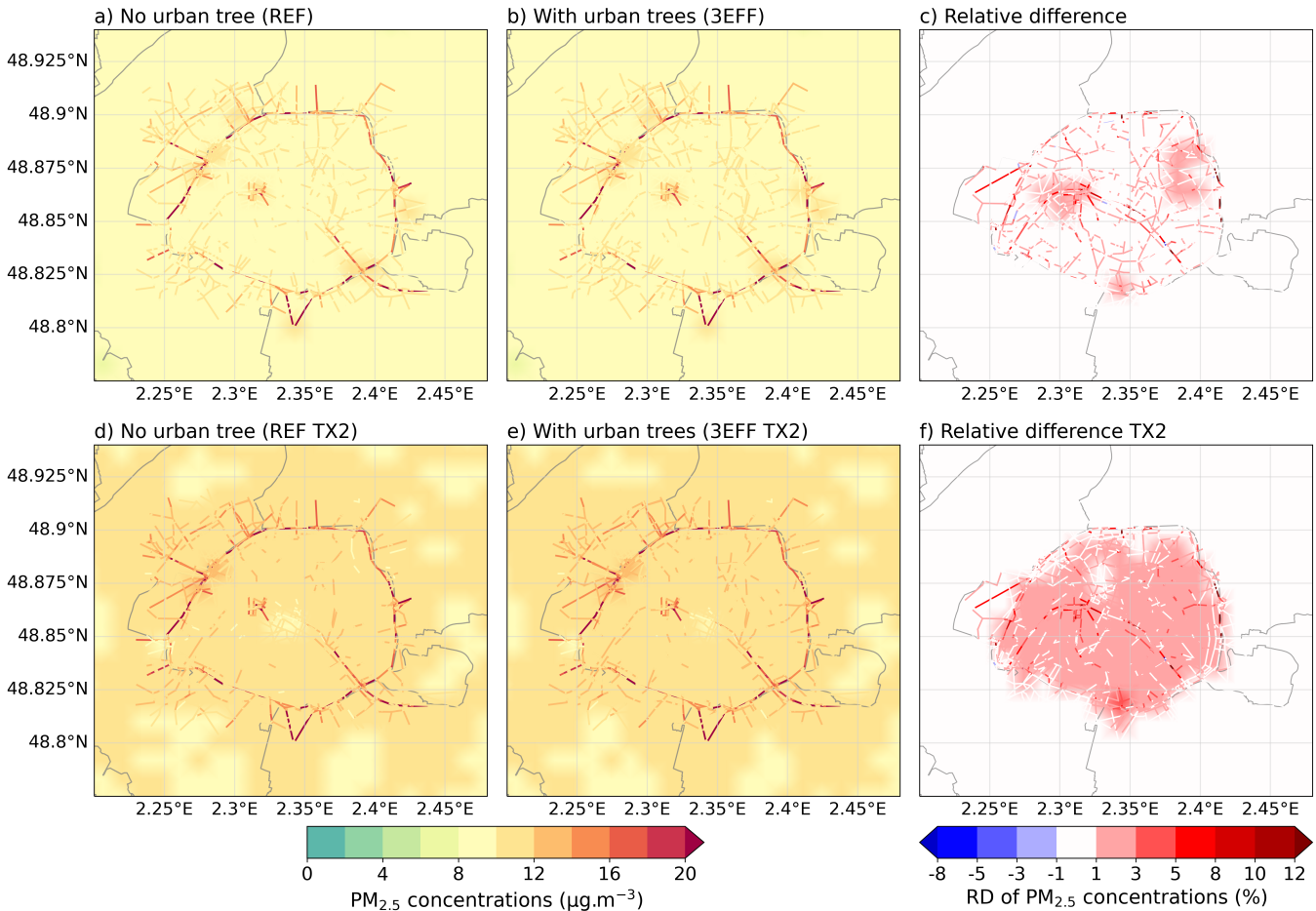


Figure 4.31: Average background and street $PM_{2.5}$ concentrations (06/06 to 31/07/22) simulated with CHIMERE/MUNICH a) without trees (REF) and b) with all tree effects (3EFF) and c) mean relative difference between the two. Panels d), e) and f) show the same results with TX2 scenario.

To summarize, $PM_{2.5}$ concentrations increase because of biogenic emissions from urban trees and in particular monoterpene and sesquiterpene emissions that leads to the formation of OM. In addition, there is an increase in concentrations in streets with trees due to the aerodynamic effect and a small decrease in adjacent streets.

4.4 Conclusion

In the literature, a growing number of studies attempt to quantify the effects of trees on air quality in urban environments. The three main effects of trees, i.e. reduced ventilation (aerodynamic effect), dry deposition on leaves and biogenic emissions are rarely all taken into account over large urban areas (Mircea et al., 2023). This study aims to estimate the urban tree effects on air quality at the street and Paris city scale, which to our knowledge, has never been studied before. Firstly, the three main effects of urban trees on air quality were added to the modeling chain CHIMERE/MUNICH. The tree aerodynamical effect in street canyons has been parameterized based on CFD simulations by Maison et al. (2022b) and is applied here to the city of Paris. The dry deposition of gaseous and particulate species on street and leaf surfaces is computed with a classical resistive approach. The characteristics of each tree are computed from the tree inventory of the municipality of Paris along with urban tree allometric equations (Chapter 3). The BVOC emissions of each tree are estimated with these computed characteristics along with tree species dependent emission factors and activity factors for MEGANv3.2 and Guenther et al. (2012). The trees located in the streets emit biogenic species in the street volume and those outside the streets (in parks, cemeteries etc.) emit in the background.

The simulations show that the dry deposition reduces the concentrations of gas and particles by at most a few percents. This decrease is only slightly significant for ozone in streets with trees. The tree aerodynamic effect affects mainly the species emitted in the street either by traffic or trees. The aerodynamic effect increases with emission intensity and tree LAI. It is significant in streets with high and medium emissions depending on the LAI, and reaches +37% for NO₂. Although ozone is a secondary pollutant, and is therefore not emitted in the street, concentrations are also modified by the aerodynamic effect of trees, because of the increase in NO_x concentrations and titration. The tree aerodynamical effect also impacts, but to a lesser extent, isoprene and monoterpene concentrations emitted in the streets, and OM and PM_{2.5} concentrations through the effect on primary organic aerosols.

As expected, the biogenic emissions from urban trees increase exponentially the concentrations of isoprene and monoterpenes both in the streets and the background. This increase is higher during heatwaves due to higher emissions. Compared with measurements, isoprene concentrations are globally well estimated, but they tend to be overestimated during the heatwave. However, for monoterpenes and sesquiterpenes, the scenario where their emissions are doubled leads to the best correlation between simulated and observed monoterpene concentrations. The urban tree biogenic emissions do not significantly impact NO₂ concentrations and induce a slight increase in O₃ street concentrations of 1% on average over the 14 days and of 2.1% during the 4-day heatwave. The OM concentrations significantly increase because of biogenic emissions (+2.5% on average over the 14 days and +3.5% during the heatwave). This increase is larger when monoterpene and sesquiterpene emissions are doubled, and this scenario gives a better comparison to measurements. This suggests the importance of monoterpenes and sesquiterpenes from urban vegetation in the formation of OM concentrations in summer.

To summarize, this study shows that trees cannot be considered as an effective solution for reducing air pollution via leaf deposition. However, there are large uncertainties in the dry deposition parameterizations used and more measurements of dry-deposition velocities on urban trees at the leaf scale are necessary. The aerodynamical effect locally increases the concentrations of the species

emitted in the street. This intensity depends on tree LAI and chemical species emission, suggesting that the plantation of large trees in streets with heavy traffic should be limited. Finally, the biogenic emissions induce an increase in ozone (mainly due to isoprene and OVOC emissions) and organic matter (also due to monoterpene and sesquiterpene emissions), especially during the heatwave period. It should be remembered, that there is a large uncertainty on the emission factors of BVOCs and they vary with the tree species. Therefore, the impact of urban trees on ozone and particulate concentrations varies greatly from one city to another (Owen et al., 2003; Calfapietra et al., 2013; Ren et al., 2017). More measurements of emission factors specific to urban trees are needed to lower down the uncertainties on tree BVOC emission factors, and in particular terpenes. The impact of biogenic emissions is larger in the background over the city of Paris, and variations in ozone and OM concentrations are rather homogeneous over all streets. It would be interesting to study different tree species planting scenarios to see if certain species can limit these impacts.

Fairly significant assumptions are made in calculating biogenic emissions, notably that leaf surface temperature is equal to air temperature. The solar radiation reaching the leaves is assumed to be equal to the incoming solar radiation above the street, neglecting the effects of reflections between street surfaces and building shading. The overestimation of isoprene concentrations observed could be due to the effect of water stress on trees, which could reduce isoprene emissions, and it is not considered in this chapter. The urban canopy model used in WRF is also relatively simple. Indeed, only a term of anthropogenic sensible heat is added and there is no consideration of all processes affecting the urban climate (dark materials, radiation reflections on buildings etc.). The urban micro-climate representation and the biogenic emissions computation will be refined in the Chapter 5 by coupling MUNICH to the Town Energy Balance Model (TEB) (Masson, 2000) and the soil-plant-atmosphere continuum SPAC (Tuzet et al., 2017).

4.A List of measurement stations

Table 4.7: Location of HdV and Airparif air-quality stations with the species measured and used in this study. All stations are of traffic type.

station address	city/district	location	species measured
Hôtel de Ville (HdV)	PARIS 4eme	48.855752°N, 2.351913°E	NO ₂ , OM, C ₅ H ₈ , MTs
Quai des Célestins	PARIS 4eme	48.852557°N, 2.359963°E	NO ₂
Rue Bonaparte	PARIS 6eme	48.856281°N, 2.334484°E	NO ₂
Avenue des Champs Elysées	PARIS 8eme	48.868608°N, 2.311339°E	NO ₂ , PM ₁₀
Boulevard Haussmann	PARIS 9eme	48.873316°N, 2.330433°E	NO ₂ , PM _{2.5} , PM ₁₀
Boulevard Soutl	PARIS 12eme	48.837948°N, 2.408196°E	NO ₂
Boulevard Périphérique Est	PARIS 12eme	48.838523°N, 2.413070°E	NO ₂ , PM _{2.5} , PM ₁₀ , OM
Place Victor Basch	PARIS 14eme	48.827796°N, 2.327492°E	NO ₂ , PM ₁₀
Boulevard Périphérique Auteuil	PARIS 16eme	48.849938°N, 2.252514°E	NO ₂ , PM _{2.5} , PM ₁₀
Route Nationale 2 Pantin	93500 PANTIN	48.902323°N, 2.390601°E	NO ₂ , PM ₁₀

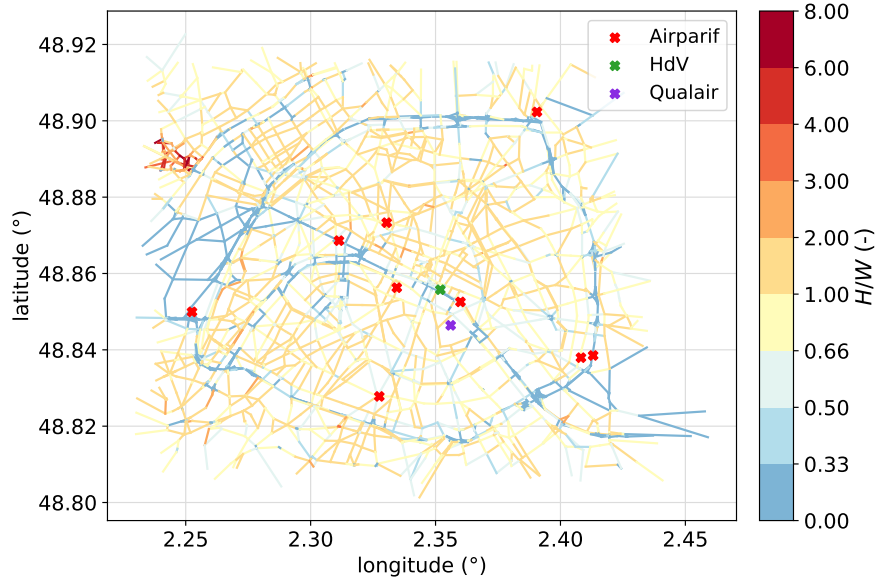


Figure 4.32: Map of the street aspect ratio (H/W) in Paris street network with location of the Airparif and HdV stations and Qualair platform (crosses).

4.B Computation of the dry deposition of gas and aerosols on street and leaf surfaces

4.B.1 Dry deposition of gaseous species

For each street, the dry deposition flux of a gas i on each surface \diamond , $Q_{dep,\diamond}$ (in $\mu\text{g}\cdot\text{s}^{-1}$), is computed as:

$$Q_{dep,w}^i = S_w v_{d,w}^i C_{street}^i, \quad (4.9)$$

$$Q_{dep,g}^i = S_g v_{d,g}^i C_{street}^i, \quad (4.10)$$

$$Q_{dep,t}^i = S_t v_{d,t}^i C_{street}^i, \quad (4.11)$$

where $\diamond = w$ stands for wall, g for ground and t for tree leaves. S_\diamond is the area of each component of the street (m^2), $S_w = 2HL$, $S_s = WL$ and $S_t = LA_s$. C_{street}^i is the average street concentration of the gas i (in $\mu\text{g}\cdot\text{m}^{-3}$). The list of gaseous compounds that can be deposited and their associated model parameters are presented in Table 4.9.

For gases, the deposition velocities $v_{d,\diamond}^i$ ($\text{m}\cdot\text{s}^{-1}$) are calculated as:

$$v_{d,w}^i = \frac{1}{R_{b,w}^i + R_{g,w}^i}, \quad (4.12)$$

$$v_{d,s}^i = \frac{1}{R_{b,s}^i + R_{g,s}^i}, \quad (4.13)$$

$$v_{d,t}^i = \frac{1}{R_{b,t}^i + R_{s,t}^i}, \quad (4.14)$$

with:

$R_{b,\diamond}^i$ the quasi-laminar sublayer resistance, computed from Hicks et al. (1987); Wesely et al. (1977)

$R_{g,\diamond}^i$ the ground or wall surface resistance, computed from Zhang et al. (2002, 2003)

$R_{s,t}^i$ the tree leaves surface resistance that includes the stomatal R_{sto}^i (Wesely, 1989), the cuticular

R_{cut}^i (Zhang et al., 2003) and the mesophyll R_{mes}^i (Wesely, 1989) resistances:

$$\frac{1}{R_{s,t}^i} = \frac{1}{R_{sto}^i + R_{mes}^i} + \frac{1}{R_{cut}^i}. \quad (4.15)$$

All the resistances are in $\text{s}\cdot\text{m}^{-1}$ and the corresponding resistive scheme is shown in Fig. 4.33. As the street concentration is considered homogeneous in the street, no aerodynamical resistance is included inside the street. The aerodynamical resistance between the street and the background (see Fig. 4.33) corresponds to the turbulent transfer between the background and the street, which is computed by the vertical transfer coefficient q_{vert} (sections 2.2 and 2.3). The computation of each resistance is detailed in the following paragraphs.

- Quasi-laminar sublayer resistance

The transfer resistance in the boundary layer above the street or tree leaf surfaces, $R_{b,\diamond}^i$, is computed from Hicks et al. (1987) as:

$$R_{b,\diamond}^i = \frac{1}{\kappa u_{*,\diamond}} \left(\frac{S_c^i}{P_r} \right)^p, \quad (4.16)$$

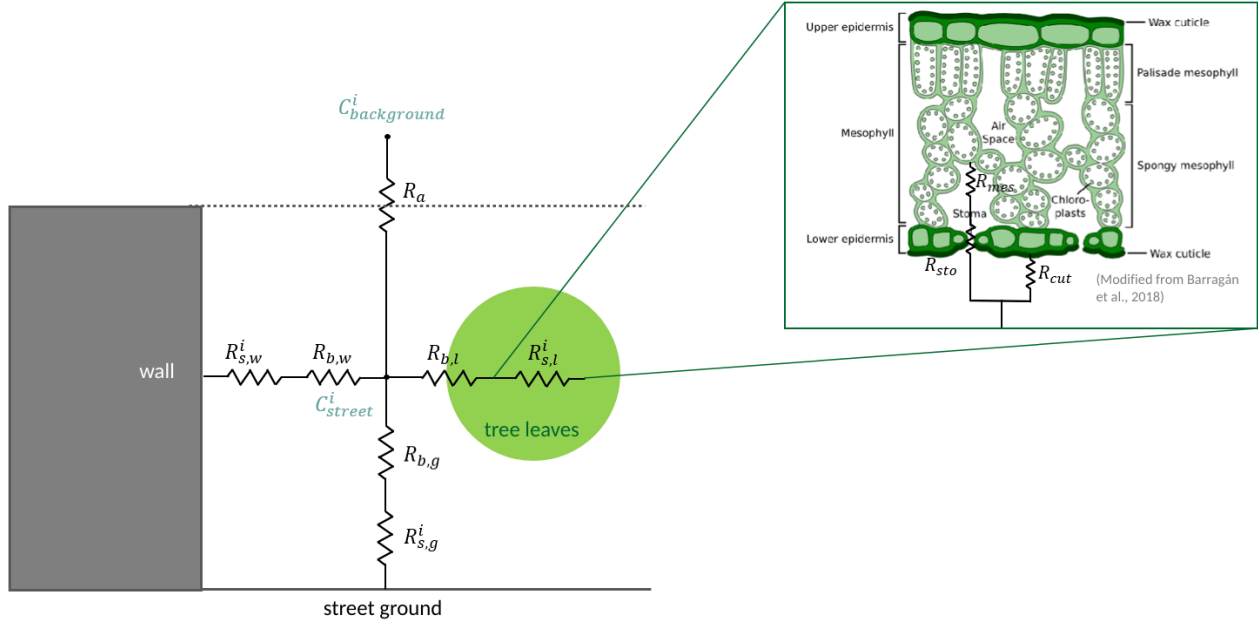


Figure 4.33: Diagram of the resistive scheme used to compute dry deposition of gas and aerosols on street and tree leaves surfaces. Leaf scheme modified from Barragán et al. (2018).

where S_c^i is the Schmidt number and P_r is the Prandtl number for air (Wesely et al., 1977):

$$S_c^i = \frac{\nu}{D_i}, \quad (4.17)$$

$$P_r = 0.74, \quad (4.18)$$

where ν is the kinematic viscosity of air ($\nu = 0.15 \text{ cm}^2 \cdot \text{s}^{-1}$) and D_i is the molecular diffusivity of the gas i . p is equal to $\frac{2}{3}$ (Baldocchi et al., 1987) and $u_{*,\diamond}$ is the friction velocity over the surface and is estimated from the wind speed profile parameterized in the sections 2.2 and 2.3 (see Section 4.B.3 for the detailed calculation).

- Ground or wall surface resistance

The surface resistance of the street ground and walls, R_g^i , is estimated for each compound according to SO_2 and O_3 surface resistances ($R_g^{\text{SO}_2}$ and $R_g^{\text{O}_3}$ in $\text{s} \cdot \text{m}^{-1}$) from Zhang et al. (2002, 2003). $R_g^{\text{SO}_2}$ is dependent on surface wetness (dew deposition or wet surface after rain). As these processes are not taken into account in the model, dry wall and ground surfaces are considered here. For dry surfaces $R_g^{\text{SO}_2} = 300$ and $R_g^{\text{O}_3} = 500 \text{ s} \cdot \text{m}^{-1}$. The wall and ground surface resistances are considered equal and are computed for a gas i as:

$$R_g^i = \left(\frac{\alpha_i}{R_g^{\text{SO}_2}} + \frac{\beta_i}{R_g^{\text{O}_3}} \right)^{-1}, \quad (4.19)$$

where α_i and β_i are dimensionless coefficients (Table 4.9). When the air temperature (T_{air} in $^\circ\text{C}$) is low, the following correction is applied:

$$\text{If } T_{air} < -1^\circ\text{C}, R_g^i(T_{air}) = R_g^i \exp(-0.2(1 + T_{air})). \quad (4.20)$$

- Cuticular resistance

The cuticle is the waxy outer layer that covers and protects the leaf epidermis. It is impermeable to gases, which cannot pass through it but can be deposited on it. The cuticular resistance of a gaseous compound i , R_{cut}^i , is computed depending on SO_2 and O_3 resistances based on Zhang et al. (2003) as:

$$R_{cut}^i = \left(\frac{\alpha_i}{R_{cut}^{SO_2}} + \frac{\beta_i}{R_{cut}^{O_3}} \right)^{-1}, \quad (4.21)$$

where $R_{cut}^{O_3}$ and $R_{cut}^{SO_2}$ are computed:

$$R_{cut}^x = \frac{R_{cut_{d0}}^x}{\exp(0.03RH) LAI^{1/4} u_{*,t}} \quad \text{if dry surface.} \quad (4.22)$$

LAI is the tree Leaf Area Index ($m_{leaves}^2 \cdot m_{sol}^{-2}$) and RH is the air relative humidity (-). x stands for SO_2 or O_3 and $u_{*,t}$ is the friction velocity at tree crown level (computed in Section 4.B.3). $R_{cut_d}^{SO_2}$ and $R_{cut_d}^{O_3}$ depend on the tree type and are listed in the Table 4.8 for dry surfaces. A correction is applied when the air temperature (T_{air} in $^{\circ}C$) is low:

$$\text{If } T_{air} < -1^{\circ}C, R_{cut}^i(T_{air}) = R_{cut}^i * \exp(-0.2(T_{air} + 1)). \quad (4.23)$$

- Stomatal resistance

Depending on light and meteorological (temperature, humidity and wind) conditions, stomata, that are small pore located on the leaves, open to allow gas exchange necessary for photosynthesis. They give access to a maze of gaps in which air is saturated with water. Other gases than H_2O , O_2 and CO_2 can enter ; and the stomatal resistance for a compound i , R_{sto}^i , is computed from the stomatal resistance for water vapor ($R_{sto}^{H_2O}$) and the compound (D_i) and water vapor (D_{H_2O}) molecular diffusivities ($cm^2 \cdot s^{-1}$) as (Wesely, 1989):

$$R_{sto}^i = R_{sto}^{H_2O} \frac{D_{H_2O}}{D_i}. \quad (4.24)$$

$R_{sto}^{H_2O}$ is calculated:

$$R_{sto}^{H_2O} = R_{sto_{min}}^{H_2O} (1 + (200(G + 0.1)^{-1})^2)(400(T_s(40 - T_s))^{-1}), \quad (4.25)$$

where $R_{sto_{min}}^{H_2O}$ is the minimal stomatal resistance for water vapor, that depends on tree species (Table 4.8) in $s \cdot m^{-1}$, G the downwards solar radiation in $W \cdot m^{-2}$, and T_s is the air temperature near the leaves surface (in $^{\circ}C$). In MUNICH, this temperature is approximated by the air temperature, so $T_s = T_{air}$. If $T_s > 40^{\circ}C$, stomata are closed and a high value of R_{sto}^i is fixed.

- Mesophyll resistance

The gas that enter in the leaf through the stomata can be deposited on the mesophyll tissues. The mesophyll resistance, R_{mes}^i , is computed from Wesely (1989) as:

$$R_{mes}^i = \left(\frac{H^{*i}}{3000} + 100 f_0^i \right)^{-1}, \quad (4.26)$$

where H^{*i} is the Henry constant and f_0^i is the reactivity factor (Table 4.9). These coefficients depend on compound species and take into account the compound solubility and reactivity.

Table 4.8: List of resistance values used to computed dry deposition of gas on dry tree leaves according to tree type (s.m^{-1}) (Zhang et al., 2003).

Tree type	$R_{cut_{d0}}^{SO_2}$	$R_{cut_{d0}}^{O_3}$	$R_{stom_{in}}^{H_2O}$
evergreen needleleaf trees	2000	4000	250
evergreen broadleaf trees	2500	6000	150
deciduous needleleaf trees	2000	4000	250
deciduous broadleaf trees	2500	6000	150
mixed broadleaf and needleleaf trees	2500	6000	250

Table 4.9: List of gaseous species that are deposited on street and tree leaf surfaces with associated model parameters.

gas species	D	α	β	H^*	f_0
CO	0.18	0.01	0.0	10^3	0.0
NH3	0.20	1.0	0.0	62.0	0.0
NO2	0.14	0.0	0.8	$1.2 \cdot 10^{-2}$	0.1
O3	0.14	0.0	1.0	$1.14 \cdot 10^{-2}$	1.0
H2O2	0.16	1.0	1.0	$1.02 \cdot 10^5$	1.0
HNO3	0.12	10.0	10.0	$2.1 \cdot 10^5$	0.0
HONO	0.14	2.0	2.0	49.0	0.1
NO	0.17	0.0	0.0	$1.9 \cdot 10^{-3}$	0.0
PAN	0.08	0.0	0.6	5.0	0.1
SO2	0.12	1.0	0.0	1.23	0.0
HCL	0.14	1.0	0.0	1.10	-
POAIP	0.0634	0.0	0.05	$1.6 \cdot 10^5$	0.1
POAmP	0.0634	0.0	0.05	$1.6 \cdot 10^5$	0.1
POAhP	0.0634	0.0	0.05	$1.6 \cdot 10^5$	0.1

4.B.2 Dry deposition of aerosols

As for gases, the dry deposition flux of a particle j on each surface \diamond , $Q_{dep,\diamond}$, is computed as:

$$Q_{dep,w}^j = S_w v_{d,w}^j C_{street}^j, \quad (4.27)$$

$$Q_{dep,g}^j = S_g v_{d,g}^j C_{street}^j, \quad (4.28)$$

$$Q_{dep,t}^j = S_t v_{d,t}^j C_{street}^j, \quad (4.29)$$

where $\diamond = w$ stands for wall, g for ground and t for tree.

The deposition velocities are calculated from the sedimentation velocity (v_s^j in m.s^{-1}) and the surface resistance ($R_{s_\diamond}^j$ in s.m^{-1}):

- For the street ground and tree leaves (Venkatram and Pleim, 1999):

$$v_{d,\diamond}^j = \frac{v_s^j}{1 - \exp(-v_s^j \times R_{s_\diamond}^j)}. \quad (4.30)$$

- For the walls, the sedimentation velocity is not considered:

$$v_{d,w}^j = \frac{1}{R_{s_w}^j}. \quad (4.31)$$

The sedimentation velocity calculation is detailed in Appendix 4.B.2 and the surface resistance is calculated from the friction velocity near the surface, $u_{*,\diamond}$ (in m.s^{-1}) and from four dimensionless coefficients that each represent a different physical process according to the Zhang et al. (2001) parameterization:

$$R_{s_\diamond}^j = \frac{1}{\varepsilon_0 u_{*,\diamond} (E_{im_\diamond}^j + E_{in_\diamond}^j + E_{b_\diamond}^j) R_{r_\diamond}^j}, \quad (4.32)$$

where $\varepsilon_0 = 3$ for all surface type. $E_{im_\diamond}^j$ is the impaction efficiency coefficient, $E_{in_\diamond}^j$ the interception efficiency coefficient, $E_{b_\diamond}^j$ the Brownian diffusion efficiency coefficient. A $R_{r_\diamond}^j$ coefficient is added to account for the particle rebound. The computation of each coefficient is developed in the following paragraphs. The expression of these coefficients is the same for street ground, walls and tree leaves, but some of the parameters listed in Table 4.10 differ.

- Impaction efficiency coefficient

The impaction efficiency coefficient of a particle j , $E_{im_\diamond}^j$, is expressed as:

$$E_{im_\diamond}^j = \left(\frac{St_{j_\diamond}}{\alpha_\diamond + St_{j_\diamond}} \right)^\beta, \quad (4.33)$$

where β is a dimensionless constant equal to 2.0 for all surfaces, α_\diamond is a dimensionless constant depending on surface type (Table 4.10) and St_{j_\diamond} is the Stokes number (-) computed depending of the characteristic radius of the collection surface, A_\diamond (in m) (Table 4.10), as:

$$St_{j_\diamond} = \frac{v_s^j u_{*,\diamond}^2}{g \nu} \quad \text{if } A_\diamond = 0 \text{ (smooth surface),} \quad (4.34)$$

$$St_{j_\diamond} = \frac{v_s^j u_{*,\diamond}}{g A_\diamond} \quad \text{otherwise (rough surface).} \quad (4.35)$$

where ν is the kinematic viscosity of air here in $\text{m}^2.\text{s}^{-1}$ and $u_{*,\diamond}$ is the friction velocity near the surface in $\text{m}.\text{s}^{-1}$ (Section 4.B.3).

- Interception efficiency coefficient

The interception efficiency coefficient of a particle j , $E_{in_\diamond}^j$, is calculated as:

$$E_{in_\diamond}^j = 0, \text{ if } A_\diamond = 0 \quad (4.36)$$

$$E_{in_\diamond}^j = \frac{1}{2} \left(\frac{d_j}{A_\diamond} \right)^2, \text{ otherwise} \quad (4.37)$$

where d_j is the particle diameter (m).

- Brownian diffusion efficiency coefficient

The Brownian diffusion efficiency coefficient of a particle j , $E_{b_\diamond}^j$, is expressed as:

$$E_{b_\diamond}^j = Sc_{j_\diamond}^{-\gamma_\diamond}. \quad (4.38)$$

- Rebound coefficient

The rebound coefficient of a particle j , $R_{r_\diamond}^j$, is computed depending on the Stokes number as:

$$R_{r_\diamond}^j = \exp \left(-2\sqrt{St_{j_\diamond}} \right). \quad (4.39)$$

- Sedimentation velocity

Both for street ground and tree leaves, the sedimentation velocity is expressed as:

$$v_s^j = \frac{\rho_j d_j^2 g C u_j}{18\mu}, \quad (4.40)$$

with:

ρ_j and d_j the particle density ($\text{kg}.\text{m}^{-3}$) and diameter (m), $g = 9.81 \text{ m}.\text{s}^{-2}$ gravity acceleration, μ dynamic viscosity of air ($\text{kg}.\text{m}^{-1}.\text{s}^{-1}$) and $C u_j$ the Cunningham number (-):

$$C u_j = 1 + \frac{2\lambda}{d_j} \left(1.257 + 0.4 \exp \left(-0.55 \frac{d_j}{\lambda} \right) \right), \quad (4.41)$$

with λ the mean free path in air (m):

$$\lambda = 2 \frac{\mu}{P_{air}} \left(\frac{8}{\pi R_{air} T_{air}} \right)^{-0.5}. \quad (4.42)$$

T_{air} and P_{air} are the air temperature (K) and pressure (Pa) and $R_{air} = 287.05 \text{ J}.\text{K}^{-1}.\text{kg}^{-1}$ is the specific constant of the dry air.

Table 4.10: List of resistance values used to computed dry deposition of aerosols on tree leaves according to tree type (Zhang et al., 2001).

Land-use category	A	α	γ
Unit	m	-	-
urban	0.01	1.5	0.56
evergreen needleleaf trees	0.002	1.0	0.56
evergreen broadleaf trees	0.005	0.6	0.58
deciduous needleleaf trees	0.002	1.1	0.56
deciduous broadleaf trees	0.005	0.8	0.56
mixed broadleaf and needleleaf trees	0.005	0.8	0.56

4.B.3 Computation of the surface friction velocity

To compute the deposition fluxes, the friction velocity near street surfaces (street ground, walls and tree leaves) needs to be estimated. Indeed, friction velocity is an important parameter which influences the deposition of both gas and aerosols on the different street surfaces (see equations in Appendices 4.B.1 and 4.B.2). To be consistent, the friction velocities near the different surfaces are estimated based on the same parameterizations developed in the sections 2.2 and 2.3.

In the street, the friction velocity vertical profile is expressed from the turbulent flux τ which is the product of the eddy diffusivity coefficient, K , and the derivation of the horizontal wind speed $\frac{\partial U}{\partial z}$:

$$\tau(z) = K(z) \frac{\partial U(z)}{\partial z} = u_*(z)^2. \quad (4.43)$$

Knowing $K(z)$ and $\frac{\partial U(z)}{\partial z}$, a vertical profile can be calculated. According to the parameterizations developed in sections 2.2 and 2.3, $K(z)$ is computed from the mixing length profile $l_m(z)$ and from the friction velocity above the urban canopy u_{*c} :

$$K(z) = u_{*c} l_m(z) \quad \text{with} \quad l_m(z) = \kappa z s_H. \quad (4.44)$$

Equations (4.43) and (4.44) give:

$$u_{*c} \kappa z s_H \frac{\partial U}{\partial z} = u_*(z)^2, \quad (4.45)$$

and the vertical profile of the friction velocity in the street is computed as:

$$u_*(z) = \sqrt{u_{*c} \kappa z s_H \frac{\partial U}{\partial z}}, \quad (4.46)$$

$$\text{with} \quad \frac{\partial U}{\partial z} = \frac{g(z)}{2z} [C_1 I_1(g(z)) - C_2 K_1(g(z))], \quad (4.47)$$

where g is a function of z and the canopy density, C_1 and C_2 are dimensionless integration coefficients, I_1 and K_1 are the first and second type modified Bessel functions of order 1 as detailed in sections 2.2 and 2.3 and in Wang (2012, 2014). For walls and street ground, the friction velocity is computed at $z = z_{0s}$, where z_{0s} is the surface roughness length (m). For tree crown, it is computed at $z = h$, where h is the height of the middle of the tree crown, computed from the top tree height and trunk height as $h = h_{tk} + \frac{h_{max} - h_{tk}}{2}$ (see Chapter 5). Note that the friction velocity profile continuity is ensured at the building height altitude, i.e. at $z = H$, $u_*(H) = u_{*c}$.

4.C Impact on tree aerodynamical effect on isoprene and monoterpene emissions in the street

To assess the impact of the aerodynamic effect on the biogenic isoprene emitted in the streets, the MRD between the simulations 3EFF and BVOC, which quantifies the aerodynamic effect considering isoprene emissions from both traffic and trees, is compared to the MRD between the simulations AERO and REF, which quantifies the aerodynamic effect considering only isoprene emissions from traffic, in Table 4.11. It shows that the minimum of MRD is lower and the average is higher when isoprene BVOC emissions are taken into account, corresponding to higher aerodynamic effect.

Table 4.11: Comparison of the minimum, average and maximum mean relative difference (MRD) of isoprene concentrations in the street network due to the tree aerodynamical effect (AERO) without (left column) and with (right column) BVOC emissions.

	MRD AERO traffic emissions only	MRD AERO traffic + BVOC emissions
min	-11.0	-23.0
mean	0.5	1.8
max	22.8	55.7

As for isoprene, the aerodynamical effect of trees is higher when monoterpene biogenic emissions from trees are taken into account (Table 4.12). In the homogeneous version of MUNICH used here, all the emissions are diluted in the street volume. Therefore, the tree aerodynamical effect limits in the same way the dispersion of the compounds emitted by traffic or by the trees. To better take into account the vertical gradients of concentrations inside the street, a discretized version of MUNICH, in which the street is divided into 3 sub-volumes, should be used (Sarica et al., 2023). In this more realistic version, traffic emissions are added in the grid close to the ground, and it would be desirable to add the tree biogenic emissions at the vertical level of the tree crowns.

Table 4.12: Comparison of the minimum, average and maximum mean relative difference (MRD) of monoterpene concentrations due to the tree aerodynamical effect (AERO) without and with BVOC emissions.

	MRD AERO traffic emissions only	MRD AERO traffic + BVOC emissions
min	-15.3	-27.2
mean	-0.2	2.7
max	11.2	56.6

4.D Definition of the statistical indicators

To compare the simulation results to measured data, classical statistical indicators are computed where obs_i and sim_i are respectively the hourly observed and simulated concentrations. n is the total number of concentrations and \overline{obs} and \overline{sim} are the average observed and simulated concentrations.

- Root Mean Square Error (same unit as the concentration):

$$RMSE = \sqrt{\frac{1}{n} \sum_{i=1}^n (obs_i - sim_i)^2}. \quad (4.48)$$

- Normalized Absolute Difference (dimensionless):

$$NAD = \frac{\sum_{i=1}^n |obs_i - sim_i|}{\sum_{i=1}^n obs_i + \sum_{i=1}^n sim_i}. \quad (4.49)$$

- Bias (same unit as the concentration):

$$Bias = \frac{1}{n} \sum_{i=1}^n (sim_i - obs_i). \quad (4.50)$$

- Correlation coefficient (dimensionless):

$$R = \frac{\sum_{i=1}^n [(sim_i - \overline{sim})(obs_i - \overline{obs})]}{\sqrt{\sum_{i=1}^n (sim_i - \overline{sim})^2 \sum_{i=1}^n (obs_i - \overline{obs})^2}}. \quad (4.51)$$

To compare the simulations with trees to the reference simulation without tree, the Mean Relative Difference (MRD in %) between two simulations is calculated as:

$$MRD = 100 \times \sum_{i=1}^n \left(\frac{sim_{ti} - ref_i}{sim_{ti}} \right), \quad (4.52)$$

where ref_i and sim_{ti} are respectively the hourly concentrations simulated without and with trees and n is the total number of concentrations.

The average (\bar{x}) and standard deviation (σ) of observed or simulated hourly concentrations x_i are calculated as (with same unit as the concentration):

$$\bar{x} = \frac{1}{n} \sum_{i=1}^n x_i \quad \text{and} \quad \sigma = \sqrt{\frac{1}{n} \sum_{i=1}^n (x_i - \bar{x})^2}. \quad (4.53)$$

Chapter 5

Towards a finer representation of the urban micro-climate and BVOC emissions in air-quality models.

Contents

5.1	Introduction	178
5.2	Materials & Methods	178
5.2.1	Presentation of TEB-Veg	178
5.2.2	Presentation of SPAC	179
5.2.3	TEB-SPAC coupling	181
5.2.4	TEB-SPAC-MUNICH coupling	183
5.2.5	Simulation set-up and input data	187
5.3	Results	197
5.3.1	Comparison of simulated and observed meteorological fields in HdV	197
5.3.2	Analysis of the tree energetic and hydraulic functioning	199
5.3.3	Impacts of the MUNICH-TEB-SPAC coupling on the modeled urban micro-climate	205
5.3.4	Impacts of the urban micro-climate on street concentrations	212
5.3.5	Impacts of the urban micro-climate and tree water stress simulated by TEB-SPAC on BVOC emissions	217
5.4	Conclusion	222

5.1 Introduction

By intercepting radiation and evapotranspiration, urban trees help to reduce temperatures and improve thermal comfort. They appear to be an effective solution for mitigating the urban heat island. For those reasons, the impacts of the urban vegetation, and more specifically of trees, on city climate is increasingly being studied. Few studies take into account the major impacts of trees on both climate and air quality, and even fewer consider the impact of trees over an entire city.

On the other hand, local urban air-quality models take mesoscale meteorological data as input. They recalculate pollutant transfer velocities at a street scale, but do not compute a street-specific energy balance to estimate the street's own micro-meteorology. However, the interactions between air quality and meteorology are close at various levels. First, chemical reactions are dependent on temperature, humidity and pressure. A change in the urban climate can therefore lead to changes in chemical kinetics and aerosol dynamics and hence in concentrations. Then, the impacts of trees on the street micro-meteo could also impact the concentrations. Above all, BVOC emissions, that are computed with the weather data of the mesoscale model, should be impacted if the leaf temperature and the effective radiation received by the tree inside the street are considered. Besides, with models that compute urban soil and vegetation water budget, it is possible to add the effect of water stress on isoprene emissions. Then, the shade created by buildings (and trees) modifies not only the temperatures but can also affect photolysis in the street. Finally, a more detailed computation of the fluxes between the surface and the atmosphere could have a significant effect on pollutant concentrations. In fact, pollutant concentrations in the street are very sensitive to atmospheric stability which determines the level of turbulence and hence the transport of pollutants. A better estimate of temperatures and latent and sensible heat fluxes should improve the estimation of the street concentrations. The objectives of this study are multiple. First, by coupling the air-quality model MUNICH and the urban energy balance model TEB, we will try to improve the representation of the street micro-meteorology and its impact on pollutant concentrations in MUNICH, initially without trees, and then by adding trees. TEB is also coupled to the soil-plant-atmosphere model (SPAC) to better simulate the water transfers in the trees and estimate tree water stress. The energetic and hydraulic functioning of urban trees during the summer 2022 will be analyzed and simulated by TEB-SPAC, whose output fields are used as forcing data for MUNICH simulations of air quality. The biogenic emissions, previously calculated with the air temperature and incoming solar radiation above the street, are estimated more accurately by taking the leaf surface temperature and the effective radiation received by the leaves (accounting for reflections and shade effects). Finally, the effect of tree water stress will be added in the isoprene emissions computation.

5.2 Materials & Methods

5.2.1 Presentation of TEB-Veg

In mesoscale atmospheric models, the impacts of cities on the boundary layer can be represented with varying degrees of complexity, from simple parameterizations of rough bare soil to more complex multi-layer urban modules such as [Martilli et al. \(2002\)](#). The Town Energy Balance (TEB) scheme aims to simulate the local-scale urban surface energy balance by resolving the energy budget with heat and water exchanges for each surface (road, wall and roof) ([Masson, 2000](#); [Lemonsu and Masson, 2002](#)). It is originally a single-layer module where the urban canopy is represented by an

isotropic array of street canyons. To account for the vertical effects of buildings, a surface boundary layer (SBL) scheme was developed by including a drag force approach (Hamdi and Masson, 2008; Masson and Seity, 2009). It allows the model to simulate vertical profiles of momentum, turbulent kinetic energy, air temperature, humidity and pressure in and above the street canyon. Then, the effect of vegetation in the street was added in the model by coupling TEB to the Interaction between Soil Biosphere and Atmosphere (ISBA) model (Noilhan and Planton, 1989). A fraction of vegetation was firstly added on the same urban tile but located outside the street canyon without direct micro-scale interactions (Lemonsu et al., 2004). Then Lemonsu et al. (2012) developed a model version (TEB-Veg) in which the vegetation (lawn) is directly included inside the street canyon. It allows a more accurate representation of the street canyon, its interactions with vegetation (computation of shadow effect in the canyon and turbulent fluxes) and the micro-climatic fields. Then, a module was developed in TEB to simulate the hydrological and energetic impacts of green roofs (De Munck et al., 2013). Recently, TEB has been improved to include street trees and their impacts on radiative transfers (Redon et al., 2017) and turbulent fluxes (Redon et al., 2020). The tree cover is represented by its horizontal coverage fraction in the street and its vertical thickness between the tree trunk and crown heights. The Leaf Area Index (LAI) is prescribed as input data and tree crowns are considered to have a rectangular shape, so the Leaf Area Density (LAD) is constant over the crown thickness. Tree foliage can intercept, reflect, transmit, and absorb incoming radiation and participates in radiation inter-reflections so it can shade the wall, road, soil and low vegetation. The tree foliage also modifies the vertical profiles of momentum, turbulent kinetic energy, air temperature and humidity in the urban canopy. The fluxes are computed following the big-leaf approach used in ISBA, so homogeneous fluxes are computed by square meters of foliage and there is no interaction between the leaves within the tree cover (i.e. shade effects). The SBL scheme allows to reallocate the turbulent fluxes computed with the big leaf approach in ISBA at the crown layer height. Finally, the hydrological processes taking place in the urban subsoil are represented with the TEB-hydro scheme (Stavropoulos-Laffaille et al., 2018; Bernard, 2021), that allows to take into account, among other things, the surface runoff going from the roofs and roads into the soil compartment. TEB and ISBA are both integrated in the externalized land surface modeling system, SURFEX, developed by Météo-France (Masson et al., 2013) and can be used offline with forcing data or coupled online with atmospheric models such as Meso-NH (Lac et al., 2018) or AROME (Seity et al., 2011).

5.2.2 Presentation of SPAC

The soil-plant-atmosphere continuum (SPAC) model is a process-based model aiming to simulate plant energy budget and water balance (Tuzet et al., 2003; Tuzet and Perrier, 2008; Tuzet et al., 2017). It couples stomatal conductance, water transport through the soil and the plant, and leaf energy balance. Stomatal conductance is regulated by photosynthesis, inter-cellular carbon dioxide (CO₂) concentration and leaf water status and is computed with a modified Leuning et al. (1995) model. Stomatal opening is directly linked to the soil water availability via the different hydraulic potentials of plants, allowing a fine representation of the impact of water stress on transpiration. An empirical logistic function is used to describe the sensitivity of stomata to leaf hydraulic potential. The model also includes a plant storage compartment with a capacitance discharge and recharge (Tuzet and Perrier, 2008). It was applied to simulate the hydraulic functioning of a forest beech stand (Tuzet et al., 2017) under various soil water conditions in Eastern France and was adapted to model the hydraulic functioning of urban linden trees in a park of Strasbourg, France (Maison,

2019). The tree evapotranspiration depends on the potential transpiration (function of the tree energy balance), stomatal regulation, tree water status and radial diffusion of water from the soil to the roots.

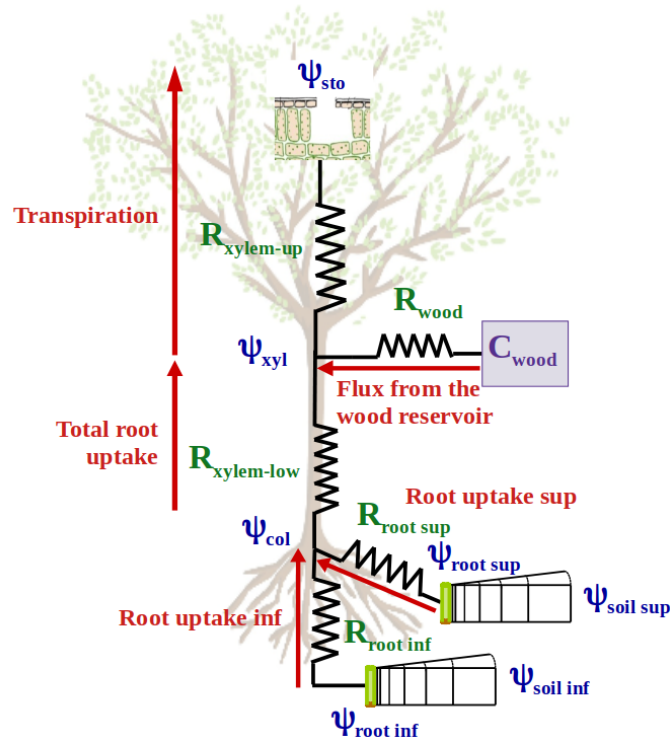


Figure 5.1: Resistive scheme of the SPAC hydraulic model (modified from Tuzet et al. (2017)). Hydraulic resistances are in green, hydraulic potential in blue, water fluxes in red and capacitance in purple.

As shown in Fig. 5.1, the leaf hydraulic potential is linked to the other plant and soil potentials via a resistive scheme. Water is stored into the plant compartments: leaves for grasses (Tuzet and Perrier, 2008) and leaves and woody organs (branches, trunk and large roots) for trees (Tuzet et al., 2017). As the storage of water into the wood compartment is predominant compared to the leaves (Tuzet et al., 2017), the version used here regroups all the compartments in a single reservoir called "wood", with the associated capacitance C_{wood} (Fig. 5.1). To model the water transport in the soil and the root absorption, cylindrical geometry and the concept of effective soil volume per unit root length have been used. The roots are taken to be long cylinders with uniform radius and water absorbing properties, and water is assumed to move by diffusion only in the radial direction. The two SPAC layers are themselves subdivided into several sublayers and water uptake by the roots is then calculated dynamically by solving Richard's equation at each time step. At root level, a flux condition corresponding to the root uptake is imposed. In the last sublayer far from the roots (external sublayer), the water flux is set zero and the water content of all soil sublayers is homogenized during the night following rainy days. The values of the hydraulic resistances of the upper and lower xylem ($R_{xylem up}$ and $R_{xylem low}$), the wood reservoir (R_{wood}) and the two roots ($R_{root sup}$ and $R_{root inf}$) are constant and must be specified (see Table 5.5).

5.2.3 TEB-SPAC coupling

As the objective is to simulate the hydraulic functioning, and especially the effect of water stress, of street trees, SPAC has to be adapted to the specificities of the urban environment. To this end, the hydraulic model of SPAC is integrated into TEB-Veg, which computes the street tree radiation exchanges and energy balance taking into account the urban environment, for example the solar and infrared (IR) radiation exchanges between surfaces and the drag effect of buildings.

5.2.3.1 Coupling methodology

The hydraulic model of SPAC is directly added in the TEB-Veg code and the numerical resolution of SPAC has been modified to limit the number of iterations. The methodology and the variable connection are the following. At the beginning of the time step, TEB-Veg computes the energy balance of street trees depending on the shortwave and long wave radiations absorbed by the leaves and the air temperature, humidity and wind speed at the tree crown level. The tree latent heat flux (LE) is calculated with the stomatal resistance that depends on the soil water content of the previous time step. The empirical function used to represent the water stress in the stomatal resistance computation (F_2) is replaced by the $f(\psi_{leaf})$ function computed by SPAC at the previous time step. Here, the stomatal resistance (R_s) is computed using the Jarvis method (Jarvis, 1976) as described by Noilhan and Planton (1989):

$$R_s = \frac{R_{smin}}{LAI} \times \frac{1}{F_1(PAR) F_2(W_g) F_3(VPD) F_4(T_a)}, \quad (5.1)$$

where R_{smin} is the minimum stomatal resistance, LAI is the Leaf Area Index, F_1 , F_2 , F_3 and F_4 are empirical functions representing respectively the effects of photosynthetically active radiation (PAR), soil water content (W_g), vapor pressure deficit (VPD) and air temperature (T_a). The soil water stress factor is computed in ISBA as:

$$F_2 = \sum_{i=1}^{n_{layer}} \left(\frac{W_{g_i} - W_{wilt_i}}{W_{fc_i} - W_{wilt_i}} f_{root_i} \right) = \sum_{i=1}^{n_{layer}} (SWI_i f_{root_i}), \quad (5.2)$$

where i is the soil layer number of ISBA, n_{layer} the total number of soil layer including roots, W_g is the soil water content, W_{wilt} is the wilting point, W_{fc} is the field capacity, and f_{root} is the root fraction. This ratio is a normalized Soil Water Content (SWC) and is also called the Soil Water Index (SWI). In the TEB-SPAC coupling, this F_2 function is replaced by the $f(\psi_{leaf})$ calculated as:

$$f(\psi_{leaf}) = \frac{1 + \exp[-\lambda_{leaf} \psi_{ref_{leaf}}]}{1 + \exp[\lambda_{leaf} (\psi_{leaf} - \psi_{ref_{leaf}})]}, \quad (5.3)$$

where $\psi_{ref_{leaf}}$ is the reference potential (MPa) and λ_{leaf} is the stomatal sensitivity parameter to the leaf hydraulic potential (-). These parameters depend on morphological adaptations. Photosynthesis and CO_2 fluxes are not included here, and the TEB-SPAC coupling has been only tested with this simple stomatal resistance formulation but could become operational for use with more advanced version of ISBA such as ISBA-A-gs.

The tree transpiration is provided to SPAC that computes the flux partition between the wood reservoir and the root uptake from the two SPAC soil layers. In parallel, the water flux entering each soil layer is computed as the variation in water content calculated by TEB-Veg that includes

all the processes (precipitation, evaporation, vertical diffusion, drainage etc.) except root water uptake. It is a major difference with the model version of Tuzet et al. (2017), because precipitation and the other processes of the urban water budget are included at each time step by a flux condition in the external sublayers. Then, knowing the two fluxes at the SPAC soil layer limits, the hydraulic potential, hydraulic conductivity and water content of each sublayer is computed by resolving the Richard's diffusion equations in a radial direction. A coefficient of partition of the root uptake between the superior and inferior soil layers is computed as a function of root and soil hydraulic potentials, root hydraulic resistance and total root water uptake. The tree potentials are recalculated for the next time step and the root uptake is given to TEB-Veg to compute the soil water budget of the current time step. SPAC computes all the water fluxes per square meter of tree crown, and then the fraction of each surface is used to weight the fluxes between the different surfaces.

5.2.3.2 Additional developments made in TEB-Veg

Independently of the coupling with SPAC, two developments were made to calculate the turbulent transfer resistance and to include the water interception on tree leaves. In the TEB-Veg version with SBL scheme, air temperature and humidity used to compute the leaf energy budget are computed directly at the tree crown level. So the turbulent transfer resistance between the leaf and the level where meteorological data are taken can be summarized here to a surface boundary layer resistance (R_{bl} in s.m^{-1}). It is computed as (Schuepp, 1972; Finnigan and Raupach, 1987; Maison, 2019):

$$R_{bl} = \frac{\eta}{LAI} \sqrt{\frac{D_l}{U}}, \quad (5.4)$$

where $\eta = 76.84$ is a dimensionless constant, $D_l = 0.07\text{m}$ is the characteristic length of individual leaves and U is the average wind speed in the tree crown (m.s^{-1}).

The water interception by leaves, that was already taken into account in TEB-Veg for low vegetation (lawn), is added for trees. The same methodology as ISBA is used, where the leaf interception reservoir is modeled as a single layer-bucket, with a surface equal to the leaf area. The fraction of leaf covered by water depends on the precipitation rate and the bucket maximum capacity. Depending on the climatic demand, water on leaves evaporates and transpiration occurs on the remaining water-free leaf surface. So the tree evapotranspiration (ETR) is the sum of the transpiration (TR) and the evaporation (EV) (all in W.m^{-2}):

$$ETR = TR + EV \quad (5.5)$$

When the maximum capacity is exceeded, water drips on the ground. The main difference with ISBA is that depending on the tree, soil, lawn and road fractions, water can drip either on the road, lawn or soil.

5.2.4 TEB-SPAC-MUNICH coupling

5.2.4.1 Coupling methodology

To take the effects of urban micro-climate and trees into account in air-quality simulations, TEB-SPAC is coupled to MUNICH. The two codes run independently and certain variables simulated by TEB-SPAC are sent to MUNICH. Figure 5.2 presents the meteorological fields calculated and exchanged between the mesoscale model Weather Research and Forecasting (WRF) and the street-scale models TEB and MUNICH. The description of the WRF simulation set-up is done in Chapter 3. The middle and right canyons in Fig. 5.2 shows respectively the meteorological fields used and calculated in MUNICH (alone) and exchanged when MUNICH is coupled to TEB. The variables are also listed in Table 5.1. Note that in the figure, TEB refers both to the version with and without trees, as SPAC is directly integrated into TEB, the coupling methodology is identical. The variables exchanges are the same but there are computed differently with parameterizations including tree effects.

First, SURFEX that includes TEB is used here offline, so WRF meteorological fields are given as input data to TEB and there is no feedback from TEB to WRF (Fig. 5.2 left canyon). For each street, the reference height is fixed to 25 m above the building height (see the left canyon in Fig. 5.2). WRF meteorological fields are therefore extracted in the vertical layer containing this reference height and in the horizontal cell containing the middle of the street. MUNICH recomputes its vertical and horizontal transfer coefficients (as described in Chapter 2) even when it is coupled to TEB. A comparison and development work described in Section 5.2.4.2 was therefore carried out to ensure that pollutant, water and heat flows are transported at similar velocities.

Then, as shown in the MUNICH-TEB canyon in Fig. 5.2, the vertical gradients of air temperature (T), specific humidity (Q) and pressure (P) simulated by TEB are averaged over the street height to compute the street average micro-meteorological variables that are used in MUNICH simulations. To try to improve calculations of atmospheric stability and instability, the Monin-Obukhov length (MOL) computed from [Soulhac et al. \(2011\)](#) in MUNICH is also replaced by the MOL simulated above the street by TEB and TEB-SPAC. The standard deviation of the vertical wind speed, σ_W (see Chapter 2) computed from the two MOL is compared.

Table 5.1: MUNICH variables modified with the coupling to TEB-SPAC.

type	variable taken from TEB-SPAC	variable taken from WRF
meteo	- average air temperature in the street	- 2 m air temperature
	- average atmospheric pressure in the street	- surface pressure
	- average air specific humidity in the street	- surface air specific humidity
	- MOL above the street	- MOL computed from Soulhac et al. (2011)
dry deposition	- stomatal resistance	- stomatal resistance from Wesely (1989) (eq. (4.25))
biogenic emissions	- leaf surface temperature	- 2 m air temperature
	- shortwave radiation received by vegetation with shadow and reflection effects	- incident shortwave radiation reaching the surface
	- soil water content to compute tree water stress	- not taken into account

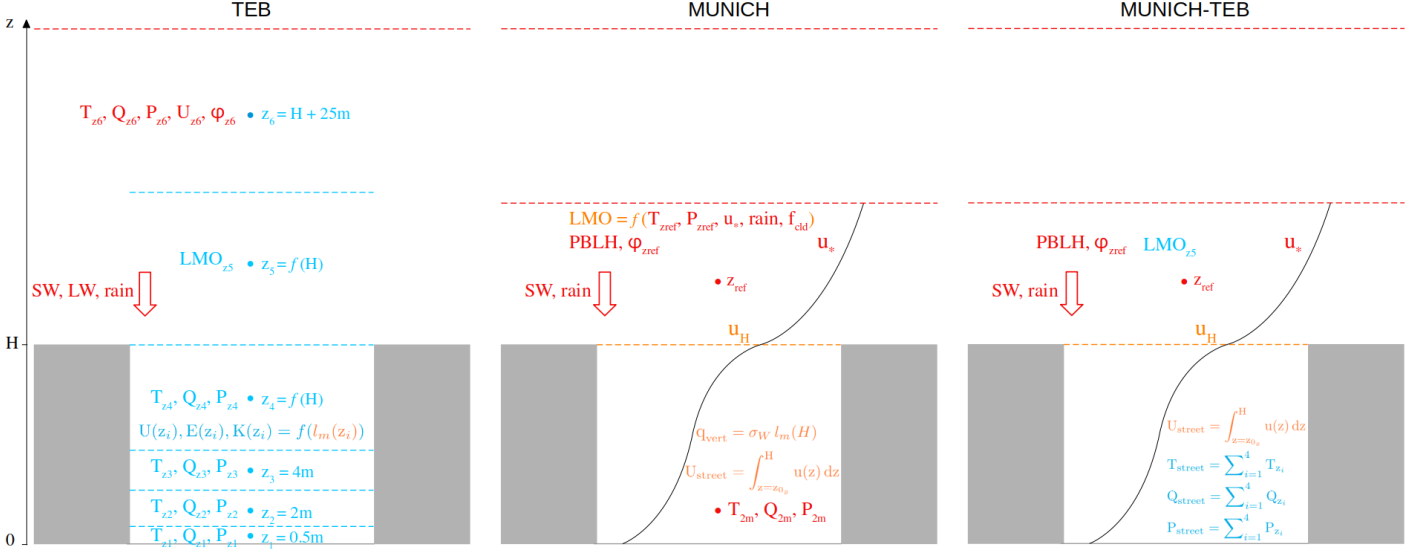


Figure 5.2: Scheme of meteorological fields calculated and exchanged by the 3 models **WRF**, **MUNICH** and **TEB**. The left and the middle street canyons illustrate the fields used as input data (from WRF) and computed respectively in TEB and MUNICH. The right street canyon illustrates the fields used as input data (from WRF and TEB) for the coupled MUNICH-TEB simulations. Dotted lines represent the boundaries of the vertical layers and small circles the middle or the height where fields are taken. Downwards arrows represent flows reaching the surface and black lines the vertical profiles computed in MUNICH. φ is the wind speed direction, PBLH the planetary boundary layer height and f_{cl} the cloud fraction.

Finally, the computation of biogenic emissions is modified by taking the leaf temperature and the solar radiation received by the tree leaves simulated by TEB-SPAC. The effect of water stress is also included in biogenic emissions by testing three parameterizations of the activity factor function of soil moisture, γ_{SM} (Guenther et al., 2012; Bonn et al., 2019; Otu-Larbi et al., 2020).

5.2.4.2 Calculation of consistent transfer velocities between MUNICH and TEB

A particular attention was paid to the calculation of the momentum and turbulent fluxes between the two models. Indeed, the momentum, heat and water amounts simulated by TEB-Veg and the pollutants concentrations simulated by MUNICH should be transported with the same transfer velocities. To do this, the expressions of vertical profiles of wind speed and turbulent transfer coefficient were first compared. The SBL scheme uses the turbulent kinetic energy scheme developed by Cuxart et al. (2000) where the turbulent flux ($\overline{u'w'}$) is calculated as:

$$\overline{u'w'} = -K \frac{\partial U}{\partial z}, \quad (5.6)$$

where K is an eddy diffusivity coefficient ($\text{m}^2 \cdot \text{s}^{-1}$) computed as:

$$K = C_u l_m E^{1/2}, \quad (5.7)$$

where $C_u = 0.126$ is a dimensionless constant, l_m is the mixing length (m) and E is the turbulent kinetic energy ($\text{m}^2 \cdot \text{s}^{-2}$). Mixing and dissipative lengths are not equal and the mixing length can be either computed as in Redelsperger et al. (2001) or in Santiago and Martilli (2010). The K coefficient is comparable to the vertical transfer coefficient in MUNICH, q_{vert} . To calculate the

transfer between the vertical levels, K is estimated as the half-sum of the K coefficients calculated at the middle of the levels. The full description of the SBL turbulent scheme is given in [Masson and Seity \(2009\)](#).

[Redon et al. \(2020\)](#) added the drag effect of trees inside the canyon in the SBL scheme developed by [Hamdi and Masson \(2008\)](#); [Masson and Seity \(2009\)](#), by including a drag term in the equations of momentum and turbulent kinetic energy vertical profiles. This term depends on the drag coefficient of trees (taken equal to 0.20 as in MUNICH) and of the tree canopy leaf area density (LAD) in each vertical layer (which is considered vertically constant). [Redon et al. \(2020\)](#) showed that it reduces the wind speed and allows a better comparison to measurements, but the wind speed was still overestimated during the day. In this TEB-Veg version, the impact of the tree crown on the mixing length is not considered. However, in Chapter 2, we showed that trees also modify the mixing length in the street. So, to try to obtain close vertical and horizontal transfer velocities between MUNICH and TEB, the mixing-length parameterization developed by [Maison et al. \(2022a,b\)](#) was added in TEB. The comparison of the vertical profiles of the K coefficient and the horizontal wind speed U between MUNICH and TEB-Veg with the mixing-length parameterization developed in the Chapter 2 is presented in figures 5.3 and 5.4 for the same three street canyons as in Chapter 2 and for a neutral atmospheric stability. Figure 5.3 presents the K vertical profiles computed in TEB-Veg and MUNICH mixing length. It is compared to the vertical transfer coefficient profile in MUNICH, which is computed as a linear function of the vertical transfer coefficient between the street and the background at $z = H$, $q_{vert}(H)$ ([Maison et al., 2022b](#)):

$$K(z) = q_{vert}(z) = \sigma_W l_m(z) = \sigma_W \kappa s_H z, \quad (5.8)$$

where σ_W is the standard deviation of the vertical wind speed ($\text{m}\cdot\text{s}^{-1}$) function of the friction velocity above the street and the atmospheric stability (see eq. (2) in Section 2.2 and [Soulhac et al. \(2011\)](#)). κ is the Von Kàrmàn constant (-) and s_H is a dimensionless coefficient taken into account the effect of rough soil, buildings and trees on the mixing length in the street.

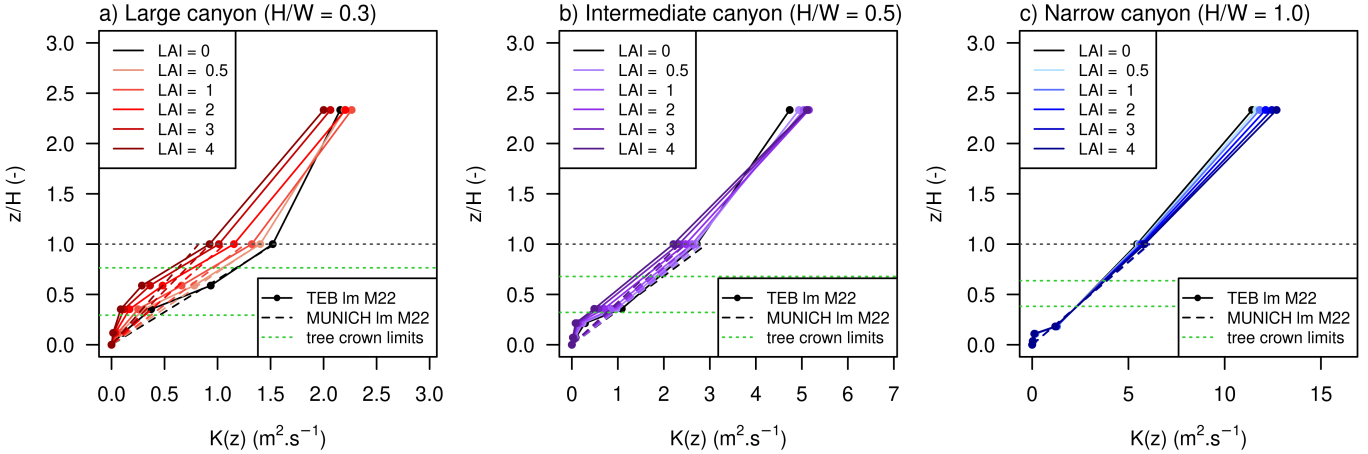


Figure 5.3: Comparison of the vertical profiles of the turbulent transfer coefficient computed in MUNICH and in TEB with the mixing-length parameterization of [Maison et al. \(2022a,b\)](#) (M22). The profiles are compared in three street canyons of various aspect ratios as presented in [Maison et al. \(2022a,b\)](#). The tree LAI varies but the tree height and crown volume fraction (CVF) are fixed to $h_{max}/H = 0.5$ and $CVF = 10\%$.

Figure 5.3 shows that the K profiles computed in MUNICH and in TEB-Veg with the same mixing-length parameterization and from the same friction velocity above the street are very close in the three street canyons of various aspect ratio and for each tree LAI. This should result in close vertical transfer velocities between the two models.

Similarly, the vertical profiles of horizontal velocities are compared in Fig. 5.4. The profiles are computed from the same wind speed at the reference height above the street. The parameterizations used to calculate the wind speed profile above the street being different, the wind speed at $z = H$ is slightly lower in MUNICH. In the street, the shape of profiles are similar but the wind attenuation seems stronger in MUNICH.

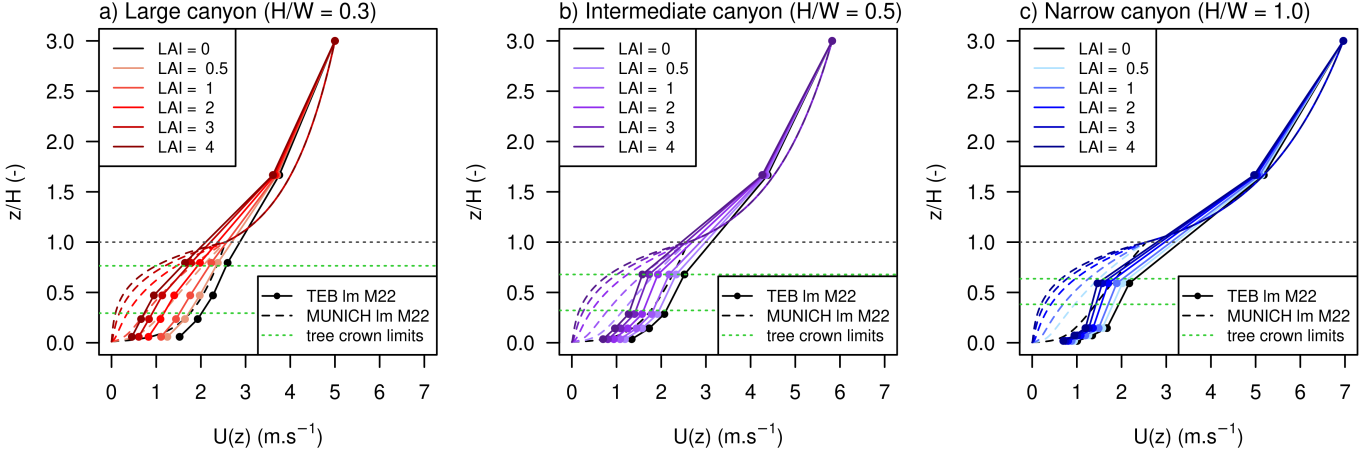


Figure 5.4: Comparison of the vertical profiles of the horizontal wind speed computed in MUNICH and in TEB with the mixing-length parameterization of [Maison et al. \(2022a,b\)](#) (M22). The profiles are compared in three street canyons of various aspect ratios as presented in [Maison et al. \(2022a,b\)](#). The tree LAI varies but the tree height and crown volume fraction (CVF) are fixed to $h_{max}/H = 0.5$ and $CVF = 10\%$. The angle between the street orientation and wind direction is equal to 0° .

The average wind speed in the street (U_{street}) and the relative difference of wind speed between the cases with trees and without are also compared in Fig. 5.4. It shows that the average wind speed is higher in TEB than in MUNICH (Fig. 5.4a), the tree effect computed with the relative difference is also a little higher in TEB than in MUNICH (Fig. 5.4b). However, the differences are acceptable and should again enable us to obtain close transfer velocities for pollutants, water and heat between the two models.

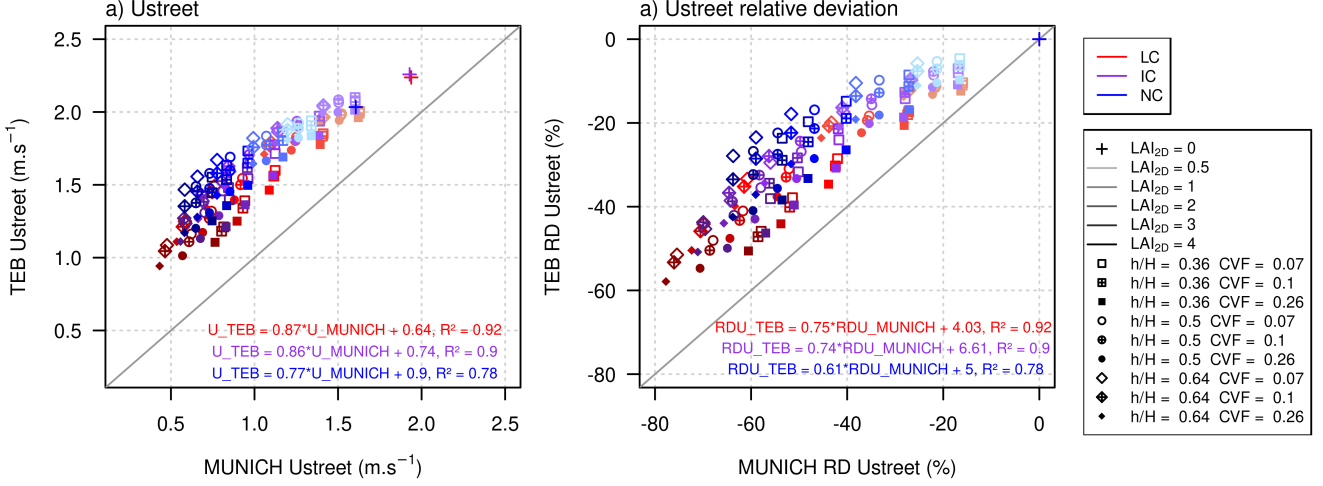


Figure 5.5: Comparison of a) street average horizontal wind speed (U_{street}) and b) relative difference (RD) of wind speed computed in MUNICH and in TEB with the mixing-length parameterization of Maison et al. (2022a,b). The results are presented for the three street canyons studied in Maison et al. (2022a,b): large, intermediate and narrow canyons (LC, IC and NC) and for each tree type with various LAI, tree heights (h/H) and crown volume fractions (CVF). The angle between the street orientation and wind direction is equal to 0° .

5.2.5 Simulation set-up and input data

5.2.5.1 Computation of the TEB grid

The spatial approach is different between MUNICH and TEB. MUNICH is a street network model and the chemical species mass balance is computed for each street of known height, width and length. Species are horizontally transported between the street segments and exchanged vertically with the background. TEB-Veg computes the energy balance of a street canyon per square or rectangular grid point. The canyon characteristics are then calculated as the average of the street characteristics in each mesh. The minimum horizontal resolution is 250×250 m and there is no horizontal transfer between grid points. In TEB-Veg, fluxes are computed per square meter and there is no notion of street length. The methodology adopted here is to run TEB-Veg on grid points corresponding to MUNICH streets. A grid point is therefore equal to a "real" street and not to an average street. Street coordinates cannot be used directly to define the TEB-Veg mesh because the streets are too close compared to the minimum resolution. A regular mesh of 250×250 m centered on Paris city is used and the longitudes and latitudes of each grid point are recalculated. As the study area is rather small, the offset between real and equivalent coordinates does not significantly affect the results.

As MUNICH and TEB-Veg assume the street canyon hypothesis and require similar input data (building height, street width, street angle, tree height, etc.), many street and tree characteristics calculated in MUNICH are used directly in TEB-Veg. The computation of the additional tree characteristics needed and the parameters fixed in TEB are presented in sections 5.2.5.2 and 5.2.5.5.

5.2.5.2 Computation of additional street and tree characteristics

The parameters presented in the Table 5.2 are street dependent and are directly taken from MUNICH.

Table 5.2: Street and tree dependent parameters used directly from MUNICH to TEB-Veg.

Parameter	Definition	Unit
H	building height	m
W	street width	m
θ	street orientation	°
h_{max}	top tree height	m
DBH	trunk diameter at breast height	cm

Then, as in MUNICH, the building fraction is fixed to $f_{bld} = 0.5$ (-) for all streets (De Munck, 2013). The computation of the other surface fractions for TEB-Veg is presented below. A representation of the TEB-Veg street canyon with the different heights, surface fractions and atmospheric vertical levels of the SBL scheme is presented in Fig. 5.6.

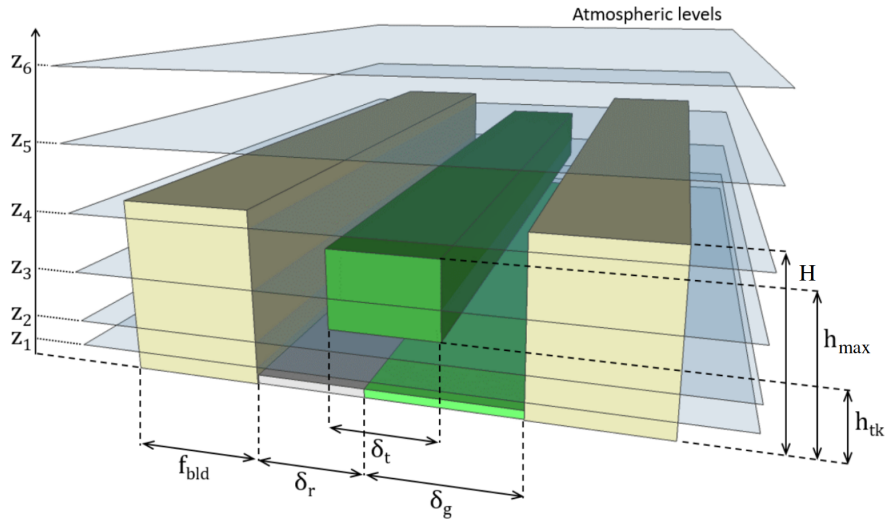


Figure 5.6: Scheme of the TEB-Veg urban canyon with the atmospheric vertical levels of the surface boundary layer (SBL) scheme (modified from Redon et al. (2020)).

The Fraction of high vegetation (tree) (-) is calculated as:

$$\delta_t = \frac{TF}{1 - f_{bld}}, \quad (5.9)$$

where TF is the tree fraction per street area computed in equation (4.5). The tree fractions computed in Paris street network are presented in Fig. 5.7.

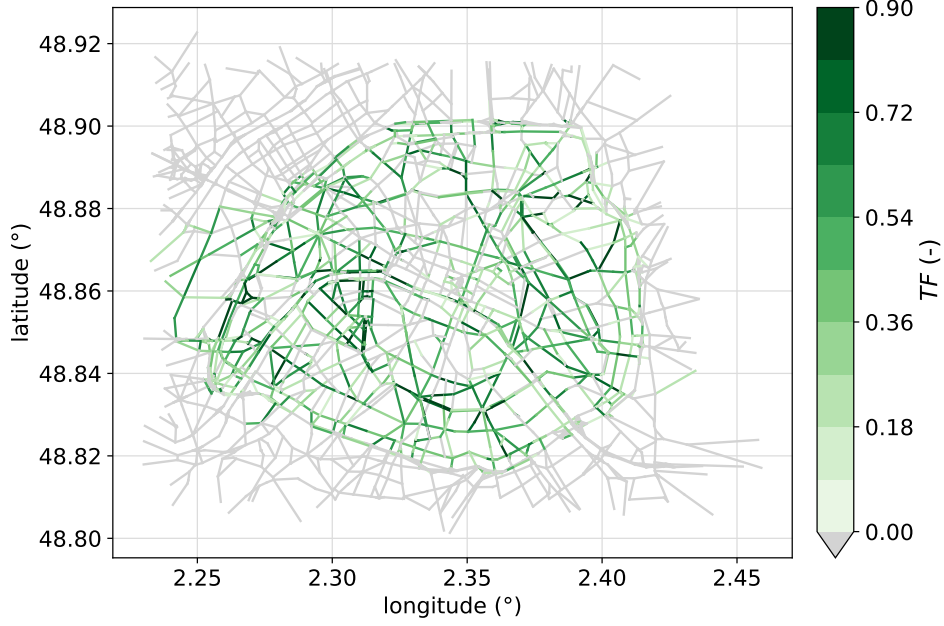


Figure 5.7: Map of the tree fraction (TF) computed in Paris street network.

The fraction of bare soil, δ_s (-) is computed assuming that each tree has a pit of volume $V_{pit} = 9 \text{ m}^3$ and of maximum depth $d_{max} = 1.5 \text{ m}$. The total soil volume in the street is therefore $V_{pit} N_t$, where N_t is the number of trees in the street:

$$\delta_s = \frac{S_s}{S_{street}} \times \frac{1}{1 - f_{bld}}, \quad (5.10)$$

$$\text{with } S_s = \frac{V_{pit} N_t}{d_{max}}, \quad (5.11)$$

$$\text{and } S_{street} = WL. \quad (5.12)$$

S_{street} is the surface of the street ground (road + bare soil) in m^2 . No low vegetation (lawn) fraction (δ_l) is considered, so the garden fraction is equal to the bare ground fraction: $\delta_g = \delta_s$. The soil surface in the street is therefore computed assuming that each tree has the same soil volume of 9 m^3 and same surface of 6 m^2 . Root uptake is computed per square meter of tree crown and is then multiplied by the tree crown to soil surface ratio to computed the water drawn from the soil volume. A very large tree surface compared to the soil volume can lead to numerical issues, so the tree fraction is limited to 10 times the soil fraction, i.e. $\delta_t \leq 10 \delta_g$. In those streets, the leaf surface is conserved, so the crown width is reduced and the LAI is increased. This correction is made in 44% of the streets, underlying the fact that many trees might explore a soil volume greater than 9 m^2 .

The road fraction (-) is computed to ensure that the sum of the fractions is equal to 1:

$$\delta_r = 1 - (f_{bld} + \delta_s) \quad (5.13)$$

The wall surface density is:

$$\delta_w = \frac{2H}{W}(1 - f_{bld}). \quad (5.14)$$

Then, for the trees, the LAI_{street} used in MUNICH (eq. 4.1) is converted to compute the leaf surface per crown projected area (LAI) used in TEB-Veg that depends on the crown width, W_c (m):

$$LAI = LAI_{street} \frac{W}{W_c}, \quad (5.15)$$

$$W_c = TF \times W. \quad (5.16)$$

The modeled trunk height ($h_{tk_{mod}}$) is estimated from the crown ($h_{crown_{mod}}$) and tree ($h_{tree_{mod}}$) heights computed with McPherson et al. (2016) equations and is corrected by the ratio of the actual tree height measured by the Paris municipality ($h_{tree_{obs}}$) to the modeled tree height ($h_{tree_{mod}}$):

$$h_{tk} = h_{tk_{mod}} \frac{h_{tree_{obs}}}{h_{tree_{mod}}} = (h_{tree_{mod}} - h_{crown_{mod}}) \frac{h_{tree_{obs}}}{h_{tree_{mod}}} \quad (5.17)$$

Note that in McPherson et al. (2016) equations, the tree crown can be an ellipsoid so the crown diameter is different from the crown height.

The trunk volume per crown surface ($\text{m}^3 \cdot \text{m}^{-2}$) is needed in SPAC to compute the wood reservoir volume, it is estimated assuming a cylindrical trunk as:

$$V_{trunk} = \pi \left(\frac{DBH \times 10^{-2}}{2} \right)^2 h_{tk} \times \frac{1}{CPA}, \quad (5.18)$$

where CPA is the crown projected area (m^2) computed in eq. (4.5).

The trunk heights and volumes are simply averaged for trees belonging to the same street, to compute the street average trunk height and volume.

The minimum and maximum volume of the wood reservoir, $V_{res_{min}}$ and $V_{res_{max}}$ ($\text{m}^3 \cdot \text{m}^{-2}$) are then computed from the street average trunk volume ($\overline{V_{trunk}}$) as:

$$V_{res_{max}} = P_{wood} \times \overline{V_{trunk}}, \quad (5.19)$$

$$V_{res_{min}} = 0.4 \times V_{res_{max}}, \quad (5.20)$$

where P_{wood} is the wood porosity (-), that generally varies between 0.4 and 0.8 (Varivodina et al., 2010) and depends on tree age and species. Here, the wood porosity is fixed to $P_{wood} = 0.6$ for all trees, and should be tested in a sensitivity analysis.

5.2.5.3 Estimation of the reference leaf hydraulic potential

Physiological responses to drought vary according to tree species. Some tree species maintain a constant midday leaf water potential when water is non-limited, as well as under drought conditions, reducing stomatal conductance if necessary to limit transpiration (isohydric strategy). Other tree species have a more variable midday leaf water potential and keep their stomata open and photosynthetic rates high longer, even in the presence of decreasing leaf water potential (anisohydric strategy) (Sade et al., 2012). These different behaviors can be related to the hydraulic characteristics of the tree, and in particular the type of xylem. To take account of this physiological diversity, the reference hydraulic potential of the leaf sub-stomatal cavity, $\psi_{ref_{leaf}}$ involved in the $f(\psi_{leaf})$ function (eq. (5.3)) is expressed depending on the tree xylem type. Firstly, the xylem type of each tree species found in Paris is determined using two databases: The Xylem Database developed by the Swiss Federal Research Institute WSL and available at <https://www.wsl.ch/>

dendropro/xylemdb/ and the Xylem Functional Traits Database from Choat et al. (2012) available at <https://xylemfunctionaltraits.org/>. When several xylem types coexist on the same street, the predominant xylem type is selected. Secondly, the Xylem Functional Traits Database also lists many experimental measurements on tree hydraulic traits or anatomy. It especially includes minimum predawn and midday stem hydraulic potential measurements. The minimum midday stem hydraulic potentials under drought conditions ($\psi_{midday_{min}}$ in MPa) are compared by xylem type in Fig. 5.8, which shows lower potentials for ring porous and semi-ring porous xylem types.

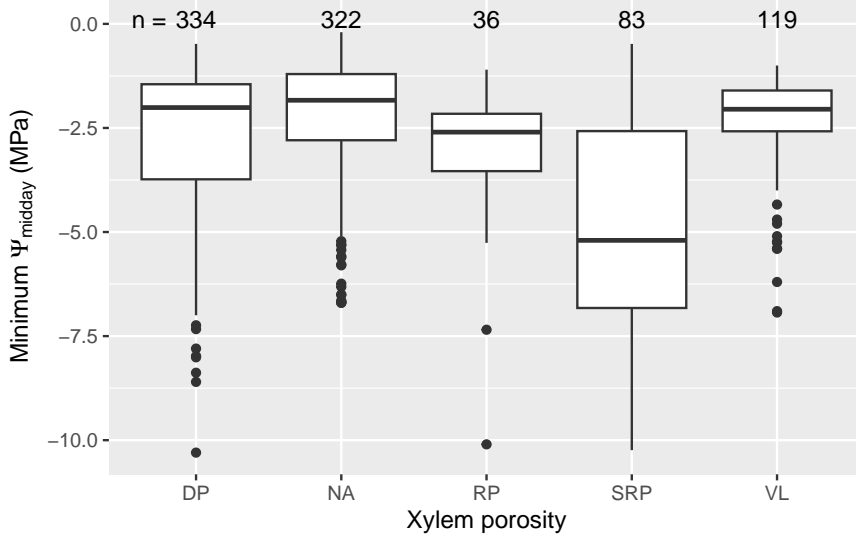


Figure 5.8: Minimum predawn stem hydraulic potential measurements available in the Xylem Functional Traits Database depending on the xylem type (DP: diffuse porous, RP: ring porous, SRP: semi-ring porous, VL: vesselless and NA: not available). n is the number of sample for each xylem type.

$\psi_{ref_{leaf}}$ is then expressed for each xylem type category as a function of the average minimum predawn stem hydraulic potential ($\overline{\psi_{midday_{min}}}$):

$$\psi_{ref_{leaf}} = a \times \overline{\psi_{midday_{min}}} \quad (5.21)$$

where a is a dimensionless constant estimated to 0.65 with the data used. The obtained $f(\psi_{leaf})$ functions are presented for each xylem type category in Fig. 5.9.

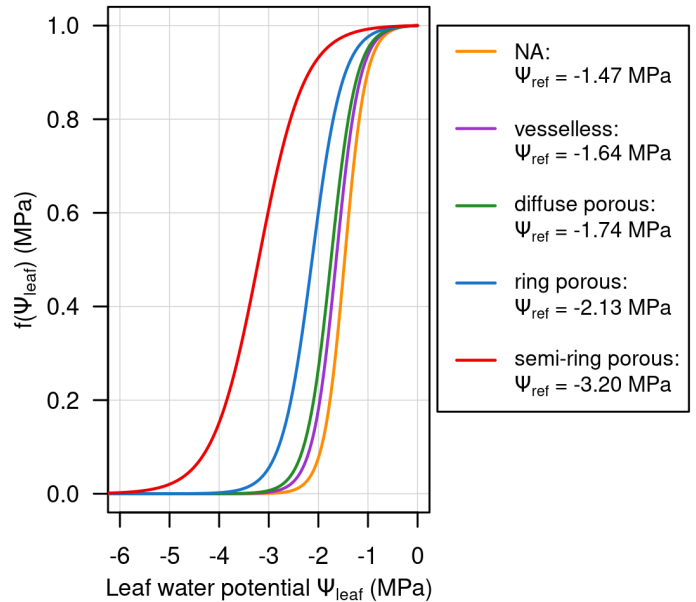


Figure 5.9: $f(\psi_{leaf})$ functions depending on the $\psi_{ref_{leaf}}$ that are computed from the xylem types (DP: diffuse porous, RP: ring porous, SRP: semi-ring porous, VL: vesselless and NA: not available).

The value of $\psi_{ref_{leaf}}$ for each street is mapped for the Paris street network in Fig. 5.10. It shows a predominance of streets with diffuse, ring and semi-ring porous xylem type.

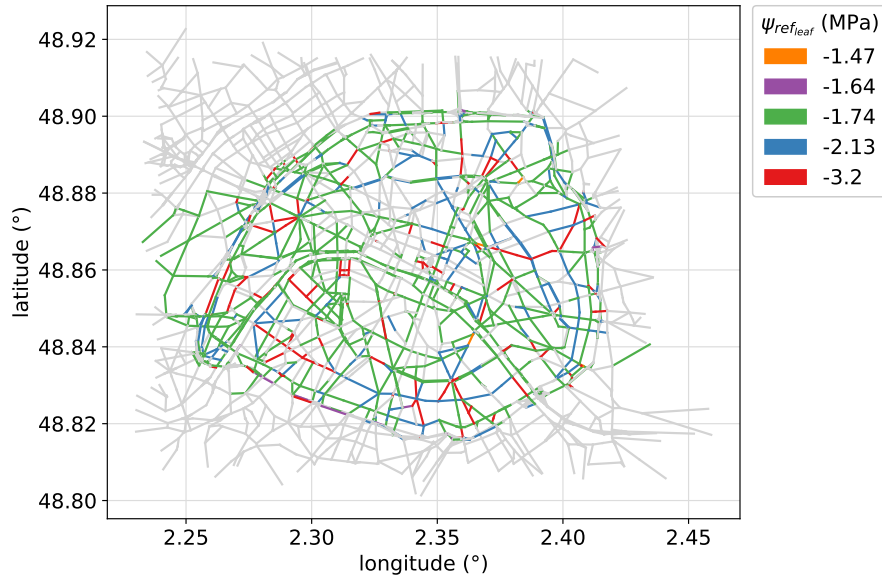


Figure 5.10: Map of the reference leaf hydraulic potential ($\psi_{ref_{leaf}}$) computed from the Paris street network from the xylem types.

5.2.5.4 Computation of soil characteristics and root profile

Analyses of soil samples from 32 pits in Paris streets were carried out by the [Paris City agronomy laboratory \(2019\)](#). The pits are located in different streets in Paris and contain various tree species, as shown in the Table 5.3.

Table 5.3: Location of analyzed pits and tree species planted ([Paris City agronomy laboratory, 2019](#)).

Street	Paris arr.	pit nb.	detailed tree number and species
avenue de Flandres	19	12	3 <i>Celtis australis</i> , 3 <i>Sophora japonica</i> , 3 <i>Tilia cordata</i> , 3 <i>Ulmus</i>
rue de Bretagne	3	3	3 <i>Celtis australis</i>
rue du Temple	3	6	3 <i>Platanus x hispanica</i> , 3 <i>Quercus ilex</i>
rue Ordener	18	2	2 <i>Gledistia triacanthos</i>
rue Franc Nohain	13	3	3 <i>Quercus Cerris</i>
boulevard Victor	15	6	3 <i>Platanus x hispanica</i> , 3 <i>Zelkova carpinifolia</i>

The average fraction of sand, silt and clay is calculated for each street with the associated standard deviation (σ) and presented in Fig. 5.11a. This figure also shows the average texture computed on the 32 pits, called "all streets".

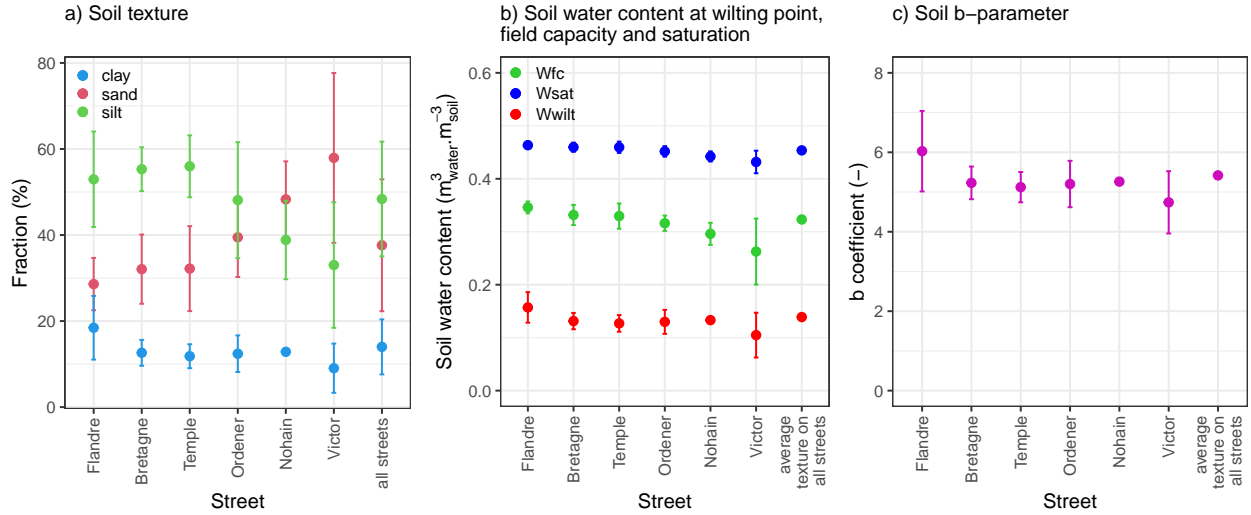


Figure 5.11: a) Measured soil texture with (b, c) soil hydrodynamic characteristics computed from the textures and [Clapp and Hornberger \(1978\)](#) equations. The circles correspond to the average values and the error bars to $\pm\sigma$.

Figure 5.11a shows that the predominant texture of the soils studied is a sandy clay loam but there is a certain heterogeneity both between pits on the same street and between streets. The soil hydro-dynamic parameters used in the pedo-transfer functions (wilting point W_{wilt} , field capacity W_{fc} , soil water content at saturation W_{sat} and b coefficient) are calculated for these different pits using the [Clapp and Hornberger \(1978\)](#) equations. The results are presented in panels b) and c) and show that despite the texture heterogeneities, the computed W_{wilt} , W_{fc} and W_{sat} are rather homogeneous between the streets and have a smaller intra-street variability. The b coefficient is sensitive to the clay fraction and slightly higher in the Flandre avenue. Overall, the hydro-dynamic parameters calculated from the average texture on all streets (right column) are very close to the parameters calculated for each street. The soil texture is therefore assumed to be homogeneous in all the tree pits modeled in Paris and the average soil texture is used in TEB-SPAC simulations: $f_{sand} = 0.376$, $f_{clay} = 0.140$ and $f_{silt} = 0.484$ (-). It gives the following hydro-dynamic parameters: $W_{wilt} = 0.139$, $W_{fc} = 0.323$, $W_{sat} = 0.454$ $m^3 \cdot m^{-3}$ and $b = 5.42$ (-). A homogeneous texture is also assumed vertically in the soil and there is no distinction of different soil horizons.

The vertical transfers of water in the soil are computed in TEB-Veg using the ISBA-DIF model (Boone, 2000). The version with 12 vertical soil layers is used here and a root fraction profile is defined to weight the root water uptake between the different ISBA-DIF soil layers. Since urban trees are planted in a limited soil volume, we assume that the roots explore the soil volume with a constant density. The profile is computed assuming a homogeneous root density in each soil layer. As presented in Fig. 5.12, the root fraction is proportional to the soil layer thickness and the cumulated root fraction is therefore linear in the layers containing roots. The maximum rooting depth (d_{max}) is set to 1.5 m, so there is no root in the two deep layers. Note that to avoid instability due to soil evaporation in a very thin surface soil layer, the layer thickness of the two first layers (near the surface) have been increased (0.01 m instead of 0.001 m and 0.03 m instead of 0.01 m). We also assume that there is no root in the first layer.

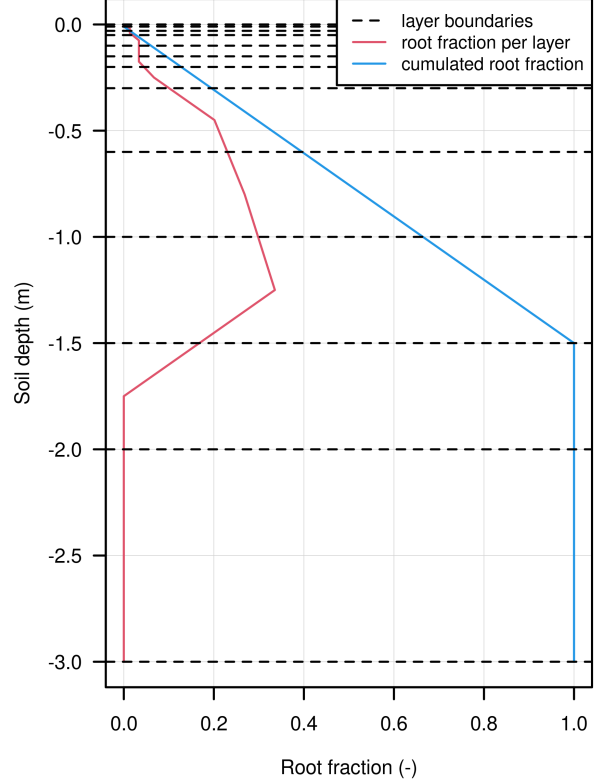


Figure 5.12: Vertical profile of root fraction per soil layer and cumulated.

Then, the two SPAC layers are distributed on ISBA-DIF layers to get about 50% of the root fraction in each SPAC soil layer. The two SPAC layers along with ISBA-DIF corresponding soil layers, root fraction and normalized soil volume (containing roots) are presented in the Table 5.4.

Table 5.4: Description of the two SPAC layers.

SPAC soil layer	ISBA-DIF layer	root fraction (-)	soil volume ($\text{m}^3_{\text{soil}} \cdot \text{m}^{-2}$)
1 (sup)	2 - 8	0.396	0.59
2 (inf)	9 - 10	0.604	0.90

Each soil layer is divided into 15 sublayers. These sublayers are hollow cylinders through which the water will circulate by radial diffusion. The thickness of these 15 sublayers is constant in each soil layer and is calculated based on the radius of each cylinder and the radius of the roots. The radius of the fine absorbing roots is fixed at 0.00035 m in both layer and for all tree canopies. The radius of the two SPAC layers are computed from the normalized root length (L_{root_l} , in $\text{m} \cdot \text{m}^{-2}$) and soil volume (V_{sol_l} in $\text{m}^3 \cdot \text{m}^{-2}$), which is conserved between SPAC soil layers and ISBA-DIF equivalent layers:

$$R_{soilcyl_l} = \sqrt{\frac{V_{sol_l}}{\pi L_{root_l}}}, \quad (5.22)$$

where l stand for the soil layer number. The root length is computed from the total surface of the root envelope (S_{root} in m^2) and the root fraction in each soil layer (f_{root_l} (-)) in equation (5.25). Data on tree roots in urban areas being quite rare, a simple parameterization is proposed to calculate the root surface density ($d_{S_{root}}$ in $\text{m}^2 \cdot \text{m}^{-3}$) as a function of the DBH of trees. It is inspired by

the values measured in [Ermák et al. \(2000\)](#); [Grabosky et al. \(2001\)](#). This simple parameterization represents the fact that root surface density increases with tree growth.

$$d_{S_{root}} = 0.10 DBH \quad (5.23)$$

$$S_{root} = d_{S_{root}} d_{max} \times 1 \times 1 \quad (5.24)$$

$$L_{root_l} = \left(\frac{S_{root}}{2\pi r} \right) \times f_{root_l} \quad (5.25)$$

Therefore, the fine root length and soil layer radius varies from a street to another.

5.2.5.5 Parameters fixed in all streets

SPAC needs additional parameters to compute the $f(\psi_{leaf})$ function and the water transfers within the tree. This parameters vary with tree species and could be fixed depending on the isohydric or anisohydric behavior of trees. In the absence of measurements to determine these parameters, they are considered constant and remain equal to those used by [Tuzet et al. \(2017\)](#) for beech trees. The values prescribed in the simulation presented in Section 5.3.2 are shown in Table 5.5. The influence of each parameter on the results should be tested in future sensitivity analyses.

Table 5.5: List of SPAC tree parameters fixed identical for every street.

Variable	Definition	Value	Unit
$R_{s_{min}}$	Minimum stomatal resistance	150	s.m ⁻¹
λ_{leaf}	Stomatal sensitivity parameter to $f(\psi_{leaf})$	$\ln(0.003)/(-\psi_{ref_{leaf}})$	-
$\psi_{ref_{wood}}$	Reference potential for water transfer in the reservoir	-1.4	MPa
λ_{wood}	Model parameter for water transfer in the reservoir	0.9	-
$R_{xylem\ up}$	Upper part xylem hydraulic resistance	3.0×10^{-6}	MPa.m ⁻³ .m ² .s
$R_{xylem\ low}$	Lower part xylem hydraulic resistance	2.5×10^{-6}	MPa.m ⁻³ .m ² .s
R_{wood}	Wood reservoir hydraulic resistance	60.0×10^{-6}	MPa.m ⁻³ .m ² .s
$R_{root\ sup}$	Root hydraulic resistance of soil layer 1	1.0×10^{-6}	MPa.m ⁻³ .m ² .s
$R_{root\ inf}$	Root hydraulic resistance of soil layer 2	2.5×10^{-6}	MPa.m ⁻³ .m ² .s

Finally, the roof and wall characteristics (albedo, conductivity, layer thickness, etc.) are fixed for Haussmannian buildings following [De Munck \(2013\)](#). The roughness lengths of the different surfaces are taken from [Masson et al. \(2002\)](#); [Hamdi and Masson \(2008\)](#) and the roughness length of the walls is the same as used in MUNICH ($z_{0_s} = 0.01$ m). The TEB-HYDRO module is used to account for the water runoff from the roofs and road into the soil, and the model parameters are taken from [Stavropoulos-Laffaille et al. \(2018\)](#); [Bernard \(2021\)](#). Note that the soil water content is initialized at the field capacity in all streets.

5.2.5.6 Description of simulations performed

- TEB and TEB-SPAC simulations

First, TEB simulations of two months are performed on the Paris street-network. One without tree (on all streets), called TEB and one with trees called TEB-SPAC (only on streets with trees). One additional simulation is performed with TEB-Veg and ISBA parameterizations to illustrate the changes in stomatal resistance through the coupling with SPAC.

To evaluate the model, the simulated air temperature, humidity and pressure at 2 m height are compared to WRF fields and to observations performed in Hôtel de Ville garden (HdV). The results of these simulations are analyzed, firstly in terms of energetic and hydraulic tree functioning (Section 5.3.2).

- MUNICH simulations

MUNICH simulations are performed for 2 months on all streets with the street meteo computed by WRF, TEB and TEB-SPAC. The list of simulations with the meteo fields taken is presented in the Table 5.6. Two one-week simulations are also carried out, the first by just modifying the temperature, humidity and pressure in the street (TEB street meteo), and the second by just modifying the MOL (TEB MOL). In the simulation TEB-SPAC, the stomatal resistance computed from [Wesely \(1989\)](#) parameterization in MUNICH is replaced by the stomatal resistance simulated by TEB-SPAC. The REF and 3EFF simulations are fully described in Chapter 4.

Table 5.6: Description of the MUNICH simulations performed with the simulated period, the tree effect(s) considered and the corresponding meteorological fields. W89: [Wesely \(1989\)](#)

Simulation name	start and end dates	tree aero. effect	dry dep. on leaves	urban tree bio. emis.	meteorological fields				
					Tair	Qair	Patm	MOL	Rs
REF	06/06 - 31/07	-	-	-	WRF				-
3EFF	06/06 - 31/07	yes	yes	yes	WRF				W89
TEB	06/06 - 31/07	-	-	-	TEB				-
TEB-SPAC	06/06 - 31/07	yes	yes	yes	TEB - SPAC				-
TEB MOL	13/06 - 20/06	-	-	-	WRF		TEB		-
TEB street meteo	13/06 - 20/06	-	-	-	TEB		WRF		-

5.3 Results

First, the meteorological fields simulated by WRF, TEB and TEB-SPAC at 2 m above ground layer are compared to measurements performed in Paris HdV street.

5.3.1 Comparison of simulated and observed meteorological fields in HdV

As described in the Chapter 4, meteorological measurements were performed in the HdV street between the 2nd of June and the 7th of July. The air temperature, specific humidity and pressure at 2 m simulated by TEB and TEB-SPAC in the HdV street are compared to the measurements. The fields simulated by WRF are also added in the comparison. The list of the street and tree parameters used in the TEB and TEB-SPAC simulations are listed in Table 5.8.

Table 5.7: Comparison of observed and modeled air temperature, humidity and pressure in HdV with statistical indicators. su: same unit as the variable.

Variable		Min su	Mean su	Max su	RMSE su	NAD -	Bias su	R -
T_{air} (°C)	obs.	13.5	21.3	37.3				
	WRF	12.3	20.8	37.2	1.58	0.03	-0.54	0.94
	TEB	12.2	21.5	38.2	1.28	0.02	0.16	0.96
	TEB-SPAC	12.2	21.5	38.1	1.27	0.02	0.16	0.96
Q_{air} (kg.kg ⁻¹)	obs.	0.0048	0.0084	0.0128				
	WRF	0.0039	0.0077	0.0130	0.0013	0.058	-0.0007	0.79
	TEB	0.0047	0.0092	0.0156	0.0015	0.070	0.0008	0.78
	TEB-SPAC	0.0047	0.0093	0.0157	0.0015	0.071	0.0009	0.78
P_{atm} (hPa)	obs.	1001.6	1012.8	1023.4				
	WRF	1000.8	1011.7	1021.5	1.25	0.00	-1.11	0.99
	TEB	1001.8	1012.8	1022.5	0.57	0.00	-0.07	0.99
	TEB-SPAC	1001.8	1012.8	1022.5	0.57	0.00	-0.07	0.99

Figure 5.13 shows that the air temperatures at 2 m simulated by TEB are closer to the observations compared to WRF, especially the daily maximum air temperatures that are higher. Compared to WRF, TEB and TEB-SPAC simulations have lower RMSE and bias and a better correlation (R) (Table 5.7).

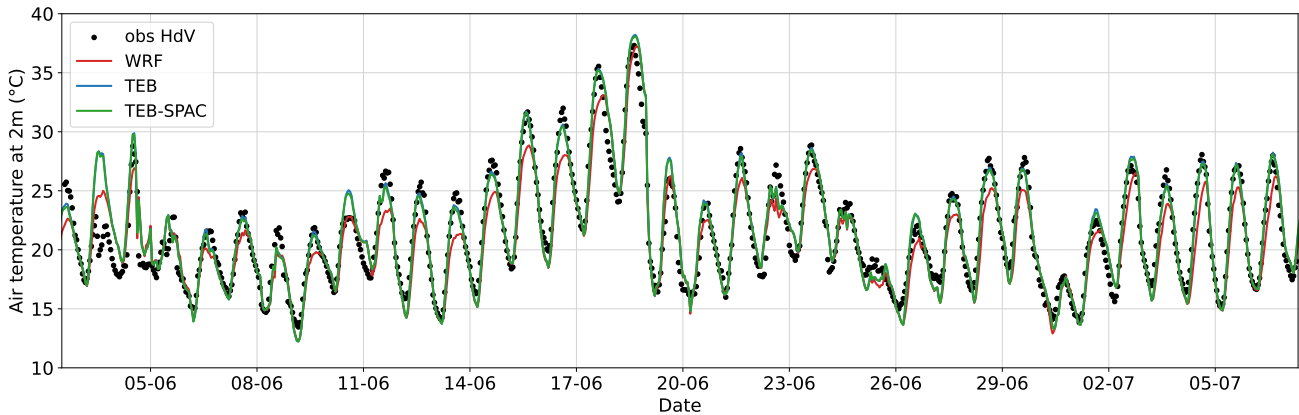


Figure 5.13: Comparison of observed and simulated air temperature at 2 m in HdV street.

The comparison of the observed and modeled air specific humidity presented in Fig. 5.14 shows that TEB and TEB-SPAC tend to overestimate the humidity some days (e.g. from 04/06 to 14/06) but simulate it better on other days (e.g. from 15/06 to 22/06 and from 28/06 to 03/07). These over-estimations seem to occur on rainy days (see Fig. 5.17), so they can be due to overestimation of evaporation and therefore of the amount of water retained on roofs and roads after rainfall. The maximum retention capacity of the road and roof surface reservoirs are respectively fixed to 3.0 and 1.5 mm and the infiltration rate through the road to $5.0 \cdot 10^{-7} \text{ m.s}^{-1}$ as suggested by [Stavropoulos-Laffaille et al. \(2018\)](#); [Bernard \(2021\)](#). The sensitivity of air humidity to these parameters has still to be quantified in current simulations. Over the whole period, the RMSE, NAD and bias are higher with TEB than with WRF but the specific humidity modeling remains satisfactory.

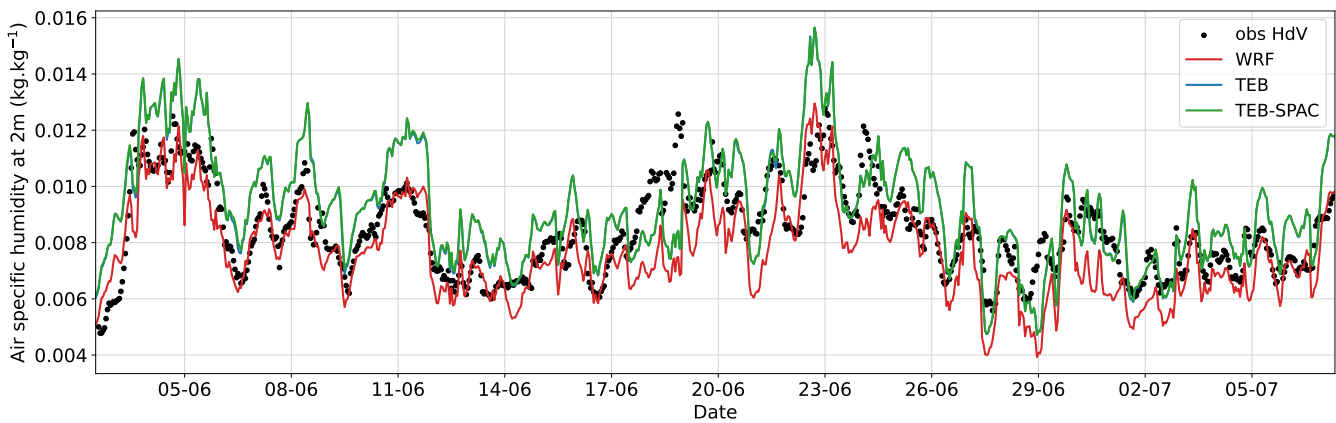


Figure 5.14: Comparison of observed and simulated air specific humidity at 2 m in HdV street.

Then, the atmospheric pressure is well modeled in the three simulations (Fig. 5.15). Compared to WRF, TEB simulates higher pressures that are closer to the observations, the RMSE and bias are therefore improved (Table 5.7).

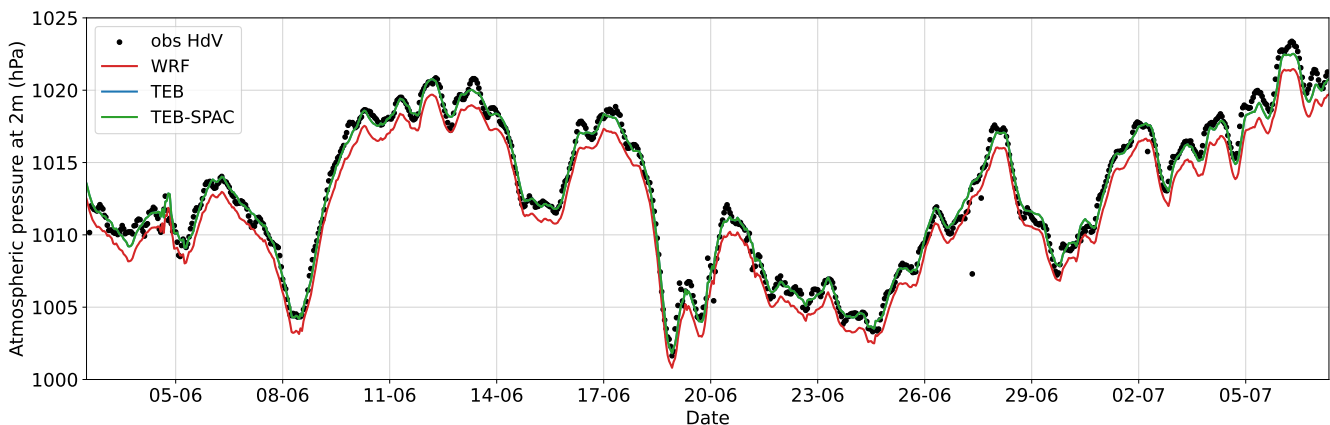


Figure 5.15: Comparison of observed and simulated atmospheric pressure at 2 m in HdV street.

No large difference of temperature, humidity and pressure is observed when trees and soil are added in the model (TEB-SPAC). This could be explained by the relatively low fraction of trees (16%) and soil (1.6%) in this street (Table 5.8).

5.3.2 Analysis of the tree energetic and hydraulic functioning

Key variables of the tree canopy energetic and hydraulic functioning modeled by TEB-SPAC are presented in this section. The results are analyzed in the Haussmann street, a street canyon with trees located in the center of Paris. The street and tree characteristics are presented in the Table 5.8. Note that a spin-up period of one day is considered in TEB, so the results are presented from the 2nd of June.

Table 5.8: List of street and tree characteristics of Haussmann and HdV streets.

Parameter	Definition	Haussmann	HdV	Unit
lon	longitude	2.329134	2.351848	°
lat	latitude	48.87351	48.85556	°
H	building height	20.9	10.9	m
W	street width	26.0	29.4	m
L	street length	316.0	158.9	m
H/W	street aspect ratio	0.80	0.37	m
θ	street orientation	281.8	122.4	°
δ_r	road fraction	0.489	0.492	-
δ_s	bare soil fraction	0.011	0.008	-
δ_t	tree canopy fraction	0.11	0.08	-
h_{max}	tree canyon height	14.5	10.9	m
h_{tk}	tree trunk height	4.8	3.6	m
DBH	tree trunk diameter	28.8	49.2	cm
V_{trunk}	tree trunk volume	0.00478	0.00724	$m^3 \cdot m_{CPA}^{-2}$
LAI	leaf area index	2.95	3.35	$m_{leaf}^2 \cdot m_{CPA}^{-2}$
$\psi_{ref_{leaf}}$	reference leaf hydraulic potential	-1.74	-1.74	MPa
N_t	number of trees in the street	30	13	-

First, the energy budget of the tree canopy is illustrated in Fig. 5.16. It shows that during the first two weeks the latent heat flux (LE) of evapotranspiration reaches around $350 \text{ W} \cdot \text{m}^2$ in non rainy days. On June 14, the LE starts to decrease up to low values around $50 \text{ W} \cdot \text{m}^2$. In parallel, the sensible heat flux (H) increases because the net radiation (RN) remains around $650 \text{ W} \cdot \text{m}^2$. From June 17 to July 31, the tree evapotranspiration stays low, except some increases during and after rain. Trees greatly reduce their transpiration and most of the energy received is dissipated as heat, signifying that the leaves are heating up. The heat storage by conductivity (G) in the leaf is low, this is not surprising given the limited volume and thermal proprieties of the leaves. Disturbed peaks in the LE curve correspond to rainy days when direct water evaporation from the leaves occurs. Indeed, several rainfall episodes of varying intensities occur over the period, as presented in Fig. 5.17. This figure also shows the fraction of the leaves covered by water. This fraction increases with rainfall and decreases more or less rapidly depending on the intensity of evaporation. The resulting LE partition between transpiration and evaporation is shown in Fig. 5.18.

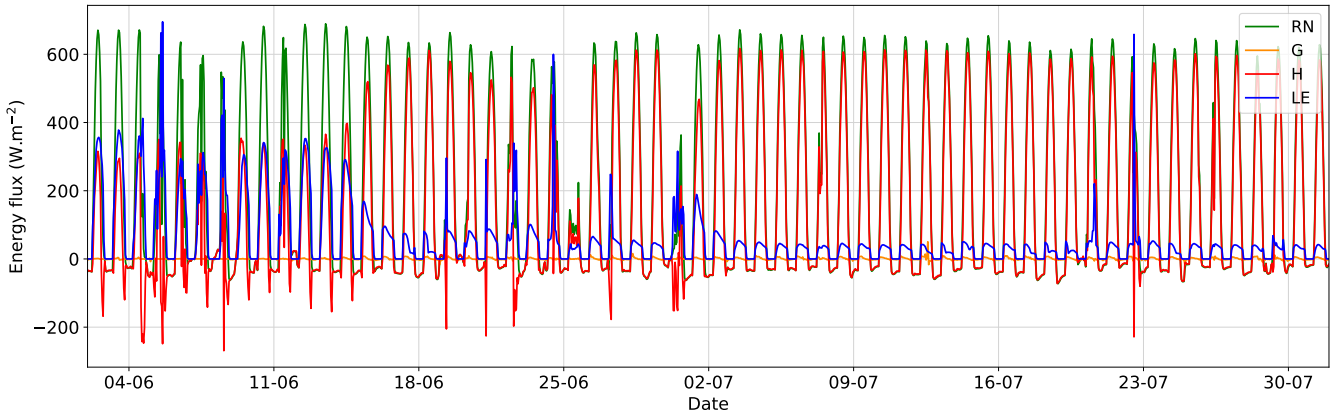


Figure 5.16: Energy budget of the tree canopy simulated with TEB-SPAC in Haussmann street. RN: net radiation, G: conduction flux (storage), H: sensible heat flux, LE: latent heat flux.

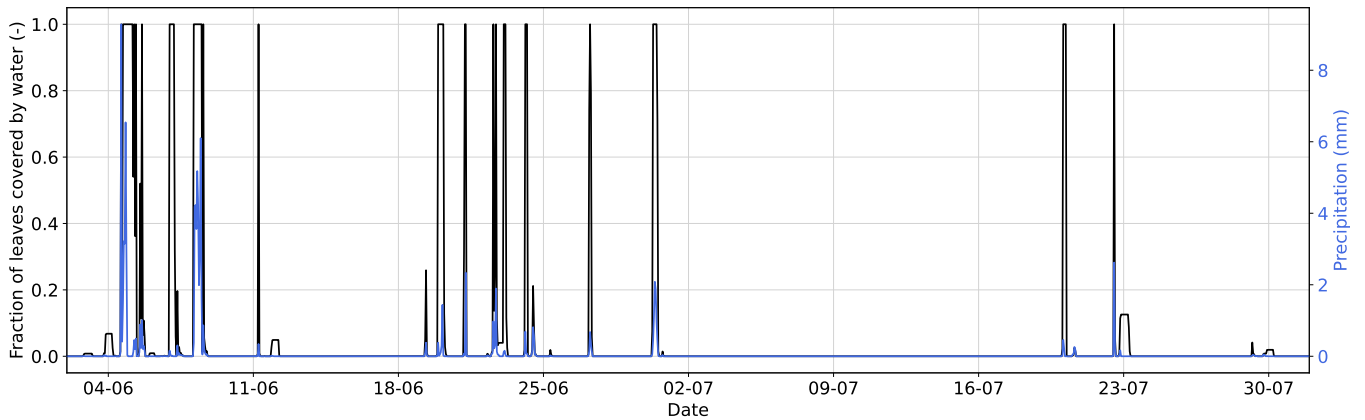


Figure 5.17: Precipitation and fraction of tree leaves covered by water simulated with TEB-SPAC in Haussmann street.

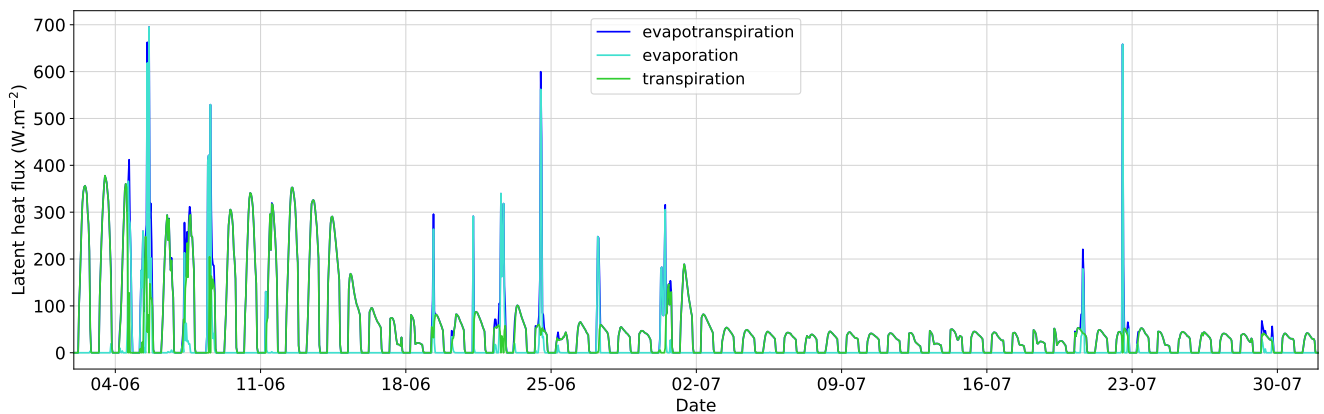


Figure 5.18: Partition of the latent heat flux of the tree canopy simulated with TEB-SPAC in Haussmann street.

Then, it is also possible to distinguish the water flows and potentials in the tree modeled by SPAC (Fig. 5.19 and 5.20). The drop in transpiration around the 14th of June is clearly visible, as are the increases after the rains both on the water fluxes and potentials. The potential of the leaf sub-stomatal cavity stabilizes at -2.3 MPa during water stress. This value is sensitive to $\psi_{refleaf}$

that depends on the tree xylem type (see Section 5.2.5.3). Root uptake occurs preferentially in the SPAC soil layer with the highest water content. So, the trees draws water from both soil layers, with a relative proportion depending on the water content of the layers. The reservoir contributes to transpiration during the day and is recharged at night, but its contribution is very small and its hydraulic potential is always very close to the xylem potential. The flux depends on the reservoir volume and the value of hydraulic resistance connecting wood water storage to the main flow.

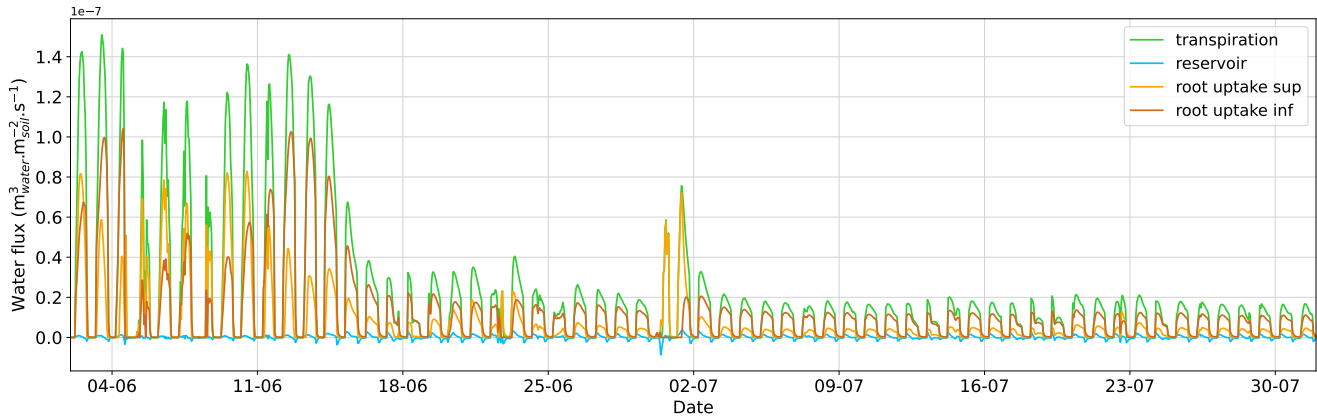


Figure 5.19: Water fluxes in the tree canopy simulated with TEB-SPAC in Haussmann street.

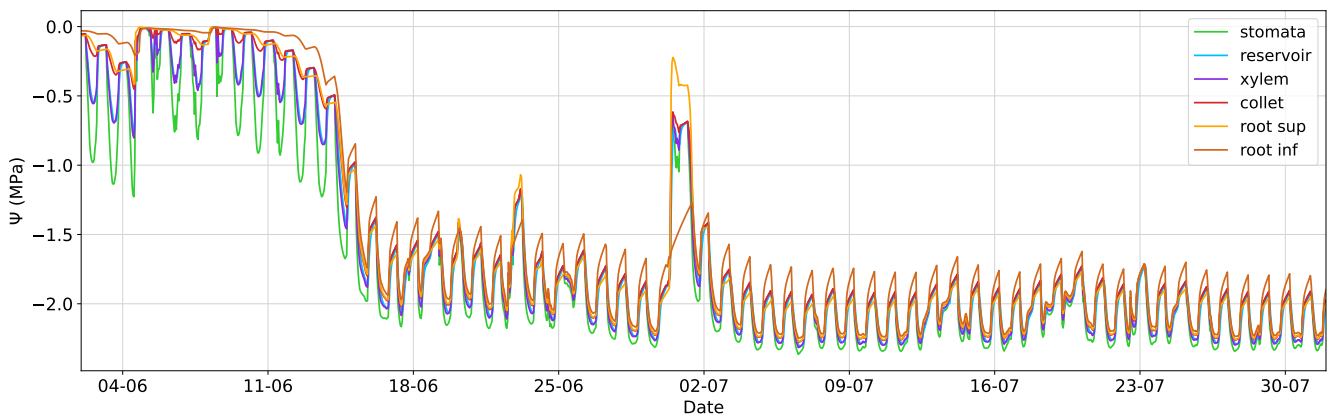


Figure 5.20: Hydraulic potentials of the tree canopy simulated with TEB-SPAC in Haussmann street.

This temporal variations are also observed on the stomatal conductance presented in Fig. 5.21. A fall in stomatal conductance and hence stomatal closure is observed around midday on almost all days. TEB-ISBA also models the fall in stomatal conductance in the middle of June and the stomatal conductance values are close. The main difference between ISBA and SPAC is that SPAC represents a greater increase in stomatal conductance after rainfall events. This is due to the $f(\psi_{leaf})$ function (Fig. 5.22), which is more sensitive to soil water content through the tree's series of hydraulic potentials. With this sensibility, SPAC simulates also a greater daily variability in the $f(\psi_{leaf})$ function and the stomatal conductance.

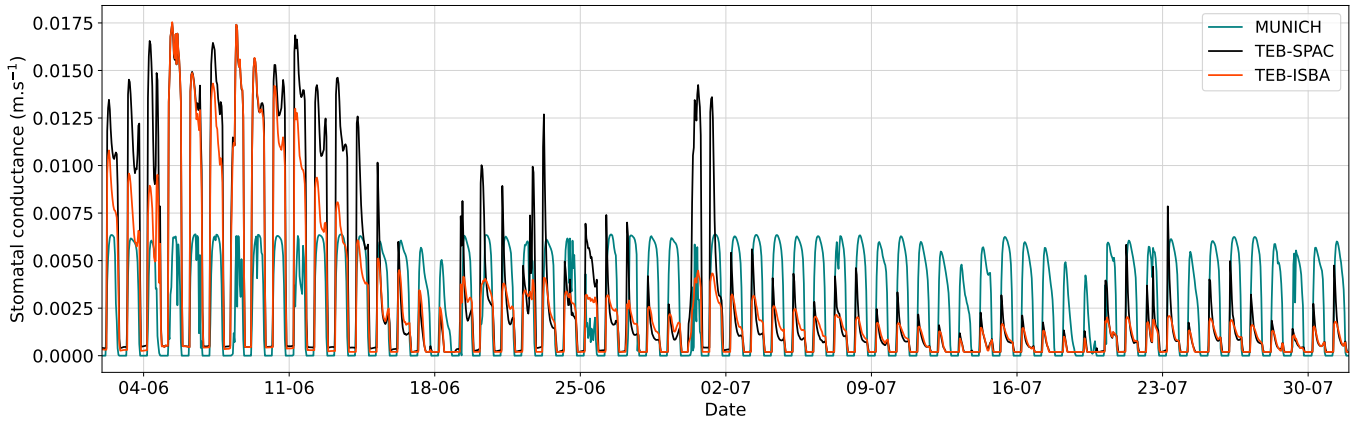


Figure 5.21: Stomatal conductance of the tree canopy simulated with TEB-SPAC and TEB-ISBA in Haussmann street.

For comparison, the stomatal conductance calculated in MUNICH for gas deposition on leaves (eq. (4.25)) is also shown in Fig. 5.21. This parameterization depends on temperature and solar radiation, but not on water stress. The conductance is therefore more constant over the period, with a decrease on cloudy days and high temperatures.

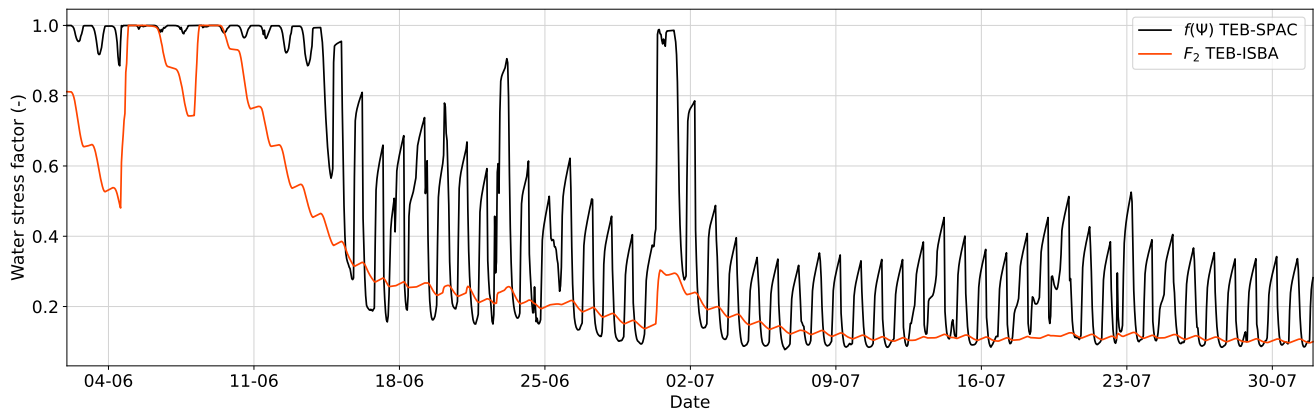


Figure 5.22: Water stress function simulated with TEB-SPAC and TEB-ISBA in Haussmann street.

The SWC evolution is illustrated in Fig. 5.23. The figure represents the gradients in the 15 sublayers of each SPAC soil layer but the SWC is rather homogeneous between the sublayers and the gradient is not visible. This is due to the soil texture (sandy clay loam), which has rather good diffusive properties. The curves are presented from the 1st of June here to illustrate that the initial condition is the field capacity in both SPAC layers. Soil water is rapidly absorbed by trees due to the high tree crown to soil surface ratio (10). During heavy rains at the beginning of June, the soil content almost reaches saturation point, but quickly falls back down with root uptake. Small soil water content increases occur during the night and are due to diffusive vertical flows between the bare soil layers, and also to horizontal flows with the soil layers beneath the road.

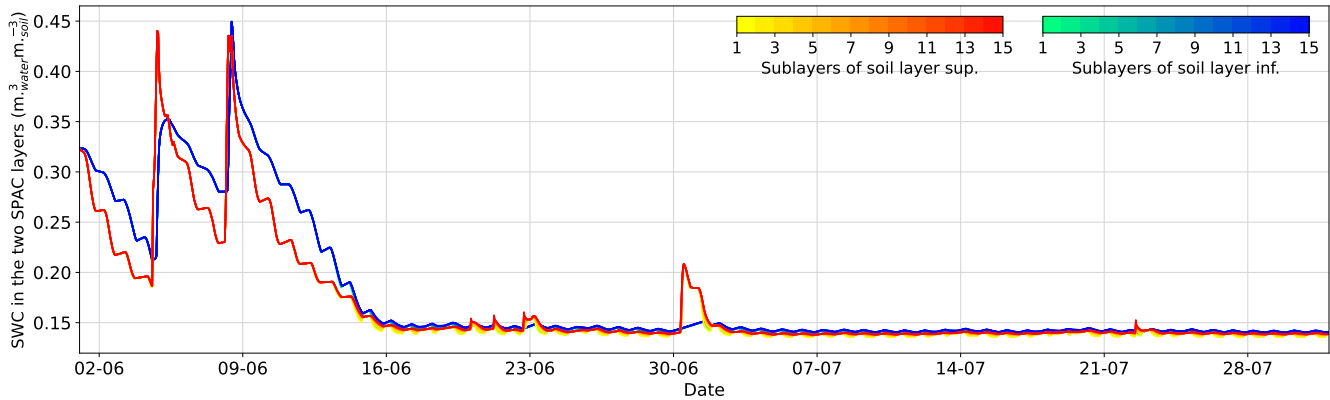


Figure 5.23: Soil water content in the 15 sublayers of each SPAC soil layer simulated with TEB-SPAC in Haussmann street.

Finally, the temperatures of the different surfaces in the street are compared in Fig. 5.24. During daytime, the roof and road have larger surface temperatures following by the bare soil and the south-facing wall (B). The north-facing wall (A) is more often in the shadow of trees and of the other building due to the relatively high aspect ratio (0.8), so its temperature is lower. The leaf surface temperature is most of the time comprised between the two walls temperature and it can reach 40°C during heatwave. This value is rather high but coherent with the low evapotranspiration and high sensible heat fluxes observed during these periods (Fig. 5.16).

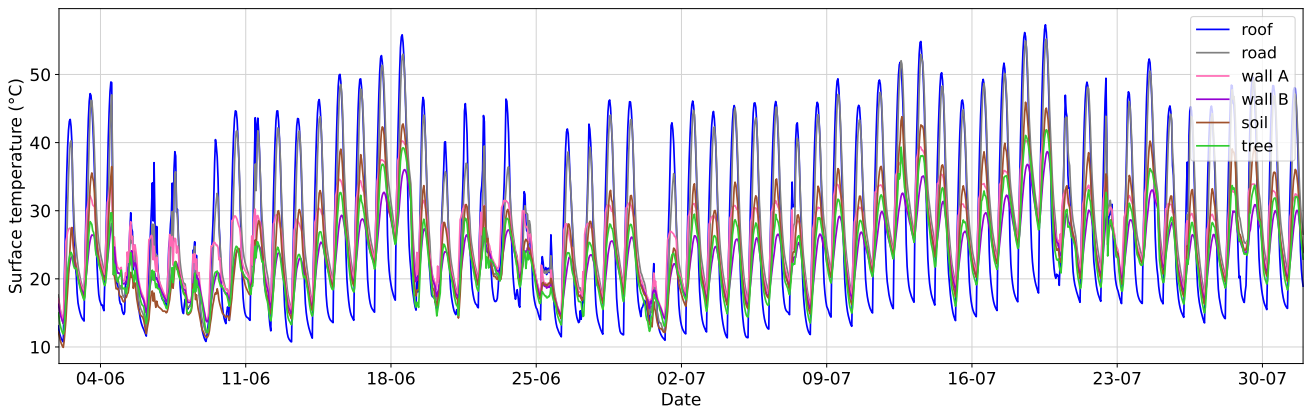


Figure 5.24: Surface temperature of the different street components simulated with TEB-SPAC in Haussmann street.

To complete the temporal analysis of the tree energetic and hydraulic functioning done in one street, maps of *SWI* and tree *LE* at three different dates are shown in figures 5.25 and 5.26.

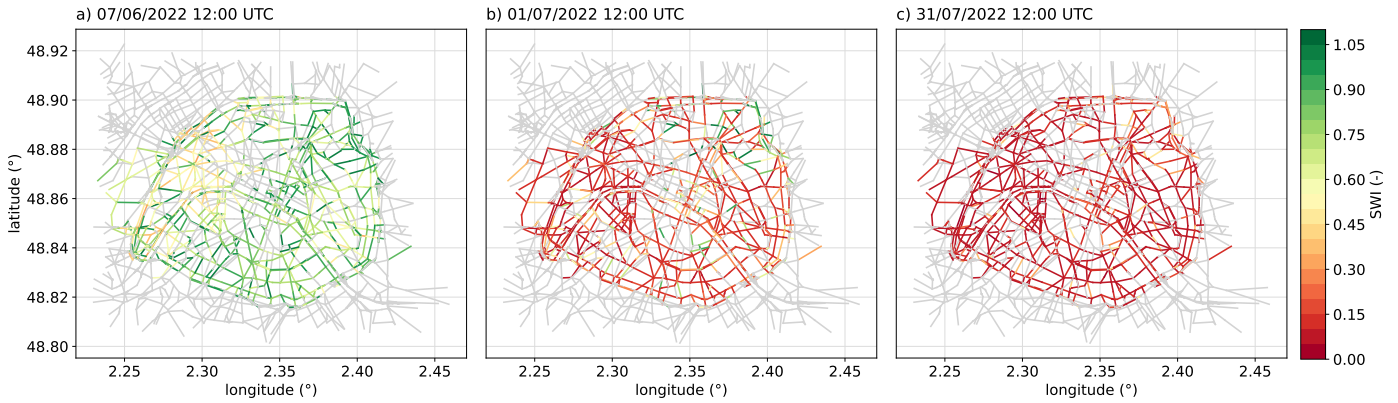


Figure 5.25: Soil water index (SWI) simulated with TEB-SPAC in Paris streets at three different dates.

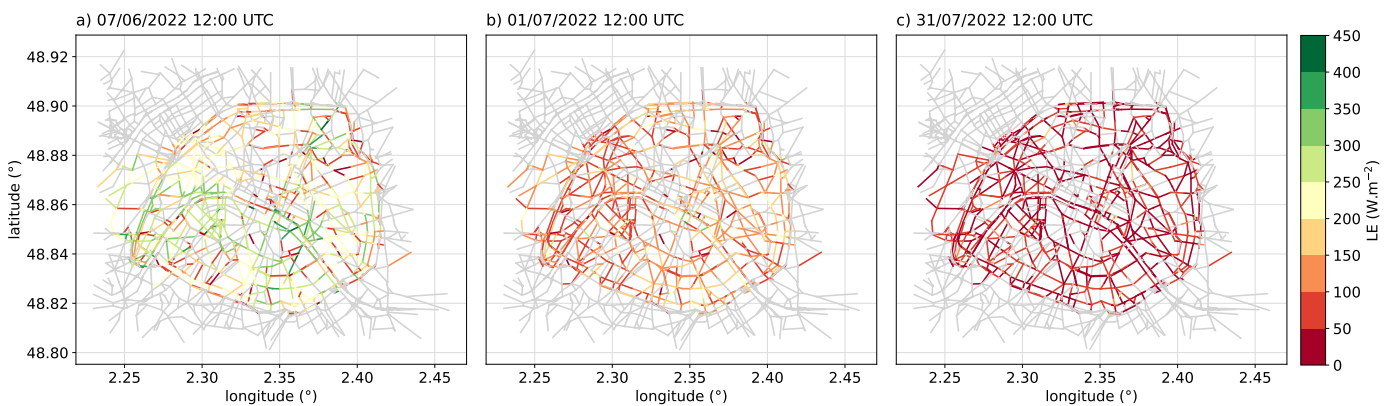


Figure 5.26: Tree canopy latent heat flux (LE) simulated with TEB-SPAC in Paris streets at three different dates.

After one week of simulation (Fig. 5.25a and 5.26a), the SWI is relatively high, between 0.5 and 1 with a certain heterogeneity between the streets. As the water content in all streets is initialized to the field capacity, this heterogeneity depends on street and tree characteristics and especially on the $\psi_{refleaf}$ value, the tree LAI and crown to soil surface ratio. On the same day the tree evapotranspiration is around 300 W.m^2 as in Haussmann street. Then after one month of simulation (Fig. 5.25b and 5.26b) the SWI has decreased but the recent rainfall has raised the water content. The LE is quite heterogeneous and seems correlated with the SWI . Finally, on the 31st of July and after many days without rain, the SWI is very low (around 0.1) in almost all streets. This induced a very low LE (around 50 W.m^2) in all streets.

This spatial and temporal analysis of SWI and LE variations is consistent with the variations observed in Haussmann street, with heterogeneities between streets due to their own characteristics. The conclusions drawn from the analysis of one street can therefore be generalized to all Paris streets. There is a rather humid period at the beginning of June when the trees are not suffering from water stress and evapotranspiration will be quite high. SWC decreases rapidly due to high root uptakes. Low rainfalls in July lead to low SWC close to the wilting point. As transpiration is very sensitive to the SWC through the series of hydraulic potentials, trees transpiration is limited from June 15 to July 31. To analyze the impacts of the trees on street micro-climate in the next sections, the results will be averaged on the "no water stress" period from 02 or 06/06 to 15/06 (depending on the variable due to spin-up time) and on the "water stress" period from 16/06 to 31/07.

5.3.3 Impacts of the MUNICH-TEB-SPAC coupling on the modeled urban micro-climate

The meteorological fields simulated by TEB (without tree) and by TEB-SPAC (with trees) in the street are compared to WRF surface meteorological fields that are used in the MUNICH REF simulation. Note that some fields are different i.e. the air temperature at 2 m in WRF and the average air temperature in the street volume in TEB, but they are both used in MUNICH simulations, so they are compared in order to interpret the impacts on concentrations.

5.3.3.1 Comparison of meteorological fields simulated by WRF and TEB (without tree) and used in MUNICH

In this section, the meteorological fields simulated by TEB without tree are compared to WRF. Given the wide daily variation in weather data, the fields are averaged over day and nighttime. The following figures present the WRF average fields along with the mean absolute difference of the variables simulated by TEB. First, the comparison of the daytime and nighttime air temperatures is presented in Fig. 5.27.

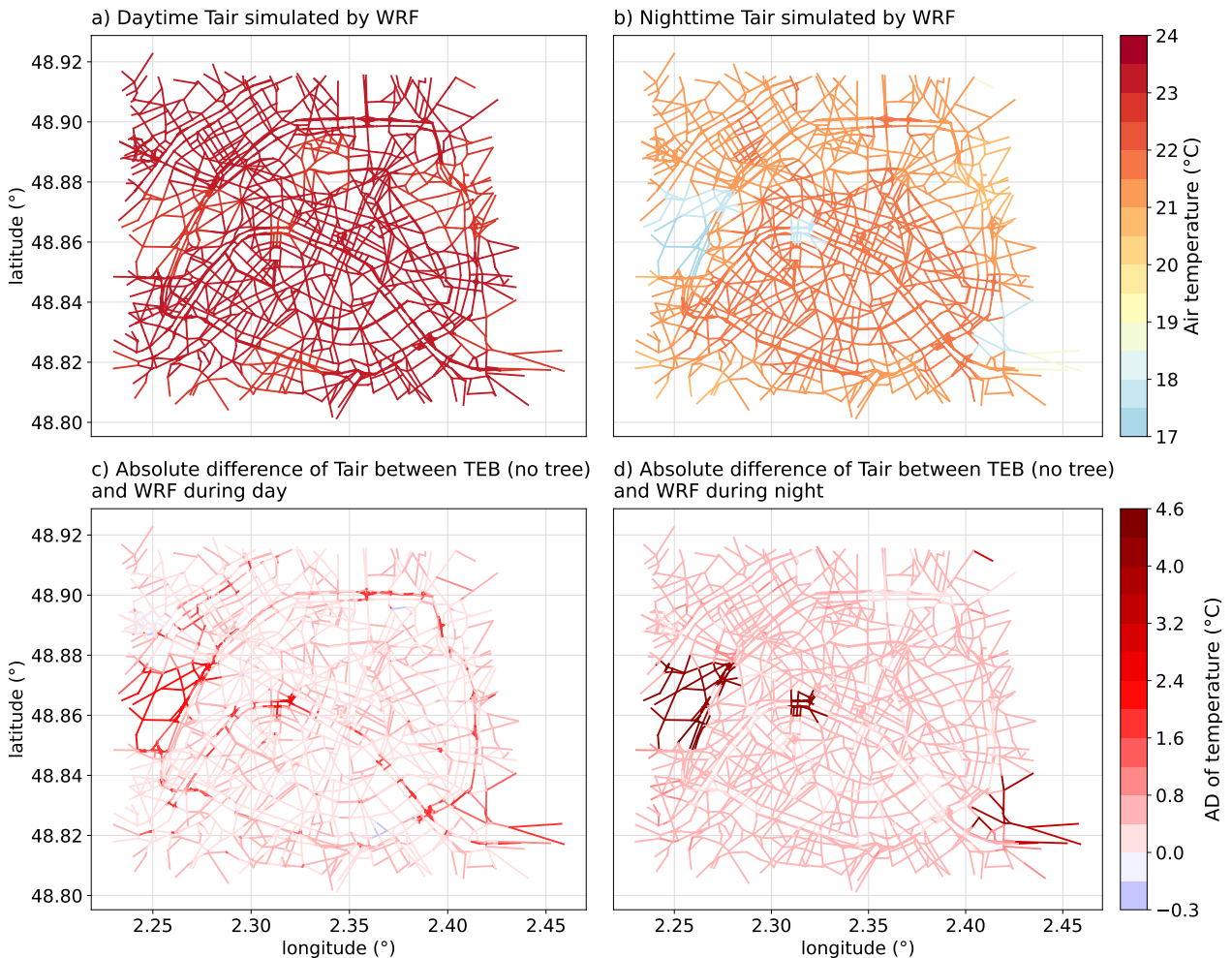


Figure 5.27: a) Daytime and b) nighttime average air temperature at 2 m simulated by WRF and c) daytime and d) nighttime mean absolute difference with the average air temperature in the street simulated by TEB.

Figure 5.27 shows that WRF simulates a quite homogeneous air temperature at 2 m during the day. Temperature are lower in the cells containing vegetation as the Vincennes and Boulogne woods. This difference is higher during the night with 18°C on average in these areas and 21°C in the urban cells. TEB simulates higher air temperatures in the vegetated meshes ($+1^{\circ}\text{C}$ by day $+4^{\circ}\text{C}$ by night). Indeed, TEB computes the temperature gradient from the WRF air temperature well above the surface ($H + 25$ m), which is less impacted by the land-use type. In other streets, compared to the WRF 2 m temperature, TEB simulates higher air temperatures, on average $+1.2^{\circ}\text{C}$ during day and $+0.5^{\circ}\text{C}$ during night. This may be due to the ability of the TEB model to more accurately represent thermo-radiative processes at street level, and in particular radiation reflection and heat storage in street surfaces.

Figure 5.28 shows that the specific humidity is globally larger during the night than during the day and that TEB induces a quite spatially homogeneous increase in Q_{air} of 0.00145 kg.kg^{-1} during day and 0.00142 kg.kg^{-1} during night. This could be due to the finer representation of the urban water budget, and in particular the evaporation of water accumulated on roofs and walls after rainfall as discussed in the Section 5.3.1.

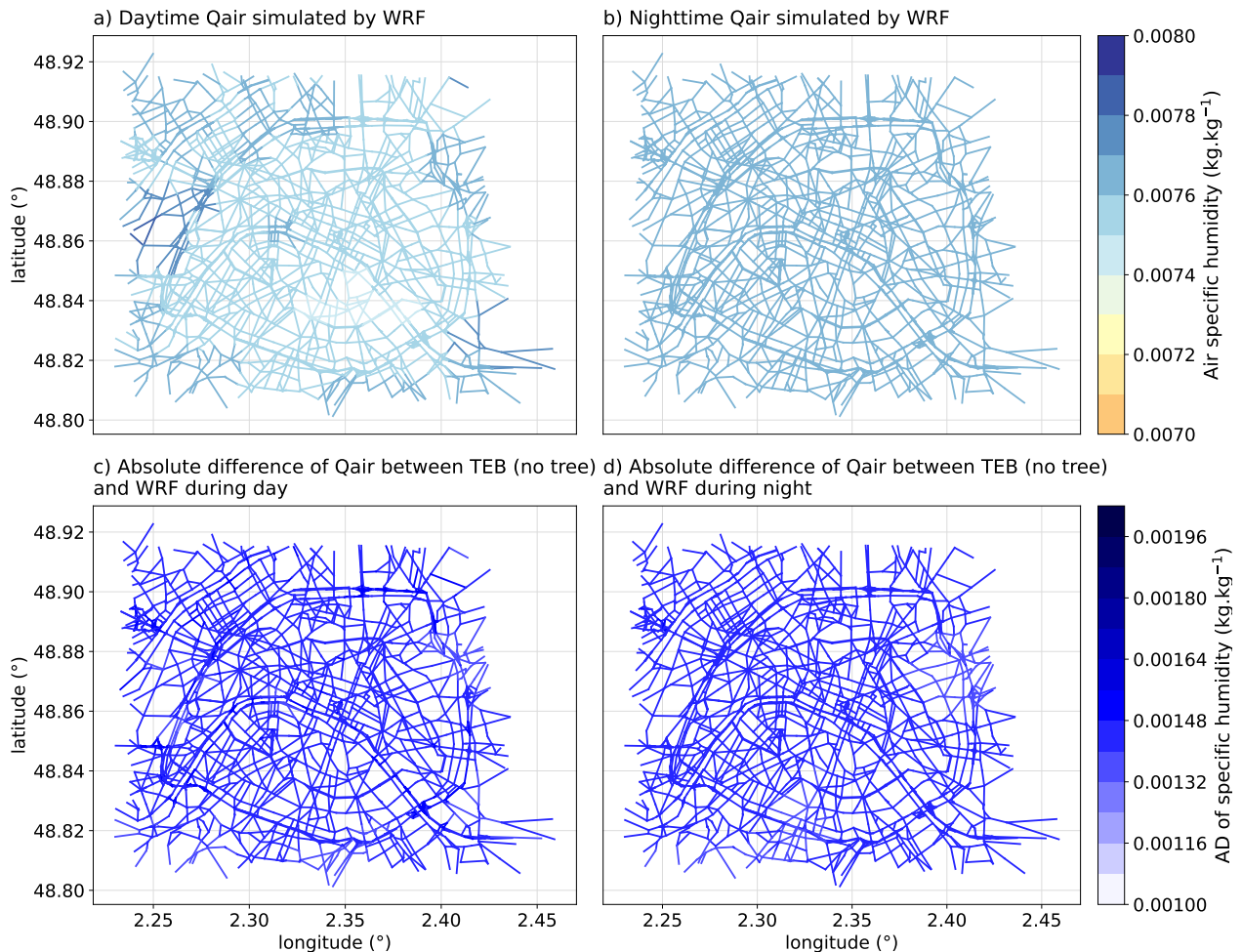


Figure 5.28: a) Daytime and b) nighttime average surface air specific humidity simulated by WRF and c) daytime and d) nighttime mean absolute difference with the average air specific humidity in the street simulated by TEB.

Figure 5.29 presents the standard deviation of the vertical wind speed, σ_W . This variable is used to parameterize the vertical exchange coefficient that regulates the vertical transfer of gas and particles in the street, so the street concentrations of the chemical species are sensitive to this variable. This variable depends on the friction velocity, boundary layer height, MOL and building height (see chap. 2 and [Soulhac et al. \(2011\)](#)). In WRF, the friction velocity is particularly sensitive to the anthropogenic sensible heat flux, which is prescribed in the urban canopy model depending on the land-use. This sensible heat flux is larger in transport and commercial areas, than in the city center, in the suburb and nil over natural areas, as described in the Chapter 3. On figures 5.29a and b, the different areas are clearly visible and gives different average σ_W . In particular σ_W is lower both during day and night in the Vincennes and Boulogne woods and near the Invalides. The impact of the σ_W computed from TEB MOL is completely different during day and night. During day, TEB simulates a greater stability and σ_W is on average -0.04 m.s^{-1} lower. During night, a greater instability is simulated, and σ_W is on average 0.03 m.s^{-1} higher. Like the air temperature, TEB does not simulate the impact of the vegetation in the cells containing woods.

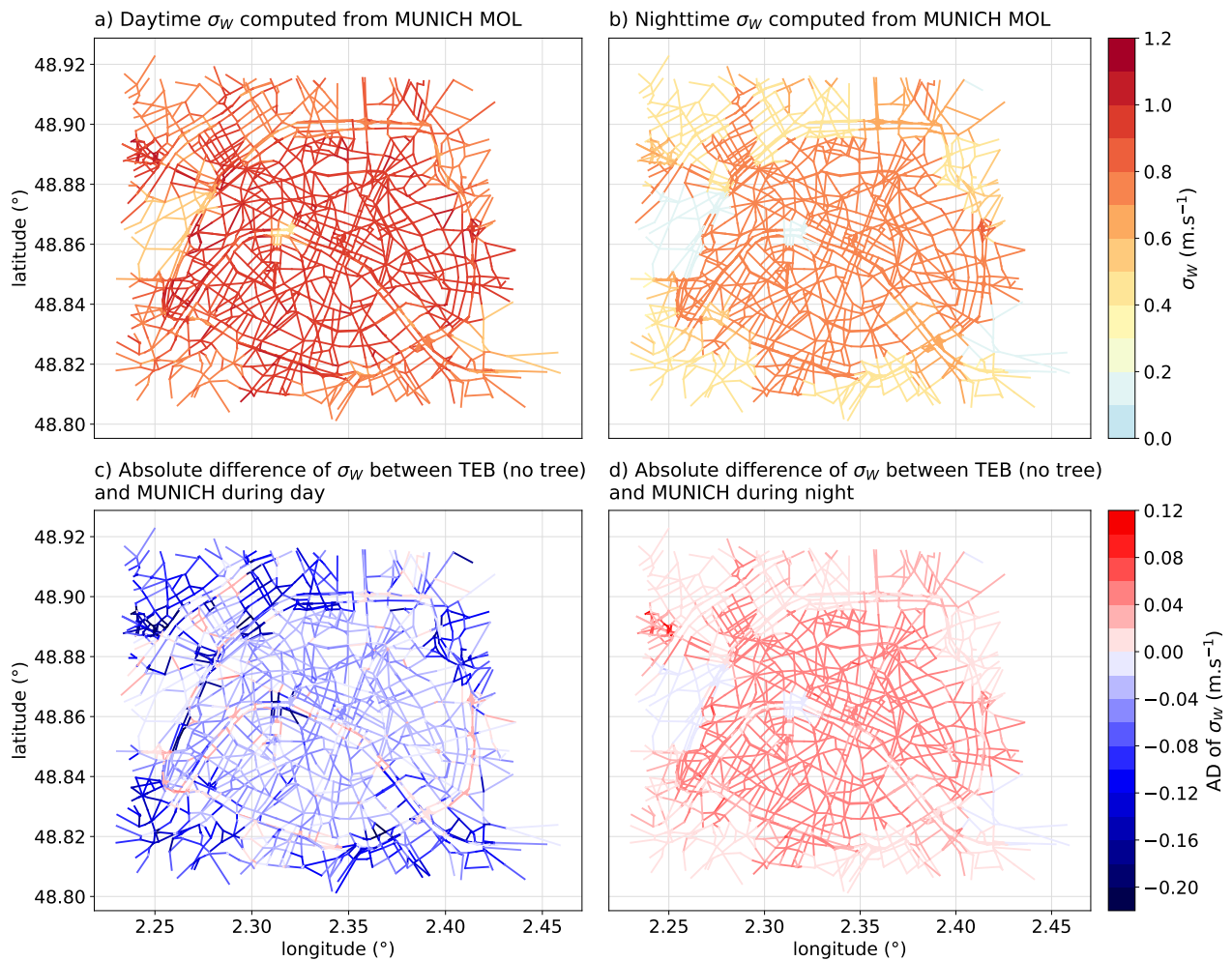


Figure 5.29: a) Daytime and b) nighttime average σ_W computed from MUNICH MOL and c) daytime and d) nighttime mean absolute difference with the average σ_W simulated from TEB MOL.

5.3.3.2 Impacts of trees on urban micro-climate simulated by TEB-SPAC

This section presents the impact of street trees on air temperature, humidity and σ_W . The TEB-SPAC simulation, that includes tree canopy and bare soil in the street, is compared to the TEB simulation, that includes only urbanized artificial surfaces.

Figure 5.30 illustrates the street air temperatures simulated by TEB-SPAC and the absolute difference of temperature between TEB-SPAC and TEB. Because trees limit their transpiration from June 15, the results are averaged on two periods: before the water stress period (from 02 to 15/06) and during the water stress period (from 16/06 to 31/07).

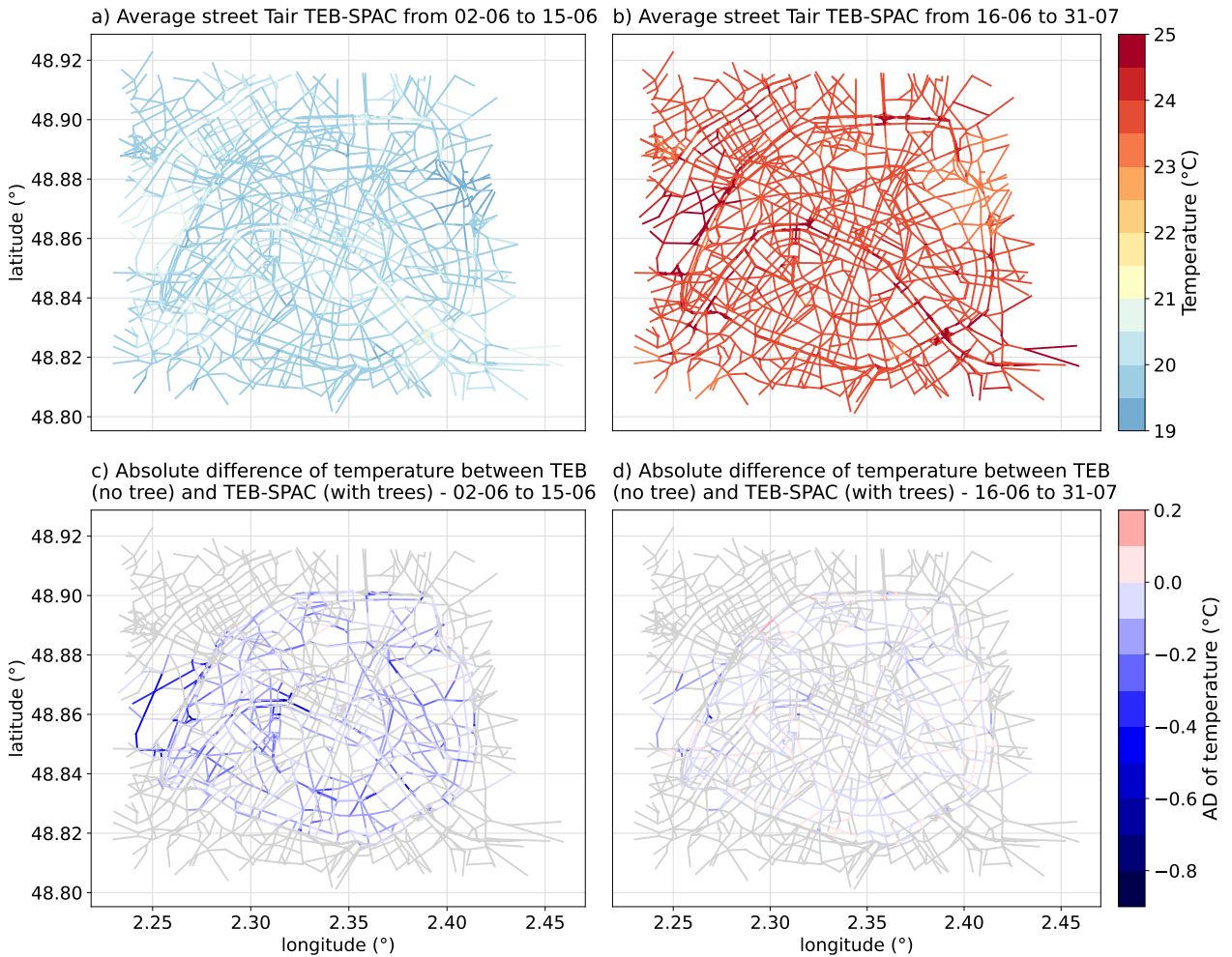


Figure 5.30: Street average air temperature simulated by TEB-SPAC averaged a) before the water stress period (from 02/06 to 15/06) and b) during the water stress period (from 16/06 to 31/06) and mean absolute difference with the street average air temperature simulated by TEB c) before and d) during the water stress period.

Temperatures simulated by TEB-SPAC are higher during the second period because forcing temperature are also higher. The tree and bare soil effect on temperature is contrasted between the two periods. Indeed, when trees transpire and soils evaporate water, air temperatures in street with trees are globally lower in TEB-SPAC simulations, -0.12°C on average and up to -0.77°C (Fig. 5.30c). The cooling intensity seems to correlate rather well with LAI (Fig. 4.4a). When trees suffer from water stress (Fig. 4.4b), the tree cooling effect is much more reduced, -0.02°C on average and up to -0.46°C . In some streets, the presence of trees even slightly increases temperatures (up

to $+0.17^{\circ}\text{C}$). This may be due to the tree aerodynamic effect that limits the street ventilation and therefore heat dissipation. This effect is not compensated by tree transpiration, so temperatures increase. The positive effect of shading on temperature reduction is less visible because it affects mainly the temperatures under the tree crown and the effect on the average temperature in the street is less strong. To confirm this, the same maps with the temperature at 2 m height in the street are presented in Fig. 5.31.

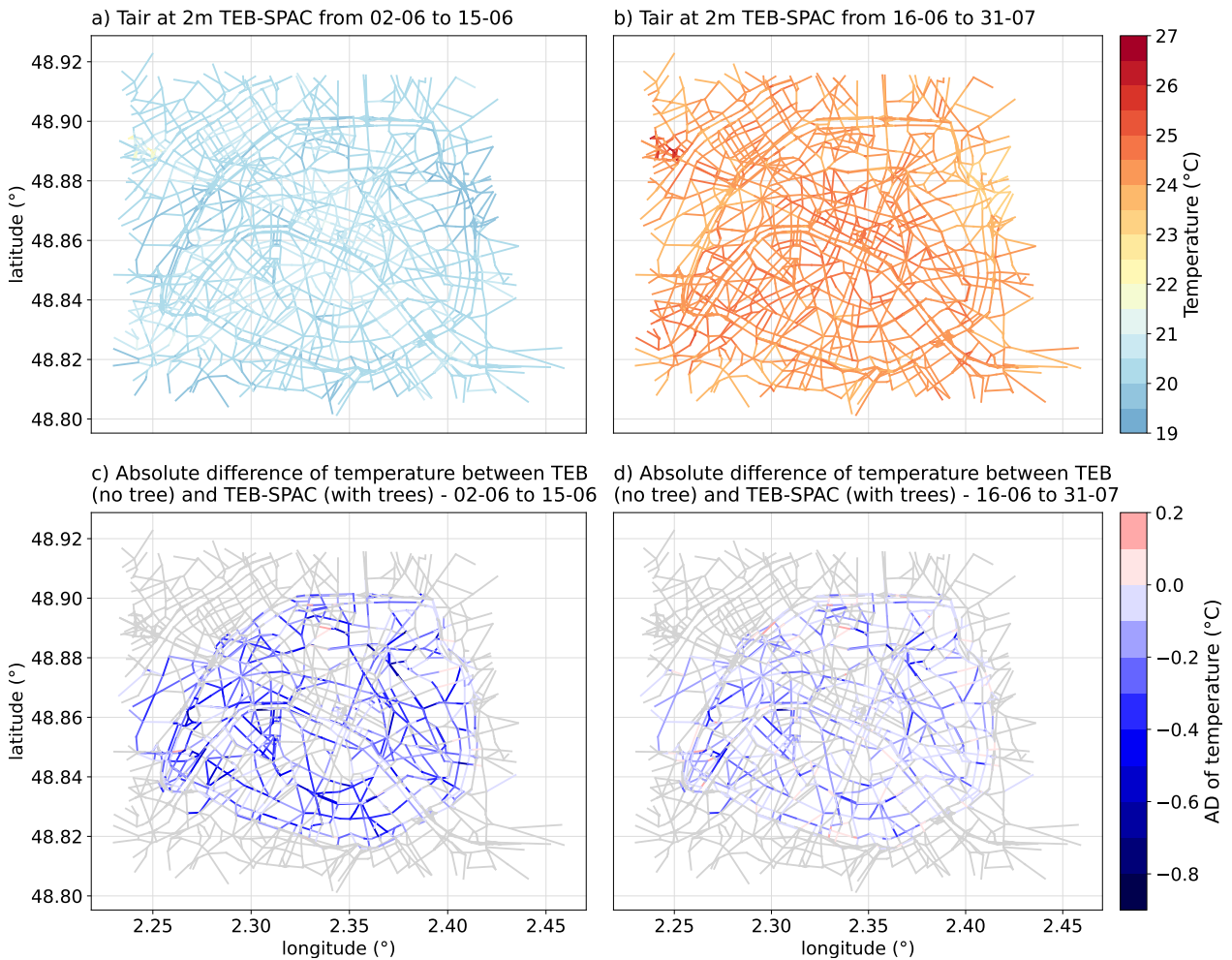


Figure 5.31: Air temperature at 2 m simulated by TEB-SPAC averaged a) before the water stress period (from 02/06 to 15/06) and b) during the water stress period (from 16/06 to 31/06) and mean absolute difference with the air temperature at 2 m simulated by TEB c) before and d) during the water stress period.

Figure 5.31c shows that before the water stress period, the tree cooling effect is on average higher on the 2 m air temperatures than on the street average temperatures (-0.19°C on average and up to -0.81°C). During the water stress period (Fig. 5.31d), some streets with trees have a higher temperature at 2 m than without (up to $+0.26^{\circ}\text{C}$), but the cooling effect of trees on the temperature under the crown at 2 m is still visible in many streets (-0.09°C on average and up to -0.67°C). These are streets with high *LAI* (Fig. 4.4a) and large tree fractions (Fig. 5.7). This suggests that the effects of shading can indeed reduce the air temperature under trees with wide crowns and high *LAI*. It would be possible, with further development, to capture these vertical gradients in MUNICH using the discretized version of the model developed by Sarica et al. (2023).

Figure 5.32 presents the relative difference of air temperature between the TEB and TEB-SPAC simulations for streets with trees and averaged over different periods. Note that to maintain the visibility of the figures, outliers are not displayed on the box-plots for all simulations and periods. They are, nevertheless, taken into account in the calculation of the statistics and in the other figures. Figure 5.32 shows that compared to the TEB simulation without trees, the presence of trees and soil in TEB-SPAC simulation induces on average in streets with trees a few percent (but significant) temperature decrease during the all period, nighttime, and the period before water stress. The temperature decrease is less significant during the water stress period.

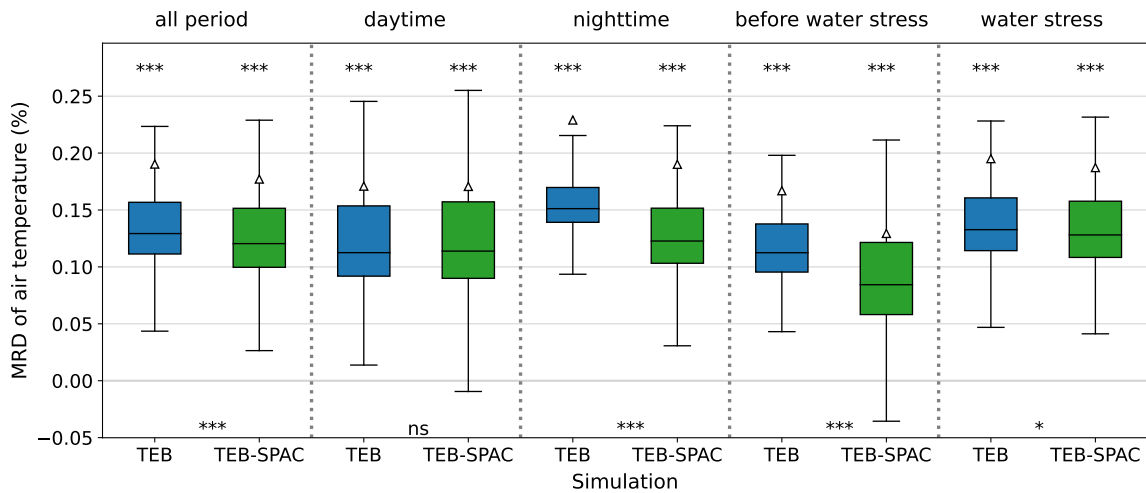


Figure 5.32: Box-plot of Mean Relative Difference (MRD) of street air temperature in streets with trees during the whole period, daytime, nighttime, before water stress (from 06/06 to 12/06) and during water stress (from 16/06 to 31/07). The mean is represented by a white triangle and the result of a T-test between TEB and REF and TEB-SPAC and 3EFF is indicated at the top of each box-plot. The result of a T-test between TEB and TEB-SPAC is indicated at bottom. '***': p-value < 0.001, '**': p-value < 0.01, '*': p-value < 0.05 and 'ns' (non-significant): p-value \geq 0.1.

Concerning the specific humidity (Fig. 5.33), an large increase from +17% to +31% is observed in all streets containing trees and in all periods. This increase is larger during daytime than nighttime and before water stress than during water stress. This can be explain by the evapotranspiration of trees and the soil evaporation which are higher during the day than the night due to the higher climatic demand and lower during the water stress due to limited soil water.

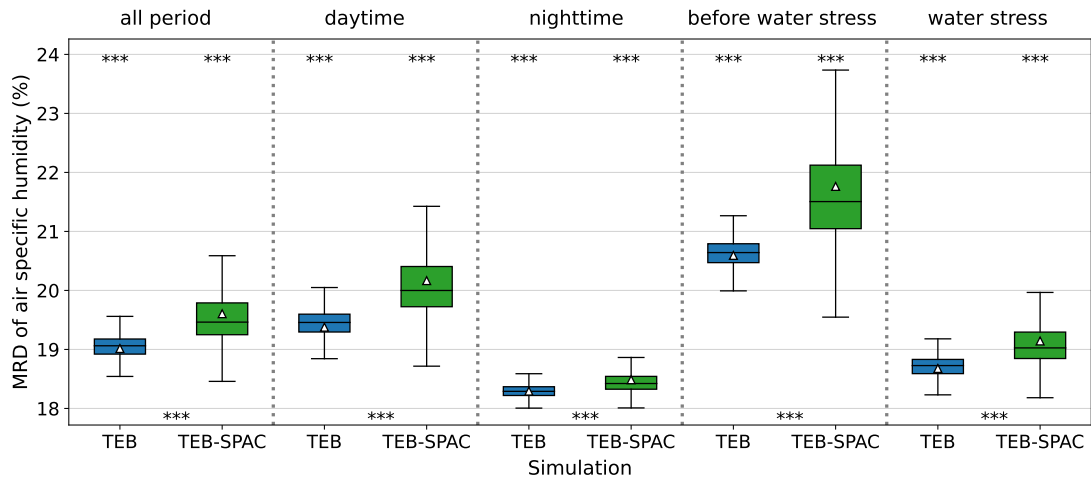


Figure 5.33: Box-plot of Mean Relative Difference (MRD) of street air specific humidity in streets with trees during the whole period, daytime, nighttime, before water stress (from 06/06 to 12/06) and during water stress (from 16/06 to 31/07). The mean is represented by a white triangle and the result of a T-test between TEB and REF and TEB-SPAC and 3EFF is indicated at the top of each box-plot. The result of a T-test between TEB and TEB-SPAC is indicated at bottom. '***': p-value < 0.001, '**': p-value < 0.01, '*': p-value < 0.05 and 'ns' (non-significant): p-value \geq 0.1.

As shown previously, TEB tends to decrease σ_W during day and increase it during night. The MOL above the street is modified by the presence of trees in the street, inducing a decrease in σ_W of a few percent compared to the TEB simulation without trees during all different periods.

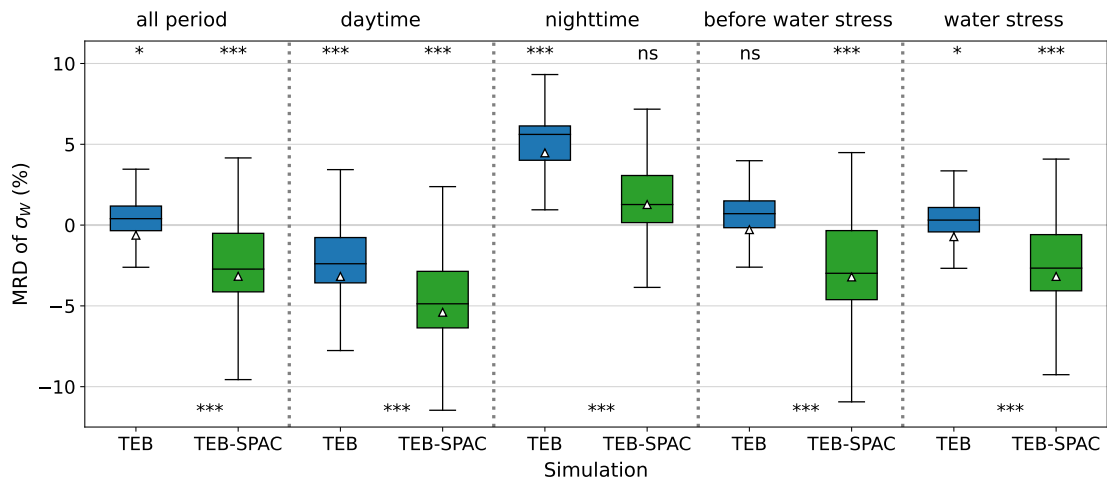


Figure 5.34: Box-plot of Mean Relative Difference (MRD) of σ_W in streets with trees during the whole period, daytime, nighttime, before water stress (from 06/06 to 12/06) and during water stress (from 16/06 to 31/07). The mean is represented by a white triangle and the result of a T-test between TEB and REF and TEB-SPAC and 3EFF is indicated at the top of each box-plot. The result of a T-test between TEB and TEB-SPAC is indicated at bottom. '***': p-value < 0.001, '**': p-value < 0.01, '*': p-value < 0.05 and 'ns' (non-significant): p-value \geq 0.1.

5.3.4 Impacts of the urban micro-climate on street concentrations

After studying the impacts of trees on the street meteorology, this section presents the impacts of the modification of meteorology by trees on NO_2 and particle concentrations. The impacts of modeling the local meteorology without trees are first assessed, before quantifying the impacts of the tree modifications of local meteorology on the concentrations.

5.3.4.1 Impacts on NO_2 concentrations

To illustrate the impact of modeling the local meteorology on NO_2 concentrations, Fig. 5.35 shows the NO_2 concentrations in Haussmann street for one-week simulations with different assumptions: MUNICH simulations are performed with TEB street meteorology (temperature, humidity, pressure) only or MOL only and the two combined, and they are compared to the reference simulation (REF).

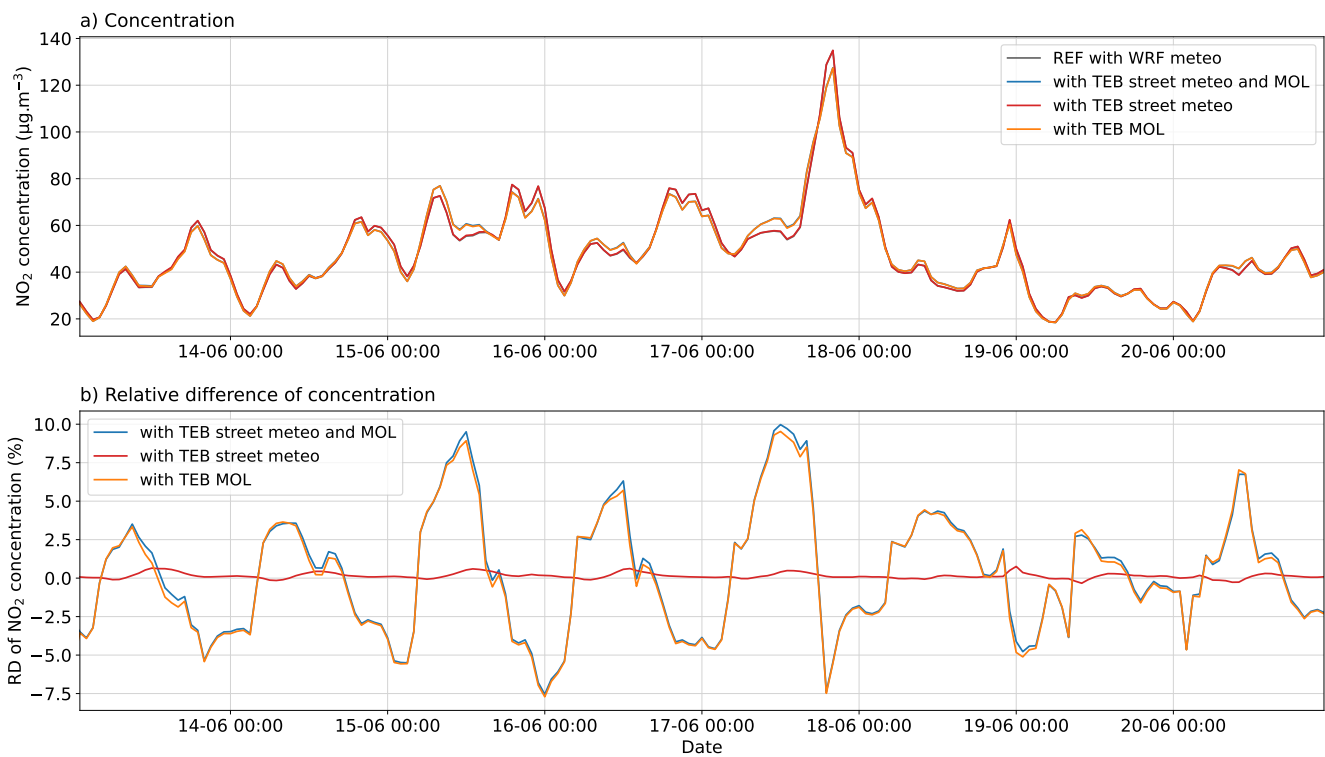


Figure 5.35: Comparison of a) NO_2 concentrations simulated in Haussmann street with WRF meteo (REF), TEB street meteo only, TEB MOL only and TEB street meteo and MOL (see Table 5.6) and b) relative deviation (RD) of NO_2 concentrations compared to the REF simulation.

Figure 5.35 shows that the street meteorology has a limited impact on NO_2 concentrations, but the change in MOL and therefore in σ_W and in the vertical transfer between the street and the background induces large increases in concentrations during the day (up to +10%) and decreases during the night (up to -7.5%). This is coherent with the variations of σ_W observed in Fig. 5.29 and 5.34. σ_W is lower during the day, inducing less dispersion of NO_2 , which is emitted in the street, and so higher concentrations.

For all streets during this week, the minimum, average and maximum RD of NO_2 concentrations due to street meteorology changes are respectively equal to -0.1, 0.2 and 0.8%. The minimum, average and maximum RD of NO_2 concentrations due to MOL changes are respectively equal to

−3.4, 1.1 and 15.6%. So NO_2 concentrations are mainly influenced by the representation of the vertical transfer between the street and the background (variation of σ_W). The impact of the street meteorology and in particular the temperature is lower.

Figure 5.36 presents the map of NO_2 concentrations simulated in the REF simulation and the relative difference of concentrations between TEB and REF simulations averaged over daytime and nighttime. The variation of NO_2 concentrations (average increase during the day of +2.2% and average decrease during the night of −0.79%) is very well anti-correlated with the variation of σ_W (Fig. 5.29). This is coherent with the results presented in Fig. 5.35.

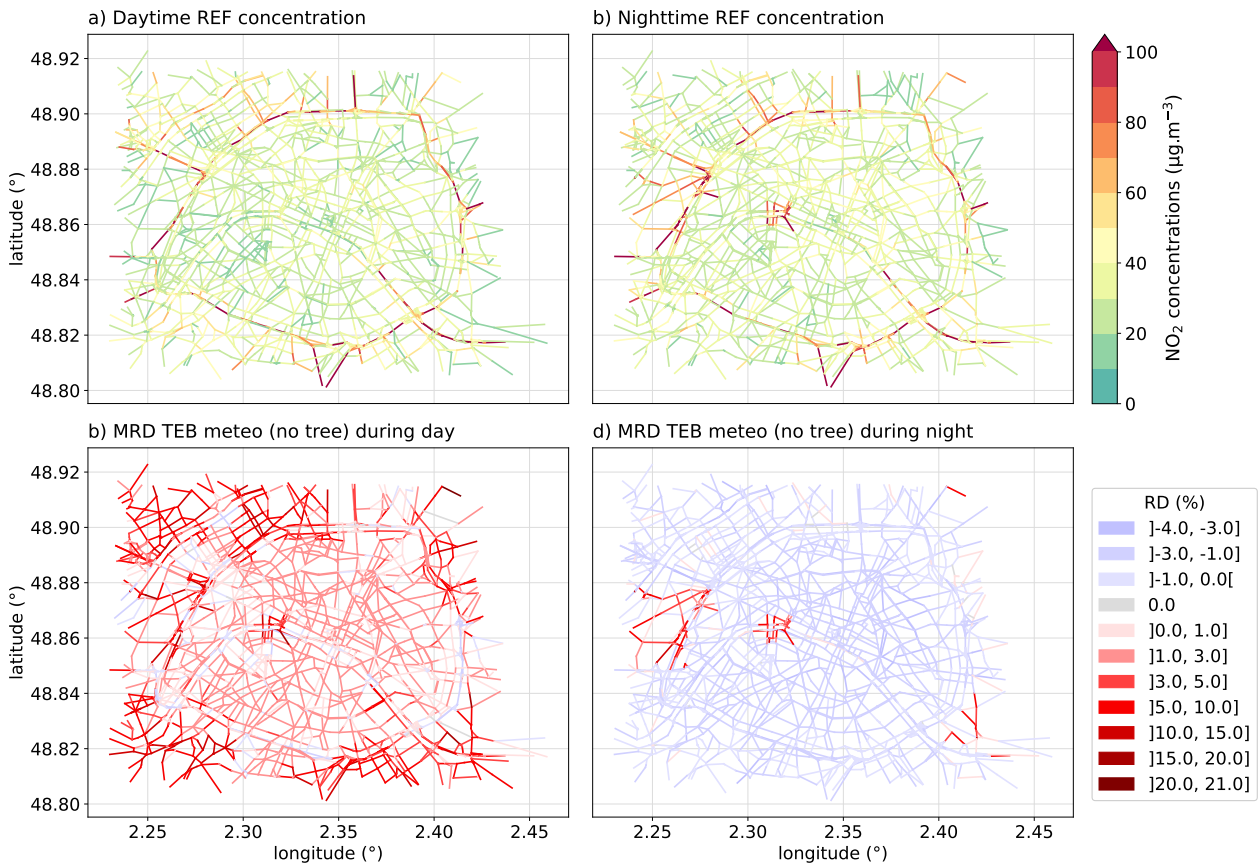


Figure 5.36: Comparison of average a) daytime and b) nighttime NO_2 concentrations simulated by MUNICH and WRF meteo and relative difference of c) daytime and d) nighttime NO_2 concentrations simulated by MUNICH with TEB street meteo and MOL.

To determine the impacts of the tree modifications of local meteorology on the concentrations, Fig. 5.37 represents the mean relative difference of NO_2 concentrations due to the global tree effect without modification of street meteo (3EFF / REF) and with modification of street meteo by MUNICH-TEB-SPAC coupling (TEB-SPAC / TEB). In Chapter 4, where the impact of trees on the micro-meteorology was not taken into account, the trees induce a NO_2 concentration increase due to the aerodynamic effect in streets with trees. Figure 5.37 shows that on average over the two months, the global tree effect is the same whether or not the street micro-meteorology is considered. Small differences are observed when concentrations are averaged on shorter periods and could be due to changes in the vertical transfer between the street and the background (σ_W) and to a lesser extend in air temperatures.

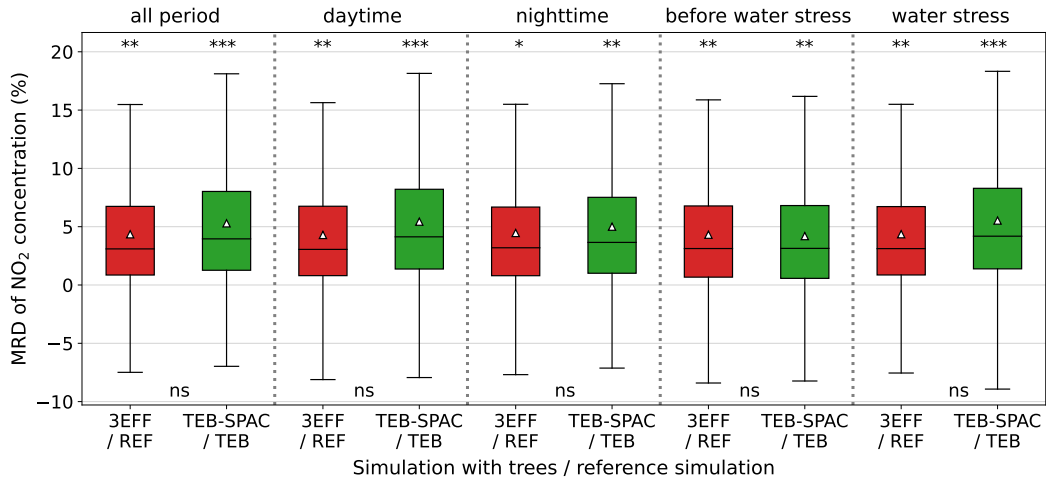


Figure 5.37: Box-plot of Mean Relative Difference (MRD) of NO_2 concentrations in streets with trees averaged during the whole period, daytime, nighttime, before water stress (from 06/06 to 12/06) and during water stress (from 16/06 to 31/07). The mean is represented by a white triangle and the result of a T-test between 3EFF and REF and TEB-SPAC and TEB is indicated at the top of each box-plot. The result of a T-test between 3EFF and TEB-SPAC is indicated at bottom. '***': p-value < 0.001, '**': p-value < 0.01, '*': p-value < 0.05 and 'ns' (non-significant): p-value \geq 0.1.

The same type of analysis is carried out for $\text{PM}_{2.5}$ concentrations in the next section.

5.3.4.2 Impacts on $\text{PM}_{2.5}$ concentrations

Figure 5.38 presents the results of the sensitivity analysis in Haussmann street for $\text{PM}_{2.5}$.

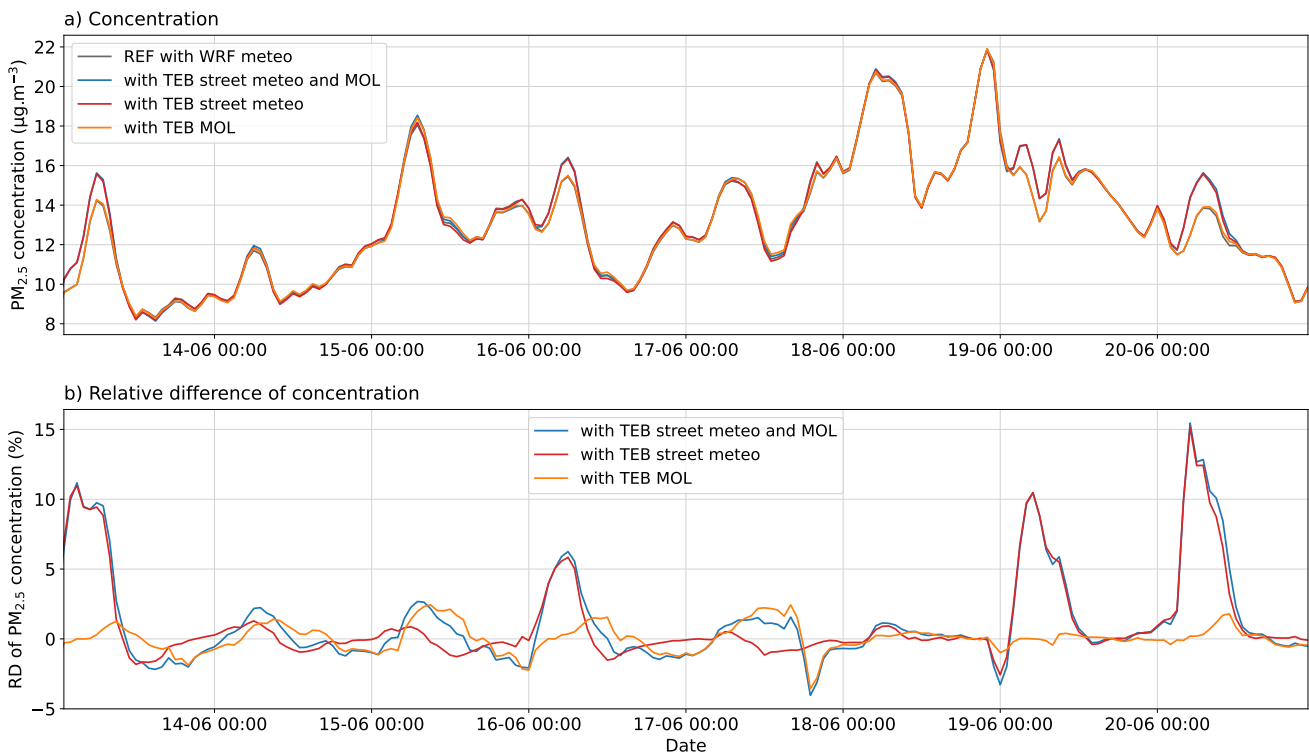


Figure 5.38: Comparison of a) $\text{PM}_{2.5}$ concentrations simulated in Haussmann street with WRF meteo (REF), TEB street meteo only, TEB MOL only and TEB street meteo and MOL (see Table 5.6) and b) relative deviation (RD) of $\text{PM}_{2.5}$ concentrations compared to the REF simulation.

Fig. 5.38, shows that both changes in street meteo and MOL impact $PM_{2.5}$ concentrations. As for NO_2 , the decrease in vertical transfer (σ_W) during the day leads to higher concentrations and the increase during the night leads to slightly lower concentrations. The street meteorology leads to the opposite effect, with generally a concentration increase during night and a decrease during day. The increases due to both effects are larger than the decreases so the net effect on $PM_{2.5}$ concentrations is positive. Then, large RD peaks due to the change in street meteo are observed on the mornings of June 13, 16, 19 and 20. To understand the origin of these sharp increases, the effect on the various components of $PM_{2.5}$ is now studied.

Figure 5.39 presents the RD of particle concentrations obtain a) in the TEB street meteo simulation as a function of the RD of air temperature and b) in the TEB MOL simulation as a function of the RD of σ_W . Each point represents a hourly concentration simulated in Haussmann street. The different compounds of $PM_{2.5}$ are represented: Black carbon (BC), a primary pollutant emitted in the street by traffic and assumed to be inert in the model, organic aerosols separated into primary organic aerosols (POAs) emitted in the street and secondary organic aerosols (SOAs), formed by reactions involving POAs, atmospheric oxidants and VOCs (especially BVOCs as shown in the previous chapters), secondary inorganic aerosols (SIAs), which in the urban environment of Paris, are mainly ammonium nitrate.

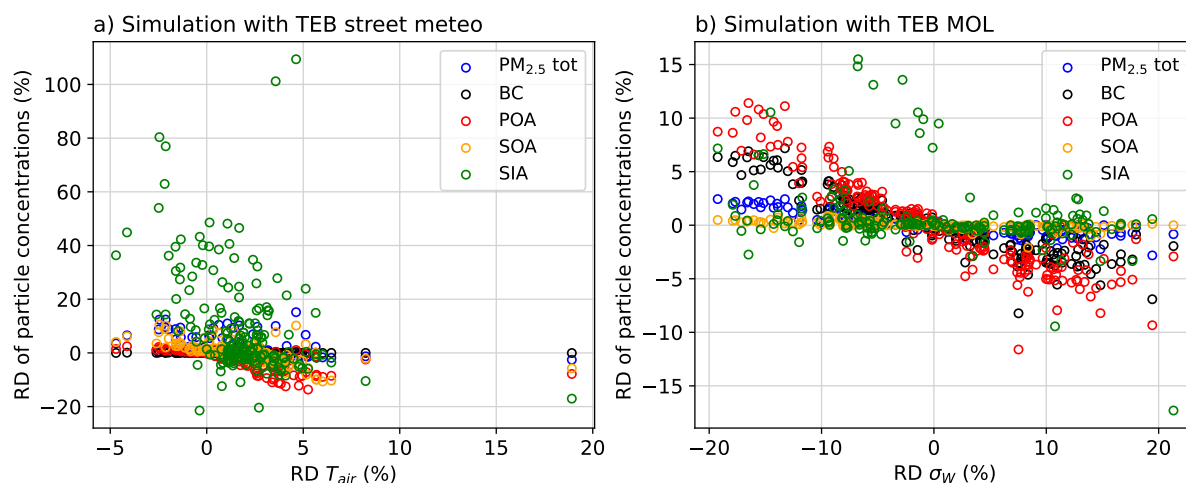


Figure 5.39: Relative difference of $PM_{2.5}$ concentrations simulated by MUNICH with a) TEB street meteo and b) TEB MOL compared to REF as a function of the relative difference of air temperature and σ_W . The particle chemical composition is detailed, BC: Black Carbon, POA: Primary Organic Aerosols, SOA: Secondary Organic Aerosols and SIA: Secondary Inorganic Aerosols (ammonium nitrate).

Figure 5.39 shows that BC is not impacted by the change of temperature (Fig. 5.39a) and its concentration decreases when σ_W increases and inversely (Fig. 5.39b). BC is a primary pollutant, so like NO_x , its concentrations are mainly impacted by atmospheric stability, via the transfer velocity. Conversely, SOAs are not much impacted by the variation of σ_W (Fig. 5.39b) but SOA concentrations increase when the RD of temperature are negative and inversely (Fig. 5.39a). Both POA and SOA concentrations are sensitive to temperature through the processes of evaporation and condensation. Indeed, higher temperature leads to evaporation of semi-volatile organic compounds (SVOCs) absorbed on the aerosol, and therefore a decrease in POA and SOA concentrations. Inversely, lower temperature leads to condensation of SVOCs on the aerosol, and therefore an increase

in SOA concentrations. POAs concentrations are also impacted by σ_W changes (Fig. 5.39b). POAs are primary particles emitted by traffic, so like BC, their dispersion is impacted by stability. The large increases in $PM_{2.5}$ concentrations observed on a few mornings are due to the formation of SIAs (Fig. 5.39a). The formation of SIAs is also very sensitive to temperature through the evaporation and condensation processes and the four RD peaks are observed when the RD of air temperature is negative. SIAs are to a lesser extent also sensitive to stability. They are indeed formed from ammonia (NH_3) emitted into the street by traffic. Its dispersion is modified due to variation of σ_W . In the TEB street meteo simulation, the effect of the change of specific humidity has also been studied but its effect on concentrations is less significant than the temperature effect. The net impact on $PM_{2.5}$ concentrations is therefore the result of these different effects.

At the city scale over the 2-month period, the $PM_{2.5}$ concentrations simulated by MUNICH with TEB street meteo and MOL are on average 1.7% higher during day and 0.13% during night as shown in Fig. 5.40 and 5.41.

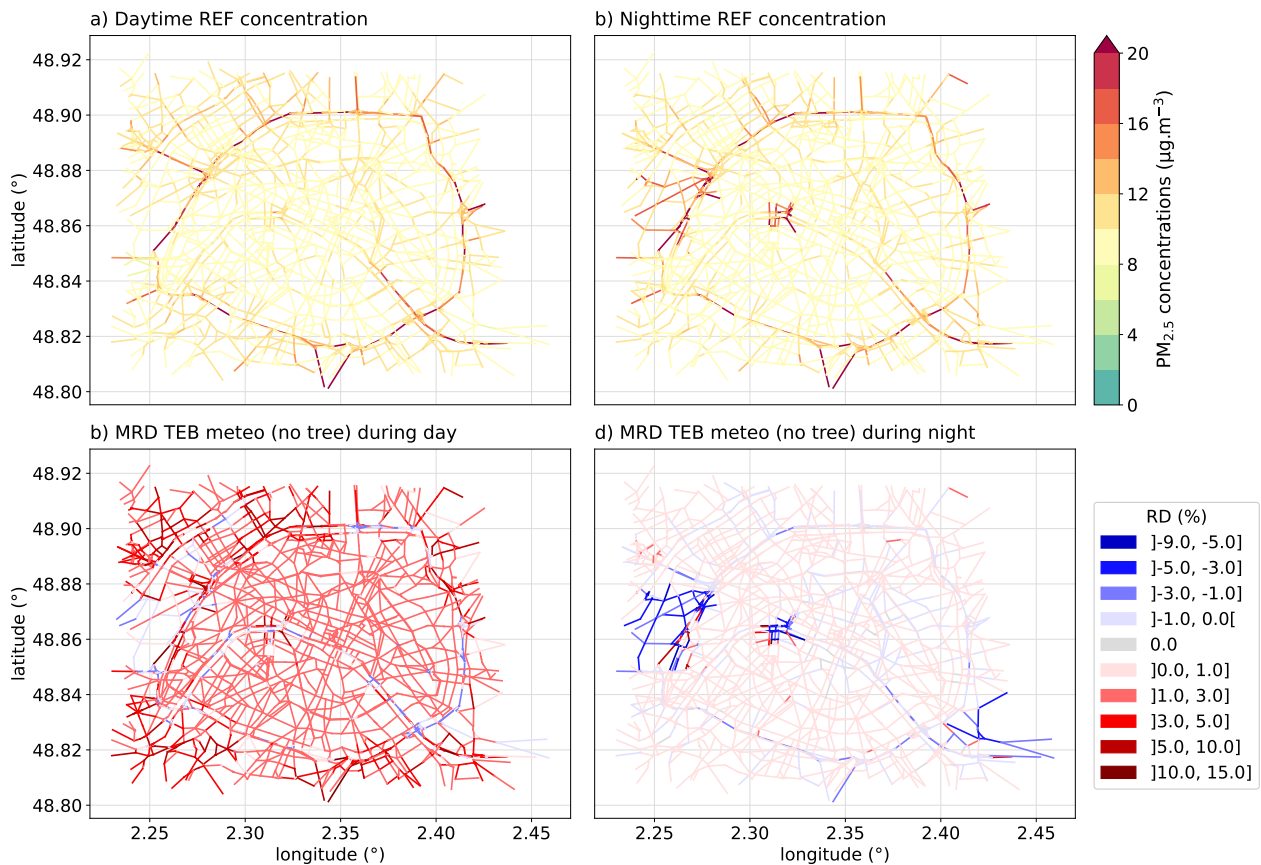


Figure 5.40: Comparison of average a) daytime and b) nighttime $PM_{2.5}$ concentrations simulated by MUNICH and WRF meteo and relative difference of c) daytime and d) nighttime $PM_{2.5}$ concentrations simulated by MUNICH with TEB street meteo and MOL.

Figure 5.41 also shows that the tree effect on $PM_{2.5}$ concentrations is slightly higher during all periods when the street micro-meteo is considered, due to the changes of stability and temperatures as shown previously. The average global tree effect on $PM_{2.5}$ concentrations remains below 2%.

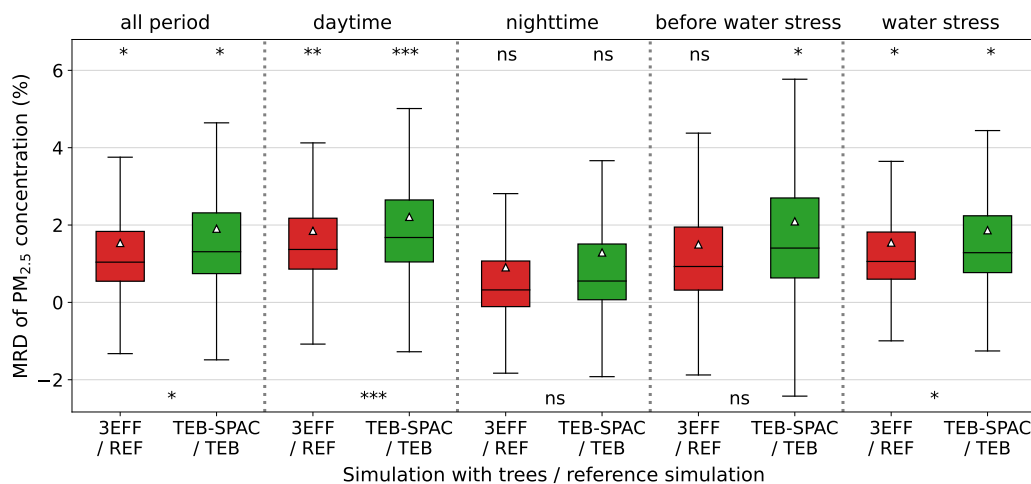


Figure 5.41: Box-plot of Mean Relative Difference (MRD) of $PM_{2.5}$ concentrations in streets with trees averaged during the whole period, daytime, nighttime, before water stress (from 06/06 to 12/06) and during water stress (from 16/06 to 31/07). The mean is represented by a white triangle and the result of a T-test between 3EFF and REF and TEB-SPAC and TEB is indicated at the top of each box-plot. The result of a T-test between 3EFF and TEB-SPAC is indicated at bottom. '***': p-value < 0.001, '**': p-value < 0.01, '*': p-value < 0.05 and 'ns' (non-significant): p-value ≥ 0.1 .

A change in the micro-meteo in the street simulated by TEB and TEB-SPAC, in particular temperature and atmospheric stability, induces modifications in the physico-chemical processes and therefore in the pollutant concentrations in the street. The use of the TEB-SPAC model also makes it possible to refine the calculation of biogenic emissions. The impact on biogenic emissions is detailed in the following section.

5.3.5 Impacts of the urban micro-climate and tree water stress simulated by TEB-SPAC on BVOC emissions

To estimate the biogenic emissions in the chapters 3 and 4, it was assumed that the leaf surface temperature is equal to the air temperature at 2 m. Furthermore, the incident solar radiation used does not consider the complex radiative processes occurring in the street, with reflections and shading effects. The TEB-SPAC model simulates the leaf surface temperature, which is the variable that should be used in emission models (Guenther et al., 2012), as well as the solar radiation received by the leaves computed from the street radiative budget (Redon et al., 2017). Note that this solar radiation received by leaves includes reflections on the different street surfaces and shading effect of buildings on leaves but no shading effect between leaves within the tree canopy is modeled. The simulated leaf surface temperatures and received solar radiations are compared to WRF variables in Fig. 5.42. It shows that on average over the two months, the leaf surface temperatures are largely higher than the air temperature at 2 m, with an average increase of $+1.2^{\circ}C$, that can reach $+3.7^{\circ}C$. The leaf surface temperature is closely linked to tree water status. Indeed, as long as the tree is transpiring, its leaf temperature can be lower than the air temperature. However, when the tree is under water stress and limits its transpiration (from June 16 in the simulation as shown in Fig. 5.16 and 5.21), the leaf surface temperature rises and becomes warmer than the air temperature. The solar radiation received by the leaves is much more heterogeneous than the incoming solar radiation because of the local effects of reflections and shading. The increase in solar radiation

can reach $+124 \text{ W.m}^{-2}$ (+25.5%) and the decrease -272 W.m^{-2} (-50.6%). By comparison to the street aspect ratio map shown in Fig. 4.1, the solar radiation received by the trees is generally lower than the incoming solar radiation in the narrow streets and is larger in the more opened streets, due to building shade.

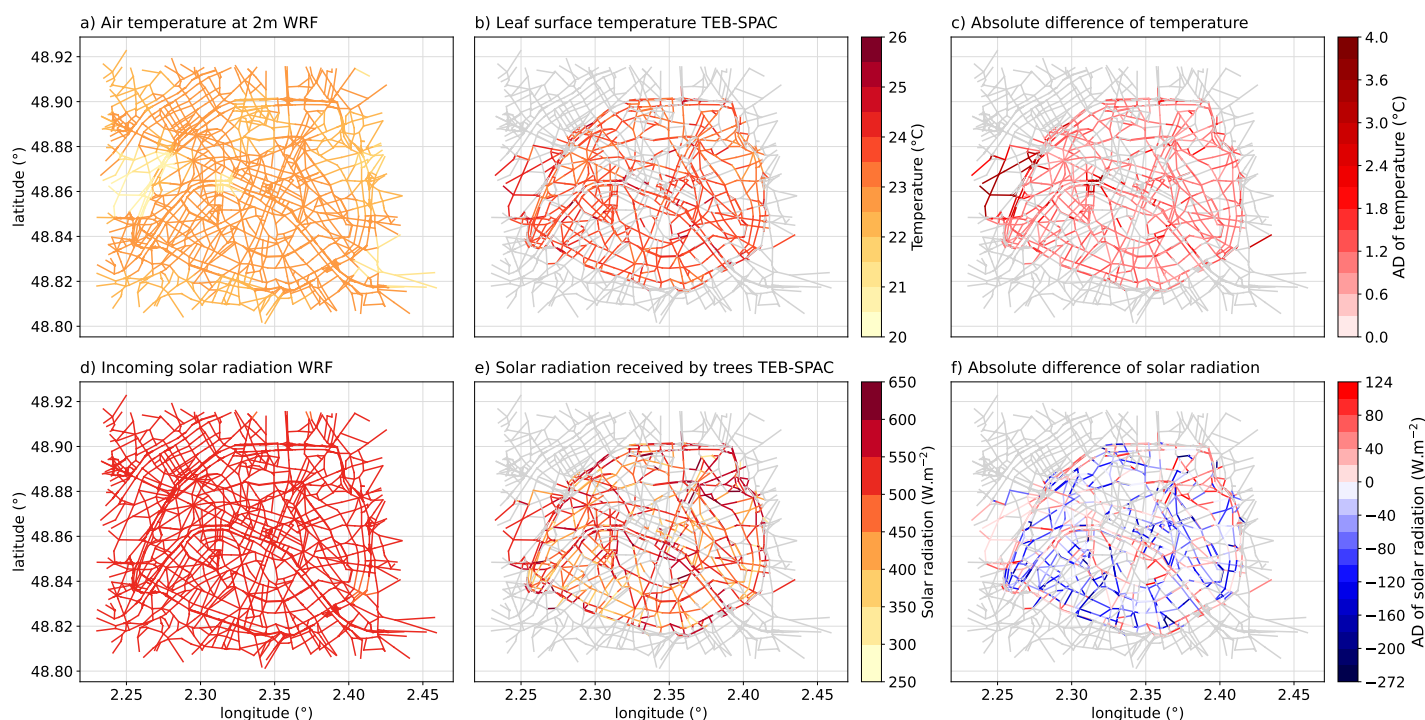


Figure 5.42: Comparison of the (a, b) temperatures and solar radiation (d, e) used to compute BVOC emissions in MUNICH (a, d) and in MUNICH-TEB-SPAC (b, e) along with the relative difference (RD) of c) temperature and f) solar radiation averaged on the two months.

Then, as TEB-SPAC also simulates a detailed street water balance it is possible to introduce the water stress effect on isoprene emissions with the γ_{SM} activity factor. Three parameterizations, in which γ_{SM} is function of the soil water content, are tested: [Guenther et al. \(2012\)](#); [Otu-Larbi et al. \(2020\)](#) and [Bonn et al. \(2019\)](#). The γ_{SM} evolution as a function of the SWI is represented in Fig. 5.43. For the soil texture considered in Paris (see Section 5.2.5.4), the parameterizations simulate a decrease in isoprene emissions from around $SWI = 0.38$ for [Otu-Larbi et al. \(2020\)](#); [Bonn et al. \(2019\)](#) and from $SWI = 0.22$ for [Guenther et al. \(2012\)](#). Then, γ_{SM} decrease at different rates and for $SWI = 0$, it reaches $\gamma_{SM} = 0$ for [Guenther et al. \(2012\)](#); [Otu-Larbi et al. \(2020\)](#) and $\gamma_{SM} = 0.15$ for [Bonn et al. \(2019\)](#). The [Guenther et al. \(2012\)](#) parameterization simulates a decrease in emissions starting from a lower soil water content, but the decrease is then greater. These three parameterizations simulate a decrease in isoprene emissions from June 15 as shown in Fig. 5.44. This decrease is the lowest with [Guenther et al. \(2012\)](#) parameterization, followed by [Otu-Larbi et al. \(2020\)](#) and [Bonn et al. \(2019\)](#). This figure also shows that the isoprene emissions computed from the leaf surface temperature and solar radiation received by the trees are on average in all streets higher than the emissions computed from the air temperature and the incoming radiation.

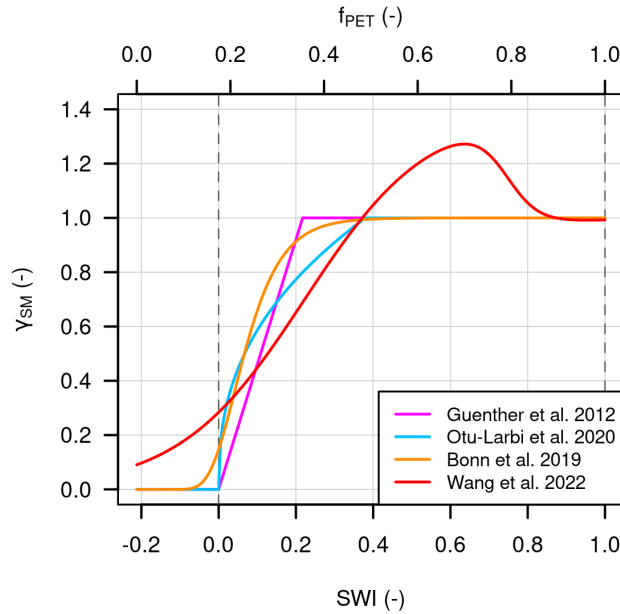


Figure 5.43: Comparison of the γ_{SM} activity factor computed from Guenther et al. (2012); Otu-Larbi et al. (2020); Bonn et al. (2019) as a function of the Soil Water Index (SWI) and from Wang et al. (2022) as a function of the evapotranspiration to potential evapotranspiration ratio (f_{PET}).

On average over the two months, the isoprene emissions computed from the leaf surface temperature and solar radiation received by the trees are higher by +35.6% than when meteorological fields from above the street are used. When γ_{SM} of Bonn et al. (2019) is considered, this increase is limited to -2.2%, so the water stress effect partly offsets the increase due to temperature and radiation changes in the street. With the γ_{SM} of Guenther et al. (2012), the emissions are even decreased compared to the reference by -42.1% on average. The variation of emissions with the γ_{SM} of Otu-Larbi et al. (2020) is between the two previous parameterizations with an average decrease of -25.6%. The average net decrease in isoprene emissions due to the water stress is equal to -28.2% for Bonn et al. (2019), -45.7% for Otu-Larbi et al. (2020) and -58.0% for Guenther et al. (2012).

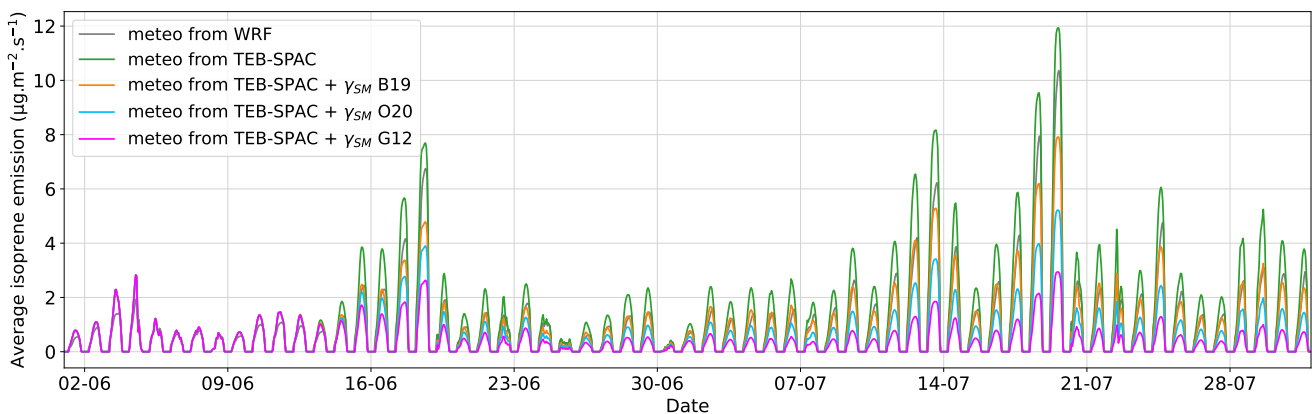


Figure 5.44: Temporal evolution of isoprene emissions computed with WRF and TEB-SPAC meteo averaged on all streets and with or without water stress factor γ_{SM} (G12: Guenther et al. (2012), B19: Bonn et al. (2019), O20: Otu-Larbi et al. (2020)).

Figure 5.45 presents the 2-month average isoprene emissions computed from WRF meteo and the MRD of emissions when leaf surface temperature and radiation received by the tree in the street, as well as the γ_{SM} of [Bonn et al. \(2019\)](#) and [Guenther et al. \(2012\)](#) are considered. By comparing the figures 5.42c and 5.45b, the increase in isoprene emissions seems to be mainly due to the rise in temperature. In fact, above a certain radiation level (around $300 \text{ W}\cdot\text{m}^{-2}$), emissions no longer increase when radiation levels rise as shown in Fig. 5 of Chapter 3. For high levels of solar radiation such as those obtained during the simulation period, a variation in radiation causes only small variations in emissions. On the other hand, over the temperature range obtained, an increase in temperature leads to a larger increase in emissions (Fig. 5 of Chapter 3). The decrease in isoprene emissions with the water stress effect offsets the increase due to temperature in many streets, as shown in Fig. 5.45c and 5.45d. The emission decrease is heterogeneous and seems to be correlated with the tree fraction in the street (Fig. 5.7). As shown previously, soil water content decreases faster in streets with large crown fraction due to larger root uptake, inducing higher water stress for trees.

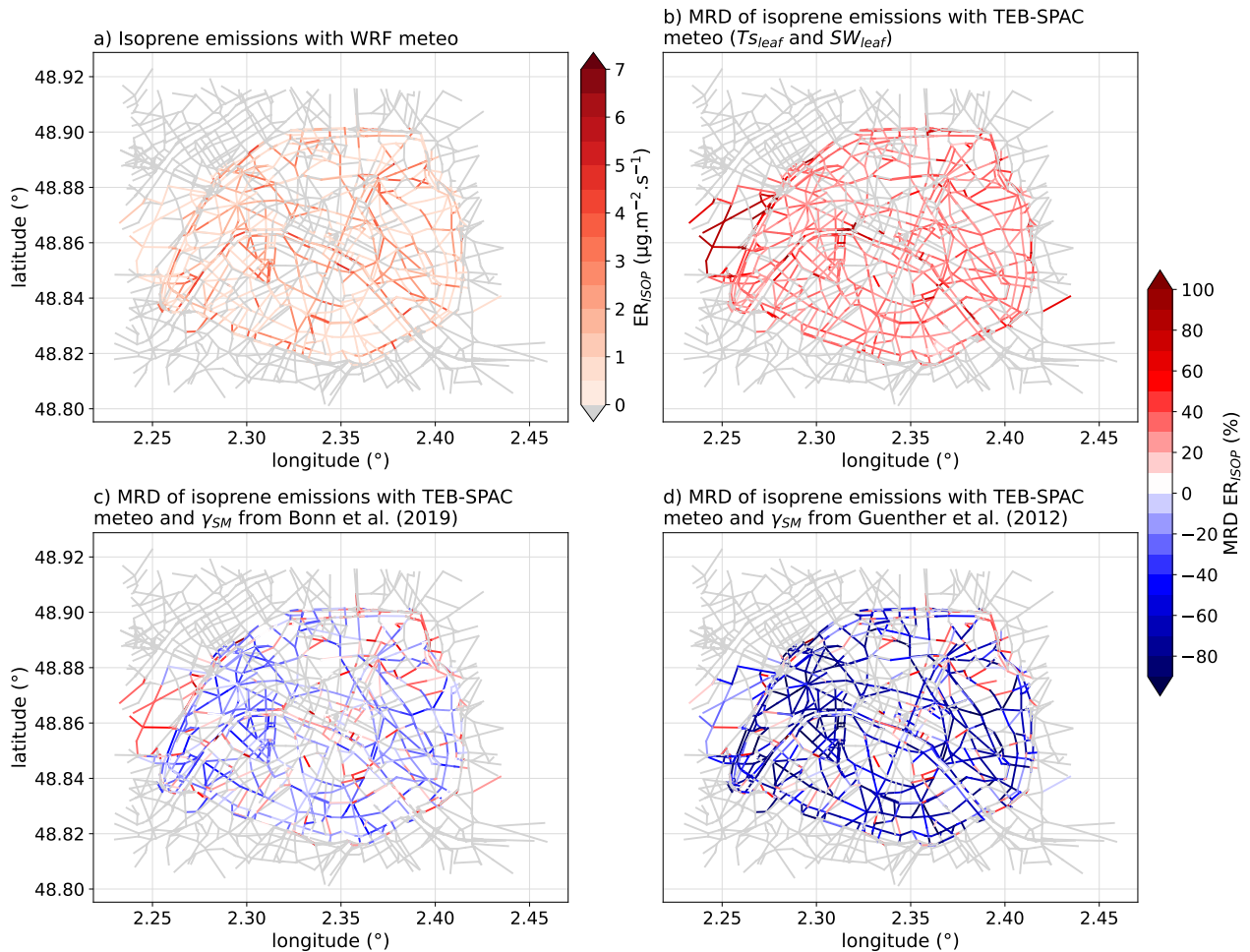


Figure 5.45: a) Average isoprene emissions computed with WRF meteo and mean relative difference of isoprene emissions computed with TEB-SPAC meteo (leaf surface temperature T_{sleaf} and solar radiation received by the leaves SW_{leaf}) b) without and with water stress factor γ_{SM} from c) [Bonn et al. \(2019\)](#) and d) [Guenther et al. \(2012\)](#).

The temporal and spatial variations of monoterpene emissions are also compared in Fig. 5.46 and 5.47. As for isoprene, using the leaf surface temperature increases the monoterpene emissions in all streets, of +25.1% on average. Emissions of other biogenic species also increase, on average of +48.5% for sesquiterpenes, +19.4% for nitrogen monoxide (NO), +25.1% for carbon monoxide (CO) and +23.3% for other BVOCs (mainly oxygenated BVOCs). The effect of water stress on monoterpene and sesquiterpene emissions is more complex, because the effect can be different depending on the isomer considered, and is not yet represented.

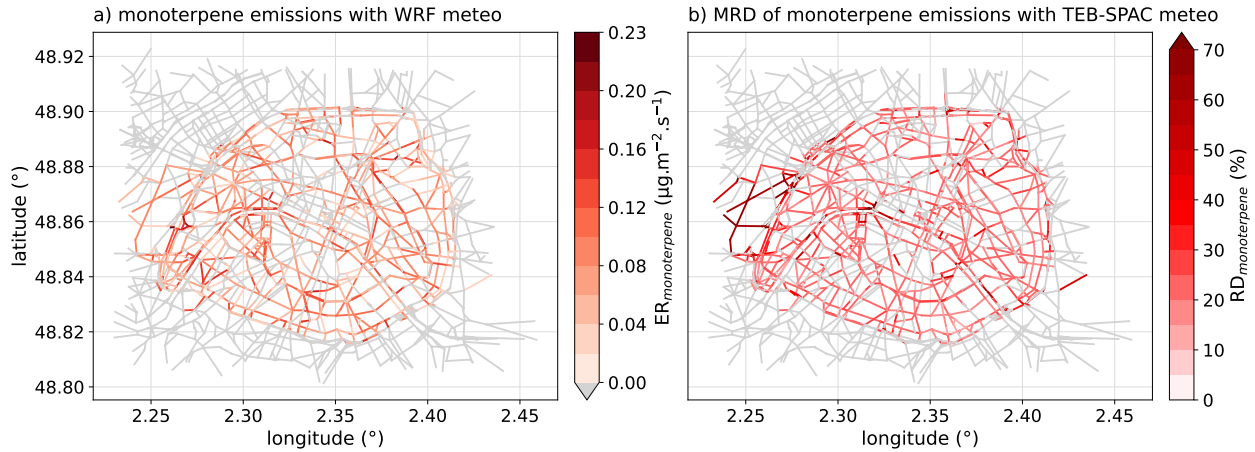


Figure 5.46: a) Average monoterpene emissions computed with WRF meteo and b) mean relative difference of isoprene emissions computed with TEB-SPAC meteo.

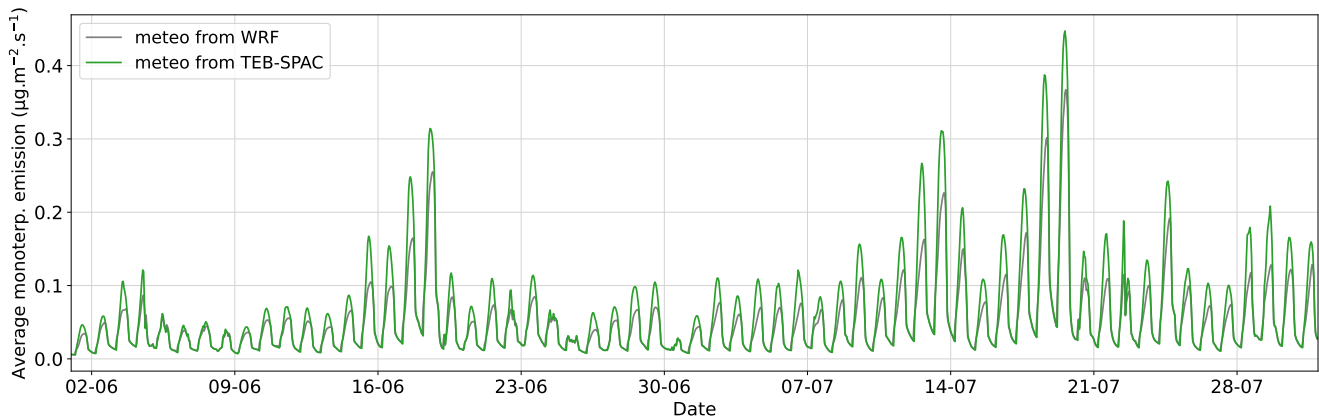


Figure 5.47: Temporal evolution of monoterpene emissions computed with WRF and TEB-SPAC meteo averaged over all streets.

5.4 Conclusion

As shown in Chapter 4, urban trees significantly impact the gas and particle concentrations through their aerodynamical effect and biogenic emissions at the street and city levels. However, this impact was estimated without taking into account the effect of trees on the micro-meteorology. Trees also modify the street radiative, thermal and water budgets. To estimate the global impact of trees on air quality, taking into account the impact on micro-meteorology, this chapter presents the development of a modeling chain based on the street-level air-quality model MUNICH, the urban surface model TEB-Veg and the soil-plant-atmosphere continuum model SPAC. The hydraulic model of SPAC is directly integrated into TEB-Veg, providing a detailed representation of the street tree hydraulic functioning, and in particular of water stress. Meteorological data simulated by TEB (without tree) and TEB-SPAC (with trees) at the street level are used as input data in MUNICH simulations. To be consistent with the homogeneous street approach of MUNICH, street average air temperature, humidity and pressure are computed from TEB simulations. The Monin-Obukhov length (MOL) above the street, that represents atmospheric stability and has a strong impact on vertical pollutant transfer, is also taken from TEB simulations. The vertical transfer coefficient and horizontal wind speed are calculated by each model separately. In order to obtain close transfer velocities for water, heat and pollutants, the mixing-length parameterization developed in [Maison et al. \(2022a,b\)](#) for MUNICH is also integrated in the TEB-Veg model. The inclusion of this parameterization both in TEB-Veg and MUNICH results in similar vertical and horizontal transfer velocities between the two models.

To study the impact of micro-meteorology in streets without trees, a comparison of the meteorological fields estimated in MUNICH from the mesoscale model (WRF) and of those computed by TEB is carried out. Differences are observed between the variables, due to their nature (e.g. air temperature at 2 m vs. average street temperature), and the processes represented in the models. Compared to the parameterized MUNICH meteorological fields, the explicit computation of micro-meteorology in TEB leads to on average over the 2 months and all streets higher temperatures (+0.63°C), higher humidity (+0.0014 kg.kg⁻¹) and slightly higher pressure (+0.76 hPa). The atmospheric stability is higher during the day (-4.7% in σ_W) and lower during the night (+4.9% in σ_W) compared to the MOL computed in MUNICH.

The study of the trees hydraulic and energetic functioning over the 2 summer months showed that due to the low volume of soil in which they are planted, the trees suffer from water stress quite quickly from June 15. The effect of trees on street-average air temperature and humidity is different before and during this period of water stress. From 02 to 15/06, in streets including trees and soil, the air temperature is on average -0.12°C lower, this decrease can reach -0.77°C. The air specific humidity is increased of +1.0% on average and up to +8.3%. From 16/06 to 31/07, transpiration is limited and the effect of shade on street-average temperature is weak, so the cooling effect of trees is reduced, with temperatures even rising in some streets due to the aerodynamic effect (-0.02°C on average and from -0.46 to +0.17°C). The air specific humidity is also less increased with +0.40% on average and up to +5.1%. The presence of trees in the street induces an average decrease in σ_W of -2.5% over the all period. The atmospheric pressure is not significantly modified by trees.

The impact on pollutant concentrations depends on the nature of the chemical species, in particular on its origin (primary or secondary). The primary compounds emitted in the streets, for example NO₂ and black carbon are particularly sensitive to the stability that drives the vertical transport between the street and the background. The secondary particles are sensitive to tem-

perature through the oxidation, evaporation and condensation processes and to stability when the precursors are emitted in the street. In the 2-month simulation performed, NO_2 concentrations are on average increased during the day by +2.2% and decreased during the night by -0.79%. $\text{PM}_{2.5}$ concentrations are on average 1.7% higher during day and 0.13% higher during night. The average global tree effect including aerodynamic effect, dry deposition on leaves and biogenic emissions on NO_2 concentration is the same whether street micro-meteo is considered or not. The effect on $\text{PM}_{2.5}$ is slightly greater when micro-meteo is taken into account, but remains below the 2% increase in concentrations.

Then, the MUNICH-TEB-SPAC coupling enables us to refine the calculation of biogenic emissions. The emissions are computed from leaf-surface temperature instead of the air temperature, and from the solar radiation received by the trees, which takes into account reflections and shading in the street instead of the incoming solar radiation above the street. The detailed water budget in the street gives the soil water content that is used to compute the water stress impact on isoprene emissions with the γ_{SM} activity factor. The leaf surface temperature is largely higher than the air temperature (+1.2°C on average) inducing higher biogenic emissions (+35.6% for isoprene, +25.1% for monoterpenes and +48.5% for sesquiterpenes). The solar radiation received by the trees is much more heterogeneous than the incoming radiation above the street (from -50.6% up to +25.5%), because of local effects of reflections and shading. However, due to a plateau effect in the light activity factor, this variation in radiation has a much less impact on emissions than the temperature. Three parameterizations of the γ_{SM} depending of the soil water content are compared (Guenther et al., 2012; Otu-Larbi et al., 2020; Bonn et al., 2019). They lead to a decrease in isoprene emissions of varying intensity starting from June 15. With leaf surface temperature, radiation received by trees and γ_{SM} taken into account, the net isoprene emission variation with respect to the reference is -2.2% for γ_{SM} of Bonn et al. (2019), -25.6% for γ_{SM} of Otu-Larbi et al. (2020), and -42.1% for γ_{SM} of Guenther (2013). A fourth parameterization (Wang et al., 2022) is also shown in Fig. 5.43. It depends not on soil water content but on the ratio of evapotranspiration to potential evapotranspiration (LE/PLE). It allows to represent the increase in isoprene emissions due to the heat stress on leaf temperature under moderate water stress. This is an integrated ratio calculated at the mesoscale and it is not directly applicable to the LE/PLE ratio computed by SPAC by each time step. With further research, it could be adapted to the ratio of evapotranspiration to potential evapotranspiration computed by TEB-SPAC.

The presented results depend on the soil water content and tree hydraulic functioning that are known to be particularly sensitive to the value of the reference leaf hydraulic potential. This parameter depends on the trees adaptation to drought and therefore on the hydraulic characteristics of the tree species. The reference leaf hydraulic potential has been expressed here as a function of the xylem porosity (diffuse, ring-porous, etc.) by using xylem databases. Other parameters such as the tree hydraulic resistances are known to be sensitive parameters (Tuzet et al., 2017). More sensitivity analyses need to be carried out to identify other sensitive parameters. Tree physiological measurements (sap flows, minimum leaf hydraulic potentials) and soil water contents could guide us to set the hydraulic parameters of the trees, but given the number and diversity of trees in Paris, it would be complicated to determine the parameters for each tree species. Here, many tree parameters were therefore considered identical for all trees.

Besides, the TEB MOL was used in MUNICH as a first approach to test the model's sensitivity to this parameter. The street concentrations of pollutants emitted in the street or reacting with them are sensitive to this value, as it is used to quantify the atmospheric stability above the street that

impacts the vertical transport of compounds. To be more coherent, the other variables involved in the computation of the vertical transport such as the friction velocity should be taken from the same energy budget modeled by TEB.

The biogenic emissions are strongly dependent on temperature, solar radiation and water stress (for isoprene), it is therefore important to estimate them accurately. Taking the leaf surface temperature, solar radiation with reflections and building shading and soil water content is an improvement and strongly modify the simulated emissions. Other processes such as the shading effects between leaves within the tree cover and the effect of past light conditions could also be taken into account. In addition, the activity factor parameterizations have been developed in forests and fields so their generalization for urban trees can be questioned. The effect of water stress was parameterized only for isoprene emissions. However it could impact other biogenic emitted compounds, such as monoterpenes, and more research is necessary to estimate its effect on other compounds.

Finally, CHIMERE/MUNICH simulations that take into account the effect of micro-meteorology on biogenic emissions (in particular via effects on the leaf surface temperature, the radiation received by trees and the water stress effect), and on the formation of secondary compounds should be performed to estimate the global tree impacts on gas and particles concentrations at the street and city scale. These simulations require new CHIMERE simulations to recompute the background concentrations with the updated emissions from street trees. As micro-meteorology leads to an increase of biogenic emissions by 19% to 49% depending on chemical species, the impact of urban trees may be greater than that observed in chapters 3 and 4, in particular on secondary organic aerosols and ozone concentrations.

Chapter 6

Conclusions and perspectives

6.1 Conclusions

The main objective of this thesis was to quantify the impact of urban trees on concentrations of chemical species at the street and city scales. To do so, the various effects of urban trees were integrated in air-quality models at the street and regional scales. First, the three main effects of trees (aerodynamic effect, dry deposition and biogenic emissions) on urban air quality were added in the modeling chain CHIMERE/MUNICH. The tree aerodynamic effect in street canyons was parameterized in the street-network model MUNICH based on computational fluid dynamics (CFD) simulations. It represents the impact of tree crowns on street air flow, by parameterizing the effect of the crown size and Leaf Area Index (LAI) on horizontal and vertical transfer velocities. This parameterization was first developed for a treeless canyon. This is a generic parameterization function of common street and tree characteristics. It can be applied to other street air-quality models but also to urban surface-atmosphere models, as done in the Chapter 5.

Dry deposition of gas and particles on leaves was added to MUNICH, deposition velocities were calculated using a resistive scheme adapted to trees in streets. The resistance and coefficient formulations were taken from the literature, while ensuring consistency with the parameterizations developed in the first chapter.

Biogenic emissions were estimated at the tree scale based on the empirical approach of the MEGAN model (Guenther et al., 2012) that uses leaf dry biomass, tree species dependent emission factors and activity factors representing the effect of meteorology on emissions. Location and characterization of urban trees were therefore required. The tree database of the Paris city, which includes most of the city's public trees (excluding woods), was used in this thesis (Municipality of Paris, 2023). It provides information about the tree coordinates, species, trunk circumference and tree crown height. These information were crossed with a database of allometric equations, developed for urban trees in the US (McPherson et al., 2016), to estimate the tree characteristics required as model inputs such as the crown width, trunk height, leaf area and dry biomass. Based on the tree location coordinates, this characteristics were then integrated at the street level in MUNICH and at the cell level of CHIMERE to compute the biogenic emissions. They were also used to compute the aerodynamical effect and the dry deposition on leaves in MUNICH.

The impact of biogenic emissions from urban trees on regional air quality was quantified using CHIMERE-WRF simulations over the Île-de-France region and during June and July 2022. For this purpose, simulations with emissions from urban trees were compared with reference simulations without trees. Concentrations of biogenic species greatly increase in Paris when emissions from urban trees are added, by more than a factor 10 for isoprene and monoterpenes. These compounds induce a significant increase in particulate organic matter (OM) concentrations by 4.6% on

average over the two months and 5.4% during the heatwave periods. As OM is a significant part of PM_{2.5} in summer, PM_{2.5} concentrations also increase, but to a lesser extent (+0.6% on average and +1.3% during the heat wave periods). Urban tree emissions also induce a slight increase in O₃ concentrations, by 1.0% on average over the 2 months and by 2.4% during the heat waves, this increase can locally reach 2.4% on average over the two months and 5.7% during the heat waves. The effects remain localized over the Paris city area, except for the increase in O₃ concentrations that can expand over Paris suburbs during heat waves.

To quantify the tree impacts at the street scale, MUNICH simulations were performed over the Paris street network. The impacts of the different tree effects were quantified over a 2-week sensitivity analysis and the global tree effect over 2-month simulations. The results show that the aerodynamical effect induces an increase in the concentrations of primary compounds emitted in the street. The aerodynamic effect increases with tree LAI and traffic emission rates. Compared to the 2-week reference simulation, it increases the NO₂ concentrations by 4.6% on average in streets with trees and up to 37%. This increase in NO₂ induces a titration of O₃, whose concentrations decrease on average by -2.7% in streets with trees. The aerodynamic effect also increases OM and PM_{2.5} concentrations (mainly through the primary compounds) by respectively 1.6 and 1.2% on average in streets with trees and up to 29 and 22%. The aerodynamic effect also modifies the distribution of pollutants between streets, increasing concentrations in streets with trees and reducing them in adjacent streets. Based on these results, planting trees with wide crown and high LAI in streets with heavy traffic should be avoided.

The impact of dry deposition of gas and particles is limited and reduces concentrations by up to -3% only, for all species studied. It nevertheless induces a significant reduction in O₃ concentrations in streets with trees of -0.6% on average and up to -2.5%. Therefore, dry deposition on tree leaves does not seem to be a very effective processes to reduce pollutant concentrations. However, measurements of dry deposition on urban tree leaves would be useful to assess the parameterizations used for the different pollutants.

The effect of biogenic emissions in the streets is similar to that observed at a regional scale. The concentrations of biogenic species is largely higher, leading to an increase in concentrations of O₃ (1% on average over the 2 weeks and 2.1% during the heat waves), OM (2.5% on average over the 2 weeks and 3.5% during the heat waves) and PM_{2.5} (0.5% on average over the 2 weeks and 1% during the heat waves). Biogenic emissions have no significant impact on NO₂ concentrations, and affect mainly secondary compounds of particles.

The overall effect of the trees on concentrations corresponds to the sum of each individual effect. Over the 2-month, the net variation of concentrations on average in all streets is equal to +1.5% for NO₂ (and varies from -16.6 to +35.6%), +0.03% for O₃ (from -23.9 to +25.2%), +3.8% for OM (from -10.4 to +33.2%) and +0.8% (from -8.2 to +21.7%) for PM_{2.5} concentrations.

The MUNICH simulations presented in Chapter 4 were performed using street meteorological fields parameterized from the meso-scale meteorology. However, the urban micro-climate and the presence of street trees modify the micro-meteorological conditions, which could influence pollutant concentrations. To better take this into account and to determine the impact on street concentrations, MUNICH has been coupled to the TEB-SPAC model. The TEB-Veg model, which includes a representation of the impact of trees on the thermo-radiative and water budgets of the street canyon was first coupled to the soil-plant-atmosphere continuum model, SPAC. This provides a more refined representation of water flows within trees and of the impact of water stress on tree functioning.

The stomata opening that regulates transpiration is function of the leaf hydraulic potential. This potential is closely connected to soil water content through the tree's series of water potentials and resistances. In the two simulated months of summer 2022, trees transpire without limitation by soil water until June 15. As the crown surface area is large in comparison to the soil volume, soil water is very quickly absorbed by trees, decreasing rapidly the soil water content. Rainfall in late June and in July is fairly low, so water content remains close to the wilting point and trees suffer from water stress. The impact of trees on the micro-meteorology depends on their water status. In the streets with trees, the cooling effect of trees is greatly reduced when they stop transpiring (on average from -0.12°C before water stress to -0.02°C during water stress). The average street temperature is even slightly increased due to the aerodynamical effect that limits the heat dissipation in the street. During the water stress period, the tree shading effect still participates to decrease the temperature under the tree crown, but mainly in streets with high tree fraction and LAI. To maintain the benefit effects of trees on thermal comfort, it is therefore important to find urban planning solutions to ensure access to water and limit water stress (EPA, 2013).

The impact of micro-meteorology on concentrations was estimated without considering urban trees by performing MUNICH simulations with and without the detailed micro-meteorology, i.e. with or without coupling to TEB. The comparison of the meteorological fields simulated by WRF (used in the MUNICH reference simulation) with those simulated by TEB shows that the street average temperature simulated by TEB is on average $+0.63^{\circ}\text{C}$ higher than the temperature at 2 m given by WRF. Locally, the temperature can decrease by -0.16°C and increase by $+3.0^{\circ}\text{C}$ when the micro-meteorology is taken into account. These temperature variations mainly have an impact on the concentrations of secondary species. Temperature governs in particular the processes of oxidation, condensation and evaporation, and the formation of secondary particles are very sensitive to this processes. Then, the transfer between the street and the background above strongly influences the street concentrations, and it depends on the Monin-Obukhov length (MOL). Rather than using the parameterization of the MOL available in MUNICH, simulations were carried out taking as input data the MOL above the street simulated by TEB. TEB simulates more stable conditions during the day and a slightly more unstable conditions during the night. This leads to a lower dispersion of pollutants emitted in the street and therefore higher concentrations during the day ($+2.2\%$ on average for NO_2) and inversely at night (-0.79% on average for NO_2). The variation of atmospheric stability impacts directly the primary aerosols and indirectly the secondary aerosols when a precursor is emitted by traffic.

Then, the impact of micro-meteorology on concentrations was estimated considering urban trees. To do so, MUNICH simulations are performed with the three tree effects and the street meteo provided by TEB-SPAC. The global effect of trees on NO_2 and $\text{PM}_{2.5}$ concentrations taking into account or not the street meteo is generally similar with only a few tenths of a percent of difference. Nevertheless, the biogenic emissions computed more precisely, from the leaf surface temperature and the solar radiation received by the tree in the street (with reflections and shade), increase very significantly. It is mainly due to the leaf surface temperature, which is on average 1.2°C higher than the air temperature (up to $+3.7^{\circ}\text{C}$) and which leads to an increase in emissions of 35.6% for isoprene, 25.1% for monoterpenes and 48.5% for sesquiterpenes.

Finally, the effect of water stress on isoprene emissions was also investigated. Three parameterizations of the literature representing the decrease in isoprene emissions with the soil water content were compared (Guenther et al., 2012; Bonn et al., 2019; Otu-Larbi et al., 2020). They all simulate a decrease in isoprene emissions from the 15th of June, when the soil water content starts to be

very low, but of varying intensity. They counterbalance the increase in emissions due to increased temperatures with a net variation of -2.2% for [Bonn et al. \(2019\)](#), -25.6% for [Otu-Larbi et al. \(2020\)](#) and -42.1% for [Guenther et al. \(2012\)](#). It is a very wide range of variation which contains uncertainties due to the parameterizations themselves but also of the tree hydraulic parameters fixed in SPAC.

6.2 Perspectives

In terms of development of the MUNICH model, the parametrizations of the vertical profiles of horizontal wind speed and vertical transfer coefficient in [Maison et al. \(2022a\)](#) have enabled us to develop a model version where the street is discretized into three vertical levels ([Sarica et al., 2023](#)). The vertical gradients of concentrations are better represented in this version, which does not currently include trees. It would be possible to add the trees by adding the different effects in the levels where the crown is located. The aerodynamic effect and BVOC emissions would be better localized in the street, and it would be possible to use directly the meteorological variables simulated by TEB-SPAC at the different vertical levels. A work has already been initiated as part of a student project to estimate the impact of the vertical discretization on the vertical exchange coefficient with trees. In fact this coefficient represents the transfer between the street and the background, and CFD simulations were also used to estimate the vertical transfer coefficient between the different levels in the street. The results showed that the linear profile from the coefficient value at $z = H$ was overall a good approximation.

Then, the tree energetic and hydraulic functioning is sensitive to the tree parameters. To consider the diversity of the tree hydraulic characteristics among species, the reference leaf hydraulic potential was expressed depending on the xylem type. The model includes other parameters such as hydraulic resistances that were considered constant. It is necessary to performed additional analyses to identify the other sensitive parameters and try to improve their estimations for the different tree species based on tree physiological measurements (sap flows, minimum leaf hydraulic potentials).

Since 2020, eco-physiological parameters and isoprene emissions have been measured on plate trees under water stress conditions in the Paris suburb. These results were used to compare the biogenic emissions algorithms and in particular the water stress factor ([Puga Freitas et al., 2023](#)). Difficulties were encountered in modeling the soil texture (potting soil), so the analysis was not pursued further but could be extended in order to better guide us in the isoprene emission parameterizations.

The effect of water stress on other BVOCs such as monoterpenes and sesquiterpene is more complex than for isoprene, especially because the effect can be different depending on the isomer considered. This was not considered here, but few studies based on measurements try to characterize this effect ([Yani et al., 1993](#); [Ormeño et al., 2007](#); [Lavoir et al., 2009](#)), and parameterizations are developed for certain tree species ([Lavoir et al., 2011](#)).

The results of this thesis showed that OM urban concentrations are very sensitive to monoterpene and sesquiterpene emissions. Taking into account urban trees improve the modeling of OM concentrations compared to observations, but they are still underestimated, so to simulate them more accurately, the urban vegetation should be better characterized. In particular the 30% of private trees missing in the Paris city database but also the numerous suburban trees. Participatory science actions could be implemented to list more trees in large parks and private residences (e.g. <https://www.tela-botanica.org/projets/streets-suivi-des-pieds-darbres-de-ma-rue/>). Remote sensing of vegetation based on aerial images is also a promising technique for identifying urban

vegetation cover. This method is developed by APUR in the Greater Paris city (APUR, 2012) and could be used to complete the inventory of both public and private trees, as long as the tree species can be identified and at a sufficiently fine spatial resolution.

The street concentrations of compounds emitted into the street or reacting with them are sensitive to wind speed over the street and atmospheric stability, so it is essential to estimate these parameters accurately. The use of more detailed urban canopy models could improve the estimation of the impact of surface roughness and fluxes on these variables (Martilli et al., 2002; Barlage et al., 2016). Besides, this thesis focused mainly on representing the effects of trees at the street scale and considered no feedback of the ground vegetation to the atmosphere. A bidirectional coupling between the local and the mesoscale weather model could be set up to better represent the multi-scale interactions between meteorology and air quality.

List of Figures

1.1	Processes affecting air quality and atmospheric chemistry (EPA).	14
1.2	Major micro-physical and chemical processes that influence the size distribution and chemical composition of atmospheric aerosols (Brasseur and Jacob, 2017).	15
1.3	Schematic diagram showing flow and scale lengths within an urban boundary layer (UBL) (PBL: Planetary boundary layer) (Fisher et al., 2006).	16
1.4	Schematic diagram of air flow and pollutant dispersion within a street canyon (Silver et al., 2013).	17
1.5	Urban structure, cover, fabric and metabolism contribute to the UHI effect in highly developed areas (Soltani and Sharifi, 2017).	18
1.6	UHI diagram - spatial variations of day and nighttime temperatures over a city (US EPA, 2014).	18
1.7	Ecosystem services provided by trees in cities (Livesley et al., 2016).	19
1.8	Number of publications containing terms related to vegetation in cities in title or abstract (Dimensions, 1980-2022).	20
1.9	Impact of rows of trees and hedges on wind speed and dispersion of pollutants emitted by traffic in a street canyon modeled by Vos et al. (2013).	21
1.10	Impact of urban environment on tree development compared to forest (www.eskp.de).	21
1.11	Modeling chain developed to simulate the effects of trees on climate and air quality at the street and city scale. Variables are in normal font and models and database in bold.	25
4.1	Map of the street aspect ratio (H/W) in Paris street network.	132
4.2	Trees integrated in the Paris street network depending on the search street width.	133
4.3	Trees integrated in the Paris street network depending on the search street width. Zoom over the a) Champs Elysées and b) Hôtel de Ville neighborhoods.	134
4.4	Maps of a) the street Leaf Area Index (LAI_{street}) and b) the tree to building height ratio (h_{max}/H) computed in Paris street network.	136
4.5	Map of the tree leaf dry biomass (DB) per area of street computed in Paris street network.	137
4.6	Comparison of the temporal variation of a) air temperature at 2 m height and b) global solar radiation modeled by WRF (mod) and observed (obs) at the HdV (48.85574°N, 2.35191°E) and Qualair (48.84638°N, 2.35598°E) sites at a 10 min temporal resolution. T_{air} observations are 10-min average of 10 s data measured by a meteorological station was located at 2 m height on the edge of the Paris city hall garden (HdV). SW_g observations are 10-min average of 1 s data measured by a radiometer located in the Qualair platform, on the roof of Sorbonne university at 35 m above the ground (https://qualair.fr).	138

4.7	Temporal variation of spatially averaged BVOC emissions. Due to their different emission rates, the BVOC species are separated into two panels a) for isoprene and other BVOCs and b) for monoterpenes, sesquiterpenes, NO and CO. Emissions are averaged over the streets with trees.	139
4.8	Maps of temporal average BVOC emissions over the 2-month period without multiplication of monoterpene emissions. a) Isoprene, e) NO and f) CO are directly emitted whereas b) monoterpenes, d) sesquiterpenes and d) other VOCs (OVOCs, mainly oxygenated BVOCs) represent the sum of several emitted species.	140
4.9	a) Average isoprene concentrations in the reference simulation (REF) and mean relative difference (MRD) of isoprene concentrations between the simulation b) with tree aerodynamic effect (AERO), c) with dry deposition on leaves (DEP), d) with urban tree biogenic emissions (BVOC) and the REF simulation without trees averaged from June 13 to 26.	143
4.10	Box-plots of the Mean Relative Difference (MRD) of isoprene concentrations in a) all streets and b) streets with trees for each simulation. Concentrations are averaged from June 13 to 26 (left panel) and during the heatwave period (June 15 to 18) (right panel). The mean is represented by a white triangle and the result of a T-test between each simulation with trees and the reference simulation is indicated at the top of each box-plot '***': p-value < 0.001, '**': p-value < 0.01, '*': p-value < 0.05 and 'ns' (non-significant): p-value \geq 0.1.	144
4.11	Average background and street isoprene concentrations (06/06 to 31/07/22) simulated with CHIMERE/MUNICH a) without trees (REF) and b) with all tree effects (3EFF) and c) mean relative difference between the two. Panels d), e) and f) show the same results with TX2 scenario.	145
4.12	Temporal evolution of measured (black dots) and simulated with MUNICH (lines) isoprene concentrations in Paris Hôtel de Ville.	146
4.13	a) Average monoterpene concentrations in the reference simulation (REF) and mean relative difference (MRD) of monoterpene concentrations between the simulation b) with tree aerodynamic effect (AERO), c) with dry deposition on leaves (DEP), d) with urban tree biogenic emissions (BVOC) and the REF simulation without trees averaged from June 13 to 26.	147
4.14	Box-plot of the Mean Relative Difference (MRD) of monoterpene concentrations in a) all streets, b) streets with trees and c) streets without tree for each simulation. Concentrations are averaged from June 13 to 26, on the all period (left part), during daytime (middle part) and nighttime (right part). The mean is represented by a white triangle and the result of a T-test between each simulation with trees and the reference simulation is indicated at the top of each box-plot '***': p-value < 0.001, '**': p-value < 0.01, '*': p-value < 0.05 and 'ns' (non-significant): p-value \geq 0.1.	148
4.15	Average background and street monoterpene concentrations (06/06 to 31/07/22) simulated with CHIMERE/MUNICH a) without trees (REF) and b) with all tree effects (3EFF) and c) mean relative difference between the two. Panels d), e) and f) show the same results with TX2 scenario.	149
4.16	Hourly evolution of measured (black dots) and simulated (lines) monoterpene concentrations at Paris HdV station.	150

4.17	a) Average NO ₂ concentrations in the reference simulation (REF) and mean relative difference (MRD) of NO ₂ concentrations between the simulation b) with tree aerodynamic effect (AERO), c) with dry deposition on leaves (DEP), d) with urban tree biogenic emissions (BVOC) and the REF simulation without trees averaged from June 13 to 26.	151
4.18	Box-plot of the Mean Relative Difference (MRD) of NO ₂ concentrations in a) all streets, b) streets with trees and c) streets without tree for each simulation. Concentrations are averaged from June 13 to 26, over the whole period (left part), during daytime (middle part) and nighttime (right part). The mean is represented by a white triangle and the result of a T-test between each simulation with trees and the reference simulation is indicated at the top of each box-plot '***': p-value < 0.001, '**': p-value < 0.01, '*': p-value < 0.05 and 'ns' (non-significant): p-value ≥ 0.1. . .	152
4.19	Average background and street NO ₂ concentrations (06/06 to 31/07/22) simulated with CHIMERE/MUNICH a) without trees (REF) and b) with all tree effects (3EFF) and c) mean relative difference between the two. Panels d), e) and f) show the same results with TX2 scenario.	153
4.20	Mean relative difference of NO ₂ concentrations between the simulations AERO and REF as a function of the street LAI and the average NO ₂ emission (for each street averaged from 13 to 26/06).	153
4.21	a) Average O ₃ concentrations in the reference simulation (REF) and mean relative difference (MRD) of O ₃ concentrations between the simulation b) with tree aerodynamic effect (AERO), c) with dry deposition on leaves (DEP), d) with urban tree biogenic emissions (BVOC) and the REF simulation without trees averaged from June 13 to 26.	154
4.22	Mean relative difference due to aerodynamical effect (MRD AERO) of O ₃ concentrations as a function of MRD AERO of NO ₂ concentrations (for each street averaged from 13 to 26/06).	154
4.23	Box-plot of the Mean Relative Difference (MRD) of O ₃ concentrations in a) all streets, b) streets with trees and c) streets without tree for each simulation. Concentrations are averaged from June 13 to 26, over the whole period (left part), during daytime (middle part) and nighttime (right part). The mean is represented by a white triangle and the result of a T-test between each simulation with trees and the reference simulation is indicated at the top of each box-plot '***': p-value < 0.001, '**': p-value < 0.01, '*': p-value < 0.05 and 'ns' (non-significant): p-value ≥ 0.1. . .	155
4.24	Average background and street O ₃ concentrations (06/06 to 31/07/22) simulated with CHIMERE/MUNICH a) without trees (REF) and b) with all tree effects (3EFF) and c) mean relative difference between the two. Panels d), e) and f) show the same results with TX2 scenario.	156
4.25	a) Average organic matter (OM) concentrations in the reference simulation (REF) and mean relative difference (MRD) of OM concentrations between the simulation b) with tree aerodynamic effect (AERO), c) with dry deposition on leaves (DEP), d) with urban tree biogenic emissions (BVOC) and the REF simulation without trees averaged from June 13 to 26.	157

4.26	Box-plot of the Mean Relative Difference (MRD) of organic matter concentrations in a) all streets, b) streets with trees and c) streets without tree for each simulation. Concentrations are averaged from June 13 to 26, over the whole period (left part), during daytime (middle part) and nighttime (right part). The mean is represented by a white triangle and the result of a T-test between each simulation with trees and the reference simulation is indicated at the top of each box-plot '***': p-value < 0.001, '**': p-value < 0.01, '*': p-value < 0.05 and 'ns' (non-significant): p-value \geq 0.1.	158
4.27	Temporal evolution of measured (black dots) and simulated (lines) OM concentrations at Paris HdV station.	159
4.28	Average background and street organic matter (OM) concentrations (06/06 to 31/07/22) simulated with CHIMERE/MUNICH a) without trees (REF) and b) with all tree effects (3EFF) and c) mean relative difference between the two. Panels d), e) and f) show the same results with TX2 scenario.	160
4.29	a) Average PM _{2.5} concentrations in the reference simulation (REF) and mean relative difference (MRD) of PM _{2.5} concentrations between the simulation b) with tree aerodynamic effect (AERO), c) with dry deposition on leaves (DEP), d) with urban tree biogenic emissions (BVOC) and the REF simulation without trees averaged from June 13 to 26.	161
4.30	Box-plot of the Mean Relative Difference (MRD) of PM _{2.5} concentrations in a) all streets, b) streets with trees and c) streets without tree for each simulation. Concentrations are averaged from June 13 to 26, over the whole period (left part), during daytime (middle part) and nighttime (right part). The mean is represented by a white triangle and the result of a T-test between each simulation with trees and the reference simulation is indicated at the top of each box-plot '***': p-value < 0.001, '**': p-value < 0.01, '*': p-value < 0.05 and 'ns' (non-significant): p-value \geq 0.1.	162
4.31	Average background and street PM _{2.5} concentrations (06/06 to 31/07/22) simulated with CHIMERE/MUNICH a) without trees (REF) and b) with all tree effects (3EFF) and c) mean relative difference between the two. Panels d), e) and f) show the same results with TX2 scenario.	163
4.32	Map of the street aspect ratio (H/W) in Paris street network with location of the Airparif and HdV stations and Qualair platform (crosses).	166
4.33	Diagram of the resistive scheme used to compute dry deposition of gas and aerosols on street and tree leaves surfaces. Leaf scheme modified from Barragán et al. (2018)	168
5.1	Resistive scheme of the SPAC hydraulic model (modified from Tuzet et al. (2017)). Hydraulic resistances are in green, hydraulic potential in blue, water fluxes in red and capacitance in purple.	180

5.2	Scheme of meteorological fields calculated and exchanged by the 3 models WRF , MUNICH and TEB . The left and the middle street canyons illustrate the fields used as input data (from WRF) and computed respectively in TEB and MUNICH. The right street canyon illustrates the fields used as input data (from WRF and TEB) for the coupled MUNICH-TEB simulations. Dotted lines represent the boundaries of the vertical layers and small circles the middle or the height where fields are taken. Downwards arrows represent flows reaching the surface and black lines the vertical profiles computed in MUNICH. φ is the wind speed direction, PBLH the planetary boundary layer height and f_{cl} the cloud fraction.	184
5.3	Comparison of the vertical profiles of the turbulent transfer coefficient computed in MUNICH and in TEB with the mixing-length parameterization of Maison et al. (2022a,b) (M22). The profiles are compared in three street canyons of various aspect ratios as presented in Maison et al. (2022a,b) . The tree LAI varies but the tree height and crown volume fraction (CVF) are fixed to $h_{\text{max}}/H = 0.5$ and $CVF = 10\%$.	185
5.4	Comparison of the vertical profiles of the horizontal wind speed computed in MUNICH and in TEB with the mixing-length parameterization of Maison et al. (2022a,b) (M22). The profiles are compared in three street canyons of various aspect ratios as presented in Maison et al. (2022a,b) . The tree LAI varies but the tree height and crown volume fraction (CVF) are fixed to $h_{\text{max}}/H = 0.5$ and $CVF = 10\%$. The angle between the street orientation and wind direction is equal to 0°	186
5.5	Comparison of a) street average horizontal wind speed (U_{street}) and b) relative difference (RD) of wind speed computed in MUNICH and in TEB with the mixing-length parameterization of Maison et al. (2022a,b) . The results are presented for the three street canyons studied in Maison et al. (2022a,b) : large, intermediate and narrow canyons (LC, IC and NC) and for each tree type with various LAI, tree heights (h/H) and crown volume fractions (CVF). The angle between the street orientation and wind direction is equal to 0°	187
5.6	Scheme of the TEB-Veg urban canyon with the atmospheric vertical levels of the surface boundary layer (SBL) scheme (modified from Redon et al. (2020)).	188
5.7	Map of the tree fraction (TF) computed in Paris street network.	189
5.8	Minimum predawn stem hydraulic potential measurements available in the Xylem Functional Traits Database depending on the xylem type (DP: diffuse porous, RP: ring porous, SRP: semi-ring porous, VL: vesselless and NA: not available). n is the number of sample for each xylem type.	191
5.9	$f(\psi_{\text{leaf}})$ functions depending on the ψ_{refleaf} that are computed from the xylem types (DP: diffuse porous, RP: ring porous, SRP: semi-ring porous, VL: vesselless and NA: not available).	191
5.10	Map of the reference leaf hydraulic potential (ψ_{refleaf}) computed from the Paris street network from the xylem types.	192
5.11	a) Measured soil texture with (b, c) soil hydrodynamic characteristics computed from the textures and Clapp and Hornberger (1978) equations. The circles correspond to the average values and the error bars to $\pm\sigma$	193
5.12	Vertical profile of root fraction per soil layer and cumulated.	194
5.13	Comparison of observed and simulated air temperature at 2 m in HdV street.	197
5.14	Comparison of observed and simulated air specific humidity at 2 m in HdV street.	198

5.15	Comparison of observed and simulated atmospheric pressure at 2 m in HdV street. .	198
5.16	Energy budget of the tree canopy simulated with TEB-SPAC in Haussmann street. RN: net radiation, G: conduction flux (storage), H: sensible heat flux, LE: latent heat flux.	200
5.17	Precipitation and fraction of tree leaves covered by water simulated with TEB-SPAC in Haussmann street.	200
5.18	Partition of the latent heat flux of the tree canopy simulated with TEB-SPAC in Haussmann street.	200
5.19	Water fluxes in the tree canopy simulated with TEB-SPAC in Haussmann street. . .	201
5.20	Hydraulic potentials of the tree canopy simulated with TEB-SPAC in Haussmann street.	201
5.21	Stomatal conductance of the tree canopy simulated with TEB-SPAC and TEB-ISBA in Haussmann street.	202
5.22	Water stress function simulated with TEB-SPAC and TEB-ISBA in Haussmann street.	202
5.23	Soil water content in the 15 sublayers of each SPAC soil layer simulated with TEB- SPAC in Haussmann street.	203
5.24	Surface temperature of the different street components simulated with TEB-SPAC in Haussmann street.	203
5.25	Soil water index (SWI) simulated with TEB-SPAC in Paris streets at three different dates.	204
5.26	Tree canopy latent heat flux (LE) simulated with TEB-SPAC in Paris streets at three different dates.	204
5.27	a) Daytime and b) nighttime average air temperature at 2 m simulated by WRF and c) daytime and d) nighttime mean absolute difference with the average air temper- ature in the street simulated by TEB.	205
5.28	a) Daytime and b) nighttime average surface air specific humidity simulated by WRF and c) daytime and d) nighttime mean absolute difference with the average air specific humidity in the street simulated by TEB.	206
5.29	a) Daytime and b) nighttime average σ_W computed from MUNICH MOL and c) daytime and d) nighttime mean absolute difference with the average σ_W simulated from TEB MOL.	207
5.30	Street average air temperature simulated by TEB-SPAC averaged a) before the water stress period (from 02/06 to 15/06) and b) during the water stress period (from 16/06 to 31/06) and mean absolute difference with the street average air temperature simulated by TEB c) before and d) during the water stress period.	208
5.31	Air temperature at 2 m simulated by TEB-SPAC averaged a) before the water stress period (from 02/06 to 15/06) and b) during the water stress period (from 16/06 to 31/06) and mean absolute difference with the air temperature at 2 m simulated by TEB c) before and d) during the water stress period.	209

- 5.32 Box-plot of Mean Relative Difference (MRD) of street air temperature in streets with trees during the whole period, daytime, nighttime, before water stress (from 06/06 to 12/06) and during water stress (from 16/06 to 31/07). The mean is represented by a white triangle and the result of a T-test between TEB and REF and TEB-SPAC and 3EFF is indicated at the top of each box-plot. The result of a T-test between TEB and TEB-SPAC is indicated at bottom. '***': p-value < 0.001, '**': p-value < 0.01, '*': p-value < 0.05 and 'ns' (non-significant): p-value \geq 0.1. 210
- 5.33 Box-plot of Mean Relative Difference (MRD) of street air specific humidity in streets with trees during the whole period, daytime, nighttime, before water stress (from 06/06 to 12/06) and during water stress (from 16/06 to 31/07). The mean is represented by a white triangle and the result of a T-test between TEB and REF and TEB-SPAC and 3EFF is indicated at the top of each box-plot. The result of a T-test between TEB and TEB-SPAC is indicated at bottom. '***': p-value < 0.001, '**': p-value < 0.01, '*': p-value < 0.05 and 'ns' (non-significant): p-value \geq 0.1. 211
- 5.34 Box-plot of Mean Relative Difference (MRD) of σ_W in streets with trees during the whole period, daytime, nighttime, before water stress (from 06/06 to 12/06) and during water stress (from 16/06 to 31/07). The mean is represented by a white triangle and the result of a T-test between TEB and REF and TEB-SPAC and 3EFF is indicated at the top of each box-plot. The result of a T-test between TEB and TEB-SPAC is indicated at bottom. '***': p-value < 0.001, '**': p-value < 0.01, '*': p-value < 0.05 and 'ns' (non-significant): p-value \geq 0.1. 211
- 5.35 Comparison of a) NO₂ concentrations simulated in Haussmann street with WRF meteo (REF), TEB street meteo only, TEB MOL only and TEB street meteo and MOL (see Table 5.6) and b) relative deviation (RD) of NO₂ concentrations compared to the REF simulation. 212
- 5.36 Comparison of average a) daytime and b) nighttime NO₂ concentrations simulated by MUNICH and WRF meteo and relative difference of c) daytime and d) nighttime NO₂ concentrations simulated by MUNICH with TEB street meteo and MOL. . . . 213
- 5.37 Box-plot of Mean Relative Difference (MRD) of NO₂ concentrations in streets with trees averaged during the whole period, daytime, nighttime, before water stress (from 06/06 to 12/06) and during water stress (from 16/06 to 31/07). The mean is represented by a white triangle and the result of a T-test between 3EFF and REF and TEB-SPAC and TEB is indicated at the top of each box-plot. The result of a T-test between 3EFF and TEB-SPAC is indicated at bottom. '***': p-value < 0.001, '**': p-value < 0.01, '*': p-value < 0.05 and 'ns' (non-significant): p-value \geq 0.1. 214
- 5.38 Comparison of a) PM_{2.5} concentrations simulated in Haussmann street with WRF meteo (REF), TEB street meteo only, TEB MOL only and TEB street meteo and MOL (see Table 5.6) and b) relative deviation (RD) of PM_{2.5} concentrations compared to the REF simulation. 214
- 5.39 Relative difference of PM_{2.5} concentrations simulated by MUNICH with a) TEB street meteo and b) TEB MOL compared to REF as a function of the relative difference of air temperature and σ_W . The particle chemical composition is detailed, BC: Black Carbon, POA: Primary Organic Aerosols, SOA: Secondary Organic Aerosols and SIA: Secondary Inorganic Aerosols (ammonium nitrate). 215

5.40	Comparison of average a) daytime and b) nighttime $PM_{2.5}$ concentrations simulated by MUNICH and WRF meteo and relative difference of c) daytime and d) nighttime $PM_{2.5}$ concentrations simulated by MUNICH with TEB street meteo and MOL.	216
5.41	Box-plot of Mean Relative Difference (MRD) of $PM_{2.5}$ concentrations in streets with trees averaged during the whole period, daytime, nighttime, before water stress (from 06/06 to 12/06) and during water stress (from 16/06 to 31/07). The mean is represented by a white triangle and the result of a T-test between 3EFF and REF and TEB-SPAC and TEB is indicated at the top of each box-plot. The result of a T-test between 3EFF and TEB-SPAC is indicated at bottom. '***': p-value < 0.001, '**': p-value < 0.01, '*': p-value < 0.05 and 'ns' (non-significant): p-value \geq 0.1.	217
5.42	Comparison of the (a, b) temperatures and solar radiation (d, e) used to compute BVOC emissions in MUNICH (a, d) and in MUNICH-TEB-SPAC (b, e) along with the relative difference (RD) of c) temperature and f) solar radiation averaged on the two months.	218
5.43	Comparison of the γ_{SM} activity factor computed from Guenther et al. (2012) ; Otu-Larbi et al. (2020) ; Bonn et al. (2019) as a function of the Soil Water Index (SWI) and from Wang et al. (2022) as a function of the evapotranspiration to potential evapotranspiration ratio (f_{PET}).	219
5.44	Temporal evolution of isoprene emissions computed with WRF and TEB-SPAC meteo averaged on all streets and with or without water stress factor γ_{SM} (G12: Guenther et al. (2012) , B19: Bonn et al. (2019) , O20: Otu-Larbi et al. (2020)).	219
5.45	a) Average isoprene emissions computed with WRF meteo and mean relative difference of isoprene emissions computed with TEB-SPAC meteo (leaf surface temperature T_{sleaf} and solar radiation received by the leaves SW_{leaf}) b) without and with water stress factor γ_{SM} from c) Bonn et al. (2019) and d) Guenther et al. (2012)	220
5.46	a) Average monoterpene emissions computed with WRF meteo and b) mean relative difference of isoprene emissions computed with TEB-SPAC meteo.	221
5.47	Temporal evolution of monoterpene emissions computed with WRF and TEB-SPAC meteo averaged over all streets.	221

List of Tables

4.1	Comparison of observed and modeled air temperature (T_{air}) in HdV and global solar radiation (SW_g) in Qualair with statistical indicators (defined in Appendix 4.D). su: same unit as the variable.	138
4.2	Description of the MUNICH simulations performed with the simulated period, the tree effect(s) considered and the corresponding background concentrations.	141
4.3	Comparison of pollutants and BVOC concentrations observed at HdV and Airparif traffic stations and simulated with MUNICH without tree (REF). The definition of the statistical indicators is given in Appendix 4.D.	142
4.4	Comparison of isoprene concentrations observed and simulated at HdV with and without urban trees and TX2 scenario. The definition of the statistical indicators is given in Appendix 4.D and $n = 619$	146
4.5	Comparison of monoterpene concentrations observed and simulated at HdV with and without urban trees and TX2 scenario. The definition of the statistical indicators is given in Appendix 4.D.	150
4.6	Comparison of OM concentrations observed and simulated at Paris HdV station with and without urban trees and TX2 scenario. The definition of the statistical indicators is given in Appendix 4.D.	159
4.7	Location of HdV and Airparif air-quality stations with the species measured and used in this study. All stations are of traffic type.	166
4.8	List of resistance values used to computed dry deposition of gas on dry tree leaves according to tree type ($s.m^{-1}$) (Zhang et al., 2003).	170
4.9	List of gaseous species that are deposited on street and tree leaf surfaces with associated model parameters.	170
4.10	List of resistance values used to computed dry deposition of aerosols on tree leaves according to tree type (Zhang et al., 2001).	173
4.11	Comparison of the minimum, average and maximum mean relative difference (MRD) of isoprene concentrations in the street network due to the tree aerodynamical effect (AERO) without (left column) and with (right column) BVOC emissions.	174
4.12	Comparison of the minimum, average and maximum mean relative difference (MRD) of monoterpene concentrations due to the tree aerodynamical effect (AERO) without and with BVOC emissions.	174
5.1	MUNICH variables modified with the coupling to TEB-SPAC.	183
5.2	Street and tree dependent parameters used directly from MUNICH to TEB-Veg.	188
5.3	Location of analyzed pits and tree species planted (Paris City agronomy laboratory, 2019).	192
5.4	Description of the two SPAC layers.	194

5.5	List of SPAC tree parameters fixed identical for every street.	195
5.6	Description of the MUNICH simulations performed with the simulated period, the tree effect(s) considered and the corresponding meteorological fields. W89: Wesely (1989)	196
5.7	Comparison of observed and modeled air temperature, humidity and pressure in HdV with statistical indicators. su: same unit as the variable.	197
5.8	List of street and tree characteristics of Haussmann and HdV streets.	199

Bibliography

- K. Ahmad, M. Khare, and K. K. Chaudhry. Wind tunnel simulation studies on dispersion at urban street canyons and intersections - a review. *J. Wind Eng. Ind. Aerod.*, 93(9):697–717, 2005. doi: 10.1016/j.jweia.2005.04.002. URL <https://www.sciencedirect.com/science/article/pii/S0167610505000504>.
- H. Akimoto. Global Air Quality and Pollution. *Science*, 302(5651):1716–1719, Dec. 2003. ISSN 0036-8075, 1095-9203. doi: 10.1126/science.1092666. URL <https://www.sciencemag.org/lookup/doi/10.1126/science.1092666>.
- J. H. Amorim, V. Rodrigues, R. Tavares, J. Valente, and C. Borrego. CFD modelling of the aerodynamic effect of trees on urban air pollution dispersion. *Sci. Total. Environ.*, 461-462: 541–551, 2013. doi: 10.1016/j.scitotenv.2013.05.031. URL <https://www.sciencedirect.com/science/article/pii/S0048969713005743>.
- S. Angel, J. Parent, D. L. Civco, A. Blei, and D. Potere. The dimensions of global urban expansion: Estimates and projections for all countries, 2000–2050. *Prog. Plann.*, 75(2):53–107, 2011. doi: 10.1016/j.progress.2011.04.001. URL <https://www.sciencedirect.com/science/article/pii/S0305900611000109>.
- K. W. Appel, J. O. Bash, K. M. Fahey, K. M. Foley, R. C. Gilliam, C. Hogrefe, W. T. Hutzell, D. Kang, R. Mathur, B. N. Murphy, S. L. Napelenok, C. G. Nolte, J. E. Pleim, G. A. Pouliot, H. O. T. Pye, L. Ran, S. J. Roselle, G. Sarwar, D. B. Schwede, F. I. Sidi, T. L. Spero, and D. C. Wong. The community multiscale air quality (CMAQ) model versions 5.3 and 5.3.1: system upyears and evaluation. *Geosci. Model Dev.*, 14(5):2867–2897, 2021. doi: 10.5194/gmd-14-2867-2021. URL <https://gmd.copernicus.org/articles/14/2867/2021/>.
- APUR. Les arbres dans la Métropole du Grand Paris. Vers une base de données de décompte et d’identification. Technical report, Atelier parisien d’urbanisme, 2012. URL https://www.apur.org/sites/default/files/4p203_arbres_mgp.pdf?token=lxP9tayU.
- F. Archambeau, N. Méchitoua, and M. Sakiz. Code Saturne: A finite volume code for the computation of turbulent incompressible flows-Industrial applications. *International Journal on Finite Volumes*, 1(1):1–62, 2004. URL <https://hal.archives-ouvertes.fr/hal-01115371>.
- R. Arimoto. Atmospheric deposition of chemical contaminants to the great lakes. *Journal of Great Lakes Research*, 15(2):339–356, 1989. doi: 10.1016/S0380-1330(89)71487-8. URL <https://www.sciencedirect.com/science/article/pii/S0380133089714878>.
- D. Armson, M. A. Rahman, and A. R. Ennos. A comparison of the shading effectiveness of five different street tree species in manchester, UK. *Arboriculture & Urban Forestry*, 39(4):157–164, 2013a. doi: 10.48044/jauf.2013.021. URL <https://www.cabdirect.org/cabdirect/abstract/20133290871>.

- D. Armson, P. Stringer, and A. R. Ennos. The effect of street trees and amenity grass on urban surface water runoff in manchester, UK. *Urban For. Urban Gree.*, 12(3):282–286, 2013b. doi: 10.1016/j.ufug.2013.04.001. URL <https://www.sciencedirect.com/science/article/pii/S1618866713000460>.
- A. Arnfield. Two decades of urban climate research: A review of turbulence, exchanges of energy and water, and the urban heat island. *Int. J. Climatol.*, 23(1):1–26, 2003. doi: 10.1002/joc.859.
- M. H. Askariyeh, M. Venugopal, H. Khreis, A. Birt, and J. Zietsman. Near-road traffic-related air pollution: Resuspended PM_{2.5} from highways and arterials. *Int. J. Env. Res. Pub. He.*, 17(8): 2851, 2020. doi: 10.3390/ijerph17082851. URL <https://www.mdpi.com/1660-4601/17/8/2851>.
- R. W. Atkinson, I. C. Mills, H. A. Walton, and H. R. Anderson. Fine particle components and health—a systematic review and meta-analysis of epidemiological time series studies of daily mortality and hospital admissions. *Journal of Exposure Science & Environmental Epidemiology*, 25(2):208–214, 2015. doi: 10.1038/jes.2014.63. URL <https://www.nature.com/articles/jes201463>.
- A. H. Auer. Urban boundary layer. In S. A. Changnon, editor, *Metromex: A Review and Summary*, Meteorological Monographs, pages 41–62. American Meteorological Society, 1981. ISBN 978-1-935704-29-4. doi: 10.1007/978-1-935704-29-4_3. URL 10.1007/978-1-935704-29-4_3.
- M. Baccini, A. Biggeri, G. Accetta, T. Kosatsky, K. Katsouyanni, A. Analitis, H. R. Anderson, L. Bisanti, D. D’Ippoliti, J. Danova, B. Forsberg, S. Medina, A. Paldy, D. Rabczenko, C. Schindler, and P. Michelozzi. Heat effects on mortality in 15 european cities. *Epidemiology*, 19(5):711, 2008. doi: 10.1097/EDE.0b013e318176bfcd. URL https://journals.lww.com/epidem/Fulltext/2008/09000/Heat_Effects_on_Mortality_in_15_European_Cities.13.aspx.
- J. Badach, M. Dymnicka, and A. Baranowski. Urban vegetation in air quality management: A review and policy framework. *Sustainability*, 12(3):1258, 2020. doi: 10.3390/su12031258. URL <https://www.mdpi.com/2071-1050/12/3/1258>.
- R. Baghi, D. Helmig, A. Guenther, T. Duhl, and R. Daly. Contribution of flowering trees to urban atmospheric biogenic volatile organic compound emissions. *Biogeosciences*, 9(10):3777–3785, 2012. doi: 10.5194/bg-9-3777-2012. URL <https://bg.copernicus.org/articles/9/3777/2012/>.
- D. D. Baldocchi, B. B. Hicks, and P. Camara. A canopy stomatal resistance model for gaseous deposition to vegetated surfaces. *Atmos. Environ.*, 21(1):91–101, 1987. doi: 10.1016/0004-6981(87)90274-5.
- M. Barlage, S. Miao, and F. Chen. Impact of physics parameterizations on high-resolution weather prediction over two chinese megacities. *J. Geophys. Res-Atmos.*, 121(9):4487–4498, 2016. doi: 10.1002/2015JD024450. URL <https://onlinelibrary.wiley.com/doi/abs/10.1002/2015JD024450>.
- R. C. Barragán, M. Strojnik, A. Rodríguez-Rivas, G. G. Torales, and F. J. González. Optical spectral characterization of leaves for *Quercus Resinosa* and *Magnolifolia* species in two senescent states. In M. Strojnik and M. S. Kirk, editors, *Infrared Remote Sensing and Instrumentation XXVI*, volume 10765, page 1076511. International Society for Optics and Photonics, SPIE, 2018. doi: 10.1117/12.2321710. URL 10.1117/12.2321710.
- R. Basu. High ambient temperature and mortality: a review of epidemiologic studies from 2001 to 2008. *Environmental Health*, 8(1):40, 2009. doi: 10.1186/1476-069X-8-40. URL 10.1186/1476-069X-8-40.
- A. Berchet, K. Zink, C. Muller, D. Oettl, J. Brunner, L. Emmenegger, and D. Brunner. A cost-effective method for simulating city-wide air flow and pollutant dispersion at building resolving

- scale. *Atmos. Environ.*, 158:181–196, 2017. doi: 10.1016/j.atmosenv.2017.03.030. URL <https://linkinghub.elsevier.com/retrieve/pii/S1352231017301620>.
- R. Berkowicz. OSPM - a parameterised street pollution model. *Environmental Monitoring and Assessment*, 65(1):323–331, 2000. doi: 10.1023/A:1006448321977. URL 10.1023/A:1006448321977.
- A. Berland. The role of trees in urban stormwater management. *Landscape Urban Plan.*, 162:167–177, 2017. doi: 10.1016/j.landurbplan.2017.02.017.
- E. Bernard. *Réponse hydro-climatique de Paris et sa petite couronne*. PhD thesis, Université Toulouse 3 - Paul Sabatier, 2021.
- J. A. Bernstein, N. Alexis, C. Barnes, I. L. Bernstein, A. Nel, D. Peden, D. Diaz-Sanchez, S. M. Tarlo, P. B. Williams, and J. A. Bernstein. Health effects of air pollution. *Journal of Allergy and Clinical Immunology*, 114(5):1116–1123, 2004. doi: 10.1016/j.jaci.2004.08.030. URL <https://linkinghub.elsevier.com/retrieve/pii/S0091674904022663>.
- C. Bertram and K. Rehdanz. The role of urban green space for human well-being. *Ecological Economics*, 120:139–152, 2015. doi: 10.1016/j.ecolecon.2015.10.013.
- B. Blocken, Y. Tominaga, and T. Stathopoulos. CFD simulation of micro-scale pollutant dispersion in the built environment. *Build Environ.*, 64:225–230, 2013. doi: 10.1016/j.buildenv.2013.01.001. URL <https://lirias.kuleuven.be/1113606>.
- B. Bonn, R.-K. Magh, J. Rombach, and J. Kreuzwieser. Biogenic isoprenoid emissions under drought stress: different responses for isoprene and terpenes. *Biogeosciences*, 16(23):4627–4645, 2019. doi: 10.5194/bg-16-4627-2019. URL <https://bg.copernicus.org/articles/16/4627/2019/>.
- A. Boone. *Modélisation des processus hydrologiques dans le schéma desurface ISBA: Inclusion d’un réservoir hydrologique, du gel et modélisation de la neige*. PhD thesis, Université Toulouse 3 - Paul Sabatier, 2000.
- C. Borrego, H. Martins, O. Tchepel, L. Salmim, A. Monteiro, and A. I. Miranda. How urban structure can affect city sustainability from an air quality perspective. *Environ. Modell. Softw.*, 21(4):461–467, 2006. doi: 10.1016/j.envsoft.2004.07.009. URL <https://www.sciencedirect.com/science/article/pii/S1364815204003081>.
- J. Boutahar, S. Lacour, V. Mallet, D. Quelo, Y. Roustan, and B. Sportisse. Development and validation of a fully modular platform for numerical modelling of air pollution: POLAIR. *International Journal of Environment and Pollution*, 22(1):17–28, 2004. doi: 10.1504/IJEP.2004.005474. URL <https://www.inderscienceonline.com/doi/abs/10.1504/IJEP.2004.005474>.
- G. P. Brasseur and D. J. Jacob. *Modeling of Atmospheric Chemistry*. Cambridge University Press, 2017. ISBN 978-1-107-14696-9. doi: 10.1017/97811316544754. URL <https://www.cambridge.org/core/books/modeling-of-atmospheric-chemistry/88C5AEAD7C28EA3E17FFA6D2CE92DE06>.
- M. Bruse and H. Fleer. Simulating surface–plant–air interactions inside urban environments with a three dimensional numerical model. *Environ. Modell. Softw.*, 13(3):373–384, 1998. doi: 10.1016/S1364-8152(98)00042-5. URL <https://www.sciencedirect.com/science/article/pii/S1364815298000425>.
- R. Buccolieri, C. Gromke, S. Di Sabatino, and B. Ruck. Aerodynamic effects of trees on pollutant concentration in street canyons. *Sci. Total. Environ.*, 407(19):5247–5256, 2009. doi: 10.1016/j.scitotenv.2009.06.016. URL <https://linkinghub.elsevier.com/retrieve/pii/S0048969709005944>.

- R. Buccolieri, S. M. Salim, L. S. Leo, S. Di Sabatino, A. Chan, P. Ielpo, G. de Gennaro, and C. Gromke. Analysis of local scale tree–atmosphere interaction on pollutant concentration in idealized street canyons and application to a real urban junction. *Atmos. Environ.*, 45(9):1702–1713, 2011. doi: 10.1016/j.atmosenv.2010.12.058. URL <https://linkinghub.elsevier.com/retrieve/pii/S1352231011000057>.
- R. Buccolieri, J.-L. Santiago, E. Rivas, and B. Sanchez. Review on urban tree modelling in CFD simulations: Aerodynamic, deposition and thermal effects. *Urban For. Urban Gree.*, 31:212–220, 2018. doi: 10.1016/j.ufug.2018.03.003. URL <https://linkinghub.elsevier.com/retrieve/pii/S1618866717304600>.
- D. Byun and K. L. Schere. Review of the governing equations, computational algorithms, and other components of the models-3 community multiscale air quality (CMAQ) modeling system. *Applied Mechanics Reviews*, 59(2):51–77, 2006. doi: 10.1115/1.2128636. URL 10.1115/1.2128636.
- C. Calfapietra, S. Fares, F. Manes, A. Morani, G. Sgrigna, and F. Loreto. Role of biogenic volatile organic compounds (BVOC) emitted by urban trees on ozone concentration in cities: A review. *Environ. Pollut.*, 183:71–80, 2013. doi: 10.1016/j.envpol.2013.03.012. URL <https://www.sciencedirect.com/science/article/pii/S0269749113001310>.
- E. Canaval, D. B. Millet, I. Zimmer, T. Nosenko, E. Georgii, E. M. Partoll, L. Fischer, H. D. Alwe, M. Kulmala, T. Karl, J.-P. Schnitzler, and A. Hansel. Rapid conversion of isoprene photooxidation products in terrestrial plants. *Communications Earth & Environment*, 1(1):44, 2020. doi: 10.1038/s43247-020-00041-2. URL <https://www.nature.com/articles/s43247-020-00041-2>.
- D. Carruthers, H. Edmunds, A. Lester, C. McHugh, and R. Singles. Use and validation of ADMS-urban in contrasting urban and industrial locations. *International Journal of Environment and Pollution*, 14(1):364–374, 2000. doi: 10.1504/IJEP.2000.000558. URL <https://www.inderscienceonline.com/doi/abs/10.1504/IJEP.2000.000558>.
- A. Chan, J. C. H. Fung, and A. K. H. Lau. Influence of urban morphometric modification on regional boundary-layer dynamics. *J. Geophys. Res-Atmos.*, 118(7):2729–2747, 2013. doi: 10.1002/jgrd.50263. URL <https://onlinelibrary.wiley.com/doi/abs/10.1002/jgrd.50263>.
- A. T. Chan, W. T. W. Au, and E. S. P. So. Strategic guidelines for street canyon geometry to achieve sustainable street air quality-part II: multiple canopies and canyons. *Atmos. Environ.*, 37(20):2761–2772, 2003. doi: 10.1016/S1352-2310(03)00252-8. URL <https://www.sciencedirect.com/science/article/pii/S1352231003002528>.
- J. Chang, Z. Qu, R. Xu, K. Pan, B. Xu, Y. Min, Y. Ren, G. Yang, and Y. Ge. Assessing the ecosystem services provided by urban green spaces along urban center-edge gradients. *Scientific Reports*, 7(1):11226, 2017. doi: 10.1038/s41598-017-11559-5. URL <https://www.nature.com/articles/s41598-017-11559-5>.
- A. Charalampopoulos, M. Lazarina, I. Tsiripidis, and D. Vokou. Quantifying the relationship between airborne pollen and vegetation in the urban environment. *Aerobiologia*, 34(3):285–300, 2018. doi: 10.1007/s10453-018-9513-y. URL 10.1007/s10453-018-9513-y.
- B. Choat, S. Jansen, T. Brodribb, H. Cochard, S. Delzon, R. Bhaskar, S. Bucci, T. Feild, S. Gleason, U. Hacke, A. Jacobsen, F. Lens, H. Maherali, J. Martinez-Vilalta, S. Mayr, M. Mencuccini, P. Mitchell, A. Nardini, J. Pittermann, R. Pratt, J. Sperry, M. Westoby, I. Wright, and A. Zanne. Global convergence in the vulnerability of forests to drought. *Nature*, 491:752–755, 2012. URL <https://xylemfunctionaltraits.org/>.

- R. B. Clapp and G. M. Hornberger. Empirical equations for some soil hydraulic properties. *Water Resources Research*, 14(4):601–604, 1978. doi: 10.1029/WR014i004p00601. URL <https://onlinelibrary.wiley.com/doi/abs/10.1029/WR014i004p00601>.
- C. G. Collier. The impact of urban areas on weather. *Quart. J. Roy. Meteorol. Soc.*, 132(614):1–25, 2006. doi: 10.1256/qj.05.199. URL <https://onlinelibrary.wiley.com/doi/abs/10.1256/qj.05.199>.
- J. Cuxart, P. Bougeault, and J.-L. Redelsperger. A turbulence scheme allowing for mesoscale and large-eddy simulations. *Quart. J. Roy. Meteorol. Soc.*, 126(562):1–30, 2000. doi: 10.1002/qj.49712656202. URL <https://onlinelibrary.wiley.com/doi/abs/10.1002/qj.49712656202>.
- M. Czaja, A. Kołton, and P. Muras. The complex issue of urban trees-stress factor accumulation and ecological service possibilities. *Forests*, 11(9):932, 2020. doi: 10.3390/f11090932. URL <https://www.mdpi.com/1999-4907/11/9/932>.
- W. F. Dabberdt, F. L. Ludwig, and W. B. Johnson. Validation and applications of an urban diffusion model for vehicular pollutants. *Atmos. Environ.*, 7(6):603–618, 1973. ISSN 0004-6981. doi: 10.1016/0004-6981(73)90019-X. URL <https://www.sciencedirect.com/science/article/pii/S000469817390019X>.
- C. De Munck. *Modélisation de la végétation urbaine et stratégies d’adaptation pour l’amélioration du confort climatique et de la demande énergétique en ville*. PhD thesis, Institut National Polytechnique de Toulouse (INP Toulouse), 2013.
- C. De Munck, A. Lemonsu, R. Bouzouidja, V. Masson, and R. Claverie. The GREENROOF module (v7.3) for modelling green roof hydrological and energetic performances within TEB. *Geosci. Model Dev.*, 6(6):1941–1960, 2013. doi: 10.5194/gmd-6-1941-2013. URL <https://gmd.copernicus.org/articles/6/1941/2013/>.
- Department of Economics and Social Affairs. World urbanization prospects the 2018 revision. Technical report, United Nations, 2018. URL <https://population.un.org/wup/Publications/Files/WUP2018-Report.pdf>.
- A. Diener and P. Mudu. How can vegetation protect us from air pollution? a critical review on green spaces’ mitigation abilities for air-borne particles from a public health perspective - with implications for urban planning. *Sci. Total. Environ.*, 796:148605, 2021. doi: 10.1016/j.scitotenv.2021.148605. URL <https://linkinghub.elsevier.com/retrieve/pii/S0048969721036779>.
- Dimensions. Publication number timeline overview, 1980-2022. URL https://app.dimensions.ai/analytics/publication/overview/timeline?search_mode=content&year_from=1980&year_to=2022. Last access: 02/06/2023.
- D. D’Ippoliti, P. Michelozzi, C. Marino, F. de’Donato, B. Menne, K. Katsouyanni, U. Kirchmayer, A. Analitis, M. Medina-Ramón, A. Paldy, R. Atkinson, S. Kovats, L. Bisanti, A. Schneider, A. Lefranc, C. Iñiguez, and C. A. Perucci. The impact of heat waves on mortality in 9 european cities: results from the EuroHEAT project. *Environmental Health*, 9(1):37, 2010. doi: 10.1186/1476-069X-9-37. URL [10.1186/1476-069X-9-37](https://doi.org/10.1186/1476-069X-9-37).
- M. El-Harbawi. Air quality modelling, simulation, and computational methods: a review. *Environmental Reviews*, 21(3):149–179, 2013. doi: 10.1139/er-2012-0056. URL <https://cdnsiencepub.com/doi/10.1139/er-2012-0056>.
- I. Eliasson, B. Offerle, C. Grimmond, and S. Lindqvist. Wind fields and turbulence statistics in an urban street canyon. *Atmos. Environ.*, 40(1):1–16, 2006. doi: 10.1016/j.atmosenv.2005.03.031. URL <https://linkinghub.elsevier.com/retrieve/pii/S1352231005002967>.

- C. Elichegaray, S. Bouallala, A. Maitre, and M. Ba. État et évolution de la pollution atmosphérique. *Revue Française d'Allergologie*, 50(4):381–393, 2010. doi: 10.1016/j.reval.2009.08.003. URL <https://www.sciencedirect.com/science/article/pii/S1877032009002000>.
- EPA. Stormwater to Street Trees: Engineering Urban Forests for Stormwater Management. Technical report, U.S. Environmental Protection Agency, Office of Wetlands, Oceans and Watersheds, 2013. URL <https://www.epa.gov/sites/default/files/2015-11/documents/stormwater2streettrees.pdf>.
- J. Ermák, J. Hruška, M. Martinková, and A. Prax. Urban tree root systems and their survival near houses analyzed using ground penetrating radar and sap flow techniques. *Plant and Soil*, 219(1): 103–116, 2000. doi: 10.1023/A:1004736310417. URL 10.1023/A:1004736310417.
- F. J. Escobedo and D. J. Nowak. Spatial heterogeneity and air pollution removal by an urban forest. *Landscape Urban Plan.*, 90(3):102–110, 2009. doi: 10.1016/j.landurbplan.2008.10.021. URL <https://www.sciencedirect.com/science/article/pii/S0169204608001801>.
- European Environment Agency. Europe's air quality status 2023, 2023. URL <https://www.eea.europa.eu/publications/europes-air-quality-status-2023>.
- S. Fares, E. Paoletti, C. Calfapietra, T. N. Mikkelsen, R. Samson, and D. Le Thiec. Carbon sequestration by urban trees. In D. Pearlmutter, C. Calfapietra, R. Samson, L. O'Brien, S. Kratjer Ostoić, G. Sanesi, and R. Alonso Del Amo, editors, *The Urban Forest*, volume 7, pages 31–39. Springer International Publishing, 2017. ISBN 978-3-319-50279-3 978-3-319-50280-9. doi: 10.1007/978-3-319-50280-9_4. URL http://link.springer.com/10.1007/978-3-319-50280-9_4.
- H. Feng, B. Zou, J. Wang, and X. Gu. Dominant variables of global air pollution-climate interaction: Geographic insight. *Ecological Indicators*, 99:251–260, 2019. doi: 10.1016/j.ecolind.2018.12.038. URL <https://linkinghub.elsevier.com/retrieve/pii/S1470160X18309713>.
- J. Fenger. Urban air quality. *Atmos. Environ.*, 33(29):4877–4900, 1999. doi: 10.1016/S1352-2310(99)00290-3. URL <https://www.sciencedirect.com/science/article/pii/S1352231099002903>.
- J. Finnigan and M. Raupach. Modern theory of transfer in plant canopies in relation to stomatal characteristics. In E. Zeiger, G. Farquhar, and I. Cowan, editors, *Stomatal Function*, pages 385–429. Stanford University Press, CA, 1987.
- A. M. Fiore, V. Naik, and E. M. Leibensperger. Air quality and climate connections. *Journal of the Air & Waste Management Association*, 65(6):645–685, 2015. doi: 10.1080/10962247.2015.1040526. URL 10.1080/10962247.2015.1040526.
- B. Fisher, J. Kukkonen, M. Piringer, M. W. Rotach, and M. Schatzmann. Meteorology applied to urban air pollution problems: concepts from COST 715. *Atmos. Chem. Phys.*, 6:555–564, 2006. doi: 10.5194/acp-6-555-2006. URL www.atmos-chem-phys.net/6/555/2006/.
- S. Fuzzi, U. Baltensperger, K. Carslaw, S. Decesari, H. Denier van der Gon, M. C. Facchini, D. Fowler, I. Koren, B. Langford, U. Lohmann, E. Nemitz, S. Pandis, I. Riipinen, Y. Rudich, M. Schaap, J. G. Slowik, D. V. Spracklen, E. Vignati, M. Wild, M. Williams, and S. Gilarioni. Particulate matter, air quality and climate: lessons learned and future needs. *Atmos. Chem. Phys.*, 15(14):8217–8299, 2015. ISSN 1680-7316. doi: 10.5194/acp-15-8217-2015. URL <https://acp.copernicus.org/articles/15/8217/2015/>.
- K. Gao, M. Santamouris, and J. Feng. On the efficiency of using transpiration cooling to mitigate urban heat. *Climate*, 8(6):69, 2020. doi: 10.3390/cli806069. URL <https://www.mdpi.com/2225-1154/8/6/69>.

- J. Grabosky, N. Bassuk, L. Irwin, and H. Van Es. Shoot and root growth of three tree species in sidewalks. *Journal of Environmental Horticulture*, 19(4):206–211, 2001. doi: 10.24266/0738-2898-19.4.206. URL <http://meridian.allenpress.com/jeh/article/19/4/206/79930/Shoot-and-Root-Growth-of-Three-Tree-Species-in>.
- C. Gromke and B. Blocken. Influence of avenue-trees on air quality at the urban neighborhood scale. part II: Traffic pollutant concentrations at pedestrian level. *Environ. Pollut.*, 196:176–184, 2015. doi: 10.1016/j.envpol.2014.10.015. URL <https://linkinghub.elsevier.com/retrieve/pii/S0269749114004382>.
- C. Gromke and B. Ruck. Influence of trees on the dispersion of pollutants in an urban street canyon-experimental investigation of the flow and concentration field. *Atmos. Environ.*, 41(16):3287–3302, 2007. doi: 10.1016/j.atmosenv.2006.12.043. URL <https://www.sciencedirect.com/science/article/pii/S1352231007000076>.
- A. Guenther. Biological and chemical diversity of biogenic volatile organic emissions into the atmosphere. *International Scholarly Research Notices*, 2013:e786290, 2013. doi: 10.1155/2013/786290. URL <https://www.hindawi.com/journals/isrn/2013/786290/>.
- A. Guenther, C. N. Hewitt, D. Erickson, R. Fall, C. Geron, T. Graedel, P. Harley, L. Klinger, M. Lerdau, W. Mckay, T. Pierce, B. Scholes, R. Steinbrecher, R. Tallamraju, J. Taylor, and P. Zimmerman. A global model of natural volatile organic compound emissions. *Journal of geophysical research*, 100:8873–8892, 1995. doi: 10.1029/94JD02950.
- A. Guenther, X. Jiang, C. L. Heald, T. Sakulyanontvittaya, T. Duhl, L. K. Emmons, and X. Wang. The model of emissions of gases and aerosols from nature version 2.1 (MEGAN2.1): an extended and upyeard framework for modeling biogenic emissions. *Geosci. Model Dev.*, 5(6):1471–1492, 2012. doi: 10.5194/gmd-5-1471-2012. URL <https://gmd.copernicus.org/articles/5/1471/2012/>.
- S. Hajat, S. Vardoulakis, C. Heaviside, and B. Eggen. Climate change effects on human health: projections of temperature-related mortality for the UK during the 2020s, 2050s and 2080s. *J. Epidemiol. Community. Health.*, 68(7):641–648, 2014. doi: 10.1136/jech-2013-202449. URL <https://jech.bmj.com/content/68/7/641>.
- R. Hamdi and V. Masson. Inclusion of a drag approach in the town energy balance (TEB) scheme: Offline 1d evaluation in a street canyon. *J. Appl. Meteorol. Clim.*, 47(10):2627–2644, 2008. doi: 10.1175/2008JAMC1865.1. URL <https://journals.ametsoc.org/doi/10.1175/2008JAMC1865.1>.
- A. Hami, B. Abdi, D. Zarehaghi, and S. B. Maulan. Assessing the thermal comfort effects of green spaces: A systematic review of methods, parameters, and plants’ attributes. *Sustain. Cities. Soc.*, 49:101634, 2019. doi: 10.1016/j.scs.2019.101634. URL <https://linkinghub.elsevier.com/retrieve/pii/S2210670718327306>.
- S. Hanna and J. Chang. Acceptance criteria for urban dispersion model evaluation. *Meteorol. Atmos. Phys.*, 116(3-4):133–146, 2012. doi: 10.1007/s00703-011-0177-1.
- I. N. Harman, J. F. Barlow, and S. E. Belcher. Scalar fluxes from urban street canyons. Part II Model. *Bound.-Lay. Meteorol.*, 113:387–409, 2004a. doi: 10.1007/s10546-004-6205-7.
- I. N. Harman, M. J. Best, and S. E. Belcher. Radiative exchange in an urban street canyon. *Bound.-Lay. Meteorol.*, 110(2):301–316, 2004b. doi: 10.1023/A:1026029822517. URL 10.1023/A:1026029822517.

- A. L. Hass, K. N. Ellis, L. Reyes Mason, J. M. Hathaway, and D. A. Howe. Heat and humidity in the city: Neighborhood heat index variability in a mid-sized city in the southeastern United States. *Int. J. Env. Res. Pub. He.*, 13(1):117, 2016. doi: 10.3390/ijerph13010117. URL <https://www.ncbi.nlm.nih.gov/pmc/articles/PMC4730508/>.
- C. Heaviside, H. Macintyre, and S. Vardoulakis. The urban heat island: Implications for health in a changing environment. *Current Environmental Health Reports*, 4(3):296–305, 2017. doi: 10.1007/s40572-017-0150-3. URL [10.1007/s40572-017-0150-3](https://doi.org/10.1007/s40572-017-0150-3).
- B. Hicks, D. Baldocchi, T. Meyers, R. Hosker, and D. Matt. A preliminary multiple resistance routine for deriving dry deposition velocities from measured quantities. *Water, Air, Soil, Poll.*, 36(3-4):311–330, 1987. doi: 10.1007/BF00229675.
- R. Hotchkiss and F. Harlow. Air pollution transport in street canyons, epa-r4-73-029. Technical report, EPA, 1973.
- C. Huang, A. G. Barnett, X. Wang, P. Vaneckova, G. FitzGerald, and S. Tong. Projecting future heat-related mortality under climate change scenarios: A systematic review. *Environmental Health Perspectives*, 119(12):1681–1690, 2011. doi: 10.1289/ehp.1103456. URL <https://ehp.niehs.nih.gov/doi/10.1289/ehp.1103456>.
- Y. Huang, C. Lei, C.-H. Liu, P. Perez, H. Forehead, S. Kong, and J. L. Zhou. A review of strategies for mitigating roadside air pollution in urban street canyons. *Environ. Pollut.*, 280:116971, 2021. doi: 10.1016/j.envpol.2021.116971. URL <https://www.sciencedirect.com/science/article/pii/S0269749121005534>.
- Y.-d. Huang, M.-z. Li, S.-q. Ren, M.-j. Wang, and P.-y. Cui. Impacts of tree-planting pattern and trunk height on the airflow and pollutant dispersion inside a street canyon. *Build Environ.*, 165:106385, 2019. doi: 10.1016/j.buildenv.2019.106385. URL <https://www.sciencedirect.com/science/article/pii/S0360132319305955>.
- L. Hunter, G. Johnson, and I. Watson. An investigation of three-dimensional characteristics of flow regimes within the urban canyon. *Atmospheric Environment. Part B. Urban Atmosphere*, 26(4):425–432, 1992. doi: 10.1016/0957-1272(92)90049-X. URL <https://linkinghub.elsevier.com/retrieve/pii/095712729290049X>.
- R. Huston, Y. Chan, T. Gardner, G. Shaw, and H. Chapman. Characterisation of atmospheric deposition as a source of contaminants in urban rainwater tanks. *Water Research*, 43(6):1630–1640, 2009. doi: 10.1016/j.watres.2008.12.045. URL <https://linkinghub.elsevier.com/retrieve/pii/S004313540800657X>.
- IPCC. Climate Change 2021: The Physical Science Basis. Contribution of Working Group I to the Sixth Assessment Report of the Intergovernmental Panel on Climate Change. Report, Intergovernmental Panel on Climate Change, United Nations, 2021. [Masson-Delmotte V., Zhai P., Pirani A., Connors S.L., Péan C., Berger S., Caud N., Chen Y., Goldfarb L., Gomis M.I., Huang M., Leitzell K., Lonnoy E., Matthews J.B.R., Maycock T.K., Waterfield T., Yelekçi O., Yu R., and Zhou B. (eds.)]. Cambridge University Press. In Press.
- J. Irwin and M. Williams. Acid rain: Chemistry and transport. *Environ. Pollut.*, 50(1):29–59, 1988. doi: 10.1016/0269-7491(88)90184-4. URL <https://linkinghub.elsevier.com/retrieve/pii/0269749188901844>.
- E. Jamei, P. Rajagopalan, M. Seyedmahmoudian, and Y. Jamei. Review on the impact of urban geometry and pedestrian level greening on outdoor thermal comfort. *Renewable and Sustainable Energy Reviews*, 54:1002–1017, 2016. doi: 10.1016/j.rser.2015.10.104. URL <https://linkinghub.elsevier.com/retrieve/pii/S1364032115011831>.

- S. Janhäll. Review on urban vegetation and particle air pollution – deposition and dispersion. *Atmos. Environ.*, 105:130–137, 2015. doi: 10.1016/j.atmosenv.2015.01.052. URL <https://www.sciencedirect.com/science/article/pii/S1352231015000758>.
- P. G. Jarvis. The interpretation of the variations in leaf water potential and stomatal conductance found in canopies in the field. *Philosophical Transactions of the Royal Society of London. Series B, Biological Sciences*, 273(927):593–610, 1976. URL <https://www.jstor.org/stable/2417554>.
- A. P. R. Jeanjean, P. S. Monks, and R. J. Leigh. Modelling the effectiveness of urban trees and grass on PM_{2.5} reduction via dispersion and deposition at a city scale. *Atmos. Environ.*, 147:1–10, 2016. doi: 10.1016/j.atmosenv.2016.09.033. URL <https://www.sciencedirect.com/science/article/pii/S1352231016307336>.
- W. Johnson, F. Ludwig, W. Dabberdt, and R. Allen. An urban diffusion simulation model for carbon monoxide. *J. Air Pollut. Control Assoc.*, 23(6):490–498, 1973. doi: 10.1080/00022470.1973.10469794. URL 10.1080/00022470.1973.10469794.
- M. Kampa and E. Castanas. Human health effects of air pollution. *Environ. Pollut.*, 151(2):362–367, 2008. doi: 10.1016/j.envpol.2007.06.012. URL <https://linkinghub.elsevier.com/retrieve/pii/S0269749107002849>.
- T. Karl, P. Harley, L. Emmons, B. Thornton, A. Guenther, C. Basu, A. Turnipseed, and K. Jardine. Efficient atmospheric cleansing of oxidized organic trace gases by vegetation. *Science*, 330(6005):816–819, 2010. doi: 10.1126/science.1192534. URL <https://www.science.org/doi/10.1126/science.1192534>.
- S. Karra, L. Malki-Epshtein, and M. K. A. Neophytou. Air flow and pollution in a real, heterogeneous urban street canyon: A field and laboratory study. *Atmos. Environ.*, 165:370–384, 2017. doi: 10.1016/j.atmosenv.2017.06.035. URL <https://www.sciencedirect.com/science/article/pii/S1352231017304168>.
- I. Kasprzyk, A. Ćwik, K. Kluska, T. Wójcik, and P. Cariñanos. Allergenic pollen concentrations in the air of urban parks in relation to their vegetation. *Urban For. Urban Gree.*, 46:126486, 2019. doi: 10.1016/j.ufug.2019.126486. URL <https://www.sciencedirect.com/science/article/pii/S1618866719302171>.
- P. Kastner-Klein, R. Berkowicz, and R. Britter. The influence of street architecture on flow and dispersion in street canyons. *Meteorol. Atmos. Phys.*, 87(1):121–131, 2004. doi: 10.1007/s00703-003-0065-4. URL 10.1007/s00703-003-0065-4.
- M. Katz and V. C. Shore. Air pollution damage to vegetation. *J. Air Pollut. Control Assoc.*, 5(3):144–182, 1955. doi: 10.1080/00966665.1955.10467697. URL <http://www.tandfonline.com/doi/abs/10.1080/00966665.1955.10467697>.
- H. H. Kim. Urban heat island. *Int. J. Remote Sens.*, 13(12):2319–2336, 1992. doi: 10.1080/01431169208904271. URL 10.1080/01431169208904271.
- Y. Kim, Y. Wu, C. Seigneur, and Y. Roustan. Multi-scale modeling of urban air pollution: development and application of a street-in-grid model (v1.0) by coupling MUNICH (v1.0) and polair3d (v1.8.1). *Geosci. Model Dev.*, 11(2):611–629, 2018. doi: 10.5194/gmd-11-611-2018. URL <https://www.geosci-model-dev.net/11/611/2018/>.
- Y. Kim, L. Lugon, A. Maison, T. Sarica, Y. Roustan, M. Valari, Y. Zhang, M. André, and K. Sartelet. MUNICH v2.0: a street-network model coupled with SSH-aerosol (v1.2) for multi-pollutant modelling. *Geosci. Model Dev.*, 15(19):7371–7396, 2022. doi: 10.5194/gmd-15-7371-2022. URL <https://gmd.copernicus.org/articles/15/7371/2022/>.

- A. Kinnunen, I. Talvitie, J. Ottelin, J. Heinonen, and S. Junnila. Carbon sequestration and storage potential of urban residential environment – a review. *Sustain. Cities. Soc.*, 84:104027, 2022. doi: 10.1016/j.scs.2022.104027. URL <https://linkinghub.elsevier.com/retrieve/pii/S221067072200347X>.
- J. Konarska, F. Lindberg, A. Larsson, S. Thorsson, and B. Holmer. Transmissivity of solar radiation through crowns of single urban trees-application for outdoor thermal comfort modelling. *Theoretical and Applied Climatology*, 117(3):363–376, 2014. doi: 10.1007/s00704-013-1000-3. URL 10.1007/s00704-013-1000-3.
- J. Konarska, J. Uddling, B. Holmer, M. Lutz, F. Lindberg, H. Pleijel, and S. Thorsson. Transpiration of urban trees and its cooling effect in a high latitude city. *Int. J. Biometeorol.*, 60(1):159–172, 2016. doi: 10.1007/s00484-015-1014-x. URL 10.1007/s00484-015-1014-x.
- Ku Donggyun, Bencekri Madiha, Kim Jooyoung, Lee Shinhae, and Lee Seungjae. Review of european low emission zone policy. *Chemical Engineering Transactions*, 78:241–246, 2020. doi: 10.3303/CET2078041. URL 10.3303/CET2078041.
- W. Kuttler. The urban climate – basic and applied aspects. In J. M. Marzluff, E. Shulenberger, W. Endlicher, M. Alberti, G. Bradley, C. Ryan, U. Simon, and C. ZumBrunnen, editors, *Urban Ecology: An International Perspective on the Interaction Between Humans and Nature*, pages 233–248. Springer US, 2008a. ISBN 978-0-387-73412-5. doi: 10.1007/978-0-387-73412-5_13. URL 10.1007/978-0-387-73412-5_13.
- W. Kuttler. The urban climate – basic and applied aspects. In J. M. Marzluff, E. Shulenberger, W. Endlicher, M. Alberti, G. Bradley, C. Ryan, U. Simon, and C. ZumBrunnen, editors, *Urban Ecology: An International Perspective on the Interaction Between Humans and Nature*, pages 233–248. Springer US, 2008b. ISBN 978-0-387-73412-5. doi: 10.1007/978-0-387-73412-5_13. URL 10.1007/978-0-387-73412-5_13.
- K. Laaidi, A. Zeghnoun, B. Dousset, P. Bretin, S. Vandentorren, E. Giraudet, and P. Beaudeau. The impact of heat islands on mortality in paris during the august 2003 heat wave. *Environmental Health Perspectives*, 120(2):254–259, 2012. doi: 10.1289/ehp.1103532. URL <https://ehp.niehs.nih.gov/doi/10.1289/ehp.1103532>.
- C. Lac, J.-P. Chaboureaud, V. Masson, J.-P. Pinty, P. Tulet, J. Escobar, M. Leriche, C. Barthe, B. Aouizerats, C. Augros, P. Aumond, F. Auguste, P. Bechtold, S. Berthet, S. Bielli, F. Bosseur, O. Caumont, J.-M. Cohard, J. Colin, F. Couvreux, J. Cuxart, G. Delautier, T. Dauhut, V. Ducrocq, J.-B. Filippi, D. Gazen, O. Geoffroy, F. Gheusi, R. Honnert, J.-P. Lafore, C. Lebeau-pin Brossier, Q. Libois, T. Lunet, C. Mari, T. Maric, P. Mascart, M. Mogé, G. Molinié, O. Nuissier, F. Pantillon, P. Peyrillé, J. Pergaud, E. Perraud, J. Pianezze, J.-L. Redelsperger, D. Ricard, E. Richard, S. Riette, Q. Rodier, R. Schoetter, L. Seyfried, J. Stein, K. Suhre, M. Taufour, O. Thouron, S. Turner, A. Verrelle, B. Vié, F. Visentin, V. Vionnet, and P. Wautelet. Overview of the meso-NH model version 5.4 and its applications. *Geosci. Model Dev.*, 11(5):1929–1969, 2018. doi: 10.5194/gmd-11-1929-2018. URL <https://gmd.copernicus.org/articles/11/1929/2018/>.
- D. Lai, W. Liu, T. Gan, K. Liu, and Q. Chen. A review of mitigating strategies to improve the thermal environment and thermal comfort in urban outdoor spaces. *Sci. Total. Environ.*, 661:337–353, 2019. doi: 10.1016/j.scitotenv.2019.01.062. URL <https://linkinghub.elsevier.com/retrieve/pii/S0048969719300683>.
- A.-V. Lavoie, M. Staudt, J. P. Schnitzler, D. Landais, F. Massol, A. Rocheteau, R. Rodriguez, I. Zimmer, and S. Rambal. Drought reduced monoterpene emissions from the evergreen mediterranean oak quercus ilex: results from a throughfall displacement experiment. *Biogeosciences*, 6(7):

- 1167–1180, 2009. doi: 10.5194/bg-6-1167-2009. URL <https://bg.copernicus.org/articles/6/1167/2009/>.
- A. V. Lavoit, C. Duffet, F. Mouillot, S. Rambal, J. P. Ratte, J. P. Schnitzler, and M. Staudt. Scaling-up leaf monoterpene emissions from a water limited quercus ilex woodland. *Atmos. Environ.*, 45(17):2888–2897, 2011. doi: 10.1016/j.atmosenv.2011.02.005. URL <https://www.sciencedirect.com/science/article/pii/S1352231011001294>.
- A. Le Tertre, A. Lefranc, D. Eilstein, C. Declercq, S. Medina, M. Blanchard, B. Chardon, P. Fabre, L. Filleul, J.-F. Jusot, L. Pascal, H. Prouvost, S. Cassadou, and M. Ledrans. Impact of the 2003 heatwave on all-cause mortality in 9 french cities. *Epidemiology (Cambridge, Mass.)*, 17(1):75–79, 2006. doi: 10.1097/01.ede.0000187650.36636.1f.
- A. Lemonsu and V. Masson. Simulation of a summer urban breeze over paris. *Bound.-Lay. Meteorol.*, 104(3):463–490, 2002. doi: 10.1023/A:1016509614936. URL <http://link.springer.com/10.1023/A:1016509614936>.
- A. Lemonsu, C. S. B. Grimmond, and V. Masson. Modeling the Surface Energy Balance of the Core of an Old Mediterranean City: Marseille. *Journal of Applied Meteorology*, 43(2):312 – 327, 2004. doi: 10.1175/1520-0450(2004)043(0312:MTSEBO)2.0.CO;2.
- A. Lemonsu, V. Masson, L. Shashua-Bar, E. Erell, and D. Pearlmutter. Inclusion of vegetation in the town energy balance model for modelling urban green areas. *Geosci. Model Dev.*, 5(6):1377–1393, 2012. doi: 10.5194/gmd-5-1377-2012. URL <https://gmd.copernicus.org/articles/5/1377/2012/>.
- A. Lemonsu, V. Vigi e, M. Daniel, and V. Masson. Vulnerability to heat waves: Impact of urban expansion scenarios on urban heat island and heat stress in paris (france). *Urban Climate*, 14: 586–605, 2015. doi: 10.1016/j.uclim.2015.10.007. URL <https://linkinghub.elsevier.com/retrieve/pii/S2212095515300316>.
- L. B. Leopold. Hydrology for urban land planning - A guidebook on the hydrologic effects of urban land use. *US. Geological Survey*, 554(554):18, 1968.
- D. Y. C. Leung, J. K. Y. Tsui, F. Chen, W.-K. Yip, L. L. P. Vrijmoed, and C.-H. Liu. Effects of urban vegetation on urban air quality. *Landscape Research*, 36(2):173–188, 2011. doi: 10.1080/01426397.2010.547570. URL 10.1080/01426397.2010.547570.
- R. Leuning, F. M. Kelliher, D. G. G. De Pury, and E.-D. Schulze. Leaf nitrogen, photosynthesis, conductance and transpiration: scaling from leaves to canopies. *Plant, Cell & Environment*, 18(10):1183–1200, 1995. doi: 10.1111/j.1365-3040.1995.tb00628.x. URL <https://onlinelibrary.wiley.com/doi/abs/10.1111/j.1365-3040.1995.tb00628.x>.
- C. Li, Z. Wang, B. Li, Z.-R. Peng, and Q. Fu. Investigating the relationship between air pollution variation and urban form. *Build Environ.*, 147:559–568, 2019. doi: 10.1016/j.buildenv.2018.06.038. URL <https://www.sciencedirect.com/science/article/pii/S0360132318303810>.
- Z. Li, F. Niu, J. Fan, Y. Liu, D. Rosenfeld, and Y. Ding. Long-term impacts of aerosols on the vertical development of clouds and precipitation. *Nature Geoscience*, 4(12):888–894, 2011. doi: 10.1038/ngeo1313. URL <https://www.nature.com/articles/ngeo1313>. Number: 12 Publisher: Nature Publishing Group.
- C. Lin, R. Ooka, H. Kikumoto, C. Flageul, Y. Kim, Y. Wang, A. Maison, Y. Zhang, and K. Sartelet. Large-eddy simulations on pollutant reduction effects of road-center hedge and solid barriers in an idealized street canyon. *Build Environ.*, page 110464, 2023a. doi: 10.1016/j.buildenv.2023.110464. URL <https://www.sciencedirect.com/science/article/pii/S0360132323004912>.

- C. Lin, Y. Wang, R. Ooka, C. Flageul, Y. Kim, H. Kikumoto, Z. Wang, and K. Sartelet. Modeling of street-scale pollutant dispersion by coupled simulation of chemical reaction, aerosol dynamics, and CFD. *Atmos. Chem. Phys.*, 23(2):1421–1436, 2023b. doi: 10.5194/acp-23-1421-2023. URL <https://acp.copernicus.org/articles/23/1421/2023/>.
- F. Lindberg and C. S. B. Grimmond. The influence of vegetation and building morphology on shadow patterns and mean radiant temperatures in urban areas: model development and evaluation. *Theoretical and Applied Climatology*, 105(3):311–323, 2011. doi: 10.1007/s00704-010-0382-8. URL 10.1007/s00704-010-0382-8.
- F. Lindberg, B. Holmer, and S. Thorsson. SOLWEIG 1.0 – modelling spatial variations of 3d radiant fluxes and mean radiant temperature in complex urban settings. *Int. J. Biometeorol.*, 52(7):697–713, 2008. doi: 10.1007/s00484-008-0162-7. URL 10.1007/s00484-008-0162-7.
- J. Lindén, M. Gustafsson, J. Uddling, A. Watne, and H. Pleijel. Air pollution removal through deposition on urban vegetation: The importance of vegetation characteristics. *Urban For. Urban Gree.*, 81:127843, 2023. doi: 10.1016/j.ufug.2023.127843. URL <https://www.sciencedirect.com/science/article/pii/S1618866723000146>.
- S. J. Livesley, E. G. McPherson, and C. Calfapietra. The Urban Forest and Ecosystem Services: Impacts on Urban Water, Heat, and Pollution Cycles at the Tree, Street, and City Scale. *Journal of Environmental Quality*, 45(1):119–124, 2016. doi: 10.2134/jeq2015.11.0567.
- L. Lugon, K. Sartelet, Y. Kim, J. Vigneron, and O. Chrétien. Nonstationary modeling of NO₂, NO and NO_x in paris using the street-in-grid model: coupling local and regional scales with a two-way dynamic approach. *Atmos. Chem. Phys.*, 20(13):7717–7740, 2020. doi: 10.5194/acp-20-7717-2020. URL <https://acp.copernicus.org/articles/20/7717/2020/>.
- L. Lugon, K. Sartelet, Y. Kim, J. Vigneron, and O. Chrétien. Simulation of primary and secondary particles in the streets of paris using MUNICH. *Faraday Discuss.*, 226(0):432–456, 2021a. doi: 10.1039/D0FD00092B. URL <http://dx.doi.org/10.1039/D0FD00092B>.
- L. Lugon, J. Vigneron, C. Debert, O. Chrétien, and K. Sartelet. Black carbon modeling in urban areas: investigating the influence of resuspension and non-exhaust emissions in streets using the street-in-grid model for inert particles (sing-inert). *Geosci. Model Dev.*, 14:7001–7019, 2021b. doi: 10.5194/gmd-14-7001-2021.
- T. Lyons, J. Kenworthy, and P. Newman. Urban structure and air pollution. *Atmospheric Environment. Part B. Urban Atmosphere*, 24(1):43–48, 1990. doi: 10.1016/0957-1272(90)90008-I. URL <https://linkinghub.elsevier.com/retrieve/pii/095712729090008I>.
- U. Lüttge and M. Buckeridge. Trees: structure and function and the challenges of urbanization. *Trees*, 37(1):9–16, 2023. doi: 10.1007/s00468-020-01964-1. URL 10.1007/s00468-020-01964-1.
- A. Maison. Understanding of the hydric functioning of vegetation in an urban park. Master’s thesis, AgroParisTech, Université Paris-Saclay, 2019. URL <https://hal.inrae.fr/hal-02787739>.
- A. Maison, C. Flageul, B. Carissimo, A. Tuzet, and K. Sartelet. Parametrization of horizontal and vertical transfers for the street-network model MUNICH using the CFD model code `saturne`. *Atmosphere*, 13(4):527, 2022a. doi: 10.3390/atmos13040527. URL <https://www.mdpi.com/2073-4433/13/4/527>.
- A. Maison, C. Flageul, B. Carissimo, Y. Wang, A. Tuzet, and K. Sartelet. Parameterizing the aerodynamic effect of trees in street canyons for the street network model MUNICH using the CFD model code `saturne`. *Atmos. Chem. Phys.*, 22(14):9369–9388, 2022b. doi: 10.5194/acp-22-9369-2022. URL <https://acp.copernicus.org/articles/22/9369/2022/>.

- A. Martilli, A. Clappier, and M. W. Rotach. An urban surface exchange parameterisation for mesoscale models. *Bound.-Lay. Meteorol.*, 104(2):261–304, 2002. doi: 10.1023/A:1016099921195. URL <http://link.springer.com/10.1023/A:1016099921195>.
- D. Martuzevicius, L. Kliucininkas, T. Prasauskas, E. Krugly, V. Kauneliene, and B. Strandberg. Resuspension of particulate matter and PAHs from street dust. *Atmos. Environ.*, 45(2):310–317, 2011. doi: 10.1016/j.atmosenv.2010.10.026. URL <https://www.sciencedirect.com/science/article/pii/S1352231010009015>.
- V. Masson. A Physically-Based Scheme For The Urban Energy Budget In Atmospheric Models. *Bound.-Lay. Meteorol.*, 94:357–397, 2000. doi: 10.1023/A:1002463829265.
- V. Masson and Y. Seity. Including atmospheric layers in vegetation and urban offline surface schemes. *J. Appl. Meteorol. Clim.*, 48(7):1377–1397, 2009. doi: 10.1175/2009JAMC1866.1. URL <https://journals.ametsoc.org/view/journals/apme/48/7/2009jamc1866.1.xml>.
- V. Masson, C. S. B. Grimmond, and T. R. Oke. Evaluation of the town energy balance (TEB) scheme with direct measurements from dry districts in two cities. *J. Appl. Meteorol. Clim.*, 41(10):1011–1026, 2002. doi: 10.1175/1520-0450(2002)041<1011:EOTTEB>2.0.CO;2. URL https://journals.ametsoc.org/view/journals/apme/41/10/1520-0450_2002_041_1011_eotteb_2.0.co_2.xml.
- V. Masson, P. Le Moigne, E. Martin, S. Faroux, A. Alias, R. Alkama, S. Belamari, A. Barbu, A. Boone, F. Bouyssel, P. Brousseau, E. Brun, J.-C. Calvet, D. Carrer, B. Decharme, C. Delire, S. Donier, K. Essaouini, A.-L. Gibelin, H. Giordani, F. Habets, M. Jidane, G. Kerdraon, E. Kourzeneva, M. Lafaysse, S. Lafont, C. Lebeaupin Brossier, A. Lemonsu, J.-F. Mahfouf, P. Marguinaud, M. Mokhtari, S. Morin, G. Pigeon, R. Salgado, Y. Seity, F. Taillefer, G. Tanguy, P. Tulet, B. Vincendon, V. Vionnet, and A. Voldoire. The SURFEXv7.2 land and ocean surface platform for coupled or offline simulation of earth surface variables and fluxes. *Geosci. Model Dev.*, 6(4):929–960, 2013. doi: 10.5194/gmd-6-929-2013. URL <https://gmd.copernicus.org/articles/6/929/2013/>.
- V. Masson, A. Lemonsu, J. Hidalgo, and J. Voogt. Urban climates and climate change. *Annu. Rev. Environ. Resour.*, 45(1):411–444, 2020. doi: 10.1146/annurev-environ-012320-083623. URL <https://www.annualreviews.org/doi/10.1146/annurev-environ-012320-083623>.
- A. Matzarakis, F. Rutz, and H. Mayer. Modelling radiation fluxes in simple and complex environments-application of the RayMan model. *Int. J. Biometeorol.*, 51(4):323–334, 2007. doi: 10.1007/s00484-006-0061-8. URL [10.1007/s00484-006-0061-8](https://doi.org/10.1007/s00484-006-0061-8).
- A. Matzarakis, F. Rutz, and H. Mayer. Modelling radiation fluxes in simple and complex environments: basics of the RayMan model. *Int. J. Biometeorol.*, 54(2):131–139, 2010. doi: 10.1007/s00484-009-0261-0. URL [10.1007/s00484-009-0261-0](https://doi.org/10.1007/s00484-009-0261-0).
- C. McHugh, D. Carruthers, and H. Edmunds. ADMS and ADMS–urban. *International Journal of Environment and Pollution*, 8(3):438–440, 1997. doi: 10.1504/IJEP.1997.028193. URL <https://www.inderscienceonline.com/doi/abs/10.1504/IJEP.1997.028193>.
- E. G. McPherson, N. S. van Doorn, and P. J. Peper. Urban tree database and allometric equations. Technical Report PSW-GTR-253, U.S. Department of Agriculture, Forest Service, Pacific Southwest Research Station, 2016. URL <https://www.fs.usda.gov/treesearch/pubs/52933>.
- L. Menut, B. Bessagnet, R. Briant, A. Cholakian, F. Couvidat, S. Mailler, R. Pennel, G. Siour, P. Tuccella, S. Turquety, and M. Valari. The CHIMERE v2020r1 online chemistry-transport model. *Geosci. Model Dev.*, 14(11):6781–6811, 2021. doi: 10.5194/gmd-14-6781-2021. URL <https://gmd.copernicus.org/articles/14/6781/2021/>.

- M. Mircea, R. Borge, S. Finardi, G. Briganti, F. Russo, D. de la Paz, M. D'Isidoro, G. Cremona, M. G. Villani, A. Cappelletti, M. Adani, I. D'Elia, A. Piersanti, B. Sorrentino, E. Petralia, J. M. de Andrés, A. Narros, C. Silibello, N. Pepe, R. Prandi, and G. Carlino. The role of vegetation on urban atmosphere of three european cities. part 2: Evaluation of vegetation impact on air pollutant concentrations and depositions. *Forests*, 14(6):1255, 2023. doi: 10.3390/f14061255. URL <https://www.mdpi.com/1999-4907/14/6/1255>.
- D. Mitchell, C. Heaviside, S. Vardoulakis, C. Huntingford, G. Masato, B. P. Guillod, P. Frumhoff, A. Bowery, D. Wallom, and M. Allen. Attributing human mortality during extreme heat waves to anthropogenic climate change. *Environ. Res. Lett.*, 11(7):074006, 2016. doi: 10.1088/1748-9326/11/7/074006. URL <https://dx.doi.org/10.1088/1748-9326/11/7/074006>.
- P. Moonen, C. Gromke, and V. Dorer. Performance assessment of large eddy simulation (LES) for modeling dispersion in an urban street canyon with tree planting. *Atmos. Environ.*, 75:66–76, 2013. doi: 10.1016/j.atmosenv.2013.04.016. URL <https://www.sciencedirect.com/science/article/pii/S1352231013002616>.
- M. Moradpour and V. Hosseini. An investigation into the effects of green space on air quality of an urban area using CFD modeling. *Urban Climate*, 34:100686, 2020. doi: 10.1016/j.uclim.2020.100686. URL <https://www.sciencedirect.com/science/article/pii/S2212095519303633>.
- Municipality of Paris. Paris Data : Les arbres. <https://opendata.paris.fr/explore/dataset/les-arbres/>, 2023. Accessed: 2023-03-03.
- Y. Nakamura and T. Oke. Wind, temperature and stability conditions in an east-west oriented urban canyon. *Atmos. Environ.*, 22(12):2691–2700, 1988. doi: 10.1016/0004-6981(88)90437-4. URL <https://linkinghub.elsevier.com/retrieve/pii/0004698188904374>.
- N. Nasrollahi, A. Ghosouri, J. Khodakarami, and M. Taleghani. Heat-mitigation strategies to improve pedestrian thermal comfort in urban environments: A review. *Sustainability*, 12(23):10000, 2020. doi: 10.3390/su122310000. URL <https://www.mdpi.com/2071-1050/12/23/10000>.
- E. Nemitz, M. Vieno, E. Carnell, A. Fitch, C. Steadman, P. Cryle, M. Holland, R. D. Morton, J. Hall, G. Mills, F. Hayes, I. Dickie, D. Carruthers, D. Fowler, S. Reis, and L. Jones. Potential and limitation of air pollution mitigation by vegetation and uncertainties of deposition-based evaluations. *Philosophical Transactions of the Royal Society A: Mathematical, Physical and Engineering Sciences*, 378(2183):20190320, 2020. doi: 10.1098/rsta.2019.0320. URL <https://royalsocietypublishing.org/doi/full/10.1098/rsta.2019.0320>.
- T. B. Nguyen, J. D. Crouse, A. P. Teng, J. M. St. Clair, F. Paulot, G. M. Wolfe, and P. O. Wennberg. Rapid deposition of oxidized biogenic compounds to a temperate forest. *Proceedings of the National Academy of Sciences*, 112(5), 2015. doi: 10.1073/pnas.1418702112. URL <https://pnas.org/doi/full/10.1073/pnas.1418702112>.
- S. E. Nicholson. A pollution model for street-level air. *Atmos. Environ.*, 9(1):19–31, 1975. doi: 10.1016/0004-6981(75)90051-7. URL <https://www.sciencedirect.com/science/article/pii/0004698175900517>.
- U. Niinemets. Mild versus severe stress and BVOCs: thresholds, priming and consequences. *Trends in Plant Science*, 15(3):145–153, 2010. doi: 10.1016/j.tplants.2009.11.008. URL <https://www.sciencedirect.com/science/article/pii/S1360138509002921>.
- U. Niinemets, F. Loreto, and M. Reichstein. Physiological and physicochemical controls on foliar volatile organic compound emissions. *Trends in Plant Science*, 9(4):180–186, 2004. doi: 10.1016/j.tplants.2004.02.006. URL <https://www.sciencedirect.com/science/article/pii/S1360138504000524>.

- NOAA/ESRL. WRF-Chem - Weather Research and Forecasting model coupled to Chemistry, 2023. URL <https://ruc.noaa.gov/wrf/wrf-chem/>. last access: 2023-06-06.
- J. Noilhan and S. Planton. A simple parameterization of land surface processes for meteorological models. *Monthly Weather Review*, 117(3):536–549, 1989. doi: 10.1175/1520-0493(1989)117<0536:ASPOLS>2.0.CO;2. URL https://journals.ametsoc.org/view/journals/mwre/117/3/1520-0493_1989_117_0536_aspols_2_0_co_2.xml.
- D. J. Nowak and D. E. Crane. Carbon storage and sequestration by urban trees in the USA. *Environ. Pollut.*, 116:381–389, 2002. doi: 10.1016/S0269-7491(01)00214-7.
- D. J. Nowak, D. E. Crane, and J. C. Stevens. Air pollution removal by urban trees and shrubs in the united states. *Urban For. Urban Gree.*, 4(3):115–123, 2006. doi: 10.1016/j.ufug.2006.01.007. URL <https://linkinghub.elsevier.com/retrieve/pii/S1618866706000173>.
- M. Nunez and T. R. Oke. The energy balance of an urban canyon. *J. Appl. Meteorol. Clim.*, 16(1):11–19, 1977. doi: 10.1175/1520-0450(1977)016<0011:TEBOAU>2.0.CO;2. URL https://journals.ametsoc.org/view/journals/apme/16/1/1520-0450_1977_016_0011_teboau_2_0_co_2.xml.
- T. R. Oke. The energetic basis of the urban heat island. *Quart. J. Roy. Meteorol. Soc.*, 108(455):1–24, 1982. doi: 10.1002/qj.49710845502. URL <http://doi.wiley.com/10.1002/qj.49710845502>.
- T. R. Oke. Street Design and Urban Canopy Layer Climate. *Energy and Buildings*, 11:103–113, 1998. doi: 10.1016/0378-7788(88)90026-6.
- T. R. Oke, G. Mills, A. Christen, and J. A. Voogt. *Urban Climates*. Cambridge University Press, 2017. ISBN 978-0-521-84950-0.
- G. Oliveri Conti, B. Heibati, I. Kloog, M. Fiore, and M. Ferrante. A review of AirQ models and their applications for forecasting the air pollution health outcomes. *Environ. Sci. Pollut. Res.*, 24(7):6426–6445, 2017. doi: 10.1007/s11356-016-8180-1. URL [10.1007/s11356-016-8180-1](https://doi.org/10.1007/s11356-016-8180-1).
- E. Ormeño, J. Mévy, B. Vila, A. Bousquet-Mélou, S. Greff, G. Bonin, and C. Fernandez. Water deficit stress induces different monoterpene and sesquiterpene emission changes in mediterranean species. relationship between terpene emissions and plant water potential. *Chemosphere*, 67(2):276–284, 2007. doi: 10.1016/j.chemosphere.2006.10.029. URL <https://linkinghub.elsevier.com/retrieve/pii/S0045653506013658>.
- F. Otu-Larbi, C. G. Bolas, V. Ferracci, Z. Staniaszek, R. L. Jones, Y. Malhi, N. R. P. Harris, O. Wild, and K. Ashworth. Modelling the effect of the 2018 summer heatwave and drought on isoprene emissions in a UK woodland. *Global Change Biology*, 26(4):2320–2335, 2020. doi: 10.1111/gcb.14963. URL <https://onlinelibrary.wiley.com/doi/abs/10.1111/gcb.14963>.
- S. M. Owen, A. R. MacKenzie, H. Stewart, R. Donovan, and C. N. Hewitt. BIOGENIC VOLATILE ORGANIC COMPOUND (VOC) EMISSION ESTIMATES FROM AN URBAN TREE CANOPY. *Ecological Applications*, 13(4):927–938, 2003. doi: 10.1890/01-5177. URL <http://doi.wiley.com/10.1890/01-5177>.
- J. Pandey, K. Shubhashish, and R. Pandey. Metal contamination of ganga river (india) as influenced by atmospheric deposition. *Bull. Environ. Contam. Toxicol.*, 83(2):204–209, 2009. doi: 10.1007/s00128-009-9744-2. URL [10.1007/s00128-009-9744-2](https://doi.org/10.1007/s00128-009-9744-2).
- M. Pantusheva, R. Mitkov, P. O. Hristov, and D. Petrova-Antonova. Air pollution dispersion modelling in urban environment using CFD: A systematic review. *Atmosphere*, 13(10):1640, 2022. doi: 10.3390/atmos13101640. URL <https://www.mdpi.com/2073-4433/13/10/1640>.

- Paris City agronomy laboratory. Soil analysis. Technical report, Paris municipal department of green spaces and environment (DEVE), Parc Floral - Pavillon 5 – Rond-Point de la Pyramide, 75012 Paris, France, 2019.
- J. A. Patz, D. Campbell-Lendrum, T. Holloway, and J. A. Foley. Impact of regional climate change on human health. *Nature*, 438(7066):310–317, 2005. doi: 10.1038/nature04188. URL <https://www.nature.com/articles/nature04188>.
- V.-H. Peuch, M. Amodei, T. Barthet, M. L. Cathala, M. Michou, and P. Simon. Mocage, modèle de chimie atmosphérique à grande échelle. In *Proceedings of Météo France: Workshop on atmospheric modelling*, pages 33–36, Toulouse, France, 1999.
- G. Pigeon, D. Legain, P. Durand, and V. Masson. Anthropogenic heat release in an old European agglomeration (Toulouse, France). *Int. J. Climatol.*, 27(14):1969–1981, 2007. doi: 10.1002/joc.1530. URL <http://doi.wiley.com/10.1002/joc.1530>.
- A. Piracha and M. T. Chaudhary. Urban air pollution, urban heat island and human health: A review of the literature. *Sustainability*, 14(15):9234, 2022. doi: 10.3390/su14159234. URL <https://www.mdpi.com/2071-1050/14/15/9234>.
- R. Puga Freitas, A. Claude, A. Maison, L. Leitao, A. Repellin, P. Nadam, C. Kalalian, C. Boissard, V. Gros, K. Sartelet, A. Tuzet, and J. Leymarie. Drought effect on urban plane tree ecophysiology and its isoprene emissions. EGU General Assembly 2023, Vienna, Austria, EGU23-13401, 2023. doi: 10.5194/egusphere-egu23-13401. URL <https://meetingorganizer.copernicus.org/EGU23/EGU23-13401.html>.
- C. Pénard-Morand and I. Annesi-Maesano. Air pollution: from sources of emissions to health effects. *Breathe*, 1(2):108–119, 2004. doi: 10.1183/18106838.0102.108. URL <https://breath.ersjournals.com/content/1/2/108>.
- V. Ramanathan, P. Crutzen, J. Kiehl, and D. Rosenfeld. Atmosphere: Aerosols, climate, and the hydrological cycle. *Science*, 294(5549):2119–2124, 2001. doi: 10.1126/science.1064034.
- J. L. Redelsperger, F. Mahé, and P. Carlotti. A simple and general subgrid model suitable both for surface layer and free-stream turbulence. *Bound.-Lay. Meteorol.*, 101(3):375–408, 2001. doi: 10.1023/A:1019206001292. URL [10.1023/A:1019206001292](https://doi.org/10.1023/A:1019206001292).
- E. Redon, A. Lemonsu, and V. Masson. An urban trees parameterization for modeling microclimatic variables and thermal comfort conditions at street level with the town energy balance model (TEB-SURFEX v8.0). *Geosci. Model Dev.*, 13(2):385–399, 2020. doi: 10.5194/gmd-13-385-2020. URL <https://gmd.copernicus.org/articles/13/385/2020/>.
- E. C. Redon, A. Lemonsu, V. Masson, B. Morille, and M. Musy. Implementation of street trees within the solar radiative exchange parameterization of TEB in SURFEX v8.0. *Geosci. Model Dev.*, 10(1):385–411, 2017. doi: 10.5194/gmd-10-385-2017. URL <https://gmd.copernicus.org/articles/10/385/2017/>.
- Y. Ren, Z. Qu, Y. Du, R. Xu, D. Ma, G. Yang, Y. Shi, X. Fan, A. Tani, P. Guo, Y. Ge, and J. Chang. Air quality and health effects of biogenic volatile organic compounds emissions from urban green spaces and the mitigation strategies. *Environ. Pollut.*, 230:849–861, 2017. doi: 10.1016/j.envpol.2017.06.049. URL <https://www.sciencedirect.com/science/article/pii/S0269749117309491>.
- J. Robine, S. Cheung, and S. L. Roy. Report on excess mortality in Europe during summer 2003. *EU Community Action Programme for Public Health*, pages 1–15, 2007.

- S. Roeland, M. Moretti, J. H. Amorim, C. Branquinho, S. Fares, F. Morelli, U. Niinemets, E. Paoletti, P. Pinho, G. Sgrigna, V. Stojanovski, A. Tiwary, P. Sicard, and C. Calfapietra. Towards an integrative approach to evaluate the environmental ecosystem services provided by urban forest. *Journal of Forestry Research*, 30(6):1981–1996, 2019. doi: 10.1007/s11676-019-00916-x. URL <http://link.springer.com/10.1007/s11676-019-00916-x>.
- A. C. Rohr and R. E. Wyzga. Attributing health effects to individual particulate matter constituents. *Atmos. Environ.*, 62:130–152, 2012. doi: 10.1016/j.atmosenv.2012.07.036. URL <https://www.sciencedirect.com/science/article/pii/S135223101200708X>.
- M. W. Rotach. Profiles of turbulence statistics in and above an urban street canyon. *Atmos. Environ.*, 29(13):1473–1486, 1995. doi: 10.1016/1352-2310(95)00084-C. URL <https://www.sciencedirect.com/science/article/pii/135223109500084C>.
- Y. Rybarczyk and R. Zalakeviciute. Machine learning approaches for outdoor air quality modelling: A systematic review. *Applied Sciences*, 8(12):2570, 2018. doi: 10.3390/app8122570. URL <https://www.mdpi.com/2076-3417/8/12/2570>.
- N. Sade, A. Gebremedhin, and M. Moshelion. Risk-taking plants. *Plant Signaling & Behavior*, 7(7):767–770, 2012. doi: 10.4161/psb.20505. URL <https://www.ncbi.nlm.nih.gov/pmc/articles/PMC3583960/>.
- S. M. Salim, R. Buccolieri, A. Chan, and S. Di Sabatino. Numerical simulation of atmospheric pollutant dispersion in an urban street canyon: Comparison between RANS and LES. *J. Wind Eng. Ind. Aerod.*, 99(2):103–113, 2011. doi: 10.1016/j.jweia.2010.12.002. URL <https://linkinghub.elsevier.com/retrieve/pii/S0167610510001248>.
- P. Salizzoni, L. Soulhac, and P. Mejean. Street canyon ventilation and atmospheric turbulence. *Atmos. Environ.*, 43(32):5056–5067, 2009. doi: 10.1016/j.atmosenv.2009.06.045. URL <https://linkinghub.elsevier.com/retrieve/pii/S1352231009005585>.
- R. San Jose and J. L. Perez-Camanyo. High-resolution impacts of green areas on air quality in madrid. *Air Quality, Atmosphere & Health*, 2022. doi: 10.1007/s11869-022-01263-3. URL <https://link.springer.com/10.1007/s11869-022-01263-3>.
- J. L. Santiago and A. Martilli. A dynamic urban canopy parameterization for mesoscale models based on computational fluid dynamics reynolds-averaged navier–stokes microscale simulations. *Bound.-Lay. Meteorol.*, 137(3):417–439, 2010. doi: 10.1007/s10546-010-9538-4. URL 10.1007/s10546-010-9538-4.
- J. L. Santiago, R. Borge, F. Martin, D. de la Paz, A. Martilli, J. Lumbreras, and B. Sanchez. Evaluation of a CFD-based approach to estimate pollutant distribution within a real urban canopy by means of passive samplers. *Sci. Total. Environ.*, 576:46–58, 2017a. doi: 10.1016/j.scitotenv.2016.09.234. URL <https://www.sciencedirect.com/science/article/pii/S0048969716321647>.
- J.-L. Santiago, E. Rivas, B. Sanchez, R. Buccolieri, and F. Martin. The impact of planting trees on NOx concentrations: The case of the plaza de la cruz neighborhood in pamplona (spain). *Atmosphere*, 8(12):131, 2017b. doi: 10.3390/atmos8070131. URL <http://www.mdpi.com/2073-4433/8/7/131>.
- T. Sarica, A. Maison, Y. Roustan, M. Ketznel, S. S. Jensen, Y. Kim, C. Chaillou, and K. Sartelet. Modelling concentration heterogeneities in streets using the street-network model MUNICH. *Geosci. Model Dev.*, 16(17):5281–5303, 2023. doi: 10.5194/gmd-16-5281-2023. URL <https://gmd.copernicus.org/articles/16/5281/2023/>.

- C. Sarrat, A. Lemonsu, V. Masson, and D. Guedalia. Impact of urban heat island on regional atmospheric pollution. *Atmos. Environ.*, 40(10):1743–1758, 2006. doi: 10.1016/j.atmosenv.2005.11.037. URL <https://www.sciencedirect.com/science/article/pii/S1352231005010885>.
- K. Sartelet, F. Couvidat, Z. Wang, C. Flageul, and Y. Kim. SSH-aerosol v1.1: A modular box model to simulate the evolution of primary and secondary aerosols. *Atmosphere*, 11(5):525, 2020. doi: 10.3390/atmos11050525. URL <https://www.mdpi.com/2073-4433/11/5/525>.
- P. Schuepp. Studies of forced-convection heat and mass transfer of fluttering realistic leaf models. *Bound.-Lay. Meteorol.*, 2:263–274, 1972. doi: 10.1007/BF02184768.
- Y. Seity, P. Brousseau, S. Malardel, G. Hello, P. Bénard, F. Bouttier, C. Lac, and V. Masson. The AROME-france convective-scale operational model. *Monthly Weather Review*, 139(3):976–991, 2011. doi: 10.1175/2010MWR3425.1. URL <https://journals.ametsoc.org/view/journals/mwre/139/3/2010mwr3425.1.xml>.
- W. Selmi, C. Weber, E. Rivière, N. Blond, L. Mehdi, and D. Nowak. Air pollution removal by trees in public green spaces in strasbourg city, france. *Urban For. Urban Gree.*, 17:192–201, 2016. doi: 10.1016/j.ufug.2016.04.010. URL <https://linkinghub.elsevier.com/retrieve/pii/S1618866716301571>.
- H. Setälä, V. Viippola, A.-L. Rantalainen, A. Pennanen, and V. Yli-Pelkonen. Does urban vegetation mitigate air pollution in northern conditions? *Environ. Pollut.*, 183:104–112, 2013. doi: 10.1016/j.envpol.2012.11.010. URL <https://www.sciencedirect.com/science/article/pii/S0269749112004885>.
- A. Shackell, R. Walter, Great Britain, Forestry Commission, Centre for Sustainable Healthcare, National Health Service in Scotland, Great Britain, National Health Service, and Sustainable Development Unit. Greenspace design for health and well-being. Technical report, Forestry Commission, 2012.
- L. Shashua-Bar and M. E. Hoffman. The green CTTC model for predicting the air temperature in small urban wooded sites. *Build Environ.*, 37(12):1279–1288, 2002. doi: 10.1016/S0360-1323(01)00120-2. URL <https://www.sciencedirect.com/science/article/pii/S0360132301001202>.
- J. D. Silver, M. Ketzler, and J. Brandt. Dynamic parameter estimation for a street canyon air quality model. *Environ. Modell. Softw.*, 47:235–252, 2013. doi: 10.1016/j.envsoft.2013.05.012. URL <https://linkinghub.elsevier.com/retrieve/pii/S1364815213001333>.
- J.-F. Sini, S. Anquetin, and P. G. Mestayer. Pollutant dispersion and thermal effects in urban street canyons. *Atmos. Environ.*, 30(15):2659–2677, 1996. doi: 10.1016/1352-2310(95)00321-5. URL <https://linkinghub.elsevier.com/retrieve/pii/1352231095003215>.
- W. H. Smith. *Air Pollution and Forests: Interactions Between Air Contaminants and Forest Ecosystems*. Springer Science & Business Media, 2012. ISBN 978-1-4684-0104-2.
- A. Soltani and E. Sharifi. Daily variation of urban heat island effect and its correlations to urban greenery: A case study of adelaide. *Frontiers of Architectural Research*, 6(4):529–538, 2017. doi: 10.1016/j.foar.2017.08.001. URL <https://www.sciencedirect.com/science/article/pii/S2095263517300432>.
- L. Soulhac, P. Salizzoni, F.-X. Cierco, and R. Perkins. The model SIRANE for atmospheric urban pollutant dispersion; part i, presentation of the model. *Atmos. Environ.*, 45(39):7379–7395, 2011. doi: 10.1016/j.atmosenv.2011.07.008. URL <https://linkinghub.elsevier.com/retrieve/pii/S1352231011007096>.

- L. Soulhac, P. Salizzoni, P. Mejean, D. Didier, and I. Rios. The model SIRANE for atmospheric urban pollutant dispersion; PART II, validation of the model on a real case study. *Atmos. Environ.*, 49:320–337, 2012. doi: 10.1016/j.atmosenv.2011.11.031. URL <https://linkinghub.elsevier.com/retrieve/pii/S1352231011012143>.
- L. Soulhac, C. Nguyen, P. Volta, and P. Salizzoni. The model SIRANE for atmospheric urban pollutant dispersion. PART III: Validation against NO₂ yearly concentration measurements in a large urban agglomeration. *Atmos. Environ.*, 167:377–388, 2017. doi: 10.1016/j.atmosenv.2017.08.034. URL <https://linkinghub.elsevier.com/retrieve/pii/S1352231017305472>.
- B. Sportisse. *Fundamentals in Air Pollution: From Processes to Modelling*. Springer Science & Business Media, 2009. ISBN 978-90-481-2970-6.
- X. Stavropoulos-Laffaille, K. Chancibault, J.-M. Brun, A. Lemonsu, V. Masson, A. Boone, and H. Andrieu. Improvements to the hydrological processes of the town energy balance model (TEB-veg, SURFEX v7.3) for urban modelling and impact assessment. *Geosci. Model Dev.*, 11(10):4175–4194, 2018. doi: 10.5194/gmd-11-4175-2018. URL <https://gmd.copernicus.org/articles/11/4175/2018/>.
- P. Stier, J. H. Seinfeld, S. Kinne, and O. Boucher. Aerosol absorption and radiative forcing. *Atmos. Chem. Phys.*, 7(19):5237–5261, 2007. doi: 10.5194/acp-7-5237-2007. URL <https://acp.copernicus.org/articles/7/5237/2007/>.
- J. Stocker, C. Hood, D. Carruthers, and C. McHugh. ADMS-urban: developments in modelling dispersion from the city scale to the local scale. *International Journal of Environment and Pollution*, 50(1):308–316, 2012. doi: 10.1504/IJEP.2012.051202. URL <https://www.inderscienceonline.com/doi/abs/10.1504/IJEP.2012.051202>.
- F. C. Sulaiman. The mature trees in recreation areas and its role in enhancing quality of life. *Procedia - Social and Behavioral Sciences*, 234:289–298, 2016. doi: 10.1016/j.sbspro.2016.10.245.
- A. Svirejeva-Hopkins, H. J. Schellnhuber, and V. L. Pomaz. Urbanised territories as a specific component of the global carbon cycle. *Ecological Modelling*, 173:295–312, 2004. doi: 10.1016/j.ecolmodel.2003.09.022.
- H. Taha. Urban climates and heat islands: albedo, evapotranspiration, and anthropogenic heat. *Energy and Buildings*, 25(2):99–103, 1997. doi: 10.1016/S0378-7788(96)00999-1. URL <https://www.sciencedirect.com/science/article/pii/S0378778896009991>.
- H. Taha, H. Akbari, A. Rosenfeld, and J. Huang. Residential cooling loads and the urban heat island—the effects of albedo. *Build Environ.*, 23(4):271–283, 1988. doi: 10.1016/0360-1323(88)90033-9. URL <https://www.sciencedirect.com/science/article/pii/0360132388900339>.
- M. Taleghani. Outdoor thermal comfort by different heat mitigation strategies- a review. *Renewable and Sustainable Energy Reviews*, 81:2011–2018, 2018. doi: 10.1016/j.rser.2017.06.010. URL <https://linkinghub.elsevier.com/retrieve/pii/S1364032117309474>.
- P. Thunis. On the validity of the incremental approach to estimate the impact of cities on air quality. *Atmos. Environ.*, 173:210–222, 2018. doi: 10.1016/j.atmosenv.2017.11.012. URL <https://linkinghub.elsevier.com/retrieve/pii/S1352231017307574>.
- Y. Tominaga and T. Stathopoulos. CFD simulation of near-field pollutant dispersion in the urban environment: A review of current modeling techniques. *Atmos. Environ.*, 79:716–730, 2013. doi: 10.1016/j.atmosenv.2013.07.028. URL <https://linkinghub.elsevier.com/retrieve/pii/S1352231013005499>.

- A. Tuzet and A. Perrier. Modeling the dynamics of water flow through plants, role of capacitance in stomatal conductance, and plant water relations. In *Response of crops to limited water: Understanding and modeling water stress effects on plant growth processes*, volume 1 of *Advances in Agricultural Systems Modeling*, chapter 5, pages 145–164. ASA/CSSA/SSSA edition, 2008. doi: 10.2134/advagricysystmodell.c5.
- A. Tuzet, A. Perrier, and R. Leuning. A coupled model of stomatal conductance, photosynthesis and transpiration. *Plant, Cell & Environment*, 26(7):1097–1116, 2003. doi: 10.1046/j.1365-3040.2003.01035.x. URL <https://onlinelibrary.wiley.com/doi/abs/10.1046/j.1365-3040.2003.01035.x>.
- A. Tuzet, A. Granier, P. Betsch, M. Peiffer, and A. Perrier. Modelling hydraulic functioning of an adult beech stand under non-limiting soil water and severe drought condition. *Ecological Modelling*, 348:56–77, 2017. doi: 10.1016/j.ecolmodel.2017.01.007. URL <https://www.sciencedirect.com/science/article/pii/S0304380016305117>.
- I. Uno, S. Wakamatsu, H. Ueda, and A. Nakamura. An observational study of the structure of the nocturnal urban boundary layer. *Bound.-Lay. Meteorol.*, 45(1):59–82, 1988. doi: 10.1007/BF00120815. URL 10.1007/BF00120815.
- R. Upreti, Z.-H. Wang, and J. Yang. Radiative shading effect of urban trees on cooling the regional built environment. *Urban For. Urban Gree.*, 26:18–24, 2017. doi: 10.1016/j.ufug.2017.05.008. URL <https://www.sciencedirect.com/science/article/pii/S1618866716303776>.
- O. US EPA. Learn about heat islands, 2014. URL <https://www.epa.gov/heatislands/learn-about-heat-islands>.
- D. Vallero. *Fundamentals of Air Pollution 5th edition*. Elsevier, 2014. ISBN 0-12-401733-9, 978-0-12-401733-7. doi: 10.1016/B978-0-12-401733-7.00007-4.
- S. Vardoulakis, B. E. Fisher, K. Pericleous, and N. Gonzalez-Flesca. Modelling air quality in street canyons: a review. *Atmos. Environ.*, 37(2):155–182, 2003-01. doi: 10.1016/S1352-2310(02)00857-9. URL <https://linkinghub.elsevier.com/retrieve/pii/S1352231002008579>.
- S. Vardoulakis, K. Dear, S. Hajat, C. Heaviside, B. Eggen, and A. J. McMichael. Comparative assessment of the effects of climate change on heat- and cold-related mortality in the united kingdom and australia. *Environmental Health Perspectives*, 122(12):1285–1292, 2014. doi: 10.1289/ehp.1307524. URL <https://www.ncbi.nlm.nih.gov/pmc/articles/PMC4256046/>.
- I. Varivodina, N. Kosichenko, V. Varivodin, and J. Sedliačik. Interconnections among the rate of growth, porosity and wood water absorption. *Wood research*, 55:59–66, 2010. URL <http://www.woodresearch.sk/wr/201001/07.pdf>.
- E. Velasco, M. Roth, L. Norford, and L. T. Molina. Does urban vegetation enhance carbon sequestration? *Landscape Urban Plan.*, 148:99–107, 2016. doi: 10.1016/j.landurbplan.2015.12.003. URL <https://www.sciencedirect.com/science/article/pii/S0169204615002455>.
- A. Venkatram and J. Pleim. The electrical analogy does not apply to modeling deposition of particles. *Atmos. Environ.*, 33:3075–3076, 1999. doi: 10.1016/S1352-2310(99)00094-1.
- D. Voordeckers, T. Lauriks, S. Denys, P. Billen, T. Tytgat, and M. Van Acker. Guidelines for passive control of traffic-related air pollution in street canyons: An overview for urban planning. *Landscape Urban Plan.*, 207:103980, 2021. doi: 10.1016/j.landurbplan.2020.103980. URL <https://linkinghub.elsevier.com/retrieve/pii/S0169204620314638>.

- P. E. Vos, B. Maiheu, J. Vankerkom, and S. Janssen. Improving local air quality in cities: To tree or not to tree? *Environ. Pollut.*, 183:113–122, 2013. doi: 10.1016/j.envpol.2012.10.021. URL <https://linkinghub.elsevier.com/retrieve/pii/S0269749112004605>.
- C. J. Walcek and H.-H. Yuan. Calculated influence of temperature-related factors on ozone formation rates in the lower troposphere. *J. Appl. Meteorol. Clim.*, 34(5):1056–1069, 1995. doi: 10.1175/1520-0450(1995)034<1056:CIOTRF>2.0.CO;2. URL https://journals.ametsoc.org/view/journals/apme/34/5/1520-0450_1995_034_1056_ciotrf_2_0_co_2.xml.
- J. V. d. Walle, O. Brousse, L. Arnalsteen, C. Brimicombe, D. Byarugaba, M. Demuzere, E. Jjemba, S. Lwasa, H. Misiani, G. Nsangi, F. Soetewey, H. Sseviiri, W. Thiery, R. Vanhaeren, B. F. Zaitchik, and N. P. M. v. Lipzig. Lack of vegetation exacerbates exposure to dangerous heat in dense settlements in a tropical african city. *Environ. Res. Lett.*, 17(2):024004, 2022. doi: 10.1088/1748-9326/ac47c3. URL <https://dx.doi.org/10.1088/1748-9326/ac47c3>.
- J. Walmsley and M. Wesely. Modification of coded parametrizations of surface resistances to gaseous dry deposition. *Atmos. Environ.*, 30(7):1181–1188, 1996. doi: 10.1016/1352-2310(95)00403-3.
- C. J. Walsh, T. D. Fletcher, and M. J. Burns. Urban stormwater runoff: A new class of environmental flow problem. *PLOS ONE*, 7(9):e45814, 2012. doi: 10.1371/journal.pone.0045814. URL <https://journals.plos.org/plosone/article?id=10.1371/journal.pone.0045814>.
- H. Wang, X. Lu, R. Seco, T. Stavrakou, T. Karl, X. Jiang, L. Gu, and A. B. Guenther. Modeling isoprene emission response to drought and heatwaves within MEGAN using evapotranspiration data and by coupling with the community land model. *Journal of Advances in Modeling Earth Systems*, 14(12), 2022. doi: 10.1029/2022MS003174. URL <https://onlinelibrary.wiley.com/doi/10.1029/2022MS003174>.
- W. Wang. An Analytical Model for Mean Wind Profiles in Sparse Canopies. *Bound.-Lay. Meteorol.*, 142:383–399, 2012. doi: 10.1007/s10546-011-9687-0.
- W. Wang. Analytically modelling mean wind and stress profiles in canopies. *Bound.-Lay. Meteorol.*, 151:239–256, 2014. doi: 10.1007/s10546-013-9899-6.
- Y. Wang, C. Flageul, A. Maison, B. Carissimo, and K. Sartelet. Impact of trees on gas concentrations and condensables in a 2-D street canyon using CFD coupled to chemistry modeling. *Environ. Pollut.*, page 121210, 2023. doi: 10.1016/j.envpol.2023.121210. URL <https://www.sciencedirect.com/science/article/pii/S0269749123002129>.
- R. Wankhade, G. Pernigotto, and M. Larcher. A literature review on methods and metrics for the analysis of outdoor air displacement conditions in the urban environment. *Energies*, 16(6):2577, 2023. doi: 10.3390/en16062577. URL <https://www.mdpi.com/1996-1073/16/6/2577>.
- M. Wesely. Parameterization of surface resistances to gaseous dry deposition in regional-scale numerical models. *Atmos. Environ.*, 23(6):1293–1304, 1989. doi: 10.1016/j.atmosenv.2007.10.058.
- M. Wesely, B. Hicks, W. Dannevik, S. Frisella, and R. Husar. An eddy-correlation measurement of particulate deposition from the atmosphere. *Atmos. Environ.*, 11(6):561–563, 1977. doi: 10.1016/0004-6981(77)90076-2.
- R. C. Wissmar, R. K. Timm, and M. G. Logsdon. Effects of changing forest and impervious land covers on discharge characteristics of watersheds. *Environmental Management*, 34(1):91–98, 2004. doi: 10.1007/s00267-004-0224-5.
- www.eskp.de. Climate change: trees in cities. URL <https://www.eskp.de/en/climate-change/trees-city-climate-change-935846/>.

- Y. Xing and P. Brimblecombe. Role of vegetation in deposition and dispersion of air pollution in urban parks. *Atmos. Environ.*, 201:73–83, 2019. doi: 10.1016/j.atmosenv.2018.12.027. URL <https://www.sciencedirect.com/science/article/pii/S1352231018308847>.
- F. Xue and X. Li. The impact of roadside trees on traffic released PM 10 in urban street canyon: Aerodynamic and deposition effects. *Sustain. Cities. Soc.*, 30:195–204, 2017. doi: 10.1016/j.scs.2017.02.001. URL <https://linkinghub.elsevier.com/retrieve/pii/S2210670716304528>.
- H. Yang, T. Chen, Y. Lin, R. Buccolieri, M. Mattsson, M. Zhang, J. Hang, and Q. Wang. Integrated impacts of tree planting and street aspect ratios on CO dispersion and personal exposure in full-scale street canyons. *Build Environ.*, 169:106529, 2020a. doi: 10.1016/j.buildenv.2019.106529. URL <https://linkinghub.elsevier.com/retrieve/pii/S0360132319307413>.
- J. Yang, B. Shi, Y. Shi, S. Marvin, Y. Zheng, and G. Xia. Air pollution dispersal in high density urban areas: Research on the triadic relation of wind, air pollution, and urban form. *Sustain. Cities. Soc.*, 54:101941, 2020b. doi: 10.1016/j.scs.2019.101941. URL <https://www.sciencedirect.com/science/article/pii/S2210670719322474>.
- Y. Yang, E. Gatto, Z. Gao, R. Buccolieri, T. E. Morakinyo, and H. Lan. The “plant evaluation model” for the assessment of the impact of vegetation on outdoor microclimate in the urban environment. *Build Environ.*, 159:106151, 2019. doi: 10.1016/j.buildenv.2019.05.029. URL <https://linkinghub.elsevier.com/retrieve/pii/S0360132319303476>.
- A. Yani, G. Pauly, M. Faye, F. Salin, and M. Gleizes. The effect of a long-term water stress on the metabolism and emission of terpenes of the foliage of cupressus sempervirens. *Plant, Cell & Environment*, 16(8):975–981, 1993. doi: 10.1111/j.1365-3040.1993.tb00521.x. URL <https://onlinelibrary.wiley.com/doi/abs/10.1111/j.1365-3040.1993.tb00521.x>.
- A. W. M. Yazid, N. A. C. Sidik, S. M. Salim, and K. M. Saqr. A review on the flow structure and pollutant dispersion in urban street canyons for urban planning strategies. *SIMULATION*, 90(8): 892–916, 2014. doi: 10.1177/0037549714528046. URL <http://journals.sagepub.com/doi/10.1177/0037549714528046>.
- D. Zajic, H. J. S. Fernando, R. Calhoun, M. Princevac, M. J. Brown, and E. R. Pardyjak. Flow and turbulence in an urban canyon. *J. Appl. Meteorol. Clim.*, 50(1):203–223, 2011. doi: 10.1175/2010JAMC2525.1. URL <https://journals.ametsoc.org/view/journals/apme/50/1/2010jamc2525.1.xml>.
- L. Zhang, S. Gong, J. Padro, and B. L. A size-segregated particle dry deposition scheme for an atmospheric aerosol module. *Atmos. Environ.*, 35:549–560, 2001. doi: 10.1016/S1352-2310(00)00326-5.
- L. Zhang, M. D. Moran, P. A. Makar, J. R. Brook, and S. Gong. Modelling gaseous dry deposition in AURAMS: a unified regional air-quality modelling system. *Atmos. Environ.*, 36(3): 537–560, 2002. doi: 10.1016/S1352-2310(01)00447-2. URL <https://linkinghub.elsevier.com/retrieve/pii/S1352231001004472>.
- L. Zhang, J. R. Brook, and R. Vet. A revised parameterization for gaseous dry deposition in air-quality models. *Atmos. Chem. Phys.*, page 16, 2003. doi: 10.5194/acp-3-2067-2003.
- Y. Zhang, Z. Gu, and C. W. Yu. Impact factors on airflow and pollutant dispersion in urban street canyons and comprehensive simulations: a review. *Current Pollution Reports*, 6(4):425–439, 2020. doi: 10.1007/s40726-020-00166-0. URL [10.1007/s40726-020-00166-0](https://doi.org/10.1007/s40726-020-00166-0).
- Y. Zhao, L. W. Chew, A. Kubilay, and J. Carmeliet. Isothermal and non-isothermal flow in street canyons: A review from theoretical, experimental and numerical perspectives. *Build Environ.*,

- 184:107163, 2020. doi: 10.1016/j.buildenv.2020.107163. URL <https://linkinghub.elsevier.com/retrieve/pii/S0360132320305370>.
- J. Zhong, X.-M. Cai, and W. J. Bloss. Coupling dynamics and chemistry in the air pollution modelling of street canyons: A review. *Environ. Pollut.*, 214:690–704, 2016. doi: 10.1016/j.envpol.2016.04.052. URL <https://www.sciencedirect.com/science/article/pii/S0269749116303207>.
- J. Zou, Y. Yu, J. Liu, J. Niu, K. Chauhan, and C. Lei. Field measurement of the urban pedestrian level wind turbulence. *Build Environ.*, 194:107713, 2021. doi: 10.1016/j.buildenv.2021.107713. URL <https://linkinghub.elsevier.com/retrieve/pii/S0360132321001244>.